UC Davis

UC Davis Electronic Theses and Dissertations

Title

Architecture of the shallow magma storage system across a caldera-forming cycle in the Okataina Volcanic Center, Taupō Volcanic Zone, New Zealand

Permalink

https://escholarship.org/uc/item/8b4062qs

Author

Grant, Elizabeth R. G.

Publication Date

2024

Supplemental Material

https://escholarship.org/uc/item/8b4062qs#supplemental

Peer reviewed|Thesis/dissertation

eScholarship.org Powered by the California Digital Library
University of California

Architecture of the shallow magma storage system across a caldera-forming cycle in the Okataina Volcanic Center, Taupo Volcanic Zone, New Zealand

By

ELIZABETH R.G. GRANT
DISSERTATION

Submitted in partial satisfaction of the requirements for the degree of

DOCTOR OF PHILOSOPHY

in

GEOLOGY

in the

OFFICE OF GRADUATE STUDIES

of the

UNIVERSITY OF CALIFORNIA

DAVIS

Approved:

Kari M. Cooper, Chair

Darren M. Gravley

Sujoy Mukhopadhyay

Committee in Charge

2024

ACKNOWLEDGEMENTS

I would first like express my deepest gratitude to my advisor, Dr. Kari Cooper, for her support and guidance throughout my time at UC Davis. Kari was very patient with my many questions, and my dissertation would not be as strong without her keen eye for data interpretation and probing questions. Kari also gave me the freedom to explore subdisciplines within igneous petrology and volcanology beyond isotope geochemistry, and her support of my intellectual curiosity and faith in my abilities opened the door for me to a lifetime in science.

A very special thank you to my Ph.D. committee members Darren Gravley and Sujoy Mukhopadhyay, whose review and feedback has helped to improve the quality of my dissertation, and to Gordon Moore and Chip Lesher, all of whom served on my qualifying exam committee. Thank you to Chad Deering and Darren Gravley for their field assistance and expertise. They helped our team to locate and sample 27 tephra and tuff deposits around the North Island of New Zealand during our 2017 field season. I would also like to thank Justin Glessner and Greg Baxter for helping with the technical work that made my research possible.

A huge thank you to Dawnika Blatter, Tom Sisson, and the entire USGS California Volcano Observatory for their support over the years. Chapter one would not have been possible without Dawnika and Tom's guidance and expertise, and I am grateful that they gave me the opportunity to master new techniques, explore new ideas, and broaden my network of colleagues. It my sincerest hope that we will continue to work together in the future.

I would like to thank all of the UC Davis Earth and Planetary Science department faculty and staff. With the EPS department I have explored geology locally, regionally, and globally, from structure lunch field trips to visit the Franciscan melange at the coast, to class field trips to look at sedimentology in Anza-Borrego Desert State Park, to a field trip to Northern Greece, led

by Eldridge Moores, where we saw the Vourinos Ophiolite that Eldrigde mapped in the 60s. I am so grateful for the opportunities that the EPS department offered both in the classroom and in the field; it is because of this department that I feel like a geologist.

I would like to thank my graduate student peers, especially the "6th year cohort" for their support, teamwork, and laughter throughout the years, especially Kaitlyn Amodeo, Becky Fildes, Sydney Salley, Emilia Hernandez, Supratim Dey, and honorary member Hannah Kempf. It's been a wild ride, and I wouldn't want to have experienced it with anyone else.

Thank you to the Cooper Group members both new and old, Tyler Schlieder, Anjelica Guerrier, and Julia Walker, for their support over the years. A special thank you to Tyler for suffering through multiple 24-hour mass spec sessions, being game for 4:30 am car rides to the SHRIMP, enduring strange AirBnB situations, and accompanying me on countless coffee runs.

I'd also like to thank my friends from home and new friends from Sacramento for their patience and understanding as I lived through the Ph.D. journey. I've missed many of my friends' important life events because of my work schedule, but I know that we'll be able to pick up where we left off because of their grace. Thank you to my family for their unconditional support, especially my parents who have been exceedingly patient with my busy schedule. A huge thank you to my sister, who did her Ph.D. at the same time and who, despite the drudgery, was always ready to go on an adventure.

Thank you to Lou and Elliott, our two rescue cats who helped with my mental and emotional well-being, and who were especially comforting companions during the COVID-19 pandemic. No, you can't go outside now; it's dark out.

Finally, thank you to my husband Jeff. Not only has he been patient and supportive, but he has actively participated in this journey alongside me: weekends spent working at coffee

shops, nights editing my grant and proposal drafts, driving to Davis to bring me dinner during late night analytical sessions, and patiently enduring my growing rock “collection.” To Jeff I am eternally grateful, I could not have made it through with process without him.

CONTRIBUTION OF AUTHORS

The research in chapter one was designed by Elizabeth Grant, Dawnika Blatter (USGS), and Thomas Sisson (USGS). The research was conducted, collected, assembled, and reviewed by Elizabeth Grant with input and guidance from Dawnika Blatter and Thomas Sisson. The chapter one manuscript was written by Elizabeth Grant with significant input, editing, and revisions from Dawnika Blatter and Tom Sisson. The research of chapters two, three, and four was designed, conducted, and reviewed by Elizabeth Grant with significant input from Kari Cooper. Additionally, chapters two, three, and four were written by Elizabeth Grant, with significant editing and review from Kari Cooper. Darren Gravley (University of Canterbury) was involved with project design, chapter review, and editing for chapters two, three, and four.
As part of the PhD committee, Sujoy Mukhopadhyay contributed to the review and editing of chapters two, three, and four. Chad Deering (Michigan Technological University) and Adam Kent (Oregon State University) both contributed to the project design. All of these authors have provided important feedback, discussion, and interpretations of these data.

TABLES OF CONTENTS

Acknowledgements……... ii
Contribution of Authors……. v
Abstract……. ix

Chapter 1: Shallow storage of the explosive Earthquake Flat Pyroclastics magma body, Okataina Volcanic Center, Taupo Volcanic Zone, New Zealand: evidence from phase-equilibria experiments
Introduction to published manuscript…….. 1
Published manuscript……... 2

Chapter 2: Sustained compositional and thermal heterogeneity in distributed melts across a caldera-forming cycle in the Okataina Volcanic Center, Taupo Volcanic Zone, New Zealand
2.1 Abstract…….. 32
2.2 Introduction…… 32
2.3 Geologic Background…… 38
2.3.1 Deposits……. 40
2.4 Methods…… 44
2.4.1 Sample collection……... 44
2.4.2 Sample processing…… 45
2.4.3 Mounting and imaging……... 45
2.4.4 Zircon morphology ……... 46
2.4.5 Analytical procedure: SHRIMP-RG…….. 47
2.4.6 Analytical procedure: MC-ICP-MS……... 49
2.4.7 Zircon melt modeling…… 49
2.5 Results…… 50
2.5.1 Zircon model ages…….. 50
2.5.2 Temperature……... 53
2.5.2.1 Ti-in-Zircon thermometry…….. 53
2.5.2.2 Zircon saturation thermometry…….. 57
2.5.2.3 Fe-Ti oxide thermometry……... 58
2.5.3 Geochemistry……. 59
2.5.3.1 Eu/Eu*……... 59
2.5.3.2 Zr/Hf in glass……. 60
2.5.3.3 Zr/Hf in zircon……... 61
2.5.3.4 Yb/Gd……. 61
2.5.3.5 ΣREE+Y/P and Y/P……... 62
2.5.4 Zircon-glass equilibrium modeling…… 63
2.6 Discussion…….. 65
2.6.1 Evidence for a long-lived mush system……. 65
2.6.2 Thermal evidence for zircon growth conditions throughout mush history… 74
2.6.3 Trace element geochemistry in rhyolites……... 78

2.6.3.1 Apatite and xenotime fractionation: Y/P and (ΣREE+Y)/P……... 82
2.6.3.2 Mafic phase fractionation: Yb/Gd……. 85
2.6.4 Evidence for compositional evolution……... 87
2.6.5 Compositional variability as revealed by zircon-glass equilibrium modeling…… 94
2.6.6 Evidence for the growth of physically separate melt lenses within a greater mush system…….. 96
2.6.7 Implications for caldera cyclicity…….. 100
2.7 Conclusions…… 103
2.8 References…….. 104
Chapter 2 Appendix A……. 114

Chapter 3: Improving the Accuracy of (^{238}U)/(^{230}Th) Bulk Crystallization Ages of Major Phase Silicate Minerals in Volcanic Rocks
3.1 Abstract…….. 134
3.2 Introduction…… 135
3.2.1 Materials and equipment…… 138
3.2.2 Sample collection……... 138
3.3 Methods……. 140
3.3.1 Imaging of mineral inclusions……... 140
3.3.2 Laboratory sample separation…… 142
3.3.3 Mass spectrometry……. 147
3.4 Results…… 149
3.4.1 Kakapiko Dome……. 152
3.4.2 Rotoiti…… 153
3.4.3 Earthquake Flat…… 153
3.4.4 Hauparu…….. 154
3.4.5 BSE imaging…….. 154
3.5 Discussion…….. 158
3.5.1 Expected behavior of U-series nuclides in mineral separates……... 158
3.5.2 Okataina Volcanic Center minerals…… 166
3.5.3 Comparison to other studies…….. 171
3.5.4 Complexities of growth from a magma mush……... 175
3.6 Conclusions…… 176
3.7 References…….. 177

Chapter 4: Trace element diffusion modeling in plagioclase from the Okataina Volcanic Center, Taupo Volcanic Zone, New Zealand
4.1 Abstract…….. 184
4.2 Overview…… 185
4.3 Samples…….. 187
4.4 Methods……. 190
4.5 Results…… 196
4.6 Discussion…….. 221

4.6.1 Diffusive modelling with Ti-in-zircon thermometry……. 222
4.6.2 Diffusive modelling with Fe-Ti oxide thermometry…….. 225
4.6.3 Implications for hazard mitigation……. 230
4.7 Conclusions…… 231
4.8 References…….. 231
Chapter 4 Appendix A: Table of diffusion modeling results……... 237
Chapter 4 Appendix B: Model results……. 239
Chapter 4 Appendix C: Trace element plots…… 261

ABSTRACT

Caldera-forming eruptions are some of the largest eruptions on Earth. Although infrequent, they can produce >5,000 km^3 of pyroclastic flows and fall deposits and can generate collapse features ~100 km in diameter. Understanding how such large bodies of magma are assembled and stored in the crust is an important parameter in our future ability to forecast eruption but this requires a well-understood foundational framework of the architecture of the magma reservoir. Caldera-forming magma reservoirs are broadly composed of an interconnected network of smaller melt bodies of variable crystallinity that are fed by a large crystal mush zone. Recent studies have shown these large magma reservoirs can persist on timescales of 10^4–10^5 years, and temporal and geochemical evidence suggests that long-lived bodies chiefly consist of crystal-rich magmas in a "mush" system, where melt exists within the interstices of a crystalline framework, and any melt-dominated bodies are ephemeral features existing only for a short time prior to eruption. Some well-studied systems record simple mineral growth histories which can lead to a clear understanding of how a magma evolved prior to eruption (e.g. Yellowstone), and others preserve stratigraphic relationships that can reveal simple zoning patterns within magma reservoirs prior to eruption (e.g. Bishop Tuff). The Okataina Volcanic Center, Taupō Volcanic Zone, New Zealand is a highly complicated system that reveals neither simple growth histories nor simple zoning patterns and which requires a more complicated explanation for magma assembly and storage pathways. My work focuses on understanding changes within the magma reservoir across a caldera cycle at the Okataina Volcanic Center.

The Okataina Volcanic Center has hosted at least two caldera-forming eruptions in its modern history, the most recent of which is the Rotoiti eruption. The Rotoiti eruption occurred around ~45 ka and evacuated 100 km^3 of magma which produced pyroclastic flow and fall

deposits. The Rotoiti eruption was immediately followed by the Earthquake Flat eruption, which erupted days to weeks after the Rotoiti eruption producing ~10 km^3 of pyroclastic flow and fall deposits. The Earthquake Flat eruption is broadly considered syn-eruptive with the Rotoiti eruption. Pre-caldera dome growth was dominant ~50–150 kyrs prior to the Rotoiti eruption. An apparent lapse in volcanism between the dome growth period (~96 ka) and the Rotoiti eruption (~45 ka) may suggest less magmatic activity during that time, with the caveat that the lack of 45–96 ka eruptive deposits in the rock record does not preclude their existence; caldera-forming pyroclastic flow deposits have been documented to destroy and/or cover preceding older eruptive deposits. At least twenty-three post-caldera eruptions follow the Rotoiti and Earthquake Flat eruptions, and are dominated by smaller volume, crystal-poor to crystal-moderate eruptions. This work examines the petrologic, geochemical, and geochronological signatures from deposits across a caldera-forming cycle (pre-caldera Kakapiko Dome; caldera-forming eruption Rotoiti, syn-caldera eruption Earthquake Flat; and post-caldera eruption Hauparu) to better understand the overall variations in the architecture of the magma system throughout the caldera-forming cycle.

Throughout this study, I investigate the intensive parameters that govern petrologic storages conditions, and geochemical, thermal, and geochronological variation across a caldera-forming cycle to understand the broad architecture of the system. In chapter one, I present results of a phase-equilibrium experimental study to constrain the pressure, temperature, and oxygen fugacity of the Earthquake Flat magma body immediately prior to eruption. I present results of H_2O-saturated phase equilibrium experiments buffered at NNO on a glass concentrate of the Earthquake Flat rhyolitic tuff. Based on co-saturation of the melt concentrate with quartz and plagioclase, our experiments show that the Earthquake Flat rhyolitic magma was most likely

stored at crystal-rich conditions between 75–200 MPa, and 710–760 °C, saturated with H_2O-rich magmatic vapor. In particular, we find co-saturation of quartz, plagioclase, and biotite at 140 MPa, and 755 ºC. Prior experimental work on the Rotoiti rhyolite estimated its pre-eruptive temperature and pressure by cummingtonite stability to ≤750 °C and ≤300 MPa if H_2O-saturated. Although the two eruptions vented only ~20 km apart, connections between the two magma bodies are unknown. Despite similar shallow, low-temperature storage conditions of the Earthquake Flat and Rotoiti magma bodies, the higher K_2O concentration of the former accounts for the presence of biotite versus cummingtonite (and/or orthopyroxene + hornblende) in the latter. The high crystallinity of the Earthquake Flat tuff, combined with abundant poly- and mono-mineralic clusters, suggests that the Earthquake Flat magma body was a shallow, mushy proto-pluton prior to mobilization and eruption.

In chapter two, I present trace element compositional data and ^{238}U-^{230}Th ages measured in zircon to constrain the chemical, thermal, and temporal variation across a caldera-forming cycle in the Okataina Volcanic Center. In-situ U-series ages in zircon surfaces and interiors reveal ages from secular equilibrium to within error of eruption for all eruption stages throughout the caldera-forming cycle. Despite this range in ages, there are no systematic patterns in Ti-in-zircon thermometry or common geochemical indices (U/Th, Yb/Gd, (ΣREE + Y)/P, [Hf]) over time. Rather, signatures in zircon reveal that co-crystallization of accessory and major phases complicate simple progressive evolution histories. I also present a zircon-melt model that uses zircon chemistries to predict the initial host melt from which that zircon crystallized. The results show that zircon crystallized from a much wider range of melt compositions than the host glass, which suggests that geochemically diverse melts must have been sustained throughout the zircon crystallization history.

In chapter three, I present a new workflow to decrease impurities in bulk mineral separates in order to accurately ^{238}U-^{230}Th bulk mineral ages for major phases. Due to the low concentrations of U and Th in major phases (e.g. plagioclase, biotite, oxides), I measure U and Th concentrations and isotopic compositions by bulk dissolution of hundreds to thousands of grains, which homogenizes any inclusions present within the grains. My results show that even at very low abundances, inclusions of zircon and glass dominate the U and Th budgets of the bulk sample, resulting in an inaccurate (^{238}U)/(^{230}Th) age. While there was some success with the Earthquake Flat and Rotoiti plagioclase separates, the results yield isochrons with large uncertainties that do not constrain the bulk crystallization age. I interpret these results to suggest that the bulk mineral separates are still dominated by mineral inclusions of glass and in some cases, zircon. The complexity of these results compared to other systems is consistent with complex and protracted crystallization and residence of major minerals within a crystal mush.

In chapter four, I use trace element diffusion chronometry to constrain the timescales on which plagioclase crystals resided at magmatic temperatures prior to eruption. Using Sr diffusion in plagioclase modeled at a range of temperatures (600–850 ºC), my results show that Sr diffusion time scales are short for the crystal-moderate and crystal poor-eruptions (10^0–10^1 years) but only slightly longer for the crystal-rich eruptions (10^1–10^2 years). The bulk of the Okataina Volcanic Center plagioclase contain flat Sr profiles, which indicate that either the plagioclase grew rapidly enough such that Sr did not have time to diffuse, or the plagioclase grew in the presence of a compositionally changing magma that supplied continuous Sr contents such that there was no progressive depletion in the Sr composition of the melt. These results provide a point of comparison with previous work modeling plagioclase diffusion in magmas from the Taupō Volcanic Center.

Collectively, these chapters help to understand the pressure and temperature regimes at which magmas are stored in the shallow crust, the timescales that minerals are stored prior to eruption, and the different chemical environments in which those minerals are stored. These lines of evidence reveal that there are no systematic variations in the compositional, thermal, and temporal diversity within or between eruptive bodies across a caldera-forming cycle at the Okataina Volcanic Center. These observations are distinct from trends found in other caldera-forming systems and are important characteristics of the architecture of the shallow plumbing system beneath the Okataina Volcanic Center. This work has important implications for caldera cyclicity and hazard mitigation. The results of this study are consistent with others from the Okataina Volcanic Center that support models of caldera cyclicity. This work suggests that the Okataina Volcanic Center magma reservoir is in the early- to mid-maturation phase of caldera growth, which can last hundreds of thousands of years, but which is typically followed by caldera-forming eruption. Furthermore, this work documents how large eruptions do not always occur from crystal-poor magmas within the caldera margins but can also form from crystal-rich magmas that occur at extra-caldera locations. This observation suggests that geophysical monitoring efforts should be expanded to include extra-caldera monitoring.

CHAPTER ONE

Shallow storage of the explosive Earthquake Flat Pyroclastics magma body, Okataina Volcanic Center, Taupo Volcanic Zone, New Zealand: evidence from phase-equilibria experiments

Elizabeth R. G. Grant
Dawnika L. Blatter
Thomas W. Sisson
Kari M. Cooper

1.1 Introduction to published manuscript

The work of chapter one was published in Contributions to Mineralogy and Petrology in July 2024. The manuscript was published under an open access agreement between University of California Davis and Springer Nature.

Contributions to Mineralogy and Petrology (2024) 179:81
https://doi.org/10.1007/s00410-024-02151-y

ORIGINAL PAPER

Shallow storage of the explosive Earthquake Flat Pyroclastics magma body, Okataina Volcanic Center, Taupo Volcanic Zone, New Zealand: evidence from phase-equilibria experiments

Elizabeth R. G. Grant[1] · Dawnika L. Blatter[2] · Thomas W. Sisson[2] · Kari M. Cooper[1]

Received: 17 October 2023 / Accepted: 31 May 2024
© The Author(s) 2024

Abstract
Rhyolitic tuffs range widely in their crystal contents from nearly aphyric to crystal-rich, and their crystal cargoes inform concepts of upper crustal magma reservoirs. The Earthquake Flat pyroclastics (Okataina Volcanic Center, Taupo Volcanic Zone, New Zealand) are 10 km^3 of rhyolitic tuffs with abundant (~40 vol.%) plagioclase and quartz, minor biotite, hornblende, and orthopyroxene, and accessory Fe-Ti oxides, apatite, and zircon, set in high-silica rhyolitic glass. Major minerals form large, euhedral phenocrysts and abundant glomerocrysts with few disequilibrium textures excepting some faintly resorbed quartz. Plagioclase phenocrysts have thick rims of nearly constant composition near An_{30}, and hornblende is weakly zoned or unzoned. The abundant and texturally complex mineral assemblage contrasts with the nearby (~25 km), nearly synchronous, but more voluminous and crystal-moderate rhyolite tuffs from Rotoiti caldera. New H_2O-saturated phase-equilibria results on the erupted Earthquake Flat melt (glass) determine its co-saturation with the partial phenocryst assemblage of plagioclase, quartz, biotite, and Fe-Ti oxides at: 140 MPa, 755 ºC. These closely approximate the conditions of the pre-eruptive magma body assuming it was saturated with nearly pure H_2O and at an fO_2 of ~Ni–NiO. Absence of hornblende and orthopyroxene from the synthesized assemblages may result from those minerals being in a peritectic reaction relation with melt to produce biotite, so they would not grow from the liquid used as starting material. Experimental results on Rotoiti rhyolite (Nicholls et al. 1992) show that the two bodies resided at similar pressures, temperatures, and fO_2s. Lower crystal abundance of the Rotoiti tuffs may result from slight compositional differences. We interpret that the Earthquake Flat pyroclastics were sourced from the crystal-rich periphery of a mushy reservoir system with the Rotoiti occupying a more melt-rich central location. Uncertain is whether this was a single intrusion zoned continuously in crystallinity, or discrete adjacent intrusions, but our results illustrate and quantify complexities of magma storage across relatively short distances.

Keywords Taupo Volcanic Zone · Earthquake Flat Pyroclastics · Rotoiti · Rhyolite · Phase equilibria · Experimental petrology

Introduction

The magmas that feed large rhyolitic eruptions are complex mixtures of melt, crystals, and gases with minerals that routinely have compositions, zoning, and ages inconsistent with having formed by the simple, progressive crystallization of a closed body of melt (Bachmann and Bergantz 2004; Befus and Gardner 2016; Caricchi and Blundy 2015; Cashman et al. 2017; Chamberlain et al. 2015; Ellis et al. 2014; Hildreth 2004; Hildreth and Mahood. 1986; Pichavant et al. 2007; Swallow et al. 2019). Instead, mineral interiors can have distinct compositional zones, some truncated by overgrown resorption surfaces, and even the rims of mineral grains need

Communicated by Dante Canil.

✉ Elizabeth R. G. Grant
ergrant@ucdavis.edu

[1] University of California, Davis, CA, USA

[2] U.S. Geological Survey, California Volcano Observatory, Moffett Field, CA, USA

Published online: 25 July 2024

not be in equilibrium[1] with the melt that accompanied them upon eruption. These and other features point to varied and protracted pre-eruptive histories involving recharge, partial solidification — in some cases to advanced extents — remelting, and remobilization (Reid 2003, 2008), and the diverse crystal cargoes can impede inferring magmatic storage conditions (Ellis et al. 2014). One commonly endorsed scenario (the "mush model") is that shallow silicic magma reservoirs reside over most of their spans of activity in highly crystalline states with small melt fractions, with eruptions being brought about by melt that segregates and accumulates as a transitory melt-rich zone or cap, or that, at times, the crystal mush is in some way partly remelted (or "defrosted," Mahood 1990) locally or widely and thereby remobilized (Bachmann and Bergantz 2004, 2006; Cashman and Giordano 2014; Ellis et al. 2014; Hildreth 2004; Lipman et al. 1997). Melt segregation and defrosting are not mutually exclusive processes. Timespans over which shallow silicic magmas remain in eruptible melt-rich states are matters of active research, but estimates are 10^3–10^5 years (Bachmann and Bergantz 2004; Charlier et al. 2005; Cooper 2015, 2019; Reid and Vazquez 2017), considerably briefer than the overall lifespans of their respective magmatic systems.

Shallow silicic magmatic systems must be more complex and diverse than these simplified representations, with melt versus crystal abundances also differing with proximity to the system's margins where heat is lost, and toward its sites of recharge where heat and replenishing melts are gained, as well as with the times elapsed since recharges, recharge volumes and compositions, reservoir depth and size, and other factors. Such complexities lead to multiple potential origins for the cognate crystals in silicic magmas including as true autocrysts formed by the progressive partial crystallization of a closed body of melt; as partially remelted relicts of a remobilized, formerly crystal-rich reservoir or domain; as grains entrained from highly crystalline regions by transiting melt; and as composite grains grown from multiple replenishing silicic melts. In all cases, if melt and crystals then remain together sufficiently long, mineral rims and melt can approach equilibrium. Discerning the processes that assembled a magma body and then brought it to eruption therefore requires examining its crystal assemblage and its state of equilibrium with coexisting melt.

Experimentally determined phase-equilibria assemblages can reveal important intensive parameters (P–T-H_2O-fO_2) of magma reservoirs (Rutherford et al. 1985; Scaillet and Evans 1999; Cadoux et al. 2014; Befus and Gardner 2016). We present new experimental phase-equilibria results for the Earthquake Flat (EQF) rhyolitic deposit (Okataina Volcanic Center, Taupo Volcanic Zone, New Zealand), which establish the storage conditions of the magma body immediately prior to eruption. The EQF crystal-rich (~ 40 vol.%) rhyolitic tuff provides an excellent example of a complicated assemblage of minerals that might have been entrained from different parts of the magma reservoir, including crystal-rich peripheral regions. Large (≤ 1mm), chemically evolved crystals (e.g., low An content across plagioclase rims), and abundant glomerocrysts suggest that the crystals had ample time to grow from evolved melt, to nucleate heterogeneously on one another forming glomerocrysts, or potentially to have been scavenged from highly crystalline regions.

These textural observations, alone, do not resolve whether the crystals in this eruption were scoured and entrained from the mushy regions or largely grew in equilibrium with the host melt. To address this problem, we performed phase-equilibria experiments using separated EQF glass as the starting material to establish the P–T conditions of the EQF magma immediately prior to eruption. The experimental results place the EQF magma storage conditions at 140 ± 10 MPa and 755 ± 5 ºC, if saturated with H_2O-rich vapor at Δ Ni–NiO = 0, based on the liquidus co-saturation of the natural melt with plagioclase, quartz, and biotite. These results and observations support a crystal-mush model, where the EQF crystals and melt were largely cogenetic, most crystals having grown from or equilibrated with the melt, rather than scoured from other portions of the system.

Geologic and petrologic background

The Taupo Volcanic Zone (TVZ), North Island of New Zealand, is the on-shore continuation of the Tonga-Kermadec arc and its spreading back-arc Havre Trough rift system. It is marked by 1.6 Myr of active rhyolitic volcanism and by high rifting rates (Wilson et al. 1995) (Fig. 1A). Back-arc rifting ranges from 15 mm/yr near the Bay of Plenty to 5 mm/yr near Lake Taupo and is partly controlled by the geometry of the adjacent subduction zone (Cole et al. 2014). The Pacific Plate subducts beneath the Australian Plate, but obliquity of the plate boundary increases southward as the Hikurangi Plateau subducts (Cole and Spinks 2009). The TVZ is defined by eight volcanic centers, the northernmost of which is the Okataina Volcanic Center (OVC). The most recent caldera-forming eruption from the OVC was the Rotoiti eruption at ~ 45 ka (Cole et al. 2014; Danišík et al. 2012; Gravley et al. 2016). The Rotoiti eruption produced > 100 km^3 of moderately crystalline (15–25 vol.%) rhyolitic pyroclastic flow and fall deposits (Schmitz 1995; Davis 1985; Nairn 1972) (Fig. 1B). Shortly after the Rotoiti eruption, EQF erupted ~ 20–25 km to the southwest, producing 10 km^3 of crystal-rich (25–45 vol.%), non-welded

[1] Growth of minerals from melt is a disequilibrium process, so minerals capable of solid-solution need not have compositions strictly in equilibrium with the melt from which they are growing, but for simplicity of discussion this growth disequilibrium is ignored.

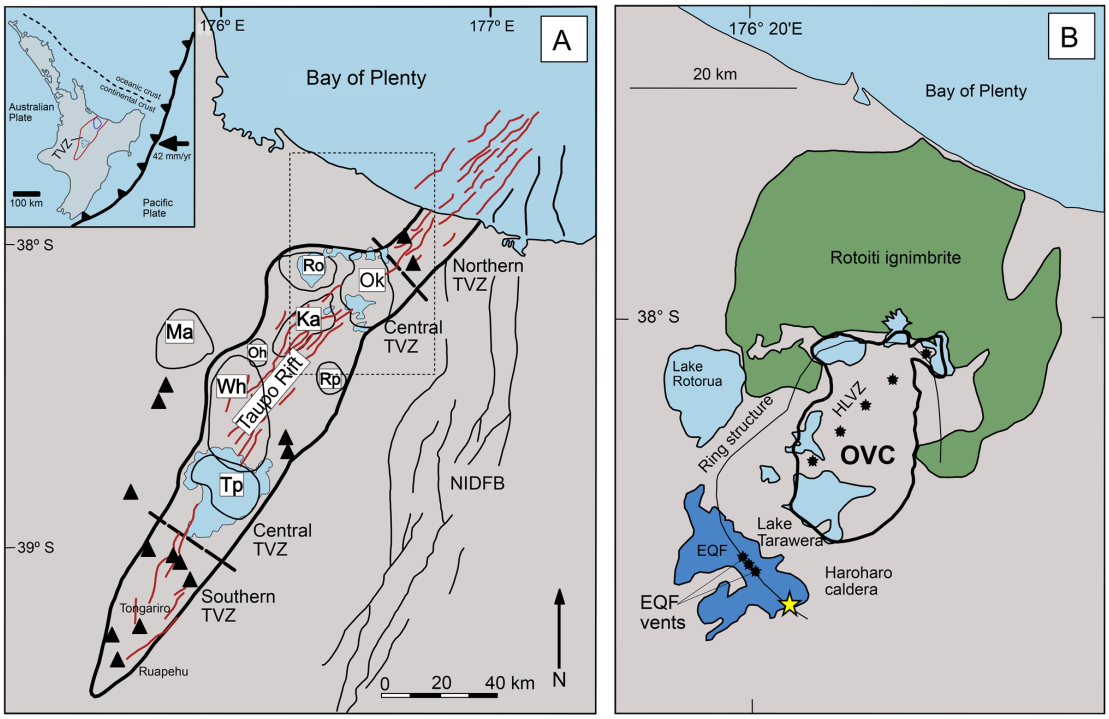


Fig. 1 (**A**) Tectonic and volcanic map of the central portion of the North Island of New Zealand (after Deering et al. 2011). Taupo Volcanic Zone (TVZ) outlined by thick black line, with its eight major volcanic centers outlined by light & medium black lines and labeled: Ok = Okataina, Ro = Rotorua, Ka = Kapenga, Rp = Reporoa, Oh = Ohakuri, Ma = Mangakino, Wh = Whakatane, Tp = Taupo. Red and black squiggly lines are intra-TVZ faults, and faults of the North Island dextral fault belt (NIDFB), respectively. Black triangles are stratovolcanoes. Black dashed lines indicate the boundaries between the northern, central, and southern TVZ volcanic regions. The inset shows the regional tectonic environment, the TVZ is outlined in red, the Okataina Volcanic Center (OVC) is outlined in blue. Dashed rectangle demarcates the region of panel B. **B** Map modified from Molloy et al. (2008) showing the distribution map for the Rotoiti (green area) and Earthquake Flat (EQF) (blue area) eruptions and their likely source vents (stars). Rotoiti vents coincide with the Haroharo Linear Vent Zone (HLVZ). Collapsed portion of Haroharo caldera defined by dark black line, and the inferred ring structure defined by the light black line. EQF vents are located along the inferred ring structure. Yellow star marks the approximate sampling location

rhyolitic pyroclastic flow and fall deposits. The EQF tuffs consist overwhelmingly of juvenile pumiceous lapilli and ash; pumice are composed of filamentous and bubble-rich glass with dominant phenocrysts of plagioclase and quartz, minor-to-trace biotite, hornblende, and orthopyroxene, plus accessory apatite, zircon, and Fe-Ti oxides. Juvenile Rotoiti deposits differ from the EQF both by their lower abundance of crystals, by the lack of biotite and hornblende, and by the presence of cummingtonite, but the mineral assemblages are otherwise generally similar, although not strictly the same. Field relations suggest that the EQF erupted immediately following the Rotoiti as evinced by the EQF Rifle Range ash conformably overlying the reworked upper Rotoiti Unit 5 (Nairn and Kohn 1973). Furthermore, lack of paleosol development between the two units confirms a short duration between eruptions (Nairn and Kohn 1973). Subsequent eruptions from the OVC have obscured the Rotoiti vents; however, it has been inferred that the eruption originated from the NE–SW-trending Haroharo Linear Vent Zone in the OVC (Fig. 1B) based on pyroclastic distribution maps (Schmitz and Smith 2004). Lithic lag breccia exposed on the caldera rim suggests that vents were intra-caldera (Shane et al. 2005). EQF erupted from inferred NW–SE trending linear vents (Fig. 1B) along the SW corner of the extra-caldera OVC ring structure (Nairn 2002; Molloy et al. 2008). Despite the temporal and spatial proximity of these two eruptive bodies, and their similar compositions and crystal assemblages, subtle isotopic differences between the two deposits precludes their having derived from a homogenous magma that differed solely in extent of crystallization across ~ 20 km (Molloy et al. 2008; Schmitz and Smith 2004). Broad mineralogical similarities between the two eruptions suggest that the pre-eruptive storage conditions

for the two bodies were likely similar; however, this has not previously been tested quantitatively.

Petrologic summary of the Rotoiti and Earthquake Flat rhyolites

The bulk of the Rotoiti tuffs are chemically homogenous, with the exception of the small proportion (< 10 vol.% of total erupted materials) of biotite-bearing deposits that top the Rotoiti stratigraphy (Davis 1985; Schmitz and Smith 2004; Shane et al. 2005). Schmitz (1995) and Shane et al. (2005) both reported a lack of compositional diversity throughout the Rotoiti stratigraphic section in terms of mineralogy and glass composition (glass $SiO_2 = 77.8 \pm 0.3$ wt.%, $K_2O = 3.34 \pm 0.10$ wt.%). The small-volume upper units differ in mineralogy by the appearance of biotite, increase in hornblende content, disappearance of cummingtonite, and by subtle changes in glass composition (glass $SiO_2 = 77.4 \pm 0.3$ wt.%, $K_2O = 4.07 \pm 0.17$ wt.%). Single-clast pumice chemical compositions for the entire Rotoiti section range from 71.8–75.9 wt.% SiO_2, and average 74.5 wt.% SiO_2 (Schmitz 1995). Charlier et al. (2003) identified weak zoning based on mineral contents throughout the stratigraphy. Some studies argued that the late, biotite-bearing, small-volume magma was sourced from an injection of the EQF magma into the Rotoiti reservoir (Schmitz 1995), while others interpreted that the biotite-bearing magma was sourced from some other evolved rhyolitic magma adjacent to the Rotoiti reservoir and not from the Earthquake Flat magma (Shane et al. 2005; Schmitz and Smith 2004).

The Earthquake Flat tuffs consist of 14 intercalated flow and fall deposits that, where well exposed, range from 0.5 to 7 m in thickness, but with no systematic stratigraphic changes in mineralogy, crystallinity, or bulk composition as seen in other large silicic tuff deposits such as the Bishop Tuff (Davis 1985). Davis (1985) argued that EQF shows weak chemical zoning, with MgO, total Fe as Fe_2O_3, and TiO_2 slightly enriched in the upper EQF deposits relative to the lower deposits, but with no obvious trend in CaO concentrations throughout the entire sequence. Conversely, Molloy et al. (2008) found no evidence for chemical zoning in the EQF deposits. Reports of crystallinity range from 23–34 vol.% (Davis 1985; Schmitz 1995), but Molloy et al. (2008) expanded this range to 25–45 vol.% crystallinity, which is consistent with our observations. Davis (1985) interpreted the presence of two distinguishable magma types: "type 1" magmas are represented by single-pumice $SiO_2 = 73.1$–75.1 wt.% and $K_2O = 2.80$–3.15 wt.%, and "type 2" pumices that are defined by $SiO_2 = 71.0$–72.3 wt.% and $K_2O = 2.36$–2.47 wt.%. By Davis' classification, our samples are of "type 1" magmas (single-pumice $SiO_2 = 73.9$–74.4 wt.%, $K_2O = 3.02$–3.30 wt.%). Schmitz (1995) confirmed that "type 1" samples dominate the deposits, but that the relationship between the two magma types is both discontinuous and unclear. From these reports, and from the compositional information we present below, we conclude that our samples are representative of the majority of the EQF tuff deposits.

Methods

Starting Material

The EQF pumice sample employed herein was collected from non-welded tuff exposed along New Zealand State Highway 38 (− 38.31112°, 176.3791°, NZGD 1949). Ten to fifteen large (6–25 cm) irregularly shaped pumice clasts were collected from a poorly sorted, matrix-supported, massive flow deposit. The single largest (~ 25 cm) pumice fragment without discoloration or visible vapor-phase alteration was selected for all analyses presented here. Analyzed materials were prepared by scrubbing the pumice clast clean of organic debris, drying, then coarse-crushing with a stainless-steel mortar and pestle. An aliquot of the cleaned, crushed single pumice was retained for whole-rock geochemical analyses and the remainder of the crushed sample was sieved into > 2, 1–2, 0.5–1, 0.125–0.5, 0.063–0.125, and < 0.063 mm size fractions. The 0.063–0.125 and 0.125–0.5 mm samples were passed through a Frantz magnetic separator at increasing amperages to separate minerals from glass. Some quartz and plagioclase grains in EQF pumice contain glass, Fe-Ti oxides, zircon, and apatite inclusions, which have a significant net effect on the magnetic susceptibility of such grains. As a result, the glass-rich split from the Frantz magnetic separator retained significant quartz and plagioclase. To remove the quartz and plagioclase from the glass (0.125–0.5 mm size fraction), we twice passed the concentrated glass split through a lithium heteropolytungstate (LST) solution of known density, resulting in a glass concentrate with < 5 vol.% mineral grain fragments (plagioclase > quartz). The resulting glass concentrate was washed and sonicated repeatedly, first in deionized water, then in acetone, and then again in deionized water to remove residual LST. This concentrate of natural glass, rather than the bulk pumice, was employed for experimental syntheses. Sparse remaining phenocryst fragments were easily identified in the experimental syntheses by their irregular, angular shapes, overgrowths, and their compositions. Splits of the purified glass concentrate and of the bulk crushed pumice were analyzed for major- and trace-element concentrations by X-ray fluorescence (XRF) at Hamilton Analytical Laboratory, Hamilton College, Clinton, New

Table 1. Anhydrous-normalized chemical compositions of starting materials

	Whole rock (XRF)[1]		Pumice matrix glass (EMP)[2]		Superliquidus glass for phase proportions (EMP)[3]		Glass concentrate starting material (XRF)[4]	
	wt.%	1 SD	wt.%	1 SD	wt.%	1 SD	wt.%	% error
SiO_2	74.2	0.19	77.8	0.15	77.4	0.46	77.7	0.09
TiO_2	0.30	0.00	0.10	0.02	0.10	0.02	0.13	6.31
Al_2O_3	13.9	0.16	12.5	0.09	13.0	0.16	12.5	0.75
FeO	2.02	0.05	0.87	0.12	0.68	0.05	0.78	0.43
MnO	0.07	0.00	0.05	0.02	0.04	0.03	0.04	0.60
MgO	0.43	0.01	0.08	0.01	0.07	0.02	0.06	13.1
CaO	2.02	0.03	0.79	0.02	0.80	0.03	0.82	2.87
Na_2O	3.85	0.10	3.30	0.10	3.22	0.13	3.45	0.03
K_2O	3.15	0.11	4.26	0.12	4.57	0.10	4.49	0.85
P_2O_5	0.06	0.00	0.01	0.01	0.02	0.00	0.02	5.43
Original total	99.7	--	98.3	--	93.8	--	99.6	--

[1]Whole rock compositional data is an average of seven different pumice clasts analyzed by XRF (ranging from 73.9 to 74.4 wt% SiO_2 normalized anhydrous) with 1 standard deviation.

[2]Natural matrix glass is an average of 28 spot analyses meaured by EMP (ranging from 77.5 to 78.2 wt% SiO_2 normalized anhydrous), 1 standard deviation is presented.

[3]An average of 82 spot analyses from three superliquidus experimental glasses (Runs 12, 14, and 27) used as the starting material and composition for phase proportion calcluations, measured by EMP with average 1 standard deviation.

[4]A single 5 g aliquot of glass concentrate starting material was analyzed by XRF, we present % error for replicate analyses of USGS obsidian standard Rhyolite, Glass Mountain (RGM-1).

Original totals are presented with normalized oxide data

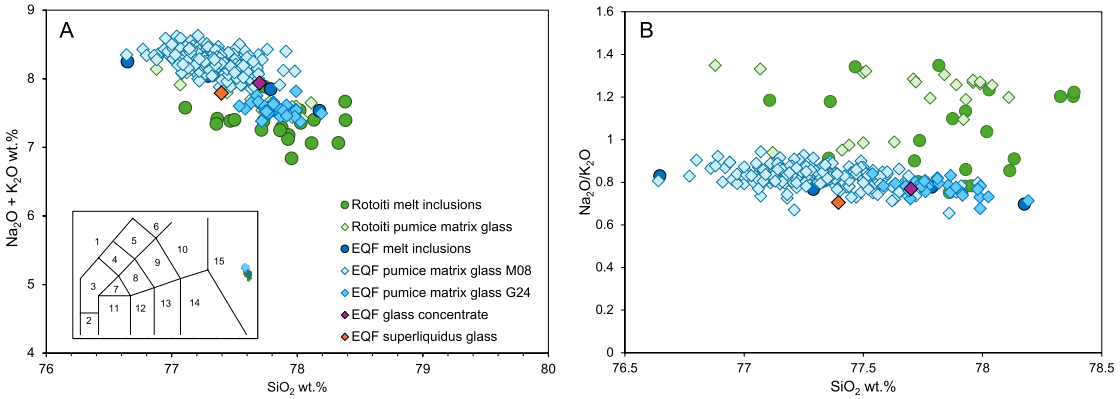


Fig. 2 **A** Total alkali-silica (TAS) diagram illustrating the relationship between Rotoiti matrix glass and melt inclusion glass, Earthquake Flat (EQF) matrix glass and melt inclusion glass, and the glass concentrate starting material. Rotoiti melt inclusion glass (dark green circles: Smith et al. 2010; Johnson et al. 2013); Rotoiti matrix glass (light green diamonds: Shane et al. 2005; Johnson et al. 2013); EQF melt inclusion glass (dark blue circles: Smith et al. 2010); EQF matrix glass (light blue diamonds "M08": Molloy et al. 2008, medium blue diamonds "G24": this study); glass concentrate starting material for this study (purple diamond); superliquidus glass used for phase proportion mass balance in this study (orange diamond). Inset shows full TAS diagram: (1) Foidite; (2) Picro-basalt; (3) Basanite; (4) Phonotephrite; (5) Tephriphonolite; (6) Phonolite; (7) Trachybasalt; (8) Basaltic trachyandesite; (9) Trachyandesite; (10) Trachyte; (11) Basalt; (12) Basaltic andesite; (13) Andesite; (14) Dacite; (15) Rhyolite (lines after Le Maitre et al. 2005). **B** Na_2O/K_2O versus SiO_2 diagram illustrating the relative offset between the Rotoiti and EQF melt inclusion and matrix glasses. In both cases melt inclusion glass is not offset from matrix glass indicating minimal to no alkali migration

York (Table 1). Volcanic glass is prone to hydration and alteration, which can be accompanied by alkali exchange. Typical TVZ fresh glass alkali concentrations are > 3 wt.% Na_2O and < 4.5 wt.% K_2O (Shane 2000). Vesicular pumice glasses from EQF and from Rotoiti have Na_2O and K_2O concentrations indistinguishable from those of those

deposits' respective melt inclusions (Fig. 2) indicating little-to-no alkali losses. Our pumice glass and glass concentrate materials (Table 1) are well within the thresholds of what is considered hydrated but otherwise fresh glass.

Use of separated natural glass, versus bulk pumice, for experimental syntheses

The primary objective of this work was to identify the temperature and pressure (depth) representative of the bulk of the EQF magma body immediately prior to its eruption, and this was accomplished by finding the conditions at which the natural melt (the erupted glass) is saturated on its liquidus with the dominant phenocrysts. The textures and mineral chemistry of the EQF pumices are consistent with the phenocrysts in a growth regime: quartz, plagioclase, and biotite grains are large and sub-to-euhedral, and their rim compositions are homogenous or nearly so across relatively large distances (> 200 µm). Rim compositions are also similar from grain to grain, and the subtle oscillatory zoning of the thick, sodic plagioclase rims lack prominent resorption intervals. These features are consistent with the minerals having grown approaching the time of eruption. Some quartz grains are faintly resorbed, but this could have resulted from decompression rather than from heating (Luth et al. 1964; Tuttle and Bowen 1958). Practical advantages of using the separated glass, rather than bulk pumice, include that the natural glass's liquidus is identified readily, its composition along the liquidus is guaranteed to be that of the natural melt at the time of eruption, and the run products are uncomplicated by the presence of abundant fragments of phenocrysts, antecrysts, and glomerocrysts that can remain unreacted or thinly armored in syntheses on crushed bulk pumices at the relatively low temperatures of rhyolites. An alternative approach is to prepare a glass with the composition of the bulk pumice, but nucleation and undercooled growth of crystals can be problematic in attaining the approximately 40 vol.% crystallinity, representative of the EQF magma at its time of eruption. A drawback of employing separated natural glass is that any peritectic reactant minerals will not grow from the melt despite being stable, and so will be absent from synthesized assemblages.

Capsule configuration and fO_2 buffering

Experiments were performed in H_2O-pressurized cold-seal vessels employing the classic double-capsule configuration developed by Eugster (1957) where the sample plus H_2O were sealed in an inner capsule (herein, Au) and this plus fO_2 buffer (herein, Ni–NiO) and H_2O were sealed in an outer Au capsule. The configuration was modified, owing to the long durations of the syntheses and the propensity of Ni to alloy with Au at the investigated temperatures. Modifications included containing the Ni–NiO buffers in two crimped but unsealed Pt tubes within the sealed outer Au capsule, thereby preventing Ni from touching Au, and by accompanying each synthesis with an additional Pt buffer capsule packed with Ni, NiO, and H_2O to prolong fO_2 buffered conditions (Electronic Supplementary Materials (ESM) 1).

Internal buffer capsules were 2 mm OD (outer diameter) Pt tubes loaded with a Ni–NiO (1:1 by weight) powder mixture (Ni metal and NiO powders) and a 1 mm diameter, ¼ inch (~ 7 mm) length of nickel wire, such that experiments were buffered at Ni–NiO, chosen based on calculated fO_2 from Fe-Ti oxide (titanomagnetite-ilmenite) touching pairs in the EQF pumice as discussed subsequently. The internal buffer capsules were welded at one end, loaded with buffer, and the second capsule end was squeezed shut and folded over with pliers so that buffer was contained but exposed to the H_2O environment.

The inner capsule containing the sample consisted of a 3/8-inch (9.5 mm) length of 3 mm OD annealed Au tubing into which 15–20 mg of the powdered natural glass concentrate and 7 wt.% distilled H_2O were loaded, and this was then triple crimped and welded closed using a tungsten-inert-gas welder.

The internal buffer capsules and the inner sealed Au capsule containing the wet sample were inserted in the outer Au capsule constructed of 4 mm OD annealed Au, along with ~ 60 μL H_2O, and this was finally triple crimped and welded shut. The external buffer capsules were constructed of 5 mm OD annealed Pt, loaded with ~ 50 mg of Ni–NiO (1:1 by weight) powder and ~ 50 μL distilled H_2O. The weigh, heat (several minutes at 112 °C), reweigh technique was employed at each stage to confirm welds were complete, and capsules that failed this test were rebuilt.

All experiments were H_2O-saturated, which yields ~ 2.7–7 wt.% H_2O dissolved in the melt, varying with pressure (Ghiorso and Gualda 2015; Liu et al. 2005; Moore et al. 1998; Iacovino et al. 2021; Table 2). These H_2O concentrations are consistent with those dissolved in Rotoiti melt inclusions (CO_2 < 10 ppm (~ limit of detection), and H_2O ≤ 5.1 wt.%, Johnson et al. 2011; and CO_2 = 210–960 ppm, and H_2O ≤ 7.5 wt.%, Smith et al. 2010), and available EQF melt inclusions (H_2O = 3.4–7.5 wt.%, Smith et al. 2010) and discussed in more detail below.

Experimental Setup

All experiments employed H_2O-pressurized, externally heated cold-seal pressure vessels without filler rods, other than the supplementary buffer capsule, with the vessels oriented vertically (synthesis conditions listed in Table 2). Temperatures were measured and controlled with a type-K thermocouple inserted into a 2.3 cm long well in the base of each vessel that places the thermocouple junction adjacent

Table 2. Experimental conditions

Run #	Pressure (MPa)	Temperature (°C)	Duration (hrs)[1]	Phases[2]	% glass	Liq-Plg K_D (Ca-Na)[3]	Dissolved H_2O (wt.%)				
							By difference (STD (1σ))[4]	Solubility models[5]			Measured (ATR-FTIR)
Phase equilibirum experments								Ghiorso and Gualda[6]	Liu[7]	Moore[8]	(avg FD)[9]
42	250	680	531	kfsp (16), plg (10), qtz (17), bte (1), tmt, zr, ap	55	1.51	6.10 (0.84)	6.20	7.01	6.83	--
28	250	700	191	qtz (4), bte (1), tmt, zr, ap	95	--	6.86 (0.41)	6.30	6.97	6.71	--
29	250	714	239	qtz (1), bte (<1), tmt, zr, ap	98	--	7.42 (0.37)	6.57	6.93	6.93	--
31	250	740	192	tmt, zr, ap	>99	--	6.88 (0.37)	6.66	6.90	6.88	6.4
11	200	700	333	kfsp (5), plg (4), qtz (8), bte (1), tmt, zr, ap	83	1.96	5.95 (0.01)	5.62	6.23	6.04	--
15	200	720	333	qtz (1), bte (<1), tmt, zr, ap	98	--	6.09 (0.46)	5.76	6.17	6.08	--
32	200	740	190	bte (<1), tmt, zr, ap	99	--	6.86 (0.29)	5.86	6.12	6.08	--
12	200	760	333	tmt, zr, ap	>99	--	6.21 (0.58)	5.90	6.07	6.01	6.2
14	200	780	307	tmt, zr, ap	>99	--	6.62 (0.53)	5.96	6.02	5.98	5.5
41	150	720	531	plg (1), qtz (2), bte (1), tmt, zr, ap	96	2.86	5.99 (0.37)	4.97	5.30	5.30	--
24	150	740	332	plg (2), qtz (<1), bte (<1), tmt, zr, ap	96	3.41	5.78 (0.41)	5.03	5.24	5.27	--
26	150	760	331	tmt, zr, ap	>99	--	5.45 (0.35)	5.07	5.18	5.22	5.7
27	150	780	331	tmt, zr, ap	>99	--	5.86 (0.43)	5.09	5.13	5.17	5.5
16	100	720	330	kfsp (39), plg (13), qtz (25), bte (1), tmt, zr, ap	21	1.71	6.16 (0.72)	3.85	4.25	4.19	--
18	100	740	330	plg (4), qtz (1), bte (<1), tmt, zr, ap	94	2.71	4.05 (0.67)	4.01	4.19	4.30	--
19	100	760	330	plg (2), qtz (1), bte (1), tmt, zr, ap	96	3.20	4.63 (0.72)	4.02	4.14	4.24	--
20	100	780	330	plg (1), tmt, zr, ap	99	3.67	3.63 (0.40)	4.03	4.08	4.19	3.8
43	50	750	343	kfsp, plg, qtz, bte, tmt, zr, ap	<5	2.36	--	3.19	2.84	3.21	--
40	50	790	531	plg (3), qtz (2), tmt, zr, ap	94	3.36	2.20 (0.37)	2.70	2.75	2.90	--
Reversals											
37	250	740	159; 335	tmt, zr, ap		--	--	--	--	--	--
35	200	720	161; 335	qtz, bte, tmt, zr, ap		--	--	--	--	--	--
36	200	740	159; 335	bte, tmt, zr, ap		--	--	--	--	--	--
38	150	760	162; 335	tmt, zr, ap		--	--	--	--	--	--

[1]Durations for reversal experiments are the time held above the liquidus, and the time spent at run conditions, respectively

[2]Phases: potassium feldspar (kfsp), plagioclase (plg), quartz (qtz), biotite (bte), titanomagnetite +/- ilmenite oxides (tmt), zircon (zr), apatite (ap); phase proportions in wt.% indicated in parentheses; no phase estimates for Exp 43; tmt, zr, and ap are all trace phases

[3]K_D (Ca-Na) = $[(Ca/Na)_{plg}/(Ca/Na)_{liq}]$

[4]"By difference" refers to the difference between the total oxide sum for glass compostional analyses and 100

[5]Dissolved volatile concentrations using VESIcal (Iacovino et al. 2021)

[6]MagmaSat Ghiorso and Gualda (2015)

[7]Liu et al. (2005)

[8]Moore et al. (1998)

[9]Measured ATR-FTIR H_2O concentration realative to Fisher Dacite standard (FD); data presented for runs where we are confident that analysis only measured glass

Probe run conditions listed in ESM 4

Double dash indicates not applicable

to the base of the vessel's bore. Temperatures were controlled accounting for small differences between the control thermocouple's temperature and the internal temperature at the sample's position as determined by prior calibrations at run temperatures employing an internal type-K thermocouple. Calibrations included profiling the vessel's internal temperature with the vessel inserted at different depths into the furnace to locate the optimal conditions of minimum thermal gradient across the sample position and a minimum difference between internal versus external temperature. Four vessels were generally run simultaneously in adjacent furnaces, and all the hotspots were located within the bottom 1–2 cm of the vessel's bore, with offsets between external control thermocouple and internal sample position no greater than Δ 3 °C (e.g., 723 vs. 726 °C in bottom 15 mm of furnace #4). The sample capsule was placed in the bottom of the vessel's bore with the sample positioned at the base to ensure it was in the hotspot and adjacent to the control thermocouple. The supplementary buffer capsule was placed above the sample capsule, and the bore was filled with water prior to closing of the vessel, connecting it to the H_2O pressure system, and inserting it the appropriate distance into the cold furnace. The vessels were water-pressurized using an air-driven pump, and pressure was monitored with a Heise Bourdon tube gauge. The vessels were brought to pressure before heating to prevent the sample capsule from expanding and bursting or (and) sticking in the vessel. Once the vessels were securely pressurized, the furnaces were turned on and adjusted to run temperature. During heating, the pressure was monitored and adjusted to not exceed the intended run pressure by more than about 50 bars. Once the intended temperature was reached, the pressure was adjusted to the intended value. Both pressure and temperature were maintained over the experimental durations to within ± 1 °C and ± 10 bars, therefore, the uncertainties on pressure and temperature measurements are small: temperature uncertainties are ≤ 5 °C based on replicate calibrations of temperature offsets and hotspot gradients, and pressure uncertainties are on the order of several bars. Syntheses brought directly to pressure and temperature were held at intended conditions for 8–22 days, generally increasing with proximity to the solidus. Reversal experiments, designed to approach equilibrium from high temperature conditions, were brought to silicate superliquidus conditions for 6.5–6.75 days, then temperature and pressure were adjusted to the conditions of prior direct syntheses and held for 14 days (Table 2). After the intended synthesis durations, vessels were extracted from the furnaces and cooled by a jet of compressed air. No evidence of quench crystallization was observed (no microlites in glass, no graphic textures, no quench overgrowths on stable crystals discernable at optical and electron-beam resolutions). A magnet was used to check that the internal and supplementary buffer capsules retained Ni metal, and internal buffer capsules that occasionally tore open on capsule disassembly consistently showed yellow-green NiO, collectively showing that fO_2s were buffered for the synthesis durations. The inner capsules containing the samples were then ground to expose the glassy slug, epoxy impregnated, mounted, and polished for analytical work.

Electron Microprobe (EMP)

The synthesized products and natural EQF pumice phases (polished thin sections) were analyzed on a five-spectrometer JEOL JXA-8530 F + electron microprobe at the U.S. Geological Survey, Menlo Park, California, using wavelength-dispersive methods. Instrument conditions were 15 kV accelerating potential, a 10 nanoamp, 2–5 µm diameter beam for minerals, or a 2 nanoamp, 5–20 µm diameter beam for glass. For minerals, elements were measured for 10–40 s, whereas in glass, Na and K were measured first for 10 s, and the other elements for 20–30 s. Backgrounds were determined every 6th point, and background-corrected count rates were reduced to concentrations with the JEOL-proprietary version of the ZAF method, standardized with natural and synthetic materials. Primary and secondary standards were analyzed as unknowns periodically during analysis sessions to monitor and post-process for drift. Analytical results, uncertainties, and instrument conditions are reported in Tables 3 and 4, analytical results of unknown and standards are both available in ESM 2 and 4.

ATR-FTIR

Dissolved H_2O concentrations of the experimental glasses, EQF pumice glass, EQF quartz-hosted embayment glasses, and EQF melt inclusions were determined by the attenuated total reflectance (ATR) method (Lowenstern and Pitcher 2013) using a germanium crystal on singly-polished surfaces with the Nicolet iN10 Fourier transform infrared imaging microscope (FTIR) at the U.S. Geological Survey in Menlo Park, California, with liquid-N_2-cooled MCT-B detector. This method limits light penetration to ~ 1 µm below the surface, allowing avoidance of crystals. The aperture size (30–150 µm) was adjusted according to the size of the glass pools in each sample and spectra were collected from 4,000 to 1,200 cm^{-1} with 256 scans for each spot and spectral resolution of 8–16 cm^{-1}. A reference spectrum was collected in air prior to each sample measurement and a straight baseline was used to determine the height of the 3,450 cm^{-1} band. An internal dacite glass standard with known H_2O concentration was analyzed periodically throughout each analytical session to verify that the ATR crystal and sample were oriented for optimal contact. Several spots were analyzed in distributed melt pools across each experimental or EQF pumice glass sample, and maps

Table 3 Average chemical compositions of minerals and glass in EQF pumice (oxide wt.%) measured by EMP

Phase	n[1]	Composition	SiO_2	TiO_2	Al_2O_3	V_2O_3	Cr_2O_3	FeO_T[2]	MnO	MgO	CaO	Na_2O	K_2O	P_2O_5	BaO	Cl	F	SO_3	Total[3]	(H_2O)[4]
Glass (anhydrous)[5]	28		77.9	0.10	12.5	--	--	0.88	0.05	0.08	0.79	3.30	4.27	b.d.l.	--	0.19	b.d.l.	b.d.l.	98.3	1.7
SD (1σ)			0.1	0.02	0.1	--	--	0.12	0.02	0.01	0.02	0.10	0.12	b.d.l.	--	0.02	b.d.l.	b.d.l.	--	0.1
Plagioclase cores[6]	37	$An_{41}Ab_{56}Or_2$	57.7	--	26.7	--	--	0.21	--	b.d.l.	8.63	6.46	0.43	--	0.06	--	--	--	100.2	--
SD (1σ)			3.5	--	2.4	--	--	0.12	--	b.d.l.	2.75	1.53	0.22	--	0.03	--	--	--	--	--
Plagioclase rims[6]	32	$An_{28}Ab_{69}Or_4$	61.6	--	24.3	--	--	0.18	--	b.d.l.	5.83	7.93	0.65	--	0.06	--	--	--	100.5	--
SD (1σ)			0.9	--	0.4	--	--	0.03	--	b.d.l.	0.36	0.30	0.06	--	0.04	--	--	--	--	--
Biotite cores[7]	35	Mg# = 50	37.0	4.48	14.0	--	b.d.l.	19.7	0.22	10.9	0.05	0.47	7.92	--	--	0.29	0.27	--	95.2	--
SD (1σ)			1.1	0.19	0.5	--	b.d.l.	0.75	0.03	0.60	0.04	0.11	0.39	--	--	0.02	0.08	--	--	--
Biotite rims[7]	34	Mg# = 49	36.9	4.46	14.0	--	b.d.l.	19.2	0.21	10.6	0.08	0.43	7.74	--	--	0.28	0.27	--	94.3	--
SD (1σ)			0.7	0.22	0.5	--	b.d.l.	0.90	0.04	0.73	0.06	0.11	0.53	--	--	0.02	0.13	--	--	--
Hornblende cores[7]	5		47.2	1.12	5.9	--	b.d.l.	17.3	0.66	12.7	10.2	1.31	0.36	--	--	0.13	0.17	--	97.0	--
SD (1σ)			0.3	0.11	0.4	--	b.d.l.	0.16	0.04	0.25	0.08	0.06	0.04	--	--	0.02	0.04	--	--	--
Hornblende rims[7]	9		46.4	1.29	6.3	--	b.d.l.	17.3	0.62	12.2	10.3	1.40	0.44	--	--	0.15	0.18	--	96.7	--
SD (1σ)			0.6	0.14	0.5	--	b.d.l.	0.26	0.02	0.29	0.07	0.11	0.05	--	--	0.01	0.05	--	--	--
Pyroxene cores[7]	14	$Wo_2En_{47}Fs_{52}$	50.5	0.08	0.3	--	b.d.l.	29.4	2.27	16.0	0.83	0.01	b.d.l.	--	--	--	--	--	99.5	--
SD (1σ)			0.2	0.02	0.0	--	b.d.l.	0.18	0.25	0.28	0.06	0.01	b.d.l.	--	--	--	--	--	--	--
Pyroxene rims[7]	33	$Wo_2En_{48}Fs_{50}$	50.4	0.10	0.3	--	b.d.l.	28.8	2.04	16.4	0.78	0.01	0.01	--	--	--	--	--	98.9	--
SD (1σ)			0.3	0.03	0.0	--	b.d.l.	0.38	0.11	0.27	0.02	0.01	0.01	--	--	--	--	--	--	--
Magnetite[7]	8		0.1	9.53	1.3	0.26	0.04	82.8	0.76	0.56	b.d.l.	--	--	--	--	--	--	--	95.4	--
SD (1σ)			0.0	0.20	0.0	0.02	0.01	0.42	0.03	0.01	b.d.l.	--	--	--	--	--	--	--	--	--
Ilmenite[7] (n=8)	8		0.0	50.2	0.1	0.15	b.d.l.	48.1	1.43	1.36	0.02	--	--	--	--	--	--	--	101.4	--
SD (1σ)			0.0	0.19	0.0	0.08	b.d.l.	0.17	0.02	0.05	0.03	--	--	--	--	--	--	--	--	--
Quartz embayment glass (anhydrous)	5		77.7	0.09	12.4	--	--	0.89	0.04	0.06	0.72	3.48	4.33	b.d.l.	--	0.20	b.d.l.	b.d.l.	99.9	1.2
SD (1σ)			0.4	0.01	0.1	--	--	0.02	0.01	0.01	0.04	0.10	0.06	b.d.l.	--	0.03	b.d.l.	b.d.l.	--	0.3

[1]Number of analyses

[2]FeO_T, all Fe as FeO

[3]Total indicates original analytical sum

[4]H_2O measured by ATR-FTIR; H_2O not included in glass total

[5]Hydrous glass was analyzed at 15 kV accelerating voltage, 20 µm spot, 2 nA current. Where MnO and P_2O_5 returned negative values these were reported as below detection limit (bdl); glass composition normalized anhydrous, original glass total is presented

[6]Feldspar was analyzed at 15 kV accelerating voltage, 1-5 µm spot (depending on grain size), 5 nA current. Reported averages exclude excessive low/high mass totals (< 98.5 and > 101.5). We ran K_2O and Na_2O first in the analytical routine to mitigate potential loss by alkali migration. We checked for Na loss at the feldspar analysis conditions, confirming no detectable migration, altough we continued to count Na_2O and K_2O for short times

[7]Fe-Ti oxides, pyroxene, amphibole (EQF pumice samples only) were analyzed at 15 kV accelerating voltage, 20 nA current, focused beam. Biotite (EQF pumice samples only) was analyzed 15 kV accelerating voltage, 10 nA current, 5 µm spot. We corrected for the overlap of interfering peaks on oxide analyses (Ti on V, and V on Cr). We tested Fe-Ti oxides for Mg/Mn equilibration using Bacon and Hirschmann (1988), all grains plotted within the 2-sigma envelope

were collected for EQF melt inclusions (results not discussed here but available in ESM 3). Experimental products with high crystallinities prohibit accurate and precise H_2O measurements as there is not sufficient area for the germanium crystal to make complete contact without interfering with synthesized grains. Highly crystalline experiments yield H_2O concentrations that differ by up to 1.5 wt.% H_2O and are therefore not reported. For low crystallinity experiments, complete contact between glassy pools and germanium crystal yield H_2O concentration that vary no more than 0.6 wt.% H_2O within a single experiment (Table 2, ESM 3); H_2O concentrations of EQF melt inclusions are not reported in Table 2 as they presented analytical challenges beyond the scope of this study; however, these results are included in ESM 1 and 3.

Results

Characteristics of EQF pumices

The EQF pyroclastics are dominantly pumice lapilli and pumiceous ash with abundant crystals set in microlite-free highly vesicular glass. Compositions are presented for EQF pumice glass, glass concentrate starting material, and the average of seven EQF single pumices in Table 1, compositions of EQF pumice minerals are presented in Table 3, and those of experimentally synthesized minerals are presented in Table 4. The natural EQF mineral assemblage is characterized (all in vol.%) by plagioclase (16–23%) > quartz (4–11%) > biotite (1–3%) > hornblende (1–2%) > oxides (< 1.5%) > orthopyroxene (< 0.5%) > trace phases (clinopyroxene, apatite, zircon, pyrrhotite) (Fig. 3A–H) (Molloy et al. 2008). We note that the EQF pumice phase proportions are not directly comparable to our experimental results as we used the glass concentrate as a starting material. As presented previously, total crystallinity spans 25–45 vol.%, with the majority of samples near the upper end of that range (Molloy et al. 2008; and this study). The pumice glass and glass concentrate starting material share similar compositions, both have > 77 wt.% SiO_2, and identical concentrations of 12.5 wt.% Al_2O_3, but EMP alkali values are ~ 5 relative % lower than XRF values, either due to minor alkali migration during EMP analyses or to differences in standardization of the two methods. Molloy et al. (2008) reported 205 individual point analyses of EQF glasses. Of these, six have distinctly high K_2O concentrations (> 5 wt.%, normalized anhydrous), one has aberrantly high MgO (1.8 wt.%), possibly reflecting a transcription error, and one has slightly low CaO (< 0.65 wt.%). The remaining 197 analyses are highly homogeneous high-SiO_2 rhyolitic compositions yielding low standard deviations on concentrations of oxides sensitive to rhyolitic differentiation (e.g., average CaO = 0.80 ± 0.06 wt.%, average total Fe as FeO = 0.88 ± 0.22 wt.%,

Table 3 (continued)

Primary standards: RLS75 Obsidian, Or1 Orthoclase, Tiburon Albite, VG2 Basaltic Glass, Crystal Bay Bytownite, Barite, Strontanite, CPX1 Diopside, Springwater Olivine, Sodalite, Synthetic MgF2, Tiebaghi Chromite, Ilmenite, TiO2, Hematite, Spinel, MnO, Wilbur Apatite (see supplement for additional details)

Monitors measured as unknowns during analysis sessions: RLS75, Or1, Tiburon Albite, VG2, Crystal Bay Bytownite, Barite, Strontanite, CPX1, Springwater Olivine, Sodalite, MgF2, Tiebaghi Chromite, Ilmenite, TiO2, Hematite, Spinel, MnO, Wilbur Apatite

For all phases, we re-peaked Si and Al every six points to reduce any instrumental drift but did not include these spots in data compilation; any points that returned low totals were excluded. Na and K were measured first for 10 seconds, followed by all other elements which we measured between 10 and 40 seconds, except for glasses in which Na and K were measured for 10 seconds, and all other elements were measured between 20 and 30 seconds; Analytical details available in ESM 2

Double dash indicates not applicable

Table 4 Average chemical composition (oxide wt.%) of synthesized glass, plagioclase (Plg), and alkali feldspar (Kfsp) measured by EMP

Run #	*Phase*[1]	n[2]	SiO_2	TiO_2	Al_2O_3	FeO_T[3]	MnO	MgO	CaO	Na_2O	K_2O	P_2O_5	Cl	BaO	Original Total	H_2O[4]	An	Ab	Or
Exp 11	*Glass*	*6*	77.0	0.06	13.6	0.6	0.05	0.03	0.80	3.14	4.72	b.d.l.	0.07	--	94.1	--	--	--	--
700 ℃, 200 MPa	*SD (1σ)*		0.26	0.02	0.20	0.07	0.03	0.02	0.04	0.12	0.12	--	0.01	--	--	--	--	--	--
	Plg	*27*	63.6	--	22.5	0.11	--	b.d.l.	4.21	8.23	1.13	--	--	0.11	99.9	--	21	73	7
	SD (1σ)		1.2	--	0.7	0.05	--	--	0.51	0.32	0.20	--	--	0.09	--	--	--	--	--
	Kfsp	*11*	65.3	--	18.1	0.12	--	b.d.l.	0.19	2.61	11.1	--	--	1.73	99.2	--	1	26	73
	SD (1σ)		1.5	--	0.6	0.04	--	--	0.05	0.10	0.52	--	--	0.35	--	--	--	--	--
Exp 16	*Glass*	*24*	77.7	0.03	14.2	1.10	0.22	0.06	0.36	1.77	4.51	0.05	0.18	--	93.8	--	--	--	--
720 ℃, 100 MPa	*SD (1σ)*		1.29	0.04	0.82	0.10	0.06	0.01	0.10	0.37	0.37	0.04	0.02	--	--	--	--	--	--
	Plg	*34*	67.7	--	19.4	0.23	--	b.d.l.	2.43	6.94	3.11	--	--	0.16	100.0	--	13	67	20
	SD (1σ)		1.9	--	1.1	0.19	--	--	0.49	0.60	1.21	--	--	0.10	--	--	--	--	--
	Kfsp	*10*	67.4	--	18.3	0.27	--	b.d.l.	0.85	4.82	7.80	--	--	0.16	99.6	--	4	46	49
	SD (1σ)		2.8	--	1.3	0.16	--	--	0.34	0.70	1.16	--	--	0.10	--	--	--	--	--
Exp 18	*Glass*	*30*	77.7	0.10	12.8	0.70	0.05	0.06	0.67	3.15	4.81	b.d.l.	0.13	--	96.0	--	--	--	--
740 ℃, 100 MPa	*SD (1σ)*		0.5	0.06	0.3	0.07	0.03	0.02	0.08	0.15	0.14	--	0.02	--	--	--	--	--	--
	Plg	*24*	64.8	--	21.8	0.16	--	b.d.l.	4.30	7.47	1.39	--	--	0.16	100.1	--	22	69	9
	SD (1σ)		1.8	--	1.3	0.05	--	--	0.64	0.45	0.35	--	--	0.10	--	--	--	--	--
Exp 19	*Glass*	*29*	77.4	0.09	13.0	0.72	0.06	0.07	0.73	3.22	4.69	b.d.l.	0.13	--	95.4	--	--	--	--
760 ℃, 100 MPa	*SD (1σ)*		0.33	0.02	0.13	0.05	0.04	0.02	0.06	0.19	0.39	--	0.02	--	--	--	--	--	--
	Plg	*24*	63.8	--	22.9	0.19	--	0.02	5.22	7.24	1.08	--	--	0.12	100.6	--	27	67	7
	SD (1σ)		1.7	--	1.1	0.04	--	0.01	0.49	0.48	0.27	--	--	0.07	--	--	--	--	--
Exp 20	*Glass*	*35*	77.3	0.10	13.0	0.71	0.04	0.08	0.69	3.28	4.82	b.d.l.	0.09	--	96.4	3.8	--	--	--
780 ℃, 100 MPa	*SD (1σ)*		0.28	0.03	0.17	0.06	0.03	0.01	0.04	0.12	0.13	--	0.01	--	--	0.3	--	--	--
	Plg	*24*	63.2	--	23.2	0.19	--	b.d.l.	5.50	7.10	1.10	--	--	0.08	100.4	--	28	65	7
	SD (1σ)		1.6	--	1.1	0.07	--	--	0.71	0.43	0.34	--	--	0.09	--	--	--	--	--
Exp 24	*Glass*	*30*	77.9	0.09	12.7	0.66	b.d.l.	0.06	0.77	3.22	4.60	b.d.l.	0.11	--	94.2	--	--	--	--
740 ℃, 150 MPa	*SD (1σ)*		0.21	0.04	0.16	0.07	--	0.02	0.03	0.14	0.11	--	0.02	--	--	--	--	--	--
	Plg	*7*	62.9	--	23.6	0.20	--	b.d.l.	5.79	7.13	0.89	--	--	0.12	100.7	--	29	65	5
	SD (1σ)		1.9	--	1.5	0.06	--	--	0.94	0.29	0.33	--	--	0.07	--	--	--	--	--
Exp 43	*Plg*	*10*	67.0	--	20.0	0.19	--	b.d.l.	2.56	6.95	3.52	--	--	0.22	100.5	--	13	65	22
750 ℃, 50 MPa	*SD (1σ)*		3.3	--	2.3	0.07	--	--	1.33	0.76	1.77	--	--	0.17	--	--	--	--	--
	Kfsp	*30*	66.9	--	18.7	0.12	--	b.d.l.	0.55	4.66	9.13	--	--	0.13	100.3	--	3	42	55
	SD (1σ)		2.4	--	1.6	0.04	--	--	0.34	0.77	1.19	--	--	0.20	--	--	--	--	--
Exp 40	*Glass*	*29*	77.7	0.10	12.5	0.72	0.05	0.08	0.68	3.44	4.74	b.d.l.	0.12	--	97.9	--	--	--	--
790 ℃, 50 MPa	*SD (1σ)*		0.26	0.03	0.17	0.07	0.04	0.01	0.04	0.15	0.10	--	0.01	--	--	--	--	--	--
	Plg	*30*	64.0	--	22.3	0.29	--	b.d.l.	4.68	7.62	1.25	--	--	0.17	100.4	--	23	69	8
	SD (1σ)		1.9	--	1.3	0.07	--	--	0.64	0.57	0.35	--	--	0.10	--	--	--	--	--
Exp 41	*Glass*	*30*	78.0	0.08	12.7	0.64	0.04	0.04	0.76	3.17	4.55	0.03	0.09	--	94.1	--	--	--	--
720 ℃, 150 MPa	*SD (1σ)*		0.27	0.03	0.19	0.07	0.03	0.02	0.04	0.14	0.12	0.02	0.02	--	--	--	--	--	--
	Plg	*22*	63.3	--	23.4	0.18	--	b.d.l.	5.28	7.70	0.94	--	--	0.10	100.9	--	26	69	6
	SD (1σ)		1.4	--	0.9	0.05	--	--	0.41	0.38	0.25	--	--	0.06	--	--	--	--	--

Table 4 (continued)

Run #	*Phase*[1]	n[2]	SiO_2	TiO_2	Al_2O_3	FeO_T[3]	MnO	MgO	CaO	Na_2O	K_2O	P_2O_5	Cl	BaO	Original Total	H_2O[4]	An	Ab	Or
Exp 42	*Glass*	*29*	77.2	0.07	13.6	0.65	0.06	0.05	0.90	3.21	4.24	b.d.l.	0.05	--	93.9	--	--	--	--
680 °C, 250 MPa	*SD (1σ)*		0.27	0.06	0.19	0.28	0.03	0.06	0.07	0.19	0.18	--	0.02	--	--	--	--	--	--
	Plg	*5*	64.5	--	21.4	0.08	--	b.d.l.	3.44	8.20	1.53	--	--	0.13	99.3	--	17	74	9
	SD (1σ)		0.7	--	1.2	0.04	--	--	0.47	0.85	0.63	--	--	0.05	--	--	--	--	--
	Kfsp	*23*	65.2	--	18.7	0.10	--	b.d.l.	0.20	2.79	11.6	--	--	1.08	99.6	--	1	26	72
	SD (1σ)		0.7	--	0.5	0.04	--	--	0.07	0.15	0.48	--	--	0.44	--	--	--	--	--
Exp 26	*Glass*	*29*	77.7	0.10	12.7	0.72	0.07	0.08	0.78	3.24	4.60	b.d.l.	0.11	--	94.6	5.7	--	--	--
760 °C, 150 MPa	*SD (1σ)*		0.18	0.03	0.15	0.05	0.04	0.02	0.03	0.10	0.10	--	0.01	--	--	0.2	--	--	--
Exp 27	*Glass*	*28*	77.7	0.11	12.8	0.69	b.d.l.	0.07	0.80	3.25	4.61	b.d.l.	0.12	--	94.1	5.5	--	--	--
780 °C, 150 MPa	*SD (1σ)*		0.24	0.03	0.18	0.06	--	0.02	0.03	0.11	0.11	--	0.02	--	--	0.4	--	--	--
Exp 15	*Glass*	*28*	77.4	0.08	13.18	0.63	0.06	0.06	0.79	3.20	4.58	b.d.l.	0.08	--	93.9	--	--	--	--
720 °C, 200 MPa	*SD (1σ)*		0.25	0.03	0.10	0.07	0.03	0.01	0.03	0.15	0.15	--	0.02	--	--	--	--	--	--
Exp 32	*Glass*	*29*	77.8	0.12	12.8	0.65	0.05	0.08	0.79	3.17	4.54	b.d.l.	0.09	--	93.2	--	--	--	--
740 °C, 200 MPa	*SD (1σ)*		0.17	0.03	0.15	0.06	0.04	0.02	0.04	0.16	0.14	--	0.02	--	--	--	--	--	--
Exp 12	*Glass*	*28*	77.4	0.09	13.2	0.69	0.06	0.07	0.79	3.20	4.54	b.d.l.	0.09	--	93.8	6.2	--	--	--
760 °C, 200 MPa	*SD (1σ)*		0.25	0.02	0.12	0.05	0.04	0.02	0.03	0.14	0.12	--	0.01	--	--	0.7	--	--	--
Exp 14	*Glass*	*27*	77.4	0.10	13.1	0.68	0.04	0.07	0.79	3.23	4.59	b.d.l.	0.04	--	93.4	5.5	--	--	--
780 °C, 200 MPa	*SD (1σ)*		0.18	0.02	0.15	0.06	0.03	0.01	0.03	0.17	0.11	--	0.01	--	--	0.4	--	--	--
Exp 28	*Glass*	*30*	77.7	0.07	13.3	0.59	0.04	0.04	0.81	2.77	4.63	b.d.l.	0.07	--	93.2	--	--	--	--
700 °C, 250 MPa	*SD (1σ)*		0.27	0.03	0.16	0.06	0.03	0.02	0.03	0.10	0.12	--	0.02	--	--	--	--	--	--
Exp 29	*Glass*	*30*	77.7	0.08	12.7	0.69	0.05	0.07	0.80	3.26	4.61	b.d.l.	0.08	--	92.6	--	--	--	--
714 °C, 250 MPa	*SD (1σ)*		0.21	0.03	0.16	0.07	0.04	0.02	0.04	0.11	0.11	--	0.02	--	--	--	--	--	--
Exp 31	*Glass*	*30*	78.0	0.09	12.7	0.71	b.d.l.	0.08	0.80	3.15	4.50	b.d.l.	0.08	--	93.1	6.4	--	--	--
740 °C, 250 MPa	*SD (1σ)*		0.22	0.03	0.15	0.08	--	0.02	0.04	0.11	0.11	--	0.01	--	--	0.2	--	--	--

[1]Phase compositions are averages of all EMP analyses; glasses are normalized anhydrous; original totals are presented

[2]Number of analyses

[3]All Fe reported as FeO (FeO_T for glasses)

[4]H_2O concentrations are measured by ATR-FTIR and are only presented for experiments with glassy pools large enough for analysis but without interferences from other phases

No glass data is presented for Exp 43 as glass pools were smaller than beam diameter

Analytical details available in ESM 4

Double dash indicates not applicable

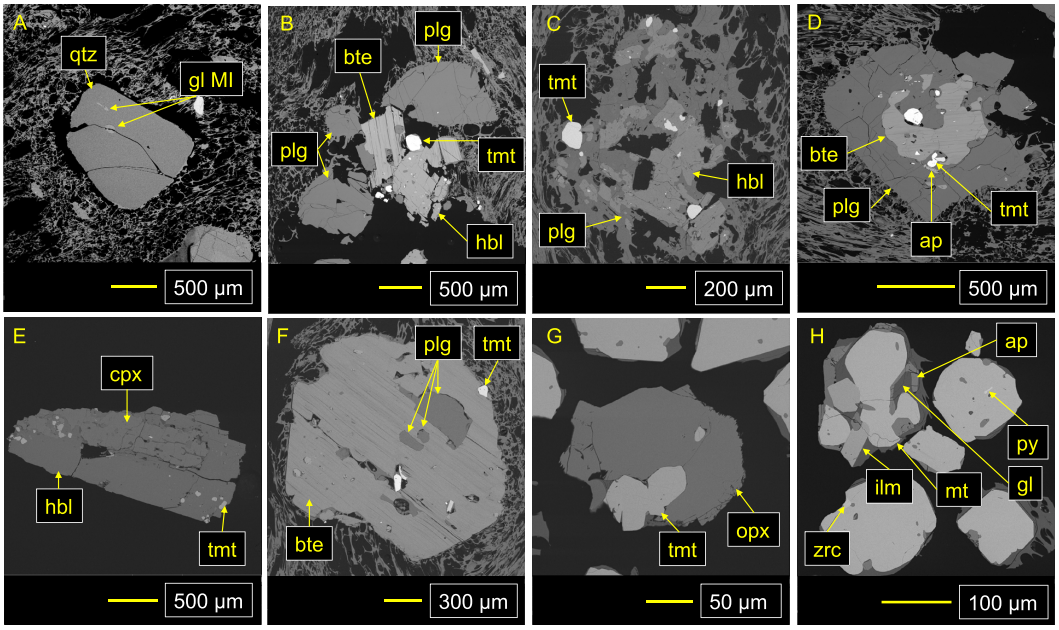


Fig. 3 Back-scattered electron (BSE) images of Earthquake Flat (EQF) pumices, *qtz* quartz; *plg* plagioclase; *bte* biotite; *ap* apatite; *tmt* titanomagnetite ± ilmenite (*ilm* ilmenite, *mt* magnetite, where identifiable); *hbl* hornblende; *cpx* clinopyroxene; *opx* orthopyroxene; *zrc* zircon; *py* pyrrhotite; *gl MI* glassy melt inclusion; **A** Quartz phenocryst in thin section with glassy melt inclusions, contrast adjusted to distinguish melt inclusions glass from quartz; **B** Plagioclase-biotite-hornblende phenocrystic cluster, phenocrysts in these clusters are ≥ 1 mm; **C** Plagioclase and hornblende micro-phenocryst cluster, micro-phenocrysts in this cluster are ~ 200μm; poikilitic hornblende grains are enveloped by plagioclase oikocrysts although individual grain boundaries are somewhat indistinct; **D** Plagioclase phenocryst with biotite sheet juxtaposed on top, both plagioclase and biotite phenocrysts contain titanomagnetite inclusions, plagioclase also contains apatite and glass inclusions; **E** Hornblende grain (grain mount), with inclusions of glass, titanomagnetite, apatite, zircon, and a resorbed clinopyroxene core (clinoferrosilite); **F** Biotite phenocryst in thin section with inclusions of plagioclase, titanomagnetite, and apatite; **G** Characteristic orthopyroxene phenocryst in a grain mount with titanomagnetite inclusions that display faintly visible exsolution lamellae; **H** Fe-Ti oxide (titanomagnetite and ilmenite) grain mount, the grain in the upper left corner shows the relationship between touching pairs of magnetite and ilmenite grains which were used for thermometry and oximetry

average $K_2O = 4.53 \pm 0.10$ wt.%) and are effectively identical to pumice glass compositions determined in the present study (Fig. 2). The samples analyzed by Molloy et al. (2008) were collected by those authors and by Davis (1985) from locations throughout the EQF stratigraphy; they present data from four samples from the upper stratigraphy, six samples from the middle stratigraphy, two samples from the lower stratigraphy, and six samples from the lowest/basal stratigraphy. Collectively, these results indicate that, excepting a trace K-rich component, EQF melt was uniform in composition across the ~ 10 km^3 of erupted magma. Because of high phenocryst contents, the average single-pumice composition is slightly less enriched in SiO_2 and K_2O (74.2 ± 0.2 wt.% SiO_2 and 3.15 ± 0.11 wt.% K_2O) than the glasses and has significantly higher concentrations of total Fe as FeO, MgO, and CaO. H_2O concentrations measured by ATR-FTIR in pumice glasses range from 1.4–1.9 wt.% H_2O (average 1.7 ± 0.1 wt.% H_2O) some of which could be from post-eruptive hydration but this was not assessed.

Quartz

Quartz grains range in size from 0.25 to > 2 mm, although many smaller quartz grains in thin section and in mineral separates appear to be shattered pieces of larger grains. Euhedral, bipyramidal quartz grains are commonly 1–2 mm across, although some rounded grains are present (Fig. 3A). The highest proportion of quartz grains are > 2 mm and tend to be anhedral shattered pieces of larger grains, suggesting that even larger grains existed prior to eruption. Almost all quartz grains have abundant inclusions of glass, apatite, zircon, or (and) opaque oxides; the exteriors of the grains have a pockmarked appearance (ESM 1).

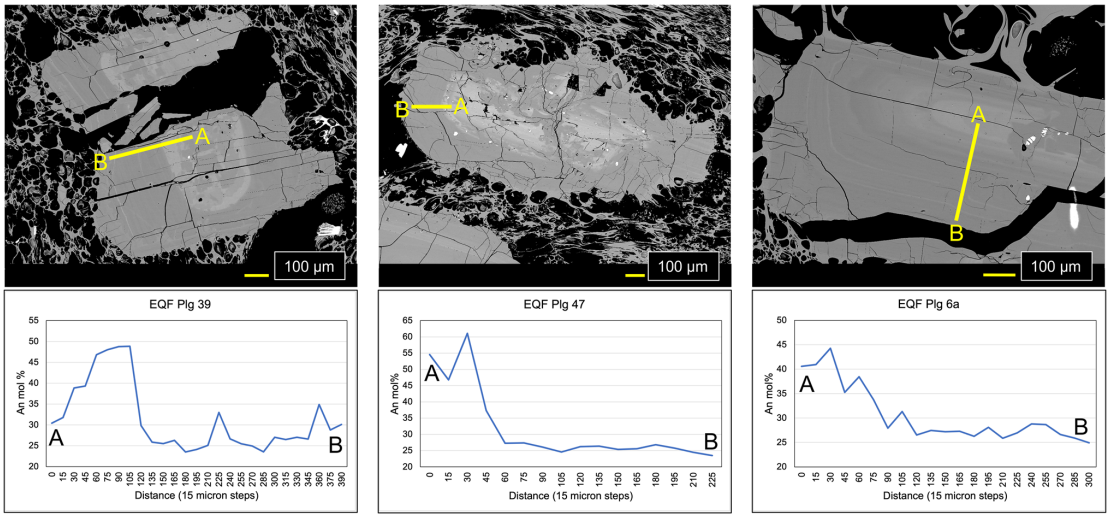


Fig. 4 Back-scattered electron (BSE) images of Earthquake Flat (EQF) plagioclase phenocrysts with core-rim analytical transects labeled (**A, B**) and corresponding anorthite content (mole percent An) vs. distance graphs below. Plagioclase rims are typically thick and faintly normally zoned with compositions of about $An_{30\text{-}24}$. Distinctly more calcic cores are common, in most cases with evidence of resorption prior to sodic overgrowth; EQF plg 39 shows patchy zoning in the core, and subtle resorption along the bright calcic core boundary; EQF plg 47 contains a calcic core with a distinct bright boundary, both show significant resorption textures; EQF plg 6a has a calcic core and subtle resorption textures.

Plagioclase

Most plagioclase grains are < 1 mm and occur as poly- and mono-mineralic glomerocrysts (Fig. 3B–D), although there is a less abundant population of individual plagioclase grains that are as large 2 mm. Most plagioclase crystals are subhedral and are commonly twinned. Many plagioclase crystals (Fig. 4) have narrow, resorbed, calcic cores, to An_{67}, overgrown over short distances by plagioclase zoned normally to ~ An_{25}, within thick sodic rims continuing that nearly constant composition to their margins (mole percent anorthite, An, is 100Ca/[Ca + Na + K]). Grain rims generally show subtle oscillatory zoning, some with rare, thin, calcic intervals, while most cores show oscillatory zoning and patchy zoning owing to resorption (Fig. 4).

Glomerocrysts

We identify two populations of glomerocrysts: (1) "large" (mineral grains 0.5–1 mm) plagioclase-dominated clusters which also contain quartz and mafic minerals (hornblende, biotite, oxides, and rare orthopyroxene), and which are easily identifiable in thin section, but which are not well preserved in mineral separates (ESM 1); and (2) "small" (mineral grains < 0.25 mm) clusters dominated by plagioclase and hornblende (ESM 1). The "small" clusters are rarely observed in thin section but are relatively common in mineral separates.

Biotite

Biotite grains are large (0.5–2 mm) and euhedral, commonly forming thick books (≤ 1.5 mm) with characteristic hexagonal habits (Fig. 3F). Most biotite grains occur individually within vesicular glass, but some occur in the "large" glomerocrystic clusters. Biotite cores and rims have nearly homogenous compositions with Mg# of cores = 47–51 and those of rims = 46–51 (Mg# is 100 Mg/[Mg + Fe], molar, employing total Fe).

Hornblende

Amphibole grains are large (0.5–2 mm), euhedral, and commonly prismatic. Pleochroism ranges from light green to dark brown. They occur as sparse individual grains within vesicular glass and abundantly in both populations of glomerocrysts (Fig. 3B, 3C, 3E; ESM 1). The amphiboles are magnesio-hornblende (Hawthorne 1981) approximating their ferric iron concentrations as the average of all-ferrous and 13eCNK methods. Hornblende compositions are relatively homogenous with cores ranging from Mg # = 56–57 and rims ranging from Mg # = 55–58. Molloy et al. (2008) reported transect and spot analyses of EQF hornblendes and

an overall tendency for Al_2O_3 concentrations to increase modestly from grain cores to rims, an attribute those authors interpret as evidence that temperatures increased as the hornblendes grew. Excluding one outlier low-Al_2O_3 analysis, the average Al_2O_3 concentrations of hornblende rims (within 100 µm of grain edges), and their standard deviations, are similar for that and the present study (6.49 ± 0.37 and 6.35 ± 0.48 wt.%, respectively). No cummingtonite has been observed in any EQF samples.

Fe-Ti Oxides

Titanomagnetite and ilmenite are abundant as individual grains in vesicular glass, in glomerocrysts, and as inclusions in other minerals (Fig. 3G, 3H). Two populations of euhedral titanomagnetite-ilmenite pairs were examined for temperature and fO_2 determinations: 1) touching pairs in contact with glass and 2) euhedral grains within glass separated by no more than 25 µm. Both touching pairs and pairs separated by glass (n = 8) yield temperatures of 694–722 °C (average 703 °C) by the Ghiorso and Evans (2008) calibration, 718–746 °C (average 733 °C) by Lepage ("ILMAT", 2003), and 708–731 °C (average 714 °C) by Andersen et al. (1993) ("QUILF") (Fig. 7). Average oxide compositions are X_{ulsp} mol = 0.275 and X_{ilm} mol = 0.926 (n = 8). All grains pass the Mg/Mn partitioning test of Bacon and Hirschmann (1988) within the 2 σ uncertainty envelope. Titanomagnetite-ilmenite pairs yield fO_2 estimates between Δ Ni–NiO = 0 to − 1, which guided our choice of experimental fO_2 buffering (ESM 1). Trellis and lamellar intergrowths of titanomagnetite and ilmenite are also present and result from oxidation (Buddington and Lindsley 1964), probably during deposit cooling, and are excluded from consideration. Molloy et al. (2008) reported compositions of 29 titanomagnetite-ilmenite pairs that, employing the Ghiorso and Evans (2008) calibration, yield a wider range and higher average temperature: 702–805 °C (average 748 ± 24 °C), including 705–778 °C for pairs within a single pumice. The principal difference is that TiO_2 concentrations of the Molloy et al. (2008) Fe-Ti oxides average ~ 5 relative % lower than those in the present study; average Fe-Ti oxide compositions are otherwise effectively identical in the two studies. The disparity in TiO_2 concentrations, and therefore in derived temperatures, may result from a standardization difference, since mineral and glass compositions were determined by Molloy et al. (2008) with energy-dispersive (EDS) methods on a scanning electron microscope that are less precise and accurate than the wavelength-dispersive electron-microprobe methods employed herein.

Orthopyroxene

Rare orthopyroxene microphenocrysts are present as euhedral to anhedral grains and range from 0.1–0.25 mm with a range of textures (Fig. 3G). Common orthopyroxene textures include ragged edges, broken grains, and sieved cores. Compositionally, orthopyroxene grains are nearly identical across cores (En_{48}) and rims (En_{50}) (En = 100 Mg/[Mg + Fe + Ca], molar, employing total Fe).

Inclusions in ferromagnesian phases

All mafic mineral phases contain diverse inclusions. Hornblende and biotite contain abundant inclusions of glass, apatite, zircon, and titanomagnetite-ilmenite. Notably, we have observed a hornblende grain with a clinopyroxenitic core (Fig. 3E), and biotite grains with plagioclase inclusions (Fig. 3F). Titanomagnetite grains have inclusions of glass, apatite, zircon, and pyrrhotite (Fig. 3H). Orthopyroxene grains have the fewest inclusions but still contain devitrified glass, titanomagnetite, and apatite.

Melt inclusions and embayments

Melt inclusions are present in nearly all mineral phases. Those in quartz and plagioclase range from glassy to fully devitrified, whereas those in mafic minerals are almost all devitrified or contain significant post-entrapment crystals grown along host-mineral boundaries. In quartz, there are both melt inclusions and melt embayments. The melt inclusions are large (≤ 200 µm), rectangular in cross section, and are partially or entirely devitrified (ESM 1). We attempted reconnaissance analyses of H_2O concentrations in the quartz-hosted melt inclusions by ATR-FTIR and obtained diverse results from 0.8 to 6.0 wt.% H_2O, with an average of 3.9 ± 1.7 wt.% H_2O. The higher H_2O concentrations may have been influenced by crystallization of anhydrous minerals, thereby concentrating H_2O in the melt, whereas the low concentrations could result from inadvertent analysis of inclusions that were not fully sealed and so partly degassed upon eruption; post-eruptive hydration of incompletely sealed inclusions is also possible. A focused study of acid-treated quartz grains to isolate truly sealed inclusions, coupled with experimental re-homogenization of those so identified, would be necessary to better understand the dissolved H_2O concentrations at the time of entrapment. The quartz–hosted embayments are elongate and almost always glassy (ESM 1) with H_2O concentrations ranging from 0.6–1.9 wt.% H_2O (average 1.2 ± 0.3 wt.% H_2O) and SiO_2 between 77.1 and 77.9 wt.% (average 77.7 wt.% SiO_2), both of which are similar to the host glass (Table 3). Since the matrix glass and the melt embayments were exposed to the surficial environment for ca. 45 kyrs, hydration is likely

to have raised H_2O concentrations of both. Assessing hydration would require measurements by transmission FTIR to distinguish molecular H_2O from that dissolved as hydroxyl groups, or by measurements of stable isotopes of glass. Plagioclase-hosted melt inclusions are an order of magnitude smaller (10 s of μm in size) than the quartz-hosted melt inclusions and are restricted to the interior zones of the grains (ESM 1). We observe hundreds of small melt inclusions clustered into arrays, just outside of heavily resorbed zones. Resorbed surfaces are effective substrates for new melt inclusion development and entrapment (Lowenstern and Thompson 1995), which are then efficiently captured within the grain by subsequent plagioclase growth (ESM 1). We were unable to measure H_2O concentrations in plagioclase-hosted melt inclusions due to size limitations, but other studies report H_2O concentrations (3.4–7.5 wt.% H_2O, Smith et al. 2010), which are further supported by volatile solubility models.

Experimental results

The unaltered EQF pumice glass composition (Tables 1 and 3) was chosen and carefully refined as the starting material for this experimental study as it is representative of the melt composition present in the majority of EQF magma immediately prior to eruption. The goal of the approach is to identify the conditions at which that melt is multiply saturated on its liquidus with the major minerals present in the natural pumice, and with the natural compositions for those minerals capable of solid solution. By comparing our experimental results to the EQF pumice, we can resolve the pressure and temperature, assuming H_2O saturation and oxygen fugacity, of the magma body immediately prior to eruption. We present experimental results, including phase assemblages and proportions (where feasible) in Table 2 and phase compositions in Table 4. We could not adequately quantify the phase compositions or proportions for low pressure/temperature experiments #16 and #43 due to small crystals (< 1 μm) and melt pools (< 10 μm). As our experiments were loaded with H_2O in amounts exceeding saturation, and the runs products contain vapor bubbles, we estimated H_2O concentrations dissolved in melt (glass) as: H_2O by difference from microprobe analysis (Table 2), H_2O measured directly by ATR-FTIR (Table 2 and ESM 3), and H_2O estimated from volatile solubility models assuming saturation with pure H_2O (Ghiorso and Gualda 2015; Liu et al. 2005; Moore et al. 1998; Iacovino et al. 2021) (Table 2).

Approach to equilibrium

The combination of long experimental durations, precise temperature and pressure calibrations and control, successful fO_2 buffering (Δ Ni–NiO = 0 with all buffer components present after a given experiment was completed), H_2O saturation, and consistent phase appearances and shifts in mineral composition point to a close approach to equilibrium conditions. Nineteen experiments were brought directly to experimental conditions, and to confirm the stability limits for quartz and plagioclase, four reversal experiments were held above the liquidus and then brought to the conditions of prior direct syntheses (Table 2). These reversals produced the same phase assemblages and abundances as the direct-to-temperature experiments, thereby confirming quartz and plagioclase stability limits. Phase compositions and abundances change systematically with temperature and pressure as shown by plagioclase anorthite content, with isopleths subparallel to the plagioclase stability curve (Fig. 5). All of our synthesis conditions were above the H_2O-saturated haplogranitic solidus, although two experiments (#16 at 100 MPa/720 °C, and #43 at 50 MPa/750 °C) were highly crystalline with low melt abundances, suggesting that these conditions were very near the solidus (> 95 vol.% crystallinity).

Phase stability

Mineral stability curves are plotted relative to phase appearance at specific synthesis conditions (Fig. 5). Five of the experimental charges were sufficiently above the liquidus such that they did not saturate with any of the major silicate minerals despite the long duration run times. These syntheses (12, 14, 26, 27, and 31) contain only melt (glass), rare relict apatite and zircon, and H_2O vapor (vesicles). Plagioclase is the highest temperature silicate mineral at low pressure but is replaced by quartz and biotite at pressures ≥ 140 MPa. K-feldspar is the lowest temperature silicate mineral and the last silicate mineral to join the crystallizing mineral assemblage upon cooling. At high pressure (≥ 200 MPa) and low temperature (< 710 ºC), plagioclase overtakes K-feldspar as the lowest temperature silicate mineral. For the investigated range in pressure and temperature conditions, the mineral appearance curves have negative slopes. Plagioclase has the shallowest negative slope, approximately – 1.25 °C/MPa. K-feldspar has a steep negative slope, approximately – 5.8 °C/MPa, between 250 and 75 MPa, but shallows to a slope of – 0.5 °C/MPa between 75 and 50 MPa. Quartz has a slope of – 3 °C/MPa between 225 and 75 MPa, and shallows to a slope of – 2.5 °C/MPa. Biotite has a slope of – 8.75 °C/MPa. Below 75 MPa the biotite curve is dashed to approximate the well-established behavior of biotite at low pressures in which the saturation curve

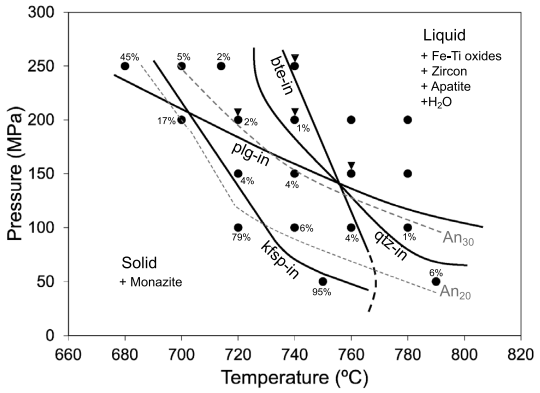


Fig. 5 Experimentally derived pressure–temperature phase diagram for Earthquake Flat (EQF) melt, H_2O-saturated, at Ni–NiO fO_2; black circles show syntheses brought directly to pressure and temperature, and black triangles indicate reversals at the conditions of the adjacent direct syntheses. Black lines represent mineral saturation limits, with labels: qtz (quartz), kfsp (K-feldspar), plg (plagioclase), bte (biotite); all runs contain relict Fe-Ti oxides, zircon, and apatite which are stable at the experimental run conditions in this study. Crystallinity estimates (wt.%) are presented next to respective syntheses; trace amounts of titanomagnetite ± ilmenite, zircon, and apatite are present hotter than the plagioclase, biotite, and quartz saturation limits. Compositions of synthesized plagioclase (mole % anorthite, An) are contoured in dashed gray

transitions to a positive slope (Piwinskii and Wyllie 1968; Gardner et al. 2014; Waters and Andrews 2016; First et al. 2021). The quartz, biotite, and plagioclase saturation curves intersect at ~ 140 MPa and ~ 755 °C. Given the spacing in our synthesis conditions (50 MPa and 20 °C steps), there is a small amount of imprecision in the exact conditions of the quartz–plagioclase–biotite saturation curve intersection point, but the steep slope defined by the biotite-in curve anchors the intersection to 140 ± 10 MPa and 755 ± 5 °C.

Experimental phase descriptions

Characteristic images of experimental phases are presented in Fig. 6. Table 4 presents the compositions of the experimentally synthesized glass and feldspars. Synthesized quartz grains have euhedral, sharp rims, equant habits, and range from 1–10 µm. Quartz grains are nearly indistinguishable from the glass in back-scattered electron (BSE) images except for their relatively bright rims (an edge-effect artifact in high-contrast BSE imaging). Some relict plagioclase grain fragments from the glass concentrate starting material are present in the experimental products and are distinguished by their angular shapes and sizes atypically larger than newly synthesized plagioclase grains. Newly synthesized plagioclase grains are euhedral to subhedral with sharp boundaries, where grown as individual grains, and new grains commonly nucleated on and/or overgrew relict plagioclase grains (< 100 µm) (Fig. 6B); minor numbers of plagioclase grains are skeletal (Fig. 6B). Traces of relict plagioclase grains are present above the depicted plagioclase saturation curve in experiments brought directly to pressure and temperature and are distinguished as unstable by their rounded edges, dissolved portions of grains, and lack of overgrowths or coexisting homogeneously nucleated plagioclase grains. Such relict grains are absent from reversal experiments initially brought to superliquidus conditions, confirming the location of the plagioclase saturation curve. K-feldspar grains are euhedral with sharp grain edges and equant to tabular habits ranging from 1 to 20 µm in length. In several runs, K-feldspar overgrew the rims of relict plagioclase grains (Fig. 6A) and, in some instances, encase an entire relict grain (Fig. 6B). Individual K-feldspar grains also commonly encase other co-precipitating phases, and in higher pressure experiments (≥ 200 MPa) they exhibit sector zoning indicating rapid growth (Fig. 6C). Compositions of synthesized plagioclase and K-feldspar range from $An_{13\text{-}29}$, and $Or_{49\text{-}73}$(Or is 100K/[Ca + Na + K + Ba]) respectively, with plagioclase grains decreasing in anorthite component approaching the solidus (Fig. 5). K-feldspar in melt-poor, near-solidus experiments (#43 at 50 MPa/740 °C and #16 at 100 MPa/720 °C) has compositions of $Or_{55\ \&\ 49}$, whereas K-feldpsar in somewhat cooler but higher pressure and more melt-rich experiments (#11 at 200 MPa/700 °C and #42 at 250 MPa/680 °C) are $Or_{73\ \&\ 72}$. Biotite grains form thin laths < 5 µm in length, and < 1 µm in width (Fig. 6A–C, E) and were too small to analyze quantitatively by EMP; however, biotite was confirmed by EDS, as well as by their characteristic tendency to erode preferentially during polishing. Mineralogy of the natural EQF pumices indicate that hornblende and orthopyroxene should also be members of the equilibrium assemblage, but we did not identify either mineral in our experiments despite extensive, high-magnification examination by EDS. Absence of hornblende and pyroxene are discussed subsequently. Fe-Ti oxide grains are < 1 µm, too small for quantitative analyses, but their identities as titanomagnetite and ilmenite were confirmed by EDS. Since magnetic methods were included in purifying the natural glass, these Fe-Ti oxides are unlikely to be relicts from the natural pumice. Traces of relict apatite and rare relict zircon are also observed in some of the run products, and micron-scale monazite was found in the four most crystalline experiments (#16 at 100 MPa/720 °C, #43 at 50 MPa/750 °C, #42 at 250 MPa/680 °C, #11 at 200 MPa/700 °C). As monazite is not part of the EQF pumice mineral assemblage, and it only appeared in run products much more crystallized than the natural pumice, the monazite grains were synthesized and are not relicts. Additionally, upon finding monazite and subsequently examining phases with high backscatter brightness at high magnification, we found a few exceptionally sparse,

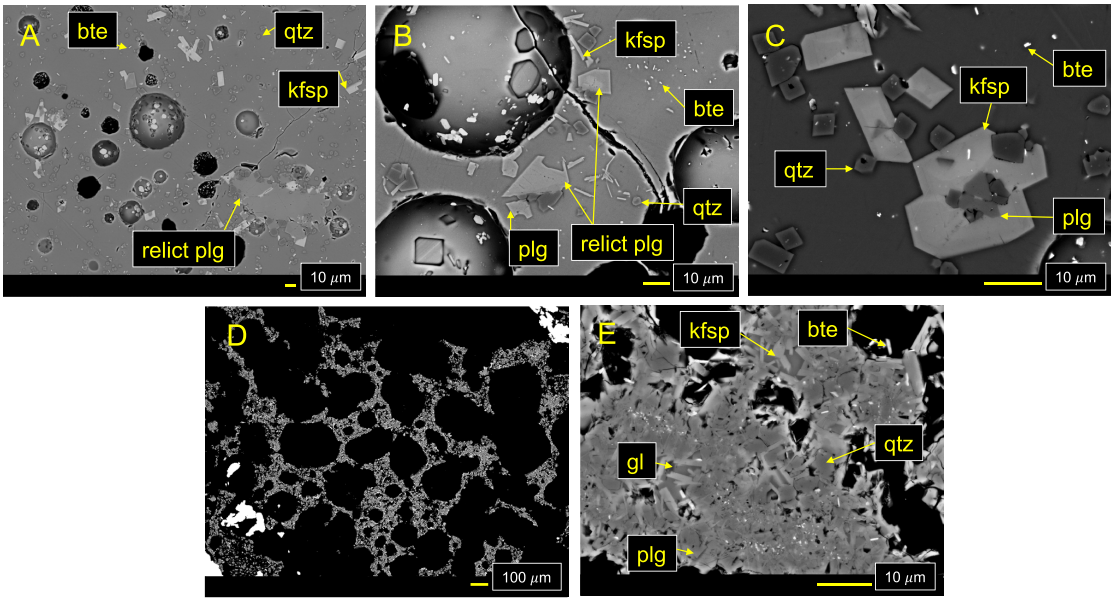


Fig. 6 Characteristic back-scattered electron (BSE) images of experimental products, *qtz* quartz; *kfsp* K-feldspar; *plg* plagioclase; *bte* biotite; *gl* glass. **A** Run 11, 200 MPa, 700 ºC; Experimentally grown quartz, plagioclase, K-feldspar, and biotite. Relict feldspar grain (~60 *μm*, irregular shaped grain in bottom right corner of image) provides nucleation site for synthesized grains. **B** Run 18, 100 MPa, 740 ºC; Plagioclase, quartz, K-feldspar, and biotite (shown polished and inside a vesicle), synthesized plagioclase is visible on relict plagioclase cores. **C** Run 42, 250 MPa, 680 ºC; Early saturated plagioclase and quartz armored by later saturating K-feldspar, bright white grains are biotite. **D** Run 43: 50 MPa, 750 ºC; Large-scale capsule view showing minerals crystallizing in a melt (lacy patchwork) and an exsolved vapor phase (rounded void spaces), bright white amorphous blebs are gold pieces from capsule wall. **E** Run 16, 100 MPa, 720 ºC; Extremely low-melt "plutonic" phase assemblage and textures

sub-micron specks of a tungsten-rich phase in a few experimental products. These lack a Ca peak on EDS spectra, so they are not scheelite. They are probably WO_3 derived from traces of the lithium heteropolytungstate employed in separating the glass. Their exceptionally low abundance, along with the saturation with H_2O that would absorb lithium, are evidence that the trace contaminant would not have affected phase stability within the resolution of our study.

Phase proportions

Phase proportions were calculated by linear least-squares multiple regression (Table 2) mass-balancing the composition of the average super-liquidus glass with those of coexisting minerals and melt all measured by electron microprobe. H_2O was included as a phase and component in the linear regressions since experimental capsules were loaded with more than sufficient H_2O to saturate the melt at run conditions, and the runs were pressurized with water throughout their durations. Four near-liquidus experiments (#s 28, 29, 40, and 41) returned inconsistent phase-proportion results but superior results were obtained using the XRF-determined glass as the bulk composition (ESM 1). Attempts to measure phase proportions by processing X-ray elemental maps failed owing to an inability to set thresholds that consistently differentiated between glass, quartz, and feldspars. Crystallinity is low (< 10 wt.%) for about 40–60 °C below the silicate liquidus and then increases sharply once K-feldspar joins the assemblage. For example, syntheses 18 and 16 differed only by 20 °C (740 vs. 720 °C at 100 MPa), yet the crystallinity of their products differ by 73 wt.% (6 and 79 wt.% crystals, respectively). The abrupt increase in silicate minerals (plagioclase, K-feldspar, quartz) approaching the solidus excludes biotite. For all syntheses, biotite was ≤ 1 wt.% of total products.

Discussion

Experimental studies of high-silica rhyolitic compositions are relatively few in comparison to their more mafic counterparts. Slow diffusivity in silicic melts inhibits nucleation and crystal growth, requiring long experimental durations which can be difficult to sustain, especially with appropriate fO_2 buffering. Nucleation and crystal-growth issues in such experiments extend to the analytical realm where small

crystal sizes hinder reliably analyzing phase compositions. Although challenging, such studies are important because petrologic tools such as thermometers, barometers, and thermodynamic models are calibrated on experimental results, and limited work in high-silica rhyolites could lead to inaccurate extrapolations. To improve our fundamental understanding of these potentially highly explosive systems and to test and calibrate models, it is important to produce quality high-silica rhyolitic experimental data. Our experimental results determine the co-saturation conditions of quartz, plagioclase, and biotite, all of which grew in equilibrium between 75–200 MPa and 710–760 ºC. Notably, the three stability curves intersect on the natural melt's H_2O-saturated liquidus at 140 ± 10 MPa and 755 ± 5 ºC with minimal uncertainty since the three curves are well defined by experimental constraints and differing pressure–temperature slopes (Fig. 5). Despite the EQF tuff's large erupted volume, its melt was nearly homogenous, matching that employed for the experiments, and all the EQF rhyolitic tuffs contain at minimum quartz, sodic plagioclase, biotite, and Fe-Ti oxides. Collectively, these observations and results indicate that the experimentally determined pressure–temperature conditions are representative of those that prevailed across much of the immediately pre-eruptive EQF magma reservoir. Based on these findings, we explore how these conditions compare to those estimated from other petrologic methods and models and consider the implications of these storage conditions for the assembly and eruption of the EQF magmatic system.

Thermometry

Fe-Ti oxide pairs in the EQF pumice samples provide estimates of pre-eruptive temperatures. Fe-Ti oxide compositions are sensitive to changes in temperature and oxygen fugacity and, due to rapid elemental diffusion at magmatic temperatures, can reset their recorded temperatures to conditions shortly prior to eruption; times to re-equilibrate are by some estimations on the order of days to months (Devine 2003; Hammond and Taylor 1982; Venezky and Rutherford 1999). Figure 7 illustrates the range in the temperatures calculated from five different geothermometers, which should caution against overinterpreting the accuracy of the results given the relatively small temperature range (694–761 ºC). While the precision is relatively good for the presented thermometry, the accuracy is less well understood as demonstrated by the dispersion in each set of calculated thermometry data, which itself is a function of the calibration of each thermometer.

The basic observation (Fig. 7) is that temperatures derived with various calibrations of the Fe-Ti oxide-exchange reaction are on average lower than that determined experimentally by tens (Powell and Powell 1977; Andersen and Lindsley 1985) to a few tens of degrees (Spencer and Lindsley 1981; Andersen et al. 1993), to as much as 40–50 degrees (Ghiorso and Evans 2008). The spread in derived temperatures is also greater for the newer calibrations. Higher temperatures can be derived with the Fe–Mg exchange reaction, and although Ghiorso and Evans (2008) interpreted that such a divergence in temperatures may reflect disequilibrium within a magma body, Mg concentrations are low in the Fe-Ti oxides of silicic magmas, including those of EQF, hindering their accurate and precise analysis. Commencing with Buddington and Lindsley (1964), experimental studies have focused mainly on the Fe-Ti oxide-exchange reaction owing to those elements' higher concentrations and that reaction's ability to provide information on oxidation state, so the Fe-Ti oxide-exchange reaction is also more solidly calibrated. For these reasons, most published studies rely on the Fe-Ti results, as do we herein. As noted previously, titanomagnetite and ilmenite compositions presented by Molloy et al. (2008) for the EQF have TiO_2 concentrations about 5 relative % lower than those determined herein and yield temperatures closer to the experimental determination. This highlights the sensitivity of Fe-Ti oxide temperature determinations to the accuracy of oxide analyses, probably also in the calibrating experiments. Given these factors, we refrain from assigning geological significance to the temperature difference between our experimental determination for the EQF magma and those provided by the various Fe-Ti oxide models.

Molina et al. (2021) presented a new amphibole–plagioclase geothermometer, which updates previous iterations, such as the plagioclase–amphibole model of Holland and Blundy (1994). Using the pressure-independent Molina et al. (2021) expression, EQF samples yield temperatures averaging 703 and 696 °C for amphibole rim compositions of this study and Molloy et al. (2008), respectively (Fig. 8). Molina et al. (2021) stated the precision of the geothermometer as approximately ± 50 °C, so the calculated temperatures do not strictly differ from the experimental determination of 755 ± 5 °C. A further caution is that only 15 of the 203 experimental amphibole–plagioclase pairs used to calibrate and validate the geothermometer have plagioclase ≤ An_{30}, similar to plagioclase rims in the EQF and many other rhyolites, so application to rhyolites is at the compositional limit of the geothermometer's calibration. Although we did not recognize amphibole in our synthesis products, hornblende grains in the EQF pumice samples are large, euhedral, and lack breakdown rims so they were probably stable up to the time of eruption as part of the equilibrium assemblage. Molloy et al. (2008) documented modest rim-ward increases in Al_2O_3 concentrations of some EQF amphibole phenocrysts that those authors interpret as evidence that magmatic temperatures increased as the amphiboles grew. Perhaps, but the lack of research on amphibole chemistry (especially under different oxygen fugacity conditions) urges circumspection. A robust study quantifying how

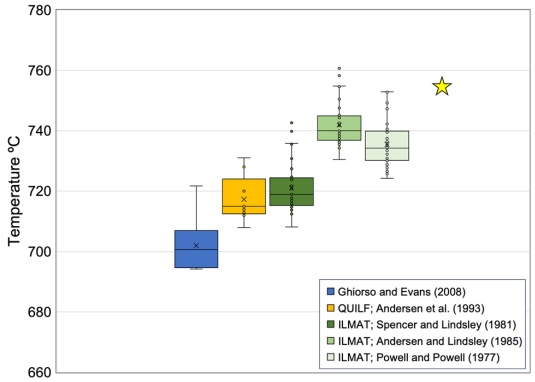


Fig. 7 Comparison of Earthquake Flat (EQF) temperatures derived with various Fe-Ti oxide calibrations. Each thermometer uses titanomagnetite-ilmenite compositions from oxide pairs ($n=8$) that pass the Mg/Mn test plot. The box and whisker plots show the average (black ×), median (black line), and first and third quartile ranges of the derived temperatures with the individual results plotted as open circles, the whiskers represent the upper and lower adjustment values (boundaries at which all other values are considered outliers), outliers are determined as any value that exceeds 1.5 times the interquartile range. From left to right: (1) (dark blue) Ghiorso and Evans (2008) yields an average of 703 ºC and a range of 694–722 ºC; (2) (yellow) Andersen et al. 1993 (QUILF) yields an average of 714 ºC and a range of 708–731 ºC; (3) (dark green) Spencer and Lindsley (1981) and Lepage (2003) yields an average of 721 ºC and a range of 718–726 ºC; (4) (medium green) Andersen and Lindsley (1985) and Lepage (2003) yields an average of 742 ºC and a range of 739–746 ºC; (5) (light green) Powell and Powell (1977) and Lepage (2003) yields an average of 736 ºC and a range of 732–738 ºC; the yellow star marks our experimentally derived storage temperature at 755 ± 5 ºC

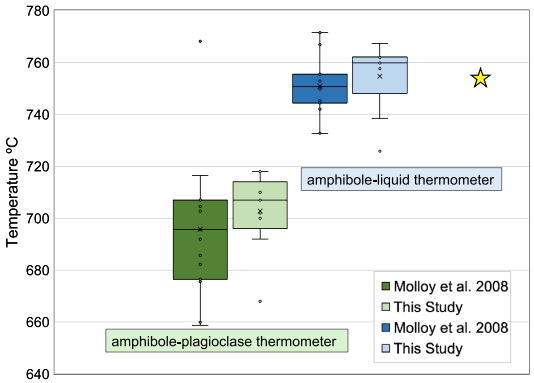


Fig. 8 Earthquake Flat (EQF) amphibole-plagioclase and amphibole-melt temperatures derived with the expressions of Molina et al. (2021) and Putirka (2016), respectively. The box and whisker plots show the average (black ×), median (black line), and first and third quartile ranges of the derived temperatures with the individual results plotted as open circles, the whiskers represent the upper and lower adjustment values (boundaries at which all other values are considered outliers), outliers are determined as any value that exceeds 1.5 times the interquartile range. Dark green symbols are amphibole-plagioclase temperatures using mineral compositions from Molloy et al. (2008) ($n=15$); light green symbols are amphibole-plagioclase temperatures using mineral compositions from this study (n = 10); dark blue symbols are amphibole-liquid temperatures using amphibole and glass compositions from Molloy et al. (2008) ($n=15$); light blue symbols are amphibole-liquid temperatures using amphibole and glass compositions from this study ($n=10$); the yellow star marks the experimental results at 755 ± 5 ºC

tetrahedral alumina behaves at different P–T-fO_2 conditions is necessary in order to interpret such slight gradients in Al_2O_3 concentration. The Putirka (2016) amphibole–liquid geothermometer estimates the temperatures at which amphiboles may have been in equilibrium with host melt. Using the Putirka (2016) geothermometer, amphibole rim and glass compositions from this study and from Molloy et al. (2008) yield apparent equilibration temperatures averaging 755 ± 53 and 751 ± 53 °C, respectively. Again, within uncertainties, these overlap with amphibole–plagioclase and the directly determined experimental temperatures for the EQF magma body (Fig. 8). While the EQF magma body may have increased in temperature approaching its eruption (Molloy et al. 2008), the uniform composition of its erupted melt and the consistency of its phenocryst assemblage are evidence that temperatures were at or close to the experimentally determined value of 755 °C across the wide portions of the magma body that erupted.

Barometry

Melt inclusion barometry effectively provides the pressure that an inclusion of melt was entrapped within its crystal host, contingent on the melt having been saturated with an H_2O–CO_2 vapor; such pressures can be converted to approximate depths employing a mean density for overlying magma and roof rocks. These depths can be those of magma accumulation and storage before eruption, although complexities include the melt may not have been vapor saturated, some melt inclusions may have entrapped deeper than the site of storage, other inclusion-bearing crystals may have been entrained from shallower levels during eruption, as well as the prosaic issue that incompletely sealed inclusions can go unrecognized and if analyzed give aberrant low pressures owing to eruptive partial degassing. Nevertheless, inclusion-derived pressures are plausible proxies for those of magma storage if melt inclusions are present in late-crystallizing quartz and feldspar crystals, if compositions of included melts are similar to that of co-erupted host glass, and if the inclusions give consistent results. There are very few melt-inclusion-derived volatile concentration determinations for EQF, but abundant determinations are available for the

nearby Rotoiti system, allowing assessment of whether magmas of the two systems resided at similar depths prior to eruption. Using the Liu et al. (2005) solubility model, a study by Johnson et al. (2013) derived Rotoiti entrapment pressures of 76–147 MPa. A similar study by Bégué et al. (2014) used the rhyoliteMELTS geobarometer of Gualda and Ghiorso (2014) to estimate pressures where Rotoiti inclusion glasses could be melts in equilibrium with quartz, plagioclase, and H_2O-vapor, obtaining 75–223 MPa. In this study, we use melt inclusion compositions presented in Smith et al. (2010) and the MagmaSat model of Ghiorso and Gualda (2015) to estimate Rotoiti entrapment pressures isothermally (740 ºC), yielding 81–261 MPa. Such pressures equate to shallow crustal depths, as is found in studies of the products of other explosive silicic eruptions and that are expected from the Rotoiti caldera environment. The derived pressure ranges are relatively large, however, reaching particularly low values, but the significance of those low values is unclear for the complexities previously presented and cannot be assessed without further focused study.

Mutch et al. (2016) presented an updated iteration of Al-in-amphibole barometry, which uses compositions of near-solidus amphiboles co-saturated with plagioclase, quartz, and melt to calculate an equilibration pressure; this expression has an estimated minimum uncertainty of ± 60 MPa based on the limiting precision of Al analyses in amphiboles. EQF amphibole rim compositions from this study and Molloy et al. (2008) yield pressures of 168–233 and 150–202 MPa, respectively (Fig. 9). We also derive pressures for the small volume, uppermost Rotoiti deposits, which are similar in mineralogy and composition to EQF (trace biotite and hornblende, absence of cummingtonite) (Schmitz and Smith 2004), yielding crystallization pressures of 105–552 MPa, which includes outliers. Excluding outliers, the barometer gives pressures of 179–282 MPa. The similarity of the Al-in-amphibole derived pressures supports that the hornblende in Rotoiti and EQF crystallized at similar shallow, sub-caldera depths, and as with temperatures, the pressures are indistinguishable within formal uncertainty with the experimental determination of 140 ± 10 MPa.

Absence of experimental hornblende and orthopyroxene

As mentioned, we did not observe synthetically grown hornblende or orthopyroxene in our experimental products, despite those minerals being relatively large, well formed, and compositionally little zoned in the natural pumice. The only hydrous Fe–Mg silicate that we produced was biotite, which was too small to analyze quantitatively by EMP, but which was confirmed by EDS spectra. Probable causes for the absence of hornblende and orthopyroxene are either that the natural melt employed as starting material is too evolved to grow those minerals appreciably upon cooling below the liquidus, despite their

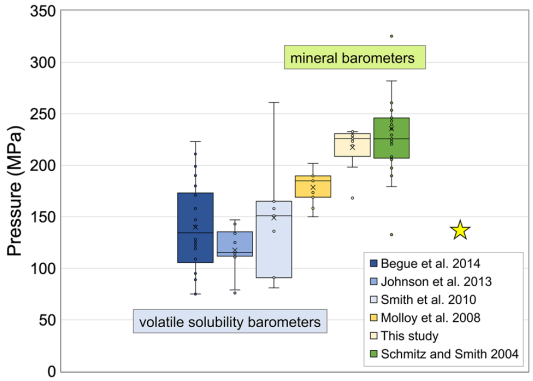


Fig. 9 Distribution of pressures derived from Earthquake Flat (EQF) and Rotoiti melt inclusions and amphibole compositions. Pressures are derived assuming melt inclusions were saturated with mixed H_2O–CO_2 fluid and assuming amphibole was a near-solidus mineral employing the geobarometer of Mutch et al. (2016); plot definitions are the same as in Fig. 7. From left to right, dark blue symbols: Rotoiti melt inclusion vapor-saturation pressures from Bégué et al. (2014) using the Gualda and Ghiorso (2014) RhyoliteMELTS solubility model ($n = 22$); medium blue symbols: Rotoiti melt inclusion vapor-saturation pressures from Johnson et al. (2013) using the Liu et al. (2005) volatile solubility model ($n = 12$); light blue symbols: Rotoiti melt inclusion vapor-saturation pressures using results of Smith et al. (2010) calculated with the solubility model of Ghiorso and Gualda (2015), modeled here isothermally at 740 °C ($n = 7$); dark yellow symbols: pressures for EQF amphibole rim compositions of Molloy et al. (2008) ($n = 11$); light yellow symbols: pressures for EQF amphibole rim compositions of this study ($n = 10$); green symbols: pressures for amphibole compositions from the upper Rotoiti unit (Schmitz and Smith 2004) ($n = 31$); the yellow star shows the experimental result, 140 ± 10 MPa

being equilibrium phases, or that those minerals are equilibrium phases but are in reaction relation with the natural EQF melt to produce biotite. Consistent with these hypotheses is that hornblende generally disappears in common arc granitoids as whole-rock SiO_2 concentrations exceed 70–72 wt.% (Dodge et al. 1982), and evidence for a reaction relation between hornblende and biotite is long known from petrographic observations of plutonic rocks (Speer 1987). First et al. (2021) presented BSE images and other experimental evidence for an orthopyroxene to biotite reaction in the presence of rhyolitic melt. It's possible to write many amphibole to biotite reactions owing to the many amphibole endmembers, but two simple H_2O conservative ones are:

$$KAlSi_3O_{8(sanidine,melt)} + Ca_2\left(Mg,Fe^{2+}\right)_3Al_2Si_6Al_2O_{22}(OH)_{2(tschermakite)} = 2\,CaAl_2Si_2O_{8(plagioclase)} + K\left(Mg,Fe^{2+}\right)_3AlSi_3O_{10}(OH)_{2(biotite)} + 2\,SiO_{2(quartz)}$$

and:

$$KAlSi_3O_{8(sanidine,melt)} + Ca_2Fe_5^{2+}Si_8O_{22}(OH)_{2(ferro-actinolite)} + {}^1/_2\,O_{2(vapor,melt)} + 2\,Al_2O_{3(melt)} = KFe_3^{2+}AlSi_3O_{10}(OH)_{2(annite)} + 2\,CaAl_2Si_2O_{8(plagioclase)} + 4\,SiO_{2(quartz)} + Fe_2O_{3(ilmeno-hematite)}$$

An orthopyroxene consuming reaction is:

$$KAlSi_3O_{8(sanidine,melt)} + 3(Mg,Fe^{2+})SiO_{3(orthopyroxene)} + H_2O_{(vapor,melt)} = K(Mg,Fe^{2+})_3AlSi_3O_{10}(OH)_{2(biotite)} + 3\,SiO_{2(quartz)}$$

Quartz saturation fixes the activity of SiO_2, and subsequent fractionation increasing the activity of sanidine component and decreasing the activity of anorthite component drives the reactions to the right, forming biotite. Amphiboles are expected to have low concentrations of octahedral Al at the upper crustal pressures inferred for the EQF magma body, so the actinolite consuming reaction may dominate with a secondary effect of increasing the Al concentration of the residual amphibole. This could provide a potential alternative to heating to account for the weak rim-ward increases in Al reported by Molloy et al. (2008) in some EQF hornblendes. The amphibole consuming reactions also produce anorthite component, potentially contributing to the nearly constant compositions of the thick rims on EQF plagioclase grains. A straightforward experimental test of reaction relations would involve seeding the natural melt with grains of hornblende and orthopyroxene, similar to Blatter et al. (2017), who investigated pyroxene to amphibole reactions in dacitic melt, but such tests are beyond the resources available to us at the time of this report.

Alternative explanations for the absence of amphibole and orthopyroxene are kinetic barriers to their nucleation and growth, that the fO_2 of our experiments differed appreciably from that of the natural magma body, and that the EQF glass lost alkalis during hydration and chemical weathering. Hammer and Rutherford (2003) presented experimental evidence for sluggish re-equilibration between amphibole and melt at temperatures similar to those investigated herein, but barriers to nucleation and growth are expected to be greater for quartz than for mafic silicates owing to slow diffusion of Si in melts and the need for all other chemical components to diffuse away from growing quartz grains. However, quartz's stability limits and growth proportions vary regularly with pressure and temperature, and its grains lack skeletal habits, consistent with a close approach to equilibrium. The essential chemical components in hornblende and orthopyroxene all diffuse faster through melt than does Si, and experiments on less evolved melts are notoriously prone to quench-crystallizing amphibole and pyroxene, so kinetic barriers (disequilibrium) are unlikely to account for the absence of hornblende and orthopyroxene in the EQF experiments. First et al. (2021) showed, with H_2O saturated experiments on a dacite, that distinctly low fO_2 conditions reduced the low-pressure stability limits of amphibole and biotite. At < 850 ºC and ΔNi–NiO = − 2, amphibole is stable at > 110 MPa, whereas at those temperatures and ΔNi–NiO = + 0.2 it's stable to as low as 75 MPa (First et al. 2021). High fO_2 can also destabilize amphibole and biotite, as shown by isobaric studies on end-member compositions (ferropargasite: Gilbert 1966; ferrotremolite: Ernst 1966, annite: Eugster and Wones 1962, among others), and high fO_2 also can destabilize amphibole in melting experiments on igneous rocks (Spear 1981; Sisson et al. 2005). The influences of fO_2 on amphibole and biotite stability limits are not abrupt, however, and since our experiments were directly Ni–NiO buffered to closely match the fO_2 given by EQF Fe-Ti oxides, incorrect fO_2 is unlikely to account for the absence of amphibole and orthopyroxene from the synthesis products. Loss of alkalis by chemical weathering of pumice glass was previously assessed for both the Rotoiti and the EQF deposits by comparing their glass's Na_2O and K_2O concentrations with those of their respective melt inclusions. Alkali concentrations are indistinguishable in the pumice glasses and their respective melt inclusions (Fig. 2), so any losses by chemical weathering are below the measurement resolution. For these reasons we prefer amphibole – melt and orthopyroxene – melt reactions to explain the absence of those minerals from the synthesis products.

RhyoliteMELTS model comparison

To investigate similarities and differences between our experimental results and thermodynamic predictions from RhyoliteMELTS (v 1.1.0) (Gualda et al. 2012), we input the composition of the EQF glass concentrate and modeled this at H_2O-saturated conditions (H_2O = 8.0 wt.%) and fO_2 = Ni–NiO to generate a phase diagram (Fig. 10). Neither amphibole nor biotite were predicted as stable in the RhyoliteMELTS simulations, although no significance is assigned to this since thermochemistries and activities of those minerals are not well established in that program. The resultant predicted mineral saturation curves generally align with our experimental results; however, there are some key differences. First, RhyoliteMELTS derives the crossover between liquidus quartz and plagioclase at 100 MPa and 795 ºC, whereas we found this crossover experimentally at 140 MPa and 755 ºC. Second, RhyoliteMELTS simulates the plagioclase and K-feldspar appearance curves as intersecting at 300 MPa and 732 ºC, whereas we find this experimentally around 210 MPa and 700 ºC. The latter difference

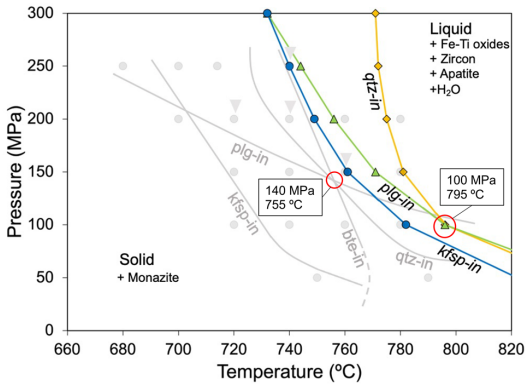


Fig. 10 Mineral appearance limits derived from RhyoliteMELTS for the erupted Earthquake Flat (EQF) melt composition compared with those determined experimentally (gray). RhyoliteMELTS simulations used glass starting material as the bulk composition, $H_2O = 8.0$ wt.% (H_2O-saturated), and fO_2 = Ni–NiO. Stability curves: yellow diamonds, quartz; green triangles, plagioclase; blue circles, sanidine (K-feldspar). Experimental crossover in quartz-plagioclase (and biotite) saturation curves found at 140 ± 10 MPa and 755 ± 5 ºC, circled in red; RhyoliteMELTS crossover in quartz-plagioclase saturation curves predicted at 100 MPa and 795 ºC, circled in red

reflects that in the RhyoliteMELTS model, plagioclase and K-feldspar stabilities respond nearly equally to changing H_2O-pressure, whereas in the experiments, plagioclase is the more sensitive of the two for the investigated bulk composition. For geological and volcanological applications the agreement is generally good in that both the experiments and the simulations indicate shallow crustal storage if the EQF magma was saturated with pure or nearly pure H_2O. The temperature difference appears relatively large but because output from RhyoliteMELTS, and the other members of the MELTS family of programs, do not propagate and report uncertainties on phase stability limits, the significance of the differences in temperature and pressure cannot be assessed quantitatively – perhaps the uncertainties on the MELTS-predicted crossover at 100 MPa and 795 ºC are sufficiently large as to overlap the direct experimental determination at 140 MPa and 755 ºC.

Mineralogical controls on magma storage

A puzzling aspect of the modern (~45 ka to present) Taupo Volcanic Zone has been the absence of K-rich alkali feldspar in all melt-bearing volcanic products, including highly evolved rhyolites (Danišík et al. 2012; Wilson et al. 1995); however, Burt et al. (1998) reported the presence of rare K-feldspar-bearing plutonic lithics in the Rotoiti lag breccia and EQF flow deposits. Sanidine in plutonic lithics is chiefly preserved as granophyric intergrowths, which Burt et al. (1998) interpreted as having formed by high-temperature, rapid ascent from mobilization of the Rotoiti magma body. Burt et al. (1998) presented two-feldspar temperatures between 700 and 800 °C, confirming that the lithics were at or close to solidus conditions, potentially as part of the outer, crystal-rich 'rigid sponge' or roof portions of the magma reservoir where cooler conditions dominate. Experimentally, we found that the erupted EQF melt composition saturates with K-feldspar only at temperatures < 760 °C at 50 MPa through < 700 °C at 200 MPa (Fig. 5), close to the probable H_2O-saturated granite (rhyolite) solidus. Thus, the EQF magma, stored at 140 MPa and 755 °C, would have had to cool a further ~ 60 °C and would have attained high crystallinity in order to produce K-feldspar.

Rhyolites in other parts of the world have erupted with alkali feldspar phenocrysts and at temperatures greater than the effective H_2O-saturated solidus, and the absence of K-feldspar from EQF and other modern Taupo rhyolites may simply be a product of their relatively K_2O-poor compositions. Among rhyolitic tuffs globally, those lacking K-feldspar typically have low K_2O concentrations in their glasses (< 4.5 wt.%). For example, Rotoiti, Novarupta, Usu, Krafla, and EQF tuffs all have $K_2O < 4.5$ wt.%, lack K-feldspar in the pumice samples, and correspondingly, did not grow K-feldspar in any experimental studies (Coombs and Gardner 2001; Nicholls et al. 1992; Rooyakers et al. 2021; Tomiya et al. 2010). Conversely, we stabilized K-feldspar in four runs for a similarly low-K_2O starting composition, thereby defining a K-feldspar saturation curve. Potentially this is due to our use of a highly evolved glass separate as our starting material, which allowed productive experiments to near-solidus conditions, whereas the other studies used whole-rocks whose less-evolved compositions and relict phenocrysts yielded more crystalline and difficult to interpret products at similar conditions that experimentalists tend to avoid. Figure 11 shows glass and whole-rock compositions of some well-known global rhyolites plotted in the haplogranitic ternary and the tonalite-trondhjemite-granite (TTG) discrimination diagram (Barker 1979). This comparison shows that the K-feldspar-free magmas plot closer to the quartz–albite join than do the K-feldspar-bearing magmas in the haplogranitic ternary. Similarly, the K-feldspar-free magmas plot closer to the trondhjemite region of the TTG ternary relative to the K-feldspar-bearing magmas which plot in the granite region. Notably, the EQF glass composition plots in between the K-feldspar-free and the K-feldspar-bearing groups in the haplogranitic plot and in the TTG diagram. The EQF whole-rock composition falls within the K-feldspar-free region on the haplogranitic ternary plot and on the granodiorite boundary region on the TTG plot. Since the EQF pumice lacks K-feldspar, the EQF glass composition must be at the threshold of K-feldspar saturation–a modest increase in normative orthoclase component or a moderate decrease in temperature and increase in crystallinity would

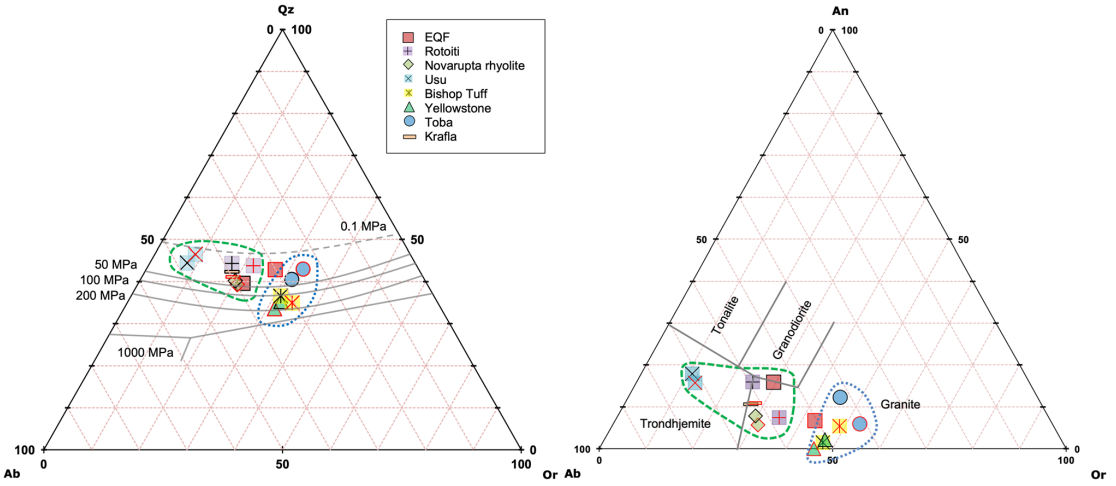


Fig. 11 Whole-rock or glass compositions for representative rhyolites with and without alkali feldspar phenocrysts plotted in the haplogranitic ternary (left, weight units) and the tonalite-trondhjemite-granite (TTG) diagram (right, Barker 1979, molecular units). Black symbols are whole-rock compositions, and corresponding red symbols are glass. On the haplogranitic ternary, minima curves are shown for 0.1, 50, 100, and 200 MPa, and the eutectic at 1000 MPa from Tuttle and Bowen (1958). Rhyolites lacking modal alkali feldspar are included within the dashed-green line, and those with alkali feldspar are included in the dotted-blue line. The Earthquake Flat (EQF) glass composition is in a shaded red square and plots between the two groups. Melt or whole-rock pumice compositions of EQF (red filled squares) from this study, Rotoiti (purple filled plus signs) from Schmitz and Smith (2004), Usu (light blue filled crosses) from Tomiya et al. (2010), Krafla (orange rectangles) from Rooyakkers et al. (2021), Novarupta (olive green diamonds) from Coombs and Gardner (2001), Bishop Tuff (yellow filled stars) from Gardner et al. (2014), Yellowstone (bright green triangles) from Befus and Gardner (2016), and Toba (blue circles) from Chesner (1998)

push the EQF glass composition into the K-feldspar-bearing group.

The absence of K-feldspar provides a secondary limit on the storage conditions of the EQF magma body, which must have resided at higher temperature and greater H_2O-pressure than K-feldspar-in, or > 760 °C if close to 50 MPa and > 700 °C if close to 200 MPa. In our K-feldspar-bearing experiments, we saw a wide range in crystallinity between 17 and 95 wt.% crystals. The highly crystalline experimental products show that K-feldspar appears very near the system solidus. Therefore, we suggest that K-feldspar phenocrysts are absent in TVZ volcanic products because those magmas are poor in K_2O (trondhjemitic or low-K granitic), so they only saturate in K-rich alkali feldspar close to the solidus where the magmas are much too crystalline to erupt. Similarly, if such compositions are heated, K-feldspar melts out close to the solidus, precluding K-feldspar in erupted products that originate by remobilizing (defrosting) near-solidus and sub-solidus intrusions.

Magma storage in a broader context

The widely advocated "mush model" for large, subvolcanic silicic systems, illustrated in Fig. 12 (after Hildreth 2004), envisions a dominantly crystal-rich shallow intrusion with highly evolved melts percolating upward through a viscous crystalline framework (rigid sponge) and accumulating in a melt-rich central domain or domains. Although such conceptual diagrams often show gradual transitions from crystal-rich to melt-rich, little is actually known of such details. Recent work shows that multiple batches of crystal-poor melts may coexist within the larger crystal-rich body (Ellis et al. 2014; Storm et al. 2014; Rubin et al. 2016; Swallow et al. 2019), an interpretation presaged by discovery of the isotopic heterogeneity of some zoned plutons (Hill 1988; Kistler et al. 1986). The mineral grains within the crystal-rich region grew by various processes and in various settings, including as disaggregated cumulus crystals, autocrysts grown simply and directly from the extant melt, and as grains or zones of grains grown from prior replenishments as the shallow intrusion was constructed and sustained. In this conceptualization, an erupting rhyolite is sourced from some crystal-poor portion of the intrusion, and as that melt-rich portion evacuates, it may be followed by progressively more crystal-rich materials. This aspect of the model was developed to account for voluminous, stratigraphically zoned tuff sequences emplaced during single eruptions. Such zoned tuffs commonly increase in their crystal abundances and magmatic temperatures in successively deposited products as those products' bulk-magma, melt,

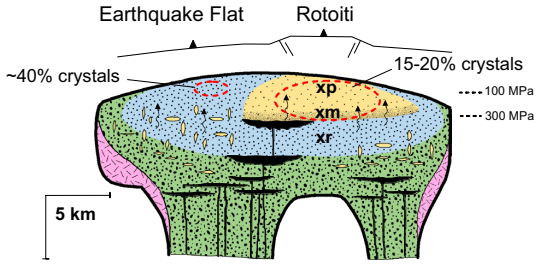


Fig. 12 Conceptual model of a large-volume, upper crustal, silicic magma storage system modified from Hildreth (2004); Canonical magma mush system consisting of high-level crystal-poor (xp) center, which increases in crystallinity margin-ward and downward through crystal-moderate (xm) and crystal-rich (xr) regions, and which transitions from melt-dominated to a crystalline framework (rigid sponge) through which melts can percolate into the melt-dominated portions of the reservoir. The outermost regions of the system are fully solidified granite or granodiorite; black signifies magmatic replenishments of various compositions. Original figure modified to model the Earthquake Flat (EQF) and Rotoiti magma system in which Rotoiti source is represented by the crystal-poor and crystal-moderate portion of the system, and in which EQF source is represented by the crystal-rich and crystalline framework portion of the system. The crystal-rich portion of the system (stippled blue) is melt-dominated despite the high crystal load (~40–50% crystals); red-dashed ellipses illustrate potential eruptive regions for EQF and Rotoiti, where Rotoiti's eruptive volume is sourced chiefly from the xp and xm regions of the reservoir, and where the EQF eruptive volume is sourced from the xr region of the reservoir; pressure scale is included to show the deepest extent to which the two bodies could have been stored based on cummingtonite stability for Rotoiti, and this study's experimental results for EQF

and mineral compositions and assemblages also become less evolved (e.g., Hildreth and Wilson 2007). In contrast, the Rotoiti tuff is largely chemically homogenous, and lacks pronounced stratigraphic zoning other than a slight variation in the proportion of trace phases (biotite, hornblende, and orthopyroxene) in the uppermost units and the presence of mingled pumice containing two distinct magma components (Shane et al. 2005; Schmitz and Smith 2004; Molloy et al. 2008). Based on the similarity between the EQF and Upper Rotoiti mineral assemblage (viz. trace biotite, and no cummingtonite), it has been suggested that the EQF magma is the second magma component identified in the mingled Rotoiti pumice, and that the EQF magma fed into the Rotoiti reservoir post-caldera collapse; however, this interpretation is unsupported by isotopic measurements (Schmitz and Smith 2004). And although mineralogical and chemical differences between Rotoiti and EQF preclude direct parental lineage, the pressure and temperature constraints support that magmas of the two volcanic centers were adjacent, coeval neighbors, residing at similar shallow depths and temperatures.

A previous experimental study by Nicholls et al. (1992) limits the Rotoiti magma's storage conditions loosely at < 300 MPa and < 750 °C, based on the presence and stability of cummingtonite, whereas our results indicate that the EQF magma was stored at ~ 140 MPa and ~ 755°C, based on liquidus co-saturation of the natural melt in quartz, plagioclase, and biotite. The pressure results are permissively the same, and based on the experiments, the Rotoiti magma may have been cooler, but this is not reflected in pronounced differences in the composition of EQF versus Rotoiti glasses, both of which are high-silica rhyolites with similar concentrations (wt.%) of TiO_2 (EQF: 0.13, Rotoiti: 0.19), FeO_T (EQF: 0.78, Rotoiti: 1.00), and CaO (EQF: 0.82, Rotoiti: 0.87), employing average Rotoiti glass compositions from Schmitz and Smith (2004).

Where the glasses do differ notably is in their alkali concentrations, Na_2O (EQF: 3.45, Rotoiti: 3.75) and K_2O (EQF: 4.49, Rotoiti: 3.44). The reaction:

$$0.5\ K_2O_{(melt)} + 0.5\ Al_2O_{3(melt)} + \left(Mg,Fe^{2+}\right)_2 \left(Mg,Fe^{2+}\right)_5Si_8O_{22}(OH)_{2(cummingtonite)} = K\left(Mg,Fe^{2+}\right)_3AlSi_3O_{10}(OH)_{2(biotite)} + 4\left(Mg,Fe^{2+}\right)SiO_{3(orthopyroxene)} + SiO_{2(quartz)}$$

indicates that for melts saturated with quartz and orthopyroxene, and with similar Al_2O_3 concentrations (~ activities), lower K_2O concentration enhances cummingtonite at the expense of biotite. Smith et al. (2005) also showed that glasses in cummingtonite bearing OVC deposits have lower K_2O concentrations than for glasses that contain biotite. Cummingtonite is also known from other distinctly low-K_2O silicic magmas (Geschwind and Rutherford 1992; Nadeau et al. 2015). Potentially, the Rotoiti tuffs contains cummingtonite not because it's storage conditions were appreciably cooler than the EQF but because its melt was less potassic, a possibility best explored by narrowing the experimental limits on Rotoiti mineral–melt stabilities. The petrologic observations and experimental results, combined with the near contemporaneity of the eruptions and the adjacent proximity of their vents (~ 20–25 km) support that the Rotoiti and EQF were lateral members of the same overall intrusive complex (pluton), with the crystal-moderate Rotoiti magma in its central area, and the crystal-rich EQF magma occupying the mushy periphery (Fig. 12).

Conclusions

Our experimental results determine the pre-eruptive storage conditions for the Earthquake Flat (EQF) magma body by locating the liquidus co-saturation of its natural melt with quartz, plagioclase, biotite, and H_2O-rich fluid. Based on

our experiments, this corresponds to 140 MPa ± 10 MPa and 755 ºC ± 5 ºC for a H_2O-saturated rhyolitic magma at fO_2 = Ni–NiO. By using a glass concentrate starting material, our experimentally defined conditions represent the conditions under which the magma body was staged immediately prior to eruption. Our experiments on the natural erupted glass did not produce hornblende and orthopyroxene that are sparse but widespread in the EQF pumices, a difference we provisionally ascribe to those minerals being in reaction relation with melt. Our experimental results are within error of results from Fe-Ti oxide thermometry, amphibole-plagioclase thermometry, amphibole barometry, and melt inclusion volatile barometry, and are similar to results from RhyoliteMELTS, which predicts the intersection of the quartz and plagioclase saturation curves moderately shallower and hotter than the experimental determination. If the temperature of the EQF magma body increased approaching its eruption (Molloy et al. 2008), then temperature had stabilized sufficiently such that there was negligible diversity in melt composition and mineral assemblage across nearly all of the ~ 10 km^3 of erupted EQF magma. A general absence of K-feldspar in rhyolites of the larger Taupo Volcanic Zone (TVZ), including EQF, is largely a consequence of their low-K_2O concentrations more similar to trondhjemites than to granites. K-feldspar appears in our experiments approximately 60 ºC cooler than the melt's H_2O-saturated liquidus at upper crustal pressures, close to the probable solidus. The low-K_2O concentration also accounts for the presence of cummingtonite in some TVZ rhyolites, which is controlled by a combination of the system's temperature and the low K_2O concentration of the melt in the larger TVZ system. We show that the EQF magma system did not have sufficient K_2O component in the pre-eruptive melt and was stored slightly too hot for K-feldspar saturation. Our findings provide pressure, temperature, and compositional constraints for H_2O-saturated, high-fO_2 (~ Δ Ni–NiO = 0) rhyolite systems globally.

Compositional differences between the Rotoiti and EQF glasses, and mineralogical differences between the two tuffs, require that the source magmas must have evolved along separate lines of descent, and therefore, that they were not stored in a well-mixed magma reservoir, although they could have been portions of the same intrusion assembled from slightly differing supplied magmas. Combined with our experimental results, which show that the two bodies were broadly stored at similar conditions, we propose a model of lateral variability in the shallow crustal intrusion, where multiple melt-rich bodies developed at similar storage conditions, but from different parental magmas, yielding different chemical signatures. Based on the observed textures in the EQF tuff, we interpret that it originated from a higher crystallinity marginal portion of the active intrusion (pluton) whose crystal-moderate center sourced the Rotoiti rhyolites only shortly earlier.

Supplementary Information The online version contains supplementary material available at https://doi.org/10.1007/s00410-024-02151-y.

Acknowledgements The project was funded through an NSF GRIP grant written by Elizabeth Grant, with input from Dawnika Blatter, Laura Waters, and Kari Cooper, and from an NSF INTERN grant, supplemental to Kari Cooper's existing NSF grant. This research was supported by the USGS Volcano Hazards Program. We would like to thank our reviewers Emily First, Michelle Coombs, and an anonymous reviewer, whose input and guidance greatly improved this manuscript. We are grateful to Greg Baxter for sample preparation, Dawn Ruth for guidance on the SEM and EMPA, and Darren Gravley and Chad Deering for their field guidance. Any use of trade, firm, or product names is for descriptive purposes only and does not imply endorsement by the U.S. Government.

Author contributions This work was conceived of and designed by Elizabeth Grant, Dawnika Blatter, and Tom Sisson. Sample preparation and analyses were performed by Elizabeth Grant. The manuscript was written by Elizabeth Grant with significant input from Dawnika Blatter, Tom Sisson, and Kari Cooper.

Funding National Science Foundation, EAR-1654506, Kari M. Cooper.

Data availability Data are available in the Tables (1–4), and electronic supplemental material files (ESM 1 – 4). All data are also available in the U.S. Geological Survey data release from Grant et al. (2024; https://doi.org/10.5066/P13IM4QQ).

Declarations

Conflict of interest The authors declare no competing interests.

Open Access This article is licensed under a Creative Commons Attribution 4.0 International License, which permits use, sharing, adaptation, distribution and reproduction in any medium or format, as long as you give appropriate credit to the original author(s) and the source, provide a link to the Creative Commons licence, and indicate if changes were made. The images or other third party material in this article are included in the article's Creative Commons licence, unless indicated otherwise in a credit line to the material. If material is not included in the article's Creative Commons licence and your intended use is not permitted by statutory regulation or exceeds the permitted use, you will need to obtain permission directly from the copyright holder. To view a copy of this licence, visit http://creativecommons.org/licenses/by/4.0/.

References

Andersen DJ, Lindsley DH, Davidson PM (1993) QUILF: A pascal program to assess equilibria among Fe-Mg-Mn-Ti oxides, pyroxenes, olivine, and quartz. Comput Geosci 19(9):1333–1350. https://doi.org/10.1016/0098-3004(93)90033-2

Andersen D Lindsley DH 1985 New (and final!) models for the Ti-magnetite/ilmenite geothermometer and oxygen barometer. Abstracts of American Geophysical Union 1985 Spring Meeting.

Bachmann O, Bergantz GW (2004) On the origin of crystal-poor rhyolites: extracted from batholithic crystal mushes. J Petrol 45(8):1565–1582. https://doi.org/10.1093/petrology/egh019

Bachmann O, Bergantz GW (2006) Gas percolation in upper-crustal silicic crystal mushes as a mechanism for upward heat advection and rejuvenation of near-solidus magma bodies. J Volcanol Geoth Res 149(1–2):85–102. https://doi.org/10.1016/j.volgeores.2005.06.002

Bacon CR, Hirschmann MM (1988) Mg/Mn partitioning as a test for equilibrium between coexisting Fe-Ti oxides. Am Miner 73(1–2):57–61

Barker F (1979) Trondhjemite: Definition, environment, and hypotheses of origin. In: Barker F (ed) Trondhjemites, dacites, and related rocks. Elsevier, New York, pp 1–12

Befus KS, Gardner JE (2016) Magma storage and evolution of the most recent effusive and explosive eruptions from Yellowstone Caldera. Contrib Miner Petrol 171(4):1–19. https://doi.org/10.1007/s00410-016-1244-x

Bégué F, Gualda GA, Ghiorso MS, Pamukcu AS, Kennedy BM, Gravley DM, Deering CD, Chambefort I (2014) Phase-equilibrium geobarometers for silicic rocks based on rhyolite-MELTS. Part 2: application to Taupo Volcanic Zone rhyolites. Contrib Miner Petrol 168:1–16. https://doi.org/10.1007/s00410-014-1082-7

Blatter DL, Sisson TW, Hankins WB (2017) Voluminous arc dacites as amphibole reaction-boundary liquids. Contrib Miner Petrol 172:1–37. https://doi.org/10.1007/s00410-017-1340-6

Buddington AF, Lindsley DH (1964) Iron-titanium oxide minerals and synthetic equivalents. J Petrol 5(2):310–357. https://doi.org/10.1093/petrology/5.2.310

Burt RM, Brown SJA, Cole JW, Shelley D, Waight TE (1998) Glass-bearing plutonic fragments from ignimbrites of the Okataina caldera complex, Taupo Volcanic Zone, New Zealand: remnants of a partially molten intrusion associated with preceding eruptions. J Volcanol Geoth Res 84(3–4):209–237. https://doi.org/10.1016/S0009-2541(98)00026-6

Cadoux A, Scaillet B, Druitt TH, Deloule E (2014) Magma storage conditions of large Plinian eruptions of Santorini Volcano (Greece). J Petrol 55(6):1129–1171. https://doi.org/10.1093/petrology/egu021

Caricchi L, Blundy J (2015) The temporal evolution of chemical and physical properties of magmatic systems. Geological Society, London, Special Publications 422(1):1–15. https://doi.org/10.1144/SP422.11

Cashman KV, Giordano G (2014) Calderas and magma reservoirs. J Volcanol Geoth Res 288:28–45. https://doi.org/10.1016/j.volgeores.2014.09.007

Cashman KV, Sparks RSJ, Blundy JD (2017) Vertically extensive and unstable magmatic systems: A unified view of igneous processes. Science 355(6331):eaag055. https://doi.org/10.1126/science.aag3055

Chamberlain KJ, Wilson CJN, Wallace PJ, Millet MA (2015) Micro-analytical perspectives on the Bishop Tuff and its magma chamber. J Petrol 56(3):605–640. https://doi.org/10.1093/petrology/egv012

Charlier BL, Peate DW, Wilson CJ, Lowenstern JB, Storey M, Brown SJ (2003) Crystallisation ages in coeval silicic magma bodies: 238U–230Th disequilibrium evidence from the Rotoiti and Earthquake Flat eruption deposits, Taupo Volcanic Zone, New Zealand. Earth Planet Sci Lett 206(3–4):441–457. https://doi.org/10.1016/S0012-821X(02)01109-3

Charlier BLA, Wilson CJN, Lowenstern JB, Blake S, Van Calsteren PW, Davidson JP (2005) Magma generation at a large, hyperactive silicic volcano (Taupo, New Zealand) Revealed by U-Th and U–Pb Systematics in Zircons. J Petrol 46(1):3–32. https://doi.org/10.1093/petrology/egh060

Chesner CA (1998) Petrogenesis of the Toba tuffs, Sumatra. Indonesia Journal of Petrology 39(3):397–438. https://doi.org/10.1093/petroj/39.3.397

Cole JW, Spinks KD (2009) Caldera volcanism and rift structure in the Taupo Volcanic Zone, New Zealand. Geological Society, London, Special Publications 327(1):9–29. https://doi.org/10.1144/SP327.2

Cole JW, Deering CD, Burt RM, Sewell S, Shane PAR, Matthews NE (2014) Okataina Volcanic Centre, Taupo Volcanic Zone, New Zealand: a review of volcanism and synchronous pluton development in an active, dominantly silicic caldera system. Earth Sci Rev 128:1–17. https://doi.org/10.1016/j.earscirev.2013.10.008

Coombs ML, Gardner JE (2001) Shallow-storage conditions for the rhyolite of the 1912 eruption at Novarupta. Alaska Geology 29(9):775–778. https://doi.org/10.1130/0091-7613(2001)029%3c0775:SSCFTR%3e2.0.CO;2

Cooper KM (2015) Timescales of crustal magma reservoir processes: insights from U-series crystal ages. Geological Society, London, Special Publications 422(1):141–174. https://doi.org/10.1144/SP422.7

Cooper KM (2019) Time scales and temperatures of crystal storage in magma reservoirs: implications for magma reservoir dynamics. Philosophical Transactions of the Royal Society a: Mathematical, Physical and Engineering Sciences 377(2139):20180009. https://doi.org/10.1098/rsta.2018.0009

Danišík M, Shane P, Schmitt AK, Hogg A, Santos GM, Storm S, Evans NJ, Keith Fifield L, Lindsay JM (2012) Re-anchoring the late Pleistocene tephrochronology of New Zealand based on concordant radiocarbon ages and combined 238U/230Th disequilibrium and (U–Th)/He zircon ages. Earth Planet Sci Lett 349–350:240–250. https://doi.org/10.1016/j.epsl.2012.06.041

Davis WJ (1985) Geochemistry and petrology of the Rotoiti and Earthquake Flat pyroclastic deposits. University of Auckland, New Zealand

Deering CD, Bachmann O, Dufek J, Gravley DM (2011) Rift-related transition from andesite to rhyolite volcanism in the Taupo Volcanic Zone (New Zealand) controlled by crystal–melt dynamics in mush zones with variable mineral assemblages. J Petrol 52(11):2243–2263. https://doi.org/10.1093/petrology/egr046

Devine JD (2003) Magma storage region processes inferred from geochemistry of Fe-Ti Oxides in andesitic magma, Soufriere Hills Volcano, Montserrat. W.I. Journal of Petrology 44(8):1375–1400. https://doi.org/10.1093/petrology/44.8.1375

Dodge FC, Millard HT, Elsheimer HN (1982) Compositional variations and abundances of selected elements in granitoid rocks and constituent minerals, central Sierra Nevada batholith, California (No. 1248). US Geol Surv Prof Pap 1248:24

Ellis BS, Bachmann O, Wolff JA (2014) Cumulate fragments in silicic ignimbrites: the case of the Snake River Plain. Geology 42(5):431–434. https://doi.org/10.1130/G35399.1

Ernst WG (1966) Synthesis and stability relations of ferrotremolite. Am J Sci 264:37–65

Eugster HP (1957) Heterogeneous reactions involving oxidation and reduction at high pressures and temperatures. J Chem Phys 26(6):1760–1761. https://doi.org/10.1063/1.1743626

Eugster HP, Wones DR (1962) Stability relations of the ferruginous biotite, annite. J Petrol 3:82–125

First EC, Hammer JE, Ruprecht P, Rutherford M (2021) Experimental constraints on dacite magma storage beneath Volcán Quizapu. Chile. Journal of Petrology 62(5):egab027. https://doi.org/10.1093/petrology/egab027

Gardner JE, Befus KS, Gualda GA, Ghiorso MS (2014) Experimental constraints on rhyolite-MELTS and the Late Bishop Tuff magma body. Contrib Miner Petrol 168:1–14. https://doi.org/10.1007/s00410-014-1051-1

Geschwind CH, Rutherford MJ (1992) Cummingtonite and the evolution of the Mount St. Helens Magmatic System Geology 20(11):1011–1014. https://doi.org/10.1130/0091-7613

Ghiorso MS, Evans BW (2008) Thermodynamics of rhombohedral oxide solid solutions and a revision of the Fe-Ti two-oxide geothermometer and oxygen-barometer. Am J Sci 308(9):957–1039. https://doi.org/10.2475/09.2008.01

Ghiorso MS, Gualda GAR (2015) An H_2O–CO_2 mixed fluid saturation model compatible with rhyolite-MELTS. Contrib Miner Petrol 169(6):1–30. https://doi.org/10.1007/s00410-015-1141-8

Ghiorso MS, Sack O (1991) Fe-Ti oxide geothermometry: thermodynamic formulation and the estimation of intensive variables in silicic magmas. Contrib Miner Petrol 108:485–510. https://doi.org/10.1007/BF00303452

Gilbert MC (1966) Synthesis and stability relations of the hornblende ferropargasite. Am J Sci 264:698–742

Grant ER, Blatter DL, Sisson TW, Cooper, KM. Shallow storage of the explosive Earthquake Flat Pyroclastics magma body, Okataina Volcanic Center, Taupo Volcanic Zone, New Zealand: evidence from phase-equilibria experiments. U.S. Geological Survey data release, access 2024 https://doi.org/10.5066/P13IM4QQ

Gravley DM, Deering CD, Leonard GS, Rowland JV (2016) Ignimbrite flare-ups and their drivers: a New Zealand perspective. Earth Sci Rev 162:65–82. https://doi.org/10.1016/j.earscirev.2016.09.007

Gualda GAR, Ghiorso MS (2014) Phase-equilibrium geobarometers for silicic rocks based on rhyolite-MELTS. Part 1: Principles, procedures, and evaluation of the method. Contrib Miner Petrol 168(1):1–17. https://doi.org/10.1007/s00410-014-1033-3

Gualda GA, Ghiorso MS, Lemons RV, Carley TL (2012) Rhyolite-MELTS: a modified calibration of MELTS optimized for silica-rich, fluid-bearing magmatic systems. J Petrol 53(5):875–890. https://doi.org/10.1093/petrology/egr080

Hammer JE, Rutherford MJ (2003) Petrologic indicators of preeruption magma dynamics. Geology 31(1):79–82. https://doi.org/10.1130/0091-7613(2003)031%3c0079:PIOPMD%3e2.0.CO;2

Hammond PA, Taylor LA (1982) The ilmenite/titano-magnetite assemblage: Kinetics of re-equilibration. Earth Planet Sci Lett 61(1):143–150. https://doi.org/10.1016/0012-821X(82)90047-4

Hawthorne FC (1981). Crystal chemistry of the amphiboles. In: Veblen DR (ed.) Amphiboles and other hydrous pyriboles. Reviews in Mineralogy 9A, 1–95.

Hildreth W (2004) Volcanological perspectives on Long Valley, Mammoth Mountain, and Mono Craters: several contiguous but discrete systems. J Volcanol Geoth Res 136(3–4):169–198. https://doi.org/10.1016/j.jvolgeores.2004.05.019

Hildreth W, Mahood GA (1986) Ring-fracture eruption of the Bishop Tuff. Geol Soc Am Bull 97(4):396. https://doi.org/10.1130/0016-7606(1986)97%3c396:REOTBT%3e2.0.CO;2

Hildreth W, Wilson CJ (2007) Compositional zoning of the Bishop Tuff. J Petrol 48(5):951–999. https://doi.org/10.1093/petrology/egm007

Hill RI (1988) San Jacinto Intrusive Complex: 1. Geology and mineral chemistry, and a model for intermittent recharge of tonalitic magma chambers. Journal of Geophysical Research: Solid Earth 93(B9):10325–10348. https://doi.org/10.1029/JB093iB09p10325

Holland T, Blundy J (1994) Non-ideal interactions in calcic amphiboles and their bearing on amphibole-plagioclase thermometry. Contrib Miner Petrol 116(4):433–447. https://doi.org/10.1007/BF00310910

Iacovino K, Matthews S, Wieser PE, Moore GM, Bégué F (2021) VESical Part I: An Open-Source Thermodynamic Model Engine for Mixed Volatile (H2O-CO2) Solubility in Silicate Melts. Earth and Space Science 8(11):e202EA001584. https://doi.org/10.1029/2020EA001584

Johnson ER, Kamenetsky VS, McPhie J, Wallace PJ (2011) Degassing of the H2O-rich rhyolites of the Okataina Volcanic Center, Taupo Volcanic Zone. New Zealand Geology 39(4):311–314. https://doi.org/10.1130/G31543.1

Johnson ER, Kamenetsky VS, McPhie J (2013) The behavior of metals (Pb, Zn, As, Mo, Cu) during crystallization and degassing of rhyolites from the Okataina volcanic center, Taupo volcanic zone, New Zealand. J Petrol 54(8):1641–1659. https://doi.org/10.1093/petrology/egt026

Kistler RW, Chappell BW, Peck DL, Bateman PC (1986) Isotopic variation in the Tuolumne Intrusive Suite, central Sierra Nevada. California Contributions to Mineralogy and Petrology 94(2):205–220. https://doi.org/10.1007/BF00592937

Lepage LD (2003) ILMAT: An Excel worksheet for ilmenite–magnetite geothermometry and geobarometry. Comput Geosci 29(5):673–678. https://doi.org/10.1016/S0098-3004(03)00042-6

Lipman P, Dungan M, Bachmann O (1997) Comagmatic granophyric granite in the Fish Canyon Tuff, Colorado: Implications for magma-chamber processes during a large ash-flow eruption. Geology 25(10):915–918. https://doi.org/10.1130/0091-7613(1997)025%3c0915:CGGITF%3e2.3.CO;2

Liu Y, Zhang Y, Behrens H (2005) Solubility of H_2O in rhyolitic melts at low pressures and a new empirical model for mixed H_2O–CO_2 solubility in rhyolitic melts. J Volcanol Geoth Res 143(1–3):219–235. https://doi.org/10.1016/j.jvolgeores.2004.09.019

Lowenstern JB, Pitcher BW (2013) Analysis of H_2O in silicate glass using attenuated total reflectance (ATR) micro-FTIR spectroscopy. Am Miner 98(10):1660–1668. https://doi.org/10.2138/am.2013.4466

Lowenstern JB, Thompson JFH (1995) Applications of silicate-melt inclusions to the study of magmatic volatiles. Magmas, Fluids and Ore Deposits 23:71–99

Luth WC, Jahns RH, Tuttle OF (1964) The granite system at pressures of 4 to 10 kilobars. J Geophys Res 69(4):759–773. https://doi.org/10.1029/JZ069i004p00759

Mahood GA (1990) Second reply to comment of RSJ Sparks, HE Huppert and CJN Wilson on "Evidence for long residence times of rhyolitic magma in the Long Valley magmatic system: The isotopic record in the precaldera lavas of Glass Mountain." Earth Planet Sci Lett 99(4):395–399. https://doi.org/10.1016/0012-821X(90)90145-N

Maitre RWL, Streckeisen A, Zanettin B, Bas MJL, Bonin B, Bateman P (eds) (2005) Igneous rocks: a classification and glossary of terms: recommendations of the International Union of Geological Sciences Subcommission on the Systematics of Igneous Rocks. Cambridge University Press, Cambridge

Molina JF, Cambeses A, Moreno JA, Morales I, Montero P, Bea F (2021) A reassessment of the amphibole-plagioclase NaSi-CaAl exchange thermometer with applications to igneous and high-grade metamorphic rocks. Am Miner 106(5):782–800. https://doi.org/10.2138/am-2021-7400

Molloy C, Shane P, Nairn I (2008) Pre-eruption thermal rejuvenation and stirring of a partly crystalline rhyolite pluton revealed by the Earthquake Flat Pyroclastics deposits, New Zealand. J Geol Soc 165(1):435–447. https://doi.org/10.1144/0016-76492007-071

Moore G, Vennemann T, Carmichael ISE (1998) An empirical model for the solubility of H_2O in magmas to 3 kilobars. Am Miner 83(1–2):36–42. https://doi.org/10.2138/am-1998-1-203

Mutch EJF, Blundy JD, Tattitch BC, Cooper FJ, Brooker RA (2016) An experimental study of amphibole stability in low-pressure granitic magmas and a revised Al-in-hornblende geobarometer. Contrib Miner Petrol 171(10):1–27. https://doi.org/10.1007/s00410-016-1298-9

Nadeau PA, Webster JD, Mandeville CW, Goldoff BA, Shimizu N, Monteleone B (2015) A glimpse into Augustine volcano's Pleistocene past: insight from the petrology of a massive rhyolite deposit. J Volcanol Geoth Res 304:304–323. https://doi.org/10.1016/j.jvolgeores.2015.07.034

Nairn IA (1972) Rotoehu ash and the Rotoiti Breccia Formation, Taupo Volcanic zone, New Zealand. NZ J Geol Geophys 15(2):251–261. https://doi.org/10.1080/00288306.1972.10421958

Nairn IA, Kohn BP (1973) Relation of the Earthquake Flat Breccia to the Rotoiti Breccia, Central North Island, New Zealand. NZ J Geol Geophys 16(2):269–279. https://doi.org/10.1080/00288306.1973.10431457

Nairn IA (2002). Geology of the Okataina Volcanic Centre, scale 1: 50,000. Institute of Geological and Nuclear Sciences geological map 25. 1 sheet+ 156 p. Institute of Geological and Nuclear Sciences Ltd.

Nicholls IA, Oba T, Conrad WK (1992) The nature of primary rhyolitic magmas involved in crustal evolution: Evidence from an experimental study of cummingtonite-bearing rhyolites, Taupo Volcanic Zone. New Zealand Geochimica Et Cosmochimica Acta 56(3):955–962. https://doi.org/10.1016/0016-7037(92)90039-L

Ochs FA III, Lange RA (1999) The density of hydrous magmatic liquids. Science 283(5406):1314–1317. https://doi.org/10.1126/science.283.5406.1314

Pichavant M, Costa F, Burgisser A, Scaillet B, Martel C, Poussineau S (2007) Equilibration scales in silicic to intermediate magmas, implications for experimental studies. J Petrol 48(10):1955–1972. https://doi.org/10.1093/petrology/egm045

Piwinskii AJ, Wyllie PJ (1968) Experimental studies of igneous rock series: a zoned pluton in the Wallowa batholith, Oregon. J Geol 76:205–234

Powell R, Powell M (1977) Geothermometry and oxygen barometry using coexisting iron-titanium oxides: a reappraisal. Mineral Mag 41(318):257–263

Putirka K (2016) Amphibole thermometers and barometers for igneous systems and some implications for eruption mechanisms of felsic magmas at arc volcanoes. Am Miner 101(4):841–858. https://doi.org/10.2138/am-2016-5506

Reid MR (2008) How long does it take to supersize an eruption? Elements 4(1):23–28. https://doi.org/10.2113/GSELEMENTS.4.1.23

Reid MR, Vazquez JA (2017) Fitful and protracted magma assembly leading to a giant eruption, Youngest Toba Tuff, Indonesia. Geochem Geophys Geosyst 18(1):156–177. https://doi.org/10.1002/2016GC006641

Reid MR (2003). Timescales of magma transfer and storage in the crust. In: HD Holland, KK Turekian (eds.) Treatise on Geochemistry: Pergamon, 167-193. https://doi.org/10.1016/B0-08-043751-6/03022-X

Rooyakkers SM, Stix J, Berlo K, Petrelli M, Hampton RL, Barker SJ, Morgavi D (2021) The origin of rhyolitic magmas at Krafla central volcano (Iceland). J Petrol 62(8):ega064. https://doi.org/10.1093/petrology/egab064

Rubin A, Cooper KM, Leever M, Wimpenny J, Deering C, Rooney T, Gravley D, Yin QZ (2016) Changes in magma storage conditions following caldera collapse at Okataina Volcanic Center, New Zealand. Contrib Miner Petrol 171:1–18. https://doi.org/10.1007/s00410-015-1216-6

Rutherford MJ, Sigurdsson H, Carey S, Davis A (1985) The May 18, 1980, eruption of Mount St. Helens: 1. Melt composition and experimental phase equilibria. Journal of Geophysical Research: Solid Earth 90(B4):2929–2947. https://doi.org/10.1029/JB090iB04p02929

Scaillet B, Evans BW (1999) The 15 June 1991 eruption of Mount Pinatubo. I. Phase equilibria and pre-eruption P-T–f O2–f H2O conditions of the dacite magma. J Petrol 40(3):381–411. https://doi.org/10.1093/petroj/40.3.381

Schmitz MD (1995) Geochemical studies of the Rotoiti Pyroclastics eruption, Okataina volcanic center, Taupo Volcanic Zone, North Island, New Zealand Doctoral dissertation. University of Auckland, New Zealand

Schmitz MD, Smith IEM (2004) The petrology of the Rotoiti eruption sequence, Taupo Volcanic Zone: An example of fractionation and mixing in a rhyolitic system. J Petrol 45(10):2045–2066. https://doi.org/10.1093/petrology/egh047

Shane P (2000) Tephrochronology: a New Zealand case study. Earth Sci Rev 49(1–4):223–259. https://doi.org/10.1016/S0012-8252(99)00058-6

Shane P, Nairn IA, Smith VC (2005) Magma mingling in the ~50 ka Rotoiti eruption from Okataina Volcanic Centre: Implications for geochemical diversity and chronology of large volume rhyolites. J Volcanol Geoth Res 139(3–4):295–313. https://doi.org/10.1016/j.jvolgeores.2004.08.012

Sisson TW, Ratajeski K, Hankins WB, Glazner AF (2005) Voluminous granitic magmas from common basaltic sources. Contrib Miner Petrol 148:635–661. https://doi.org/10.1077/s00410-004-0632-9

Smith VC, Shane P, Nairn IA (2005) Trends in rhyolite geochemistry, mineralogy, and magma storage during the last 50 kyr at Okataina and Taupo volcanic centres, Taupo Volcanic Zone, New Zealand. J Volcanol Geoth Res 148(3–4):372–406. https://doi.org/10.1016/j.jvolgeores.2005.05.005

Smith V, Shane P, Nairn I (2010) Insights into silicic melt generation using plagioclase, quartz and melt inclusions from the caldera-forming Rotoiti eruption, Taupo volcanic zone, New Zealand. Contrib Miner Petrol 160:951–971. https://doi.org/10.1007/s00410-010-0516-0

Spear FS (1981) An experimental study of hornblende stability and compositional variability in amphibolite. Am J Sci 281:697–734

Speer JA (1987) Evolution of magmatic AFM mineral assemblages in granitoid rocks: The hornblende + melt = biotite reaction in the Liberty Hill pluton, South Carolina. Am Miner 72:863–878

Spencer KJ, Lindsley DH (1981) A solution model for coexisting iron–titanium oxides. Am Miner 66(11–12):1189–1201

Storm S, Schmitt AK, Shane P, Lindsay JM (2014) Zircon trace element chemistry at sub-micrometer resolution for Tarawera volcano, New Zealand, and implications for rhyolite magma evolution. Contrib Miner Petrol 167:1–19. https://doi.org/10.1007/s00410-014-1000-z

Swallow EJ, Wilson CJN, Charlier BLA, Gamble JA (2019) The Huckleberry Ridge Tuff, Yellowstone: Evacuation of multiple magmatic systems in a complex episodic eruption. J Petrol 60(7):1371–1426. https://doi.org/10.1093/petrology/egz034

Tomiya A, Takahashi E, Furukawa N, Suzuki T (2010) Depth and Evolution of a silicic magma chamber: Melting experiments on a low-K rhyolite from Usu volcano. Japan Journal of Petrology 51(6):1333–1354. https://doi.org/10.1093/petrology/egq021

Tuttle OF, Bowen NL (1958) Origin of granite in light of experimental studies in the system NaAlSi3O8–KAlSi3 O8–SiO2-H2O. Geol Soc Am Mem 74:153

Venezky DY, Rutherford MJ (1999) Petrology and Fe-Ti oxide reequilibration of the 1991 Mount Unzen mixed magma. J Volcanol Geoth Res 89(1–4):213–230. https://doi.org/10.1016/S0377-0273(98)00133-4

Waters LE, Andrews BJ (2016) The role of superheating in the formation of Glass Mountain obsidians (Long Valley, CA) inferred through crystallization of sanidine. Contrib Miner Petrol 171:1–19. https://doi.org/10.1007/s00410-016-1291-3

Wilson CJN, Houghton BF, McWilliams MO, Lanphere MA, Weaver SD, Briggs RM (1995) Volcanic and structural evolution of Taupo Volcanic Zone, New Zealand: A review. J Volcanol Geoth Res 68(1–3):1–28. https://doi.org/10.1016/0377-0273(95)00006-G

Publisher's Note Springer Nature remains neutral with regard to jurisdictional claims in published maps and institutional affiliations.

CHAPTER TWO

Sustained compositional and thermal heterogeneity in distributed melts across a caldera-forming cycle in the Okataina Volcanic Center, Taupo Volcanic Zone, New Zealand

Elizabeth R. G. Grant
Kari M. Cooper
Darren M. Gravley
Chad D. Deering
Adam J.R. Kent

2.1 ABSTRACT

Caldera-forming eruptions are some of the largest eruptions on earth, explosively evacuating up to 10^3 km^3 of volcanic material and causing mass destruction with global impacts. In order to forecast such large-scale events, it is critical to first understand the assembly and storage timescales for the magmas that feed such large eruptions. Volcanic deposits from a caldera-forming eruption cycle (pre-caldera eruptions, caldera-forming eruption, post-caldera eruptions) preserve important information about how the magma reservoir changes in the build-up to and following caldera-forming eruptions. Here, we examine zircon compositional and temporal data across a caldera-forming cycle to see if there are systematic patterns in the magma reservoir state leading to catastrophic caldera-forming eruptions that are recorded in crystals. We capitalize on zircon's mechanical robustness and low dissolution in rhyolitic melts to probe the growth histories of magma reservoirs using zircon as a micro-lens. We present new (^{238}U)/(^{230}Th) zircon crystallization age and trace element compositional data from zircon surfaces and interiors from the Kakapiko Dome (pre-caldera-forming eruption), Rotoiti (caldera-forming eruption), Earthquake Flat (syn-caldera-forming eruption), and Hauparu (post-caldera-forming eruption) eruptions from the Okataina Volcanic Center, Taupo Volcanic Zone, New Zealand. Collectively our data show that zircon in each eruption across a caldera-forming cycle crystallized from multiple discrete geochemical environments over a sustained period of zircon growth history (~200 kyrs). The lack of any systematic differences in the zircon record across a caldera-forming cycle supports the model that long-lived and locally heterogenous melts are distributed within an upper crustal magma mush system.

2.2 INTRODUCTION

Caldera-forming eruptions (CFEs) eruptions are some of the largest explosive eruptions preserved in the rock record, erupting volumes of pyroclastic material on the order of 10^3 km^3 (Miller and Wark 2008) and leaving collapse features up to 100 km in their wake (Bachmann et al. 2002). While CFEs are infrequent, they are catastrophic in nature and can pose considerable threats to human populations (Miller and Wark 2008, Self 2005). At present, the timescales on which upper crustal magma reservoirs assemble and supply magma to caldera-forming eruptions are thought to be on the order of 10^4–10^5 years, but the timescales of mobilization to eruption are on the order of 10^1–10^2 years. (Allan et al. 2013, Bachmann and Bergantz 2004, Gualda et al. 2018, Reid et al. 1997, Vasquez and Reid 2002). These recent studies combined with the large number of geophysical studies that have imaged magmatic systems help to understand how upper crustal reservoirs are stored and assembled on a broad scale, but the precise storage conditions and assembly timescales of CFEs remain elusive. To better assess magma assembly and storage processes, it is critical to first understand the environment in which minerals grew and were stored prior to eruption, and how this environment may have changed across a caldera-forming cycle.

Communities are converging on efforts to understand the physical state of upper crustal reservoirs, but most petrological studies provide evidence based on spatial scales from crystals (centimeter–micrometer) to eruption deposits (<1 km^3 to >1000 km^3), and geophysical studies designed to image magma reservoirs using seismic tomography techniques provide evidence at the 10s of km scale. This leaves an information gap at the lower limit of geophysical techniques (km-scale) and the crystal scale of petrological techniques (cm-scale), which makes it difficult to understand the specific arrangement of melt and crystals in magma reservoirs (Paulatto et al 2022). Paulatto et al. 2022 presented a compilation of geophysical studies that attempt to

quantify the proportion of melt in the magma reservoir at active volcanoes and find a median value of 13% melt, but a range of 1–90% melt. Despite uncertainty in the scale of magma reservoir storage, there is consensus from both the petrological and geophysical community that magmas are stored in melt-poor crystalline mush systems (Allan et al. 2013, Allan et al. 2017, Bachmann and Bergantz 2004, Bégué et al. 2014, Bouvet de Maisonneuve et al. 2021, Cashman et la. 2017, Charlier et al. 2005, Charlier and Wilson 2010, Cooper et al. 2014, Cooper et al. 2016, Gravley et al. 2016, Hildreth and Wilson 2007, Holness et al. 2019, Shane et al. 2008a, Shane and Smith 2013, Smithies et al. 2023, Wilson and Charlier 2009).

Magma storage models have evolved from the concept of large, long-lived, liquid-dominated magma bodies to more recent models of storage primarily in a crystal-rich network with the liquid-dominated erupted magmas as relatively short-lived features. The magma mush model, first introduced by Hildreth and Moorbath (1988) as a possible magma storage state, envisions a magma reservoir that is dominated by a crystalline framework, through which melts will pass or pond, and incorporate crystals from different regions of the reservoir. This idea was expanded upon by Hildreth (2004) which postulates the presence of upper crustal mush zones as the storage region for the magma that fed the Bishop Tuff eruption. Although their model is specific to the magma that generated the Bishop Tuff, there are some basic features of the magma mush model that are applicable to other systems. First, in such models, rhyolitic melts are stored as a crystalline mush in upper crustal reservoirs where convection is inhibited by high crystallinity. Second, interstitial high-silica melts percolate upwards through the crystalline framework and are driven into upper crustal reservoirs of magma mush by gas-driven filter pressing or by compaction of cumulates (Sisson and Bacon 1999, Bachmann and Bergantz 2004). The generation of large rhyolitic magmas requires the presence of an intermediate

cumulate restite at depth (Allan et al. 2013, Deering et al. 2016). Crystal fractionation and cumulate settling throughout the crustal column is an important control of the formation of silicic melts because such processes facilitate the rise and stalling of evolved melts in the uppermost crust (Bacon and Druitt 1988, Bachmann and Bergantz 2004, Charlier er al. 2005, Hildreth 2004, Shane et al. 2005b, Hildreth and Wilson 2007).

Hildreth et al. (2004) used the magma mush model to explain the zoned Bishop Tuff deposits, proposing a graded crystal-rich framework that is melt-poor at the periphery and melt-rich in the top and/or center. The crystal-rich periphery grades into a the "rigid sponge," a crystal-supported framework that houses melts in its interstices. Within this model, distributed melts are not in communication with each other in the framework and can evolve along different geochemical lines of descent. Similar models have been developed to explain Taupo Volcanic Zone (TVZ) magmas. Charlier and Wilson (2005) use variations in zircon age spectra to show that the Oruanui (CFE) and Okaia (post-CFE) melt bodies were each assembled rapidly prior to eruption and that they did not have the same source magma. Ultimately this led Charlier and Wilson (2005) to develop a model wherein eruptible magmas are rapidly assembled from high-silica melts and stored in a "holding chamber" prior to eruption. The high-silica melts are generated by assimilation and crystal fractionation within a "source zone" and stored in a "root zone" where further crystallization takes place. Allan et al. (2017) streamlined this model to combine the source and the root zone into a single magma mush storage region below which mafic magmas pond. Within this zone mafic magmas mix with intermediate mushes, plutonic or basement materials are assimilated into the mush zone, and mineral crystallization occurs within geochemically distinct melt pockets producing a range of mineral compositions. Geochemically distinct high-silica melts are extracted from this mush zone and drawn into a convective eruptible

melt-rich cap where minerals grow homogenized rims. Crystal-poor rhyolites are believed to originate from the melt-rich region and typically record evolved compositions reflected in high-silica glass compositions, homogenized mineral rims, and a subset of autocrystic or phenocrystic minerals that grew in the melt-rich cap (Allan et al. 2017, Charlier et al. 2005, Wilson and Charlier 2009, Gualda et al. 2018). Crystal-rich rhyolites can contain xenocrystic and antecrystic minerals scavenged from the mush zone, as well as autocrystic minerals grown within the eruptible melt-rich cap. Mineral chemistries preserved in crystal-rich rhyolites can reveal heterogenous storage conditions thereby reflecting the minerals' diverse histories. There is a wealth of mineralogical and geochemical observations in support of magmas mush systems that ranges from cumulate entrainment (Burt et al. 1998, Cooper and Wilson 2014, Ellis et al. 2014, Shane and Smith 2013) to highly evolved Ba and Sr concentrations in glass (Hildreth 2004) to trace element ratios in amphibole ascribed to crystal fractionation (Cooper et al. 2014, Davidson et al. 2007). Mineral records from the Okataina magma reservoir suggest a more complicated reservoir than at the Taupo Volcanic Center (Charlier and Wilson 2010, Shane et al. 2005b, Shane et al. 2007, Shane et al. 2008a, Shane et al. 2008b) and a recent geophysical summary by Miller et al. (2022) shows that the locus of magmatism within the Okataina Volcanic Center (OVC) has migrated through time, creating a nested caldera structure with a highly complex subsurface. Mineralogical studies of the Rotoiti caldera-forming eruption have shown that multiple, physically separate melt bodies were assembled immediately prior to (or during) eruption (Charlier et al. 2003, Schmitz and Smith 2004, Shane et al. 2005b, Wilson and Charlier 2010), and suggest that a single magma reservoir does not exist below the OVC.

Previous studies have found success in tracking magmatic evolution in the OVC using compositional data preserved in zircon (Charlier et al. 2003, Cooper et al. 2014, Barker et al.

2014, Storm et al. 2011, Storm et al. 2014, Wilson and Charlier 2010). It has been well documented that accessory minerals such as zircon are particularly useful trackers of melt evolution, and record unique compositional, thermal, and temporal data that support their growth in distributed yet evolved silicic melts. Zircon are both ubiquitous and persistent in peraluminous and metaluminous silicic melts, making them a faithful recorder of melt geochemistry at the time of crystallization (Hanchar and van Westrenen 2007, Claiborne et al. 2006, Claiborne et al. 2010). We use zircon as a compositional and temporal tracker of magma assembly and storage (e.g., Ellis et al. 2014, Reid et al. 1997, Rubin et al. 2016, Stelten et al. 2015, Storm et al. 2014, Swallow et al. 2019), and expand upon the existing conceptual magma mush models to explore zircon crystallization, growth, and storage histories. This work allows us to understand the patchwork nature of melts within magma mush systems, the locally heterogenous melt environments from which zircon grow, and how compositional and temporal records change across a caldera-forming cycle.

The Okataina Volcanic Center (OVC), Taupo Volcanic Zone (TVZ), New Zealand, is one of the most active silicic centers of the Quaternary (Houghton et al. 1995, Wilson et al. 2009). This prolific rhyolitic volcanism, multiple caldera collapse episodes, and a range in tuff crystallinity from crystal-poor to crystal-rich, make the OVC an ideal location to study magma mush dynamics and how such magma storage systems could impact its crystal cargo across the caldera-forming cycle (Cole et al. 2014, Miller et al. 2022, Smith et al. 2005). This contribution looks at magma assembly timescales and compositional variability across a caldera forming cycle (pre-caldera eruption, caldera-forming eruption, post-caldera forming eruption). The particular changes that occur across a caldera-forming cycle are largely unconstrained and we are interested in tracking compositional, thermal, and temporal changes across a caldera-forming

cycle as a means to understanding magma assembly and storage as a magmatic system builds to large eruptions and recovers after them.

2.3 GEOLOGIC BACKGROUND

The TVZ is the onshore continuation of the Tonga-Kermadec arc and is characterized by the coincidence of subduction of the west-dipping Pacific Plate beneath the Australian Plate at 45 mm/yr, and active continental rifting between 5-15 mm/yr (Fig. 2.1) (Cole et al. 2010, Cole et al. 2014). Transtensional faulting on the eastern side of the TVZ accommodates the rotation of the Eastern North Island block further facilitating rapid extension in the TVZ (Cole et al. 1990, Wallace and Beaven 2004). Back-arc rifting coupled with transtensional extension are two processes that facilitate the prolific volcanism (Allan et al. 2012, Allan et al. 2017, Bégué et al. 2014, Bouvet de Maisonneuve et al. 2021). Additionally, the thinning crust promotes increased upwelling of asthenosphere mantle and a shallowing of the Moho, thereby accommodating higher degrees of melt at shallower levels in the crust (Bibby et al. 1995), which potentially explains why the TVZ is the most prolific producer of rhyolitic magmatism in the Quaternary (Gravley et al. 2016, Smith et al. 2005). As such, the TVZ has experienced two major caldera-forming eruptions (CFEs) in the past ~50 ka at minimum (Cole et al. 2014, Houghton et al. 1995, Smith et al. 2005, Wilson et al. 1995, Wilson et al. 2009). Rhyolitic volcanism initiated around 1.6 Ma in the TVZ and is chiefly expressed as voluminous pyroclastic tuff deposits that range in volume from 0.01 – 530 km^3 (Wilson et al. 1995, Smith et al. 2005). The TVZ is roughly defined by a lenticular shaped rift that hosts eight volcanic centers, the northernmost of which is the Okataina Volcanic Center (OVC) which experienced two definite (Rotoiti, ~45 ka; Matahina ~322 ka) and one probable CFE (Utu ~557 ka) (Leonard et al. 2010, Deering et al. 2011, Cole et

al. 2014, Miller et al 2022). The most recent major CFE, Rotoiti, has been followed by many smaller eruptions ranging from 0.1 to 17.5 km^3 of pyroclastic flows and airfall, which are well-exposed and identifiable in the volcanic stratigraphy. At least 23 eruptions have followed the CFE (Rotoiti), and while many of these eruptions are compositionally similar in broad terms, each is unique in terms of volume, mineralogy, and storage parameters including temperature and pressure. In addition, many contain major minerals with antecrystic, less evolved cores indicating that the magmatic system sourced material from a pre-existing crystal mush (Charlier et al. 2003, Sas et al. 2021).

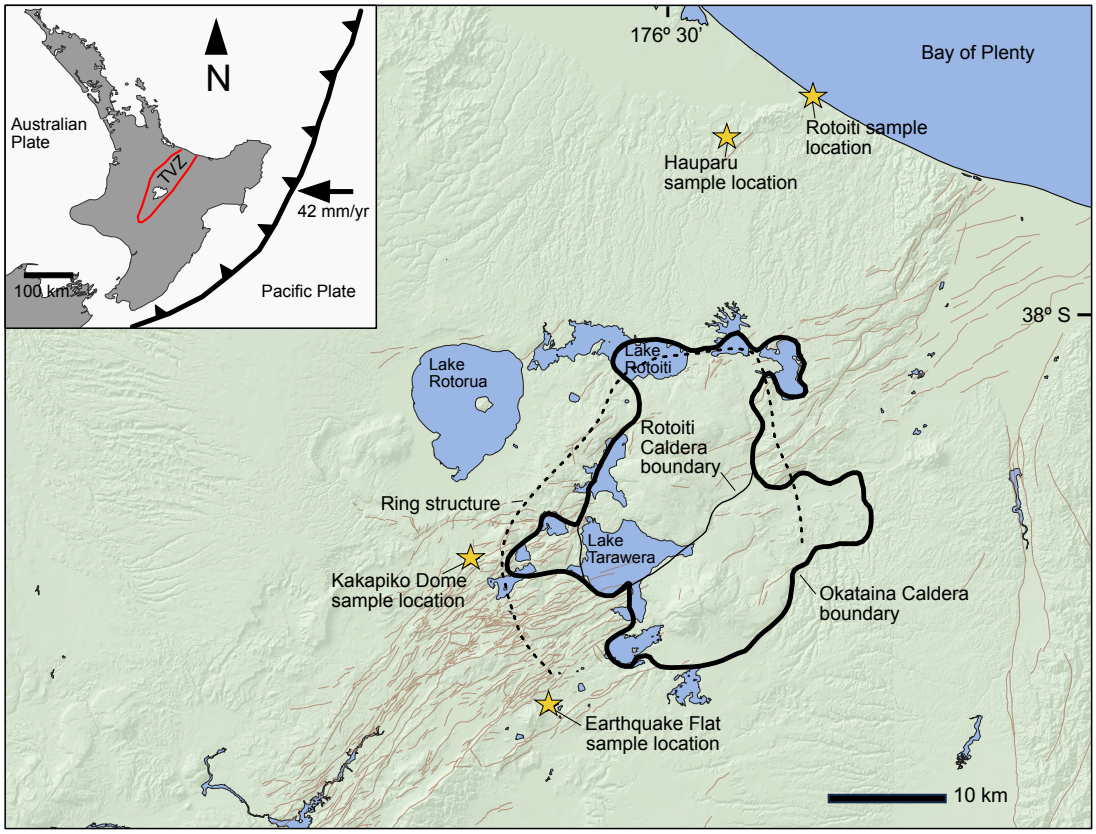


***Figure 2.1**: Map of the Okataina Volcanic Center (OVC) (thick black line), Rotoiti Caldera boundary (thin black line), and OVC ring structure (dashed black Line) from Nairn 2002 and*

Sas et al. 2021; sampling locations from this study indicated by yellow stars; hillshade and lake polygon layer publicly available at linz.govt.nz; regional fault layer from Langridge et al. (2016); Inset regional tectonic map, Pacific Plate trench location and convergence rate from Deering et al. 2011.

2.3.1 Deposits

Kakapiko dome is a small volume effusively-erupted rhyolitic lava, with a whole-rock composition of 73.9 wt.% SiO_2 (Sas et al. 2022) and anhydrous glass composition ranging from 77.4–78.3 wt.% SiO_2 (Table 2.1) (Rocco 2020). Kakapiko Dome is characterized by a high crystallinity (~45%) and a mineralogy of quartz > plagioclase >> biotite > hornblende > orthopyroxene ~ Fe-Ti oxides (Sas et al. 2022). The Kakapiko Dome eruption has not previously been dated, but surface zircon crystallization ages from this study suggest that the eruption was around or shortly after 147 ka (see below for discussion).

The Rotoiti CFE released 100 km^3 (DRE) of a moderately crystalline (~15-25%) magma deposited as an unwelded tuff, modifying the pre-existing Haroharo caldera within the OVC (Cole et al. 2009, Smith et al. 2005, Shane et al. 2005) (Fig 1). The Rotoiti vents are inferred to have originated within the Haroharo linear vent zone, along a NE-SW trending vent lineament (Miller et al. 2022, Nairn 2002, Schmitz and Smith 2004), although the precise location of the Rotoiti vents is unknown due to subsequent eruptions filling the caldera (Burt et al. 1998, Cole et al. 2014). The Rotoiti Pyroclastics, hereafter Rotoiti tuff, is defined by a combination of airfall and flow deposits. The Rotoiti tuff was preceded by the Matahi scoria, ~1 km^3 airfall unit of basaltic scoria, and immediately preceded by the Rotoehu Ash unit (Davis 1985, Shane et al. 2005, Cole et al. 2014). The Rotoiti tuff has an anhydrous whole-rock composition of 74.8 wt.% SiO_2, an anhydrous glass composition of 77.1–78.11 wt.% SiO_2, and has a mineralogy of plagioclase > quartz >> cummingtonite > Fe-Ti oxides > orthopyroxene > hornblende > biotite >

apatite/zircon (Table 2.1) (Schmitz and Smith 2004). Rotoiti is a cummingtonite-bearing tuff, with trace amounts of orthopyroxene and hornblende that increase in abundance up-section, but which do not exceed 0.1% modal abundance (Schmitz and Smith 2004). Biotite is not present in the lower units of Rotoiti but appears as a trace phase in the small volume upper units (<10% volume) (Schmitz 1995, Schmitz and Smith 2004). Cummingtonite is present throughout the entire eruptive sequence except for the uppermost ash bed of Unit 4 (Schmitz and Smith 2004). Accessory minerals zircon and apatite are present throughout the eruptive sequence. It has been suggested that the Rotoiti eruption was triggered by mafic underplating, which is supported by the stratigraphic relationship between the Matahi scoria, a small volume basaltic scoria and ash deposit, and the lower Rotoiti units. The absence of basaltic clasts or ash mingled in the Rotoiti pyroclastic deposits supports termination of the Matahi eruption prior to the Rotoiti eruption and a conformable contact and lack of paleosol development between the two eruptions suggest a short duration between eruptions (Schmitz and Smith 2004, Molloy et al. 2008). Mafic underplating is a common eruption trigger, but lack of mixing between the Matahi scoria and Rotoiti pyroclastics conceals any direct link between eruption trigger and mafic underplating (Schmitz and Smith 2004, Shane et al. 2005). It is recognized that the Matahi scoria and was likely triggered by movement along transtensional crustal faults that transect the TVZ facilitating basaltic diking (Allan et al. 2012). It is not unreasonable that transtensional crustal faults could provide pathways for the rapid rise of basalt, and/or decompression of the large rhyolitic bodies stored at shallow crustal levels. However, eruption trigger is beyond the scope of this study and will not be discussed further.

The Earthquake Flat Pyroclastics, hereafter EQF tuff, were produced by an eruption that explosively released 10 km^3 of a crystal-rich (25-45%) deposited as an unwelded tuff, along a

NW-SE segment of the inferred OVC ring structure (Molloy et al. 2008). Because the eruption vents are extra-caldera to the OVC and arguably overlap with the nearby Kapenga Volcanic Center some studies link the EQF eruption to the Kapenga Volcanic Center rather than the OVC (Charlier and Wilson 2003), and other studies cite this observation as evidence of a subsurface connectivity between the two volcanic centers (Schmitz 1995). Lack of paleosol deposits and a conformable contact between the initial EQF Rifle Range Ash unit and the uppermost Rotoiti deposits suggest that the EQF followed the Rotoiti eruption by only weeks to months (Nairn and Kohn 1973). The EQF tuff has an anhydrous whole-rock composition of 72.6 wt.% SiO_2, an anhydrous glass composition of 77.5–78.2 wt.% SiO_2, and a mineralogy of plagioclase > quartz ≫ biotite > hornblende > Fe-Ti oxides > orthopyroxene > apatite/zircon (Table 2.1) (Molloy et al. 2008, Grant et al. 2024). The EQF deposits contain abundant quartz phenocrysts (up to 2mm) and poly- and mono-mineralic clusters chiefly dominated by plagioclase and amphibole. Grant et al. (2024) documents multiple glomerocryst populations within EQF, including a larger size plagioclase-dominant population and a smaller size plagioclase-amphibole population. Large plagioclase (1-2 mm) occur as mineral clusters, while smaller shattered plagioclase grains, and few euhedral plagioclase grains range down to 0.25 mm. Conversely, almost all of the quartz grains are >2 mm in size. Plagioclase show compositional homogeneity across thick (0.25 mm) sodic rims (An_{26}) (Grant et al. 2024). Core and rim analyses of amphibole and orthopyroxene are compositionally homogenous (Grant et al. 2024). In general, major minerals lack resorption rims and other disequilibrium textures, with the exception of quartz which has a “frosted,” pock-marked texture on large (≤2 mm) doubly-terminated bipyramidal grains. It has been suggested that the upper Rotoiti biotite- and hornblende-bearing magmas were sourced from the same magma body as EQF, which would have required lateral migration within the upper crust.

Although lateral migration of magmas has been documented in the TVZ during the Oruanui eruption (Allan et al. 2012), isotopic evidence shows that the Rotoiti and EQF magmas are not consanguineous (Schmitz and Smith 2004).

The Hauparu Pyroclastics (including an unwelded pyroclastic flow and pumice fall deposits) were produced during an explosive eruption of 3.9 km^3 (DRE) of rhyodacitic magma around ~36 ka (Jurado-Chichay and Walker 2000, Shane et al. 2005, Smith et al. 2005). Hauparu is part of the Old Mangaone Subgroup, and seven Old Mangaone eruptions preceded the Hauparu Pyroclastics, collectively comprising 4.8 km^3 of eruptive deposits. The post-caldera Old Mangaone group deposits (and Unit H of Young Mangaone) are generally less compositionally evolved than the CFE itself, as demonstrated by the lack of quartz, relatively calcic anorthite contents ($An_{39–58}$) and the presence of clinopyroxene (Smith et al. 2005). In the Hauparu eruption of the Old Mangaone group, Shane et al. (2005) found two pumice populations: 1) a crystal-poor (<3%), compositionally mingled glass population, with a mineralogy of plagioclase >> orthopyroxene ~ clinopyroxene ~ Fe-Ti oxides, and ~5 mm glomerocrystic clusters; and 2) a crystal-moderate (15%), compositionally uniform glass population, with a mineralogy of plagioclase >> hornblende > Fe-Ti oxides > clinopyroxene > orthopyroxene (Table 2.1). The dominant type 1 Hauparu pumice range from 72–76 wt.% SiO_2 and 2.5–2.9 wt.% K_2O, whereas the low-volume type 2 pumice are compositionally restricted at ~77 wt.% SiO_2 and ~2.6 K_2O (Shane et al. 2005 Hauparu). Despite their evolved glass composition, Shane et al. (2005) found that the upper unit type 2 pumice have a dacitic whole-rock composition (67–68 wt.%) due to their crystal cargo. Differences between Hauparu and the pre-CFE, syn-CFE, and CFE eruption deposits could result from reorganization in the OVC magma reservoir. Post-caldera mineralogical and trace element variability in TVZ magmas have been previously documented

(Rubin et al. 2016) and require that the magmas formed at different and varied P-T-X-fO_2 conditions.

Table 2.1: Comparison of Okataina Volcanic Center eruption characteristics

Eruption	Type	Volume (km^3)	Crystallinity (%)	SiO_2 wt% (WR)	SiO_2 wt% (WR)
Kakapiko	Dome	--	20–40	73.6–74.2	77.4–78.3
Rotoiti	Plinian	100	15–25	70.2–75.4	77.1–78.1
Earthquake Flat	Plinian	10	25–45	68.8–74.4	77.5–78.2
Hauparu	Plinian	3.9	3–15	67.4–72.2	72.2–77.8

Eruption	T ºC (avg)	fO_2 (avg)	Mineralogy
Kakapiko	723	-15.80	qtz > plg ≫ bte > hbl > opx ~ oxides > ap/zrc
Rotoiti	790	-13.17	plg > qtz ≫ cmt > oxides > opx > hbl > bte > ap/zrc
Earthquake Flat	697	-16.93	plg > qtz ≫ bte > hbl > oxides > opx > ap/zrc
Hauparu	930	-10.24	plg > opx > cpx > hbl > oxides > ap/zrc

Quartz, qtz; Plagioclase, plg; Biotite, bte; Hornblende, hbl; Orthopyroxene, opx; Cummingtonite, cmt; Clinopyroxene, cpx; Fe-Ti oxides, oxides; Apatite, ap; Zircon, zrc

Whole rock (WR) and glass (gl) data normalized anhydrous

Temperature and oxygen fugacity are estimated from Fe-Ti oxide pairs

Kakapiko: Rocco 2020, Sas et al. 2021

Rotoiti: Schmitz and Smith 2004, Shane et al. 2005a

Earthquake Flat: Molloy et al. 2008, Grant et al. 2024

Hauparu sources: Smith et al. 2005, Shane et al. 2005b, Smith et al. 2002, Hopkins et al. 2021, Rocco 2020

2.4 METHODS

2.4.1 Sample collection

Pumice samples were collected from pyroclastic flows at available roadcut outcrops during three field seasons (2014, 2017, 2019). We preferentially sampled the largest pumice lapilli or blocks present, and sampled each unit from a single stratigraphic horizon. Rotoiti samples were collected at -37.842581, 176.628237; Earthquake Flat samples were collected at -38.311118, 176.37911; Hauparu samples were collected at -37.870185, 176.523368 and -38.132588, 176.805149; and Kakapiko Dome samples were collected at -38.20623, 176.28204. We targeted

these specific sample localities to ensure that we collected samples representative of the majority of the volume of magma vented during each eruption; we avoided ash beds, basal flow zones, uppermost stratigraphic beds, and reworked layers.

2.4.2 Sample processing

All samples were crushed in a stainless-steel mortar and pestle, and sieved into different size fractions (>2 mm, 1-2 mm, 0.5-1 mm, 0.25-0.5 mm, 0.125-0.25 mm, 0.063-0.125 mm, and <0.063 mm). Samples were rinsed in deionized water, methanol, and acetone, and were dried under a heat lamp. Once clean and dry, a hand magnet was used to remove Fe-Ti oxides. The 0.25-0.5 mm, 0.125-0.25 mm, and 0.063-0.125 were passed through the Frantz Magnetic Barrier Laboratory separator at increasing amperages to remove magnetic materials. Biotite, hornblende, and pyroxenes were removed from the bulk sample at amperages <0.8. Plagioclase, quartz and zircon are concentrated in the non-magnetic split at the highest amperages (>1.8). To separate zircon from the plagioclase and quartz, the samples were then passed through methylene iodide (diiodomethane) to separate the zircon fraction by density. The dense mineral split (zircon split) was rinsed in deionized water followed by acetone. The zircon sample was leached in ~10% HF acid for ~15 minutes to remove adhering glass prior to hand picking of zircon in preparation for mounting.

2.4.3 Mounting and imaging

For surface analyses, sample zircon and Early Bishop Tuff (EBT) standard zircon were pressed into indium metal on an aluminum mount such that a prismatic zircon face was flush with the indium surface; the mount was left unpolished. This approach allows the beam to capture the

outermost surface of the zircon which is representative of the youngest phase of growth (outermost 3-5 microns). This results in more effective targeting of the latest growth than analyzing exterior-most zones of sectioned zircon, which averages multiple growth zones across the diameter of the spot (30-40 microns). Mounts were washed with soap, ~10% HCl, and dried in a low temperature oven. Finally, the mounts were dusted with argon gas before entry into the SHRIMP-RG sample chamber. For interior analyses, sample zircon and EBT standard zircon were mounted in epoxy and cured overnight. The mount was sectioned using fine grit abrasion paper to expose zircon interiors. Zircon interiors were polished using an aluminum grit slurry, cleaned with soap, and dried in a low temperature oven. Zircon interiors were gold coated to a thickness of 20 microns in advance of entry into the SHRIMP-RG sample chamber to provide conductivity and reduce charging. Prior to analysis, surface mounts were imaged under reflected light, and interiors mounts are imaged under cathodoluminescence, to ensure that beam placement does not intersect surface imperfections, holes, or inclusions.

2.4.4 Zircon morphology

Zircon from all four samples are similar in character: small (<250 microns), high aspect ratio, sector, patchy, and/or oscillatory zoned, with glass inclusions and/or dissolved interior pockets. Zircon surfaces were smooth and free of adhering contaminants, and in many cases the zircon exhibited prismatic habits. When probing zircon interiors, analytical spot locations were typically placed on the innermost exposed zone of the crystal and selected to avoid any included contaminant phase or dissolved region. However, in cases where the innermost exposed zones contained inclusions or holes, spots were occasionally placed in an alternate location.

2.4.5 Analytical Procedures: SHRIMP-RG

Zircon surfaces and sectioned interiors were analyzed for ^{238}U-^{230}Th ages and trace elements on the SHRIMP-RG at the USGS/Stanford laboratory (Palo Alto, California, USA). Analyses used a primary O_2^- ion beam. Age analyses were run with beam current ranging from ~12.5 – 18 nA and mass resolution from 8000-9000 (~10% peak height; sufficient to resolve any major mass interferences), depending on the session. The accelerating voltage was 10 kV. The ^{238}U-^{230}Th age spot was typically ~40–50 microns wide, and ~5 microns deep. Trace element analyses were run with a beam current of 1.5 nA, mass resolution of 11,000 (~10% peak height; sufficient to resolve any major mass interferences), and accelerating voltage of 10 kV. The beam shape was typically 16 x 16 microns, but during some session was as large as 20 x 20 microns. The beam pit depth was ~2 microns. The shallow depth of the beam pit ensures that the analysis captures the youngest phase of growth. For zircon surfaces, the age and trace element spots were placed near each other but did not overlap, so that each analysis captures the outermost growth zone. For zircon interiors, the age and trace element spots were placed near each other and within the same zone as much as possible. In some cases, the small size of the zircon precluded adjacent placement of age and trace element spots; in these cases, the age and trace element spots were placed where the zircon exposure would allow.

Age data were culled if ZrO^{2+} and ThC^{+} counts were too low and high, respectively, and if ^{238}U-^{230}Th slopes were not within error of unity. Low ZrO^{2+} suggests that the grain is not zircon, and high ThC^{+} suggests that the beam hit an impurity (surface detritus). Less than 1% of age data were culled for each dataset. ^{238}U-^{230}Th age analyses on EBT standards were run at the beginning and end of each session and after approximately every three unknown samples to monitor instrumental U-Th fractionation. Replicate measurements of EBT were quantified to

determine the relative sensitivity factor, which was then used to correct for U-Th fractionation. To correct for fractionation, the weighted mean of the ratio of (^{230}Th)/(^{238}U) of EBT analyses is compared to the known (^{230}Th)/(^{238}U) of EBT at secular equilibrium and this is applied to the unknown (^{238}U)/(^{232}Th) data as a fractionation correction factor. Model ages were calculated from individual zircon analyses using host glasses as a proxy for the liquid from which the zircon crystallized. Uncertainties in model ages are propagated from slope error. For Kakapiko Dome, Rotoiti, Earthquake Flat, Hauparu samples we use host glass (^{238}U)/(^{232}Th) and (^{230}Th)/(^{232}Th) data from Chapter 3. In order to allow for compositional variability in liquids within the magma reservoir, we calculated an average and a range of OVC host glass value from Charlier et al. 2003, Charlier and Wilson 2010, Storm et al. 2011, and this study: average host glass values are (^{238}U)/(^{232}Th) = 0.727 and (^{230}Th)/(^{232}Th) = 0.732. Model age uncertainties were propagated using the average, high, and low (^{238}U)/(^{232}Th) and (^{230}Th)/(^{232}Th) ratios from these existing OVC data. The model surface ages show <0.5% difference, and model age interiors show <5% difference between the ages calculated using the high compared to low values for OVC glass. For trace element analyses, concentrations of unknowns are calculated relative to the well characterized MAD-559 (MADDER) standard (Coble et al. 2018). Replicate measurements of the trace element standard, MADDER, were run after every ~5 unknown analyses. The MADDER standard session reproducibility is calculated at one sigma. Reproducibility (percent) for each session was: EQF surface and interior sessions: Ti, Gd, Yb, U, Th, Hf <16 %, Sc, Y <6 %, Sm <20 %, Eu <25 %, P <13 %; Rotoiti surface and interior sessions: Y, Sc, U, Th, Hf <8 %, Ti <22 %, Sm <20 %, Eu <14 %, Gd <12 %, Yb <10 %, P <45 %; Hauparu surface and interior sessions: Ti, Sc <24 %, Sm <13 %, Eu <11 %, Yb, Gd, Y, P, U, Th <8 %, Hf <17 %; Kakapiko surface and interior session: Ti <38 %, Sm <50 %, Eu <13 %, Sc, Gd, Hf < 22 %, Yb, P, U, Th

<19 %, Y <16 %. Trace element analyses were culled if K, Fe, and Pb all exceeded one order of magnitude about the mean for each element. Coincidence of high K, Fe, and Pb suggests that the beam intersected a glass inclusion. Less than 1% of the data were culled for each dataset.

2.4.6 Analytical Procedures: MC-ICP-MS

Bulk separates of glass were prepared as described above using magnetic and density techniques. All separates were handpicked used a binocular microscope to remove any unwanted grains (e.g. other minerals, grains with large inclusions, intensely weathered grains) and weighed; glass samples were ~0.1 g. The samples were leached in a solution of 0.1 M HCl/2% H_2O_2 to remove any surface staining or organic detritus. U and Th from cleaned and leached separates were chemically separated and concentrated from the matrix using ion-exchange columns following the methods of Cooper and Donnelly (2008). Briefly, the processed glass U and Th samples were split into two aliquots, the first was spiked with a ^{233}U-^{229}Th mixed tracer for measurement of U and Th concentrations, and the second aliquot was processed to measure U and Th isotopic composition. U and Th in both aliquots were purified using Eichrom TRU resin. Samples of USGS rock standards, AGV2, BCR2, and W2 were run in parallel with unknowns during each round of U-series chemistry, in addition to a total process blank, to monitor for accuracy and background, respectively. U and Th sample aliquots were analyzed on the University of California Davis Interdisciplinary Center for Plasma Mass Spectrometry (UCD-ICPMS) Nu Plasma MC-ICP-MS.

2.4.7 Zircon melt modeling

We used the model of Claiborne et al. 2018 to calculate modeled melt-trace element concentrations that would be in equilibrium with our zircon analyses, based on empirically derived partition coefficients from Claiborne et al. (2018) and trace element concentration data for zircon measured in this study. We used the standard equation defining partition coefficients:

$$K_d = \frac{C_s}{C_l}$$

Where the partition coefficient, K_d, is equal to the ratio of the concentration of a given element in the solid to the concentration of a given element in the liquid. We compare the modeled liquid composition to measured glass compositions for each sample (Rocco 2020). All host glass and modeled glass compositions are normalized to chondritic uniform reservoir values of McDonough and Sun (1995).

2.5 RESULTS

2.5.1 Zircon model ages

Data were screened to remove analyses that show evidence for contamination by inclusions within the zircon grains. Criteria used were based on $^{96}Zr^{+}$ count rate consistent with zircon analysis (e.g. removing apatite, glass, etc) and the ThC count indicating epoxy. Less than 1% of age and trace element analyses were culled. The weighted mean and MSWD of the ^{238}U-^{230}Th isochron slopes for data from each sample were calculated using IsoPlot (Table 2.2). Here we employ the MSWD to quantify which, if any, of the age groups can be described as a single population. The weighted means were calculated twice using IsoPlot, first including all data points, and second rejecting the outliers to check if outlier removal would result in a statistically significant single population. Outliers are identified and rejected if they fall outside of the range

defined by 2σ uncertainties about the mean. In most cases of analyses of volcanic zircon interiors, crystallization occurs over 10^0–10^5 years and therefore does not represent a single population (Cooper 2015). Of our model age data, only three groups have MSWD consistent with a single population: 1) Kakapiko surfaces; 2) Kakapiko interiors (if the youngest analysis is rejected), and 3) the Rotoiti surfaces if the five oldest grains are rejected (Table 2.2).

Table 2.2: Summary of statistics for Okataina Volcanic Center U-series slopes

Spot location	Eruption	Wtd Mean	1σ	95% CI (2σ)	MSWD	n	Within acceptable range of MSWD?
Surface	Kakapiko	0.741	0.024	0.048	1.3	20	yes (95% CI)
Surface	Rotoiti all	0.399	0.029	0.058	2.5	36	no
Surface	Rt slope <0.6	0.387	0.018	0.036	1.4	31	yes (95% CI)
Surface	EQF all	0.480	0.042	0.084	3.7	32	no
Surface	Hauparu	0.564	0.057	0.114	9.6	46	no
Interior	Kakapiko	0.805	0.035	0.070	2.4	20	no
Interior	Rotoiti	0.488	0.038	0.076	4.1	46	no
Interior	EQF	0.675	0.033	0.066	4.7	40	no
Interior	Hauparu	0.512	0.067	0.134	11.3	24	no

PDFs of the zircon-glass slopes are presented for zircon surfaces and interiors from each eruption and compared to the slope corresponding to the accepted eruption age for each (Fig. 2.2). The Kakapiko Dome zircon interior ages range from secular equilibrium to within error of eruption and define a single peak at 176 ka (Fig. 2.2A). Conversely, the Kakapiko surfaces have a broader peak at 147 ka with a shoulder corresponding to higher slope values. Six of the surface ages are clustered near eruption age (and within error of eruption), although there is a tail of older ages that are not within error of eruption. There are no surface ages older than 212 ka. The Rotoiti zircon age PDF has relatively simple peaks for both surfaces and interiors at 55 ka and 73 ka, respectively, although both the interiors and surfaces have a shoulder at higher slope values (Fig. 2.2B). Rotoiti interior ages range from secular equilibrium to within error of eruption,

whereas 18 of the surface analyses out of 36 total are clustered within error of eruption age. The EQF interior PDF has a short, broad peak at 122 ka that tails off to higher slope values, and the corresponding ages range from secular equilibrium to within error of eruption (Fig. 2.2C). Conversely, the EQF surface PDF has a simpler peak at 71 ka, with a few analyses at higher slope values. EQF surface ages range from 206 ka to within error of eruption age. For Kakapiko Dome, Rotoiti, and EQF, the surface PDF peaks yield younger model ages than do those of the interiors. The Hauparu surface and interiors PDFs show complicated polymodal distributions, both with peaks near eruption age and secondary peaks at higher slope (and age) values (Fig. 2.2D). Both the Hauparu surfaces and interiors range from secular equilibrium to within error of eruption, and the weighted-mean of slopes yield an average crystallization age of 90 ka for the surfaces, and 78 ka for the interiors. Hauparu is the only eruption for which the weighted-mean of the slopes for surface analyses yields an older crystallization age then the interiors. This is likely due to sampling bias, as there are nearly double the amount of surface analyses (n=46) than interior analyses (n=24), and the overall shape of the PDFs are similar.

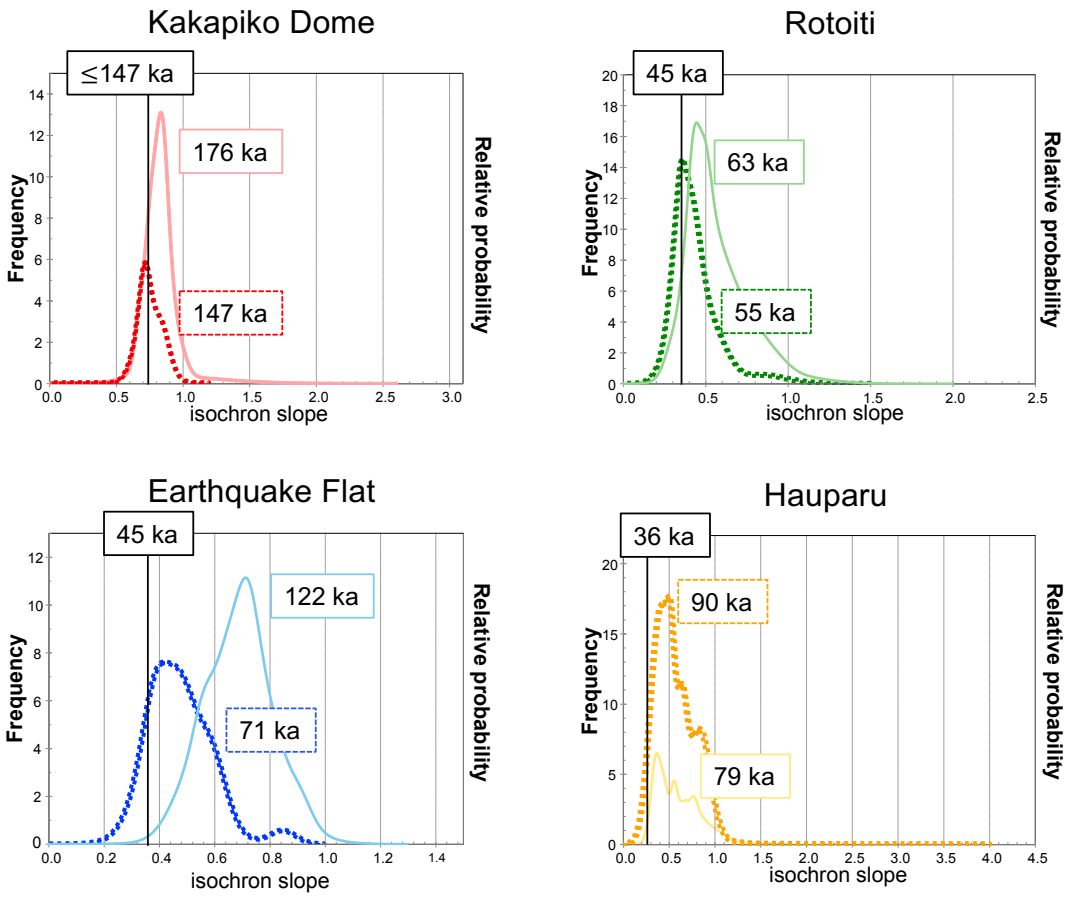


***Figure 2.2**: Probability density functions (PDFs) of the isochron slope of zircon populations from Kakapiko Dome, Rotoiti, Earthquake Flat, and Hauparu eruptions. Zircon surface populations illustrated by the dashed dark-colored line, and interiors are illustrated by the solid light-colored line, with the corresponding mean crystallization age for each population flagged in dashed and solid boxes, respectively. Eruption ages are illustrated by solid black vertical lines, and the accepted eruption age flagged with a corresponding black box. Host glass ratios and decay constants for age calculations presented in Chapter 3.*

2.5.2 Temperature

2.5.2.1 Ti-in-zircon thermometry

Temperatures were calculated from our Ti concentration data using the Ti-in-zircon thermometer of Ferry and Watson (2007). Titanium activity ($aTiO_2$) was calculated using Fe-Ti oxide pair

compositional data from Molloy et al. (2008) and Grant et al. (2024) for EQF ($aTiO_2$ = 0.461), Schmitz and Smith (2004) for Rotoiti ($aTiO_2$ = 0.683), and an estimate of $aTiO_2$ = 0.5 for Hauparu and Kakapiko Dome, and using the oximeter of Ghiorso and Evans (2008). Silica activity was set at $aSiO_2$ = 1 because quartz is present in all eruptions. Given the evolved, highly silicic composition of these deposits, it is likely that quartz was on the liquidus throughout the duration of zircon crystallization. Lowering $aSiO_2$ by 10% decreases the calculated temperatures by ~10 °C. Therefore, the temperatures that we present are maxima based on the assumption of quartz saturation. Natural variation in $aTiO_2$, on the order of +/- 0.1, changes the calculated absolute temperature <15 °C. For example, $aTiO_2$ measured from EQF oxide pairs ranges from 0.447 to 0.483, and this propagates to <7 ºC change in temperature for the EQF zircon surfaces and <8 ºC change in temperature for the EQF zircon interiors. 2σ analytical uncertainties on ^{49}Ti concentration measurements propagate to temperature uncertainties of $\pm$ 20 ºC, which places many of the Ti-in-zircon temperatures within error of each other. Importantly, here we focus on the *relative* differences in temperature between the analyses. Therefore, unless Ti activity was significantly different for melts from which the different zircon grains crystallized, our choice of Ti activity will not affect the interpretations. Furthermore, the Ferry and Watson (2007) Ti-in-zircon thermometer places $\pm$ 50 ºC uncertainties on the calibration but again, this is a systematic error that does not affect our interpretations of relative differences in temperature. We calculated the range, median, arithmetic mean of Ti-in-zircon temperatures for all grains measured for each eruption (Tables 2.3 and 2.4). Rotoiti and EQF share the most similarities in temperature range, and both have interiors which record higher temperatures than their respective surfaces, and which yield a larger range in temperature than do the surfaces (Fig. 2.3). The Hauparu surfaces and interiors are on average hotter than zircon from the other three eruptions, irrespective of the

outlier at 1211 °C. The Kakapiko interior temperatures are similar to the range of temperatures seen in EQF and Rotoiti interiors (~650 - ~900 °C), but the Kakapiko surfaces have a cluster of grains that yield cooler temperatures than the other three eruptions (~625 °C). There seems to be minimal zircon crystallization below ~640 °C, except for a cluster of Kakapiko surfaces and two interiors (Fig. 2.3).

Table 2.3: Summary of geochemical statistics for Okataina Volcanic Center zircon surfaces

Geochemical index	*Surfaces*	Min	Max	Median	Arithmetic mean	Wtd Mean	1σ	95% CI (2σ)	MSWD	n	Within acceptable range of MSWD?
Eu/Eu*	Kakapiko Dome	0.12	0.28	0.23	0.21	0.19	0.05	0.09	0.22	21	no
	Rotoiti	0.21	0.48	0.33	0.32	0.30	0.02	0.04	0.82	44	yes (95% CI)
	Earthquake Flat	0.11	0.30	0.17	0.17	0.15	0.01	0.02	0.88	47	yes (95% CI)
	Hauparu	0.12	0.67	0.32	0.35	0.25	0.01	0.02	11.2	34	no
Y/P	Kakapiko Dome	1.7	10.8	6.0	5.6	3.20	0.90	1.80	4.8	21	no
	Rotoiti	0.9	9.3	2.1	3.1	2.12	0.27	0.54	67	44	no
	Earthquake Flat	1.8	13.0	5.0	5.9	3.22	0.54	1.08	27	47	no
	Hauparu	2.0	12.3	6.1	6.2	4.47	0.71	1.42	31	34	no
ΣREE+Y/P	Kakapiko Dome	0.9	5.8	3.1	2.9	--	--	--	--	21	--
	Rotoiti	0.5	4.7	1.1	1.6	--	--	--	--	44	--
	Earthquake Flat	1.0	6.4	2.4	3.0	--	--	--	--	47	--
	Hauparu	1.0	5.5	3.2	3.1	--	--	--	--	34	--
Yb/Gd	Kakapiko Dome	14.5	35.1	22.5	22.5	20.2	2.6	5.2	0.65	21	yes (95% CI)
	Rotoiti	16.0	47.0	34.0	31.0	25.7	2.6	5.2	18	44	no
	Earthquake Flat	17.0	43.0	30.0	30.0	25.6	2.1	4.2	2.3	47	no
	Hauparu	11.5	46.3	22.3	25.1	19.5	2.5	5.0	25	34	no
Hf	Kakapiko Dome	4708	23361	7306	9246	6930	1100	2200	2.7	21	no
	Rotoiti	9511	12981	11295	11382	11336	240	480	4.5	44	no
	Earthquake Flat	5135	14819	12070	11684	10567	800	1600	3.1	47	no
	Hauparu	9825	15279	12142	12197	11926	450	900	26	34	no
Temperature (˚C)	Kakapiko Dome	573	990	653	669	--	39	78	--	21	--
	Rotoiti	636	914	679	690	--	14	28	--	44	--
	Earthquake Flat	640	731	666	670	--	5	10	--	47	--
	Hauparu	684	1211	801	807	--	34	68	--	34	--
Zr/Hf	Kakapiko Dome	20	101	65	62	--	--	--	--	21	--
	Rotoiti	37	50	42	42	--	--	--	--	44	--
	Earthquake Flat	32	93	40	43	--	--	--	--	47	--
	Hauparu	31	49	39	40	--	--	--	--	34	--

Table 2.4: Summary of geochemical statistics for Okataina Volcanic Center zircon interiors

Geochemical index	*Interiors*	Min	Max	Median	Arithmetic mean	Wtd Mean	1σ	95% CI (2σ)	MSWD	n	Within acceptable range of MSWD?
Eu/Eu*	Kakapiko Dome	0.08	0.65	0.35	0.37	0.20	0.06	0.13	1.06	19	yes (95% CI)
	Rotoiti	0.23	0.58	0.37	0.37	0.35	0.02	0.04	0.72	66	yes (95% CI)
	Earthquake Flat	0.06	0.50	0.17	0.19	0.14	0.01	0.02	5.5	30	no
	Hauparu	0.14	0.51	0.38	0.35	0.23	0.06	0.11	6.8	19	no
Y/P	Kakapiko Dome	1.7	10.6	5.3	4.8	3.16	0.78	1.56	3.6	19	no
	Rotoiti	1.9	10.4	3.8	4.0	2.78	0.27	0.54	7.3	66	no
	Earthquake Flat	2.7	10.4	4.5	4.9	4.10	0.34	0.68	17	30	no
	Hauparu	1.9	5.6	4.3	4.0	3.28	0.55	1.10	10	19	no
ΣREE+Y/P	Kakapiko Dome	0.9	5.2	2.6	2.4	--	--	--	--	19	--
	Rotoiti	1.0	5.1	2.0	2.1	--	--	--	--	66	--
	Earthquake Flat	1.5	5.0	2.3	2.5	--	--	--	--	30	--
	Hauparu	1.0	2.8	2.2	2.0	--	--	--	--	19	--
Yb/Gd	Kakapiko Dome	9.1	30.6	19.5	20.7	15.5	3.2	6.4	1.8	19	yes (95% CI)
	Rotoiti	15.0	51.0	30.0	31.0	25.4	2.0	4.0	7.5	66	no
	Earthquake Flat	8.0	36.0	19.0	20.0	18.5	2.3	4.6	9.4	30	no
	Hauparu	21.1	40.0	30.9	30.6	29.0	2.4	4.8	2.8	19	no
Hf	Kakapiko Dome	4154	11366	5322	6457	5446	730	1460	1.8	19	yes (95% CI)
	Rotoiti	7881	13235	10485	10494	10344	280	560	4.1	66	no
	Earthquake Flat	7638	39020	12634	15506	11594	780	1560	21	30	no
	Hauparu	8514	11560	9937	9865	9748	370	740	1.7	19	yes (95% CI)
Temperature (˚C)	Kakapiko Dome	621	761	697	697	--	18	36	--	19	--
	Rotoiti	620	810	698	699	--	8.4	16.8	--	66	--
	Earthquake Flat	664	807	731	734	--	12	24	--	30	--
	Hauparu	669	821	748	743	--	21	42	--	19	--
Zr/Hf	Kakapiko Dome	42	115	89	81	--	--	--	--	19	--
	Rotoiti	36	61	46	46	--	--	--	--	66	--
	Earthquake Flat	12	53	38	34	--	--	--	--	30	--
	Hauparu	41	56	48	49	--	--	--	--	19	--

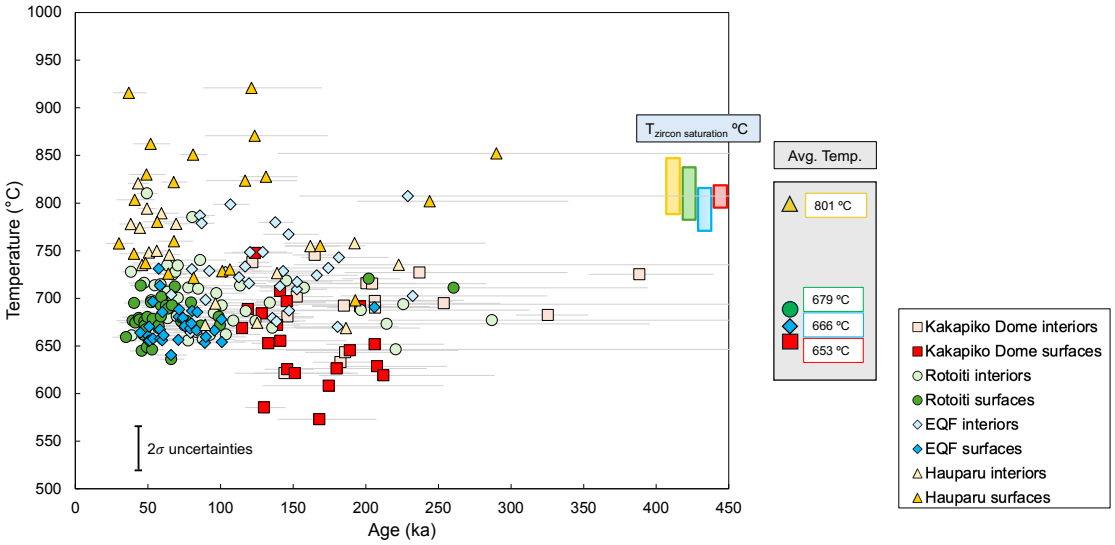


***Figure 2.3**: Ti-in-zircon temperatures versus ^{238}U-^{230}Th crystallization age measured in zircon surface and interiors for Kakapiko Dome (dark and light red squares, respectively), Rotoiti (dark and light green circles, respectively), Earthquake Flat (dark and light diamonds, respectively), and Hauparu (dark and light triangles, respectively). Uncertainties on ages are 1σ standard deviations, propagated as ages based on 1σ uncertainty in the slope.*

Uncertainties in Ti-in-zircon temperatures were propagated from the 2σ uncertainty in Ti concentration measurements, and were on the order of +/- 20 ºC. Representative 2σ uncertainties are presented. Zircon saturation temperatures were calculated using the derivation of Watson and Harrison (1983) the range of which is represented by colored boxes: yellow box indicates the Hauparu saturation temperature at 790–848 ºC; the green box indicates the Rotoiti saturation temperature range at 779–836 ºC; the blue box indicates the Earthquake Flat saturation temperature range at 773–818 ºC; the red box indicates the Kakapiko Dome saturation temperature range at 795–819 ºC. Median values of each Ti-in-zircon temperature surface population are presented on the right: Hauparu median surface crystallization temperature, 801 ºC; Rotoiti median surface crystallization temperature, 679 ºC; Earthquake Flat median surface crystallization temperature, 666 ºC; Kakapiko Dome median surface crystallization temperature, 653 ºC.

2.5.2.2 Zircon Saturation Thermometry

We calculated zircon saturation temperatures using the calibrations of Watson and Harrison (1983), Boehnke et al. (2013), and Shao et al. (2020). Watson and Harrison (1983) define a compositional parameter M based on major element oxides, and a partition coefficient $D_{Zr}^{zircon/melt}$ for Zr between zircon solid and melt, also used by the calculations of Boehnke et al. (2013) and Shao et al. (2020), the latter two of which refine thermometry calculation based on modern analytical capabilities and new experimental studies. The formulation of Watson and Harrison (1983) yields the hottest zircon temperatures for a given analysis, Boehnke et al. (2013) yields the coolest temperatures, and Shao et al. (2020) yields intermediate temperatures compared to the other two calibrations. We used Kakapiko Dome whole rock compositional data and zirconium concentration data from Sas et al. (2021) and
glass compositional data and zirconium concentrations from Rocco (2020); Rotoiti whole rock compositional data and zirconium concentration data from Schmitz and Smith (2004), and Rotoiti glass compositional data from Shane et al. 2005; EQF whole rock compositional data and zirconium concentration data from Schmitz and Smith (2004), and EQF glass compositional and zirconium concentration data from Grant et al. 2024; Hauparu whole rock and glass major

element compositional data and zirconium concentration from Rocco (2020). Using the Kakapiko Dome, Rotoiti, and EQF glass compositions yields lower saturation temperatures than the whole rock composition by ~50-100 °C (Fig. 2.4). Conversely, using the Hauparu glass composition yields higher temperatures than the whole rock composition by ~40 °C. Even when using the hotter temperatures calculated from Watson and Harrison (1983), and using Hauparu glass compositions, the hottest calculated temperature is 887 °C, which is inconsistent with the four Hauparu zircon surface analyses with crystallization temperatures exceeding 900 °C according to the Ti-in-zircon temperature calculations. However, given the uncertainties from the Ti-in-zircon thermometry (±50 ºC) three of the four >900 °C zircon grains are within error of the calculated zircon saturation thermometry.

2.5.2.3 Fe-Ti oxide thermometry

Fe-Ti oxides record pre-eruptive temperatures given fast diffusive re-equilibration rates at magmatic temperatures (Venezky and Rutherford 1999, Devine et al. 2003, Hou et al 2021). We use the calibration of Ghiorso and Evans (2008) to calculate Fe-Ti exchange temperature, which is a proxy for pre-eruptive temperature (Table 2.1). Fe-Ti oxide pair compositional data is from Schmitz and Smith (2004) for Rotoiti and Grant et al. (2024) for EQF. Rotoiti Fe-Ti oxide pairs yield a range of 751–862 °C, and an average of 780 °C. EQF Fe-Ti oxide pairs yield a range of 694–722 °C with an average of 703 °C. From Shane et al. (2005b), Hauparu Fe-Ti oxide temperatures range from 890–990 °C for the type 1 pumice, and 866–886 °C for the type 2 pumice. From Sas et al. 2021, Kakapiko Dome oxide temperatures range from 708–751 °C.

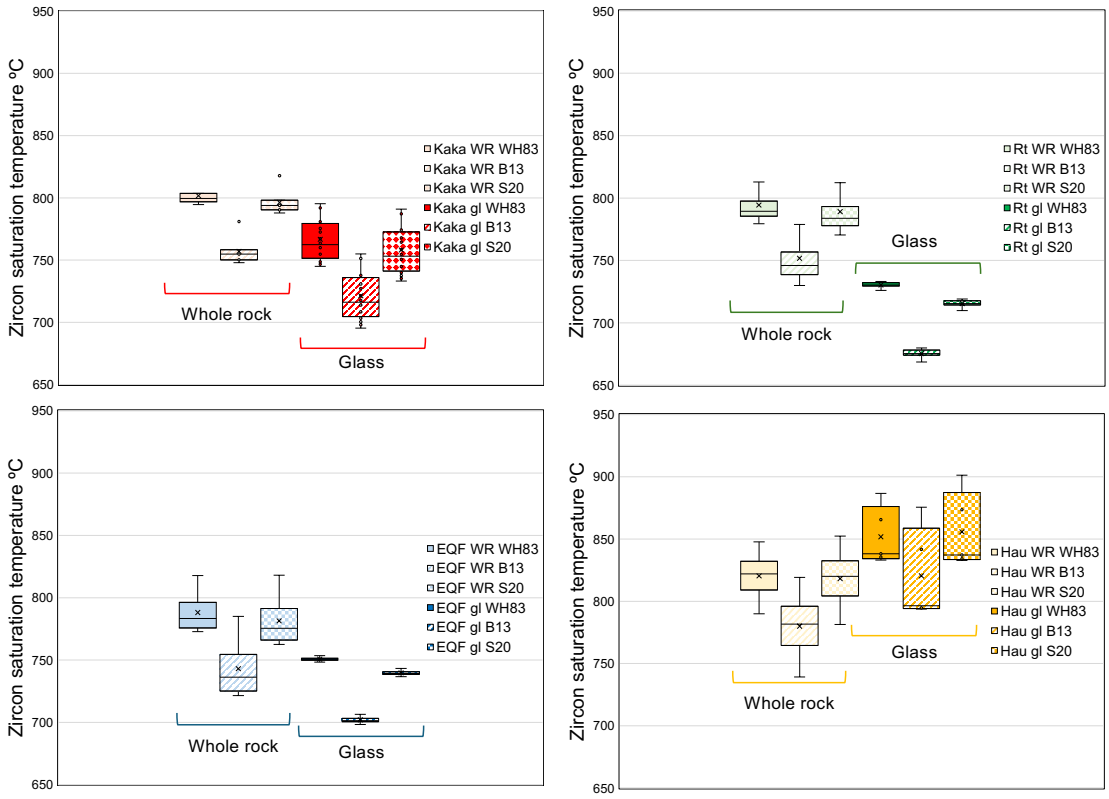


Figure 2.4*: Box and whisker plots illustrating the distribution of zircon saturation temperature using whole-rock and glass compositions. The box shows the distribution of data grouped into quartiles, where the median is defined by the black line and the average is defined by the black 'x.' The whiskers represent the range in data, and outliers are plotted beyond the whiskers if present. Outliers are determined if they exceed 1.5 times the upper or lower quartile values. Three models are presented: Watson and Harrison (1983) (solid-colored symbols), Boehnke et al. (2013) (diagonal striped symbols), and Shao et al (2020) (diamond checkerboard symbols). In most cases the whole-rock composition predicts higher saturation temperatures than the glass except for Hauparu.*

2.5.3 Geochemistry

*2.5.3.1 Eu/Eu**

The Eu/Eu* anomaly is the positive or negative deviation from a straight line propagated between CHUR normalized vales for Sm and Gd. Results for Eu/Eu* values for each eruption are reported in Tables 2.3 and 2.4. Eu/Eu* values measured in zircon surfaces and interiors are

generally understood to record the degree of plagioclase fractionation experienced by the melt from which the zircon grew. In general, Kakapiko Dome, Rotoiti, EQF, and Hauparu zircon surfaces have a more restricted range of Eu/Eu* than the interiors of grains for the same eruption. Despite the different ranges observed in corresponding surface and interior populations, the weighted-mean for each pair of populations are very similar. The MSWD of the Kakapiko surface, Rotoiti interior, and EQF surface data falls within the 99% confidence interval, suggesting that each group defines a single, normally distributed population.

2.5.3.2 Zr/Hf in glass

Zr/Hf in glass is a measure of magmatic system evolution, generally tracking the degree to which zircon has fractionated from the melt. Lower Zr/Hf ratios measured in glass or whole rock indicate a melt that has fractioned and been separated from zircon (Claiborne et al. 2006). Kakapiko Dome major element glass and trace element data (Rocco 2020) yield Zr/Hf ratios range from 25–34 and average 29 for a 77.4–78.3 wt.% SiO_2 glass (normalized anhydrous). The Rotoiti major element glass and trace element data (Rocco 2020, Hopkins et al. 2021) yield Zr/Hf ratios of 28–46 and average 34 for a 77.9–78.8 wt.% SiO_2 glass (normalized anhydrous). The EQF major element glass and trace element data (Rocco 2020, Hopkins et al. 2021) yield Zr/Hf ratios of 29–53 and average 33 for a 77.1–78.1 wt.% SiO_2 glass (normalized anhydrous). The Hauparu major element glass and trace element data (Rocco 2020, Hopkins et al. 2021) yield Zr/Hf ratios of 36–68 and average 44 for a 72.2–77.8 wt.% SiO_2 glass (normalized anhydrous). The Hauparu glass has a somewhat constant Zr/Hf ratio across a wide range of SiO_2, up to 5.5 wt.% SiO_2, whereas the Rotoiti, EQF, and Kakapiko Dome Zr/Hf ratios decrease across a nearly constant silica value, that varies <1 wt.% SiO_2 (Tables 2.3 and 2.4).

2.5.3.3 Zr/Hf in zircon

Zr/Hf in zircon can track the evolution of the melt from which the zircon crystallized. Solid solution between zircon and hafnon, Hf_2SiO_4, is common in igneous zircon and results in very high Hf concentrations in zircon compared to the liquid, in some cases on the order of wt.%. A compilation of global zircon analyses shows that hafnon component in zircon ranges from 0.7–8.3 wt.%, but averages ~2 wt.% (Hoskin and Schaltegger 2003, Claiborne et al. 2006). The zircon presented in this study range from hafnon abundance of 0.4–3.9 wt.%, and average ~1 wt.%. Zr/Hf in zircon is calculated assuming stoichiometry of pure zircon; we assume the same zirconium concentration (477,600 ppm) as used in Claiborne et al. (2006). Hf concentrations were measured by SHRIMP-RG in this study. Results for the four eruptions are presented in Tables 2.3 and 2.4.

2.5.3.4. Yb/Gd

Yb/Gd is typically considered an index of mafic phase fractionation (pyroxene, amphibole, etc.). Results of the Yb/Gd range, median, arithmetic mean, weighted mean, and MSWD for zircon from each eruption can be found in Tables 2.3 and 2.4. The Kakapiko Dome, EQF, and Hauparu surfaces have a more restricted range in Yb/Gd than the interiors, while the range in Rotoiti surfaces and interiors in nearly identical. Hauparu has the largest difference between interior and surface weighted-means, at 29 and 20, respectively, which suggests that the surfaces are crystallizing from a melt with a lower Yb concentration relative to the melt from which the interiors crystallized. For all populations, none of the MSWDs of the weighted-means are consistent with statistically simple populations. Despite general similarities in range (~10–~50)

there is no systematic difference between surfaces and interiors within that range for any of the four eruptions. MREEs are compatible in zircon and therefore increasing differentiation should be tracked by an increasing Yb/Gd ratio (Barth and Wooden 2010). No such patterns are preserved in the zircon presented here (see discussion for details). Yb and Gd are of similar incompatibility in clinopyroxene and orthopyroxene, although Gd is an order of magnitude more incompatible in orthopyroxene ($K_{D_{Gd}}^{opx/liq}$=0.03) than it is in clinopyroxene ($K_{D_{Gd}}^{cpx/liq} = 0.7$) according to a study by Fujimaki et al. (1984). The difference in partition coefficients suggests that this index might serve as a useful indicator of orthopyroxene and clinopyroxene fractionation in the absence of other mafic phases that would also incorporate Yb and Gd (i.e. amphibole), that is in dry magmas. Yb and Gd are both similarly compatible in amphibole ($K_{D_{Gd}}^{Amph/liq} = 5.4 - 7.9$; $K_{D_{Yb}}^{Amph/liq} = 5.1 - 7.9$; Nandedkar et al. 2016). Apatite partition coefficients are of similar magnitude for water-bearing melts between 700 – 800 °C (series D) in study by Fleet and Pan (1997): $K_{D_{Gd}}^{ap/liq} = 5.7$; $K_{D_{Yb}}^{ap/liq} = 1.4$.

2.5.3.5 ΣREE+Y/P and Y/P

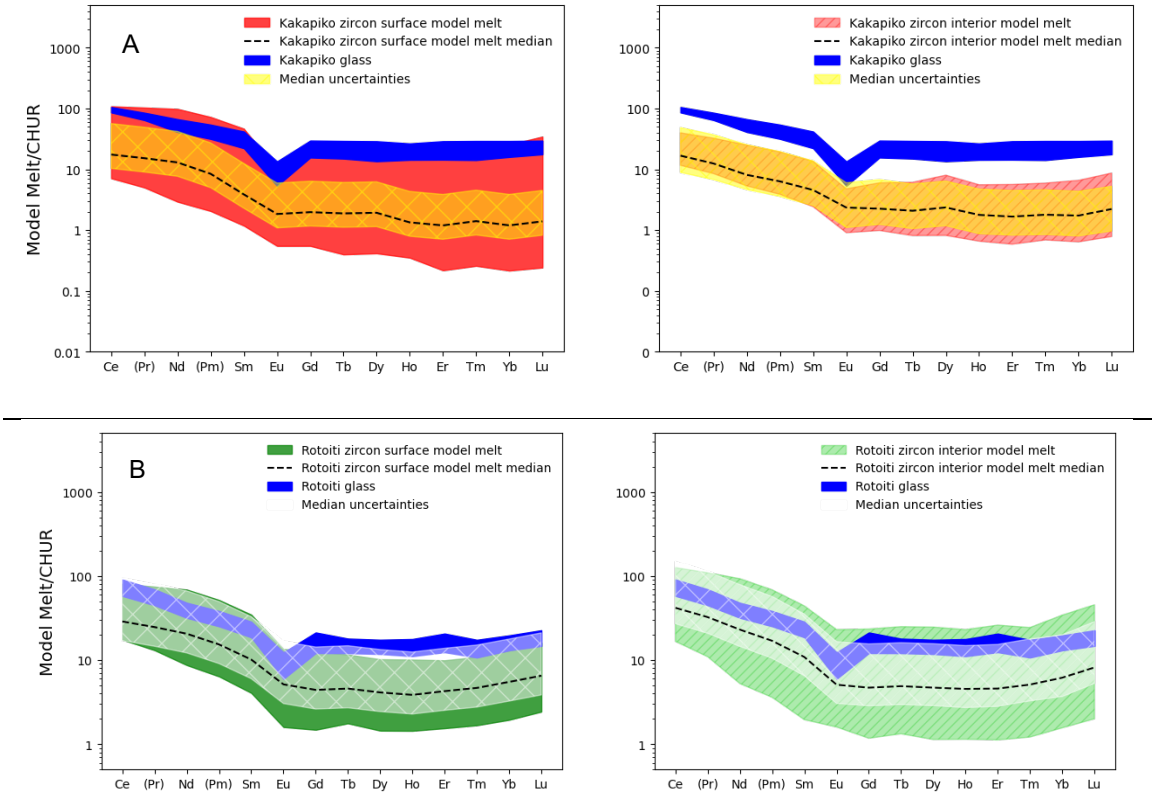
ΣREE+Y/P and Y/P can be used as an index of xenotime and apatite fractionation respectively. Results for the ΣREE+Y/P and Y/P ranges, medians, arithmetic means, weighted means, and MSWDs for zircon from each eruption can be found in Tables 2.3 and 2.4. Only Kakapiko Dome interiors and surfaces, and Rotoiti surfaces have sub-unity ΣREE+Y/P ratios, values that can be ascribed to xenotime substitution. All populations have very similar ranges in Y/P except Hauparu interiors, which have a relatively small range, but which have a similar weighted-mean

as the other populations. The data cluster between a range of 1 – 7, with a tail that extends to <14.

2.5.4 Zircon-glass equilibrium modeling

We used the model of Claiborne et al. (2018) to estimate glass compositions in equilibrium with the measured zircon. This is particularly important in the case of zircon grains or zones that are significantly older than eruption age, where the assumption that they crystallized from a melt similar to the erupted glass may not be accurate. The Claiborne model uses a geologically diverse dataset to empirically derive a set of partition coefficients, which are then applied to zircon from this study to calculate the melt concentrations in equilibrium with the zircon. We compare modeled glass trace element data to pumice glass trace element data from Rocco (2020) for Kakapiko Dome, Rotoiti, EQF, and Hauparu. In all cases, the modeled glass compositions in equilibrium with zircon show a larger range in normalized trace element concentration (for any given element) than do the actual analyses of pumice glass (Figs. 5A–D). This suggests that the host glass is in equilibrium with only a small portion of the analyzed zircon. For the Kakapiko Dome interiors, there is almost no overlap between the modeled glass and the pumice glass, with one exception: the lowest Eu concentration in the pumice glass falls within error of the modeled glass median uncertainties. Pumice glass from Kakapiko Dome overlaps with the upper end of the modeled glass range but is not within error of the median value of modeled glass. The Rotoiti pumice glass overlaps with the range of the Rotoiti zircon interior modeled glass and is within the median uncertainties of the modeled glass. The Rotoiti pumice glass partially overlaps with the Rotoiti surface modeled glass in LREE and HREEs, but does not overlap in MREE (Tb–Tm), but the pumice glass is entirely or partially within error of the median uncertainties of the

modeled glass. The EQF pumice glass overlaps with the range of the EQF zircon interior modeled glass and is within the median uncertainties of the modeled glass for LREE and MREEs, but not HREEs. The EQF pumice glass overlaps with the EQF surface modeled glass in LREEs but does not overlap in MREE or HREEs (Gd–Lu), and the similarly pumice glass is within the median uncertainties of the modeled glass in LREEs, but not in MREE or HREEs. The Hauparu pumice glass overlaps with the range of the Hauparu zircon interior modeled glass and is at least partially within the median uncertainties of the modeled glass for all elements. The Hauparu pumice glass overlaps with the Hauparu surface modeled glass and within the median uncertainties of the surface glass.



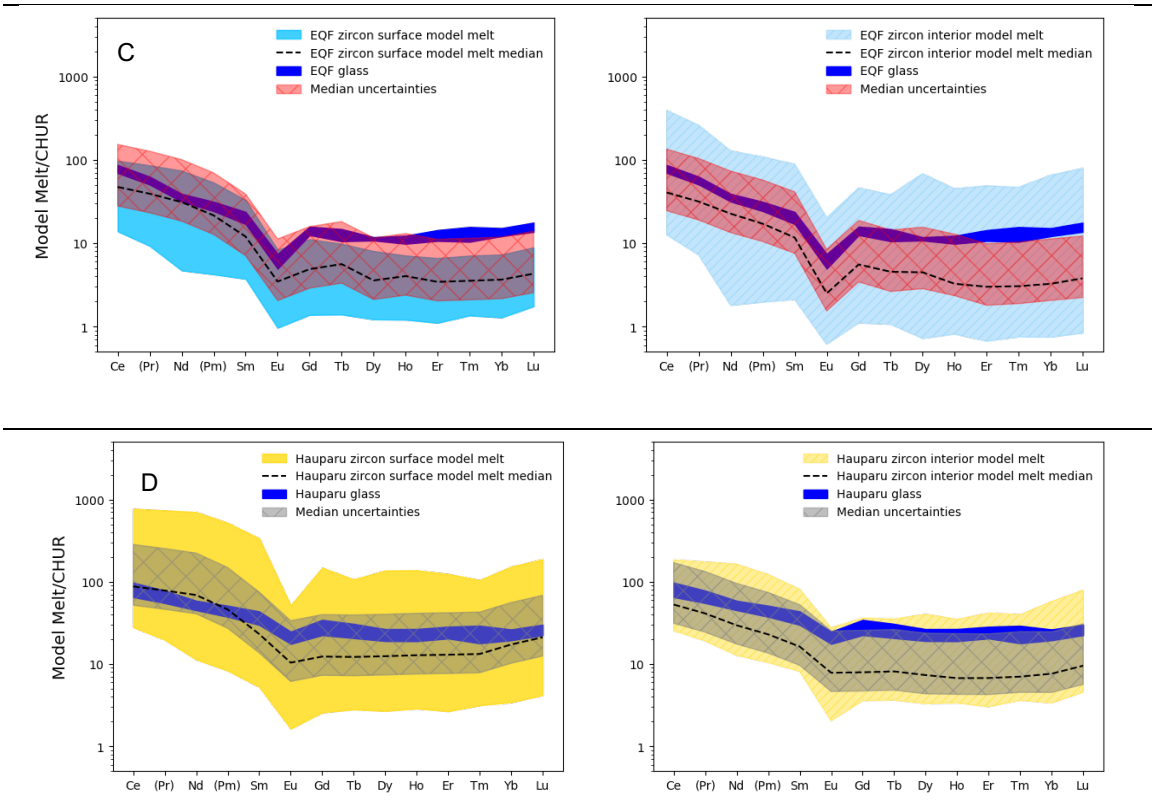


Figure 2.5*: Zircon-glass equilibrium models using the formulation of Claiborne et al. (2018). Each panel presents modeled glass trace element compositions for zircon surfaces (left) and interiors (right) from Kakapiko Dome (A), Rotoiti (B), Earthquake Flat (C), and Hauparu (D). Pumice glass from Rocco (2020) is represented for each eruption by the dark blue trace element data. The black dashed line represents the median value for the model melt results, and the pattered data represent the uncertainties about the median.*

2.6 DISCUSSION

2.6.1 Evidence for a long-lived mush system

All four eruptions contain zircon that record protracted crystallization histories from secular equilibrium to eruption age, at a wide range of Ti-in-zircon crystallization temperatures (Fig. 2.6). The Kakapiko interiors and surfaces show protracted crystallization from eruption age (~147 ka) to secular equilibrium over a range of ~200 °C (400 °C if including outlier grain with

no associated age spot) (Fig. 2.6). The oldest Rotoiti interiors preserve temperatures below 715 °C from 87–287 ka, but hotter interiors (>740 °C) are recorded starting at 86 ka, which suggests that these zircon crystallized from a hotter magma, potentially in a different part of the reservoir (Fig. 2.6). The Rotoiti surfaces are more tightly clustered than the interiors in terms of both crystallization age and temperature, suggesting that the surfaces crystallized from a relatively homogenous environment in terms of temperature whereas eruption age interiors crystallized from hotter environments. The EQF interiors preserve a range in temperature from 664–807 °C over ~200 ka. The EQF surfaces are slightly more focused between 640 and 731 °C, a range < 100 °C, and are all younger than ~100 ka (except for one 205 ka zircon), which is a crystallization duration of ~55 kyrs. The Hauparu surfaces have a larger range in calculated crystallization temperatures (Δ 245 ºC) than the interiors (Δ 152 ºC) chiefly due to four outliers grains that record temperatures >900 ºC in the surface population. (Fig. 2.2, Fig. 2.6). Overall, Hauparu interiors and surfaces both show protracted crystallization from near secular equilibrium to within error of eruption age and sustained temperature range from 684–871 °C (with the exception of the four >900 ºC outlier grains). In general, the temporal and thermal relationship between surfaces and interiors suggests that the surfaces crystallized from cooler melts (with more limited compositional variability) than the interiors, except for Hauparu for which zircon crystallization temperatures suggest that the melts from which the surfaces crystallized were slightly hotter than that of the interiors. There is small degree of overlap between the youngest interior grains and older surfaces, which means that the “hotter” interiors and “cooler” surfaces were crystallizing at the same time but from different thermal environments (and therefore likely different compositional environments). Overall, the

preservation of such large ranges in temperatures suggests that at any given time throughout the history of zircon crystallization, some parts of the magma reservoir sustained an environment conducive to zircon growth (Fig. 2.6).

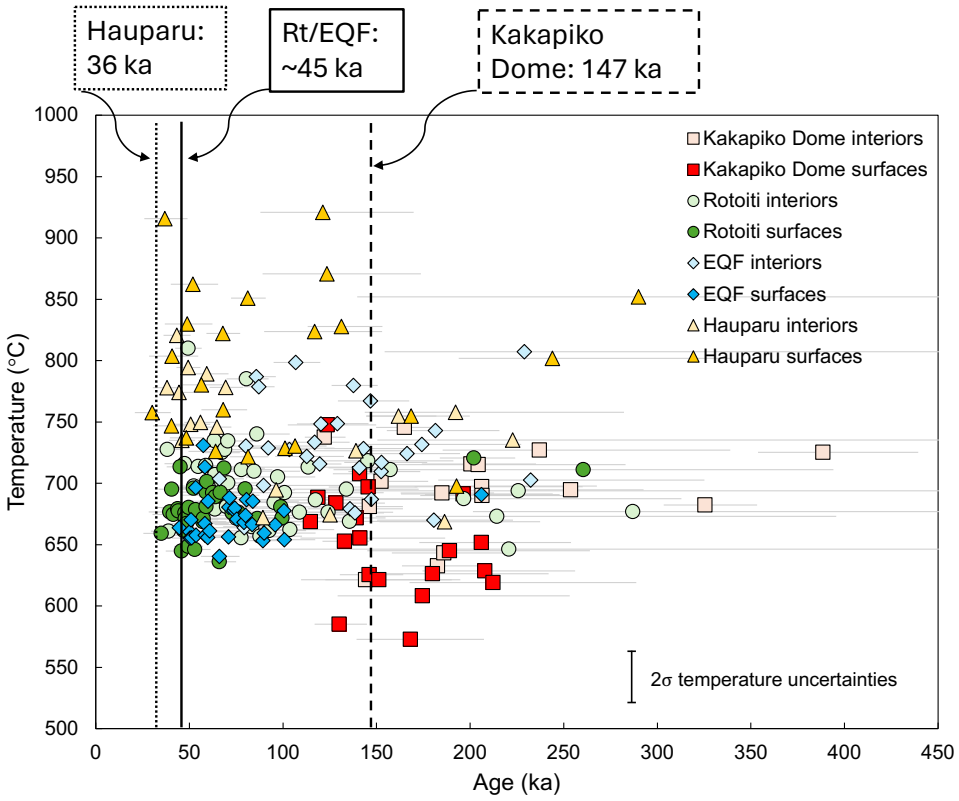


Figure 2.6: *Ti-in-zircon temperatures versus ^{238}U-^{230}Th crystallization age measured in zircon surface and interiors for Kakapiko Dome (dark and light red squares, respectively), Rotoiti (dark and light green circles, respectively), Earthquake Flat (dark and light diamonds, respectively), and Hauparu (dark and light triangles, respectively). Eruption age for each eruption is represented by the vertical lines with the accepted eruption age indicated nearby. Uncertainties on ages are 1σ standard deviations, propagated as ages based on 1σ uncertainty in the slope. Uncertainties in Ti-in-zircon temperatures were propagated from the 2σ uncertainty in Ti concentration measurements, and were on the order of +/- 20 ºC. Representative 2σ uncertainties are presented.*

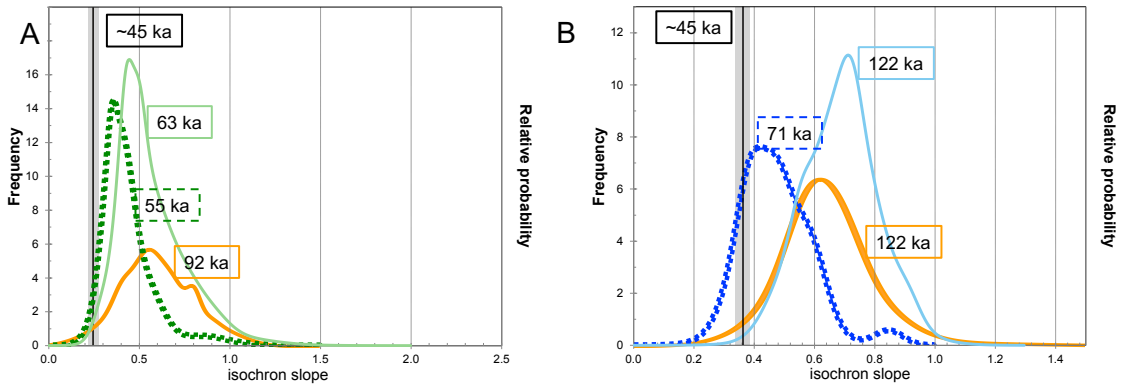
Protracted zircon crystallization in an active magma reservoir has been observed in many large silicic systems (Barker et al. 2014, Charlier et al. 2005, Cooper et al. 2014, Reid 1997, Claiborne et al. 2010, Stelten et al. 2015, Cooper 2015, Reid and Vasquez 2017, Wilson and Charlier 2010), therefore it is unsurprising that for each eruption we have zircon datasets with a large spread in ages. The pattern in preserved ages for all four of the studied eruptions indicates that the magma reservoirs were experiencing similar processes, such as zircon crystallization throughout a range of temperatures and removal from the growth environment such that their Ti-in-zircon signatures were preserved. Rotoiti and EQF are approximately syn-eruptive, but on average the EQF zircon surfaces (71 ka) crystallized prior to Rotoiti surfaces (55 ka), requiring that the EQF surfaces were stored for longer prior to eruption than the Rotoiti surfaces. This supports the model that the two magma systems operated more or less independently of each other, despite close spatial proximity. Conditions in the Rotoiti magma body were apparently more favorable to zircon growth (and perhaps nucleation) than the EQF magma body, which was not experiencing as much active zircon growth near eruption (EQF n=6, Rotoiti n=19). The Kakapiko Dome, Rotoiti, and EQF eruptions show a more limited range in surface temperatures than their corresponding interiors. Even though the surface temperatures are more restricted, there is still a range in temperature with "cool" (~650 °C), "warm" (>740 °C), and "hot" (>810 °C) (in the case of Hauparu) zircon crystallizing in a relatively short duration during the lead-up to eruption (~20 ka). The contrast between the cooler surfaces relative to warmer interiors suggests that for the pre-CFE and CFE eruptions, there was a focusing of magma temperature and composition shortly (~20 ka) prior to eruption.

Comparing our Rotoiti and EQF zircon model ages to those of Charlier et al. (2003), we find that the datasets are consistent in supporting a model where zircon are stored in separate

melt environments. The Charlier et al. (2003) zircon model ages are measured on zircon interiors, and therefore do not capture the last period of growth that is preserved by the zircon surfaces. But a first order comparison of the Charlier et al. (2003) and our zircon interior data reveals similar spectra that both attest to complicated zircon growth from physically separate melts (Fig. 2.7A). Similarly, the Charlier et al. (2003) EQF zircon interior model ages are consistent with our EQF zircon interior model ages (Fig. 2.7B), and for both datasets of zircon interiors the weighted mean of isochron slopes correspond to a crystallization age of 122 +18/-16 ka from Charlier et al. (2003), and 122 ± 3.7 ka from this study.

The OVC magma reservoir is most likely comprised of a complex network of disconnected melt pockets and pathways where zircon crystallization is protracted and where zircon are physically removed from the melt environment as inclusions in major phases or in low-melt crystal mush pockets. Given this environment it can be difficult to use zircon age spectra as a unique identifier of a specific discrete magma, but in general, we can confirm that both the Rotoiti and EQF zircon were derived from a crystalline mush where eruptible magma was accumulated shortly prior to eruption and grew some (Rotoiti) to few (EQF) autocrystic zircon from the host melt. Figures 2.7C-D plot zircon model ages as rank and order profiles which show clear differences in the Rotoiti and EQF crystallization histories. The EQF zircon interior model ages reveal protracted crystallization over ~200 kyr, whereas the surface model ages cluster <50 kyr prior to eruption (with the exception of one outlier). Our data show that the Rotoiti zircon interior model ages crystallized ~100 kyr prior to eruption but if we include the Charlier et al. (2003) data, Rotoiti zircon interior crystallization appears to have also been protracted on the order of ~200 kyr prior to eruption. The Rotoiti surfaces show crystallization over ~50 kyrs prior to eruption (except two outliers). The Rotoiti and EQF zircon surface model

ages are somewhat similar in distribution, but the EQF surfaces mean model age is ~20 kyr older than the Rotoiti surfaces, which requires that the EQF zircon were removed from the melt environment or the magma system feeding the EQF magma reservoir slowed or cooled such that zircon crystallization was not significant. The many Rotoiti zircon surface ages within error of eruption show that zircon were crystallizing immediately prior to eruption in at least some parts of the Rotoiti magma reservoir. Although there are similarities between the Rotoiti and EQF zircon model age spectra, the differences in surface crystallization history strongly suggests that Rotoiti and EQF zircon grew in separate magma systems, which is consistent with the findings of Charlier et al. (2003).



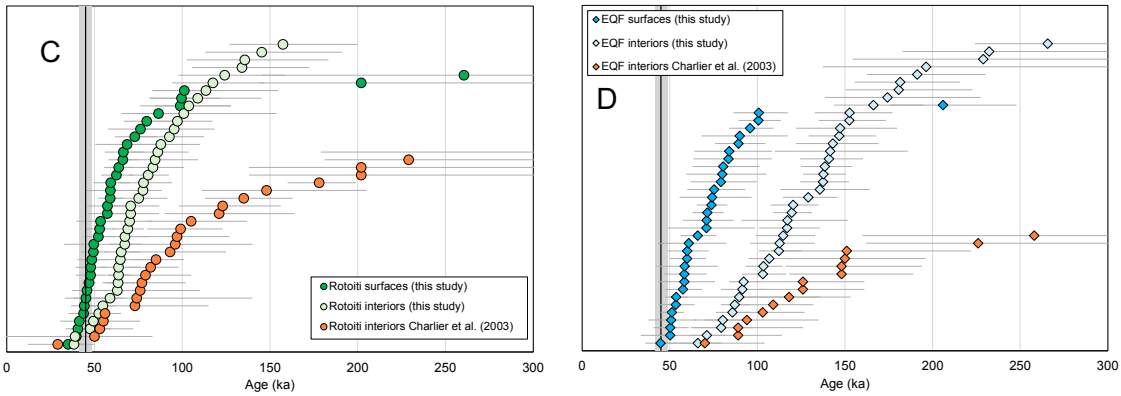


Figure 2.7*: Probability density functions of Rotoiti (A) and Earthquake Flat (B) zircon model ages from this study (solid light-colored lines are zircon interior analyses; dashed dark-colored lines are zircon surface analyses) and Charlier et al. (2003) zircon interiors analyses (solid orange line). Eruption age is marked by a solid black line with uncertainties shaded in gray (Rotoiti and Earthquake Flat eruption age and uncertainties from Danišík et al. (2012), respectively, 45.1(7) ± 3.3 ka and 45.1(6) ± 2.9 ka. The Charlier et al. (2003) zircon interiors data are consistent with our zircon interior model ages for both Rotoiti and Earthquake Flat. Rank and order profiles for Rotoiti (C) and EQF (D) zircon model ages from this study and Charlier et al. (2003).*

The distribution of Hauparu zircon ages and range in temperatures is unlike the other three eruptions. Hauparu zircon interiors and surfaces both exhibit complex polymodal distributions of similar shape (Fig. 2.2) and has a larger spread in surface temperatures to higher temperatures than its interiors, which was sustained over a large range in age from secular equilibrium to eruption age (a ~200–300 kyr duration). This requires the presence of discrete thermal environments throughout the duration of the zircon crystallization record. One question that these observations generate is: does this indicate a systematic change within the OVC reservoir? Hauparu interiors and surfaces are on average hotter than the other eruptions with average temperatures of 743 and 807 °C, respectively (Ti-in-zircon thermometry). The combination of the polymodal distribution in ages and the higher and larger range in temperature when compared to the other eruptions suggests that magma assembly post-CFE recovery

amalgamated a more heterogenous population of zircon than the magma bodies that assembled prior to the CFE. The environment from which Hauparu zircon crystallized was long-lived (at least in some parts), contained a thermal gradient of some form, and had a mechanism that effectively removed zircon from the melt environment (old surfaces). These observations are echoed by other studies which show post-CFE heterogeneity in the magma reservoir at the OVC (Shane et al. 2007, Shane et al. 2008a).

One observation that supports the persistence of a long-lived magma mush is the relatively cool zircon crystallization temperatures (<650 ºC) preserved in Kakapiko Dome and EQF zircon surfaces and interiors. The preservation of such cool temperatures could be explained by growth from a highly crystalline mush located on the periphery of the magma reservoir where cooler temperatures dominate. Alternatively, to preserve cool surface temperatures, these zircon could have been incorporated into major phase minerals thereby armoring them from the melt environment. For example, the Earthquake Flat surface population shows a continuous 160 kyr spread in crystallization ages, but the overwhelming majority of EQF zircon surfaces (n=17 out of 32) have crystallization ages much older (>35 kyr) than the ~45 ka eruption date. To preserve these surface ages, the zircon must have been removed from the growth environment. Lack of young rim growth and the preservation of sharp rim boundaries on some EQF surfaces are in support removal of zircon from the melt environment.

Another observation common to all four eruptions is the presence of eruption age zircon interiors. The eruption age interiors suggest that in some parts of the reservoir zircon was nucleating and grew relatively rapidly prior to each eruption to a similar size. Further, the fact that the eruption-age zircon were large enough to be measured by SHRIMP-RG implies that the zircon must have been present for enough time to grow a zircon large enough to be analyzed.

Given that the SHRIMP-RG spots for age analyses are ~40 microns across and ~5 microns deep, this represents a minimum diameter and surface thickness of the zircon grains. For Rotoiti, at least six of the Rotoiti zircon (based on their young interior age) must have grown very quickly prior to eruption in order to produce crystals large enough to analyze and interior ages within error of eruption, requiring enough time to grow a surface of at least ~5 microns and a diameter of ~40 microns. An implication for this growth requirement is that to produce the observed range in zircon interior ages, the magma reservoir must have hosted melt environments sufficient for zircon growth for >200 kyr.

For all four eruptions, there are four main conclusions: 1) the magma reservoir must have maintained a melt environment suitable for zircon growth throughout the duration of the recorded crystallization ages; 2) the preservation of older surface ages required that some zircon must have been removed from the growth environment either: a) as inclusions in other mineral phases, b) as part of a highly crystallinity, low permeability mush, c) in a melt depleted of zircon growth components (Zr, Hf, etc.), d) in a cool environment with slow zircon growth rates, or e) some combination of the above; 3) interiors and surfaces analyses that are both within error of eruption require that some zircon crystals (≥ 125 micron size at minimum) must have grown rapidly prior to eruption; and 4) a range in thermal environments must have existed within the magma reservoir in order to explain the range of thermal (and compositional) variation that co-existed throughout the ~200 ka history of each reservoir, and specifically immediately prior to eruption. Physically, this could be: a) introduction of hotter magma into the shallow mush reservoir creating locally hotter pockets of magma as mixing occurred, and/or b) existence of a long-lived (>200 ka) thermal (and compositional) gradient that allowed same age zircon to crystallize at different temperatures. Both scenarios are probable at the TVZ as there is evidence

of basaltic eruption and/or reactivation of the magma mush prior to the Rotoiti eruption (Shane et al. 2005b, Schmitz and Smith 2005) and as the eruption trigger for post-Rotoiti eruptions (Shane et al. 2007, Shane et al. 2008a). Numerous studies have established the presence of a long-lived magma mush zone from which zircon record can different thermal conditions (e.g., Barker et al. 2014, Cooper et al. 2014, Rubin et al. 2016).

2.6.2 Thermal evidence for zircon growth conditions throughout mush history

Temperatures calculated from Fe-Ti oxides have been documented in some cases to scale inversely with stratigraphy, with higher temperatures recorded in Fe-Ti oxides stratigraphically at the top of tuff units and cooler temperatures preserved towards the bottom, which has been interpreted to correspond with the top-down emptying of a magma reservoir (e.g., Bishop Tuff; Hildreth and Wilson 2007). Hildreth and Wilson (2007) make a similar argument for a crystallinity gradient imposed by water content and inversely correlated with temperature (crystal-poor at the top of the magma reservoir and crystal-rich toward the bottom and sides of the reservoir). However, such straightforward dynamics are not observed in OVC deposits. Shane et al. (2005b) found no systematic variation between temperature and crystallinity expected of zoned magma reservoirs in any of the studied OVC deposits. Davis (1985) suggested that there is weak compositional zoning in the EQF deposit based on major element oxide variation, but Molloy et al. (2008) found no evidence of compositional zoning. Schmitz and Smith (2004) reported zoning in Rotoiti eruptive deposits based on mineralogy and incompatible trace element geochemistry, but ultimately settled on the conclusion that two physically separate magma bodies without vertical stratification evolved along different liquid lines of descent and

were mingled immediately prior to eruption, thereby juxtaposing oxides from different regions of the reservoir that record large variations in temperature.

Our Ti-in-zircon thermometry and Fe-Ti oxide thermometry data support a model similar to that of Schmitz and Smith (2004) for Rotoiti. The Fe-Ti oxides record thermal variation on the order of ~110 °C for Rotoiti, and ~30 °C for EQF. With the exception of two grains, Rotoiti Ti-in-zircon surface temperatures (636–721°C) fall below the range of pre-eruptive (i.e. oxide) temperatures (751-863 °C), whereas the EQF Ti-in-zircon surfaces temperatures (640–731 °C) overlap significantly with the EQF pre-eruptive oxide temperatures (694–722 °C). The comparison of these two thermometers has some implicit assumptions. First, zircon growth rates are generally thought to be slower than major phase (i.e. oxide) growth. Using the radial zircon growth rates of Watson (1996) a ~5 micron surface layer would take 10^2 years to grow using their fastest growth rate of 10^{-13} cm/s, and 10^4 years to grow a 5 micron zircon rim at the intermediate growth rate of 10^{-15} cm/s (Storm et al. 2011). Second, it would take only weeks to months for oxides to re-equilibrate with the magma through diffusion at magmatic temperatures (Devine et al. 2003, Hou et al. 2021, Venezky and Rutherford 1999). Plinian eruptions will quench Fe-Ti oxides, effectively locking any inferred temperature records in place, whereas effusive eruptions cool slowly enough that the Fe-Ti oxides could be reset during cooling after eruption. Therefore, Fe-Ti oxide temperatures will reset much faster than zircon can grow, creating a lag in temperature records. Fe-Ti oxides will record the most recent temperature fluctuation, whereas Ti-in-zircon temperatures record longer-term storage temperatures.

For EQF, the significant overlap in Ti-in-zircon and Fe-Ti oxide temperature suggests that there was little to no thermal fluctuation to the system prior to eruption. If the EQF magma reservoir was recharged with a hotter magma immediately prior to eruption as the mobilization

mechanism, then the recharge and mobilization were rapid enough such that the Fe-Ti oxides did not have time to reset. For Rotoiti, the ~110 °C range in Fe-Ti oxide temperatures, and minimal overlap with the Ti-in-zircon temperatures, could be consistent with two alternative interpretations. First, that the Rotoiti magma reservoir was recharged with a hotter magma prior to eruption on a timescale long enough to reset the Fe-Ti oxides to temperatures to reflect a new thermal environment, but short enough that new zircon surface growth was not significant enough to be reflected in the surface analyses. Alternatively, if the Rotoiti zircon were stored in small, disconnected melt pockets at various regions in the magma reservoir they could record disparate temperature records. Heating from recharge of a hotter magma intrusion below could affect proximal melt pockets but would have less effect on melt pockets distal to the recharge; in this scenario, the Fe-Ti oxides would record a large range in temperature, whereas the zircon might not have time to grown new surfaces reflecting the new thermal environment.

The ~100 ºC range in Rotoiti Fe-Ti oxide equilibrium temperatures suggests either nonuniform heating of the magma reservoir prior to eruption, creating thermal diversity which was then recorded by oxides, and/or rapid scavenging of different parts of a thermally and chemically heterogeneous magma mush. It is most likely some combination of the above two that gives rise to the large range in Fe-Ti oxide temperatures further suggesting that heating of the magma body prior to eruption was rapid, such that thermal diffusion did not have time to reset all of the oxides in the magma reservoir. The Rotoiti zircon surfaces preserve relatively cool Ti-in-zircon temperatures (636-721 ºC), which roughly align with the late erupted Rotoiti (T2, Smith et al. 2005) pre-eruptive Fe-Ti oxide temperatures (712 ºC). Early erupted Rotoiti (T1, Smith et al. 2005) Fe-Ti oxide pairs record pre-eruptive temperatures around 768 ºC. Given the rapid re-equilibration times of oxides, we infer that the Rotoiti eruption evacuated the magma

chamber quickly thereby preserving the cooler temperatures of the late (T2) Rotoiti oxides. Alternatively, if the entire eruption period was shorter than the rate at which Fe-Ti oxide reset, then the ~100 ºC range in Fe-Ti temperatures could represent the ambient thermal state of the magma reservoir prior to re-heating and eruption. While the Schmitz and Smith (2004) and Shane et al. (2005b) models envision two magma bodies, our zircon data require multiple small melt environments, but the two models are not mutually exclusive. The micron-scale heterogeneity preserved in zircon that we describe could easily exist within the larger mineral-scale heterogenous magma batches that Schmitz and Smith (2004) describe.

Zircon saturation thermometry is used to predict at what temperature zircon should saturate in a liquid of a given composition, where whole-rock or glass are used as proxies for the liquid. Because our zircon age spectra provide evidence of a long-lived crystal mush, we recognize the possibility that not all zircon are cogenetic with the whole-rock composition. With the exception of two Ti-in-zircon temperatures that exceed 836 ºC, most zircon temperatures fall below the Watson and Harrison (1983) zircon saturation temperature thresholds (Fig. 2.3) for OVC glasses. This implies that Kakapiko Dome, Rotoiti, and EQF zircon were stored in an environment conducive to zircon growth (and not dissolution) prior to eruption, and by extension, that the pre-eruptive state of the magma body was also conducive to zircon growth. The Boehnke et al. (2013), Gervasoni et al. (2016), and Shao et al. (2020) zircon saturation thermometers predict slightly cooler saturation conditions for zircon. For example, 19 of the 36 Rotoiti zircon surfaces are within error of eruption age; this suggests that the conditions prior to eruption were favorable for zircon growth as per the zircon saturation thermometry estimations. Nine of the Hauparu zircon surfaces fall above the calculated saturation threshold of 848 ºC, whereas none of the Hauparu zircon interiors are above the saturation threshold. This suggests

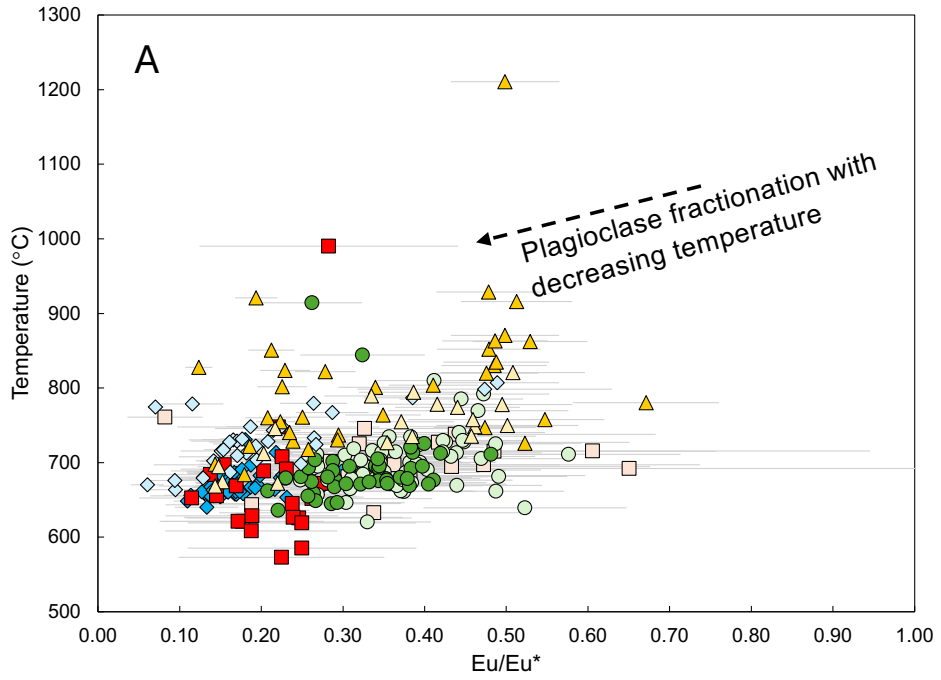
that the Hauparu surfaces must have crystallized from compositionally diverse magmas in which the zircon saturation temperature minimum was higher. Collectively, the zircon from Kakapiko Dome, Rotoiti, EQF, and Hauparu show oscillatory zoning, sector zoning, and in some cases patchy zoning, the latter could be an artifact of zircon not sectioned normal to a major crystallographic axis. Some zircon show minor resorption surfaces in the interior most portions of the grain, but we do not see evidence of significant resorption periods that would require the zircon to be stored above the zircon saturation temperature threshold.

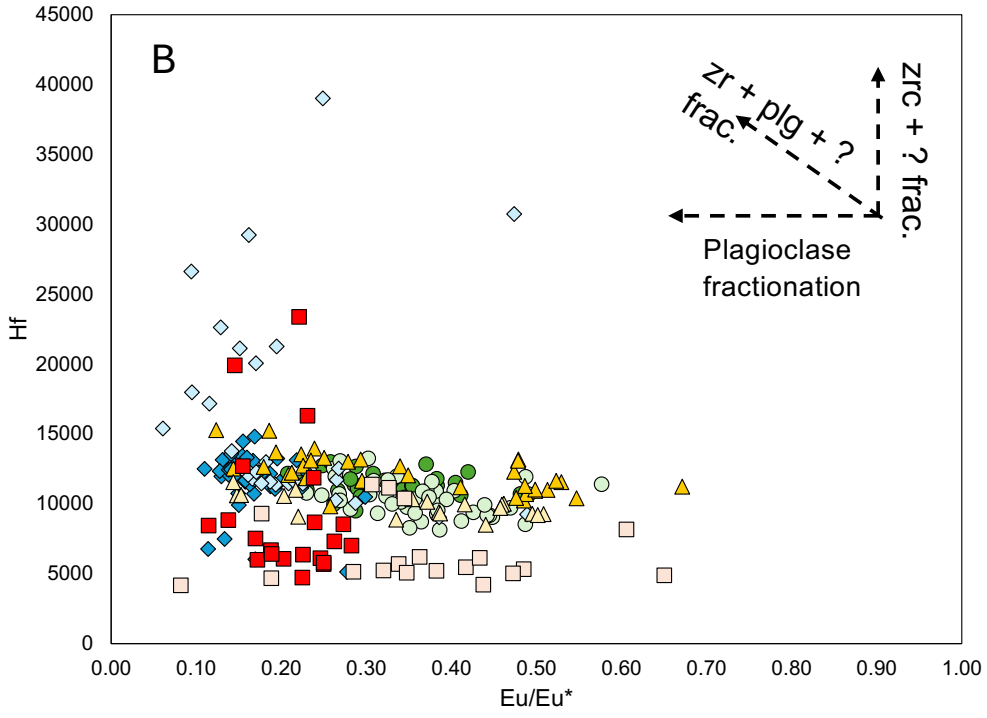
2.6.3 Trace element geochemistry in rhyolites

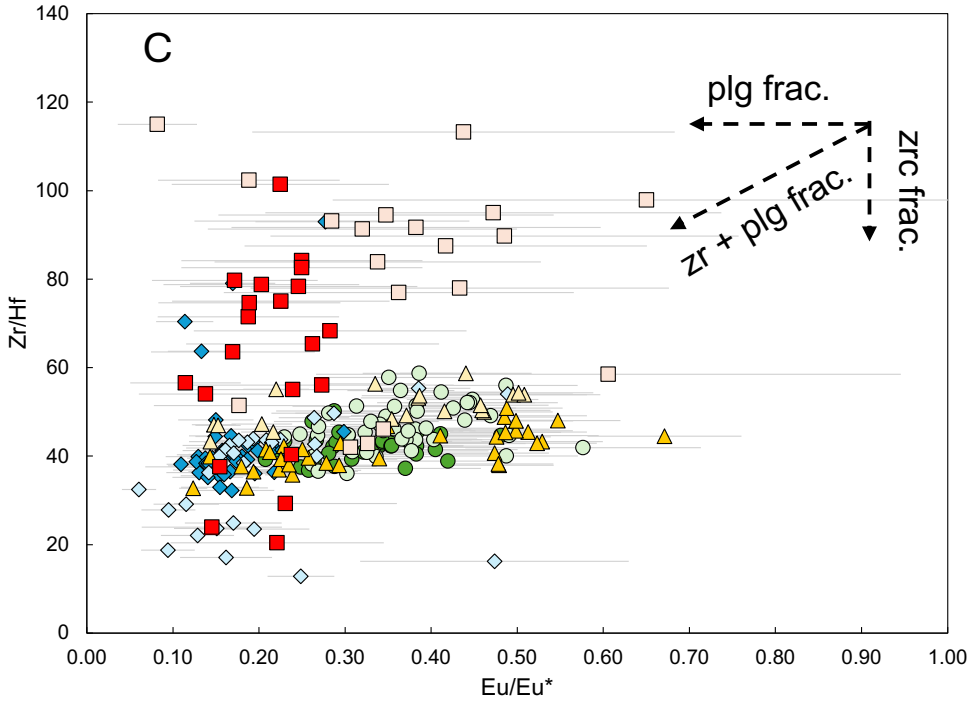
Comparing trace element signatures in different zircon populations can help to identify the unique melts from which the zircon crystallized and any genetic relationships between melts. The geochemical signatures of zircon from Kakapiko Dome, Rotoiti, EQF, and Hauparu deposits show a wide range of compositions within each eruption, and broadly similar ranges in trace element ratios across the four eruptions. The preservation of such a widespread range of compositions requires the zircon to have grown in physically separate compositional environments prior to each eruption. But despite the large range in compositional heterogeneity across interiors and surface populations for each eruption, there are no systematic patterns in trace element compositions and temperature that would suggest systematic evolution through time within the broader OVC magma reservoir. Rather, all four pre-eruptive magma reservoirs apparently contained many discrete melt environments, all of which produced zircon compositions consistent with trace element geochemistry of evolved rhyolitic melts.

We use trace element signatures in zircon as a reflection of the melt from which they crystallized, and as a general indication of the evolution of the magma system. Trace element

signatures capture the composition of the magma reservoir at the time of zircon crystallization due to very slow diffusion at magmatic temperatures (Cherniak et al. 1997). Trace elements, including rare earth elements (REEs) and Y, are indicative of both accessory and major phase fractionation, depending on the index used (Linnen and Keppler 2002, Hanchar and van Westrenen 2007, Barth and Wooden 2010, Claiborne et al. 2010, Nandedkar et al. 2016, Were and Keppler 2021, Bell et al. 2022). Factors such as coupled substitution, kinetic effects, and varied melt composition will affect the mineral-melt partition coefficients and will result in variable geochemical signatures recorded in zircon surfaces and interiors. Our zircon trace-element data do not show systematic patterns in common indices of fractionation (e.g. U/Th, Yb/Gd, LREE/HREE) (Fig. 2.8D), which suggests that there was not a simple history of melt evolution and fractionation within the OVC magma system or across the caldera-forming cycle. Similar findings have been reported for other TVZ magmas (Cooper and Wilson 2014, Cooper et al. 2016).


A
Temperature (°C)
Eu/Eu*
Plagioclase fractionation with
decreasing temperature


B
Hf
Eu/Eu*
zr + plg + ? frac.
zrc + ? frac.
Plagioclase
fractionation


C
plg frac.
zrc frac.
zr + plg frac.
Zr/Hf
Eu/Eu*
0
20
40
60
80
100
120
140
0.00
0.10
0.20
0.30
0.40
0.50
0.60
0.70
0.80
0.90
1.00

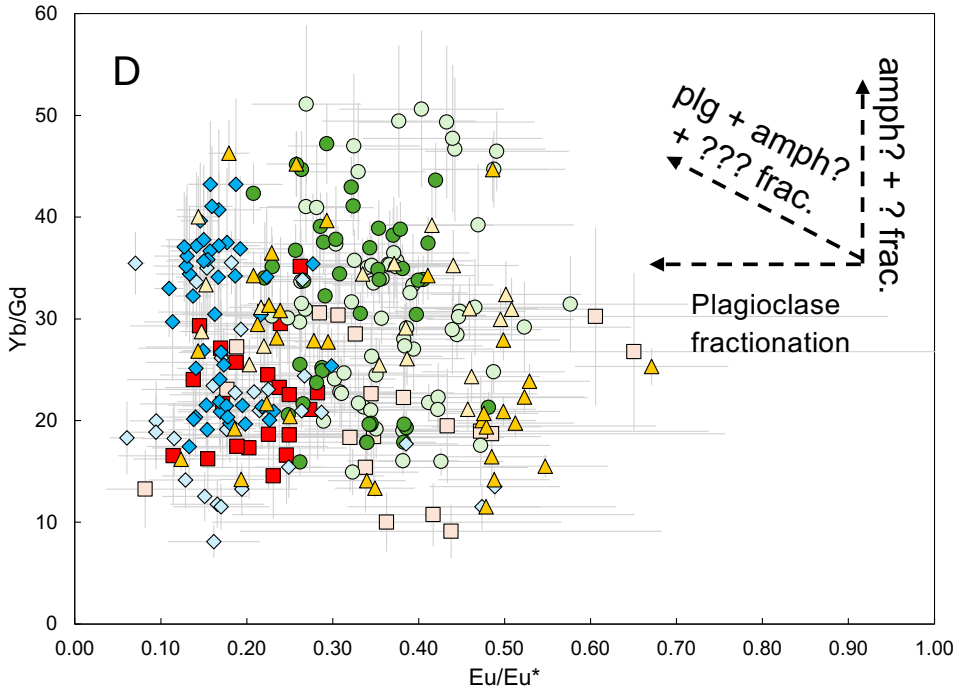

D
plg + amph?
+ ??? frac.
amph? + ? frac.
Plagioclase
fractionation
Yb/Gd
Eu/Eu*
0
10
20
30
40
50
60
0.00
0.10
0.20
0.30
0.40
0.50
0.60
0.70
0.80
0.90
1.00

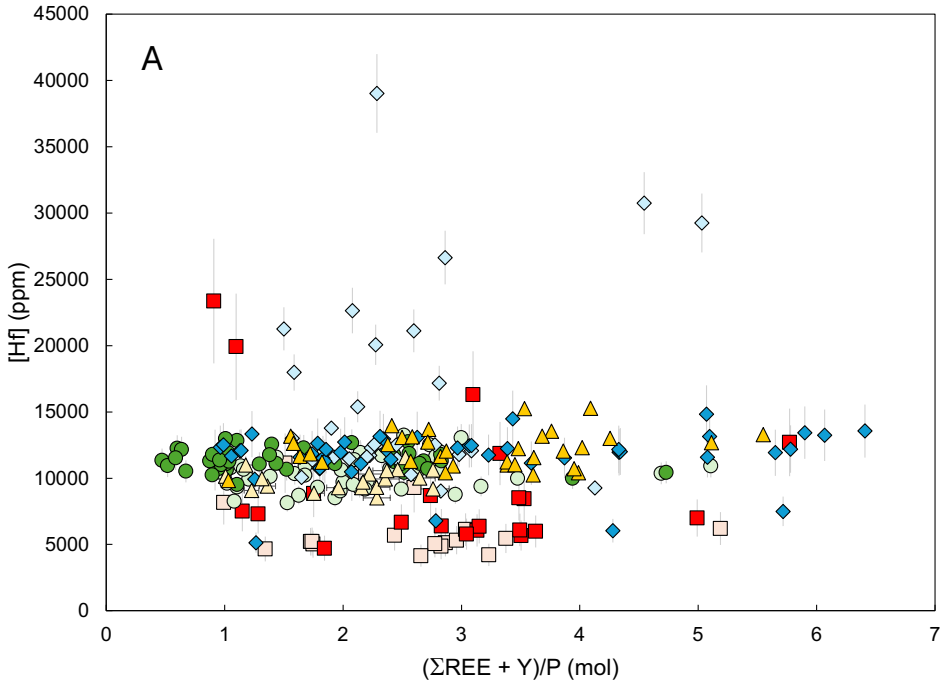
Figure 2.8*: Panel A: Ti-in-zircon temperature (A), Hf concentration (B), Zr/Hf (C), and Yb/Gd (D) versus Eu/Eu* for each of the four eruptions; typical mineral fractionation trends are illustrated on each panel. Decreasing trends in Eu/Eu* and Zr/Hf suggest plagioclase and zircon fractionation, respectively, and increasing trends in Hf concentration illustrate zircon fractionation; the lack of any systematic trends in Yb/Gd suggest that the zircon were stored in a heterogenous crystal mush; Symbols as in figure 2.6.*

2.6.3.1 Apatite and xenotime fractionation: Y/P and (ΣREE+Y)/P:

The OVC zircon lack systematic trace-element patterns in any single eruption or between eruptions, which we interpret to suggest variable amounts of major and accessory mineral co-crystallization. Some common trace element fractionation indices used in other systems to track major and accessory phase fractionation are Y/P, (ΣREE+Y)/P, and Yb/Gd; we found no systematic variation in those indices for OVC zircon (Fig. 2.8). We explore the potential explanation that the lack of any patterns in these indices is controlled by co-crystallizing phases rather than single mineral fractionation. For example, Y/P ratios serve as a relative measure of apatite fractionation if other Y-bearing phases are not significant. Apatite is the chief host of P, and can also host REEs, following the coupled substitution $REE^{3+} + Si^{4+} = Ca^{2+} + P^{5+}$ (Fleet and Pan 1997). At face value, the large range in Y/P recorded by the OVC zircon might suggest variable amounts of apatite crystallization (Tables 2.3 and 2.4), but the difficulty in using this index is that this study does not quantify to what extent apatite fractionation occurred relative to other Y-bearing phases. Yttrium strongly partitions into amphibole (Nandedkar et al. 2016), but also partitions into apatite, xenotime, and allanite to a lesser extent, thereby obscuring any clear indication of any single mineral fractionation patterns.

Although xenotime is not reported in the TVZ, it is an important reservoir of Y and REEs and can complicate trace element fractionation patterns. Xenotime solid solution in zircon occurs as: $Zr^{4+} + Si^{4+} = (Y + REE)^{3+} + P^{5+}$ where balanced xenotime substitution in zircon is (Y +

REE)$^{3+}$ + P^{5+} = 1 (Speer 1982, Finch and Hanchar 2003, Claiborne et al. 2010). OVC data presented in figure 2.8A shows a horizontal array of molar (ΣREE+Y)/P ratios in excess of that expected from xenotime substitution (Hanchar et al. 2001), with the exception of several Rotoiti surfaces, one Kakapiko Dome surface, and one Kakapiko Dome interior. This suggests an excess of REEs relative to P, resulting in a charge imbalance due to P depletion in the magma (Reid et al. 2011) that is further compounded by apatite fractionation incorporating wt.% proportions of P. In general, the range in (ΣREE+Y)/P ratios > 1 suggests the presence of another coupled substitution mechanism and/or co-crystallization of other phases, although at present it is difficult to quantify which minerals are controlling the trace element budget (Finch and Hancher 2003, Reid et al. 2011). As the only accessory phases found in the TVZ are zircon, apatite, and trace pyrrhotite (pyrrhotite is not a significant host of REEs), we surmise that the available REE hosts in the OVC must be zircon (given a REE coupled substitution mechanism), apatite, and mafic phases (pyroxene, amphibole, etc), rather than the accessory phases (e.g. allanite, monazite, xenotime, titanite) to which REE fractionation patterns are typically ascribed. While the trace element (REE, Y, P) signatures in zircon do not reveal any systematic variation within or between eruptions, the sustained and large spread in trace element values suggests that zircon crystallized from melts that had either previously co-crystallized accessory and/or mafic phases or was actively co-crystallizing accessory and/or mafic phases.


A
[Hf] (ppm)
(ΣREE + Y)/P (mol)
0
5000
10000
15000
20000
25000
30000
35000
40000
45000
0
1
2
3
4
5
6
7

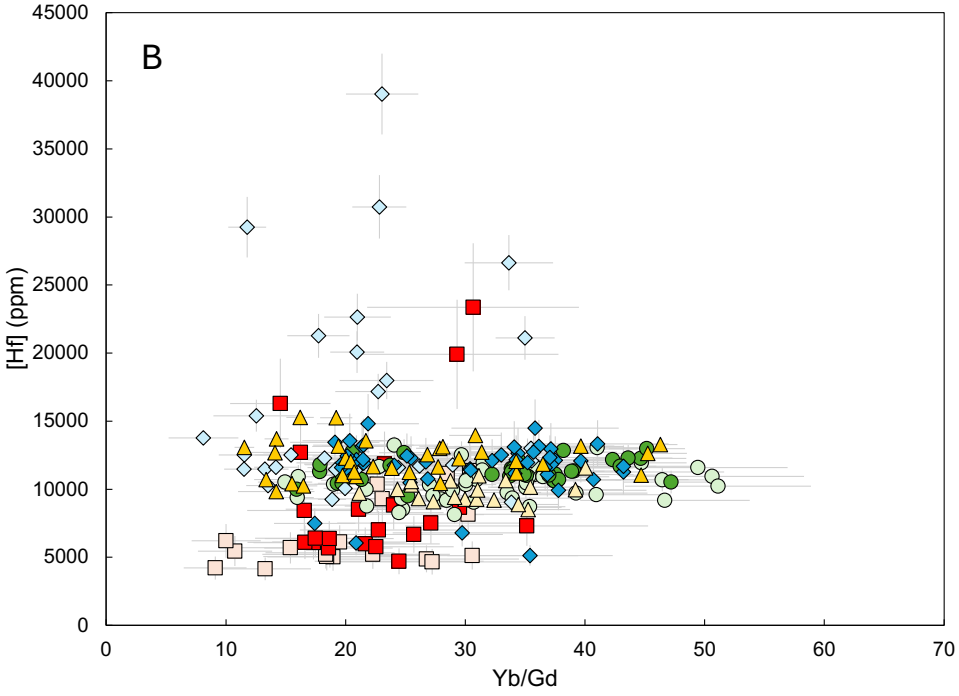

B
[Hf] (ppm)
Yb/Gd
0
5000
10000
15000
20000
25000
30000
35000
40000
45000
0
10
20
30
40
50
60
70

Figure 2.9*: Hf concentration (ppm) versus (ΣREE + Y)/P (A) and Yb/Gd (B). Symbols as in figure 2.6. The OVC zircon reveal horizontal arrays in Hf concentration (ppm) but preserve a ride range of diversity in (ΣREE + Y)/P and Yb/Gd ratios.*

2.6.3.2 Mafic phase fractionation: Yb/Gd

The Yb/Gd ratio is commonly used as an indication of mafic phase fractionation (pyroxene, amphibole), especially in systems that have abundant cogenetic mafic phases in the phase assemblage (Till et al. 2019). Andersen et al. (2019) suggested that Yb/Gd reflects titanite saturation, but there is no titanite reported in the TVZ so we do not further consider titanite saturation. Positive trends in Yb/Gd ratios versus Hf concentration in granitic rocks have been attributed to progressive depletion of the melt with zircon crystallization (Barth and Wooden 2010) and to co-crystallizing accessory minerals (Bell et al. 2022). The OVC zircon reveal mostly horizontal arrays in Yb/Gd vs Hf concentration that lack any systematic variation (Fig. 2.9B). The explanations of Barth and Wooden (2010) and Bell et al. (2022) both require progressive evolution of the melt resulting in a systematic variation recorded by zircon. Since no such patterns are present in the OVC zircon, we surmise that the widespread range in Yb/Gd, but relatively constant Hf concentrations is not due to zircon crystallization alone, but is likely due to co-crystallization of mafic phases, in particular pyroxene or amphibole.

Yb and Gd are incompatible in pyroxene relative to amphibole and in systems where amphibole is a dominant mafic phase relative to pyroxene Yb and Gd will preferentially partition into amphiboles over pyroxenes. Rotoiti and EQF contain only trace amounts of orthopyroxene, therefore, we do not expect pyroxene to be a major control on Yb and Gd in Rotoiti and Earthquake Flat. Hauparu contains 5% orthopyroxene and 5% clinopyroxene (and hornblende in the small volume upper unit) yet shows the same range in Yb/Gd as observed in the non-

pyroxene bearing eruptions. Furthermore, because the relative compatibility of Yb, Gd, and MREEs is of the same (or similar) order of magnitude in amphiboles that crystalize from rhyolitic melts (K_D = 5.1–7.8), the ratio Yb/Gd is an ineffective tool to discern fractionation of amphibole (Sisson 1994, Nandedkar et al. 2016). Biotite fractionation doesn't appreciably affect rare earth elements, as shown in experimental studies by Were and Keppler (2021) and therefore is not further considered here. Barth and Wooden (2010) show that variation in Yb/Gd is controlled by MREE incorporation into crystallizing zircon, a finding that is supported by the compilation of Hanchar and van Westrenen (2007). An outstanding question emerges from this discussion: what is the control of REE incorporation by accessory phases relative to major and minor phases? The simplest answer is that the range in Yb/Gd is due to sustained chemical heterogeneity within the magma reservoir due to unique inherited melt compositions and co-crystallization of trace pyroxenes, trace amphibole, and accessory phases (Anderson et al. 2019, Bell et al. 2021).

If the range in Yb/Gd is due to amphibole fractionation, then a possible explanation is the existence of a vertical compositional and thermal gradient in the crust, where mafic residual cumulates are stored in the lower to mid-crust. Evidence of a lower crustal mafic phase reservoir, envisioned by Davidson et al. (2007) as an amphibole sponge, could serve as a reservoir for mafic phases. A lower crustal "restite" has been identified geophysically by a rapid increase in conductivity at 10 km depth (Heise et al. 2007, Hochstein et al. 1993). And although amphibole is a liquidus phase in EQF and Rotoiti, a restitic reservoir dominated by pyroxene could explain some of the variation in MREE and HREE concentrations, and the range that we observe in Yb/Gd. If Yb/Gd ratios are controlled by pyroxene fractionation, it's possible that the Yb/Gd signatures in zircon reflect co-crystallization of zircon and pyroxene from different

compositional zones within the crustal column thereby reflecting the observed range in Yb/Gd ratios (~10-50). One flaw with this argument is that it would first require eruption-aged zircon to crystallize from melts that had experienced variable amounts of pyroxene fractionation, and second, require those zircon to assemble into an eruptive body without the co-crystallized pyroxene. Under conditions of efficient liquid extraction where zircon are carried with the liquid, this might be the case; but the challenge to this model is that rhyolitic melts are highly viscous, which could slow liquid accumulation times. Barker et al. 2016 have shown that eruptible magma bodies are rapidly assembled on the order of decades to centuries at the Taupo Volcanic Center, and Allan et al. (2012) and Begué et al. (2014) show that tectonic triggering could facilitate the rapid rise and accumulation of silicic melts. It is possible that tectonic readjustment could the rapid rise, accumulation, and eruption of melts at the OVC, which could explain the diversity of compositions preserved on mineral rims.

2.6.4 Evidence for compositional evolution

Eu/Eu* is an index of major mineral fractionation and is a useful measure to compare to other volcanic systems given the ubiquity of plagioclase in almost all calc-alkaline volcanic deposits. Trivalent Eu is the dominant species under oxidizing conditions, whereas divalent Eu is expected under reducing conditions. If all Eu is trivalent, then there should not be a deviation in CHUR-normalized values between Sm and Gd, but if all Eu is divalent, a negative Eu anomaly is expected (Hoskin and Schlategger 2003). Although Eu can be an indication of redox state, Maas et al. (1992) reported that factors such as temperatures and melt composition also play a role in Eu partitioning. Here we use the Eu anomaly as a general indication of plagioclase fractionation; magmas with low Eu/Eu* signatures indicate that the melt has experienced significant

plagioclase fractionation, whereas magmas with high Eu/Eu* signatures indicate that the melt has not experienced significant plagioclase fractionation. Eu is not compatible in zircon and therefore not an element expected to experience boundary-layer effects as zircon crystallize, thus the Eu/Eu* concentration reflects melts of varying plagioclase fractionation. Overall, there is little difference in the range or the weighted-mean of Eu/Eu* between the interiors and surfaces for each eruption (Tables 2.3 and 2.4, Fig. 2.8). While the large range in Eu/Eu* of eruption-age zircon suggests that a number of isolated compositional environments must have existed simultaneously, the similarity in weighted-means and ranges of interiors and surfaces suggests that similarly heterogenous Eu/Eu* environments were sustained over the range of zircon crystallization. That is, the large range in Eu/Eu* signature at any given time throughout zircon crystallization suggests the sustained presence of different compositional melt environments. Generally, Kakapiko Dome and EQF interiors and surfaces have slightly lower weighted means than Rotoiti and Hauparu (Fig. 2.8A), suggesting that they crystallized from melts that had experienced more plagioclase fractionation than the Rotoiti and Hauparu melts. The Rotoiti and EQF surfaces, and the Kakapiko and Rotoiti interiors are consistent with single populations based on their MSWD (Tables 2.3 and 2.4). Given their genesis from a complicated volcanic system that shows evidence for a mushy storage region, protracted crystallization up to 10^5 years, and abundant mineral armoring of zircon, it is somewhat surprising that there are single populations of zircon (Tables 2.3 and 2.4). These single zircon populations represent relatively uniform Eu/Eu* signatures in the melts from which those zircon crystallized. The zircon populations that are not characterized by single populations require that the magma reservoirs hosted isolated melt pockets within a crystal framework which allowed each melt pocket to

evolve along unique liquid lines of descent, and/or that zircon hosted by major phase minerals were separate from the melt environment and preserved a variety of Eu/Eu* signatures.

Although Zr is the chief building block in zircon, Hf is isovalent and a similar radius to Zr, and will relatively easily substitute for Zr in the zircon lattice. As Zr is depleted from the melt, zircon will incorporate increasing amounts of Hf. Thus, high Hf concentrations in zircon can be considered an indication of zircon fractionation (Linnen and Keppler 2002, Claiborne et al. 2006, Claiborne et al. 2010), and zircon crystals that record high Hf concentrations can be interpreted to have crystallized from evolved melts that has already experienced significant zircon fractionation. The OVC zircon show similar ranges in Hf concentration, with the exception of the EQF interiors which extend to very high Hf concentrations (>39,000 ppm), and the Kakapiko Dome surfaces and interiors which have slightly lower Hf concentrations than the majority of zircon (~5000 ppm) (Fig. 2.8B). In general, this suggests that zircon crystallized from a range of progressively evolving magmas. Claiborne et al. (2006) suggest that lower Hf concentrations could represent zircon crystallization within a restitic cumulate pile, an observation that is consistent with the high crystallinity of the Kakapiko Dome. In general, increasing Hf concentration with decreasing temperature is a common feature of magma evolution (Claiborne et al. 2006, Reid et al. 2011, Anderson et al. 2019, Bell et al. 2022). Other than the EQF interiors and Kakapiko Dome zircon, the Rotoiti interiors and surfaces, EQF surfaces, and Hauparu interiors and surfaces all plot in a relatively well-defined horizontal band between ~8000 and ~15,000 ppm (Fig. 2.8B). This horizontal array suggests that the melts from which these zircon crystallized were relatively homogenous in Hf concentration. It is interesting that the interiors and surfaces for Rotoiti, Hauparu, and Kakapiko Dome overlap in the range of Hf concentration, suggesting that the interiors and surfaces crystallized from melts of relatively

constant Hf concentration (with the exception of some high Hf Kakapiko Dome surfaces). Claiborne et al. (2018) show that there is a negative correlation between Hf partition coefficient and Ti concentration, which is interpreted as a temperature-dependent relationship (decreasing Hf K_D with decreasing temperature). They further show that at cool temperatures (~600 ºC) the Hf K_D is on the order of 10^2–10^3, which predicts that Hf would prefer the zircon lattice over the melt at these temperatures. If the Hf K_D temperature-dependent relationship can be extrapolated to hotter temperatures (~750 ºC), then the Hf K_D would be $>10^3$, suggesting that Hf is highly compatible in zircon. This is consistent with Hf solid solution in zircon up to wt.% abundance.

Other studies find a negative correlation between Ti (and therefore temperature) and Hf, which they attribute to zircon crystallization (Barth and Wooden 2010, Bell et al. 2022, Claiborne et al. 2010). We do not see such clear patterns in the OVC zircon data (Fig. 2.9). None of the samples show a negative relationship between temperature (or Ti concentrations) and Hf concentration. Rotoiti and EQF cluster into very similar overlapping populations, with the exception of the EQF tail to higher Hf concentrations. Hauparu clusters at similar Hf concentrations as Rotoiti and EQF but at higher temperatures, and Kakapiko Dome is clustered at lower Hf concentrations and lower temperatures. The OVC zircon do not reveal clear evidence of zircon fractionation as in other studies (Barth and Wooden 2010, Bell et al. 2022, Claiborne et al. 2010). Based on evidence from other trace elements, we suspect that the Hf concentration data is complicated by the presence of co-crystallizing phases in the presence of a magma mush system, and/or distributed melts of similar composition progressively fractionated zircon to different extents, resulting in a cluster of data rather than a single evolution trend.

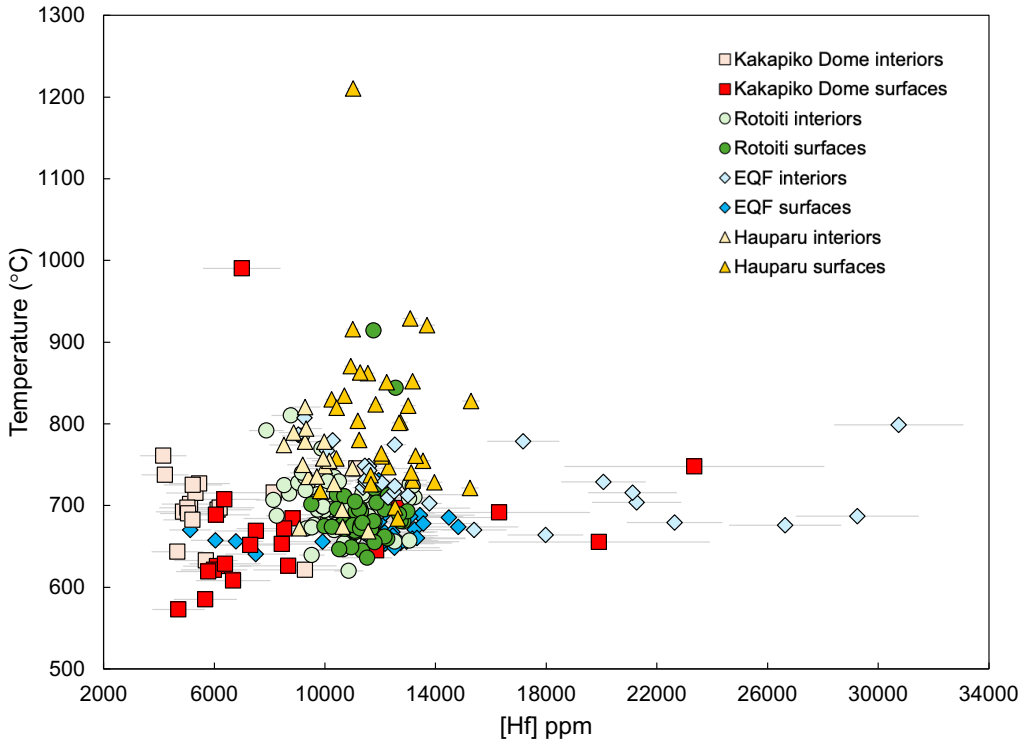


***Figure 2.10**: Ti-in-zircon concentration versus Hf concentration for the four eruptions. There is a subtle trend in decreasing Ti-in-zircon temperature with increasing Hf concentration in the Rotoiti and Earthquake Flat zircon, which is a common trend in evolving magmas, but there is no obvious correlation between Ti-in-zircon temperature and Hf concentration for the Kakapiko Dome and Hauparu zircon.*

The OVC zircons have a large range of signatures in almost every other trace element index indicating accessory phases fractionation. That Hf is relatively uniform compared to the spread in other indices implies that some mechanism is controlling zircon fractionation relative to other accessory phase fractionation. To understand the Hf concentration patterns further, we use the Zr/Hf from whole rock, glass, and zircon as an indication of zircon fractionation and extraction (Claiborne et al. 2006, Miller et al. 2005). The Rotoiti, EQF, and Hauparu surfaces and interiors define a decreasing trend of Zr/Hf, although there are no systematic differences between the interior and surfaces for each eruption (Fig. 2.8C) – a detail we also observed in the

Hf concentrations. In general, the cloud of data decreases from Zr/Hf = 59 to Zr/Hf = 12, which suggests continued zircon fractionation from melts rich in Zr (Zr/Hf = 59) and melts increasingly depleted in Zr (Zr/Hf = 12), but despite this trend, there is no systematic pattern in zircon fractionation through time (Fig. 2.8B–C, Fig. 2.12). Kakapiko Dome zircon reveal a different pattern in Zr/Hf ratios where the interiors show an extreme range in values from 42–115, and surfaces range from 20–101. When plotted against other geochemical fractionation trends such as Eu/Eu* (Fig. 2.8C), there appears to be a weak systematic fractionation trend, but given the overlapping range of Zr/Hf values, the observed trend is actually more controlled by Eu/Eu*.

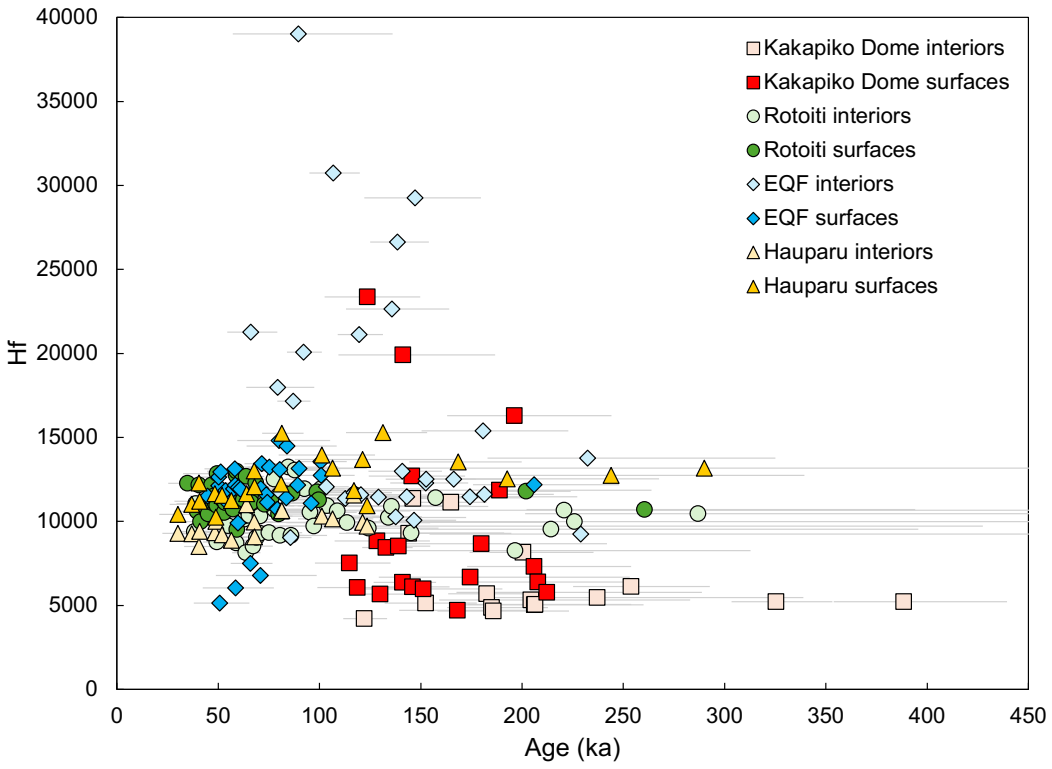


***Figure 2.11**: Hf concentration (ppm) versus ^{238}U-^{230}Th crystallization age for the four eruptions. The zircon show that there is no systematic variation in Hf concentration through*

time, which supports the idea of a complicated and geochemically heterogeneous magma mush reservoir where the zircon were stored.

Zr/Hf in glass shows bulk patterns more typical of the expected behavior presented by Claiborne et al. (2006): Zr/Hf ratios reflect chondritic values (35–40) from whole-rock SiO_2 < 73–75 wt.% and drop precipitously at whole-rock SiO_2 > 73–75 wt.%, which is ascribed to zircon fractionation. We present OVC glass Zr/Hf ratios relative to glass SiO_2 composition (Fig. 2.12) rather than whole-rock SiO_2 composition, so our data are slightly higher than the whole-rock measurements of Claiborne et al. (2006). We observe the same pattern in the OVC glasses as Claiborne et al. (2006) did in whole-rock compositions. Hauparu, the least evolved of the studied eruptions, reveals near-chondritic Zr/Hf values (36–48) over a range of SiO_2 = 72–78 wt.%, whereas Kakapiko Dome, Rotoiti, and EQF glasses reveal Zr/Hf ratios of 25–43 (with the exception of three outliers) over a tightly restricted range of SiO_2 = 77–79 wt.% (Fig. 2.12). This expected pattern suggests that evolved zircon saturation is closely tied to SiO_2 composition. One observed peculiarity is that Kakapiko Dome zircon display relatively low Hf concentrations, and therefore high Zr/Hf ratios, which may suggest accumulation of zircon in a cumulate pile, but the glass Zr/Hf ratios are very low, suggesting that the glass had experienced significant zircon fractionation. This seeming contradiction in composition requires that the zircon and glass are unrelated (see modeling discussion below). Overall, the Kakapiko Dome, Rotoiti, and Earthquake Flat zircon reveal diversity in Zr/Hf ratios over a somewhat narrow band in SiO_2 (wt.%) content, suggesting that geochemically distinct melts were amalgamated and poorly mixed prior to eruption. The Hauparu glass data reveal a large range in both Zr/Hf and SiO_2 (wt.%) content which supports a heterogenous magma reservoir post-CFE.

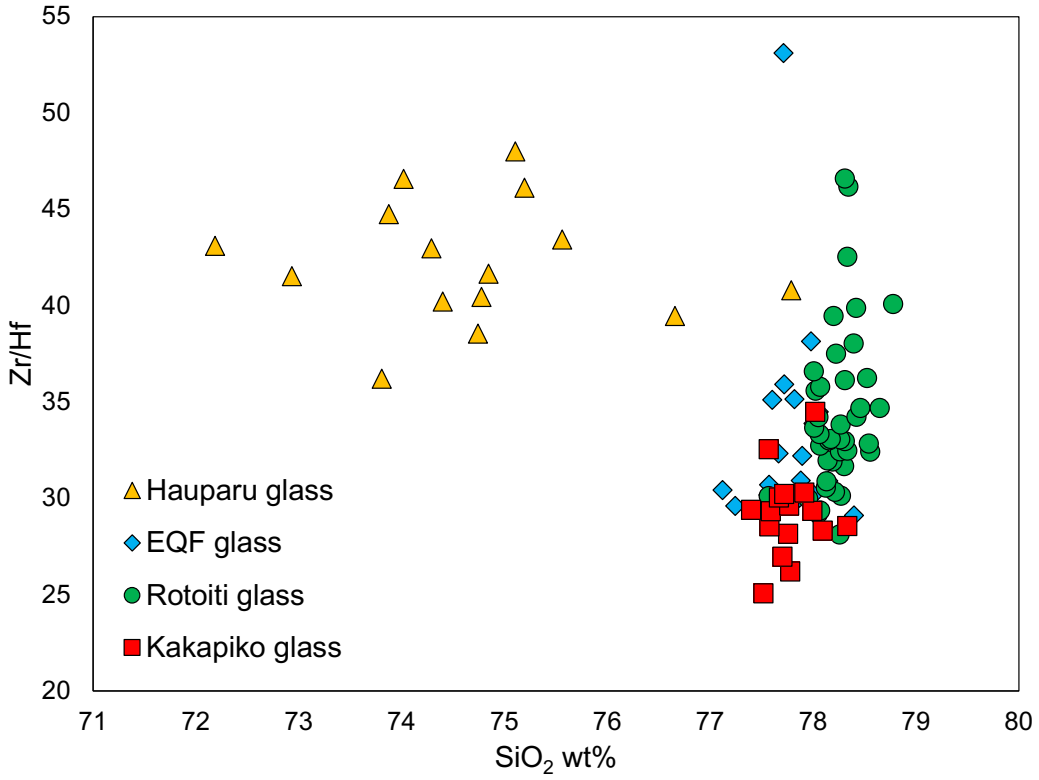


***Figure 2.12**: Zr/Hf ratios versus SiO_2 (wt.%) content in glass. Kakapiko Dome, Rotoiti, and Earthquake Flat glasses all show a range in Zr/Hf over a relatively narrow band on SiO_2 content, which suggests that heterogenous yet similarly evolved melts were amalgamated immediately prior to eruption but were inefficiently mixed. The Hauparu glass data reveal a range in both Zr/Hf content and SiO_2 content, which supports a model of significant heterogeneity post-CFE.*

2.6.5 Compositional variability as revealed by zircon-glass equilibrium modeling

Comparing OVC pumice glass trace-element compositions to glass/melt compositions modeled from zircon suggests that zircon crystallized from a wider range of melt compositions than the range in OVC pumice glass. Many of the pumice glass compositions have REE contents within error of the median modeled zircon melt compositions (Kakapiko Dome surfaces, Rotoiti interiors, Earthquake Flat interiors, and Hauparu interiors and surfaces) (Fig. 2.5A–D). Modeled

melt compositions for Rotoiti and EQF zircon surfaces overlap with the pumice glass entirely in LREEs but only fall partially within the errors of the median value for the modeled glass range of MREE and HREEs. Importantly, the MREE and HREEs preserved in zircon reveal unclear geochemical patterns that are difficult to interpret given the variation in mineral-melt partition coefficients and the effects that co-crystallization of different phases can have on REE concentration. Such complications limit our ability to discuss mineral fractionation patterns. One potential explanation for the large range of predicted MREE and HREE concentrations in the host glass is the presence of a large range of unique upper crustal melt compositions. If unique melts are distributed within a crystal mush, then each melt could evolve along a unique liquid line of descent without mixing or homogenizing. This could imprint different MREE and HREE compositions on zircon crystallized in those melts, such that when the measured zircon grains are juxtaposed the compositions do not reflect simple fractionation trends.

Geochemical diversity arises as fractionated silicic melts are stripped of their mafic componentry in the mid-crust by fractional crystallization within a large and mineralogically zoned crystal mush in upper crustal reservoirs (Allan et al. 2013, Begué et al. 2014, Charlier et al. 2005, Cooper and Wilson 2014, Shane and Smith 2013). Within these fractionated silicic melts, there is sustained micro-scale trace element heterogeneity that can explain the wide but uniform ranges of zircon trace element ratios and concentrations, and has bearing on the thermal and mineralogical differences in the studied eruptions. Such compositional heterogeneity preserved in zircon surfaces can be explained in several ways: 1) inclusion of zircon in major phases removes the zircon from melt environment thereby allowing the preservation of heterogeneous zircon surface signatures and a snapshot of melt history through time, a phenomena also documented by Wark and Miller (1993) and Charlier et al. (2003); 2) zircon

removal from the melt environment and storage in a low-melt crystal-rich cumulate pile; 3) zircon growth locally depleting the melt of Zr and Hf building blocks such that new growth cannot occur given slow diffusion rates.

2.6.6 Evidence for the growth of physically separate melt lenses within a greater mush system

As we have established, the large range in trace element concentrations observed in the OVC zircon suggests that zircon crystallized from melts that experienced variable amounts of zircon (Zr/Hf, REEs), plagioclase (Eu/Eu*), accessory (REEs) and mafic phase fractionation (REEs), which shows that chemical heterogeneity was maintained throughout the ~200 kyr preserved history of each magma reservoir, and further supports a model in which chemical diversity is maintained through physically separate melt environments. An interpretation of the OVC magma system as a single melt environment is not supported by our data as this type of environment would generate a more homogenous geochemical signature than is consistent with our observations. To explain the spread in preserved compositions and ages, the zircon must have been growing from coeval and diverse melt environments throughout the history of each magma reservoir, some zircon must have been removed from the growth environment and armored in another mineral phase as an inclusion, and some zircon must have grown very rapidly prior to eruption perhaps due to rapid ascent as the magma reservoir amalgamated an eruptive body.

All OVC zircon appear to have been stored in a crystal mush, but the details of magma storage relevant to each erupted magma body varies. At a critical crystallinity of 50-60% crystals, magmatic bodies become too viscous to erupt (Marsh 1981), and the mush framework will inhibit convection, allowing the development of isolated melt pockets and heterogeneous chemical environments. Thus, melt pockets housing zircon crystals that are inhibited from

participating in wholesale mixing and mingling by a crystal-rich network could plausibly generate the observed geochemical signatures preserved in zircon. Earthquake Flat is a notable eruption because it erupted explosively from the margins of the existing caldera and carried with it a significant cargo of individual crystals, lithics, and glomerocrysts ranging from >2– 0.1 mm, and amounting to around 40% crystal content. Neighboring, and possibly related, Rotoiti shares many compositional and petrologic characteristics with EQF but is different in the following significant ways: 1) Rotoiti contains far fewer crystals (20-25%), with few glomerocrysts; 2) Rotoiti lacks the large crystal sizes (>2mm) that characterize EQF; and 3) Rotoiti is saturated in cummingtonite, whereas EQF is saturated in hornblende and biotite (although trace amounts of hornblende and biotite in the uppermost units of Rotoiti suggest a possible link in the subsurface that could have sourced material from a laterally extensive, magma mush that also supplied hornblende and biotite to EQF). Nicholls et al. (1992) conducted a H_2O-saturated, Ni-NiO buffered experimental study that establish Rotoiti pre-eruptive storage conditions at < 300 MPa and < 750 ºC, specifically limited by the presence of cummingtonite. The experiments of Grant et al. (2024) show that EQF was stored at similarly cool and shallow conditions of 755 ºC and 140 MPa, which represents the equilibrium magma body immediately prior to eruption. A notable difference is that Nicholls et al. (1992) used whole rock as an experimental starting composition, and therefore their data provide broad pre-eruptive storage conditions, whereas Grant et al. (2024) use glass as a starting composition which focused the results on the conditions directly prior to eruption. Nevertheless, both results yield magma storage conditions within uncertainty of each other, and at reasonable pressure and temperature conditions in the shallow crust. Despite uncertainty in the intensive parameter comparison between the two eruptions, petrologic observations indicate that EQF was not primed to erupt in the same way as Rotoiti.

EQF contains abundant glomerocrysts of multiple sizes, large grains (>2 mm), and lacks resorption textures on rim boundaries (with the exception of quartz). Tightly adhered glomerocrysts lack interstitial glass, which suggest that minerals might have been stored in a cumulate mush pile. Grant et al. (2024) interpret these textures and the shallow, cool storage conditions of the magma body to propose that EQF was the crystal-rich periphery of a laterally extensive magma system. Building upon the mush model identified by other studies (Allan et al. 2013, Allan et al. 2017, Begué et al. 2014, Charlier et al. 2005, Charlier and Wilson 2010, Cooper et al. 2014, Smithies et al. 2023, Wilson and Charlier 2009), we invoke a magma mush model where high-silica interstitial melts can explain the unique and evolved geochemical signatures of Kakapiko Dome, Rotoiti, EQF and Hauparu. In such a scenario, Kakapiko Dome and EQF represent eruption of cooler crystal-rich regions of the magma mush, and Rotoiti and Hauparu represent eruption from rapidly assembled but poorly mixed melts with a moderate to low crystal cargo. It is likely that the magma system must have needed some time to rebuild post-CFE; if previous magma pathways were destroyed in a CFE and new mafic intrusions were required to reestablish the mush system then this could explain Hauparu's slightly hotter thermal state.

While there is still debate about the precise temperature of the solidus in granitic composition magma bodies, most studies agree that it likely falls within the range of 675-720 ºC for shallow, water-saturated magmas, depending on composition (Johannes and Holtz 1996, Gardner et al. 2014, Befus and Gardner 2016, Waters and Andrews 2016). The composition of Kakapiko Dome, Rotoiti, EQF, and Hauparu is within the context of these experimental results, and therefore we can reasonably assume that based on Ti-in-zircon thermometry that the OVC zircon crystallized at near-solidus conditions. Befus and Gardner (2016) conducted experiments

on a similar system (Central Plateau Member rhyolites, Yellowstone, WY, USA) and showed that ~80% of crystallization occurred within 20 degrees of the solidus. Therefore, given the range in Ti-in-zircon crystallization temperatures for the OVC zircon, we suggest that these magma reservoirs housed discrete parcels of magma that were likely in diverse states of crystallinity. Conversely, at temperatures >750 ºC the magma body is likely above the temperature of a crystal-dominated mush and is present as a melt-dominated system with varying amounts of crystal cargo. Given the range of temperatures recorded by all of the Rotoiti zircon (637-834 ºC) over a 50 kyr period, we conclude that the magma reservoir as a whole must have experienced *both* near-solidus and melt-dominated conditions simultaneously for at least 50 kyr. We interpret this to mean that that magma reservoir must have been large enough to host diverse melt conditions including environments of subsolidus, near-solidus, and melt-dominated conditions.

The zircon saturation threshold for Hauparu (848 ºC) supports slightly hotter magma lenses than the other eruptions. Hauparu is generally the least evolved of the four eruptions presented here, with the lowest whole-rock (67.4–72.2 wt.%) and glass (72.2 – 77.8 wt.%) SiO_2 contents (Table 2.1) and containing both orthopyroxene and clinopyroxene. Collectively these observations suggest that Hauparu was sourced from deeper (Smith et al. 2005) and hotter portions of the magma reservoir, but only some of the zircon record hotter and less evolved conditions. There are many zircon that show more evolved signatures similar to the caldera-forming, Rotoiti and EQF. The existence of evolved surfaces within error of eruption age shows that evolved melts must have existed in this system, and that zircon grew rapidly from these evolved melts immediately prior to eruption. Therefore, post-caldera recovery magmas not only come from deeper, more mafic melts, but also in some cases from evolved, presumably shallow, part of the system as well. Hauparu erupted ~9 ka after Rotoiti and EQF, which is a relatively

short recovery time. Although not as evolved as the CFE and syn-CFE magmas, Hauparu zircon show evidence that evolved pockets of melt either still existed within the reservoir and that survived the CFE, or that magma generation, assembly, and storage is sufficiently rapid that it can create similarly evolved magmas on timescales of 10^3 ka. Shane et al. (2007) and Shane et al. (2008a) propose a similar model for post-Rotoiti eruptions in the OVC where separate, geochemically diverse melts are rapidly assembled prior to eruption.

Our data highlight the similar behaviors of magma assembly and storage across a caldera forming cycle; crystallization occurs over long durations (~200 ka) and over a large range of temperatures (537–929 °C), and large ranges in trace element geochemistry reflect a magmatic environment in which zircon crystallize from physically separate regions within the magma reservoir and are assembled prior to eruption on short enough timescales that zircon are not overprinted by their host magma signature.

2.6.7 Implications for caldera cyclicity

A recent global summary by Bouvet de Maisonneuve et al. (2021) builds a framework to understand caldera cycles. Broadly, they define the caldera cycle as three stages: 1) "maturation:" during which assimilation and crystal fractionation create high-silica melts that are stored as separate melt pockets; 2) "fermentation:" during which eruptible melt readies itself for eruption, this is often accompanied by a volatile saturation creating an overpressure in the eruptible melt reservoir; and 3) "recovery:" post-CFE the magma reservoir rebuilds with inputs of mafic to intermediate recharge, during this period magmas are often less evolved and hotter than magma from the previous stages and might mix with remnant material from the caldera-forming magmas. Bouvet de Maisonneuve et al. (2021) suggest that the OVC is in the early to

mid-maturation phase, which our data support. We find that Kakapiko Dome (pre-CFE), Rotoiti (CFE), and Earthquake Flat (syn-CFE) show similar trends of evolved and unique geochemical signatures, suggesting that the melts were housed separately prior to eruption. The Kakapiko Dome falls into the "maturation" stage where a magma mush builds with small volume melts interspersed within the mush. The relatively simple crystallization history preserved by the Kakapiko Dome zircon age spectra and heterogeneous trace element signatures supports a model wherein a small melt body was rapidly assembled from a re-developing magma mush. Rotoiti and EQF fall into the "fermentation" stage, although for these two eruptions "fermentation" was rapid and short-lived as Rotoiti whole-rock and glass compositions are heterogenous revealing a unmixed magma (or magmas). Within this "fermentation" stage, whole rock and glass compositions suggest two different assembly pathways for the Rotoiti and the EQF magmas. The EQF tuff whole rock composition ranges from 69.3 – 73.0 wt.% SiO_2 (Molloy et al. 2008) yet the glass compositions are highly homogenized (76.6 – 78.0 wt.% SiO_2; Grant et al. 2024, Molloy et al. 2008). Whereas both the Rotoiti whole rock and glass compositions are heterogeneous at 71.8 – 75.3 wt.% SiO_2 and 74.6 – 80.5 wt.% SiO_2, respectively. The heterogenous whole-rock compositions for the two eruptions most likely represent amalgamation of variable crystal cargo from the magma mush, but the distinction between the glass compositions requires different assembly patterns. The Rotoiti glass composition is heterogenous, which suggests that separate Rotoiti melt bodies were assembled rapidly prior to eruption and the multiple melt bodies did not mix efficiently (Schmitz and Smith 2004, Shane et al. 2005). Conversely, the EQF glass compositions are homogenous. If the Rotoiti eruption was the trigger for the EQF eruption, and the time between the two eruptions was days to weeks (Nairn and Kohn 1973), then the EQF magma must have had: 1) very efficient silicic melt

production, producing the same composition of melt within a <1.5 wt.% SiO_2 range that was rapidly assembled prior to eruption, and/or 2) efficient extraction and very rapid mixing prior to eruption. The "recovery" stage occurs post-CFE and is supported by mafic and intermediate recharge into the magma mush producing heterogenous magmas that record hotter thermal conditions. Our data show that Hauparu magmas were highly heterogenous, as preserved by zircon age spectra, Ti-in-zircon thermometry, and trace element geochemistry. Other studies of post-CFE magmas in the OVC also show an increase in melt heterogeneity (Shane et al. 2007, Shane et al. 2008a).

An important caveat for hazard mitigation and planning is the rapidity of the EQF eruption following the Rotoiti CFE. The high crystallinity of the EQF eruption and its location on the periphery of the OVC caldera are both unusual factors associated with eruptive volumes the size of EQF. It is atypical for such high crystallinity, high-silica eruptions to efficiently mobilize 10 km^3 of material. Geophysical monitoring efforts can identify large melt-dominated bodies of magma but might not have the resolution to identify eruptive melt bodies of ~40% crystals, and targeted monitoring efforts are often focused within caldera boundaries rather than at extra-caldera locations. Therefore, current geophysical monitoring efforts would not necessarily flag an eruptive body like EQF as a hazard. Although high crystallinity rhyolitic eruptions of large volume are rare, it is important to consider the likelihood of eruption from all regions within a volcanic center, as the magma reservoir below is likely more complicated than the surface volcanism would suggest (Miller et al. 2022). A further caveat of caldera cyclicity for hazard mitigation is that small eruptions do not necessitate a CFE. Small eruptions are likely to occur within the "maturation" phase of the caldera cycle, but it isn't until the "fermentation" stage is reached that eruption could be imminent.

2.7 CONCLUSIONS

The temporal, chemical, and thermal heterogeneity recorded by zircon of diverse crystallization ages (eruption age through secular equilibrium) suggests that physically separate melt environments must have been sustained over a protracted growth period of ~200 kyr in order to impart chemically heterogeneous signatures on zircon. Our data show that the magma reservoir supported protracted zircon crystallization (~200 kyr) at varied (537–929 °C) mostly at cooler temperatures (~720 ºC). These observations combined with the zircon age spectra suggests that the magma reservoir as a whole supported continuous zircon growth (although any given location may not have).

We find no evidence of systematic fractionation through time or with temperature between zircon interiors and surfaces within or between eruption. In the case of each eruption, the variability in trace element signatures preserved in young interiors and old surfaces zircon suggests the existence of discrete geochemical melt environments over the zircon growth period. Based on the ages and geochemical signatures we propose that the zircon were stored in a crystal-rich framework, which housed isolated pockets of distributed melts that facilitated relatively cool, near-solidus conditions. In our model geochemical variability is chiefly controlled by physically separate melt environments within a crystal-rich mush, zircon armoring within major phases, and slow growth due to cool conditions and sluggish diffusion rates. Melts are differentiated in a mid-crustal reservoir creating a mafic phase sponge which could account for the geochemical variability imparted to silicic melts that percolate upwards and are rapidly assembled in upper crustal reservoirs prior to eruption. Different trace element signatures preserved in zircon likely arise from various amounts of major and accessory mineral

fractionation from distributed melts. This highly efficient magma processing center produces large, silicic magma reservoirs that can amalgamate individual melt pockets sufficiently rapidly that zircon growth from a single host melt composition cannot overprint the trace-element variability observed in zircon surfaces.

Our data show similar behaviors of magma assembly and storage across the caldera-forming cycle. Although for each eruption the range in trace element concentrations and ratios are similar, there does not appear to be any relationship between trace element composition and eruptive volume, nor does there appear to be any relationship between trace element compositions and temporal evolution across a caldera-forming cycle. Geochemical heterogeneity on a trace element scale from different magmas from the same volcanic center suggests that geologically ephemeral, distributed melts are present over the period the zircon growth period of ~200 kyr.

2.8 REFERENCES

Allan, A. S., Wilson, C. J., Millet, M. A., & Wysoczanski, R. J. (2012). The invisible hand: Tectonic triggering and modulation of a rhyolitic supereruption. *Geology*, *40*(6), 563-566.

Allan, A. S., Morgan, D. J., Wilson, C. J., & Millet, M. A. (2013). From mush to eruption in centuries: assembly of the super-sized Oruanui magma body. *Contributions to Mineralogy and Petrology*, *166*, 143-164.

Allan, A. S., Barker, S. J., Millet, M. A., Morgan, D. J., Rooyakkers, S. M., Schipper, C. I., & Wilson, C. J. (2017). A cascade of magmatic events during the assembly and eruption of a super-sized magma body. *Contributions to Mineralogy and Petrology*, *172*, 1-34.

Andersen, N. L., Singer, B. S., & Coble, M. A. (2019). Repeated rhyolite eruption from heterogeneous hot zones embedded within a cool, shallow magma reservoir. *Journal of Geophysical Research: Solid Earth*, *124*(3), 2582-2600.

Bachmann, O., Dungan, M. A., & Lipman, P. W. (2002). The Fish Canyon magma body, San Juan volcanic field, Colorado: rejuvenation and eruption of an upper-crustal batholith. *Journal of Petrology*, *43*(8), 1469-1503.

Bachmann, O., & Bergantz, G. W. (2004). On the origin of crystal-poor rhyolites: extracted from batholithic crystal mushes. *Journal of Petrology*, *45*(8), 1565-1582.

Bacon, C. R., & Druitt, T. H. (1988). Compositional evolution of the zoned calc-alkaline magma chamber of Mount Mazama, Crater Lake, Oregon. *Contributions to Mineralogy and Petrology*, *98*, 224-256.

Barker, S. J., Wilson, C. J. N., Smith, E. G., Charlier, B. L. A., Wooden, J. L., Hiess, J., & Ireland, T. R. (2014). Post-supereruption magmatic reconstruction of Taupo volcano (New Zealand), as reflected in zircon ages and trace elements. *Journal of Petrology*, *55*(8), 1511-1533.

Barth, A. P., & Wooden, J. L. (2010). Coupled elemental and isotopic analyses of polygenetic zircons from granitic rocks by ion microprobe, with implications for melt evolution and the sources of granitic magmas. *Chemical Geology*, *277*(1-2), 149-159.

Befus, K. S., & Gardner, J. E. (2016). Magma storage and evolution of the most recent effusive and explosive eruptions from Yellowstone Caldera. *Contributions to Mineralogy and Petrology*, *171*, 1-19.

Bégué, F., Deering, C. D., Gravley, D. M., Kennedy, B. M., Chambefort, I., Gualda, G. A., & Bachmann, O. (2014). Extraction, storage and eruption of multiple isolated magma batches in the paired Mamaku and Ohakuri eruption, Taupo Volcanic Zone, New Zealand. *Journal of Petrology*, *55*(8), 1653-1684.

Bell, E. A., & Kirkpatrick, H. M. (2022). Micro-zircon inclusions in accessory minerals reveal more complete magma compositional evolution records. *Contributions to Mineralogy and Petrology*, *177*(12), 113.

Bibby, H. M., Caldwell, T. G., Davey, F. J., & Webb, T. H. (1995). Geophysical evidence on the structure of the Taupo Volcanic Zone and its hydrothermal circulation. *Journal of volcanology and geothermal research*, *68*(1-3), 29-58.

Boehnke, P., Watson, E. B., Trail, D., Harrison, T. M., & Schmitt, A. K. (2013). Zircon saturation re-revisited. *Chemical Geology*, *351*, 324-334.

Bouvet de Maisonneuve, C., Forni, F., & Bachmann, O. (2021). Magma reservoir evolution during the build up to and recovery from caldera-forming eruptions–a generalizable model?. *Earth-Science Reviews*, *218*, 103684.

Burt, R. M., Brown, S. J. A., Cole, J. W., Shelley, D., & Waight, T. E. (1998). Glass-bearing plutonic fragments from ignimbrites of the Okataina caldera complex, Taupo Volcanic Zone,

New Zealand: remnants of a partially molten intrusion associated with preceding eruptions. *Journal of Volcanology and Geothermal Research*, *84*(3-4), 209-237.

Cashman, K. V., Sparks, R. S. J., & Blundy, J. D. (2017). Vertically extensive and unstable magmatic systems: a unified view of igneous processes. *Science*, *355*(6331), eaag3055.

Charlier, B. L., Peate, D. W., Wilson, C. J., Lowenstern, J. B., Storey, M., & Brown, S. J. (2003). Crystallisation ages in coeval silicic magma bodies: 238U–230Th disequilibrium evidence from the Rotoiti and Earthquake Flat eruption deposits, Taupo Volcanic Zone, New Zealand. *Earth and Planetary Science Letters*, *206*(3-4), 441-457.

Charlier, B. L. A., Wilson, C. J. N., Lowenstern, J. B., Blake, S., Van Calsteren, P. W., & Davidson, J. P. (2005). Magma generation at a large, hyperactive silicic volcano (Taupo, New Zealand) revealed by U–Th and U–Pb systematics in zircons. *Journal of Petrology*, *46*(1), 3-32.

Charlier, B. L. A., & Wilson, C. J. N. (2010). Chronology and evolution of caldera-forming and post-caldera magma systems at Okataina Volcano, New Zealand from zircon U–Th model-age spectra. *Journal of Petrology*, *51*(5), 1121-1141.

Cherniak, D. J., Hanchar, J. M., & Watson, E. B. (1997). Diffusion of tetravalent cations in zircon. *Contributions to Mineralogy and Petrology*, *127*, 383-390.

Claiborne, L. L., Miller, C. F., Walker, B. A., Wooden, J. L., Mazdab, F. K., & Bea, F. (2006). Tracking magmatic processes through Zr/Hf ratios in rocks and Hf and Ti zoning in zircons: an example from the Spirit Mountain batholith, Nevada. *Mineralogical Magazine*, *70*(5), 517-543.

Claiborne, L. L., Miller, C. F., Flanagan, D. M., Clynne, M. A., & Wooden, J. L. (2010). Zircon reveals protracted magma storage and recycling beneath Mount St. Helens. *Geology*, *38*(11), 1011-1014.

Claiborne, L. L., Miller, C. F., Gualda, G. A., Carley, T. L., Covey, A. K., Wooden, J. L., & Fleming, M. A. (2018). Zircon as magma monitor: Robust, temperature-dependent partition coefficients from glass and zircon surface and rim measurements from natural systems. *Microstructural geochronology: planetary records down to atom scale*, 1-33.

Coble, M. A., Vazquez, J. A., Barth, A. P., Wooden, J., Burns, D., Kylander-Clark, A., Jackson, S., & Vennari, C. E. (2018). Trace element characterisation of MAD-559 zircon reference material for ion microprobe analysis. *Geostandards and Geoanalytical Research*, *42*(4), 481-497.

Cole, J. W. (1990). Structural control and origin of volcanism in the Taupo volcanic zone, New Zealand. *Bulletin of volcanology*, *52*, 445-459.

Cole, J. W., & Spinks, K. D. (2009). Caldera volcanism and rift structure in the Taupo Volcanic Zone, New Zealand. *Geological Society, London, Special Publications*, *327*(1), 9-29.

Cole, J. W., Spinks, K. D., Deering, C. D., Nairn, I. A., & Leonard, G. S. (2010). Volcanic and structural evolution of the Okataina Volcanic Centre; dominantly silicic volcanism associated with the Taupo Rift, New Zealand. *Journal of volcanology and geothermal research*, *190*(1-2), 123-135.

Cole, J. W., Deering, C. D., Burt, R. M., Sewell, S., Shane, P. A. R., & Matthews, N. E. (2014). Okataina Volcanic Centre, Taupo Volcanic Zone, New Zealand: A review of volcanism and synchronous pluton development in an active, dominantly silicic caldera system. *Earth-Science Reviews*, *128*, 1-17.

Cooper, G. F., Wilson, C. J., Charlier, B. L., Wooden, J. L., & Ireland, T. R. (2014). Temporal evolution and compositional signatures of two supervolcanic systems recorded in zircons from Mangakino volcanic centre, New Zealand. *Contributions to Mineralogy and Petrology*, *167*, 1-23.

Cooper, G. F., & Wilson, C. J. (2014). Development, mobilisation and eruption of a large crystal-rich rhyolite: the Ongatiti ignimbrite, New Zealand. *Lithos*, *198*, 38-57.

Cooper, K. M., & Donnelly, C. T. (2004). 238U-230Th-226Ra disequilibria in dacite and plagioclase from the 2004–2005 eruption of Mount St. Helens. *A volcano rekindled: the renewed eruption of Mount St. Helens*, *2006*, 827-846.

Cooper, K. M. (2015). Timescales of crustal magma reservoir processes: insights from U-series crystal ages. *Geological Society, London, Special Publications*, *422*(1), 141-174.

Danišík, M., Shane, P., Schmitt, A. K., Hogg, A., Santos, G. M., Storm, S., Evans, N. J., Fifield, L. K., & Lindsay, J. M. (2012). Re-anchoring the late Pleistocene tephrochronology of New Zealand based on concordant radiocarbon ages and combined $^{238}U/^{230}Th$ disequilibrium and (U–Th)/He zircon ages. *Earth and Planetary Science Letters*, *349*, 240-250.

Davidson, J., Turner, S., Handley, H., Macpherson, C., & Dosseto, A. (2007). Amphibole "sponge" in arc crust?. *Geology*, *35*(9), 787-790.

Davis WJ (1985). Geochemistry and petrology of the Rotoiti and Earthquake Flat pyroclastic deposits. Unpublished MSc thesis, University of Auckland, New Zealand.

Deering, C. D., Bachmann, O., Dufek, J., & Gravley, D. M. (2011). Rift-related transition from andesite to rhyolite volcanism in the Taupo Volcanic Zone (New Zealand) controlled by crystal–melt dynamics in mush zones with variable mineral assemblages. *Journal of petrology*, *52*(11), 2243-2263.

Deering, C. D., Keller, B., Schoene, B., Bachmann, O., Beane, R., & Ovtcharova, M. (2016). Zircon record of the plutonic-volcanic connection and protracted rhyolite melt evolution. *Geology*, *44*(4), 267-270.

Devine, J. D., Rutherford, M. J., Norton, G. E., & Young, S. R. (2003). Magma storage region processes inferred from geochemistry of Fe–Ti oxides in andesitic magma, Soufriere Hills Volcano, Montserrat, WI. *Journal of Petrology*, *44*(8), 1375-1400.

Ellis, B. S., Bachmann, O., & Wolff, J. A. (2014). Cumulate fragments in silicic ignimbrites: The case of the Snake River Plain. *Geology*, *42*(5), 431-434.

Ferry, J. M., & Watson, E. B. (2007). New thermodynamic models and revised calibrations for the Ti-in-zircon and Zr-in-rutile thermometers. *Contributions to Mineralogy and Petrology*, *154*(4), 429-437.

Finch, R. J., & Hanchar, J. M. (2003). Structure and chemistry of zircon and zircon-group minerals. *Reviews in mineralogy and geochemistry*, *53*(1), 1-25.

Fleet, M. E., & Pan, Y. (1997). Site preference of rare earth elements in fluorapatite: Binary (LREE+ HREE)-substituted crystals. *American Mineralogist*, *82*(9-10), 870-877.

Fujimaki, H., Tatsumoto, M., & Aoki, K. I. (1984). Partition coefficients of Hf, Zr, and REE between phenocrysts and groundmasses. *Journal of Geophysical Research: Solid Earth*, *89*(S02), B662-B672.

Gardner, J. E., Befus, K. S., Gualda, G. A., & Ghiorso, M. S. (2014). Experimental constraints on rhyolite-MELTS and the Late Bishop Tuff magma body. *Contributions to Mineralogy and Petrology*, *168*, 1-14.

Gervasoni, F., Klemme, S., Rocha-Júnior, E. R., & Berndt, J. (2016). Zircon saturation in silicate melts: a new and improved model for aluminous and alkaline melts. *Contributions to Mineralogy and Petrology*, *171*, 1-12.

Ghiorso, M. S., & Evans, B. W. (2008). Thermodynamics of rhombohedral oxide solid solutions and a revision of the Fe-Ti two-oxide geothermometer and oxygen-barometer. *American Journal of science*, *308*(9), 957-1039.

Ghiorso, M. S., & Sack, O. (1991). Fe-Ti oxide geothermometry: thermodynamic formulation and the estimation of intensive variables in silicic magmas. *Contributions to Mineralogy and Petrology*, *108*(4), 485-510.

Grant, E. R., Blatter, D. L., Sisson, T. W., & Cooper, K. M. (2024). Shallow storage of the explosive Earthquake Flat Pyroclastics magma body, Okataina Volcanic Center, Taupo Volcanic Zone, New Zealand: evidence from phase-equilibria experiments. *Contributions to Mineralogy and Petrology*, *179*(8), 81.

Gravley, D. M., Deering, C. D., Leonard, G. S., & Rowland, J. V. (2016). Ignimbrite flare-ups and their drivers: a New Zealand perspective. *Earth-Science Reviews*, *162*, 65-82.

Gualda, G. A., Gravley, D. M., Connor, M., Hollmann, B., Pamukcu, A. S., Bégué, F., ... & Deering, C. D. (2018). Climbing the crustal ladder: Magma storage-depth evolution during a volcanic flare-up. *Science Advances*, *4*(10), eaap7567.

Hanchar, J. M., Finch, R. J., Hoskin, P. W., Watson, E. B., Cherniak, D. J., & Mariano, A. N. (2001). Rare earth elements in synthetic zircon: Part 1. Synthesis, and rare earth element and phosphorus doping. *American Mineralogist*, *86*(5-6), 667-680.

Hildreth, W., & Moorbath, S. (1988). Crustal contributions to arc magmatism in the Andes of Central Chile. *Contributions to mineralogy and petrology*, *98*, 455-489.

Hanchar, J. M., & Van Westrenen, W. (2007). Rare earth element behavior in zircon-melt systems. *Elements*, *3*(1), 37-42.

Hildreth, W. (2004). Volcanological perspectives on Long Valley, Mammoth Mountain, and Mono Craters: several contiguous but discrete systems. *Journal of Volcanology and Geothermal Research*, *136*(3-4), 169-198.

Hildreth, W., & Wilson, C. J. (2007). Compositional zoning of the Bishop Tuff. *Journal of Petrology*, *48*(5), 951-999.

Hochstein, M. P., Smith, I. E., Regenauer-Lieb, K., & Ehara, S. (1993). Geochemistry and heat transfer processes in Quaternary rhyolitic systems of the Taupo Volcanic Zone, New Zealand. *Tectonophysics*, *223*(3-4), 213-235.

Holness, M. B., Stock, M. J., & Geist, D. (2019). Magma chambers versus mush zones: constraining the architecture of sub-volcanic plumbing systems from microstructural analysis of crystalline enclaves. *Philosophical Transactions of the Royal Society A*, *377*(2139), 20180006.

Hopkins, J. L., Lowe, D. J., & Horrocks, J. L. (2021). Tephrochronology in Aotearoa New Zealand. *New Zealand Journal of Geology and Geophysics*, *64*(2-3), 153-200.

Hoskin, P. W., & Schaltegger, U. (2003). The composition of zircon and igneous and metamorphic petrogenesis. *Reviews in mineralogy and geochemistry*, *53*(1), 27-62.

Hou, T., Botcharnikov, R., Moulas, E., Just, T., Berndt, J., Koepke, J., Zhaochong, Z., Wang, M., Yang, Z., & Holtz, F. (2020). Kinetics of Fe–Ti oxide re-equilibration in magmatic systems: implications for thermo-oxybarometry. *Journal of Petrology*, *61*(11-12), egaa116.

Houghton, B. F., Wilson, C. J. N., McWilliams, M. O., Lanphere, M. A., Weaver, S. D., Briggs, R. M., & Pringle, M. S. (1995). Chronology and dynamics of a large silicic magmatic system: central Taupo Volcanic Zone, New Zealand. *Geology*, *23*(1), 13-16.

Johannes, W., & Holtz, F. (1996). The Haplogranite System Qz-Ab-Or. *Petrogenesis and Experimental Petrology of Granitic Rocks*, 18-57.

Jurado-Chichay, Z., & Walker, G. P. L. (2000). Stratigraphy and dispersal of the Mangaone Subgroup pyroclastic deposits, Okataina volcanic centre, New Zealand. *Journal of Volcanology and Geothermal Research*, *104*(1-4), 319-380.

Langridge, R.M., Ries, W.F., Litchfield, N.J., Villamor, P., Van Dissen, R.J., Barrell, D.J.A., Rattenbury, M.S., Heron, D.W., Haubrock, S., Townsend, D.B., Lee, J.M., Berryman, K.R., Nicol, A., Cox, S.C., Stirling, M.W. (2016). The New Zealand Active Faults Database. *New Zealand Journal of Geology and Geophysics 59*: 86-96. doi: 10.1080/00288306.2015.1112818.

Leonard, G. S., Begg, J. G., Wilson, C. J. N., & Leonard, G. S. (2010). *Geology of the Rotorua area*. Lower Hutt, New Zealand: GNS Science.

Linnen, R. L., & Keppler, H. (2002). Melt composition control of Zr/Hf fractionation in magmatic processes. *Geochimica et Cosmochimica Acta*, *66*(18), 3293-3301.

Maas, R., Kinny, P. D., Williams, I. S., Froude, D. O., & Compston, W. (1992). The Earth's oldest known crust: a geochronological and geochemical study of 3900–4200 Ma old detrital zircons from Mt. Narryer and Jack Hills, Western Australia. *Geochimica et Cosmochimica Acta*, *56*(3), 1281-1300.

Marsh, B. D. (1981). On the crystallinity, probability of occurrence, and rheology of lava and magma. *Contributions to Mineralogy and Petrology*, *78*, 85-98.

Miller, C. F., & Wark, D. A. (2008). Supervolcanoes and their explosive supereruptions. *Elements*, *4*(1), 11-15.

Miller, C. A., Barretto, J., Stagpoole, V., Caratori-Tontini, F., Brakenrig, T., & Bertrand, E. (2022). The integrated history of repeated caldera formation and infill at the Okataina Volcanic Centre: Insights from 3D gravity and magnetic models. *Journal of Volcanology and Geothermal Research*, *427*, 107555.

Molloy, C., Shane, P., & Nairn, I. (2008). Pre-eruption thermal rejuvenation and stirring of a partly crystalline rhyolite pluton revealed by the Earthquake Flat Pyroclastics deposits, New Zealand. *Journal of the Geological Society*, *165*(1), 435-447.

Nandedkar, R. H., Hürlimann, N., Ulmer, P., & Müntener, O. (2016). Amphibole–melt trace element partitioning of fractionating calc-alkaline magmas in the lower crust: an experimental study. *Contributions to Mineralogy and Petrology*, *171*, 1-25.

Nairn IA (2002). Geology of the Okataina Volcanic Centre, scale 1: 50,000. Institute of Geological and Nuclear Sciences geological map 25. 1 sheet+ 156 p. Institute of Geological and Nuclear Sciences Ltd.

Nicholls, I. A., Oba, T., & Conrad, W. K. (1992). The nature of primary rhyolitic magmas involved in crustal evolution: evidence from an experimental study of cummingtonite-bearing rhyolites, Taupo Volcanic Zone, New Zealand. *Geochimica et Cosmochimica Acta*, *56*(3), 955-962.

Paulatto, M., Hooft, E. E., Chrapkiewicz, K., Heath, B., Toomey, D. R., & Morgan, J. V. (2022). Advances in seismic imaging of magma and crystal mush. *Frontiers in Earth Science*, *10*, 970131.

Reid, M. R., Coath, C. D., Harrison, T. M., & McKeegan, K. D. (1997). Prolonged residence times for the youngest rhyolites associated with Long Valley Caldera: 230Th—238U ion microprobe dating of young zircons. *Earth and Planetary Science Letters*, *150*(1-2), 27-39.

Reid, M. R., Vazquez, J. A., & Schmitt, A. K. (2011). Zircon-scale insights into the history of a Supervolcano, Bishop Tuff, Long Valley, California, with implications for the Ti-in-zircon geothermometer. *Contributions to Mineralogy and Petrology*, *161*, 293-311.

Reid, M. R., & Vazquez, J. A. (2017). Fitful and protracted magma assembly leading to a giant eruption, Youngest Toba Tuff, Indonesia. *Geochemistry, Geophysics, Geosystems*, *18*(1), 156-177.

Rocco, N. D. (2020). Isotopic and geochemical signatures of mantle and crustal contributions in rhyolites from Okataina and Taupo volcanoes, New Zealand.

Rubin, A., Cooper, K. M., Leever, M., Wimpenny, J., Deering, C., Rooney, T., Gravley, D., & Yin, Q. Z. (2016). Changes in magma storage conditions following caldera collapse at Okataina Volcanic Center, New Zealand. *Contributions to Mineralogy and Petrology*, *171*, 1–18.

Sas, M., Shane, P., Kuritani, T., Zellmer, G. F., Kent, A. J., & Nakagawa, M. (2021). Mush, melts and metasediments: a history of rhyolites from the Okataina volcanic centre, New Zealand, as captured in plagioclase. *Journal of Petrology*, *62*(8), egab038.

Sas, M., Shane, P., Kawasaki, N., Sakamoto, N., Zellmer, G. F., & Yurimoto, H. (2022). Inter- and intra-crystal quartz δ18O homogeneity at Okataina volcano, Aotearoa New Zealand: Implications for rhyolite genesis. *Journal of Volcanology and Geothermal Research*, *421*, 107430.

Schmitz, M. D., & Smith, I. E. (2004). The petrology of the Rotoiti eruption sequence, Taupo Volcanic Zone: an example of fractionation and mixing in a rhyolitic system. *Journal of Petrology*, *45*(10), 2045-2066.

Self, S. (2006). The effects and consequences of very large explosive volcanic eruptions. *Philosophical Transactions of the Royal Society A: Mathematical, Physical and Engineering Sciences*, *364*(1845), 2073-2097.

Shao, T., Xia, Y., Ding, X., Cai, Y., & Song, M. (2020). Zircon saturation model in silicate melts: a review and update. *Acta Geochimica*, *39*, 387-403.

Shane, P., Nairn, I. A., & Smith, V. C. (2005a). Magma mingling in the~ 50 ka Rotoiti eruption from Okataina Volcanic Centre: implications for geochemical diversity and chronology of large volume rhyolites. *Journal of Volcanology and Geothermal Research*, *139*(3-4), 295-313.

Shane, P., Smith, V. C., & Nairn, I. A. (2005b). High temperature rhyodacites of the 36 ka Hauparu pyroclastic eruption, Okataina Volcanic Centre, New Zealand: Change in a silicic magmatic system following caldera collapse. *Journal of Volcanology and Geothermal Research*, *147*(3-4), 357-376.

Shane, P., Martin, S. B., Smith, V. C., Beggs, K. F., Darragh, M. B., Cole, J. W., & Nairn, I. A. (2007). Multiple rhyolite magmas and basalt injection in the 17.7 ka Rerewhakaaitu eruption episode from Tarawera volcanic complex, New Zealand. *Journal of Volcanology and Geothermal Research*, *164*(1-2), 1-26.

Shane, P., Nairn, I. A., Smith, V. C., Darragh, M., Beggs, K., & Cole, J. W. (2008a). Silicic recharge of multiple rhyolite magmas by basaltic intrusion during the 22.6 ka Okareka Eruption Episode, New Zealand. *Lithos*, *103*(3-4), 527-549.

Shane, P., Nairn, I. A., Martin, S. B., & Smith, V. C. (2008b). Compositional heterogeneity in tephra deposits resulting from the eruption of multiple magma bodies: implications for tephrochronology. *Quaternary International*, *178*(1), 44-53.

Shane, P., & Smith, V. C. (2013). Using amphibole crystals to reconstruct magma storage temperatures and pressures for the post-caldera collapse volcanism at Okataina volcano. *Lithos*, *156*, 159-170.

Sisson, T. W. (1994). Hornblende-melt trace-element partitioning measured by ion microprobe. *Chemical Geology*, *117*(1-4), 331-344.

Sisson, T. W., & Bacon, C. R. (1999). Gas-driven filter pressing in magmas. *Geology*, *27*(7), 613-616.

Smith, V. C., Shane, P., & Nairn, I. A. (2005). Trends in rhyolite geochemistry, mineralogy, and magma storage during the last 50 kyr at Okataina and Taupo volcanic centres, Taupo Volcanic Zone, New Zealand. *Journal of Volcanology and Geothermal Research*, *148*(3-4), 372-406.

Smithies, S. L., Harmon, L. J., Allen, S. M., Gravley, D. M., & Gualda, G. A. (2023). Following magma: the pathway of silicic magmas from extraction to storage during an ignimbrite flare-up, Taupō volcanic zone, New Zealand. *Earth and Planetary Science Letters*, *607*, 118053.

Speer, J. Alexander. (1982). Zircon. Reviews in Mineralogy and Geochemistry, 5(1), 67–112.

Stelten, M. E., Cooper, K. M., Vazquez, J. A., Calvert, A. T., & Glessner, J. J. (2015). Mechanisms and timescales of generating eruptible rhyolitic magmas at Yellowstone caldera from zircon and sanidine geochronology and geochemistry. *Journal of Petrology*, *56*(8), 1607-1642.

Storm, S., Shane, P., Schmitt, A. K., & Lindsay, J. M. (2011). Contrasting punctuated zircon growth in two syn-erupted rhyolite magmas from Tarawera volcano: Insights to crystal diversity in magmatic systems. *Earth and Planetary Science Letters*, *301*(3-4), 511-520.

Swallow, E. J., Wilson, C. J., Charlier, B. L., & Gamble, J. A. (2019). The Huckleberry Ridge Tuff, Yellowstone: evacuation of multiple magmatic systems in a complex episodic eruption. *Journal of Petrology*, *60*(7), 1371-1426.

Till, C. B., Vazquez, J. A., Stelten, M. E., Shamloo, H. I., & Shaffer, J. S. (2019). Coexisting discrete bodies of rhyolite and punctuated volcanism characterize Yellowstone's post-Lava Creek Tuff caldera evolution. *Geochemistry, Geophysics, Geosystems*, *20*(8), 3861-3881.

Venezky, D. Y., & Rutherford, M. J. (1999). Petrology and Fe–Ti oxide reequilibration of the 1991 Mount Unzen mixed magma. *Journal of Volcanology and Geothermal Research*, *89*(1-4), 213-230.

Wallace, L. M., Beavan, J., McCaffrey, R., & Darby, D. (2004). Subduction zone coupling and tectonic block rotations in the North Island, New Zealand. *Journal of Geophysical Research: Solid Earth*, *109*(B12).

Waters, L. E., & Andrews, B. J. (2016). The role of superheating in the formation of Glass Mountain obsidians (Long Valley, CA) inferred through crystallization of sanidine. *Contributions to Mineralogy and Petrology*, *171*, 1-19.

Watson, E. B., & Harrison, T. M. (1983). Zircon saturation revisited: temperature and composition effects in a variety of crustal magma types. *Earth and Planetary Science Letters*, *64*(2), 295-304.

Were, P., & Keppler, H. (2021). Trace element fractionation between biotite, allanite, and granitic melt. *Contributions to Mineralogy and Petrology*, *176*(9), 74.

Wilson, C. J., Gravley, D. M., Leonard, G. S., & Rowland, J. V. (2009). Volcanism in the central Taupo Volcanic Zone, New Zealand: tempo, styles and controls. *Studies in volcanology: the legacy of George Walker. Special Publications of IAVCEI*, *2*, 225-247.

Chapter 2 Appendix A
Table of model ages and trace element concentrations

Zircon model crystallization ages and trace element concentrations (ppm)

Grain Location	Kakapiko Dome	Model age (ka)	+1σ (ka)	-1σ (ka)	Slope	slope error	Eu/Eu*	1 SD	Yb/Gd	1 SD	Y/P	1 SD	U/Th	1 SD	Ti-in-zircon Temp (C)	Zr/Hf	Σ(REE + P)/Y
Surface	GP_102-15.1	115	20	17	0.651	0.059	0.170	0.10	27	8	2.4	0.6	1.9	0.5	669	63.6	1.1
Surface	GP_102-18.1	119	24	20	0.663	0.067	0.203	0.11	17	5	6.0	1.5	1.2	0.3	689	78.8	3.1
Surface	GP_102-10.1	124	26	21	0.678	0.069	0.221	0.12	31	9	1.7	0.4	1.9	0.5	748	20.4	0.9
Surface	GP_102-21.1	128	26	21	0.692	0.065	0.138	0.08	24	7	3.4	0.8	2.1	0.6	684	54.1	1.8
Surface	GP_102-2.1	130	15	13	0.696	0.039	0.250	0.14	19	5	7.1	1.7	1.4	0.4	585	84.2	3.5
Surface	GP_102-13.1	133	13	12	0.704	0.034	0.115	0.06	17	5	7.1	1.7	1.2	0.3	653	56.6	3.5
Surface	GP_102-19.1	139	16	14	0.721	0.037	0.273	0.15	21	6	7.0	1.7	1.3	0.4	672	56.0	3.5
Surface	GP_102-12.1	141	45	32	0.726	0.093	0.145	0.08	29	8	1.8	0.4	1.6	0.4	655	24.0	1.1
Surface	GP_102-17.1	141	16	14	0.726	0.038	0.225	0.13	19	5	6.5	1.6	1.3	0.3	708	75.0	3.2
Surface	GP_102-6.1	146	26	21	0.737	0.056	0.155	0.09	16	5	10.8	2.6	1.0	0.3	697	37.6	5.8
Surface	GP_102-7.1	146	18	16	0.738	0.040	0.246	0.14	17	5	7.0	1.7	1.4	0.4	626	78.3	3.5
Surface	GP_102-16.1	151	39	29	0.750	0.075	0.172	0.10	22	6	6.3	1.5	1.1	0.3	621	79.7	3.6
Surface	GP_102-1.1	168	39	29	0.786	0.065	0.225	0.13	24	7	3.6	0.9	2.3	0.6	573	101.4	1.8
Surface	GP_102-5.1	174	79	45	0.798	0.104	0.188	0.11	26	7	5.4	1.3	2.0	0.5	608	71.5	2.5
Surface	GP_102-3.1	180	62	39	0.808	0.083	0.239	0.13	30	9	4.8	1.2	1.8	0.5	626	55.1	2.7
Surface	GP_102-14.1	189	75	44	0.823	0.088	0.238	0.13	23	7	6.3	1.5	1.4	0.4	645	40.3	3.3
Surface	GP_102-8.1	196	48	33	0.835	0.059	0.231	0.13	15	4	6.0	1.5	1.5	0.4	691	29.3	3.1
Surface	GP_102-11.1	206	48	33	0.849	0.054	0.262	0.15	35	10	2.4	0.6	2.4	0.6	652	65	1
Surface	GP_102-9.1	208	48	33	0.851	0.053	0.189	0.11	17	5	6.3	1.5	1.6	0.4	629	75	3
Surface	GP_102-4.1	212	77	45	0.857	0.072	0.250	0.14	23	7	5.7	1.4	1.3	0.3	619	83	3
Surface	GP_102-20.1	--	--	--	--	--	0.283	0.16	23	7	10.4	2.5	1.4	0.4	990	68	5
Interior	GP102_int_17.1	122	11	10	0.673	0.032	0.438	0.25	9	3	6.6	1.6	0.7	0.2	738	113.3	3.2
Interior	GP102_int_7.2	140	51	34	0.724	0.103	--	--	--	--	--	--	--	--	--	--	--
Interior	GP102_int_14.1	144	18	15	0.733	0.040	0.177	0.10	23	7	5.3	1.3	1.6	0.4	621	51.4	2.6
Interior	GP102_int_2.1	146	25	20	0.738	0.054	0.306	0.17	30	9	1.7	0.4	2.8	0.7	681	42.0	0.9
Interior	GP102_int_15.1	153	17	15	0.753	0.037	0.285	0.16	31	9	5.7	1.4	1.8	0.5	702	93.1	2.9
Interior	GP102_int_16.1	165	23	19	0.780	0.042	0.327	0.18	28	8	2.9	0.7	3.5	0.9	746	42.9	1.5
Interior	GP102_int_18.1	183	28	22	0.813	0.042	0.338	0.19	15	4	4.9	1.2	1.5	0.4	633	83.9	2.4
Interior	GP102_int_12.1	185	37	28	0.817	0.053	0.650	0.36	27	8	5.7	1.4	1.4	0.4	692	97.9	2.8
Interior	GP102_int_3.2	186	35	26	0.818	0.050	0.188	0.11	27	8	2.6	0.6	2.1	0.6	643	102.4	1.3
Interior	GP102_int_3.1	193	79	45	0.829	0.088	--	--	--	--	--	--	--	--	-- --	--	
Interior	GP102_int_8.1	200	54	36	0.841	0.062	0.606	0.34	30	9	1.9	0.5	1.2	0.3	716	58.5	1.0
Interior	GP102_int_10.1	204	48	33	0.846	0.054	0.485	0.27	19	5	6.0	1.5	1.5	0.4	715	89.7	3.0
Interior	GP102_int_5.1	206	102	52	0.849	0.092	0.472	0.26	19	5	3.5	0.8	1.5	0.4	697	95.0	1.7
Interior	GP102_int_4.1	206	39	29	0.849	0.045	0.348	0.19	18	5	5.3	1.3	0.9	0.2	690	94.5	2.8
Interior	GP102_int_9.1	210	28	22	0.854	0.033	--	--	--	--	--	--	--	--	-- --	--	
Interior	GP102_int_11.1	217	51	35	0.863	0.051	--	--	--	--	--	--	--	--	-- --	--	
Interior	GP102_int_13.1	237	49	34	0.886	0.041	0.417	0.23	11	3	6.9	1.7	0.9	0.2	727	87.5	3.4
Interior	GP102_int_21.1	254	135	58	0.902	0.069	0.433	0.24	19	6	5.9	1.4	1.4	0.4	695	78.0	3.0
Interior	GP102_int_20.1	325	350	210	0.949	0.295	0.382	0.21	22	6	3.4	0.8	1.7	0.4	682	91.7	1.7
Interior	GP102_int_1.1	388	350	120	0.972	0.057	0.320	0.18	18	5	3.2	0.8	1.4	0.4	725	91.4	1.7
Interior	GP102_int_19.1	--	--	--	--	--	0.363	0.20	10	3	10.6	2.6	1.1	0.3	697	77.0	5.2
Interior	GP102_int_6.1	--	--	--	--	--	0.345	0.19	23	7	4.1	1.0	1.8	0.5	682	46.1	2.1
Interior	GP102_int_7.1	--	--	--	--	--	0.082	0.05	13	4	5.6	1.4	0.5	0.1	761	115.0	2.7

Zr concentration is 47760 ppm from Claiborne et al. (2006)

Zircon model crystallization ages and trace element concentrations (ppm)

Grain Location	Kakapiko Dome	P/Si	1 SD	Sc/Si	1 SD	49Ti/Si	1 SD	Fe/Si	1 SD	Y/Si	1 SD	Nb/Si	1 SD	La/Si	1 SD	Ce/Si	1 SD	Nd/Si	1 SD	Sm/Si	1 SD	Eu/Si	1 SD	Gd/Si	1 SD	
Surface	GP_102-15.1		615.4	115.8	53.2	11.4	2.1	0.8	4.5	1.4	1487.0	227.4	3.7	0.9	0.2	0.1	9.6	1.8	2.1	0.5	1.4	0.7	0.3	0.0	14.0	3.1
Surface	GP_102-18.1		215.4	40.5	22.0	4.7	2.6	1.0	2.7	0.9	1292.6	197.6	1.5	0.4	0.2	0.1	13.1	2.5	2.6	0.6	2.0	1.0	0.6	0.1	24.8	5.5
Surface	GP_102-10.1		1817.3	342.0	124.6	26.8	5.1	1.9	10.3	3.2	3157.0	482.7	6.2	1.5	0.9	0.6	22.7	4.2	2.5	0.6	5.3	2.6	0.7	0.1	39.2	8.6
Surface	GP_102-21.1		269.9	50.8	74.3	16.0	2.5	0.9	3.9	1.2	917.0	140.2	2.6	0.6	0.3	0.2	6.7	1.2	1.7	0.4	1.4	0.7	0.4	0.1	12.7	2.8
Surface	GP_102-2.1		156.2	29.4	19.4	4.2	0.7	0.2	1.7	0.5	1106.6	169.2	1.4	0.3	0.1	0.1	10.2	1.9	1.3	0.3	2.0	1.0	0.4	0.0	16.8	3.7
Surface	GP_102-13.1		376.2	70.8	38.9	8.4	1.7	0.6	3.2	1.0	2674.3	408.9	3.0	0.7	0.0	0.0	21.8	4.1	4.8	1.1	5.4	2.6	1.2	0.1	45.7	10.1
Surface	GP_102-19.1		195.9	36.9	32.3	7.0	2.1	0.8	4.6	1.4	1375.6	210.3	1.8	0.4	0.1	0.1	13.6	2.5	1.2	0.3	1.5	0.7	0.3	0.0	18.5	4.1
Surface	GP_102-12.1		1166.4	219.5	84.2	18.1	3.3	1.2	2.1	0.7	2121.2	324.3	3.9	0.9	0.2	0.2	18.0	3.4	2.2	0.5	3.8	1.9	0.7	0.1	36.9	8.1
Surface	GP_102-17.1		246.8	46.5	30.0	6.5	1.7	0.7	3.1	1.0	1595.8	244.0	2.8	0.7	0.0	0.0	11.8	2.2	1.8	0.4	2.4	1.2	0.6	0.1	22.3	4.9
Surface	GP_102-6.1		579.9	109.1	83.6	18.0	2.9	1.1	4.8	1.5	6280.0	960.2	16.6	4.0	0.1	0.1	79.5	14.9	11.7	2.8	24.0	11.8	2.1	0.3	129.8	28.6
Surface	GP_102-7.1		188.9	35.6	27.7	6.0	1.2	0.4	1.0	0.3	1324.0	202.4	1.8	0.4	0.1	0.0	9.2	1.7	1.2	0.3	2.3	1.1	0.6	0.1	22.2	4.9
Surface	GP_102-16.1		141.0	26.5	16.7	3.6	1.1	0.4	2.9	0.9	887.7	135.7	1.5	0.4	0.1	0.1	9.8	1.8	1.0	0.2	0.8	0.4	0.3	0.0	17.5	3.9
Surface	GP_102-1.1		140.7	26.5	36.2	7.8	0.5	0.2	1.4	0.4	507.9	77.7	1.7	0.4	0.1	0.0	6.0	1.1	0.3	0.1	0.7	0.3	0.1	0.0	6.8	1.5
Surface	GP_102-5.1		153.6	28.9	21.0	4.5	0.9	0.3	2.0	0.6	828.3	126.6	1.8	0.4	0.0	0.0	7.5	1.4	0.5	0.1	0.6	0.3	0.2	0.0	7.3	1.6
Surface	GP_102-3.1		137.0	25.8	19.3	4.2	1.2	0.4	2.2	0.7	662.9	101.4	2.2	0.5	0.0	0.0	8.3	1.6	0.6	0.2	1.0	0.5	0.2	0.0	9.8	2.2
Surface	GP_102-14.1		284.1	53.5	40.7	8.8	1.5	0.6	4.3	1.3	1798.6	275.0	2.5	0.6	0.1	0.1	17.5	3.3	2.5	0.6	3.7	1.8	0.6	0.1	26.7	5.9
Surface	GP_102-8.1		544.5	102.5	135.6	29.2	2.7	1.0	4.3	1.4	3283.1	502.0	4.9	1.2	0.0	0.0	24.8	4.6	3.7	0.9	6.3	3.1	1.0	0.1	66.2	14.6
Surface	GP_102-11.1		271.9	51.2	22.5	4.8	1.7	0.6	1.4	0.4	642.8	98.3	2.5	0.6	0.1	0.1	6.0	1.1	0.7	0.2	0.6	0.3	0.2	0.0	7.5	1.7
Surface	GP_102-9.1		157.6	29.7	20.1	4.3	1.2	0.5	2.0	0.6	988.9	151.2	1.0	0.2	0.0	0.0	7.0	1.3	1.0	0.2	1.0	0.5	0.3	0.0	11.3	2.5
Surface	GP_102-4.1		157.8	29.7	16.2	3.5	1.1	0.4	1.9	0.6	906.5	138.6	2.1	0.5	0.0	0.0	9.9	1.8	0.9	0.2	2.8	1.4	0.3	0.0	13.6	3.0
Surface	GP_102-20.1		104.5	19.7	21.8	4.7	40.7	15.4	1.0	0.3	1091.4	166.9	1.6	0.4	0.1	0.0	11.2	2.1	0.9	0.2	1.4	0.7	0.3	0.0	11.7	2.6
Interior	GP102_int_17.1		845.1	159.0	137.7	29.7	4.6	1.7	3.2	1.0	5538.6	846.8	11.4	2.8	0.0	0.0	39.9	7.4	26.1	6.2	24.0	11.8	8.4	1.1	141.8	31.3
Interior	GP102_int_7.2		--	--	--	--	--	--	--	--	--	--	--	--	--	--	--	--	--	--	--	--	--	--	--	--
Interior	GP102_int_14.1		208.5	39.2	27.1	5.8	1.1	0.4	2.8	0.9	1104.7	168.9	2.0	0.5	0.0	0.0	10.1	1.9	0.6	0.1	1.7	0.8	0.3	0.0	13.5	3.0
Interior	GP102_int_2.1		415.7	78.2	47.2	10.2	2.4	0.9	4.7	1.5	725.9	111.0	1.8	0.4	0.0	0.0	5.0	0.9	0.3	0.1	0.5	0.2	0.2	0.0	8.4	1.9
Interior	GP102_int_15.1		186.6	35.1	91.8	19.8	3.1	1.2	2.5	0.8	1060.3	162.1	3.6	0.9	0.0	0.0	7.8	1.5	0.5	0.1	2.2	1.1	0.5	0.1	10.9	2.4
Interior	GP102_int_16.1		327.9	61.7	66.3	14.3	5.0	1.9	4.5	1.4	956.9	146.3	4.3	1.0	0.0	0.0	8.4	1.6	0.6	0.2	0.9	0.4	0.3	0.0	11.2	2.5
Interior	GP102_int_18.1		220.1	41.4	34.7	7.5	1.3	0.5	3.2	1.0	1086.1	166.1	1.6	0.4	0.0	0.0	6.4	1.2	1.2	0.3	1.2	0.6	0.5	0.1	18.4	4.0
Interior	GP102_int_12.1		96.6	18.2	22.9	4.9	2.7	1.0	2.1	0.7	547.3	83.7	1.5	0.4	0.0	0.0	4.0	0.7	0.5	0.1	0.5	0.2	0.4	0.0	6.1	1.3
Interior	GP102_int_3.2		158.0	29.7	10.3	2.2	1.5	0.6	0.8	0.3	413.1	63.2	1.8	0.4	0.0	0.0	5.3	1.0	0.3	0.1	0.8	0.4	0.1	0.0	5.1	1.1
Interior	GP102_int_3.1		--	--	--	--	--	--	--	--	--	--	--	--	--	--	--	--	--	--	--	--	--	--	--	--
Interior	GP102_int_8.1		907.1	170.7	60.1	12.9	3.6	1.4	3.8	1.2	1689.5	258.3	2.2	0.5	0.1	0.0	10.8	2.0	1.7	0.4	1.4	0.7	1.1	0.1	21.2	4.7
Interior	GP102_int_10.1		313.2	58.9	25.9	5.6	3.6	1.3	2.2	0.7	1867.2	288.5	5.1	1.2	0.0	0.0	10.7	2.0	3.3	0.8	2.5	1.2	1.3	0.2	27.4	6.0
Interior	GP102_int_5.1		177.4	33.4	53.8	11.6	2.9	1.1	2.7	0.8	616.1	94.2	1.2	0.3	0.0	0.0	4.7	0.9	0.7	0.2	1.1	0.5	0.5	0.1	9.3	2.0
Interior	GP102_int_4.1		566.7	106.7	98.5	21.2	2.7	1.0	3.3	1.0	3026.1	462.7	4.5	1.1	0.0	0.0	22.3	4.2	6.0	1.4	10.8	5.3	2.8	0.4	54.0	11.9
Interior	GP102_int_9.1		--	--	--	--	--	--	--	--	--	--	--	--	--	--	--	--	--	--	--	--	--	--	--	--
Interior	GP102_int_11.1		--	--	--	--	--	--	--	--	--	--	--	--	--	--	--	--	--	--	--	--	--	--	--	--
Interior	GP102_int_13.1		416.4	78.4	91.2	19.6	4.1	1.5	3.1	1.0	2857.6	436.9	5.3	1.3	0.1	0.0	24.4	4.6	8.6	2.0	9.2	4.5	3.3	0.4	64.4	14.2
Interior	GP102_int_21.1		278.2	52.4	139.6	30.1	2.8	1.1	2.2	0.7	1644.7	251.5	5.4	1.3	0.1	0.0	10.6	2.0	2.5	0.6	2.8	1.4	1.2	0.2	25.6	5.7
Interior	GP102_int_20.1		156.4	29.4	37.8	8.1	2.4	0.9	1.7	0.6	533.5	81.6	1.9	0.4	0.0	0.0	4.3	0.8	0.3	0.1	0.8	0.4	0.3	0.0	7.2	1.6
Interior	GP102_int_1.1		614.6	115.7	116.2	25.0	4.0	1.5	2.7	0.9	1978.8	302.6	0.9	0.2	0.0	0.0	11.4	2.1	4.1	1.0	5.8	2.9	1.6	0.2	38.4	8.5
Interior	GP102_int_19.1		370.4	69.7	117.9	25.4	2.9	1.1	4.2	1.3	3927.7	600.5	5.8	1.4	0.0	0.0	14.1	2.6	8.7	2.1	10.7	5.2	3.7	0.5	91.0	20.1
Interior	GP102_int_6.1		364.7	68.6	56.2	12.1	2.4	0.9	4.0	1.3	1499.3	229.2	9.6	2.3	0.0	0.0	17.8	3.3	0.7	0.2	1.7	0.8	0.2	0.0	20.1	4.4
Interior	GP102_int_7.1		1422.9	267.8	299.6	64.5	5.9	2.2	3.0	0.9	7944.0	1214.6	13.7	3.3	0.0	0.0	109.5	20.5	11.6	2.7	12.6	6.2	4.6	0.6	133.0	29.3

Zr concentration is 47760 ppm from Claiborne et al. (2006)

Zircon model crystallization ages and trace element concentrations (ppm)																									
Grain Location	Kakapiko Dome	Ho/Si	1 SD	Tb/Si	1 SD	Dy/Si	1 SD	Er/Si	1 SD	Tm/Si	1 SD	Yb/Si	1 SD	Lu/Si	1 SD	Hf/Si	1 SD	Pb/Si	1 SD	Th/Si	1 SD	1 sigma	1 SD	
Surface	GP_102-15.1	36.9	5.9	6.1	0.6	97.0	10.1	165.4	30.9	41.0	12.4	380.6	70.9	99.4	20.0	7512.6	1511.5	0.0	0.0	120.5	21.5	231.6	43.9	
Surface	GP_102-18.1	47.3	7.5	8.5	0.8	141.0	14.7	199.5	37.3	48.5	14.7	428.4	79.9	103.4	20.8	6062.7	1219.8	0.0	0.0	200.8	35.9	236.8	44.9	
Surface	GP_102-10.1	97.0	15.5	15.9	1.5	197.1	20.5	464.4	86.8	121.8	36.8	1201.4	223.9	318.5	64.0	23361.1	4700.2	0.0	0.0	386.6	69.1	749.0	142.0	
Surface	GP_102-21.1	32.7	5.2	5.5	0.5	83.9	8.7	140.6	26.3	32.6	9.9	304.7	56.8	72.8	14.6	8835.0	1777.6	0.0	0.0	65.7	11.7	140.9	26.7	
Surface	GP_102-2.1	35.5	5.7	6.9	0.7	89.6	9.3	151.3	28.3	34.6	10.5	312.0	58.2	76.7	15.4	5675.5	1141.9	0.0	0.0	147.8	26.4	201.6	38.2	
Surface	GP_102-13.1	90.6	14.4	16.8	1.6	198.6	20.7	390.0	72.9	89.0	26.9	756.2	141.0	180.5	36.2	8443.8	1698.9	0.0	0.0	330.7	59.1	383.7	72.7	
Surface	GP_102-19.1	41.8	6.7	7.9	0.8	125.2	13.0	186.8	34.9	45.2	13.7	389.6	72.6	95.6	19.2	8525.2	1715.3	0.0	0.0	146.7	26.2	197.8	37.5	
Surface	GP_102-12.1	97.4	15.5	14.6	1.4	280.1	29.1	487.9	91.2	119.9	36.3	1082.4	201.8	298.3	59.9	19913.0	4006.5	0.0	0.0	490.4	87.6	799.7	151.6	
Surface	GP_102-17.1	51.9	8.3	9.7	0.9	133.3	13.9	209.5	39.2	48.8	14.7	416.0	77.5	99.8	20.0	6365.0	1280.6	0.0	0.0	173.1	30.9	226.6	43.0	
Surface	GP_102-6.1	265.4	42.3	58.0	5.6	749.0	77.9	1103.5	206.2	247.7	74.9	2108.7	393.1	506.5	101.7	12698.3	2554.9	0.0	0.0	1392.2	248.8	1344.0	254.8	
Surface	GP_102-7.1	42.4	6.8	8.9	0.9	122.4	12.7	192.1	35.9	43.8	13.2	368.4	68.7	87.3	17.5	6096.1	1226.5	0.0	0.0	108.2	19.3	150.8	28.6	
Surface	GP_102-16.1	41.9	6.7	7.5	0.7	128.7	13.4	193.9	36.2	43.1	13.0	378.7	70.6	92.3	18.5	5988.9	1205.0	0.0	0.0	174.0	31.1	195.4	37.0	
Surface	GP_102-1.1	18.1	2.9	2.4	0.2	47.5	4.9	71.6	13.4	17.0	5.1	165.5	30.8	40.2	8.1	4708.2	947.3	0.0	0.0	32.2	5.8	73.9	14.0	
Surface	GP_102-5.1	20.5	3.3	3.0	0.3	52.8	5.5	87.1	16.3	19.9	6.0	186.9	34.8	45.3	9.1	6681.1	1344.2	0.0	0.0	52.3	9.3	103.0	19.5	
Surface	GP_102-3.1	24.6	3.9	4.2	0.4	83.6	8.7	131.0	24.5	30.0	9.1	290.8	54.2	71.4	14.3	8673.4	1745.1	0.0	0.0	85.0	15.2	151.7	28.8	
Surface	GP_102-14.1	56.0	8.9	13.4	1.3	177.6	18.5	301.7	56.4	70.6	21.4	621.5	115.9	152.8	30.7	11850.9	2384.4	0.0	0.0	292.8	52.3	412.8	78.3	
Surface	GP_102-8.1	118.2	18.9	25.6	2.5	383.5	39.9	526.9	98.5	112.8	34.1	963.6	179.6	227.5	45.7	16303.8	3280.3	0.0	0.0	340.6	60.9	500.3	94.9	
Surface	GP_102-11.1	21.1	3.4	3.4	0.3	54.7	5.7	110.8	20.7	28.4	8.6	264.8	49.4	66.5	13.3	7305.5	1469.9	0.0	0.0	61.7	11.0	149.6	28.4	
Surface	GP_102-9.1	21.6	3.4	3.8	0.4	52.9	5.5	93.9	17.5	22.1	6.7	196.8	36.7	50.8	10.2	6396.7	1287.0	0.0	0.0	73.5	13.1	117.0	22.2	
Surface	GP_102-4.1	34.7	5.5	6.4	0.6	109.7	11.4	153.6	28.7	34.5	10.4	306.9	57.2	74.0	14.9	5781.9	1163.3	0.0	0.0	99.2	17.7	131.8	25.0	
Surface	GP_102-20.1	33.1	5.3	5.2	0.5	82.1	8.5	131.3	24.5	31.0	9.4	267.0	49.8	69.8	14.0	6993.7	1407.1	0.0	0.0	98.6	17.6	138.1	26.2	
Interior	GP102_int_17.1	189.0	30.1	52.4	5.1	671.4	69.8	757.8	141.6	158.9	48.0	1291.2	240.7	285.3	57.3	4216.8	848.4	0.0	0.0	392.9	70.2	277.3	52.6	
Interior	GP102_int_7.2	--	--	--	--	--	--	--	--	--	--	--	--	--	--	--	--	--	--	--	--	--	--	
Interior	GP102_int_14.1	32.5	5.2	5.5	0.5	77.5	8.1	150.4	28.1	35.4	10.7	311.4	58.0	76.6	15.4	9284.0	1867.9	0.0	0.0	97.1	17.4	158.4	30.0	
Interior	GP102_int_2.1	24.1	3.8	4.0	0.4	68.0	7.1	118.8	22.2	28.8	8.7	255.1	47.5	69.0	13.9	11366.2	2286.9	0.0	0.0	35.5	6.3	100.2	19.0	
Interior	GP102_int_15.1	31.3	5.0	5.4	0.5	84.5	8.8	150.6	28.1	37.6	11.4	334.4	62.3	83.8	16.8	5127.2	1031.6	0.0	0.0	93.7	16.7	167.0	31.7	
Interior	GP102_int_16.1	30.7	4.9	5.3	0.5	93.6	9.7	149.6	28.0	35.9	10.8	317.7	59.2	82.4	16.5	11143.0	2242.0	0.1	0.0	178.4	31.9	624.3	118.4	
Interior	GP102_int_18.1	33.5	5.3	7.1	0.7	115.6	12.0	149.5	27.9	32.1	9.7	282.5	52.6	65.3	13.1	5694.5	1145.7	0.0	0.0	80.7	14.4	117.2	22.2	
Interior	GP102_int_12.1	18.0	2.9	3.4	0.3	48.5	5.0	75.0	14.0	17.7	5.3	162.1	30.2	38.5	7.7	4877.5	981.4	0.0	0.0	41.8	7.5	57.0	10.8	
Interior	GP102_int_3.2	12.3	2.0	2.1	0.2	33.2	3.5	61.6	11.5	15.4	4.6	140.2	26.1	35.5	7.1	4665.6	938.7	0.0	0.0	30.1	5.4	63.7	12.1	
Interior	GP102_int_3.1	--	--	--	--	--	--	--	--	--	--	--	--	--	--	--	--	--	--	--	--	--	--	
Interior	GP102_int_8.1	53.5	8.5	9.5	0.9	163.4	17.0	273.0	51.0	64.4	19.5	641.7	119.6	163.3	32.8	8158.7	1641.5	0.0	0.0	250.5	44.8	289.6	54.9	
Interior	GP102_int_10.1	57.9	9.2	11.7	1.1	163.6	17.0	246.6	46.1	59.4	18.0	512.9	95.6	122.6	24.6	5322.4	1070.9	0.0	0.0	56.2	10.0	86.6	16.4	
Interior	GP102_int_5.1	19.8	3.2	4.2	0.4	63.3	6.6	91.2	17.1	20.6	6.2	175.2	32.7	41.9	8.4	5027.8	1011.6	0.0	0.0	36.1	6.4	55.1	10.5	
Interior	GP102_int_4.1	101.2	16.1	21.4	2.1	321.0	33.4	462.5	86.4	110.1	33.3	995.5	185.6	248.0	49.8	5053.3	1016.7	0.0	0.0	631.5	112.8	567.3	107.6	
Interior	GP102_int_9.1	--	--	--	--	--	--	--	--	--	--	--	--	--	--	--	--	--	--	--	--	--	--	
Interior	GP102_int_11.1	--	--	--	--	--	--	--	--	--	--	--	--	--	--	--	--	--	--	--	--	--	--	
Interior	GP102_int_13.1	92.1	14.7	19.9	1.9	320.4	33.3	394.9	73.8	82.9	25.1	692.9	129.1	155.6	31.3	5458.5	1098.3	0.0	0.0	271.9	48.6	234.4	44.4	
Interior	GP102_int_21.1	56.9	9.1	11.8	1.1	183.2	19.0	259.8	48.6	58.8	17.8	499.8	93.2	114.2	22.9	6122.9	1231.9	0.0	0.0	155.3	27.7	212.1	40.2	
Interior	GP102_int_20.1	16.7	2.7	2.9	0.3	48.7	5.1	83.4	15.6	18.7	5.6	159.5	29.7	38.9	7.8	5210.0	1048.2	0.0	0.0	37.2	6.6	62.4	11.8	
Interior	GP102_int_1.1	81.2	13.0	17.4	1.7	178.3	18.5	401.0	74.9	84.1	25.4	704.0	131.2	182.7	36.7	5227.7	1051.8	0.0	0.0	189.7	33.9	266.3	50.5	
Interior	GP102_int_19.1	127.5	20.3	27.6	2.7	458.3	47.7	532.8	99.6	112.3	34.0	911.6	169.9	200.4	40.2	6202.9	1248.0	0.0	0.0	290.1	51.8	322.5	61.2	
Interior	GP102_int_6.1	45.2	7.2	7.6	0.7	148.5	15.4	215.7	40.3	47.9	14.5	454.2	84.7	108.1	21.7	10368.6	2086.2	0.0	0.0	138.2	24.7	242.6	46.0	
Interior	GP102_int_7.1	255.9	40.8	52.5	5.1	698.5	72.6	999.3	186.8	212.4	64.2	1765.5	329.1	402.3	80.8	4153.8	835.8	0.0	0.0	2439.6	436.0	1125.3	213.4	

Zr concentration is 47760 ppm from Claiborne et al. (2006)

Zircon model crystallization ages and trace element concentrations (ppm)

Grain location	Rotoiti	Model age (ka)	+1σ (ka)	-1σ (ka)	Slope	slope error	Eu/Eu*	1 SD	Yb/Gd	1 SD	Y/P	1 SD	U/Th	1 SD	Ti-in-zircon Temp (C)	Zr/Hf	Σ(REE + P)/Y
Surface	14OVC07_2_g3_s1r	35	10	10	0.27	0.07	0.26	0.04	44.67	3.78	1.14	0.51	2.69	0.24	659	39	0.6
Surface	RT_SURF_17.1	40	13	11	0.30	0.08	0.41	0.10	37.44	2.63	1.91	0.07	2.05	0.09	677	45	1.0
Surface	14OVC07_2_g2_s1s	40	7	7	0.31	0.05	0.31	0.05	34.42	2.91	1.33	0.60	1.47	0.13	695	39	0.6
Surface	14OVC07_2_g10_s1s	41	12	11	0.32	0.07	0.26	0.04	15.93	1.35	8.31	3.72	1.20	0.11	675	48	3.9
Surface	14OVC07_2_g12_s1s	44	9	8	0.33	0.05	0.23	0.04	35.13	2.97	1.85	0.83	2.18	0.19	679	43	1.0
Surface	14OVC07_2_g7_s1s	44	8	7	0.33	0.05	0.34	0.06	19.61	1.66	2.96	1.33	1.12	0.10	678	45	1.5
Surface	14OVC07_2_g13_s1s	45	8	7	0.34	0.05	0.39	0.07	19.31	1.63	9.31	4.17	1.13	0.10	713	46	4.7
Surface	14OVC07_2_g5_s1s	46	9	8	0.34	0.05	0.29	0.05	39.07	3.30	0.91	0.41	2.48	0.22	645	42	0.5
Surface	RT_SURF_3.1	47	4	4	0.35	0.02	0.21	0.05	42.33	2.97	1.78	0.07	2.44	0.11	662	39	1.0
Surface	14OVC07_2_g2_s2s	48	9	8	0.35	0.05	0.29	0.05	32.24	2.73	2.63	1.18	1.52	0.13	676	43	1.3
Surface	RT_SURF_15.1	48	9	9	0.35	0.05	0.40	0.10	33.85	2.38	1.83	0.07	2.36	0.10	671	41	1.0
Surface	14OVC07_2_g15_s1s	48	9	8	0.36	0.05	0.29	0.05	37.52	3.17	3.67	1.64	2.26	0.20	667	43	1.9
Surface	14OVC07_2_g6_s1s	49	8	7	0.36	0.04	0.27	0.05	33.72	2.85	1.02	0.46	1.85	0.16	649	44	0.5
Surface	RT_SURF_4.1	50	20	17	0.37	0.11	0.37	0.09	38.21	2.68	2.07	0.08	2.07	0.09	680	37	1.1
Surface	RT_SURF_21.1	52	9	9	0.38	0.05	0.34	0.08	17.84	1.25	5.52	0.21	1.17	0.05	696	42	2.8
Surface	14OVC07_2_g8_s1s	53	8	8	0.38	0.05	0.29	0.05	47.20	3.99	1.01	0.45	1.37	0.12	646	45	0.7
Surface	RT_SURF_9.1	53	16	14	0.39	0.08	0.35	0.08	34.85	2.45	2.52	0.10	2.34	0.10	678	43	1.4
Surface	RT_SURF_11.1	57	12	11	0.41	0.06	0.38	0.09	34.93	2.45	1.97	0.08	2.22	0.10	669	43	1.0
Surface	14OVC07_2_g11_s1s	57	13	11	0.41	0.07	0.30	0.05	37.82	3.20	1.76	0.79	2.53	0.22	671	45	0.9
Surface	RT_SURF_16.1	59	7	7	0.42	0.04	0.25	0.06	20.56	1.44	5.34	0.21	1.43	0.06	681	37	2.6
Surface	RT_SURF_7.1	59	17	15	0.42	0.08	0.26	0.06	45.18	3.17	1.85	0.07	2.06	0.09	693	37	1.0
Surface	RT_SURF_5.1	59	11	10	0.42	0.06	0.29	0.07	25.21	1.77	2.22	0.09	1.96	0.09	701	50	1.1
Surface	RT_SURF_10.1	62	9	9	0.44	0.05	0.38	0.09	19.64	1.38	5.13	0.20	1.13	0.05	692	42	2.7
Surface	14OVC07_2_g14_s1s	64	9	8	0.44	0.04	0.29	0.05	24.90	2.11	4.02	1.80	1.28	0.11	689	38	2.1
Surface	14OVC07_2_g4_s1s	66	9	8	0.45	0.04	0.22	0.04	34.02	2.88	1.15	0.51	1.74	0.15	636	41	0.6
Surface	RT_SURF_13.1	66	12	10	0.46	0.05	0.34	0.08	19.68	1.38	5.18	0.20	1.26	0.05	693	43	2.6
Surface	14OVC07_2_g9_s1s	69	22	18	0.47	0.10	0.42	0.07	43.62	3.69	3.17	1.42	2.24	0.20	712	39	1.7
Surface	RT_SURF_1.1	73	13	11	0.49	0.06	0.34	0.08	36.98	2.60	1.81	0.07	2.04	0.09	676	43	1.0
Surface	RT_SURF_8.1	76	22	19	0.50	0.09	0.35	0.08	38.89	2.73	1.61	0.06	2.28	0.10	676	42	0.9
Surface	RT_SURF_12.1	80	15	13	0.52	0.06	0.34	0.08	19.72	1.38	4.98	0.19	1.19	0.05	696	46	2.5
Surface	RT_SURF_19.1	86	15	13	0.55	0.06	0.32	0.08	42.95	3.02	1.69	0.07	2.16	0.09	671	41	0.9
Surface	RT_SURF_2.1	99	29	23	0.60	0.09	0.28	0.07	23.71	1.67	4.84	0.19	1.22	0.05	681	41	2.4
Surface	RT_SURF_18.1	100	22	18	0.60	0.07	0.35	0.08	33.87	2.38	2.02	0.08	2.19	0.10	672	42	1.0
Surface	Rt_SURF_21.2	101	22	18	0.60	0.07	--	--	--	--	--	--	--	--	--	-- --	
Surface	RT_SURF_14.1	202	134	58	0.84	0.11	0.38	0.09	17.86	1.25	5.51	0.21	1.24	0.05	721	40	2.8
Surface	RT_SURF_20.1	260	350	115	0.91	0.17	0.48	0.11	21.31	1.50	5.17	0.20	1.24	0.05	711	45	2.7
Surface	RT_SURF_22.1	--	--	--	--	--	0.33	0.08	30.51	2.14	1.58	0.06	1.84	0.08	674	47	0.9
Surface	RT_SURF_6.1	--	--	--	--	--	0.26	0.06	36.72	2.58	1.78	0.07	2.51	0.11	655	40	0.9
Surface	GP03_16_extra	--	--	--	--	--	0.40	0.09	30.43	2.14	4.29	0.17	1.30	0.06	695	42	2.4
Surface	GP03_20_extra	--	--	--	--	--	0.32	0.08	41.08	2.89	2.27	0.09	2.51	0.11	844	38	1.4
Surface	GP03_23.1	--	--	--	--	--	0.27	0.06	21.65	1.52	5.01	0.19	1.17	0.05	704	40	2.6
Surface	GP03_24.1	--	--	--	--	--	0.34	0.08	19.63	1.38	4.80	0.19	1.23	0.05	705	43	2.5
Surface	GP03_25.1	--	--	--	--	--	0.26	0.06	25.49	1.79	2.12	0.08	1.48	0.06	914	41	1.4
Surface	GP03_26.1	--	--	--	--	--	0.40	0.09	33.80	2.37	2.00	0.08	2.37	0.10	725	40	1.0
Surface	GP03_27.1	--	--	--	--	--	0.38	0.09	38.80	2.73	1.76	0.07	2.05	0.09	679	42	1.0

Zr concentration is 47760 ppm from Claiborne et al. (2006); Samples with "14OVC07" are from Rubin (2016); Samples with "GP" or "RT" are from this study.

Zircon model crystallization ages and trace element concentrations (ppm)

Grain location	Rotoiti	P/Si	1 SD	Sc/Si	1 SD	49Ti/Si	1 SD	Fe/Si	1 SD	Y/Si	1 SD	Nb/Si	1 SD	La/Si	1 SD	Ce/Si	1 SD	Nd/Si	1 SD	Sm/Si	1 SD	Eu/Si	1 SD	Gd/Si	1 SD
Surface	14OVC07_2_g3_s1r	498.13	222.01	50.31	3.10	2.51	0.25	0.75	0.33	569.59	27.06	2.49	0.22	0.02	0.01	5.91	0.47	0.40	0.06	0.78	0.10	0.17	0.02	4.94	0.30
Surface	RT_SURF_17.1	645.80	21.31	107.10	3.00	3.12	0.27	5.69	2.11	1235.38	24.71	3.34	1.15	0.21	0.07	9.05	0.28	1.84	0.23	2.08	0.42	0.70	0.07	12.97	0.80
Surface	14OVC07_2_g2_s1s	2281.11	1016.69	190.01	11.72	3.89	0.39	0.86	0.37	3029.75	143.91	6.86	0.62	0.03	0.01	19.89	1.57	1.87	0.26	3.40	0.43	0.93	0.09	24.71	1.50
Surface	14OVC07_2_g10_s1s	296.17	132.01	93.46	5.77	3.04	0.30	1.98	0.87	2460.33	116.87	4.02	0.36	0.05	0.02	21.47	1.69	3.13	0.44	6.23	0.79	1.28	0.12	35.45	2.16
Surface	14OVC07_2_g12_s1s	619.19	275.97	95.70	5.90	3.22	0.32	0.80	0.35	1145.63	54.42	3.79	0.34	0.04	0.02	8.05	0.63	1.04	0.15	1.95	0.25	0.38	0.04	13.35	0.81
Surface	14OVC07_2_g7_s1s	727.78	324.37	71.14	4.39	3.16	0.32	1.16	0.51	2154.43	102.34	3.44	0.31	0.03	0.01	15.68	1.24	2.95	0.41	5.26	0.67	1.57	0.15	36.80	2.24
Surface	14OVC07_2_g13_s1s	201.61	89.86	71.34	4.40	4.81	0.48	29.99	13.11	1876.51	89.13	6.62	0.60	0.07	0.03	14.43	1.14	3.40	0.48	6.09	0.77	1.75	0.17	31.40	1.91
Surface	14OVC07_2_g5_s1s	913.10	406.97	74.55	4.60	2.08	0.21	0.69	0.30	834.21	39.62	3.82	0.34	0.03	0.01	6.38	0.50	0.40	0.06	1.00	0.13	0.26	0.03	7.86	0.48
Surface	RT_SURF_3.1	621.28	20.50	97.02	2.72	2.60	0.23	7.93	2.94	1108.40	22.17	5.22	1.81	0.10	0.03	8.74	0.27	0.74	0.09	1.89	0.38	0.32	0.03	11.31	0.70
Surface	14OVC07_2_g2_s2s	896.37	399.51	176.46	10.89	3.10	0.31	0.91	0.40	2361.92	112.19	5.45	0.49	0.03	0.01	15.61	1.23	1.07	0.15	2.88	0.36	0.77	0.07	22.39	1.36
Surface	RT_SURF_15.1	484.74	16.00	79.88	2.24	2.92	0.26	9.37	3.48	886.67	17.73	3.00	1.04	0.10	0.04	7.66	0.24	1.18	0.15	1.12	0.22	0.46	0.05	10.95	0.68
Surface	14OVC07_2_g15_s1s	306.66	136.68	92.35	5.70	2.78	0.28	1.18	0.52	1125.41	53.46	3.40	0.31	0.02	0.01	6.95	0.55	0.57	0.08	1.38	0.17	0.38	0.04	11.89	0.72
Surface	14OVC07_2_g6_s1s	1668.65	743.72	129.77	8.01	2.19	0.22	1.11	0.49	1705.50	81.01	3.73	0.34	0.02	0.01	10.04	0.79	0.91	0.13	1.94	0.25	0.51	0.05	17.27	1.05
Surface	RT_SURF_4.1	638.99	21.09	111.01	3.11	3.26	0.29	12.06	4.48	1321.53	26.43	3.68	1.27	0.90	0.31	12.75	0.40	2.24	0.28	2.06	0.41	0.65	0.07	13.91	0.86
Surface	RT_SURF_21.1	397.80	13.13	83.34	2.33	3.93	0.35	8.16	3.03	2195.40	43.91	1.33	0.46	0.20	0.07	22.12	0.69	3.64	0.45	5.28	1.06	1.60	0.17	38.79	2.40
Surface	14OVC07_2_g8_s1s	968.05	431.46	99.22	6.12	2.12	0.21	2.86	1.25	975.53	46.34	2.57	0.23	0.04	0.02	7.88	0.62	0.57	0.08	1.61	0.20	0.47	0.04	14.50	0.88
Surface	RT_SURF_9.1	277.62	9.16	59.47	1.67	3.19	0.28	9.39	3.48	699.83	14.00	3.13	1.08	0.03	0.01	6.85	0.21	0.48	0.06	1.35	0.27	0.41	0.04	9.37	0.58
Surface	RT_SURF_11.1	646.79	21.34	103.56	2.90	2.83	0.25	5.35	1.99	1275.69	25.51	2.99	1.04	0.11	0.04	7.84	0.24	0.94	0.12	1.92	0.39	0.63	0.07	13.24	0.82
Surface	14OVC07_2_g11_s1s	609.29	271.56	97.61	6.02	2.92	0.29	3.70	1.62	1071.79	50.91	3.12	0.28	0.04	0.02	8.39	0.66	0.54	0.08	1.36	0.17	0.40	0.04	12.11	0.74
Surface	RT_SURF_16.1	459.39	15.16	95.85	2.68	3.29	0.29	11.79	4.37	2454.35	49.09	5.86	2.03	0.10	0.03	19.84	0.61	2.32	0.29	5.44	1.09	1.05	0.11	30.45	1.89
Surface	RT_SURF_7.1	654.42	21.60	106.00	2.97	3.79	0.33	11.19	4.15	1209.42	24.19	3.84	1.33	0.08	0.03	8.74	0.27	0.82	0.10	2.78	0.56	0.48	0.05	11.79	0.73
Surface	RT_SURF_5.1	641.30	21.16	141.67	3.97	4.19	0.37	5.36	1.99	1421.95	28.44	5.32	1.84	0.03	0.01	8.28	0.26	0.93	0.12	3.09	0.62	0.68	0.07	16.91	1.05
Surface	RT_SURF_10.1	440.03	14.52	77.33	2.17	3.77	0.33	4.35	1.61	2299.30	45.19	3.70	1.28	0.01	0.00	19.03	0.59	2.94	0.37	6.19	1.24	1.99	0.21	40.33	2.50
Surface	14OVC07_2_g14_s1s	482.87	215.22	95.51	5.89	3.63	0.36	0.94	0.41	1942.23	92.26	3.48	0.31	0.02	0.01	15.43	1.22	2.11	0.30	4.76	0.60	1.08	0.10	27.41	1.67
Surface	14OVC07_2_g4_s1s	2342.08	1043.87	187.15	11.55	1.86	0.19	1.30	0.57	2689.65	127.76	7.48	0.67	0.04	0.02	16.32	1.29	1.29	0.18	3.53	0.45	0.70	0.07	26.88	1.63
Surface	RT_SURF_13.1	391.29	12.91	81.81	2.29	3.78	0.33	9.77	3.62	2027.62	40.55	3.55	1.23	0.13	0.04	18.42	0.57	2.79	0.35	5.66	1.14	1.55	0.16	33.42	2.07
Surface	14OVC07_2_g9_s1s	236.98	105.62	79.14	4.88	4.75	0.47	1.33	0.58	752.39	35.74	2.94	0.26	0.03	0.02	6.75	0.53	0.49	0.07	1.13	0.14	0.38	0.04	6.66	0.41
Surface	RT_SURF_1.1	733.44	24.20	111.20	3.11	3.09	0.27	7.03	2.61	1324.85	26.50	2.34	0.81	0.11	0.04	9.01	0.28	0.95	0.12	1.86	0.37	0.59	0.06	14.51	0.90
Surface	RT_SURF_8.1	707.53	23.35	110.80	3.10	3.11	0.27	3.60	1.34	1140.53	22.81	3.42	1.18	0.10	0.03	8.16	0.25	0.71	0.09	1.47	0.30	0.49	0.05	12.27	0.76
Surface	RT_SURF_12.1	393.52	12.99	72.72	2.04	3.91	0.34	4.85	1.80	1961.61	39.23	2.17	0.75	0.01	0.00	15.40	0.48	2.39	0.30	5.79	1.16	1.51	0.16	30.81	1.91
Surface	RT_SURF_19.1	571.73	18.87	85.54	2.40	2.92	0.26	5.41	2.01	967.57	19.35	5.70	1.97	0.22	0.08	9.98	0.31	1.78	0.22	1.93	0.39	0.47	0.05	10.21	0.63
Surface	RT_SURF_2.1	411.05	13.56	86.13	2.41	3.28	0.29	4.90	1.82	1989.56	39.79	4.08	1.41	0.01	0.00	18.45	0.57	1.58	0.20	4.32	0.87	0.97	0.10	25.80	1.60
Surface	RT_SURF_18.1	501.33	16.54	85.55	2.40	2.94	0.26	7.93	2.94	1012.85	20.26	3.99	1.38	0.28	0.10	9.93	0.31	1.96	0.25	2.15	0.43	0.56	0.06	10.68	0.66
Surface	Rt_SURF_21.2	--	--	--	--	--	--	--	--	--	--	--	--	--	--	--	--	--	--	--	--	--	--	--	--
Surface	RT_SURF_14.1	351.56	11.60	82.43	2.31	5.22	0.46	18.67	6.93	1935.62	38.71	5.86	2.03	1.05	0.36	25.90	0.80	6.94	0.87	6.62	1.33	1.91	0.20	34.78	2.16
Surface	RT_SURF_20.1	294.46	9.72	54.40	1.52	4.69	0.41	9.04	3.36	1523.59	30.47	2.69	0.93	0.12	0.04	13.81	0.43	2.89	0.36	3.95	0.79	1.59	0.17	25.63	1.59
Surface	RT_SURF_22.1	516.40	17.04	74.43	2.08	3.02	0.27	8.98	3.33	817.58	16.35	3.84	1.33	0.12	0.04	8.30	0.26	1.64	0.21	1.74	0.35	0.50	0.05	12.28	0.76
Surface	RT_SURF_6.1	469.68	15.50	74.89	2.10	2.37	0.21	9.60	3.56	837.17	16.74	3.17	1.10	0.12	0.04	7.15	0.22	0.74	0.09	1.31	0.26	0.27	0.03	7.64	0.47
Surface	GP03_16_extra	290.25	9.58	75.06	2.10	3.89	0.34	4.48	1.66	1244.39	24.89	2.55	0.88	0.19	0.07	14.26	0.44	1.90	0.24	2.47	0.50	0.89	0.09	18.91	1.17
Surface	GP03_20_extra	210.13	6.93	42.62	1.19	17.85	1.57	8.61	3.19	477.10	9.54	3.80	1.32	0.27	0.09	8.84	0.27	3.46	0.43	1.56	0.31	0.35	0.04	7.14	0.44
Surface	GP03_23.1	405.00	13.37	88.03	2.46	4.30	0.38	6.83	2.53	2030.05	40.60	4.00	1.38	0.20	0.07	20.05	0.62	2.54	0.32	6.29	1.26	1.21	0.13	30.46	1.89
Surface	GP03_24.1	316.69	10.45	59.23	1.66	4.36	0.38	6.36	2.36	1520.81	30.42	3.25	1.13	0.01	0.00	14.03	0.43	1.35	0.17	3.66	0.74	1.11	0.12	26.57	1.65
Surface	GP03_25.1	536.14	17.69	94.20	2.64	31.99	2.82	13.74	5.10	1136.32	22.73	5.07	1.75	0.49	0.17	27.90	0.86	5.09	0.64	5.03	1.01	1.02	0.11	27.76	1.72
Surface	GP03_26.1	588.00	19.40	96.33	2.70	5.51	0.48	13.43	4.98	1174.13	23.48	4.51	1.56	0.28	0.10	10.29	0.32	2.78	0.35	1.46	0.29	0.56	0.06	12.60	0.78
Surface	GP03_27.1	651.87	21.51	100.08	2.80	3.20	0.28	10.57	3.92	1149.23	22.98	2.50	0.87	0.26	0.09	10.80	0.33	3.07	0.38	1.79	0.36	0.58	0.06	12.23	0.76

Zr concentration is 47760 ppm from Claibc Zr concentration is 47760 ppm from Claiborne et al. (2006); Samples with "14OVC07" are from Rubin (2016); Samples with "GP" or "RT" are from this study.

Zircon model crystallization ages and trace element concentrations (ppm)

Grain location	Rotoiti	Ho/Si	1 SD	Tb/Si	1 SD	Dy/Si	1 SD	Er/Si	1 SD	Tm/Si	1 SD	Yb/Si	1 SD	Lu/Si	1 SD	Hf/Si	1 SD	Pb/Si	1 SD	Th/Si	1 SD	U/Si	1 SD	
Surface	14OVC07_2_g3_s1r	15.80	0.75	2.82	0.18	34.22	1.28	89.36	4.29	21.20	1.17	220.63	12.97	55.86	3.55	12261.17	971.08	0.00	0.00	24.46	1.60	65.85	3.83	
Surface	RT_SURF_17.1	37.95	0.72	6.60	0.36	91.51	5.40	204.16	10.21	48.50	2.47	485.57	16.02	120.63	4.95	10610.22	286.48	0.00	0.00	55.79	1.28	114.51	4.24	
Surface	14OVC07_2_g2_s1s	71.53	3.39	12.60	0.79	154.33	5.76	349.05	16.75	86.17	4.76	850.43	50.01	209.39	13.32	12154.28	962.62	0.00	0.00	170.46	11.16	251.14	14.62	
Surface	14OVC07_2_g10_s1s	73.54	3.49	14.84	0.94	167.12	6.23	312.35	14.99	66.00	3.65	564.71	33.21	145.31	9.24	9990.93	791.28	0.02	0.00	161.56	10.58	193.91	11.29	
Surface	14OVC07_2_g12_s1s	37.94	1.80	5.85	0.37	78.92	2.94	183.46	8.81	44.67	2.47	469.04	27.58	120.48	7.66	11013.10	872.24	0.01	0.00	52.62	3.45	114.70	6.68	
Surface	14OVC07_2_g7_s1s	69.35	3.29	15.96	1.01	177.23	6.61	338.01	16.22	75.33	4.17	721.76	42.44	166.50	10.59	10661.54	844.39	0.00	0.00	174.03	11.40	195.26	11.36	
Surface	14OVC07_2_g13_s1s	65.86	3.12	12.73	0.80	144.02	5.37	269.65	12.94	63.90	3.53	606.19	35.64	142.39	9.06	10438.18	826.70	0.02	0.00	124.55	8.16	140.38	8.17	
Surface	14OVC07_2_g5_s1s	23.50	1.11	3.79	0.24	50.74	1.89	119.34	5.73	30.12	1.67	306.96	18.05	74.03	4.71	11345.54	898.57	0.00	0.00	31.99	2.10	79.41	4.62	
Surface	RT_SURF_3.1	34.29	0.65	6.17	0.34	82.42	4.86	195.36	9.77	49.73	2.54	478.89	15.80	119.32	4.89	12162.59	328.39	0.14	0.02	60.45	1.39	147.68	5.46	
Surface	14OVC07_2_g2_s2s	61.73	2.93	10.39	0.65	133.69	4.99	298.33	14.32	76.07	4.21	721.94	42.45	180.74	11.50	11073.85	877.05	0.00	0.00	133.33	8.73	202.77	11.80	
Surface	RT_SURF_15.1	31.51	0.60	4.95	0.27	69.78	4.12	154.32	7.72	37.88	1.93	370.64	12.23	92.86	3.81	11513.76	310.87	0.11	0.01	37.74	0.87	89.03	3.29	
Surface	14OVC07_2_g15_s1s	34.53	1.64	5.60	0.35	78.82	2.94	170.34	8.18	41.79	2.31	446.15	26.23	107.76	6.85	11098.98	879.04	0.00	0.00	49.30	3.23	111.32	6.48	
Surface	14OVC07_2_g6_s1s	46.28	2.19	7.54	0.48	103.99	3.88	250.65	12.03	56.41	3.12	582.27	34.24	143.87	9.15	10955.34	867.66	0.00	0.00	80.83	5.29	149.46	8.70	
Surface	RT_SURF_4.1	40.66	0.77	7.13	0.39	97.59	5.76	220.40	11.02	53.72	2.74	531.35	17.53	133.11	5.46	12836.68	346.59	0.10	0.01	64.69	1.49	134.00	4.96	
Surface	RT_SURF_21.1	74.16	1.41	16.47	0.91	187.85	11.08	354.10	17.70	77.96	3.98	692.05	22.84	169.88	6.97	11287.20	304.75	0.03	0.00	170.07	3.91	198.74	7.35	
Surface	14OVC07_2_g8_s1s	49.46	2.34	9.72	0.61	116.18	4.33	274.38	13.17	70.84	3.92	684.44	40.25	172.35	10.96	10522.74	833.40	0.01	0.00	187.26	12.27	255.89	14.89	
Surface	RT_SURF_9.1	26.44	0.50	4.27	0.23	59.41	3.50	142.21	7.11	34.29	1.75	326.67	10.78	86.78	3.56	11119.63	300.23	0.14	0.02	37.33	0.86	87.27	3.23	
Surface	RT_SURF_11.1	36.52	0.69	5.99	0.33	75.86	4.48	187.80	9.39	45.94	2.34	462.56	15.26	113.99	4.67	11086.50	299.34	0.00	0.00	44.98	1.03	100.02	3.70	
Surface	14OVC07_2_g11_s1s	36.35	1.72	6.20	0.39	78.60	2.93	176.14	8.45	42.19	2.33	458.09	26.94	105.10	6.68	10717.71	848.84	0.00	0.00	45.03	2.95	113.78	6.62	
Surface	RT_SURF_16.1	65.96	1.25	11.96	0.66	152.99	9.03	305.87	15.29	68.87	3.51	625.94	20.66	151.84	6.23	12741.60	344.02	0.03	0.00	144.93	3.33	207.76	7.69	
Surface	RT_SURF_7.1	34.61	0.66	6.14	0.34	84.27	4.97	207.40	10.37	50.83	2.59	532.79	17.58	135.32	5.55	12980.55	350.47	0.16	0.02	73.28	1.69	151.21	5.59	
Surface	RT_SURF_5.1	43.27	0.82	7.40	0.41	91.87	5.42	201.97	10.10	46.99	2.40	426.39	14.07	113.23	4.64	9511.25	256.80	0.07	0.01	62.58	1.44	122.55	4.53	
Surface	RT_SURF_10.1	74.12	1.41	16.28	0.90	189.78	11.20	367.78	18.39	84.14	4.29	791.89	26.13	190.51	7.81	11306.87	305.29	0.00	0.00	190.06	4.37	214.49	7.94	
Surface	14OVC07_2_g14_s1s	59.66	2.83	12.51	0.79	142.98	5.33	288.15	13.83	70.69	3.91	682.37	40.12	166.00	10.56	12676.47	1003.98	0.00	0.00	173.44	11.36	221.28	12.88	
Surface	14OVC07_2_g4_s1s	81.91	3.88	13.61	0.86	174.40	6.51	412.17	19.78	90.15	4.99	914.34	53.76	220.75	14.04	11526.00	912.86	0.00	0.00	172.47	11.30	300.13	17.47	
Surface	RT_SURF_13.1	66.22	1.26	14.10	0.78	153.56	9.06	316.10	15.81	71.16	3.63	657.68	21.70	157.06	6.44	11111.99	300.02	0.00	0.00	144.28	3.32	182.00	6.73	
Surface	14OVC07_2_g9_s1s	21.27	1.01	3.06	0.19	47.88	1.79	119.54	5.74	28.48	1.57	290.57	17.09	76.81	4.89	12282.43	972.77	0.01	0.00	42.64	2.79	95.72	5.57	
Surface	RT_SURF_1.1	42.71	0.81	7.28	0.40	105.20	6.21	227.77	11.39	54.67	2.79	536.67	17.71	133.57	5.48	11022.11	297.60	0.00	0.00	70.12	1.61	142.85	5.29	
Surface	RT_SURF_8.1	37.07	0.70	6.05	0.33	85.93	5.07	198.85	9.94	48.75	2.49	477.31	15.75	120.62	4.95	11303.17	305.19	0.08	0.01	58.61	1.35	133.37	4.93	
Surface	RT_SURF_12.1	60.74	1.15	12.47	0.69	155.79	9.19	292.30	14.62	66.04	3.37	607.44	20.05	141.56	5.80	10440.56	281.90	0.05	0.01	127.96	2.94	152.50	5.64	
Surface	RT_SURF_19.1	32.28	0.61	5.46	0.30	71.16	4.20	176.32	8.82	43.41	2.21	438.66	14.48	110.93	4.55	11676.81	315.27	0.03	0.00	58.42	1.34	126.35	4.68	
Surface	RT_SURF_2.1	58.56	1.11	12.59	0.69	154.69	9.13	291.63	14.58	65.32	3.33	611.82	20.19	144.14	5.91	11758.10	317.47	0.17	0.02	143.51	3.30	175.25	6.48	
Surface	RT_SURF_18.1	30.33	0.58	4.57	0.25	57.26	3.38	148.32	7.42	36.72	1.87	361.83	11.94	93.43	3.83	11276.99	304.48	0.00	0.00	40.12	0.92	87.96	3.25	
Surface	RT_SURF_21.2	--	--	--	--	--	--	--	--	--	--	--	--	--	--	--	--	--	--	--	--	--	--	
Surface	RT_SURF_14.1	68.14	1.29	13.41	0.74	155.14	9.15	301.65	15.08	65.84	3.36	620.93	20.49	155.15	6.36	11794.28	318.45	0.00	0.00	157.22	3.62	195.25	7.22	
Surface	RT_SURF_20.1	50.72	0.96	10.77	0.59	124.76	7.36	247.46	12.37	57.08	2.91	546.16	18.02	137.27	5.63	10703.45	288.99	0.03	0.00	116.54	2.68	144.16	5.33	
Surface	RT_SURF_22.1	30.41	0.58	5.43	0.30	71.94	4.24	158.68	7.93	39.51	2.02	374.60	12.36	97.91	4.01	10253.20	276.84	0.06	0.01	45.63	1.05	84.01	3.11	
Surface	RT_SURF_6.1	22.28	0.42	3.59	0.20	49.73	2.93	111.66	5.58	29.12	1.49	280.58	9.26	76.47	3.14	11795.65	318.48	0.00	0.00	33.15	0.76	83.15	3.08	
Surface	GP03_16_extra	43.65	0.83	9.26	0.51	121.78	7.19	249.01	12.45	59.62	3.04	575.32	18.99	137.92	5.65	11242.58	303.55	0.03	0.00	115.45	2.66	150.29	5.56	
Surface	GP03_20_extra	18.25	0.35	3.20	0.18	41.14	2.43	102.29	5.11	26.43	1.35	293.47	9.68	75.43	3.09	12563.57	339.22	0.03	0.00	31.44	0.72	78.97	2.92	
Surface	GP03_23.1	62.63	1.19	13.09	0.72	163.32	9.64	311.09	15.55	71.37	3.64	659.50	21.76	154.76	6.35	11867.41	320.42	0.00	0.00	166.80	3.84	195.74	7.24	
Surface	GP03_24.1	50.27	0.96	10.55	0.58	119.66	7.06	247.61	12.38	54.89	2.80	521.63	17.21	125.34	5.14	11095.89	299.59	0.00	0.00	96.36	2.22	118.76	4.39	
Surface	GP03_25.1	65.81	1.25	12.23	0.67	149.81	8.84	316.65	15.83	74.85	3.82	707.60	23.35	179.09	7.34	11763.37	317.61	0.03	0.00	151.72	3.49	224.23	8.30	
Surface	GP03_26.1	32.98	0.63	5.89	0.32	77.18	4.55	177.81	8.89	42.95	2.19	425.77	14.05	105.69	4.33	11901.91	321.35	0.06	0.01	44.13	1.01	104.76	3.88	
Surface	GP03_27.1	38.06	0.72	6.47	0.36	89.58	5.29	206.72	10.34	48.40	2.47	474.38	15.65	123.00	5.04	11360.09	306.72	0.11	0.01	63.17	1.45	129.80	4.80	

Zr concentration is 47760 ppm from Claiborne et al. (2006); Samples with "14OVC07" are from Rubin (2016); Samples with "GP" or "RT" are from this study.

Zircon model crystallization ages and trace element concentrations (ppm)

Grain location	Rotoiti	Model age (ka)	+1σ (ka)	-1σ (ka)	Slope	slope error	Eu/Eu*	1 SD	Yb/Gd	1 SD	Y/P	1 SD	U/Th	1 SD	Ti-in-zircon Temp (C)	Zr/Hf	Σ(REE+P)/Y
Interior	14OVC07_g24_s2c	38	7	7	0.30	0.04	0.43	0.07	15.98	1.35	6.35	2.85	1.24	0.11	728	51	3.2
Interior	_14OVC07_g23_s1r	39	10	9	0.30	0.06	0.37	0.09	35.72	5.42	2.01	0.22	1.98	0.18	661	43	1.0
Interior	_14OVC07_g6_s1r	47	12	11	0.35	0.07	0.34	0.08	21.33	3.24	5.33	0.58	1.13	0.10	716	40	2.8
Interior	14OVC07_g24_s1c	49	7	7	0.36	0.04	0.41	0.07	21.77	1.84	6.05	2.71	1.13	0.10	810	54	2.9
Interior	14OVC07_g12_s2c	52	9	8	0.38	0.05	0.33	0.06	35.74	3.02	4.35	1.95	1.77	0.16	698	41	2.3
Interior	14OVC07_g28_s1c	55	7	7	0.39	0.04	0.35	0.06	33.51	2.83	4.13	1.85	1.55	0.14	714	49	2.2
Interior	14OVC07_g1_s1c	59	8	8	0.42	0.04	0.36	0.06	35.37	2.99	3.19	1.43	1.52	0.13	714	55	1.6
Interior	14OVC07_g29_s1c	63	21	18	0.44	0.10	0.34	0.06	35.07	2.97	2.68	1.20	1.52	0.13	682	47	1.4
Interior	14OVC07_g15_s2c	63	10	9	0.44	0.05	0.36	0.06	30.04	2.54	3.06	1.37	1.35	0.12	735	46	1.6
Interior	14OVC07_g25_s1c	64	7	7	0.44	0.04	0.39	0.07	29.10	2.46	3.08	1.38	1.20	0.11	707	59	1.5
Interior	_14OVC07_g16_s1r	64	12	11	0.44	0.06	0.23	0.05	30.27	4.60	2.06	0.22	1.98	0.18	679	44	1.0
Interior	_14OVC07_g7_s2r	65	23	19	0.45	0.10	0.40	0.10	50.62	7.69	3.01	0.33	1.87	0.17	690	44	1.7
Interior	14OVC07_g30_s2c	65	11	10	0.45	0.05	0.38	0.07	19.00	1.61	9.31	4.17	1.11	0.10	692	46	4.7
Interior	14OVC07_g30_s1c	67	10	9	0.46	0.05	0.49	0.08	24.79	2.10	3.84	1.72	1.15	0.10	725	56	1.9
Interior	14OVC07_g25_s2c	67	13	12	0.46	0.06	0.38	0.07	16.06	1.36	10.43	4.68	0.86	0.08	700	44	5.1
Interior	14OVC07_g19_s1c	69	9	9	0.47	0.04	0.45	0.08	30.72	2.60	3.83	1.72	1.37	0.12	728	53	2.0
Interior	14OVC07_g5_s1c	70	13	12	0.47	0.06	0.49	0.08	46.46	3.93	1.85	0.83	2.14	0.19	681	45	1.0
Interior	_14OVC07_g27_s2r	71	16	14	0.48	0.07	0.39	0.09	27.02	4.10	5.08	0.55	1.40	0.13	700	46	2.6
Interior	14OVC07_g13_s1c	71	16	14	0.48	0.07	0.38	0.07	28.00	2.37	4.16	1.87	0.79	0.07	735	51	2.1
Interior	_14OVC07_g19_s2r	75	16	14	0.50	0.07	0.36	0.08	33.93	5.15	2.18	0.24	1.91	0.17	672	51	1.1
Interior	14OVC07_g12_s1c	78	11	10	0.51	0.05	0.26	0.04	29.68	2.51	5.27	2.36	1.75	0.15	656	38	2.7
Interior	_14OVC07_g14_s1r	78	16	14	0.51	0.07	0.27	0.06	30.95	4.70	4.65	0.51	1.03	0.09	711	45	2.4
Interior	14OVC07_g18_s1c	81	12	11	0.52	0.05	0.44	0.08	28.44	2.41	4.22	1.89	1.26	0.11	785	52	2.2
Interior	_14OVC07_g15_s1r	83	18	15	0.53	0.07	0.31	0.07	22.81	3.46	5.34	0.58	1.26	0.11	665	41	2.8
Interior	_14OVC07_g18_s2r	85	25	20	0.54	0.09	0.30	0.07	24.07	3.66	4.89	0.53	1.16	0.11	710	36	2.5
Interior	_14OVC07_g10_s1r	86	18	15	0.54	0.07	0.44	0.11	46.68	7.09	4.90	0.53	1.71	0.15	740	52	2.5
Interior	14OVC07_g13_s2c	88	22	19	0.55	0.08	0.27	0.05	41.01	3.47	5.71	2.56	2.06	0.18	657	37	3.0
Interior	14OVC07_g23_s2c	93	20	17	0.57	0.07	0.49	0.08	44.72	3.78	4.06	1.82	2.16	0.19	662	40	2.1
Interior	_14OVC07_g20_s1r	95	23	19	0.58	0.08	0.32	0.08	14.94	2.27	5.81	0.63	1.11	0.10	684	45	2.8
Interior	_14OVC07_g29_s1r	97	20	17	0.59	0.07	0.47	0.11	39.24	5.96	3.88	0.42	1.89	0.17	705	49	2.0
Interior	_14OVC07_g11_s1r	101	53	36	0.60	0.15	0.26	0.06	31.51	4.79	3.64	0.40	1.83	0.17	692	40	1.8
Interior	_14OVC07_g23_s2r	104	24	19	0.61	0.08	0.37	0.09	36.48	5.54	2.17	0.24	1.93	0.18	662	44	1.1
Interior	_14OVC07_g19_s1r	109	36	27	0.63	0.10	0.25	0.06	30.07	4.57	4.01	0.44	1.71	0.15	676	45	2.0
Interior	_14OVC07_g24_s1r	113	41	30	0.65	0.11	0.44	0.10	28.94	4.40	2.21	0.24	1.64	0.15	713	48	1.2
Interior	14OVC07_g9_s1r	117	29	23	0.66	0.08	0.38	0.09	49.42	7.51	2.69	0.29	2.02	0.18	687	41	1.4
Interior	_14OVC07_g28_s1r	124	35	26	0.68	0.09	0.28	0.07	40.95	6.22	1.91	0.21	1.83	0.17	676	50	1.0
Interior	14OVC07_g5_s1r	134	38	28	0.71	0.09	0.27	0.06	51.11	7.76	3.13	0.34	2.08	0.19	695	47	1.7
Interior	_14OVC07_g24_s2r	136	48	33	0.71	0.10	0.37	0.09	35.29	5.36	1.98	0.22	1.46	0.13	669	44	1.0
Interior	_14OVC07_g8_s1r	145	46	32	0.74	0.09	0.31	0.07	24.66	3.75	3.64	0.40	1.86	0.17	718	51	1.8
Interior	_14OVC07_g14_s2r	157	42	30	0.76	0.08	0.58	0.14	31.44	4.77	3.89	0.42	1.86	0.17	711	42	2.1
Interior	_14OVC07_g25_s1r	195	79	45	0.83	0.09	--	--	--	--	--	--	--	--	--	-- --	
Interior	_14OVC07_g12_s1r	197	116	55	0.83	0.11	0.35	0.08	24.47	3.72	2.29	0.25	1.77	0.16	688	58	1.1
Interior	_14OVC07_g6_s2r	214	181	65	0.86	0.11	0.38	0.09	27.32	4.15	4.20	0.46	1.61	0.15	673	50	2.1
Interior	_14OVC07_g29_s2r	221	350	139	0.87	0.34	0.30	0.07	37.35	5.67	2.16	0.24	2.11	0.19	646	45	1.2
Interior	_14OVC07_g11_s2r	226	350	111	0.87	0.22	0.33	0.08	21.71	3.30	6.92	0.75	1.13	0.10	694	48	3.5
Interior	14OVC07_g8_s1c	287	350	85	0.93	0.09	0.37	0.06	35.13	2.97	1.87	0.84	2.17	0.19	677	46	1.0
Interior	_14OVC07_g17_s1r	--	--	--	--	--	0.47	0.11	31.12	4.73	5.87	0.64	1.18	0.11	770	48	3.0
Interior	14OVC07_g22_s1r	--	--	--	--	--	0.35	0.08	19.16	2.91	4.64	0.50	1.11	0.10	726	37	2.3
Interior	14OVC07_g16_s2r	--	--	--	--	--	0.33	0.08	44.46	6.75	2.06	0.22	1.99	0.18	620	44	1.1
Interior	14OVC07_g5_s2r	--	--	--	--	--	0.39	0.09	33.33	5.06	3.15	0.34	1.80	0.16	724	36	1.9
Interior	14OVC07_g30_s2r	--	--	--	--	--	0.35	0.08	26.30	3.99	2.46	0.27	1.47	0.13	703	49	1.3
Interior	14OVC07_g2_s1r	--	--	--	--	--	0.42	0.10	22.28	3.38	7.75	0.84	1.20	0.11	729	45	4.0
Interior	14OVC07_18_s1r	--	--	--	--	--	0.29	0.07	19.94	3.03	5.83	0.63	1.08	0.10	680	41	3.0
Interior	14OVC07_g13_s1r	--	--	--	--	--	0.34	0.08	17.88	2.72	5.85	0.64	1.24	0.11	695	49	2.9
Interior	14OVC07_g8_s2r	--	--	--	--	--	0.52	0.12	29.20	4.43	2.20	0.24	1.91	0.17	639	50	1.2
Interior	14OVC07_g7_s1r	--	--	--	--	--	0.32	0.08	46.98	7.14	2.40	0.26	1.96	0.18	684	42	1.3
Interior	14OVC07_g4_s1r	--	--	--	--	--	0.31	0.07	22.67	3.44	5.82	0.63	1.17	0.11	678	44	3.0
Interior	14OVC07_g27_s1r	--	--	--	--	--	0.26	0.06	33.68	5.11	3.48	0.38	2.00	0.18	654	45	1.8
Interior	14OVC07_g30_s1r	--	--	--	--	--	0.34	0.08	21.04	3.20	3.38	0.37	1.31	0.12	699	48	1.7
Interior	14OVC07_g1_s1r	--	--	--	--	--	0.44	0.10	47.73	7.25	2.48	0.27	1.83	0.17	670	46	1.3
Interior	14OVC07_g1_s2r	--	--	--	--	--	0.43	0.10	49.35	7.50	2.52	0.27	2.46	0.22	708	37	1.4
Interior	14OVC07_g19_s2c	--	--	--	--	--	0.45	0.08	30.19	2.55	4.66	2.09	1.19	0.10	730	47	2.5
Interior	14OVC07_g10_s1c	--	--	--	--	--	0.47	0.08	17.55	1.48	4.36	1.95	1.04	0.09	792	61	2.1
Interior	14OVC07_g27_s1c	--	--	--	--	--	0.39	0.07	32.56	2.75	2.72	1.22	1.81	0.16	698	48	1.4
Interior	14OVC07_g5_s2c	--	--	--	--	--	0.32	0.05	31.66	2.68	3.09	1.39	1.56	0.14	703	44	1.6
Interior	14OVC07_g15_s1c	--	--	--	--	--	0.42	0.07	21.09	1.78	6.86	3.07	1.13	0.10	714	42	3.4
Interior	14OVC07_g8_s2c	--	--	--	--	--	0.35	0.06	35.26	2.98	2.32	1.04	1.37	0.12	700	44	1.2

Zr concentration is 47760 ppm from Claiborne et al. (2006); Samples with "14OVC07" are from Rubin (2016); Samples with "GP" or "RT" are from this study.

Zircon model crystallization ages and trace element concentrations (ppm)

Grain location	Rotoiti	P/Si	1 SD	Sc/Si	1 SD	49Ti/Si	1 SD	Fe/Si	1 SD	Y/Si	1 SD	Nb/Si	1 SD	La/Si	1 SD	Ce/Si	1 SD	Nd/Si	1 SD	Sm/Si	1 SD	Eu/Si	1 SD	Gd/Si	1 SD	
Interior	14OVC07_g24_s2c	281.87	125.63	90.34	5.57	5.65	0.56	0.91	0.40	1790.33	85.04	3.33	0.30	0.02	0.01	8.53	0.67	3.38	0.48	5.24	0.66	1.81	0.17	32.01	1.95	
Interior	_14OVC07_g23_s1r	667.18	65.72	105.39	10.19	2.57	0.59	2.76	1.31	1339.75	61.63	4.93	0.92	0.01	0.00	7.64	0.50	0.70	0.17	1.49	0.23	0.54	0.07	13.05	1.57	
Interior	_14OVC07_g6_s1r	349.40	34.42	47.96	4.64	4.96	1.14	5.95	2.83	1863.88	85.74	3.60	0.67	0.03	0.01	12.63	0.83	3.24	0.79	4.96	0.78	1.38	0.18	31.68	3.80	
Interior	14OVC07_g24_s1c	527.01	234.89	221.46	13.66	13.10	1.31	4.59	2.01	3190.71	151.56	8.14	0.73	0.04	0.02	21.08	1.66	2.52	0.35	6.15	0.78	2.10	0.20	39.17	2.38	
Interior	14OVC07_g12_s2c	182.13	81.18	57.07	3.52	4.02	0.40	1.92	0.84	792.08	37.62	3.04	0.27	0.01	0.01	9.45	0.74	0.36	0.05	0.99	0.13	0.32	0.03	9.03	0.55	
Interior	14OVC07_g28_s1c	183.80	81.92	54.34	3.35	4.83	0.48	1.67	0.73	759.09	36.06	2.99	0.27	0.02	0.01	9.56	0.75	0.56	0.08	1.30	0.16	0.39	0.04	9.18	0.56	
Interior	14OVC07_g1_s1c	283.81	126.49	67.65	4.17	4.87	0.49	3.13	1.37	905.94	43.03	5.24	0.47	0.02	0.01	9.76	0.77	0.63	0.09	1.27	0.16	0.40	0.04	8.70	0.53	
Interior	14OVC07_g29_s1c	718.73	320.34	126.55	7.81	3.34	0.33	2.06	0.90	1926.76	91.52	4.15	0.37	0.01	0.00	12.96	1.02	1.07	0.15	2.27	0.29	0.76	0.07	20.12	1.22	
Interior	14OVC07_g15_s2c	411.53	183.42	101.44	6.26	6.10	0.61	3.98	1.74	1258.87	59.80	3.58	0.32	0.04	0.02	9.69	0.76	0.95	0.13	2.06	0.26	0.66	0.06	15.35	0.93	
Interior	14OVC07_g25_s1c	1218.31	543.00	161.82	9.98	4.47	0.45	1.37	0.60	3753.08	178.27	8.43	0.76	0.01	0.01	28.39	2.24	2.53	0.36	5.33	0.68	1.86	0.18	40.50	2.46	
Interior	_14OVC07_g16_s1r	734.92	72.39	119.38	11.54	3.21	0.74	2.05	0.98	1514.08	69.65	2.22	0.42	0.01	0.00	8.52	0.56	0.62	0.15	2.33	0.37	0.47	0.06	16.79	2.01	
Interior	_14OVC07_g7_s2r	285.95	28.17	65.70	6.35	3.68	0.84	1.94	0.92	861.02	39.61	3.35	0.63	0.02	0.01	7.77	0.51	0.40	0.10	1.00	0.16	0.37	0.05	7.93	0.95	
Interior	14OVC07_g30_s2c	225.08	100.32	64.20	3.96	3.76	0.38	1.78	0.78	2095.20	99.52	3.20	0.29	0.02	0.01	15.93	1.26	3.18	0.45	5.79	0.73	1.76	0.17	34.00	2.07	
Interior	14OVC07_g30_s1c	594.76	265.08	100.32	6.19	5.48	0.55	1.40	0.61	2281.47	108.37	5.18	0.47	0.01	0.01	19.07	1.50	3.11	0.44	4.86	0.62	1.91	0.18	29.41	1.79	
Interior	14OVC07_g25_s2c	427.81	190.68	108.45	6.69	4.14	0.41	1.33	0.58	4462.91	211.99	6.68	0.60	0.01	0.01	40.31	3.18	8.11	1.14	12.46	1.58	3.86	0.37	76.30	4.64	
Interior	14OVC07_g19_s1c	420.71	187.51	114.65	7.07	5.65	0.56	1.34	0.59	1612.09	76.57	2.87	0.26	0.01	0.01	10.04	0.79	1.39	0.20	2.64	0.33	1.03	0.10	18.67	1.13	
Interior	14OVC07_g5_s1c	505.39	225.25	74.26	4.58	3.30	0.33	1.83	0.80	936.14	44.47	2.98	0.27	0.01	0.00	6.18	0.49	0.60	0.08	0.98	0.12	0.46	0.04	8.23	0.50	
Interior	_14OVC07_g27_s2r	294.16	28.98	72.43	7.00	4.14	0.95	2.12	1.01	1495.72	68.80	5.52	1.03	0.01	0.00	11.46	0.75	1.51	0.37	2.26	0.36	0.86	0.11	19.35	2.32	
Interior	14OVC07_g13_s1c	417.04	185.88	111.47	6.88	6.09	0.61	1.30	0.57	1735.72	82.45	7.32	0.66	0.00	0.00	22.32	1.76	1.19	0.17	2.98	0.38	1.01	0.10	21.71	1.32	
Interior	_14OVC07_g19_s2r	599.53	59.05	102.19	9.88	2.93	0.67	2.37	1.13	1308.61	60.20	3.13	0.59	0.01	0.00	6.92	0.46	1.09	0.27	1.43	0.22	0.50	0.07	12.88	1.55	
Interior	14OVC07_g12_s1c	211.46	94.25	58.36	3.60	2.40	0.24	1.51	0.66	1114.23	52.93	3.22	0.29	0.01	0.01	11.46	0.90	0.74	0.10	1.83	0.23	0.43	0.04	13.53	0.82	
Interior	14OVC07_g14_s1r	446.64	43.99	115.47	11.17	4.69	1.07	2.43	1.16	2078.18	95.60	11.27	2.11	0.01	0.00	15.83	1.04	3.42	0.84	4.35	0.68	0.88	0.12	23.23	2.79	
Interior	14OVC07_g18_s1c	447.83	199.60	117.15	7.23	10.30	1.03	9.88	4.32	1889.80	89.77	7.51	0.68	0.02	0.01	14.54	1.15	1.44	0.20	3.00	0.38	1.22	0.12	23.40	1.42	
Interior	_14OVC07_g15_s1r	393.72	38.78	71.77	6.94	2.69	0.62	0.62	0.30	2102.35	96.71	3.63	0.68	0.02	0.01	17.60	1.16	2.06	0.50	4.07	0.64	1.18	0.16	33.36	4.00	
Interior	14OVC07_g18_s2r	417.21	41.10	101.89	9.85	4.63	1.06	7.86	3.74	2041.65	93.92	4.13	0.77	0.03	0.01	17.15	1.13	2.02	0.49	4.22	0.66	1.09	0.14	28.46	3.41	
Interior	_14OVC07_g10_s1r	399.24	39.33	146.88	14.20	6.47	1.48	2.60	1.24	1954.59	89.91	7.49	1.40	0.01	0.00	14.14	0.93	1.10	0.27	2.82	0.44	0.93	0.12	14.49	1.74	
Interior	14OVC07_g13_s2c	112.64	50.20	40.40	2.49	2.44	0.24	1.37	0.60	643.37	30.56	2.55	0.23	0.02	0.01	9.01	0.71	0.24	0.03	0.62	0.08	0.17	0.02	6.13	0.37	
Interior	14OVC07_g23_s2c	102.98	45.90	34.55	2.13	2.58	0.26	0.83	0.36	418.51	19.88	1.75	0.16	0.01	0.00	5.31	0.42	0.21	0.03	0.37	0.05	0.19	0.02	3.83	0.23	
Interior	_14OVC07_g20_s1r	335.63	33.06	58.79	5.69	3.43	0.79	2.21	1.05	1950.76	89.73	2.50	0.47	0.01	0.01	14.83	0.98	1.74	0.42	5.35	0.84	1.43	0.19	34.05	4.09	
Interior	_14OVC07_g29_s1r	426.00	41.96	145.60	14.08	4.39	1.00	0.70	0.33	1654.19	76.09	9.35	1.75	0.01	0.00	13.99	0.92	0.57	0.14	1.63	0.26	0.77	0.10	15.45	1.85	
Interior	_14OVC07_g11_s1r	230.39	22.69	50.10	4.84	3.77	0.86	2.11	1.00	837.58	38.53	2.09	0.39	0.00	0.00	6.93	0.46	0.47	0.12	1.72	0.27	0.34	0.05	9.12	1.09	
Interior	_14OVC07_g23_s2r	580.71	57.20	94.33	9.12	2.61	0.60	2.97	1.41	1260.21	57.97	2.60	0.49	0.01	0.00	7.33	0.48	0.92	0.22	1.83	0.29	0.59	0.08	12.76	1.53	
Interior	_14OVC07_g19_s1r	243.28	23.96	68.03	6.58	3.11	0.71	2.83	1.35	975.31	44.86	4.34	0.81	0.01	0.00	9.07	0.60	0.52	0.13	1.23	0.19	0.29	0.04	10.03	1.20	
Interior	_14OVC07_g24_s1r	528.65	52.07	93.91	9.08	4.81	1.10	2.81	1.34	1170.33	53.84	7.53	1.41	0.01	0.00	8.60	0.57	1.25	0.31	2.41	0.38	0.90	0.12	16.35	1.96	
Interior	14OVC07_g9_s1r	296.62	29.22	62.30	6.02	3.52	0.81	0.65	0.31	798.44	36.73	2.88	0.54	0.01	0.00	6.94	0.46	0.59	0.14	0.75	0.12	0.28	0.04	6.64	0.80	
Interior	14OVC07_g28_s1r	534.57	52.66	70.85	6.85	3.11	0.71	2.19	1.04	1019.46	46.90	3.28	0.61	0.01	0.00	5.33	0.35	1.14	0.28	1.50	0.24	0.36	0.05	10.12	1.21	
Interior	_14OVC07_g5_s1r	337.01	33.20	93.69	9.06	3.90	0.89	1.65	0.79	1055.52	48.55	5.27	0.98	0.00	0.00	9.57	0.63	0.45	0.11	1.60	0.25	0.33	0.04	8.67	1.04	
Interior	14OVC07_g24_s2r	675.13	66.50	111.90	10.82	2.84	0.65	2.55	1.22	1338.56	61.57	4.51	0.84	0.01	0.00	7.74	0.51	0.66	0.16	2.08	0.33	0.62	0.08	12.73	1.53	
Interior	_14OVC07_g8_s1r	281.61	27.74	88.74	8.58	5.09	1.17	4.75	2.26	1024.94	47.15	8.76	1.64	0.04	0.02	10.33	0.68	0.93	0.23	1.86	0.29	0.59	0.07	12.47	1.50	
Interior	14OVC07_g14_s2r	224.31	22.09	60.39	5.84	4.69	1.07	3.49	1.66	873.60	40.19	4.50	0.84	0.02	0.01	9.94	0.65	1.86	0.46	1.67	0.26	0.80	0.11	10.76	1.29	
Interior	_14OVC07_g25_s1r	--	--	--	--	--	--	--	--	--	--	--	--	--	--	--	--	--	--	--	--	--	--	--	--	
Interior	_14OVC07_g12_s1r	683.91	67.36	186.61	18.05	3.56	0.82	0.68	0.32	1566.18	72.04	3.46	0.65	0.01	0.00	6.58	0.43	1.24	0.30	2.10	0.33	0.66	0.09	15.69	1.88	
Interior	14OVC07_g6_s2r	263.52	25.96	57.85	5.59	2.99	0.68	5.06	2.41	1108.07	50.97	2.08	0.39	0.02	0.01	8.16	0.54	0.77	0.19	2.24	0.35	0.66	0.09	12.35	1.48	
Interior	14OVC07_g29_s2r	610.85	60.17	113.51	10.98	2.13	0.49	1.34	0.64	1321.40	60.78	5.33	1.00	0.02	0.01	7.50	0.49	0.66	0.16	1.88	0.30	0.52	0.07	14.40	1.73	
Interior	_14OVC07_g11_s2r	337.75	33.27	63.52	6.14	3.84	0.88	1.92	0.91	2337.94	107.55	4.58	0.86	0.01	0.00	13.79	0.91	3.68	0.90	7.55	1.19	1.72	0.23	33.43	4.01	
Interior	14OVC07_g8_s1c	476.93	212.57	74.69	4.61	3.13	0.31	2.57	1.12	890.73	42.31	2.22	0.20	0.01	0.01	6.20	0.49	0.40	0.06	0.94	0.12	0.36	0.03	9.21	0.56	
Interior	_14OVC07_g17_s1r	475.50	46.84	147.44	14.26	8.80	2.02	1.84	0.88	2789.58	128.32	9.49	1.78	0.03	0.01	24.50	1.61	2.80	0.68	4.61	0.72	1.80	0.24	30.06	3.61	
Interior	14OVC07_g22_s1r	554.55	54.62	132.69	12.83	5.55	1.27	1.93	0.92	2573.33	118.37	8.83	1.65	0.04	0.02	24.91	1.64	3.21	0.78	5.58	0.88	1.69	0.22	38.86	4.66	
Interior	14OVC07_g16_s2r	822.61	81.03	119.12	11.52	1.49	0.34	2.51	1.20	1692.17	77.84	3.31	0.62	0.01	0.01	8.94	0.59	1.45	0.35	2.13	0.33	0.60	0.08	14.53	1.74	
Interior	14OVC07_g5_s2r	173.32	17.07	42.96	4.15	5.41	1.24	11.20	5.34	546.26	25.13	3.55	0.66	0.09	0.04	8.89	0.58	5.00	1.22	2.61	0.41	0.61	0.08	8.61	1.03	
Interior	14OVC07_g30_s2r	563.66	55.52	76.94	7.44	4.29	0.98	2.08	0.99	1384.78	63.70	2.17	0.40	0.01	0.00	6.87	0.45	1.43	0.35	2.18	0.34	0.72	0.10	18.66	2.24	
Interior	14OVC07_g2_s1r	296.43	29.20	86.17	8.33	5.76	1.32	1.69	0.81	2296.68	105.65	4.71	0.88	0.02	0.01	13.98	0.92	3.98	0.97	5.97	0.94	1.97	0.26	33.90	4.07	
Interior	14OVC07_g8_s2r	385.46	37.97	65.58	6.34	1.94	0.44	0.29	0.14	849.40	39.07	2.87	0.54	0.00	0.00	4.35	0.29	0.54	0.13	1.01	0.16	0.59	0.08	11.64	1.40	
Interior	14OVC07_g7_s1r	348.41	34.32	60.91	5.89	3.43	0.78	3.18	1.52	835.02	38.41	3.60	0.67	0.01	0.00	6.39	0.42	0.34	0.08	1.49	0.24	0.36	0.05	7.60	0.91	
Interior	14OVC07_g4_s1r	412.18	40.60	76.72	7.42	3.18	0.73	1.34	0.64	2399.45	110.37	4.52	0.84	0.02	0.01	18.59	1.22	3.43	0.84	5.93	0.93	1.52	0.20	37.62	4.51	
Interior	14OVC07_g27_s1r	452.21	44.54	109.93	10.63	2.34	0.54	0.49	0.23	1575.93	72.49	7.92	1.48	0.01	0.00	12.32	0.81	1.22	0.30	2.63	0.41	0.59	0.08	17.82	2.14	
Interior	14OVC07_g30_s1r	500.82	49.33	82.60	7.99	4.06	0.93	1.21	0.57	1691.48	77.81	2.73	0.51	0.01	0.01	9.46	0.62	1.94	0.47	3.18	0.50	1.00	0.13	24.55	2.95	
Interior	14OVC07_g1_s1r	219.53	21.62	49.65	4.80	2.86	0.65	0.74	0.35	544.81	25.06	3.22	0.60	0.01	0.00	4.79	0.32	0.17	0.04	0.77	0.12	0.28	0.04	4.80	0.58	
Interior	14OVC07_g1_s2r	285.67	28.14	62.18	6.01	4.53	1.04	3.80	1.81	720.44	33.14	2.84	0.53	0.01	0.00	7.58	0.50	0.58	0.14	0.57	0.09	0.27	0.04	6.52	0.78	
Interior	14OVC07_g19_s2c	262.37	116.94	88.12	5.44	5.77	0.58	1.07	0.47	1223.70	58.13	4.04	0.36	0.01	0.01	14.37	1.13	1.30	0.18	2.14	0.27	0.83	0.08	15.02	0.91	
Interior	14OVC07_g10_s1c	648.42	289.00	140.10	8.64	10.98	1.10	1.52	0.66	2824.89	134.18	5.37	0.48	0.01	0.01	17.07	1.35	4.57	0.64	6.86	0.87	2.69	0.26	44.05	2.68	
Interior	14OVC07_g27_s1c	284.78	126.92	54.59	3.37	4.05	0.40	3.02	1.32	775.63	36.84	3.01	0.27	0.01	0.01	8.37	0.66	0.48	0.07	0.99	0.13	0.35	0.03	7.64	0.46	
Interior	14OVC07_g5_s2c	378.42	168.66	67.04	4.14	4.28	0.43	2.12	0.93	1170.38	55.59	2.56	0.23	0.02	0.01	8.56	0.67	0.97	0.14	2.16	0.27	0.59	0.06	14.37	0.87	
Interior	14OVC07_g15_s1c	287.18	128.00	72.99	4.50	4.87	0.49	1.28	0.56	1969.87	93.57	2.35	0.21	0.03	0.01	14.65	1.15	2.99	0.42	4.99	0.63	1.67	0.16	29.10	1.77	
Interior	14OVC07_g8_s2c	481.30	214.51	74.65	4.61	4.11	0.41	2.45	1.07	1118.05	53.11	2.42	0.22	0.03	0.01	8.54	0.67	1.13	0.16	1.84	0.23	0.51	0.05	11.17	0.68	

Zr concentration is 47760 ppm from Claiborne et al. (2006); Samples with "14OVC07" are from Rubin (2016); Samples with "GP" or "RT" are from this study.

Zircon model crystallization ages and trace element concentrations (ppm)

Grain location	Rotoiti	Ho/Si	1 SD	Tb/Si	1 SD	Dy/Si	1 SD	Er/Si	1 SD	Tm/Si	1 SD	Yb/Si	1 SD	Lu/Si	1 SD	Hf/Si	1 SD	Pb/Si	1 SD	Th/Si	1 SD	U/Si	1 SD	
Interior	14OVC07_g24_s2c	57.71	2.74	12.94	0.82	143.15	5.34	262.13	12.58	56.76	3.14	511.39	30.07	120.80	7.68	9385.89	743.36	0.00	0.00	70.78	4.64	88.12	5.13	
Interior	_14OVC07_g23_s1r	42.70	3.21	7.37	0.65	89.69	7.44	184.37	13.88	44.93	3.88	466.22	43.40	135.20	10.72	11056.72	532.93	0.08	0.01	69.48	4.05	137.50	9.56	
Interior	_14OVC07_g6_s1r	57.16	4.29	13.12	1.16	145.19	12.05	333.47	25.11	77.06	6.65	675.74	62.91	164.43	13.04	11969.68	576.94	0.00	0.00	129.34	7.54	145.80	10.13	
Interior	14OVC07_g24_s1c	106.47	5.05	18.19	1.15	217.65	8.12	443.40	21.28	95.51	5.28	852.51	50.13	203.31	12.93	8767.95	694.42	0.00	0.00	196.53	12.87	221.99	12.92	
Interior	14OVC07_g12_s2c	24.85	1.18	4.21	0.27	56.65	2.11	135.13	6.49	31.61	1.75	322.61	18.97	79.50	5.06	11699.84	926.63	0.00	0.00	53.05	3.47	94.09	5.48	
Interior	14OVC07_g28_s1c	25.43	1.21	4.46	0.28	58.37	2.18	121.55	5.83	29.37	1.62	307.66	18.09	73.38	4.67	9747.63	772.01	0.00	0.00	62.32	4.08	96.31	5.61	
Interior	14OVC07_g1_s1c	25.87	1.23	4.29	0.27	54.62	2.04	129.19	6.20	34.23	1.89	307.59	18.09	86.79	5.52	8714.31	690.17	0.00	0.00	67.48	4.42	102.82	5.98	
Interior	14OVC07_g29_s1c	57.37	2.72	10.10	0.64	128.73	4.80	284.83	13.67	72.09	3.99	705.52	41.48	167.84	10.67	10124.60	801.87	0.00	0.00	145.73	9.55	221.53	12.89	
Interior	14OVC07_g15_s2c	38.29	1.81	6.98	0.44	86.59	3.23	193.61	9.29	47.26	2.61	461.22	27.12	118.54	7.54	10341.03	819.01	0.00	0.00	97.30	6.37	131.70	7.67	
Interior	14OVC07_g25_s1c	107.40	5.09	19.07	1.20	229.00	8.54	507.67	24.37	119.67	6.62	1178.40	69.29	285.14	18.14	8136.42	644.40	0.00	0.00	297.76	19.50	357.52	20.81	
Interior	14OVC07_g16_s1r	44.21	3.32	7.99	0.71	105.78	8.78	216.36	16.29	52.02	4.49	508.15	47.31	135.11	10.71	10783.34	519.76	0.01	0.00	79.39	4.63	157.00	10.91	
Interior	_14OVC07_g7_s2r	25.67	1.93	5.47	0.48	58.13	4.83	162.33	12.22	38.33	3.31	401.35	37.37	109.66	8.70	10931.48	526.90	0.03	0.00	51.17	2.98	95.67	6.65	
Interior	14OVC07_g30_s2c	64.12	3.04	13.13	0.83	158.77	5.92	306.32	14.70	70.52	3.90	646.25	38.00	158.39	10.07	10364.70	820.88	0.00	0.00	160.77	10.53	178.62	10.40	
Interior	14OVC07_g30_s1c	66.68	3.16	12.79	0.81	152.51	5.69	327.53	15.72	76.40	4.23	729.08	42.87	188.05	11.96	8527.53	675.38	0.00	0.00	164.98	10.81	189.54	11.03	
Interior	14OVC07_g25_s2c	132.59	6.28	28.54	1.80	317.97	11.86	607.35	29.15	137.98	7.63	1225.13	72.04	280.02	17.81	10918.20	864.72	0.00	0.00	401.10	26.27	346.87	20.19	
Interior	14OVC07_g19_s1c	49.29	2.34	8.12	0.51	110.23	4.11	240.99	11.57	59.71	3.30	573.46	33.72	144.56	9.19	9039.92	715.96	0.00	0.00	91.42	5.99	125.69	7.32	
Interior	14OVC07_g5_s1c	27.32	1.29	4.23	0.27	60.44	2.25	157.55	7.56	36.75	2.03	382.57	22.50	100.68	6.40	10688.56	846.53	0.00	0.00	43.75	2.87	93.78	5.46	
Interior	_14OVC07_g27_s2r	44.31	3.33	8.86	0.78	112.04	9.30	227.54	17.13	52.36	4.52	522.77	48.67	127.73	10.13	10308.59	496.87	0.00	0.00	86.66	5.05	120.89	8.40	
Interior	14OVC07_g13_s1c	50.73	2.40	9.88	0.62	120.88	4.51	260.44	12.50	63.15	3.49	608.01	35.75	150.34	9.56	9279.59	734.94	0.00	0.00	305.88	20.04	240.44	13.99	
Interior	_14OVC07_g19_s2r	36.53	2.74	6.30	0.56	81.82	6.79	190.98	14.38	44.03	3.80	436.95	40.68	112.44	8.92	9330.81	449.75	0.02	0.00	59.65	3.48	113.95	7.92	
Interior	14OVC07_g12_s1c	34.55	1.64	6.39	0.40	79.41	2.96	171.63	8.24	40.42	2.24	401.59	23.61	99.37	6.32	12520.97	991.66	0.00	0.00	77.73	5.09	135.65	7.89	
Interior	_14OVC07_g14_s1r	66.41	4.99	12.61	1.12	144.71	12.01	326.91	24.62	79.33	6.85	718.94	66.93	171.64	13.61	10703.07	515.89	0.00	0.00	261.04	15.22	267.87	18.62	
Interior	14OVC07_g18_s1c	60.97	2.89	11.50	0.72	136.38	5.09	302.73	14.53	67.43	3.73	665.57	39.14	168.59	10.72	9170.00	726.26	0.00	0.00	99.66	6.53	125.65	7.31	
Interior	_14OVC07_g15_s1r	66.45	4.99	13.38	1.18	168.49	13.98	339.74	25.58	70.85	6.11	760.87	70.84	172.90	13.71	11649.50	561.51	0.01	0.00	168.03	9.80	211.67	14.71	
Interior	14OVC07_g18_s2r	59.32	4.46	13.15	1.16	156.78	13.01	311.89	23.49	75.99	6.56	684.94	63.77	175.19	13.89	13234.98	637.93	0.06	0.00	158.01	9.21	184.01	12.79	
Interior	_14OVC07_g10_s1r	52.25	3.92	8.87	0.79	105.02	8.72	315.32	23.74	75.89	6.55	676.40	62.97	159.42	12.64	9167.56	441.88	0.03	0.00	90.86	5.30	155.07	10.78	
Interior	14OVC07_g13_s2c	18.24	0.86	2.87	0.18	42.38	1.58	98.23	4.71	24.96	1.38	251.55	14.79	64.65	4.11	13053.23	1033.82	0.00	0.00	52.80	3.46	108.62	6.32	
Interior	14OVC07_g23_s2c	12.21	0.58	2.07	0.13	26.09	0.97	62.81	3.01	14.91	0.82	171.09	10.06	44.27	2.82	11928.91	944.77	0.00	0.00	21.69	1.42	46.89	2.73	
Interior	14OVC07_g20_s1r	59.06	4.44	13.74	1.22	137.92	11.45	245.24	18.47	53.75	4.64	508.67	47.36	135.72	10.76	10531.18	507.60	0.03	0.00	122.53	7.14	136.03	9.45	
Interior	_14OVC07_g29_s1r	48.65	3.65	8.18	0.72	95.77	7.95	250.39	18.85	54.53	4.71	606.41	56.46	155.67	12.34	9717.92	468.40	0.00	0.00	91.23	5.32	172.32	11.98	
Interior	_14OVC07_g11_s1r	23.64	1.78	4.13	0.37	51.58	4.28	121.75	9.17	27.57	2.38	287.34	26.75	67.58	5.36	11942.85	575.65	0.00	0.00	36.04	2.10	66.10	4.59	
Interior	_14OVC07_g23_s2r	38.73	2.91	7.71	0.68	90.31	7.50	192.05	14.46	42.67	3.68	465.50	43.34	134.46	10.66	10926.06	526.64	0.06	0.00	74.62	4.35	144.22	10.02	
Interior	_14OVC07_g19_s1r	26.31	1.98	4.64	0.41	59.04	4.90	125.69	9.46	31.16	2.69	301.55	28.07	80.49	6.38	10621.18	511.94	0.00	0.00	46.57	2.72	79.47	5.52	
Interior	14OVC07_g24_s1r	42.97	3.23	9.04	0.80	103.72	8.61	196.00	14.76	45.22	3.90	473.11	44.05	135.56	10.75	9921.11	478.20	0.09	0.01	88.89	5.18	145.60	10.12	
Interior	14OVC07_g9_s1r	25.00	1.88	4.43	0.39	47.80	3.97	132.02	9.94	31.56	2.72	328.14	30.55	86.92	6.89	11588.26	558.55	0.01	0.00	41.56	2.42	83.84	5.83	
Interior	_14OVC07_g28_s1r	29.79	2.24	4.84	0.43	70.81	5.88	163.33	12.30	41.21	3.56	414.51	38.59	115.91	9.19	9605.49	462.98	0.01	0.00	48.26	2.81	88.27	6.13	
Interior	14OVC07_g5_s1r	32.03	2.41	5.38	0.48	68.04	5.65	174.06	13.11	39.35	3.40	443.41	41.28	113.70	9.02	10230.87	493.13	0.04	0.00	54.90	3.20	114.35	7.95	
Interior	14OVC07_g24_s2r	38.46	2.89	7.59	0.67	91.19	7.57	180.73	13.61	44.59	3.85	449.17	41.82	125.16	9.93	10888.88	524.84	0.04	0.00	80.91	4.72	117.83	8.19	
Interior	14OVC07_g8_s1r	28.87	2.17	4.25	0.38	59.43	4.93	123.12	9.27	29.46	2.54	307.64	28.64	86.41	6.85	9310.03	448.74	0.63	0.05	42.24	2.46	78.77	5.47	
Interior	14OVC07_g14_s2r	33.31	2.50	5.19	0.46	70.28	5.83	142.55	10.73	33.74	2.91	338.16	31.48	106.09	8.41	11395.57	549.27	0.04	0.00	64.50	3.76	119.73	8.32	
Interior	14OVC07_g25_s1r	--	--	--	--	--	--	--	--	--	--	--	--	--	--	--	--	--	--	--	--	--	--	
Interior	_14OVC07_g12_s1r	41.53	3.12	8.21	0.73	95.28	7.91	185.37	13.96	40.52	3.50	383.92	35.74	95.26	7.55	8266.87	398.46	0.00	0.00	58.70	3.42	104.06	7.23	
Interior	14OVC07_g6_s2r	30.96	2.32	5.65	0.50	73.52	6.10	150.45	11.33	36.41	3.14	337.54	31.42	84.15	6.67	9527.29	459.22	0.31	0.02	47.49	2.77	76.42	5.31	
Interior	14OVC07_g29_s2r	41.76	3.14	7.27	0.64	89.97	7.47	226.80	17.08	56.02	4.83	537.78	50.07	137.87	10.93	10660.09	513.82	0.03	0.00	62.86	3.66	132.72	9.22	
Interior	_14OVC07_g11_s2r	67.54	5.07	15.10	1.34	159.80	13.26	346.35	26.08	73.52	6.34	725.92	67.58	178.14	14.13	9988.84	481.46	0.01	0.00	162.62	9.48	183.31	12.74	
Interior	14OVC07_g8_s1c	26.65	1.26	4.15	0.26	53.88	2.01	128.12	6.15	32.48	1.80	323.44	19.02	79.53	5.06	10463.07	828.68	0.00	0.00	35.87	2.35	77.81	4.53	
Interior	_14OVC07_g17_s1r	87.65	6.58	14.63	1.30	159.95	13.28	424.34	31.95	98.84	8.53	935.35	87.08	248.08	19.67	9881.18	476.27	0.02	0.00	201.34	11.74	236.70	16.45	
Interior	14OVC07_g22_s1r	84.20	6.32	17.96	1.59	190.74	15.83	384.25	28.93	76.08	6.57	744.41	69.30	195.69	15.52	13070.74	630.01	0.09	0.01	249.60	14.55	276.15	19.19	
Interior	14OVC07_g16_s2r	50.02	3.76	8.81	0.78	121.41	10.08	263.68	19.86	60.02	5.18	645.98	60.14	158.20	12.55	10864.28	523.66	0.01	0.00	83.50	4.87	165.90	11.53	
Interior	14OVC07_g5_s2r	19.93	1.50	3.92	0.35	50.23	4.17	122.53	9.23	29.50	2.55	286.85	26.71	81.66	6.48	13183.50	635.44	0.24	0.02	47.65	2.78	85.86	5.97	
Interior	14OVC07_g30_s2r	39.29	2.95	7.93	0.70	96.56	8.01	225.41	16.97	46.06	3.98	490.70	45.68	113.98	9.04	9828.01	473.71	0.02	0.00	78.03	4.55	114.76	7.98	
Interior	14OVC07_g2_s1r	72.86	5.47	13.99	1.24	182.98	15.19	357.86	26.93	81.95	7.07	755.27	70.32	177.80	14.10	10506.72	506.42	0.06	0.00	144.66	8.43	174.00	12.09	
Interior	14OVC07_19_s1r	93.61	7.03	21.10	1.87	246.26	20.44	451.11	33.97	96.72	8.35	937.28	87.26	231.66	18.37	11789.79	568.27	0.04	0.00	244.21	14.24	264.06	18.35	
Interior	14OVC07_g13_s1r	38.13	2.86	9.52	0.84	92.96	7.72	169.64	12.77	38.30	3.31	372.95	34.72	88.08	6.98	9739.75	469.46	0.00	0.00	64.76	3.78	80.26	5.58	
Interior	14OVC07_g8_s2r	25.70	1.93	4.67	0.41	58.18	4.83	137.84	10.38	36.02	3.11	339.94	31.65	90.98	7.21	9530.04	459.35	0.00	0.00	36.01	2.10	68.64	4.77	
Interior	14OVC07_g7_s1r	24.58	1.85	4.05	0.36	50.49	4.19	135.97	10.24	35.44	3.06	357.01	33.24	83.97	6.66	11304.31	544.87	0.00	0.00	41.92	2.44	82.35	5.72	
Interior	14OVC07_g4_s1r	76.85	5.77	16.42	1.45	180.42	14.97	384.52	28.95	82.44	7.11	853.08	79.42	207.44	16.45	10885.93	524.70	0.00	0.00	181.25	10.57	212.07	14.74	
Interior	14OVC07_g27_s1r	46.90	3.52	8.02	0.71	91.90	7.63	250.45	18.86	58.91	5.08	600.22	55.88	157.50	12.49	10690.03	515.26	0.00	0.00	84.00	4.90	168.14	11.69	
Interior	14OVC07_g30_s1r	52.12	3.91	10.09	0.89	115.30	9.57	231.83	17.46	56.23	4.85	516.47	48.08	128.16	10.16	9921.69	478.23	0.00	0.00	107.59	6.27	140.66	9.78	
Interior	14OVC07_g1_s1r	16.35	1.23	2.61	0.23	38.06	3.16	89.47	6.74	21.34	1.84	229.32	21.35	61.52	4.88	10338.89	498.33	0.00	0.00	30.65	1.79	56.08	3.90	
Interior	14OVC07_g1_s2r	20.78	1.56	3.31	0.29	47.00	3.90	125.24	9.43	29.68	2.56	321.56	29.94	86.81	6.88	13052.25	629.12	0.00	0.00	32.06	1.87	78.90	5.48	
Interior	14OVC07_g19_s2c	40.14	1.90	7.10	0.45	88.98	3.32	208.78	10.02	49.08	2.71	453.42	26.66	118.05	7.51	10091.49	799.25	0.00	0.00	135.49	8.87	161.84	9.42	
Interior	14OVC07_g10_s1c	90.00	4.27	17.16	1.08	205.32	7.66	389.20	18.68	81.96	4.53	772.94	45.45	185.78	11.82	7881.03	624.18	0.00	0.00	119.55	7.83	124.71	7.26	
Interior	14OVC07_g27_s1c	22.55	1.07	3.15	0.20	44.88	1.67	110.30	5.29	26.25	1.45	248.77	14.63	62.68	3.99	9935.15	786.86	0.00	0.00	37.52	2.46	67.81	3.95	
Interior	14OVC07_g5_s2c	37.02	1.75	6.43	0.41	79.44	2.96	185.22	8.89	43.63	2.41	454.99	26.75	111.61	7.10	10760.62	852.24	0.00	0.00	71.35	4.67	111.53	6.49	
Interior	14OVC07_g15_s1c	59.60	2.83	12.04	0.76	143.37	5.35	285.83	13.72	65.54	3.62	613.92	36.10	142.40	9.06	11364.34	900.06	0.00	0.00	131.70	8.63	148.18	8.62	
Interior	14OVC07_g8_s2c	30.87	1.46	5.49	0.35	66.80	2.49	158.38	7.60	37.62	2.08	393.71	23.15	91.10	5.79	10824.95	857.34	0.07	0.00	69.62	4.56	95.16	5.54	

Zr concentration is 47760 ppm from Claiborne et al. (2006); Samples with "14OVC07" are from Rubin (2016); Samples with "GP" or "RT" are from this study.

Zircon model crystallization ages and trace element concentrations (ppm)

Grain location	Earthquake Flat	Model age (ka)	+1σ (ka)	-1σ (ka)	Slope	slope error	Eu/Eu*	1 SD	Yb/Gd	1 SD	Y/P	1 SD	U/Th	1 SD	Ti-in-zircon Temp (C)	Zr/Hf	Σ(REE + P)/Y
Surface	EQF-2.1	45	10	9	0.34	0.06	0.216	0.06	30	6	3.7	0.4	2.2	0.5	664	41.5	1.8
Surface	EQF-6.1	50	20	17	0.37	0.10	0.177	0.05	38	7	4.7	0.5	2.6	0.6	661	39.4	2.4
Surface	EQF-12.1	50	11	10	0.37	0.06	0.133	0.04	34	7	3.5	0.3	2.3	0.5	655	37.8	1.8
Surface	EQF-9.1	51	15	13	0.37	0.08	0.277	0.08	35	7	2.8	0.3	1.9	0.4	670	93.0	1.3
Surface	EQF-7.1	51	7	6	0.37	0.04	0.142	0.04	37	7	4.6	0.4	2.2	0.5	656	36.9	2.3
Surface	EQF-3.1	53	11	10	0.39	0.06	0.187	0.05	43	8	3.6	0.3	1.8	0.4	697	42.4	1.8
Surface	EQF-26.1	54	7	6	0.39	0.04	0.167	0.05	37	7	3.2	0.3	2.3	0.5	658	40.4	1.7
Surface	EQF-4.1	57	11	10	0.41	0.06	0.180	0.05	20	4	8.8	0.9	1.3	0.3	731	40.0	4.3
Surface	EQF-17.1	58	17	15	0.41	0.09	0.218	0.06	21	4	9.9	1.0	1.1	0.2	713	36.4	5.1
Surface	EQF-1.1	58	13	11	0.41	0.06	0.187	0.05	34	7	3.7	0.4	2.8	0.6	667	39.3	1.9
Surface	EQF-20.1	58	19	16	0.42	0.09	0.169	0.05	21	4	9.2	0.9	1.2	0.3	658	79.1	4.3
Surface	EQF-31.1	60	11	10	0.42	0.05	0.150	0.04	38	7	2.5	0.2	2.6	0.6	656	48.2	1.3
Surface	EQF-27.1	60	12	11	0.42	0.06	0.170	0.05	27	5	8.6	0.8	1.5	0.3	685	39.8	4.3
Surface	EQF-21.1	61	21	18	0.43	0.10	0.153	0.04	22	4	11.0	1.1	1.4	0.3	661	40.1	5.7
Surface	EQF-30.1	66	11	10	0.45	0.05	0.133	0.04	17	3	12.0	1.2	1.1	0.2	640	63.7	5.7
Surface	EQF-22.1	71	28	22	0.48	0.12	0.114	0.03	30	6	5.7	0.6	1.4	0.3	656	70.4	2.8
Surface	EQF-10.1	71	15	14	0.48	0.07	0.129	0.04	35	7	3.7	0.4	1.9	0.4	680	39.9	2.0
Surface	EQF-25.1	71	9	9	0.48	0.04	0.154	0.05	19	4	11.8	1.1	1.3	0.3	688	35.5	5.9
Surface	EQF-5.1	74	9	8	0.49	0.04	0.157	0.05	37	7	3.2	0.3	2.3	0.5	678	41.2	1.6
Surface	EQF-13.1	74	23	19	0.49	0.09	0.223	0.07	34	7	5.8	0.6	1.3	0.3	680	42.9	3.6
Surface	EQF-16.1	75	18	15	0.50	0.08	0.195	0.06	21	4	12.1	1.2	1.3	0.3	671	36.1	6.1
Surface	EQF-19.1	79	21	17	0.52	0.08	0.168	0.05	41	8	3.5	0.3	2.5	0.6	668	44.6	1.8
Surface	EQF-32.1	80	25	21	0.52	0.10	0.168	0.05	22	4	10.2	1.0	1.3	0.3	674	32.2	5.1
Surface	EQF-15.1	80	21	17	0.52	0.08	0.167	0.05	34	7	5.1	0.5	1.4	0.3	687	36.5	2.6
Surface	EQF-8.1	84	25	20	0.54	0.09	0.163	0.05	30	6	5.0	0.5	1.7	0.4	666	41.9	2.4
Surface	EQF-14.1	84	24	20	0.54	0.09	0.155	0.05	36	7	6.7	0.7	2.3	0.5	685	33.0	3.4
Surface	EQF-24.1	89	15	13	0.56	0.06	0.231	0.07	21	4	8.1	0.8	1.1	0.2	653	39.2	4.3
Surface	EQF-18.1	90	27	22	0.56	0.10	0.131	0.04	36	7	4.4	0.4	2.3	0.5	660	36.3	2.3
Surface	EQF-11.1	96	13	12	0.58	0.05	0.192	0.06	37	7	4.1	0.4	2.1	0.5	666	43.1	2.1
Surface	EQF-29.1	101	13	11	0.60	0.04	0.141	0.04	20	4	13.0	1.3	1.3	0.3	678	35.2	6.4
Surface	EQF-28.1	101	17	14	0.60	0.06	0.150	0.04	36	7	3.7	0.4	2.0	0.4	654	37.5	2.0
Surface	EQF-23.1	206	42	30	0.85	0.05	0.176	0.05	21	4	11.4	1.1	1.2	0.3	691	39.2	5.8
Surface	EQF_surf2_22.1	--	--	--	--	--	0.298	0.05	25	4	3.2	0.3	0.9	0.2	688	45.5	2.1
Surface	EQF_surf2_18.1	--	--	--	--	--	0.149	0.02	27	4	3.1	0.3	1.2	0.2	686	44.4	1.8
Surface	EQF_surf2_21.1	--	--	--	--	--	0.226	0.04	20	3	8.3	0.8	1.1	0.2	684	41.4	3.9
Surface	EQF_surf_5.1	--	--	--	--	--	0.198	0.03	20	3	9.5	0.9	1.2	0.2	683	41.2	5.1
Surface	EQF_surf_6.1	--	--	--	--	--	0.158	0.02	43	6	1.9	0.2	2.2	0.4	661	40.9	1.1
Surface	EQF_surf2_8.2	--	--	--	--	--	0.169	0.03	24	3	6.5	0.6	1.3	0.2	661	40.6	3.2
Surface	EQF_surf2_19.1	--	--	--	--	--	0.146	0.02	40	6	2.0	0.2	2.8	0.5	658	39.6	1.1
Surface	EQF_surf_2.1	--	--	--	--	--	0.138	0.02	32	5	2.1	0.2	2.0	0.3	655	39.5	1.1
Surface	EQF_surf2_9.1	--	--	--	--	--	0.178	0.03	20	3	6.8	0.6	1.3	0.2	658	39.0	3.4
Surface	EQF_surf2_11.1	--	--	--	--	--	0.174	0.03	25	4	5.7	0.5	1.5	0.3	661	38.9	3.0
Surface	EQF_surf_3.1	--	--	--	--	--	0.127	0.02	37	5	1.8	0.2	2.4	0.4	661	38.7	1.0
Surface	EQF_surf2_12.1	--	--	--	--	--	0.138	0.02	20	3	6.2	0.6	1.3	0.2	668	38.4	3.1
Surface	EQF_surf2_17.1	--	--	--	--	--	0.141	0.02	25	4	6.0	0.5	1.3	0.2	663	38.3	3.1
Surface	EQF_surf2_15.1	--	--	--	--	--	0.110	0.02	33	5	2.1	0.2	1.7	0.3	649	38.2	1.0
Surface	EQF_surf2_10.1	--	--	--	--	--	0.159	0.02	41	6	2.2	0.2	2.7	0.5	660	35.8	1.2

Zr concentration is 47760 ppm from Claiborne et al. (2006)

Zircon model crystallization ages and trace element concentrations (ppm)

Grain location	Earthquake Flat	P/Si	1 SD	Sc/Si	1 SD	49Ti/Si	1 SD	Fe/Si	1 SD	Y/Si	1 SD	Nb/Si	1 SD	La/Si	1 SD	Ce/Si	1 SD	Nd/Si	1 SD	Sm/Si	1 SD	Eu/Si	1 SD	Gd/Si	1 SD	
Surface	EQF-2.1	342.3	27.6	54.5	3.0	1.8	0.3	1.2	0.1	1253.9	69.3	4.9	1.0	0.0	0.0	11.2	1.0	1.1	0.3	1.3	0.3	0.3	0.0	13.1	1.9
Surface	EQF-6.1	153.5	12.4	35.1	1.9	1.7	0.2	1.5	0.2	726.7	40.2	2.1	0.4	0.1	0.0	8.2	0.7	1.5	0.4	1.2	0.2	0.2	0.0	6.3	0.9
Surface	EQF-12.1	346.3	27.9	55.2	3.0	1.6	0.2	1.0	0.1	1217.0	67.3	4.0	0.8	0.1	0.0	10.9	0.9	1.7	0.4	1.3	0.3	0.2	0.0	12.2	1.8
Surface	EQF-9.1	345.7	27.8	36.4	2.0	1.9	0.3	2.4	0.3	970.7	53.7	3.1	0.6	0.0	0.0	7.1	0.6	1.2	0.3	1.1	0.2	0.2	0.0	6.2	0.9
Surface	EQF-7.1	297.8	24.0	58.6	3.2	1.6	0.2	1.0	0.1	1368.5	75.7	5.7	1.1	0.1	0.0	13.2	1.1	1.8	0.5	1.6	0.3	0.2	0.0	12.9	1.9
Surface	EQF-3.1	512.4	41.3	80.7	4.4	2.7	0.4	0.8	0.1	1820.8	100.7	4.6	0.9	0.1	0.0	12.4	1.1	1.5	0.4	2.2	0.4	0.4	0.1	15.5	2.3
Surface	EQF-26.1	367.8	29.6	57.0	3.1	1.7	0.2	1.2	0.1	1183.1	65.4	0.1	0.0	0.0	0.0	9.2	0.8	0.5	0.1	1.2	0.2	0.2	0.0	13.0	1.9
Surface	EQF-4.1	269.9	21.7	55.2	3.0	3.9	0.6	16.3	1.9	2370.8	131.1	5.3	1.1	0.1	0.0	21.9	1.9	3.4	0.9	5.5	1.1	0.8	0.1	34.0	5.0
Surface	EQF-17.1	182.2	14.7	60.9	3.3	3.2	0.5	1.9	0.2	1801.1	99.6	3.1	0.6	0.0	0.0	20.5	1.8	1.3	0.3	4.1	0.8	0.8	0.1	28.0	4.1
Surface	EQF-1.1	294.1	23.7	51.5	2.8	1.9	0.3	0.9	0.1	1080.7	59.8	5.7	1.1	0.0	0.0	9.4	0.8	1.0	0.2	0.9	0.2	0.2	0.0	10.8	1.6
Surface	EQF-20.1	140.1	11.3	35.4	1.9	1.6	0.2	0.7	0.1	1287.6	71.2	2.6	0.5	0.0	0.0	10.5	0.9	0.7	0.2	1.5	0.3	0.3	0.0	14.2	2.1
Surface	EQF-31.1	324.8	26.1	41.3	2.2	1.6	0.2	0.5	0.1	823.8	45.6	3.2	0.6	0.0	0.0	5.9	0.5	0.4	0.1	1.0	0.2	0.1	0.0	6.7	1.0
Surface	EQF-27.1	185.5	14.9	44.0	2.4	2.3	0.3	0.9	0.1	1591.5	88.0	6.5	1.3	0.0	0.0	16.3	1.4	1.3	0.3	2.6	0.5	0.4	0.1	19.2	2.8
Surface	EQF-21.1	187.8	15.1	44.8	2.4	1.7	0.2	0.6	0.1	2068.7	114.4	3.6	0.7	0.0	0.0	19.3	1.7	2.0	0.5	4.8	1.0	0.6	0.1	31.5	4.6
Surface	EQF-30.1	341.2	27.5	81.4	4.4	1.3	0.2	0.6	0.1	4077.8	225.5	5.6	1.1	0.0	0.0	36.4	3.2	6.0	1.5	10.6	2.1	1.1	0.2	59.5	8.8
Surface	EQF-22.1	272.4	21.9	38.3	2.1	1.6	0.2	1.3	0.2	1547.1	85.6	11.9	2.4	0.0	0.0	21.4	1.8	0.7	0.2	2.1	0.4	0.2	0.0	15.4	2.3
Surface	EQF-10.1	318.9	25.7	48.9	2.7	2.2	0.3	1.2	0.1	1174.7	65.0	3.7	0.7	0.1	0.0	10.3	0.9	1.7	0.4	1.7	0.4	0.2	0.0	13.2	1.9
Surface	EQF-25.1	208.3	16.8	50.8	2.8	2.4	0.3	1.0	0.1	2448.4	135.4	3.1	0.6	0.0	0.0	22.9	2.0	2.2	0.5	5.3	1.1	0.7	0.1	38.6	5.7
Surface	EQF-5.1	373.9	30.1	56.0	3.0	2.1	0.3	3.3	0.4	1212.3	67.0	4.2	0.8	0.1	0.0	9.6	0.8	1.7	0.4	1.2	0.3	0.2	0.0	11.1	1.6
Surface	EQF-13.1	288.5	23.2	50.3	2.7	2.2	0.3	1.0	0.1	1686.5	93.3	5.4	1.1	0.0	0.0	17.3	1.5	1.5	0.4	3.0	0.6	0.7	0.1	27.7	4.1
Surface	EQF-16.1	171.4	13.8	43.0	2.3	1.9	0.3	0.8	0.1	2075.8	114.8	4.0	0.8	0.0	0.0	18.0	1.6	1.5	0.4	3.2	0.6	0.6	0.1	29.2	4.3
Surface	EQF-19.1	319.8	25.7	53.1	2.9	1.9	0.3	2.9	0.3	1124.6	62.2	5.1	1.0	0.0	0.0	8.6	0.7	0.5	0.1	1.2	0.3	0.2	0.0	9.8	1.4
Surface	EQF-32.1	234.9	18.9	54.3	3.0	2.0	0.3	1.1	0.1	2399.0	132.7	4.4	0.9	0.0	0.0	24.4	2.1	1.7	0.4	4.1	0.8	0.6	0.1	32.3	4.8
Surface	EQF-15.1	502.1	40.4	88.4	4.8	2.4	0.3	1.1	0.1	2558.3	141.5	11.3	2.3	0.0	0.0	32.7	2.8	1.3	0.3	2.7	0.5	0.5	0.1	26.3	3.9
Surface	EQF-8.1	259.4	20.9	51.8	2.8	1.8	0.3	2.0	0.2	1292.0	71.5	6.5	1.3	0.1	0.0	13.4	1.2	1.5	0.4	2.2	0.4	0.3	0.0	12.0	1.8
Surface	EQF-14.1	107.0	8.6	28.8	1.6	2.3	0.3	0.6	0.1	713.4	39.5	2.3	0.5	0.0	0.0	9.2	0.8	0.2	0.1	1.0	0.2	0.1	0.0	7.0	1.0
Surface	EQF-24.1	270.5	21.8	71.8	3.9	1.6	0.2	0.5	0.1	2200.0	121.7	3.8	0.8	0.0	0.0	24.1	2.1	2.6	0.6	5.5	1.1	1.1	0.2	38.5	5.7
Surface	EQF-18.1	251.2	20.2	44.1	2.4	1.7	0.2	3.9	0.5	1101.4	60.9	2.2	0.4	0.0	0.0	9.0	0.8	0.6	0.1	1.6	0.3	0.2	0.0	11.9	1.8
Surface	EQF-11.1	263.9	21.2	46.7	2.5	1.8	0.3	1.3	0.1	1081.1	59.8	4.0	0.8	0.0	0.0	9.5	0.8	0.8	0.2	1.0	0.2	0.2	0.0	11.0	1.6
Surface	EQF-29.1	223.9	18.0	53.6	2.9	2.1	0.3	2.8	0.3	2917.4	161.3	6.4	1.3	0.0	0.0	26.4	2.3	3.0	0.7	7.1	1.4	0.8	0.1	41.2	6.1
Surface	EQF-28.1	298.0	24.0	47.6	2.6	1.6	0.2	0.6	0.1	1098.4	60.7	5.4	1.1	0.0	0.0	8.9	0.8	0.5	0.1	1.4	0.3	0.2	0.0	13.1	1.9
Surface	EQF-23.1	199.4	16.0	43.7	2.4	2.5	0.4	0.8	0.1	2268.3	125.4	4.0	0.8	0.0	0.0	19.1	1.7	2.5	0.6	4.9	1.0	0.7	0.1	34.2	5.0
Surface	EQF_surf2_22.1	705.5	60.0	67.9	3.8	2.8	0.2	3.8	0.6	2232.5	73.7	6.3	0.5	0.0	0.0	24.5	1.4	5.1	0.4	8.5	1.0	2.1	0.2	53.3	4.4
Surface	EQF_surf2_18.1	473.4	40.2	65.0	3.6	2.7	0.1	7.5	1.3	1464.8	48.3	7.9	0.6	0.2	0.1	30.1	1.7	2.8	0.2	4.4	0.5	0.5	0.1	26.5	2.2
Surface	EQF_surf2_21.1	524.2	44.6	76.7	4.3	2.6	0.1	4.9	0.8	4371.6	144.3	9.1	0.7	0.0	0.0	35.0	2.0	5.9	0.5	9.0	1.1	1.5	0.2	48.0	3.9
Surface	EQF_surf_5.1	253.8	21.6	39.5	2.2	2.6	0.1	7.8	1.3	2421.8	79.9	5.8	0.4	0.1	0.0	30.3	1.7	4.0	0.3	6.3	0.8	1.1	0.1	42.9	3.5
Surface	EQF_surf_6.1	477.4	40.6	45.3	2.5	2.0	0.1	6.1	1.0	914.2	30.2	3.2	0.2	0.3	0.1	9.2	0.5	2.6	0.2	1.5	0.2	0.2	0.0	9.6	0.8
Surface	EQF_surf2_8.2	313.2	26.6	46.9	2.6	2.0	0.1	13.2	2.2	2045.7	67.5	4.2	0.3	0.1	0.0	21.5	1.2	2.1	0.2	2.9	0.4	0.5	0.0	25.2	2.1
Surface	EQF_surf2_19.1	339.2	28.8	32.8	1.8	1.9	0.1	7.5	1.3	690.9	22.8	4.2	0.3	0.1	0.0	7.7	0.4	1.6	0.1	1.4	0.2	0.2	0.0	7.8	0.6
Surface	EQF_surf_2.1	638.9	54.3	55.5	3.1	1.8	0.1	8.5	1.4	1345.0	44.4	5.1	0.4	0.1	0.0	13.1	0.7	1.7	0.1	2.4	0.3	0.3	0.0	17.0	1.4
Surface	EQF_surf2_9.1	353.1	30.0	50.2	2.8	1.9	0.1	11.4	1.9	2411.5	79.6	4.9	0.4	0.5	0.1	27.7	1.6	4.7	0.4	3.9	0.5	0.7	0.1	33.4	2.7
Surface	EQF_surf2_11.1	269.5	22.9	39.9	2.2	2.0	0.1	10.0	1.7	1532.3	50.6	3.6	0.3	0.0	0.0	17.7	1.0	1.7	0.1	2.4	0.3	0.4	0.0	21.6	1.8
Surface	EQF_surf_3.1	516.5	43.9	48.6	2.7	2.0	0.1	5.5	0.9	930.6	30.7	4.0	0.3	0.1	0.0	7.8	0.4	1.1	0.1	1.7	0.2	0.2	0.0	10.1	0.8
Surface	EQF_surf2_12.1	407.6	34.6	58.2	3.3	2.2	0.1	10.4	1.8	2542.3	83.9	5.7	0.4	0.1	0.0	27.8	1.6	3.5	0.3	5.6	0.7	0.6	0.1	35.6	2.9
Surface	EQF_surf2_17.1	305.6	26.0	42.6	2.4	2.1	0.1	10.0	1.7	1833.9	60.5	3.6	0.3	0.0	0.0	16.5	0.9	1.9	0.1	4.8	0.6	0.5	0.1	23.5	1.9
Surface	EQF_surf2_15.1	1082.1	92.0	89.7	5.0	1.7	0.1	8.4	1.4	2228.2	73.5	10.8	0.8	0.0	0.0	20.8	1.2	1.0	0.1	3.2	0.4	0.3	0.0	18.6	1.5
Surface	EQF_surf2_10.1	241.8	20.6	31.3	1.8	2.0	0.1	12.2	2.1	538.6	17.8	3.7	0.3	0.4	0.1	9.5	0.5	3.2	0.2	1.3	0.2	0.1	0.0	5.7	0.5

Zr concentration is 47760 ppm from Claiborne et al. (2006)

Zircon model crystallization ages and trace element concentrations (ppm)

Grain location	Earthquake Flat	Ho/Si	1 SD	Tb/Si	1 SD	Dy/Si	1 SD	Er/Si	1 SD	Tm/Si	1 SD	Yb/Si	1 SD	Lu/Si	1 SD	Hf/Si	1 SD	Pb/Si	1 SD	Th/Si	1 SD	U/Si	1 SD	
Surface	EQF-2.1	36.8	4.8	5.9	0.8	74.3	10.3	174.9	23.7	41.4	6.1	398.7	51.0	104.0	13.6	11504.1	1688.8	0.0	0.0	119.9	18.6	259.9	39.7	
Surface	EQF-6.1	19.6	2.6	3.0	0.4	41.2	5.7	100.2	13.6	22.7	3.3	236.9	30.3	61.2	8.0	12115.5	1778.5	0.0	0.0	55.2	8.6	142.7	21.8	
Surface	EQF-12.1	34.6	4.5	5.4	0.7	72.4	10.0	176.6	24.0	42.8	6.3	420.9	53.8	103.5	13.6	12642.0	1855.8	0.1	0.0	108.1	16.8	249.9	38.1	
Surface	EQF-9.1	18.2	2.4	2.8	0.4	35.1	4.9	82.8	11.2	20.2	3.0	218.4	27.9	55.5	7.3	5134.7	753.8	0.0	0.0	49.3	7.7	95.0	14.5	
Surface	EQF-7.1	39.5	5.2	6.6	0.9	82.4	11.4	197.6	26.8	48.5	7.1	481.0	61.5	116.7	15.3	12951.7	1901.3	0.1	0.0	129.9	20.2	291.1	44.4	
Surface	EQF-3.1	55.3	7.2	9.3	1.2	118.7	16.4	282.4	38.3	68.4	10.0	671.0	85.8	170.6	22.4	11268.5	1654.2	0.0	0.0	280.9	43.6	511.7	78.1	
Surface	EQF-26.1	41.9	5.5	6.7	0.9	88.9	12.3	209.5	28.5	50.9	7.5	483.8	61.9	124.1	16.3	11828.6	1736.4	0.5	0.1	144.5	22.4	337.8	51.5	
Surface	EQF-4.1	74.7	9.8	14.1	1.8	168.1	23.3	335.5	45.6	73.6	10.8	671.5	85.9	160.3	21.0	11942.1	1753.1	0.0	0.0	303.2	47.1	386.8	59.0	
Surface	EQF-17.1	60.4	7.9	12.6	1.6	147.0	20.3	288.2	39.1	65.3	9.6	597.4	76.4	146.3	19.2	13133.9	1928.1	0.2	0.0	209.7	32.6	236.0	36.0	
Surface	EQF-1.1	30.8	4.0	4.7	0.6	63.5	8.8	149.5	20.3	37.7	5.5	369.0	47.2	91.4	12.0	12159.8	1785.1	0.1	0.0	90.2	14.0	248.3	37.9	
Surface	EQF-20.1	34.7	4.5	6.3	0.8	70.6	9.8	150.8	20.5	33.4	4.9	295.5	37.8	69.9	9.2	6040.4	886.7	0.1	0.0	110.2	17.1	129.1	19.7	
Surface	EQF-31.1	20.8	2.7	3.3	0.4	45.7	6.3	106.1	14.4	27.8	4.1	254.3	32.5	71.3	9.4	9913.6	1455.3	0.2	0.0	58.7	9.1	150.2	22.9	
Surface	EQF-27.1	50.3	6.6	9.6	1.3	116.1	16.1	241.7	32.8	54.4	8.0	513.2	65.6	117.3	15.4	12010.5	1763.1	0.2	0.0	212.8	33.1	319.3	48.7	
Surface	EQF-21.1	72.7	9.5	14.5	1.9	168.3	23.3	324.1	44.0	72.3	10.6	677.3	86.6	160.2	21.0	11921.2	1750.0	0.0	0.0	282.1	43.8	386.2	58.9	
Surface	EQF-30.1	124.4	16.3	25.6	3.3	280.6	38.8	508.3	69.0	111.4	16.4	1037.2	132.7	213.0	28.0	7498.6	1100.8	0.2	0.0	480.5	74.6	521.1	79.5	
Surface	EQF-22.1	43.5	5.7	7.6	1.0	91.4	12.7	211.9	28.8	48.2	7.1	457.8	58.6	105.5	13.9	6782.7	995.7	0.2	0.0	280.9	43.6	394.1	60.1	
Surface	EQF-10.1	40.2	5.3	6.4	0.8	83.5	11.6	209.5	28.4	50.0	7.3	465.9	59.6	122.2	16.0	11963.0	1756.2	0.1	0.0	148.7	23.1	285.8	43.6	
Surface	EQF-25.1	79.4	10.4	16.0	2.1	185.7	25.7	368.6	50.1	82.9	12.2	736.7	94.2	173.9	22.8	13436.4	1972.5	0.2	0.0	311.4	48.4	412.9	63.0	
Surface	EQF-5.1	32.1	4.2	5.2	0.7	72.5	10.0	174.3	23.7	40.6	6.0	406.0	51.9	104.7	13.8	11579.8	1699.9	0.4	0.1	110.8	17.2	257.6	39.3	
Surface	EQF-13.1	78.2	10.2	15.0	2.0	187.7	26.0	422.7	57.4	98.4	14.4	946.7	121.1	230.1	30.2	11144.3	1636.0	0.2	0.0	534.5	83.0	714.7	109.1	
Surface	EQF-16.1	65.4	8.6	13.4	1.8	154.6	21.4	302.6	41.1	69.2	10.2	626.3	80.1	156.5	20.6	13237.4	1943.2	0.1	0.0	261.2	40.6	350.1	53.4	
Surface	EQF-19.1	32.5	4.2	5.2	0.7	67.5	9.3	169.0	23.0	40.2	5.9	399.7	51.1	99.2	13.0	10718.7	1573.5	0.4	0.1	100.2	15.6	253.3	38.7	
Surface	EQF-32.1	73.3	9.6	14.2	1.9	173.1	24.0	347.3	47.2	76.4	11.2	707.3	90.5	164.9	21.6	14818.8	2175.4	0.0	0.0	289.6	45.0	385.1	58.8	
Surface	EQF-15.1	78.2	10.2	13.6	1.8	175.3	24.3	409.3	55.6	95.8	14.1	895.3	114.5	221.4	29.1	13084.5	1920.8	0.3	0.0	439.1	68.2	633.0	96.6	
Surface	EQF-8.1	33.9	4.4	5.6	0.7	68.6	9.5	160.4	21.8	37.2	5.5	366.4	46.9	89.2	11.7	11405.5	1674.3	0.0	0.0	118.7	18.4	204.3	31.2	
Surface	EQF-14.1	22.0	2.9	3.9	0.5	46.8	6.5	111.4	15.1	25.9	3.8	252.3	32.3	63.3	8.3	14479.1	2125.5	0.2	0.0	64.7	10.1	146.0	22.3	
Surface	EQF-24.1	81.7	10.7	16.9	2.2	196.7	27.2	390.9	53.1	87.6	12.9	805.1	103.0	191.2	25.1	12170.3	1786.6	0.0	0.0	281.5	43.7	303.9	46.4	
Surface	EQF-18.1	34.9	4.6	5.8	0.8	73.7	10.2	172.8	23.5	40.6	6.0	430.8	55.1	111.4	14.6	13150.6	1930.5	0.2	0.0	117.9	18.3	271.5	41.4	
Surface	EQF-11.1	34.5	4.5	6.0	0.8	76.1	10.5	178.9	24.3	42.9	6.3	405.5	51.9	98.0	12.9	11077.9	1626.2	0.1	0.0	126.6	19.7	264.2	40.3	
Surface	EQF-29.1	86.6	11.3	17.7	2.3	200.2	27.7	399.6	54.3	91.5	13.4	839.0	107.3	193.3	25.4	13557.4	1990.2	0.1	0.0	406.4	63.1	508.5	77.6	
Surface	EQF-28.1	38.7	5.1	6.3	0.8	81.9	11.3	195.3	26.5	48.3	7.1	467.5	59.8	119.9	15.7	12733.1	1869.2	0.0	0.0	168.3	26.1	340.2	51.9	
Surface	EQF-23.1	71.7	9.4	14.3	1.9	168.7	23.4	338.9	46.0	78.2	11.5	734.2	93.9	176.1	23.1	12190.4	1789.5	0.0	0.0	479.2	74.4	572.1	87.3	
Surface	EQF_surf2_22.1	128.0	5.1	28.9	3.6	380.3	63.1	654.0	59.5	146.0	13.6	1352.0	160.9	310.8	33.3	10488.2	1374.0	0.1	0.0	699.0	84.6	662.6	78.8	
Surface	EQF_surf2_18.1	72.4	2.9	11.6	1.4	138.3	23.0	330.4	30.1	72.7	6.8	711.6	84.7	171.6	18.4	10753.3	1408.7	0.0	0.0	517.7	62.6	624.8	74.4	
Surface	EQF_surf2_21.1	104.8	4.2	19.6	2.5	316.4	52.5	476.6	43.4	104.8	9.7	962.2	114.5	226.2	24.2	11530.3	1510.5	0.1	0.0	463.4	56.1	526.7	62.7	
Surface	EQF_surf_5.1	92.0	3.7	22.1	2.8	257.9	42.8	440.1	40.1	95.7	8.9	843.4	100.4	194.6	20.8	11580.4	1517.0	0.2	0.0	328.0	39.7	386.9	46.0	
Surface	EQF_surf_6.1	29.3	1.2	4.6	0.6	63.2	10.5	164.7	15.0	42.6	4.0	413.6	49.2	100.7	10.8	11683.3	1530.5	0.3	0.1	88.0	10.7	197.6	23.5	
Surface	EQF_surf2_8.2	60.2	2.4	11.0	1.4	125.5	20.8	297.3	27.1	66.3	6.2	607.5	72.3	143.3	15.3	11751.7	1539.5	0.2	0.1	249.2	30.1	324.2	38.6	
Surface	EQF_surf2_19.1	25.9	1.0	4.4	0.5	47.4	7.9	129.5	11.8	31.7	2.9	307.8	36.6	80.3	8.6	12070.5	1581.2	0.1	0.0	72.9	8.8	200.8	23.9	
Surface	EQF_surf_2.1	49.2	2.0	7.7	1.0	113.1	18.8	237.0	21.6	56.8	5.3	547.1	65.1	132.3	14.2	12092.1	1584.1	0.0	0.0	176.8	21.4	362.3	43.1	
Surface	EQF_surf2_9.1	71.0	2.8	14.0	1.8	219.4	36.4	334.8	30.5	76.3	7.1	678.2	80.7	162.9	17.4	12239.8	1603.4	0.2	0.0	297.5	36.0	394.6	47.0	
Surface	EQF_surf2_11.1	55.6	2.2	11.4	1.4	99.1	16.5	257.3	23.4	57.2	5.3	551.2	65.6	133.1	14.2	12275.5	1608.1	0.3	0.1	214.9	26.0	317.3	37.8	
Surface	EQF_surf_3.1	28.5	1.1	5.0	0.6	70.3	11.7	147.1	13.4	38.1	3.5	375.7	44.7	97.8	10.5	12337.1	1616.2	0.2	0.0	103.6	12.5	245.3	29.2	
Surface	EQF_surf2_12.1	72.6	2.9	14.6	1.8	198.0	32.9	342.5	31.2	77.9	7.2	717.3	85.4	166.6	17.8	12435.3	1629.0	0.2	0.0	309.0	37.4	408.6	48.6	
Surface	EQF_surf2_17.1	60.0	2.4	11.3	1.4	178.5	29.6	286.5	26.1	64.7	6.0	589.6	70.2	140.6	15.0	12456.2	1631.8	0.1	0.0	214.0	25.9	279.4	33.2	
Surface	EQF_surf2_15.1	55.7	2.2	9.2	1.1	126.1	20.9	275.5	25.1	63.4	5.9	613.7	73.0	147.4	15.8	12517.1	1639.7	0.2	0.1	280.8	34.0	478.9	57.0	
Surface	EQF_surf2_10.1	16.6	0.7	2.8	0.4	49.3	8.2	94.4	8.6	23.7	2.2	235.5	28.0	60.4	6.5	13325.6	1745.6	0.1	0.0	54.6	6.6	149.4	17.8	

Zr concentration is 47760 ppm from Claiborne et al. (2006)

Zircon model crystallization ages and trace element concentrations (ppm)

Grain location	Earthquake Flat	Model age (ka)	+1σ (ka)	-1σ (ka)	Slope	slope error	Eu/Eu*	1 SD	Yb/Gd	1 SD	Y/P	1 SD	U/Th	1 SD	Ti-in-zircon Temp (C)	Zr/Hf	Σ(REE + P)/Y
Interior	EQF-sm-16.1_dup	66	13	12	0.45	0.06	0.194	0.06	13	3	3.2	0.4	3.6	0.4	704	22.5	1.5
Interior	EQF-lg-2.1	71	11	10	0.48	0.05	--	--	--	--	--	--	--	--	--	--	--
Interior	EQF-sm-3.1	79	18	16	0.52	0.07	0.095	0.03	20	4	3.3	0.4	5.0	0.6	664	26.6	1.6
Interior	EQF-sm-12.1_dup	80	11	10	0.52	0.05	0.166	0.05	12	2	6.2	0.8	1.2	0.1	730	40.5	3.0
Interior	EQF_int_round2_1.1	86	10	9	0.54	0.04	0.385	0.06	18	2	5.7	0.3	0.9	0.1	787	52.9	2.8
Interior	EQF-sm-8.1	87	9	8	0.55	0.03	0.115	0.04	18	4	5.8	0.7	3.5	0.4	779	27.8	2.8
Interior	EQF-sm-9.1_dup	90	46	32	0.56	0.15	0.249	0.04	15	3	4.8	0.6	4.4	0.5	698	12.2	2.3
Interior	EQF-lg-1.1	91	14	12	0.57	0.05	--	--	--	--	--	--	--	--	--	--	--
Interior	EQF-sm-14.1	92	9	8	0.57	0.03	0.170	0.06	12	2	4.7	0.6	3.2	0.4	729	23.8	2.3
Interior	EQF-sm-7.1	103	13	12	0.61	0.04	--	--	--	--	--	--	--	--	--	--	--
Interior	EQF_int_round2_8.1	103	11	10	0.61	0.04	0.161	0.03	23	2	6.3	0.3	1.3	0.1	728	39.6	3.1
Interior	EQF-sm-1.1	107	13	12	0.62	0.04	0.474	0.16	12	2	9.3	1.2	2.1	0.2	799	15.5	4.5
Interior	EQF_int_round2_13.1	112	13	11	0.64	0.04	--	--	--	--	--	--	--	--	--	--	--
Interior	EQF_int_round2_12.1	113	20	17	0.64	0.06	0.193	0.03	29	3	3.6	0.2	1.8	0.1	722	42.0	1.7
Interior	EQF-lg-5.1	115	18	16	0.65	0.05	--	--	--	--	--	--	--	--	--	--	--
Interior	EQF_int_round2_14.1	117	19	16	0.66	0.05	0.265	0.04	34	3	4.2	0.2	2.0	0.1	733	40.8	2.2
Interior	EQF-lg-3.1	117	34	26	0.66	0.09	--	--	--	--	--	--	--	--	--	--	--
Interior	EQF-sm-4.1	120	12	11	0.67	0.03	0.151	0.05	13	2	5.4	0.7	3.2	0.4	716	22.6	2.6
Interior	EQF_int_round2_5.1	120	15	13	0.67	0.04	0.187	0.03	23	2	3.9	0.2	1.7	0.1	748	41.2	1.9
Interior	EQF_int_round2_15.1	129	17	14	0.69	0.04	0.225	0.03	23	2	4.3	0.2	2.2	0.1	749	41.7	2.2
Interior	EQF-sm-11.1	136	28	23	0.71	0.07	0.129	0.04	14	3	4.3	0.6	2.3	0.3	679	21.1	2.1
Interior	EQF-sm-5.1	137	15	13	0.72	0.04	--	--	--	--	--	--	--	--	--	--	--
Interior	EQF_int_round2_18.1	138	13	12	0.72	0.03	0.264	0.04	21	2	5.1	0.2	0.8	0.0	780	46.5	2.6
Interior	EQF-sm-2.1	138	15	14	0.72	0.04	0.094	0.03	19	4	5.9	0.7	4.9	0.6	676	17.9	2.9
Interior	EQF_int_round2_16.1	141	20	17	0.73	0.05	0.182	0.03	36	3	3.1	0.1	2.5	0.1	713	36.8	1.6
Interior	EQF-sm-13.1_dup	142	44	31	0.73	0.09	--	--	--	--	--	--	--	--	--	--	--
Interior	EQF_int_round2_7.1	143	26	21	0.73	0.06	0.208	0.03	23	2	4.2	0.2	1.6	0.1	728	41.7	2.1
Interior	EQF_int_round2_6.1	147	21	17	0.74	0.05	0.287	0.04	21	2	2.7	0.1	1.2	0.1	767	47.4	1.6
Interior	EQF-sm-10.1	147	33	25	0.74	0.07	0.162	0.05	8	2	10.4	1.3	3.0	0.3	687	16.3	5.0
Interior	EQF_int_round2_19.1	152	21	18	0.75	0.04	0.170	0.03	26	2	4.3	0.2	2.2	0.1	710	38.9	2.2
Interior	EQF_int_round2_10.1	153	24	20	0.75	0.05	0.154	0.02	35	3	4.8	0.2	1.5	0.1	717	38.2	2.5
Interior	EQF_int_round2_11.1	166	28	23	0.78	0.05	0.267	0.04	24	2	5.4	0.2	1.2	0.1	724	38.1	2.8
Interior	EQF_int_round2_9.1	174	53	36	0.80	0.08	0.177	0.03	19	2	5.0	0.2	1.9	0.1	732	41.7	2.5
Interior	EQF-sm-6.1_dup	181	42	30	0.81	0.06	0.061	0.02	18	4	4.3	0.6	4.3	0.5	670	31.0	2.1
Interior	EQF_int_round2_17.1	181	34	26	0.81	0.05	0.215	0.03	21	2	4.4	0.2	1.4	0.1	743	41.2	2.2
Interior	EQF_int_round2_21.1	191	39	29	0.83	0.05	--	--	--	--	--	--	--	--	--	--	--
Interior	EQF_int_round2_20.1	196	138	59	0.83	0.12	--	--	--	--	--	--	--	--	--	--	--
Interior	EQF_int_round2_4.1	229	442	75	0.88	0.12	0.489	0.08	14	1	8.1	0.4	1.2	0.1	807	51.6	4.1
Interior	EQF_int_round2_3.1	232	93	49	0.88	0.07	0.142	0.02	34	3	3.6	0.2	1.9	0.1	703	34.7	1.9
Interior	EQF-lg-6.1_dup	266	68	42	0.91	0.04	--	--	--	--	--	--	--	--	--	--	--
Interior	EQF_int_round2_2.1	--	--	--	--	--	0.070	0.01	35	3	3.9	0.2	1.9	0.1	775	38.1	2.3

Zr concentration is 47760 ppm from Claiborne et al. (2006); for interior measuremens, sample names with "sm" or "lg" are from Rubin (2016), samples with "int" are from this study

Zircon model crystallization ages and trace element concentrations (ppm)

Grain location	Earthquake Flat	P/Si	1 SD	Sc/Si	1 SD	49Ti/Si	1 SD	Fe/Si	1 SD	Y/Si	1 SD	Nb/Si	1 SD	La/Si	1 SD	Ce/Si	1 SD	Nd/Si	1 SD	Sm/Si	1 SD	Eu/Si	1 SD	Gd/Si	1 SD	
Interior	EQF-sm-16.1_dup	251.0	31.1	12.8	0.6	2.9	0.3	8.9	1.7	794.4	21.8	7.8	1.4	0.0	0.0	8.8	1.0	1.2	0.3	2.6	0.4	0.4	0.1	14.3	2.0	
Interior	EQF-lg-2.1	--	--	--	--	--	--	--	--	--	--	--	--	--	--	--	--	--	--	--	--	--	--	--	--	
Interior	EQF-sm-3.1	144.8	18.0	7.2	0.3	1.8	0.2	8.6	1.6	471.1	12.9	12.2	2.2	0.0	0.0	6.8	0.8	0.4	0.1	1.3	0.2	0.1	0.0	6.8	1.0	
Interior	EQF-sm-12.1_dup	182.4	22.6	8.5	0.4	3.9	0.4	11.9	2.2	1127.0	30.9	13.4	2.4	0.0	0.0	34.8	4.0	1.9	0.4	5.9	1.0	0.6	0.2	24.2	3.5	
Interior	EQF_int_round2_1.1	974.1	31.2	168.6	5.9	7.0	0.7	4.1	0.6	5566.8	167.0	12.3	1.2	0.0	0.0	52.4	1.9	10.8	1.0	18.2	2.2	5.1	0.3	90.6	7.0	
Interior	EQF-sm-8.1	104.6	13.0	7.6	0.3	6.5	0.6	9.3	1.8	608.5	16.7	4.8	0.8	0.0	0.0	11.2	1.3	0.4	0.1	1.6	0.3	0.1	0.0	9.1	1.3	
Interior	EQF-sm-9.1_dup	85.6	10.6	6.3	0.3	2.7	0.2	5.3	1.0	414.7	11.4	4.7	0.8	0.0	0.0	8.1	0.9	0.3	0.1	1.0	0.2	0.1	0.0	6.4	0.9	
Interior	EQF-lg-1.1	--	--	--	--	--	--	--	--	--	--	--	--	--	--	--	--	--	--	--	--	--	--	--	--	
Interior	EQF-sm-14.1	137.0	17.0	10.3	0.5	3.8	0.4	9.2	1.7	648.4	17.8	6.2	1.1	0.0	0.0	9.0	1.0	0.7	0.2	2.4	0.4	0.3	0.1	13.5	1.9	
Interior	EQF-sm-7.1	--	--	--	--	--	--	--	--	--	--	--	--	--	--	--	--	--	--	--	--	--	--	--	--	
Interior	EQF_int_round2_8.1	365.1	11.7	43.3	1.5	3.8	0.4	5.4	0.8	2298.3	68.9	4.6	0.4	0.0	0.0	20.0	0.7	1.6	0.2	4.1	0.5	0.6	0.0	27.8	2.1	
Interior	EQF-sm-1.1	69.6	8.6	6.2	0.3	7.9	0.7	12.2	2.3	644.7	17.7	9.5	1.7	0.1	0.0	15.1	1.7	3.5	0.8	3.9	0.6	1.2	0.3	15.6	2.2	
Interior	EQF_int_round2_13.1	--	--	--	--	--	--	--	--	--	--	--	--	--	--	--	--	--	--	--	--	--	--	--	--	
Interior	EQF_int_round2_12.1	342.3	11.0	38.8	1.4	3.6	0.3	2.7	0.4	1217.2	36.5	4.8	0.5	0.0	0.0	14.1	0.5	0.8	0.1	1.8	0.2	0.3	0.0	12.3	0.9	
Interior	EQF-lg-5.1	--	--	--	--	--	--	--	--	--	--	--	--	--	--	--	--	--	--	--	--	--	--	--	--	
Interior	EQF_int_round2_14.1	203.7	6.5	51.4	1.8	4.0	0.4	3.5	0.5	864.0	25.9	3.6	0.3	0.0	0.0	7.7	0.3	0.3	0.0	1.2	0.1	0.3	0.0	9.5	0.7	
Interior	EQF-lg-3.1	--	--	--	--	--	--	--	--	--	--	--	--	--	--	--	--	--	--	--	--	--	--	--	--	
Interior	EQF-sm-4.1	172.3	21.4	13.4	0.6	3.3	0.3	9.2	1.7	938.1	25.7	6.8	1.2	0.0	0.0	16.0	1.8	1.2	0.3	3.6	0.6	0.4	0.1	17.8	2.5	
Interior	EQF_int_round2_5.1	313.2	10.0	82.9	2.9	4.7	0.4	1.9	0.3	1218.2	36.5	4.8	0.5	0.0	0.0	11.5	0.4	0.8	0.1	2.2	0.3	0.4	0.0	15.0	1.2	
Interior	EQF_int_round2_15.1	322.3	10.3	109.5	3.8	4.7	0.4	4.1	0.6	1384.4	41.5	7.7	0.7	0.0	0.0	9.7	0.4	0.9	0.1	1.9	0.2	0.4	0.0	19.0	1.5	
Interior	EQF-sm-11.1	160.3	19.9	7.0	0.3	2.2	0.2	8.7	1.6	694.7	19.0	6.9	1.2	0.0	0.0	13.7	1.6	0.9	0.2	2.3	0.4	0.2	0.1	12.5	1.8	
Interior	EQF-sm-5.1	--	--	--	--	--	--	--	--	--	--	--	--	--	--	--	--	--	--	--	--	--	--	--	--	
Interior	EQF_int_round2_18.1	498.3	15.9	150.1	5.3	6.5	0.6	3.8	0.6	2536.9	76.1	10.4	1.0	0.0	0.0	32.1	1.2	2.1	0.2	4.8	0.6	1.2	0.1	37.0	2.8	
Interior	EQF-sm-2.1	116.9	14.5	8.5	0.4	2.1	0.2	7.6	1.4	685.8	18.8	5.5	1.0	0.0	0.0	11.2	1.3	0.7	0.2	2.2	0.4	0.1	0.0	10.1	1.4	
Interior	EQF_int_round2_16.1	388.3	12.4	66.1	2.3	3.2	0.3	3.2	0.5	1187.8	35.6	7.7	0.7	0.0	0.0	9.8	0.4	0.4	0.0	1.3	0.2	0.2	0.0	11.3	0.9	
Interior	EQF-sm-13.1_dup	--	--	--	--	--	--	--	--	--	--	--	--	--	--	--	--	--	--	--	--	--	--	--	--	
Interior	EQF_int_round2_7.1	389.3	12.5	68.0	2.4	3.8	0.4	3.9	0.6	1629.0	48.9	2.5	0.2	0.0	0.0	14.5	0.5	1.0	0.1	2.6	0.3	0.5	0.0	20.1	1.6	
Interior	EQF_int_round2_6.1	485.9	15.5	99.0	3.5	5.8	0.5	3.6	0.6	1331.7	39.9	4.1	0.4	0.0	0.0	10.0	0.4	2.3	0.2	4.0	0.5	1.0	0.1	30.6	2.4	
Interior	EQF-sm-10.1	116.7	14.5	9.6	0.4	2.4	0.2	8.7	1.6	1217.5	33.4	4.7	0.8	0.0	0.0	12.0	1.4	2.6	0.6	6.9	1.1	0.8	0.2	34.7	4.9	
Interior	EQF_int_round2_19.1	296.1	9.5	82.0	2.9	3.1	0.3	3.6	0.6	1287.7	38.6	6.4	0.6	0.0	0.0	11.0	0.4	0.5	0.0	1.8	0.2	0.3	0.0	16.1	1.2	
Interior	EQF_int_round2_10.1	546.7	17.5	169.1	5.9	3.4	0.3	3.0	0.5	2647.4	79.4	23.0	2.2	0.0	0.0	44.0	1.6	1.2	0.1	3.5	0.4	0.5	0.0	24.5	1.9	
Interior	EQF_int_round2_11.1	369.6	11.8	74.1	2.6	3.6	0.3	3.0	0.5	2011.3	60.3	2.4	0.2	0.0	0.0	20.9	0.8	1.4	0.1	3.9	0.5	0.9	0.1	26.5	2.0	
Interior	EQF_int_round2_9.1	244.1	7.8	39.6	1.4	4.0	0.4	4.5	0.7	1221.3	36.6	4.1	0.4	0.0	0.0	21.1	0.8	16.5	1.6	4.9	0.6	0.5	0.0	17.4	1.3	
Interior	EQF-sm-6.1_dup	111.3	13.8	5.7	0.3	1.9	0.2	13.7	2.6	481.8	13.2	16.9	3.0	0.0	0.0	8.8	1.0	0.6	0.1	2.3	0.4	0.1	0.0	7.5	1.1	
Interior	EQF_int_round2_17.1	407.7	13.0	79.4	2.8	4.5	0.4	3.9	0.6	1809.8	54.3	8.1	0.8	0.0	0.0	19.7	0.7	1.0	0.1	2.8	0.3	0.6	0.0	24.3	1.9	
Interior	EQF_int_round2_21.1	--	--	--	--	--	--	--	--	--	--	--	--	--	--	--	--	--	--	--	--	--	--	--	--	
Interior	EQF_int_round2_20.1	--	--	--	--	--	--	--	--	--	--	--	--	--	--	--	--	--	--	--	--	--	--	--	--	
Interior	EQF_int_round2_4.1	333.7	10.7	223.8	7.8	8.5	0.8	3.9	0.6	2706.0	81.2	4.1	0.4	0.0	0.0	9.6	0.4	5.1	0.5	8.4	1.0	3.5	0.2	58.2	4.5	
Interior	EQF_int_round2_3.1	357.0	11.4	77.1	2.7	2.8	0.3	3.6	0.6	1299.3	39.0	10.1	1.0	0.0	0.0	20.8	0.8	0.4	0.0	1.8	0.2	0.2	0.0	13.9	1.1	
Interior	EQF-lg-6.1_dup	--	--	--	--	--	--	--	--	--	--	--	--	--	--	--	--	--	--	--	--	--	--	--	--	
Interior	EQF_int_round2_2.1	871.5	27.9	63.5	2.2	6.2	0.6	5.3	0.8	3366.3	101.0	46.4	4.5	0.0	0.0	52.5	1.9	3.0	0.3	5.5	0.7	0.4	0.0	49.6	3.8	

Zr concentration is 47760 ppm from Claiborne et al. (2006)

Zircon model crystallization ages and trace element concentrations (ppm)

Grain location	Earthquake Flat	Ho/Si	1 SD	Tb/Si	1 SD	Dy/Si	1 SD	Er/Si	1 SD	Tm/Si	1 SD	Yb/Si	1 SD	Lu/Si	1 SD	Hf/Si	1 SD	Pb/Si	1 SD	Th/Si	1 SD	U/Si	1 SD	
Interior	EQF-sm-16.1_dup	22.6	1.0	5.2	1.0	52.7	11.0	93.1	14.0	20.4	3.3	189.1	25.4	45.0	4.7	21268.1	1616.4	0.0	0.0	210.0	10.6	749.8	74.8	
Interior	EQF-lg-2.1	--	--	--	--	--	--	--	--	--	--	--	--	--	--	--	--	--	--	--	--	--	--	--
Interior	EQF-sm-3.1	12.6	0.6	2.7	0.5	30.6	6.4	57.0	8.6	13.7	2.2	135.7	18.2	33.3	3.5	17975.7	1366.2	0.0	0.0	126.8	6.4	634.9	63.4	
Interior	EQF-sm-12.1_dup	30.8	1.4	9.0	1.8	85.1	17.7	135.2	20.3	30.7	4.9	284.6	38.3	68.7	7.2	11782.1	895.4	0.0	0.0	2395.3	120.5	2930.9	292.5	
Interior	EQF_int_round2_1.1	167.6	5.7	34.8	1.8	392.4	66.3	759.2	39.5	175.4	8.9	1606.6	64.3	393.5	20.5	9034.9	298.2	0.0	0.0	621.8	19.3	547.2	27.4	
Interior	EQF-sm-8.1	16.8	0.8	3.9	0.8	39.2	8.2	75.7	11.4	17.3	2.8	166.1	22.3	38.1	4.0	17167.2	1304.7	0.0	0.0	244.7	12.3	864.2	86.2	
Interior	EQF-sm-9.1_dup	11.7	0.5	2.4	0.5	26.3	5.5	45.0	6.8	11.0	1.8	98.6	13.3	26.3	2.8	39019.7	2965.5	0.0	0.0	131.4	6.6	581.4	58.0	
Interior	EQF-lg-1.1	--	--	--	--	--	--	--	--	--	--	--	--	--	--	--	--	--	--	--	--	--	--	--
Interior	EQF-sm-14.1	19.0	0.9	5.1	1.0	55.7	11.6	79.8	12.0	17.5	2.8	155.5	20.9	35.1	3.7	20065.0	1524.9	0.0	0.0	231.0	11.6	741.8	74.0	
Interior	EQF-sm-7.1	--	--	--	--	--	--	--	--	--	--	--	--	--	--	--	--	--	--	--	--	--	--	--
Interior	EQF_int_round2_8.1	69.0	2.3	12.9	0.7	151.9	25.7	316.1	16.4	70.3	3.6	652.2	26.1	153.3	8.0	12068.9	398.3	0.0	0.0	252.6	7.8	332.1	16.6	
Interior	EQF-sm-1.1	18.1	0.8	4.6	0.9	44.6	9.3	75.6	11.4	18.4	2.9	180.2	24.2	46.9	4.9	30740.7	2336.3	0.1	0.0	329.7	16.6	698.6	69.7	
Interior	EQF_int_round2_13.1	--	--	--	--	--	--	--	--	--	--	--	--	--	--	--	--	--	--	--	--	--	--	--
Interior	EQF_int_round2_12.1	34.7	1.2	6.0	0.3	72.7	12.3	161.1	8.4	37.9	1.9	356.8	14.3	87.5	4.6	11372.8	375.3	0.0	0.0	151.7	4.7	269.4	13.5	
Interior	EQF-lg-5.1	--	--	--	--	--	--	--	--	--	--	--	--	--	--	--	--	--	--	--	--	--	--	--
Interior	EQF_int_round2_14.1	29.1	1.0	5.4	0.3	61.0	10.3	147.0	7.6	33.5	1.7	319.9	12.8	76.9	4.0	11716.3	386.6	0.0	0.0	54.1	1.7	108.9	5.4	
Interior	EQF-lg-3.1	--	--	--	--	--	--	--	--	--	--	--	--	--	--	--	--	--	--	--	--	--	--	--
Interior	EQF-sm-4.1	27.7	1.2	6.7	1.3	71.6	14.9	114.9	17.3	25.0	4.0	222.8	29.9	49.7	5.2	21117.4	1604.9	0.0	0.0	317.0	15.9	998.6	99.7	
Interior	EQF_int_round2_5.1	35.9	1.2	7.1	0.4	110.7	18.7	171.1	8.9	36.6	1.9	341.6	13.7	80.3	4.2	11587.0	382.4	0.0	0.0	123.0	3.8	208.9	10.4	
Interior	EQF_int_round2_15.1	44.9	1.5	8.6	0.4	105.8	17.9	217.0	11.3	47.3	2.4	437.1	17.5	105.9	5.5	11439.6	377.5	0.2	0.0	70.5	2.2	156.0	7.8	
Interior	EQF-sm-11.1	18.8	0.8	4.7	0.9	49.0	10.2	80.7	12.1	18.7	3.0	177.3	23.8	43.7	4.6	22638.6	1720.5	0.0	0.0	611.7	30.8	1424.7	142.2	
Interior	EQF-sm-5.1	--	--	--	--	--	--	--	--	--	--	--	--	--	--	--	--	--	--	--	--	--	--	--
Interior	EQF_int_round2_18.1	86.9	3.0	17.3	0.9	197.3	33.3	402.5	20.9	86.7	4.4	775.8	31.0	176.1	9.2	10273.2	339.0	0.0	0.0	747.7	23.2	579.9	29.0	
Interior	EQF-sm-2.1	19.7	0.9	4.3	0.9	47.8	9.9	86.6	13.0	20.2	3.2	190.2	25.6	48.3	5.1	26636.0	2024.3	0.0	0.0	200.2	10.1	987.3	98.5	
Interior	EQF_int_round2_16.1	37.5	1.3	6.6	0.3	100.9	17.1	186.5	9.7	41.1	2.1	401.7	16.1	94.1	4.9	12995.7	428.9	0.1	0.0	70.8	2.2	176.9	8.8	
Interior	EQF-sm-13.1_dup	--	--	--	--	--	--	--	--	--	--	--	--	--	--	--	--	--	--	--	--	--	--	--
Interior	EQF_int_round2_7.1	49.9	1.7	8.4	0.4	109.3	18.5	232.1	12.1	49.8	2.5	459.6	18.4	106.4	5.5	11464.9	378.3	0.0	0.0	152.2	4.7	241.2	12.1	
Interior	EQF_int_round2_6.1	70.7	2.4	16.9	0.9	188.8	31.9	347.4	18.1	71.1	3.6	637.2	25.5	144.8	7.5	10065.9	332.2	0.0	0.0	172.1	5.3	210.4	10.5	
Interior	EQF-sm-10.1	39.2	1.8	11.2	2.2	102.6	21.4	155.7	23.4	32.3	5.2	281.2	37.8	64.9	6.8	29250.3	2223.0	0.0	0.0	334.5	16.8	995.4	99.3	
Interior	EQF_int_round2_19.1	43.7	1.5	8.1	0.4	116.1	19.6	209.0	10.9	46.6	2.4	421.5	16.9	98.6	5.1	12281.7	405.3	0.1	0.0	85.7	2.7	187.0	9.3	
Interior	EQF_int_round2_10.1	80.6	2.7	14.1	0.7	206.6	34.9	395.2	20.5	87.9	4.5	855.7	34.2	206.6	10.7	12504.6	412.7	0.0	0.0	284.8	8.8	420.3	21.0	
Interior	EQF_int_round2_11.1	65.7	2.2	13.9	0.7	166.4	28.1	312.4	16.2	69.2	3.5	646.1	25.8	151.2	7.9	12521.0	413.2	0.0	0.0	186.2	5.8	218.2	10.9	
Interior	EQF_int_round2_9.1	33.0	1.1	6.7	0.3	92.9	15.7	159.9	8.3	35.6	1.8	333.5	13.3	76.7	4.0	11466.6	378.4	0.1	0.0	67.0	2.1	128.2	6.4	
Interior	EQF-sm-6.1_dup	13.7	0.6	2.9	0.6	32.1	6.7	61.2	9.2	14.3	2.3	137.4	18.5	34.2	3.6	15396.2	1170.1	0.0	0.0	156.3	7.9	666.6	66.5	
Interior	EQF_int_round2_17.1	57.7	2.0	11.9	0.6	158.9	26.9	257.4	13.4	55.2	2.8	509.3	20.4	116.2	6.0	11601.4	382.8	0.0	0.0	242.8	7.5	333.8	16.7	
Interior	EQF_int_round2_21.1	--	--	--	--	--	--	--	--	--	--	--	--	--	--	--	--	--	--	--	--	--	--	--
Interior	EQF_int_round2_20.1	--	--	--	--	--	--	--	--	--	--	--	--	--	--	--	--	--	--	--	--	--	--	--
Interior	EQF_int_round2_4.1	98.7	3.4	24.8	1.3	261.8	44.2	446.0	23.2	88.7	4.5	786.3	31.5	173.5	9.0	9255.5	305.4	0.0	0.0	160.5	5.0	188.6	9.4	
Interior	EQF_int_round2_3.1	42.1	1.4	7.8	0.4	99.2	16.8	219.7	11.4	49.2	2.5	465.9	18.6	113.3	5.9	13772.9	454.5	0.0	0.0	185.4	5.7	345.7	17.3	
Interior	EQF-lg-6.1_dup	--	--	--	--	--	--	--	--	--	--	--	--	--	--	--	--	--	--	--	--	--	--	--
Interior	EQF_int_round2_2.1	131.1	4.5	25.8	1.3	282.0	47.7	733.1	38.1	178.1	9.1	1758.1	70.3	422.7	22.0	12526.7	413.4	0.2	0.0	1999.4	62.0	3813.2	190.7	

Zr concentration is 47760 ppm from Claiborne et al. (2006)

Zircon model crystallization ages and trace element concentrations (ppm)

Grain location	Hauparu	Model age (ka)	+1σ (ka)	-1σ (ka)	Slope	slope error	Eu/Eu*	1 SD	Yb/Gd	1 SD	Y/P	1 SD	U/Th	1 SD	Ti-in-zircon Temp (C)	Zr/Hf	Σ(REE + P)/Y
Surface	GP-10_6.1	30	10	9	0.24	0.07	0.55	0.07	16	1	8.1	0.6	1.0	0.1	758	46	4.0
Surface	GP-10_11.1	37	12	11	0.29	0.08	0.51	0.07	20	1	6.9	0.5	1.2	0.1	916	43	3.4
Surface	GP-10_22.1	37	7	7	0.29	0.05	--	--	--	--	--	--	--	--	--	--	--
Surface	GP-10_5.1	40	11	10	0.31	0.06	0.47	0.06	20	1	7.8	0.6	1.1	0.1	747	39	4.0
Surface	GP-10_16.1	41	14	12	0.31	0.08	0.41	0.05	34	2	3.6	0.3	1.6	0.1	804	43	1.8
Surface	GP-10_26.1	46	16	14	0.34	0.09	--	--	--	--	--	--	--	--	--	--	--
Surface	GP-10_15.1	48	9	9	0.36	0.05	0.29	0.04	28	2	3.3	0.2	2.8	0.2	737	41	1.6
Surface	GP-10_7.1	49	13	12	0.36	0.07	0.49	0.06	16	1	7.3	0.5	1.0	0.1	830	47	3.6
Surface	GP-10_33.1	50	9	9	0.37	0.05	--	--	--	--	--	--	--	--	--	--	--
Surface	GP-05_2.1	52	13	12	0.38	0.07	0.53	0.07	24	2	7.0	0.5	1.2	0.1	862	41	3.6
Surface	GP-10_19.1	52	10	10	0.38	0.06	--	--	--	--	--	--	--	--	--	--	--
Surface	GP-10_10.1	53	14	13	0.38	0.08	--	--	--	--	--	--	--	--	--	--	--
Surface	GP-10_21.1	55	19	16	0.40	0.10	--	--	--	--	--	--	--	--	--	--	--
Surface	GP-10_1.1	56	11	10	0.40	0.06	0.67	0.09	25	2	5.8	0.4	1.1	0.1	780	42	3.4
Surface	GP-10_25.1	58	16	14	0.41	0.08	--	--	--	--	--	--	--	--	--	--	--
Surface	GP-05_20.1	59	14	13	0.42	0.07	--	--	--	--	--	--	--	--	--	--	--
Surface	GP-10_12.1	64	17	14	0.44	0.08	0.52	0.07	22	2	5.6	0.4	1.3	0.1	726	41	2.8
Surface	GP-05_23.1	64	16	14	0.44	0.07	--	--	--	--	--	--	--	--	--	--	--
Surface	GP-10_14.1	68	9	9	0.46	0.04	0.28	0.04	28	2	7.2	0.5	1.6	0.1	822	37	4.3
Surface	GP-05_9.1	68	13	12	0.46	0.06	0.21	0.03	34	2	5.4	0.4	1.9	0.1	760	40	2.9
Surface	GP-05_21.1	72	14	12	0.48	0.06	--	--	--	--	--	--	--	--	--	--	--
Surface	GP-10_32.1	73	18	16	0.49	0.08	--	--	--	--	--	--	--	--	--	--	--
Surface	GP-10_27.1	74	20	17	0.49	0.08	--	--	--	--	--	--	--	--	--	--	--
Surface	GP-10_29.1	75	22	19	0.50	0.09	--	--	--	--	--	--	--	--	--	--	--
Surface	GP-10_18.1	78	18	16	0.51	0.08	--	--	--	--	--	--	--	--	--	--	--
Surface	GP-05_14.1	81	10	9	0.52	0.04	0.21	0.03	29	2	7.1	0.5	1.3	0.1	851	39	3.5
Surface	GP-05_5.1	81	11	10	0.53	0.04	0.19	0.02	19	1	7.8	0.6	1.3	0.1	722	31	3.5
Surface	GP-10_31.1	82	8	8	0.53	0.03	--	--	--	--	--	--	--	--	--	--	--
Surface	GP-05_7.1	101	26	21	0.60	0.09	0.24	0.03	31	2	4.8	0.3	2.2	0.2	729	34	2.4
Surface	GP-05_18.1	106	17	15	0.62	0.05	0.29	0.04	40	3	3.0	0.2	2.4	0.2	730	36	1.6
Surface	GP-05_6.1	108	14	12	0.63	0.04	--	--	--	--	--	--	--	--	--	--	--
Surface	GP-10_13.1	117	36	27	0.66	0.10	0.23	0.03	36	3	3.4	0.2	2.3	0.2	824	40	1.7
Surface	GP-05_22.1	119	15	13	0.66	0.04	--	--	--	--	--	--	--	--	--	--	--
Surface	GP-10_3.1	121	48	33	0.67	0.12	0.19	0.03	14	1	5.9	0.4	1.1	0.1	921	35	2.7
Surface	GP-05_19.1	123	50	34	0.68	0.12	0.50	0.07	21	1	5.8	0.4	1.1	0.1	871	44	2.9
Surface	GP-05_28.1	125	75	44	0.68	0.16	--	--	--	--	--	--	--	--	--	--	--
Surface	GP-05_4.1	131	22	18	0.70	0.05	0.12	0.02	16	1	7.0	0.5	1.2	0.1	828	31	4.1
Surface	GP-05_3.1	169	31	24	0.79	0.05	0.22	0.03	22	2	8.0	0.6	1.4	0.1	755	35	3.8
Surface	GP-10_20.1	181	350	81	0.81	0.21	--	--	--	--	--	--	--	--	--	--	--
Surface	GP-05_8.1	193	75	44	0.83	0.08	0.14	0.02	27	2	4.8	0.3	2.1	0.1	698	38	2.4
Surface	GP-05_25.1	198	42	30	0.84	0.05	--	--	--	--	--	--	--	--	--	--	--
Surface	GP-05_30.1	231	65	41	0.88	0.05	--	--	--	--	--	--	--	--	--	--	--
Surface	GP-05_10.1	244	95	50	0.89	0.06	0.23	0.03	31	2	5.6	0.4	1.9	0.1	802	38	2.7
Surface	GP-10_2.1	290	350	150	0.93	0.21	0.48	0.06	19	1	7.3	0.5	1.1	0.1	852	36	3.7
Surface	GP-05_26.1	304	291	72	0.94	0.06	--	--	--	--	--	--	--	--	--	--	--
Surface	GP-05_13.1	SE	SE	SE	1.01	0.06	0.48	0.06	12	1	5.3	0.4	1.4	0.1	929	37	2.5
Surface	GP-05_1.1	--	--	--	--	--	0.34	0.05	14	1	10.7	0.8	1.3	0.1	801	38	5.1
Surface	GP-05_11.1	--	--	--	--	--	0.26	0.03	45	3	2.0	0.1	2.4	0.2	718	38	1.0
Surface	GP-05_12.1	--	--	--	--	--	0.18	0.02	46	3	3.0	0.2	2.6	0.2	684	36	1.6
Surface	GP-05_15.1	--	--	--	--	--	0.25	0.03	20	1	12.3	0.9	1.1	0.1	761	40	5.5
Surface	GP-05_16.1	--	--	--	--	--	0.23	0.03	28	2	5.5	0.4	1.6	0.1	740	36	2.6
Surface	GP-05_17.1	--	--	--	--	--	0.35	0.05	13	1	7.7	0.6	1.2	0.1	764	45	3.9
Surface	GP-10_17.1	--	--	--	--	--	0.49	0.06	14	1	8.4	0.6	1.0	0.1	835	49	4.0
Surface	GP-10_4.1	--	--	--	--	--	0.50	0.07	28	2	6.7	0.5	1.1	0.1	1211	46	3.5
Surface	GP-10_8.1	--	--	--	--	--	0.48	0.06	21	1	6.2	0.4	1.3	0.1	820	42	2.9
Surface	GP-10_9.1	--	--	--	--	--	0.49	0.06	45	3	4.5	0.3	2.3	0.2	863	43	2.6
Interior	GP10_4.1	38	8	8	0.29	0.05	0.50	0.09	30	3	4.2	0.4	2.6	0.3	778	51	2.2
Interior	GP10_17.1	43	8	7	0.33	0.04	0.51	0.09	31	3	3.9	0.4	1.3	0.1	821	51	2.0
Interior	GP10_22.1	44	8	7	0.33	0.05	0.44	0.08	35	4	4.3	0.4	1.6	0.2	774	56	2.3
Interior	GP10_18.1	46	7	7	0.34	0.04	0.38	0.07	29	3	2.8	0.3	1.3	0.1	735	51	1.4
Interior	GP10_12.1	49	7	6	0.36	0.04	0.39	0.07	26	3	4.5	0.5	1.0	0.1	794	51	2.3
Interior	GP05_16.1	51	11	10	0.37	0.06	0.46	0.08	24	2	5.1	0.5	1.2	0.1	748	48	2.6
Interior	GP10_20.1	56	9	9	0.40	0.05	0.50	0.09	32	3	5.2	0.5	1.3	0.1	750	52	2.8
Interior	GP10_14.1	57	8	7	0.41	0.04	--	--	--	--	--	--	--	--	--	--	--
Interior	GP10_9.1	59	12	10	0.42	0.06	0.33	0.06	34	3	3.5	0.4	1.6	0.2	789	54	1.8
Interior	GP10_11.1	65	8	7	0.45	0.04	0.22	0.04	31	3	2.5	0.3	4.6	0.4	746	43	1.2
Interior	GP10_10.1	69	9	9	0.47	0.04	0.42	0.07	39	4	2.5	0.3	1.8	0.2	778	48	1.3
Interior	GP05_7.1	79	12	11	0.52	0.05	--	--	--	--	--	--	--	--	--	--	--
Interior	GP10_15.1	87	8	7	0.55	0.03	--	--	--	--	--	--	--	--	--	--	--
Interior	GP05_9.1	89	10	9	0.56	0.04	0.22	0.04	27	3	2.5	0.3	1.7	0.2	672	53	1.2
Interior	GP10_23.1	98	10	9	0.59	0.04	0.15	0.03	29	3	5.6	0.6	1.5	0.1	695	45	2.8
Interior	GP05_2.1	112	14	12	0.64	0.04	--	--	--	--	--	--	--	--	--	--	--
Interior	GP05_6.1	125	15	13	0.68	0.04	0.15	0.03	33	3	4.8	0.5	2.0	0.2	674	45	2.5
Interior	GP05_14.1	132	53	36	0.70	0.12	--	--	--	--	--	--	--	--	--	--	--
Interior	GP05_4.1	139	29	23	0.72	0.06	0.35	0.06	25	3	3.9	0.4	1.3	0.1	727	46	2.2
Interior	GP10_13.1	162	20	17	0.77	0.04	0.37	0.06	35	4	1.9	0.2	2.3	0.2	755	47	1.0
Interior	GP05_1.1	186	51	35	0.82	0.07	0.14	0.02	40	4	5.0	0.5	2.0	0.2	669	41	2.5
Interior	GP05_19.1	192	90	49	0.83	0.10	0.46	0.08	31	3	4.7	0.5	1.6	0.2	758	48	2.4
Interior	GP10_16.1	223	304	72	0.87	0.12	0.46	0.08	21	2	4.3	0.4	1.0	0.1	735	49	2.2
Interior	GP05_12.1	SE	SE	SE	1.04	0.11	0.20	0.04	25	3	4.7	0.5	1.2	0.1	712	45	2.4

Zr concentration is 47760 ppm from Claiborne et al. (2006)

Zircon model crystallization ages and tracZircon model crystallization ages and trace element concentrations (ppm)

Grain location	Haupuru	P/Si	1 SD	Sc/Si	1 SD	49Ti/Si	1 SD	Fe/Si	1 SD	Y/Si	1 SD	Nb/Si	1 SD	La/Si	1 SD	Ce/Si	1 SD	Nd/Si	1 SD	Sm/Si	1 SD	Eu/Si	1 SD	Gd/Si	1 SD	
Surface	GP-10_6.1	236.2	10.3	6.1	1.5	5.7	0.5	12.3	2.5	1920.0	110.8	1.2	0.1	0.0	0.0	11.5	0.3	2.6	0.3	4.8	0.3	2.3	0.2	33.8	1.8	
Surface	GP-10_11.1	257.9	11.2	7.6	1.9	23.6	2.0	43.4	8.8	1783.2	102.9	2.2	0.2	0.1	0.0	13.1	0.3	1.4	0.2	2.4	0.1	1.3	0.1	24.7	1.3	
Surface	GP-10_22.1	--	--	--	--	--	--	--	--	--	--	--	--	--	--	--	--	--	--	--	--	--	--	--	--	
Surface	GP-10_5.1	277.5	12.1	5.5	1.4	5.1	0.4	5.5	1.1	2158.3	124.5	1.2	0.1	0.0	0.0	13.5	0.4	2.8	0.3	5.1	0.3	2.1	0.2	35.5	1.9	
Surface	GP-10_16.1	324.8	14.1	3.8	0.9	8.9	0.8	39.3	8.0	1168.7	67.4	3.3	0.3	0.2	0.1	10.1	0.3	0.9	0.1	1.7	0.1	0.6	0.1	11.5	0.6	
Surface	GP-10_26.1	--	--	--	--	--	--	--	--	--	--	--	--	--	--	--	--	--	--	--	--	--	--	--	--	
Surface	GP-10_15.1	807.3	35.1	8.7	2.1	4.6	0.4	25.0	5.1	2677.4	154.5	2.7	0.3	0.4	0.2	3.8	0.1	1.9	0.2	3.6	0.2	1.0	0.1	29.0	1.6	
Surface	GP-10_7.1	272.2	11.8	6.0	1.5	11.4	1.0	37.7	7.7	1976.0	114.0	0.8	0.1	0.0	0.0	12.8	0.3	3.5	0.4	5.9	0.3	2.2	0.2	33.1	1.8	
Surface	GP-10_33.1	--	--	--	--	--	--	--	--	--	--	--	--	--	--	--	--	--	--	--	--	--	--	--	--	
Surface	GP-05_2.1	291.1	12.7	6.1	1.5	15.2	1.3	52.9	10.8	2043.9	117.9	1.4	0.1	0.5	0.3	13.2	0.4	2.7	0.3	4.6	0.3	2.0	0.2	28.4	1.5	
Surface	GP-10_19.1	--	--	--	--	--	--	--	--	--	--	--	--	--	--	--	--	--	--	--	--	--	--	--	--	
Surface	GP-10_10.1	--	--	--	--	--	--	--	--	--	--	--	--	--	--	--	--	--	--	--	--	--	--	--	--	
Surface	GP-10_21.1	--	--	--	--	--	--	--	--	--	--	--	--	--	--	--	--	--	--	--	--	--	--	--	--	
Surface	GP-10_1.1	192.6	8.4	7.2	1.8	7.1	0.6	9.3	1.9	1125.3	64.9	1.8	0.2	0.0	0.0	9.8	0.3	1.2	0.2	2.4	0.1	1.6	0.2	21.3	1.1	
Surface	GP-10_25.1	--	--	--	--	--	--	--	--	--	--	--	--	--	--	--	--	--	--	--	--	--	--	--	--	
Surface	GP-05_20.1	--	--	--	--	--	--	--	--	--	--	--	--	--	--	--	--	--	--	--	--	--	--	--	--	
Surface	GP-10_12.1	341.9	14.9	7.3	1.8	4.0	0.3	3.7	0.8	1898.9	109.6	3.2	0.3	0.1	0.1	13.9	0.4	2.5	0.3	4.0	0.2	1.8	0.2	27.6	1.5	
Surface	GP-05_23.1	--	--	--	--	--	--	--	--	--	--	--	--	--	--	--	--	--	--	--	--	--	--	--	--	
Surface	GP-10_14.1	174.2	7.6	4.1	1.0	10.6	0.9	24.8	5.1	1262.3	72.8	2.6	0.3	0.0	0.0	9.8	0.3	1.0	0.1	2.8	0.2	0.7	0.1	22.4	1.2	
Surface	GP-05_9.1	315.2	13.7	3.5	0.9	5.8	0.5	19.3	3.9	1686.8	97.3	6.8	0.7	0.4	0.2	20.1	0.5	1.8	0.2	2.0	0.1	0.4	0.0	20.1	1.1	
Surface	GP-05_21.1	--	--	--	--	--	--	--	--	--	--	--	--	--	--	--	--	--	--	--	--	--	--	--	--	
Surface	GP-10_32.1	--	--	--	--	--	--	--	--	--	--	--	--	--	--	--	--	--	--	--	--	--	--	--	--	
Surface	GP-10_27.1	--	--	--	--	--	--	--	--	--	--	--	--	--	--	--	--	--	--	--	--	--	--	--	--	
Surface	GP-10_29.1	--	--	--	--	--	--	--	--	--	--	--	--	--	--	--	--	--	--	--	--	--	--	--	--	
Surface	GP-10_18.1	--	--	--	--	--	--	--	--	--	--	--	--	--	--	--	--	--	--	--	--	--	--	--	--	
Surface	GP-05_14.1	330.1	14.4	7.4	1.8	13.8	1.2	121.8	24.8	2327.4	134.3	5.3	0.5	0.3	0.2	26.6	0.7	2.1	0.3	4.9	0.3	0.7	0.1	22.6	1.2	
Surface	GP-05_5.1	657.0	28.6	4.4	1.1	3.8	0.3	16.4	3.3	5108.9	294.8	7.2	0.7	1.4	0.8	41.3	1.1	4.1	0.5	8.0	0.5	1.3	0.1	54.3	2.9	
Surface	GP-10_31.1	--	--	--	--	--	--	--	--	--	--	--	--	--	--	--	--	--	--	--	--	--	--	--	--	
Surface	GP-05_7.1	320.4	13.9	9.3	2.3	4.1	0.4	8.5	1.7	1536.8	88.7	6.7	0.7	0.6	0.4	14.6	0.4	0.9	0.1	1.9	0.1	0.4	0.0	15.9	0.9	
Surface	GP-05_18.1	583.2	25.4	7.7	1.9	4.2	0.4	13.4	2.7	1733.0	100.0	4.9	0.5	1.7	1.0	11.7	0.3	1.4	0.2	2.0	0.1	0.5	0.1	16.4	0.9	
Surface	GP-05_6.1	--	--	--	--	--	--	--	--	--	--	--	--	--	--	--	--	--	--	--	--	--	--	--	--	
Surface	GP-10_13.1	120.3	5.2	7.0	1.7	10.8	0.9	16.9	3.4	404.3	23.3	2.6	0.3	0.1	0.0	6.5	0.2	0.2	0.0	0.5	0.0	0.1	0.0	4.0	0.2	
Surface	GP-05_22.1	--	--	--	--	--	--	--	--	--	--	--	--	--	--	--	--	--	--	--	--	--	--	--	--	
Surface	GP-10_3.1	833.4	36.3	3.3	0.8	24.5	2.1	48.2	9.8	4941.9	285.1	11.3	1.2	0.1	0.0	59.7	1.6	6.1	0.7	12.2	0.7	1.9	0.2	70.8	3.8	
Surface	GP-05_19.1	259.5	11.3	6.9	1.7	16.3	1.4	14.6	3.0	1505.4	86.9	1.1	0.1	0.6	0.4	10.4	0.3	1.7	0.2	3.4	0.2	1.4	0.2	22.4	1.2	
Surface	GP-05_28.1	--	--	--	--	--	--	--	--	--	--	--	--	--	--	--	--	--	--	--	--	--	--	--	--	
Surface	GP-05_4.1	447.4	19.5	5.3	1.3	11.2	0.9	83.2	16.9	3147.4	181.6	8.2	0.8	0.2	0.1	58.4	1.5	6.7	0.8	13.8	0.8	1.4	0.1	84.1	4.5	
Surface	GP-05_3.1	423.0	18.4	5.8	1.4	5.5	0.5	16.1	3.3	3372.5	194.6	3.1	0.3	0.2	0.1	25.3	0.7	3.0	0.4	5.4	0.3	1.1	0.1	38.4	2.1	
Surface	GP-10_20.1	--	--	--	--	--	--	--	--	--	--	--	--	--	--	--	--	--	--	--	--	--	--	--	--	
Surface	GP-05_8.1	226.8	9.9	3.0	0.7	2.9	0.2	5.5	1.1	1098.3	63.4	7.1	0.7	0.3	0.2	14.7	0.4	1.2	0.1	1.3	0.1	0.2	0.0	12.0	0.6	
Surface	GP-05_25.1	--	--	--	--	--	--	--	--	--	--	--	--	--	--	--	--	--	--	--	--	--	--	--	--	
Surface	GP-05_30.1	--	--	--	--	--	--	--	--	--	--	--	--	--	--	--	--	--	--	--	--	--	--	--	--	
Surface	GP-05_26.1	244.9	10.7	6.8	1.7	8.8	0.7	15.3	3.1	1375.4	79.4	4.9	0.5	0.1	0.1	14.4	0.4	0.7	0.1	1.5	0.1	0.3	0.0	12.1	0.6	
Surface	GP-10_2.1	328.5	14.3	10.2	2.5	13.9	1.2	65.2	13.3	2383.3	137.5	1.7	0.2	0.1	0.0	14.2	0.4	3.4	0.4	5.5	0.3	2.3	0.2	38.4	2.1	
Surface	GP-05_26.1	--	--	--	--	--	--	--	--	--	--	--	--	--	--	--	--	--	--	--	--	--	--	--	--	
Surface	GP-05_13.1	492.6	21.4	7.1	1.8	8.7	0.7	27.1	5.5	2593.9	149.7	1.1	0.1	3.1	1.8	13.8	0.4	8.5	1.0	8.2	0.5	3.2	0.3	50.5	2.7	
Surface	GP-05_1.1	278.1	12.1	6.6	1.6	26.1	2.2	95.3	19.4	2962.8	171.0	3.8	0.4	1.5	0.9	15.0	0.4	4.4	0.5	8.2	0.5	2.3	0.2	50.2	2.7	
Surface	GP-05_11.1	627.1	27.3	3.2	0.8	3.7	0.3	11.4	2.3	1248.9	72.1	0.0	0.0	2.0	1.1	9.5	0.3	1.3	0.2	1.5	0.1	0.3	0.0	10.2	0.5	
Surface	GP-05_12.1	349.0	15.2	6.2	1.5	2.5	0.2	6.8	1.4	1061.8	61.3	1.2	0.1	0.2	0.1	9.2	0.2	0.5	0.1	1.0	0.1	0.2	0.0	8.7	0.5	
Surface	GP-05_15.1	310.4	13.5	6.7	1.6	5.9	0.5	15.8	3.2	3803.6	219.5	5.7	0.6	0.9	0.5	29.5	0.8	2.9	0.3	6.2	0.4	1.3	0.1	38.1	2.0	
Surface	GP-05_16.1	243.0	10.6	8.2	2.0	4.7	0.4	7.3	1.5	1340.1	77.3	2.9	0.3	0.3	0.2	12.0	0.3	0.6	0.1	1.3	0.1	0.3	0.0	11.9	0.6	
Surface	GP-05_17.1	311.7	13.6	8.2	2.0	6.0	0.5	6.3	1.3	2411.6	139.2	2.5	0.3	0.4	0.2	8.2	0.2	4.5	0.5	6.7	0.4	2.1	0.2	47.5	2.5	
Surface	GP-10_17.1	362.8	15.8	7.3	1.8	11.9	1.0	20.3	4.1	3057.9	176.4	2.1	0.2	0.3	0.2	19.0	0.5	6.0	0.7	8.6	0.5	3.3	0.4	48.8	2.6	
Surface	GP-10_4.1	220.8	9.6	7.3	1.8	149.5	12.6	232.2	47.2	1476.2	85.2	1.7	0.2	0.0	0.0	8.6	0.2	1.2	0.1	3.3	0.2	1.3	0.1	18.7	1.0	
Surface	GP-10_8.1	260.1	11.3	7.6	1.9	10.4	0.9	46.2	9.4	1609.1	92.8	1.8	0.2	0.0	0.0	11.6	0.3	1.1	0.1	2.5	0.1	1.0	0.1	17.8	1.0	
Surface	GP-10_9.1	96.2	4.2	8.0	2.0	15.3	1.3	24.2	4.9	437.6	25.3	1.4	0.1	0.1	0.0	5.8	0.2	0.3	0.0	0.6	0.0	0.3	0.0	4.8	0.3	
Interior	GP10_4.1	361.6	26.3	120.3	10.0	7.0	1.6	0.8	0.1	1524.8	112.8	9.5	1.8	0.0	0.0	4.8	0.4	0.9	0.2	2.2	0.3	0.7	0.1	16.9	1.3	
Interior	GP10_17.1	342.1	24.9	103.9	8.6	10.5	2.5	1.3	0.1	1346.3	99.6	24.4	4.5	0.0	0.0	10.7	1.0	1.2	0.2	2.0	0.3	0.9	0.1	13.6	1.0	
Interior	GP10_22.1	225.7	16.4	70.0	5.8	6.7	1.6	0.9	0.1	965.8	71.5	19.3	3.5	0.0	0.0	8.8	0.8	0.4	0.1	1.5	0.2	0.6	0.1	10.7	0.8	
Interior	GP10_18.1	1013.7	73.8	125.6	10.5	4.5	1.1	0.8	0.1	2803.9	207.5	27.9	5.1	0.0	0.0	18.9	1.8	1.5	0.3	3.7	0.5	1.3	0.1	28.2	2.1	
Interior	GP10_12.1	622.5	45.3	135.6	11.3	8.2	1.9	0.7	0.1	2807.1	207.7	27.6	5.1	0.0	0.0	24.8	2.3	1.7	0.4	5.1	0.6	1.7	0.2	34.2	2.6	
Interior	GP05_16.1	204.7	14.9	52.3	4.4	5.1	1.2	0.9	0.1	1054.3	78.0	20.6	3.8	0.0	0.0	9.2	0.9	0.5	0.1	1.5	0.2	0.7	0.1	14.4	1.1	
Interior	GP10_20.1	164.2	12.0	47.0	3.9	5.2	1.2	0.4	0.0	850.9	63.0	20.0	3.7	0.0	0.0	6.5	0.6	0.7	0.1	1.3	0.2	0.6	0.1	9.8	0.7	
Interior	GP10_14.1	--	--	--	--	--	--	--	--	--	--	--	--	--	--	--	--	--	--	--	--	--	--	--	--	
Interior	GP10_9.1	436.2	31.8	103.9	8.6	7.8	1.8	0.9	0.1	1521.3	112.6	13.1	2.4	0.0	0.0	10.5	1.0	0.8	0.2	2.4	0.3	1.0	0.1	14.6	1.1	
Interior	GP10_11.1	892.9	65.0	95.3	7.9	5.0	1.2	1.1	0.1	2198.3	162.7	29.4	5.4	0.4	0.2	13.5	1.3	2.0	0.4	3.6	0.4	0.6	0.1	19.2	1.4	
Interior	GP10_10.1	232.7	16.9	55.0	4.6	7.0	1.7	1.4	0.1	589.7	43.6	21.3	3.9	0.1	0.0	5.8	0.5	0.3	0.1	0.7	0.1	0.3	0.0	5.5	0.4	
Interior	GP05_7.1	--	--	--	--	--	--	--	--	--	--	--	--	--	--	--	--	--	--	--	--	--	--	--	--	
Interior	GP10_15.1	--	--	--	--	--	--	--	--	--	--	--	--	--	--	--	--	--	--	--	--	--	--	--	--	
Interior	GP05_9.1	811.5	59.1	104.0	8.7	2.1	0.5	0.9	0.1	2027.8	150.1	25.8	4.7	0.0	0.0	9.1	0.8	0.9	0.2	3.2	0.4	0.6	0.1	21.5	1.6	
Interior	GP10_23.1	454.6	33.1	84.9	7.1	2.8	0.7	1.0	0.1	2547.6	188.5	26.8	4.9	0.0	0.0	34.8	3.2	1.3	0.3	3.8	0.5	0.5	0.0	26.1	2.0	
Interior	GP05_2.1	--	--	--	--	--	--	--	--	--	--	--	--	--	--	--	--	--	--	--	--	--	--	--	--	
Interior	GP05_6.1	279.6	20.4	57.7	4.8	2.2	0.5	1.1	0.1	1348.4	99.8	21.3	3.9	0.0	0.0	12.8	1.2	0.7	0.1	2.0	0.2	0.3	0.0	13.4	1.0	
Interior	GP05_14.1	--	--	--	--	--	--	--	--	--	--	--	--	--	--	--	--	--	--	--	--	--	--	--	--	
Interior	GP05_4.1	284.7	20.7	59.9	5.0	4.1	1.0	1.0	0.1	1116.3	82.6	22.5	4.1	0.0	0.0	10.3	1.0	1.2	0.2	2.9	0.4	0.9	0.1	19.2	1.4	
Interior	GP10_13.1	384.6	28.0	75.8	6.3	5.5	1.3	1.0	0.1	746.8	55.3	23.0	4.2	0.0	0.0	5.1	0.5	0.3	0.1	1.4	0.2	0.4	0.0	7.5	0.6	
Interior	GP05_1.1	327.6	23.8	61.1	5.1	2.1	0.5	0.7	0.1	1623.7	120.2	25.6	4.7	0.0	0.0	19.4	1.8	0.8	0.2	1.8	0.2	0.2	0.0	14.1	1.1	
Interior	GP05_19.1	258.1	18.8	75.8	6.3	5.7	1.3	1.0	0.1	1203.9	89.1	14.1	2.6	0.0	0.0	9.4	0.9	1.6	0.3	2.3	0.3	0.8	0.1	12.8	1.0	
Interior	GP10_16.1	492.3	35.8	72.0	6.0	4.5	1.1	0.7	0.1	2133.5	157.9	23.3	4.3	0.0	0.0	12.3	1.1	2.7	0.6	4.7	0.6	1.8	0.2	30.7	2.3	
Interior	GP05_12.1	356.3	25.9	51.9	4.3	3.5	0.8	0.9	0.1	1659.1	122.8	22.8	4.2	0.0	0.0	18.3	1.7	1.4	0.3	2.7	0.3	0.5	0.0	21.0	1.6	

Zr concentration is 47760 ppm from Claiborne et al. (2006)

Zircon model crystallization ages and trace element concentrations (ppm)

Grain location	Haupuru	Ho/Si	1 SD	Tb/Si	1 SD	Dy/Si	1 SD	Er/Si	1 SD	Tm/Si	1 SD	Yb/Si	1 SD	Lu/Si	1 SD	Hf/Si	1 SD	Pb/Si	1 SD	Th/Si	1 SD	U/Si	1 SD	
Surface	GP-10_6.1	65.1	3.1	12.6	0.6	128.0	21.2	268.8	9.5	57.4	3.5	525.3	24.1	128.3	3.4	10411.6	219.7	0.0	0.0	85.4	5.5	89.1	2.3	
Surface	GP-10_11.1	58.8	2.8	10.4	0.5	130.4	21.6	244.3	8.6	53.2	3.3	487.6	22.4	118.7	3.1	11004.3	232.2	0.0	0.0	87.5	5.7	103.1	2.7	
Surface	GP-10_22.1	--	--	--	--	--	--	--	--	--	--	--	--	--	--	--	--	--	--	--	--	--	--	
Surface	GP-10_5.1	76.2	3.7	14.7	0.7	183.1	30.4	355.2	12.5	76.2	4.7	710.9	32.6	172.5	4.5	12293.3	259.4	0.0	0.0	135.1	8.7	144.8	3.8	
Surface	GP-10_16.1	36.4	1.8	4.5	0.2	77.1	12.8	168.6	5.9	39.2	2.4	395.0	18.1	92.1	2.4	11194.7	236.2	0.0	0.0	58.2	3.8	90.5	2.4	
Surface	GP-10_26.1	--	--	--	--	--	--	--	--	--	--	--	--	--	--	--	--	--	--	--	--	--	--	
Surface	GP-10_15.1	80.2	3.9	13.4	0.7	149.5	24.8	363.9	12.8	84.7	5.2	803.3	36.9	206.9	5.4	11646.3	245.7	0.1	0.0	46.4	3.0	130.4	3.4	
Surface	GP-10_7.1	72.0	3.5	11.9	0.6	149.4	24.8	295.5	10.4	61.6	3.8	544.9	25.0	136.6	3.6	10244.5	216.2	0.1	0.0	97.6	6.3	101.1	2.6	
Surface	GP-10_33.1	--	--	--	--	--	--	--	--	--	--	--	--	--	--	--	--	--	--	--	--	--	--	
Surface	GP-05_2.1	69.1	3.3	12.9	0.6	165.2	27.4	321.6	11.3	72.7	4.5	677.9	31.1	166.7	4.4	11548.4	243.7	0.0	0.0	130.1	8.4	156.0	4.1	
Surface	GP-10_19.1	--	--	--	--	--	--	--	--	--	--	--	--	--	--	--	--	--	--	--	--	--	--	
Surface	GP-10_10.1	--	--	--	--	--	--	--	--	--	--	--	--	--	--	--	--	--	--	--	--	--	--	
Surface	GP-10_21.1	--	--	--	--	--	--	--	--	--	--	--	--	--	--	--	--	--	--	--	--	--	--	
Surface	GP-10_1.1	51.1	2.5	10.3	0.5	111.9	18.5	237.3	8.4	55.0	3.4	540.7	24.8	135.5	3.6	11239.8	237.2	0.0	0.0	116.6	7.5	130.9	3.4	
Surface	GP-10_25.1	--	--	--	--	--	--	--	--	--	--	--	--	--	--	--	--	--	--	--	--	--	--	
Surface	GP-05_20.1	--	--	--	--	--	--	--	--	--	--	--	--	--	--	--	--	--	--	--	--	--	--	
Surface	GP-10_12.1	58.1	2.8	11.3	0.6	135.2	22.4	294.8	10.4	63.9	3.9	615.3	28.2	149.9	3.9	11658.3	246.0	0.0	0.0	122.5	7.9	153.3	4.0	
Surface	GP-05_23.1	--	--	--	--	--	--	--	--	--	--	--	--	--	--	--	--	--	--	--	--	--	--	
Surface	GP-10_14.1	75.5	3.6	10.6	0.5	129.1	21.4	274.2	9.7	66.9	4.1	623.4	28.6	146.8	3.8	13008.6	274.5	0.0	0.0	196.1	12.7	309.1	8.0	
Surface	GP-05_9.1	60.4	2.9	9.3	0.5	124.0	20.6	289.8	10.2	68.0	4.2	689.4	31.6	159.3	4.2	12056.1	254.4	0.0	0.0	275.3	17.8	521.5	13.6	
Surface	GP-05_21.1	--	--	--	--	--	--	--	--	--	--	--	--	--	--	--	--	--	--	--	--	--	--	
Surface	GP-10_32.1	--	--	--	--	--	--	--	--	--	--	--	--	--	--	--	--	--	--	--	--	--	--	
Surface	GP-10_27.1	--	--	--	--	--	--	--	--	--	--	--	--	--	--	--	--	--	--	--	--	--	--	
Surface	GP-10_29.1	--	--	--	--	--	--	--	--	--	--	--	--	--	--	--	--	--	--	--	--	--	--	
Surface	GP-10_18.1	--	--	--	--	--	--	--	--	--	--	--	--	--	--	--	--	--	--	--	--	--	--	
Surface	GP-05_14.1	77.5	3.7	13.8	0.7	152.3	25.2	338.9	11.9	73.1	4.5	666.8	30.60	162.4	4.3	12227.1	258.0	0.0	0.0	331.4	21.4	439.1	11.4	
Surface	GP-05_5.1	130.6	6.3	23.2	1.2	257.1	42.6	539.3	19.0	119.9	7.4	1043.7	47.9	244.5	6.4	15243.3	321.6	0.0	0.0	487.4	31.5	621.7	16.2	
Surface	GP-10_31.1	--	--	--	--	--	--	--	--	--	--	--	--	--	--	--	--	--	--	--	--	--	--	
Surface	GP-05_7.1	49.5	2.4	7.8	0.4	93.9	15.6	224.5	7.9	53.0	3.3	489.6	22.5	126.2	3.3	13960.3	294.6	0.1	0.0	146.2	9.5	316.6	8.2	
Surface	GP-05_18.1	59.1	2.9	8.7	0.4	123.0	20.4	276.6	9.7	65.6	4.0	648.4	29.8	161.3	4.2	13168.6	277.9	0.0	0.0	152.9	9.9	366.8	9.5	
Surface	GP-05_6.1	--	--	--	--	--	--	--	--	--	--	--	--	--	--	--	--	--	--	--	--	--	--	
Surface	GP-10_13.1	13.5	0.7	1.8	0.1	22.5	3.7	60.0	2.1	14.5	0.9	144.4	6.6	36.3	1.0	11836.7	249.8	0.0	0.0	39.5	2.6	92.1	2.4	
Surface	GP-05_22.1	--	--	--	--	--	--	--	--	--	--	--	--	--	--	--	--	--	--	--	--	--	--	
Surface	GP-10_3.1	152.3	7.4	22.9	1.1	309.9	51.4	539.8	19.0	114.0	7.0	1006.8	46.2	227.5	6.0	13688.7	288.8	0.0	0.0	398.3	25.8	432.8	11.3	
Surface	GP-05_19.1	50.1	2.4	9.9	0.5	113.8	18.9	232.6	8.2	49.9	3.1	468.2	21.5	106.7	2.8	10932.2	230.7	0.0	0.0	68.4	4.4	76.5	2.0	
Surface	GP-05_28.1	--	--	--	--	--	--	--	--	--	--	--	--	--	--	--	--	--	--	--	--	--	--	
Surface	GP-05_4.1	162.9	7.9	26.1	1.3	424.9	70.5	754.9	26.6	156.3	9.6	1362.9	62.6	299.5	7.8	15278.6	322.4	0.0	0.0	667.1	43.2	793.3	20.6	
Surface	GP-05_3.1	95.2	4.6	17.0	0.8	176.8	29.3	414.4	14.6	91.8	5.7	833.4	38.3	188.6	4.9	13549.1	285.9	0.0	0.0	315.2	20.4	429.4	11.2	
Surface	GP-10_20.1	--	--	--	--	--	--	--	--	--	--	--	--	--	--	--	--	--	--	--	--	--	--	
Surface	GP-05_8.1	33.9	1.6	5.3	0.3	60.9	10.1	153.8	5.4	34.4	2.1	321.7	14.8	78.9	2.1	12535.8	264.5	0.0	0.0	116.1	7.5	246.9	6.4	
Surface	GP-05_25.1	--	--	--	--	--	--	--	--	--	--	--	--	--	--	--	--	--	--	--	--	--	--	
Surface	GP-05_30.1	--	--	--	--	--	--	--	--	--	--	--	--	--	--	--	--	--	--	--	--	--	--	
Surface	GP-05_10.1	37.2	1.8	5.6	0.3	81.0	13.4	178.4	6.3	41.3	2.5	379.9	17.4	96.2	2.5	12729.2	268.6	0.0	0.0	115.9	7.5	222.5	5.8	
Surface	GP-10_2.1	82.3	4.0	16.0	0.8	188.9	31.3	366.4	12.9	78.9	4.9	744.6	34.2	178.0	4.7	13171.5	277.9	0.0	0.0	120.3	7.8	130.3	3.4	
Surface	GP-05_26.1	--	--	--	--	--	--	--	--	--	--	--	--	--	--	--	--	--	--	--	--	--	--	
Surface	GP-05_13.1	81.5	3.9	17.6	0.9	181.6	30.1	334.9	11.8	68.0	4.2	583.0	26.8	132.0	3.5	13078.2	276.0	0.1	0.0	130.1	8.4	177.2	4.6	
Surface	GP-05_1.1	105.3	5.1	18.0	0.9	217.2	36.0	389.3	13.7	84.7	5.2	707.8	32.5	163.3	4.3	12682.7	267.6	0.0	0.0	202.2	13.1	266.6	6.9	
Surface	GP-05_11.1	38.6	1.9	5.9	0.3	74.1	12.3	190.6	6.7	45.8	2.8	459.9	21.1	118.7	3.1	12633.3	266.6	0.0	0.0	118.9	7.7	290.8	7.6	
Surface	GP-05_12.1	32.0	1.5	4.5	0.2	64.5	10.7	156.6	5.5	40.5	2.5	402.7	18.5	103.3	2.7	13282.0	280.2	0.0	0.0	96.1	6.2	247.4	6.4	
Surface	GP-05_15.1	90.3	4.4	16.8	0.8	201.1	33.3	384.1	13.5	81.9	5.1	777.0	35.7	184.0	4.8	12038.2	254.0	0.0	0.0	271.1	17.5	298.9	7.8	
Surface	GP-05_16.1	32.6	1.6	5.1	0.3	68.4	11.3	148.0	5.2	33.6	2.1	335.0	15.4	84.7	2.2	13114.9	276.7	0.0	0.0	112.6	7.3	185.4	4.8	
Surface	GP-05_17.1	93.6	4.5	17.9	0.9	238.0	39.5	368.8	13.0	73.7	4.5	634.5	29.1	143.3	3.8	10703.7	225.8	0.0	0.0	146.9	9.5	182.7	4.8	
Surface	GP-10_17.1	93.7	4.5	17.5	0.9	169.7	28.1	374.2	13.2	82.8	5.1	693.4	31.8	159.9	4.2	9824.7	207.3	0.0	0.0	154.1	10.0	157.9	4.1	
Surface	GP-10_4.1	44.3	2.1	9.7	0.5	102.0	16.9	233.2	8.2	53.1	3.3	520.8	23.9	125.3	3.3	10422.0	219.9	0.0	0.0	103.7	6.7	110.2	2.9	
Surface	GP-10_8.1	42.0	2.0	6.9	0.3	83.8	13.9	174.0	6.1	40.5	2.5	369.6	17.0	88.0	2.3	11275.9	237.9	0.0	0.0	47.2	3.1	62.0	1.6	
Surface	GP-10_9.1	16.0	0.8	2.3	0.1	31.0	5.1	78.2	2.8	20.2	1.2	215.4	9.9	57.1	1.5	11022.2	232.6	0.0	0.0	26.5	1.7	61.0	1.6	
Interior	GP10_4.1	47.3	3.2	7.3	0.5	105.0	6.5	238.4	20.8	55.8	3.7	507.4	33.0	133.4	12.7	9282.6	568.1	0.0	0.0	38.3	2.6	100.9	6.9	
Interior	GP10_17.1	38.7	2.6	6.3	0.5	83.3	5.1	183.5	16.0	44.6	3.0	422.2	27.5	109.6	10.4	9277.1	567.8	0.0	0.0	60.8	4.2	79.3	5.4	
Interior	GP10_22.1	32.1	2.2	4.9	0.4	73.1	4.5	164.9	14.4	41.3	2.8	376.4	24.5	98.7	9.4	8513.6	521.0	0.0	0.0	60.7	4.2	94.4	6.5	
Interior	GP10_18.1	80.0	5.5	14.5	1.0	177.1	10.9	385.9	33.6	93.9	6.3	820.5	53.4	201.9	19.2	9401.1	575.3	0.0	0.0	159.9	11.0	213.2	14.6	
Interior	GP10_12.1	86.5	5.9	16.9	1.2	202.9	12.5	423.7	36.9	101.4	6.8	893.6	58.2	220.1	20.9	9318.4	570.3	0.0	0.0	270.9	18.7	265.9	18.2	
Interior	GP05_16.1	33.8	2.3	6.8	0.5	83.3	5.1	162.6	14.2	37.7	2.5	350.3	22.8	92.5	8.8	10001.6	612.1	0.0	0.0	56.3	3.9	69.5	4.8	
Interior	GP10_20.1	27.6	1.9	5.0	0.4	71.9	4.4	148.2	12.9	35.3	2.4	318.2	20.7	84.2	8.0	9201.4	563.1	0.0	0.0	58.3	4.0	75.0	5.1	
Interior	GP10_14.1	--	--	--	--	--	--	--	--	--	--	--	--	--	--	--	--	--	--	--	--	--	--	
Interior	GP10_9.1	42.7	2.9	6.9	0.5	91.4	5.6	214.3	18.7	53.3	3.6	501.0	32.6	129.4	12.3	8873.1	543.0	0.0	0.0	57.4	4.0	93.9	6.4	
Interior	GP10_11.1	54.7	3.7	8.6	0.6	114.5	7.1	255.7	22.3	66.0	4.4	598.5	39.0	159.8	15.2	10993.9	672.8	0.0	0.0	141.6	9.8	651.6	44.7	
Interior	GP10_10.1	16.5	1.1	2.7	0.2	39.4	2.4	90.9	7.9	21.6	1.5	214.9	14.0	58.6	5.6	9973.8	610.4	0.0	0.0	24.6	1.7	44.6	3.1	
Interior	GP05_7.1	--	--	--	--	--	--	--	--	--	--	--	--	--	--	--	--	--	--	--	--	--	--	
Interior	GP10_15.1	--	--	--	--	--	--	--	--	--	--	--	--	--	--	--	--	--	--	--	--	--	--	
Interior	GP05_9.1	58.0	3.9	10.4	0.7	133.8	8.2	268.0	23.3	65.8	4.4	588.3	38.3	147.8	14.0	9078.0	555.6	0.0	0.0	175.3	12.1	294.3	20.2	
Interior	GP10_23.1	71.1	4.8	13.2	0.9	158.0	9.7	351.9	30.7	82.4	5.5	751.6	48.9	185.6	17.6	10616.0	649.7	0.0	0.0	439.2	30.3	657.3	45.1	
Interior	GP05_2.1	--	--	--	--	--	--	--	--	--	--	--	--	--	--	--	--	--	--	--	--	--	--	
Interior	GP05_6.1	41.9	2.9	6.5	0.5	89.0	5.5	201.7	17.6	52.7	3.5	448.0	29.2	123.1	11.7	10642.3	651.3	0.0	0.0	151.1	10.4	303.8	20.8	
Interior	GP05_14.1	--	--	--	--	--	--	--	--	--	--	--	--	--	--	--	--	--	--	--	--	--	--	
Interior	GP05_4.1	45.7	3.1	9.1	0.7	116.4	7.2	227.0	19.8	53.1	3.6	490.2	31.9	127.8	12.1	10324.4	631.9	0.0	0.0	95.1	6.6	128.1	8.8	
Interior	GP10_13.1	22.8	1.6	3.6	0.3	51.9	3.2	118.0	10.3	28.3	1.9	264.1	17.2	72.3	6.9	10156.5	621.6	0.0	0.0	21.4	1.5	49.7	3.4	
Interior	GP05_1.1	47.1	3.2	7.2	0.5	97.1	6.0	239.2	20.8	59.2	4.0	566.5	36.9	144.3	13.7	11559.7	707.5	0.0	0.0	183.8	12.7	362.3	24.9	
Interior	GP05_19.1	35.0	2.4	6.8	0.5	78.7	4.8	165.0	14.4	40.3	2.7	397.5	25.9	105.9	10.1	9936.9	608.1	0.0	0.0	55.2	3.8	86.1	5.9	
Interior	GP10_16.1	66.0	4.5	12.4	0.9	149.9	9.2	304.6	26.5	70.3	4.7	647.9	42.2	164.6	15.6	9710.2	594.3	0.0	0.0	137.1	9.5	143.3	9.8	
Interior	GP05_12.1	52.9	3.6	10.1	0.7	122.0	7.5	255.3	22.2	60.8	4.1	535.6	34.9	134.1	12.7	10574.7	647.2	0.0	0.0	287.7	19.9	339.2	23.3	

Zr concentration is 47760 ppm from Claiborne et al. (2006)

CHAPTER THREE

Improving the Accuracy of (^{238}U)/(^{230}Th) Bulk Crystallization Ages of Major Phase Silicate Minerals in Volcanic Rock

Elizabeth R. G. Grant
Kari M. Cooper
Darren M. Gravley
Chad D. Deering
Adam J.R. Kent

3.1 ABSTRACT

^{238}U-^{230}Th geochronology is a useful tool to date materials between ~10,000 and 250,000 ka, an age range that is difficult to resolve using other geochronometers. In-situ U-series measurements on U- and Th-rich minerals such as zircon, apatite, or allanite, by secondary ion microprobe instruments (SIMS) can yield accurate crystallization ages at relatively high precision. Major phases minerals, such as plagioclase, have significantly lower concentrations of U and Th, which precludes their analysis by in-situ methods (i.e. SIMS). Therefore, to obtain a U-series crystallization age for plagioclase, U and Th concentrations are measured by dissolution of bulk separates containing hundreds to thousands of grains, and the interpretation of the data can be complicated by the presence of mineral or glass inclusions within the separates. Here we developed a new mineral purification workflow designed to remove included phases (e.g. zircon, apatite, glass) from bulk mineral separates, with the goal of identifying the true crystallization age of the major mineral in the separate. We applied this new workflow to major phase minerals in ignimbrite deposits from the Okataina Volcanic Center (Taupo Volcanic Zone, New Zealand). Despite significant efforts to remove inclusions from major mineral phases, our results show that there is no difference between the bulk plagioclase and the glass (^{238}U)/(^{232}Th) ratios, thereby suggesting that the bulk mineral plagioclase separate was still dominated by included phases. Although other studies have found success dating bulk mineral ages using ^{238}U-^{230}Th geochronology in other systems (and in one case in the TVZ), we speculate that the complex crystal mush system that feeds TVZ eruptions could make producing a high-purity bulk mineral separate particularly challenging. Long residence times, antecrystic materials, and magmas multiply saturated in up to 8 phases complicate mineral growth and result in bulk separates that contain multiple minerals of different ages. While our attempt to remove all inclusions was

ultimately unsuccessful despite our intensive treatment of the samples, this workflow might be useful in other situations and/or for less complicated samples. We strongly suggest to those measuring U-series disequilibria in bulk mineral separates to first thoroughly characterize all target materials to ensure that the U-series crystallization age reflects the age of the target material and not the inclusions within, and to hand pick final mineral separates to minimize the number of inclusions within grains in the sample. In some cases, samples from mushy magma reservoirs with complicated crystals might be avoided for bulk analyses.

3.2 INTRODUCTION

Major phase minerals in ignimbrite deposits commonly contain many inclusions of zircon, apatite, pyrrhotite, Fe-Ti oxides, and glass. This poses problems for analytical techniques such as ^{238}U-^{230}Th geochronology, where bulk mineral separates are analyzed for some phases. Although in-situ microbeam ^{238}U-^{230}Th geochronology can provide high-resolution dates on small spatial scales when dating minerals with high concentrations of U and/or Th (e.g. zircon, allanite, monazite), current in-situ analytical techniques do not yet have the sensitivity necessary to date individual spots within minerals with the low (10^{-2}–10^{-1} ppm) concentrations of U and Th expected in, for example, plagioclase or sanidine crystals (Reid 1997, Stelten et al. 2015, Rubin et al. 2016, Reid and Vazquez 2017, Marcaida et al. 2019). Due to the low concentrations of U and Th in major phase minerals, crystallization ages for these phases are measured by bulk dissolution of hundreds to thousands of grains. In doing so, U and Th in the bulk separate reflect the volume- and concentration-weighted average of all phases in the separate, obscuring any zoning within minerals, and potentially obscuring the crystallization age of the major mineral if the budgets of U and Th are dominated by inclusions with relatively high concentrations of these

elements (e.g. glass inclusions, accessory phases). Given the challenges in dating major minerals relative to accessory minerals using ^{238}U-^{230}Th geochronology, it is unsurprising that there are relatively few major mineral crystallization dates in the literature (e.g., Cooper et al. 2001, Charlier et al. 2003, Cooper and Donnelley 2008, Eppich et al. 2012, Rubin 2016, Schlieder et al. 2022, Stelten et al. 2012, Stelten et al. 2015). Cases where major mineral analyses were attempted but were not successful are not typically published, making it difficult to assess when such analyses are likely to be successful, and potentially leading to duplicate unsuccessful efforts.

Major minerals with simple growth histories, autocrystic populations, and short magma residence times yield less complicated ^{238}U-^{230}Th crystallization ages than major minerals from long-lived and expansive magma mush systems. Experimental studies in rhyolitic and dacitic magmas show that in some cases inclusion-free plagioclase grow rapidly from degassing or decompression (ascent) (Cashman 1992, Hammer et al. 1999, Hammer et al. 2000, Waters et al. 2015). In these studies, minerals grow rapidly from the same host melt, and without the complication of many neighboring grains which allows them to grow relatively inclusion-free. And in cases where such processes are dominant, analysis of bulk separates typically yield resolvable ages. For example, Stelten et al. (2015) analyzed bulk samples of sanidine and glass from the Central Plateau Member of Yellowstone Caldera (USA) and were able to resolve crystallization ages that coincide with the eruption ages of the lava flows. They concluded that the sanidine grew from the assembled melt immediately prior to eruption and therefore had a short residence time. Cooper and Donnelley (2008) and Schlieder et al. (2022) analyzed bulk plagioclase separates from a series of Mount St. Helens eruptive deposits and were able to deconvolve multiple plagioclase populations variably tapped for different eruptions. In both

studies, plagioclase contained antecrystic cores but relatively few inclusions. Cooper et al. (2001) analyzed bulk plagioclase and clinopyroxene separates in Hawaiian lava and found that preserved ^{230}Th-^{226}Ra disequilibria in suggested that plagioclase crystallized within hundreds of years prior to eruption. Eppich et al. (2012) were also able to successfully date bulk plagioclase separates from recent eruptions at Mount Hood, OR, USA, using ^{230}Th-^{226}Ra disequilibria, yielding average ages on the order of kyrs, although the ^{238}U-^{230}Th disequilibria in the same separates yield older average ages, providing evidence for old cores (>10 ka). In contrast, although ^{230}Th-^{226}Ra dating of plagioclase in Volcan Quizapu was successful, ^{238}U-^{230}Th analyses of the same bulk mineral separates did not result in resolvable ages due to contamination with glass inclusions (Ruprecht and Cooper, 2012).

Magmatic systems that contain significant antecrystic crystal mushes scavenged as crystal cargo during eruption do not always yield clear ^{238}U-^{230}Th crystallization ages (e.g., Rubin 2016). The Okataina Volcanic Center (OVC), Taupo Volcanic Zone (TVZ), New Zealand, is an active volcanic center, with eruptions dating from ~557 (Utu Caldera-forming eruption) to 1886 CE (Tarawera basaltic fissure eruption) (Cole et al. 2014). Minerals from pyroclastic deposits, airfall deposits, and lavas show that the mineral cargo is complex: antecrystic cores with evidence of resorption, glomerocrystic clusters, and a full range of mineral inclusions including glass, and major and accessory minerals. Such complexities make it difficult to date major phases by bulk dissolution; for example, Rubin (2016) reported inconclusive ^{238}U-^{230}Th crystallization ages from TVZ plagioclase. In contrast, Charlier et al. (2003) found success dating plagioclase from the Rotoiti eruption, yielding resolvable ^{238}U-^{230}Th crystallization ages.

The presence of mineral and glass inclusions in OVC plagioclase and other major phases has been documented by other studies (Charlier et al. 2003, Molloy et al. 2008, Grant et al. 2024,

Schmitz and Smith 2004). SEM imaging of Rotoiti and EQF pumice (Fig. 3.2) show abundant accessory mineral inclusions of zircon, apatite, pyrrhotite, Fe-Ti oxides, and glass, as well as major phases included within other major phases (i.e. clinopyroxene in hornblende, biotite in hornblende, plagioclase in biotite, etc). In an effort to get a crystallization age from a multi-point isochron (in this study between glass, plagioclase, biotite, and hornblende), we have developed and tested a new mineral purification workflow in which we attempt to rid bulk mineral separates of any included phases, but chiefly zircon and apatite. Although this method was not entirely successful in the case of the Rotoiti and EQF mineral separates, this workflow could be useful in other studies.

3.2.1 Materials and equipment

This work was conducted at the University of California Davis. Materials required for this include basic laboratory glassware (beakers, separation funnels), consumables (wipes, acetone, methanol, weigh paper, sieve mesh), and laboratory equipment (heat lamp, sonicator, sieves, mortar and pestle). Specialized materials for this work include a Franz Magnetic Barrier Separator, hydrofluoric (HF) acid for leaching, and methylene iodide (diiodomethane) for density separation.

3.2.2 Sample collection

Samples were collected from the Okataina Volcanic Center (OVC), Taupo Volcanic Zone (TVZ), New Zealand, as part of an NSF-funded project to understand chemical, thermal, and temporal variations in the magma reservoir across a caldera-forming cycle (Fig 1). To address this problem, we sampled a pre-caldera forming eruption (Kakapiko Dome, eruption <~147 ka),

caldera forming eruption (Rotoiti, eruption ~45–60 ka), syn-caldera-forming eruption (Earthquake Flat, eruption ~45–60 ka), and post-caldera eruption (Hauparu, eruption ~36 ka). Earthquake Flat erupted shortly after the Rotoiti caldera-forming eruption, on the order of hours to weeks (Molloy et al. 2008) but erupted from an array of vents ~20 km southwest of the Rotoiti vent location (Haroharo linear vent zone). We collected three nonwelded tuff samples (Rotoiti, Earthquake Flat, Hauparu) and one dome sample (Kakapiko Dome/Trig Dome) from the following sampling locations (NZGD 1949): Rotoiti (IGSN: IEUCD0003) -37.842581, 176.628237; Earthquake Flat (IGSN: IEUCD000N) -38.311118, 176.37911; Hauparu (IGSNs: IEUCD0005, IEUCD0006, IEUCD000A) -37.870185, 176.523368 and -38.132588, 176.805149; Kakapiko Dome: -38.20800708, 176.28182654). Samples were collected at roadcuts and from a single stratigraphic horizon, with the exception of Hauparu which was sampled in two locations. We targeted pumice-rich lenses and preferentially sampled the largest pumice in each outcrop. Samples were not observably affected by vapor-phase alteration, devitrification, or hydrothermal alteration.

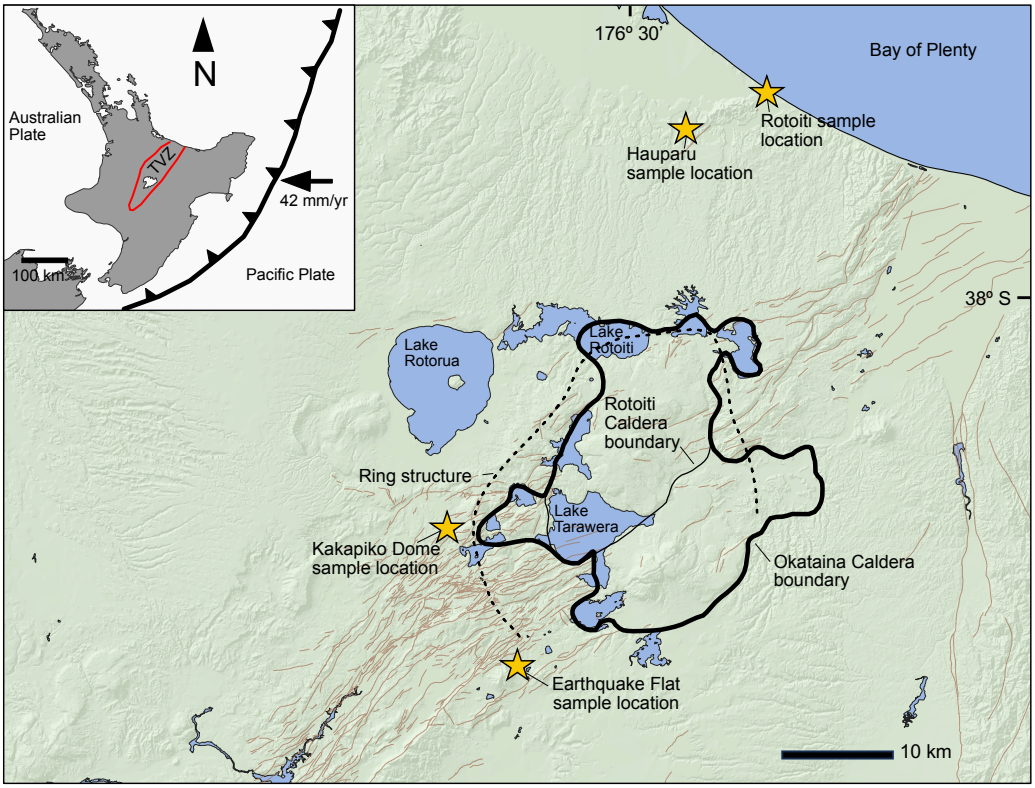


***Figure 3.1**: Map of the Okataina Volcanic Center (OVC) (thick black line), Rotoiti Caldera boundary (thin black line), and OVC ring structure (dashed black Line) from Nairn 2002 and Sas et al. 2021; sampling locations from this study indicated by yellow stars; hillshade and lake polygon layer publicly available at linz.govt.nz; regional fault layer from Langridge et al. (2016); Inset regional tectonic map, Pacific Plate trench location and convergence rate from Deering et al. 2011.*

3.3 METHODS

3.3.1 Imaging of mineral inclusions

Grain mounts and thin sections were prepared for SEM and electron microprobe (EMP) imaging. Figure 3.2 presents example images of major minerals from the EQF tuff deposit. Major minerals contain inclusions of glass, apatite, zircon, titanomagnetite, pyrrhotite, and other major minerals. Hornblende crystals contain clinopyroxenitic cores, indicative of an incomplete equilibrium

reaction, along with inclusions of glass, apatite, and titanomagnetite (Fig. 3.2A), and biotite grains contain large (>200 µm) plagioclase inclusions, indicative of co-crystalizing phases in close proximity in addition to inclusions of glass, apatite, and titanomagnetite (Fig. 3.2B). Poly-mineralic clusters with complicated spatial relationships are consistent with minerals that nucleated in close proximity (Fig. 3.2C, 3.2E). Plagioclase crystals (Fig. 3.2D, 3.2E) show calcic (An_{61}), resorbed cores, suggesting that plagioclase were not always in equilibrium with the host melt, but thick (>200 µm), sodic (An_{24}) rims suggest that the latest stage of plagioclase growth from in a relatively evolved melt without interreference by mafic rejuvenation (Grant et al. 2024). For all minerals, but especially for plagioclase, glassy melt inclusions are abundant (Fig. 3.2F).

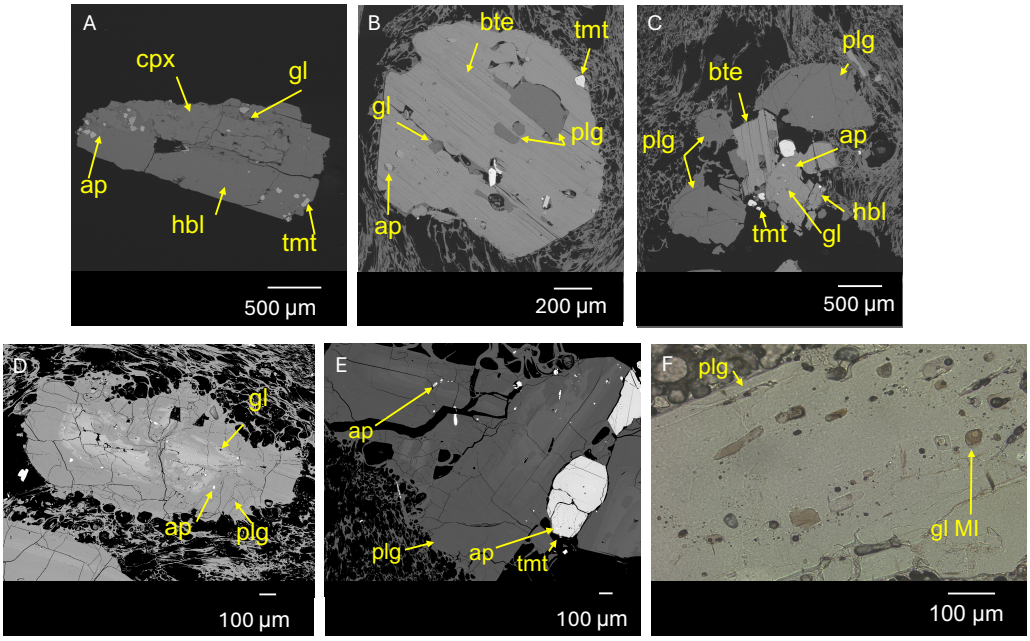


***Figure 3.2**: Back-scattered electron (BSE) images of EQF pumice phases, qtz quartz, plg plagioclase, bte biotite, ap apatite, tmt titanomagnetite (Fe-Ti oxides), hbl hornblende, cpx*

clinopyroxene, gl MI glass/melt inclusion; Panel A: subhedral hornblende with clinoferrosilite core, and apatite, glass, and titanomagnetite inclusions; Panel B: euhedral biotite grain with plagioclase, glass, and titanomagnetite inclusions; Panel C: poly-mineralic cluster including plagioclase, biotite, hornblende, and large titanomagnetite grains, biotite is included with glass, and hornblende is included with glass, apatite, and titanomagnetite grains; Panel D: subhedral plagioclase with calcic core, and with inclusions of glass and apatite; Panel E: subhedral twinned plagioclase and titanomagnetite cluster, both which contain apatite inclusions; Panel F: photomicrograph in plane polarized light of a plagioclase grain at 10x magnification showing abundant melt inclusions.

3.3.2 Laboratory Sample Separation

Each step in our separation methodology was designed to remove a specific type of inclusion (glassy melt inclusions, Fe-Ti oxides, apatite, zircon) that was observed in BSE images. Within the rest of this manuscript, each step in the flowchart (Fig. 3.3) will be italicized for clarity (e.g. Fig 3, sample *x*).

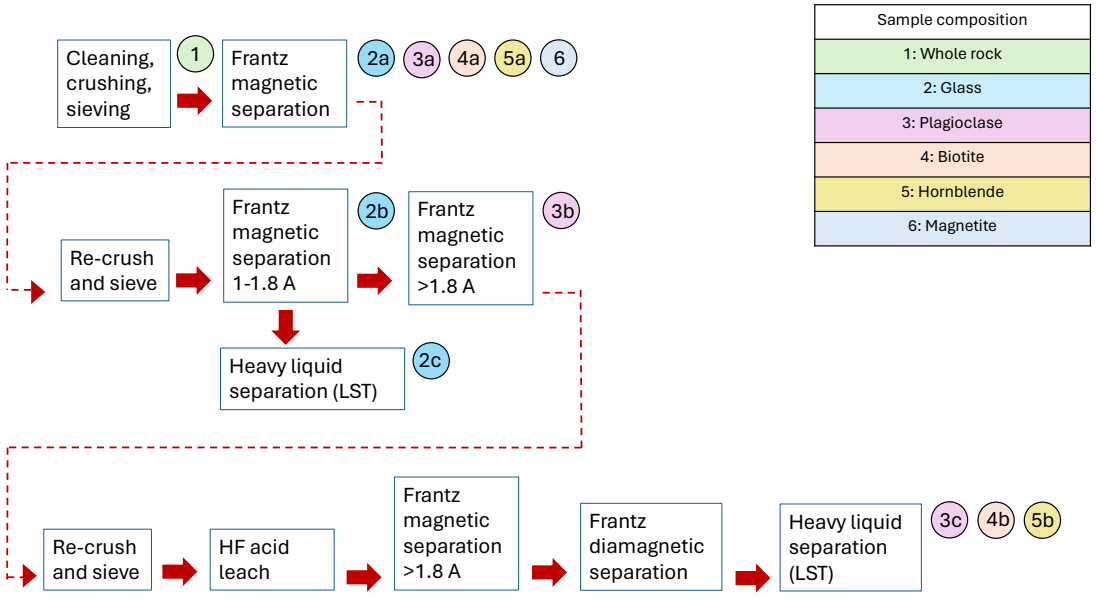


***Figure 3.3**: Flowchart of new methodology for U-series contaminant purification; steps are color keyed to a sample composition table, whole rock (green), glass (blue), plagioclase*

(purple), biotite (orange), hornblende (yellow), magnetite (blue-gray). On the flowchart, each sample name (colored circle) is located after its final step of processing.

1) All four samples were scrubbed of any surficial organic matter with a plastic bristle brush in deionized water and dried under a heat lamp. Samples were crushed in a stainless-steel mortar and pestle, and sieved into fractions of >2 mm, 0.5–1 mm, 0.25–0.5 mm (250–500 μm), 0.125–0.25 mm (125–250 μm), 0.063–0.125 mm (63–125 μm), and <0.063 mm (<63 μm). 100 mg aliquots of Rotoiti and Earthquake Flat samples were retained from the <63 μm split, which were collected as representative analyses of the whole rock (Fig. 3.3, sample *1*).

2) *Glass*:
    a. A hand magnet was passed over the sample to remove highly magnetic minerals (chiefly Fe-Ti oxides). Samples were then passed through the Frantz Magnetic Separator at increasing amperages to separate minerals by magnetic susceptibility. Mafic minerals and highly magnetic minerals were efficiently separated at low amperages (<1 A). Plagioclase and quartz were separated from glass between 1–1.8 A, and plagioclase and quartz were concentrated at amperages > 1.8. An aliquot of glass from the 1–1.8 A step was sampled as representative of a conventionally separated glass (Fig. 3.3, sample *2a*).
    b. Typically glass samples are concentrated using the Frantz Magnetic Separator and are not processed any further prior to dissolution for measurement. Numerous impurities within individual glass shards were observed after initial separation (sample *2a*) even at the 250-500 μm size fraction, rendering it impure and

therefore the glass was further processed. The glass split was re-crushed and sieved to liberate other phases from the glass shards. Then the glass was passed through the Frantz Magnetic Separator again to remove the free mineral phases. An aliquot of this re-processed glass was taken as representative of a mid-process glass that should be free of impurities, but which could still contain a small amount of liberated phases in the bulk sample (Fig. 3.3, sample *2b*).

c. Next, the sample was passed through a solution of heterolithium polytungstates (LST) ($\rho = 2.56$ g/cm^3) to separate glass from other phases by density. Given the number of zircon and apatite grains included within the glassy matrix of the pumice in BSE images, this final step was designed to remove any liberated zircon and apatite grains from the bulk separate (Fig. 3.3, sample *2c*).

3) *Plagioclase, biotite, hornblende*:

a. The typical procedures for separating plagioclase involve processing such samples using the Frantz Magnetic Separator at ≥ 1.8 A but do not process the sample any further. An aliquot of the plagioclase sample that had been passed through the Frantz Magnetic Separator at amperages >1.8 to remove all lower amperage phases was retained as the conventional plagioclase control sample for use as a comparison (Fig. 3.3, sample *3a*).

b. Because inclusions were observed in the plagioclase grains in sample *3a* at all size fractions, the plagioclase separates were further processed to remove inclusions. The plagioclase separate was re-crushed and sieved to liberate the inclusions (Fig. 3.3, *3b*)

c. Next the sample was acid leached to dissolve any adhering glass on the plagioclase rims, and to dissolve any exposed glassy melt inclusions. The sample was sonicated in 19% HF acid for 15 minutes, the HF solution was decanted, and deionized (DI) water was added to the sample. The sample was then sonicated for 10 minutes in the DI water. The DI water-rinse process was repeated twice more, so that the sample was sonicated in DI water a total of three times. Once the sample was clean, it was passed through the Frantz Magnetic Separator at amperages > 1.8 to purify the plagioclase and so that any other liberated minerals or glass pieces were separated from the plagioclase. The acid leach step aimed to remove adhering glass from plagioclase rims, which could contain small mineral inclusions. After purifying the separate, the Frantz Magnetic Separator settings were changed to complete a diamagnetic separation; the goal of the diamagnetic separation was to separate quartz from plagioclase. The pitch angle was changed from 8° to 5° to slow the rate at which the grains were moving through the magnetic field, and the tilt on the main chute was changed to -5 on the left and 1.5 on the right (Frantz chute settings). In this scenario, paramagnetic minerals (plagioclase) are attracted to the magnetic field, and diamagnetic minerals (quartz) are repelled by the magnetic field. This process is repeated 3–5 times to purify the plagioclase sample of any quartz grains. The purified plagioclase separate was passed through a calibrated solution of LST (ρ = 2.56–2.69 g/cm^3) which separated grains based on density. This range in density was effective at separating quartz and plagioclase for the EQF, Kakapiko, and Hauparu samples.

The LST was diluted to 2.5 – 2.56 g/cm^3 to separate the quartz from the plagioclase in the Rotoiti sample. (Fig. 3.3, *3c*)

d. Steps a – c were repeated with a biotite (Fig. 3.3, *4a, 4b*) and hornblende split (Fig. 3.3, *5a, 5b*).

4) Finally, prior to sample dissolution, all samples were either leached in 0.2 M HCl + 2% H_2O_2 solution or an oxalic acid + 2% H_2O_2 solution to remove any organic residue from the samples. The samples were sonicated in the solution three times for 15 minutes each round, sonicated in DI water three time for 15 minutes each, and finally rinsed in acetone and dried under a heat lamp. The repetitive washing procedure ensured that all leachates were thoroughly removed from the grains, including any cracks or pores within the grains.
5) A small split of each final sample was mounted, sectioned, and polished, and imaged on the UC Davis Cameca SX-100 electron microprobe (EMP).

To summarize, the mineral separates were crushed to expose and/or liberate inclusions, acid leached to remove adhering glass and exposed melt inclusions, magnetically separated to remove any liberated inclusions, and finally mechanically and chemically separated from quartz, zircon, and apatite. The resulting separate was an apparently pure bulk mineral sample; the sample was optically pure when imaged by picking microscope, but EMP imaging reveals an abundance of free quartz grains in the plagioclase separates, glass inclusions in plagioclase grains, apatite and glass inclusions in hornblende, and free Fe-Ti oxides and glass grains in the biotite split. Although there are still abundant inclusions and impurities in each sample, we note that the

workflow does improve the purity of the split, with the best results in the processed biotite (*4b*) and hornblende (*5c*) splits. Glassy melt inclusions in plagioclase and quartz remain a persistent problem in the plagioclase split, however this workflow could be useful for systems where quartz is not saturated and/or where melt inclusions are not as common.

3.3.3 Mass Spectrometry

Samples were weighed, dissolved, and chemically processed for U and Th separation following the procedure of Cooper and Donnelley (2004). $^{234}U/^{238}U$ and $^{230}Th/^{232}Th$ isotopic composition ratios, and $^{233}U/^{238}U$ and $^{229}Th/^{232}Th$ isotopic dilution concentrations were measured the Nu plasma multi-collector inductively coupled plasma mass spectrometer (MC-ICPMS) in the Interdisciplinary Center for Plasma Mass Spectrometry (ICPMS) facility at University of California Davis, using the analytical procedures presented in Cooper and Donnelley (2004) (Table 3.1). The uranium standard CRM-112A was used to characterize mass bias and gain throughout the duration of each run; and the NIST standard U010 was used for abundance sensitivity during Th isotopic composition runs. The solution standard IRMM-036 was used to characterize mass bias and gain throughout the duration of the Th isotopic composition analyses. The WUN standard was used to characterize the shape of the ^{232}Th peak tailing into the ^{230}Th mass range, and was used as a solution standard to assess accuracy of the mass spectrometry. Accuracy for the WUN standard was assessed relative to the WUN values of Pietruszka (2002) and Sims (2008). USGS rock standards AGV-2, BCR-2 and W2 were used to assess overall accuracy and reproducibility of the total process of chemistry and mass spectrometry. Splits of the USGS rock standards were weighed, dissolved, and chemically processed for U and Th separation along with unknown samples in each batch processed through the chemical separation

procedures. For each analytical session, the USGS rock standards returned results within 2% of ^{238}U-^{230}Th secular equilibrium (Table 2). The University of California Davis running average of (^{230}Th)/(^{238}U) for each of the USGS rock standards is also within 2% of unity (i.e. secular equilibrium), and accordingly, the accuracy of our measurements is considered to be better than 2%. A total-process blank was also run with each batch of chemistry; U and Th blanks are routinely <10 pg, negligible considering that the total amount of U and Th in each sample was on the order of 10-1000 ng. Thus, while U and Th concentrations by isotope dilution were corrected for the blank for completeness, no blank correction was made to the U or Th isotopic composition of the unknowns. (^{234}U)/(^{238}U) isotopic ratios are measured as a check of post-eruptive disturbance of the U-Th system; (^{234}U)/(^{238}U) activity ratios of USGS rock standards which are within 9‰ of secular equilibrium ((^{234}U)/(^{238}U) activity ratios of 1.000). Analytical uncertainties for Th and U concentrations reported in Table 3.1 include counting statistics during the instrument runs, blank corrections, and uncertainties in ^{229}Th-^{233}U spike calibration. The concentration of ^{229}Th and ^{233}U in the mixed spike was calibrated using an average of results from spike-standard mixes using gravimetric standards (NIST SRM 3159 for Th; NIST SRM 3164 for U), USGS rock standards AGV-2, BCR-2, and W2, and rock standard TML. Analytical uncertainties reported in Table 3.1 for Th and U isotopic ratios include counting statistics during the instrument runs only. Activity ratios were calculated using the following decay constants: λ^{232} = 4.9511 x 10-11 yr-1 (Holden et al. 1990), λ^{230} = 9.1705 x 10-6 yr-1 (Cheng et al. 2013), λ^{234} = 2.82206 x 10-6 yr-1 (Cheng et al. 2013), λ^{238} = 1.551 x 10-10 yr-1 (Jaffey et al. 1971). In the following discussion, we use the reproducibility of replicate measurements of USGS rock standards in the UC Davis laboratory (long-term running average from 2011–2024) as a measure of the overall uncertainty of our measurements, resulting in 2σ uncertainties of <2 % for

(^{230}Th)/(^{232}Th), (^{238}U)/(^{232}Th), and (^{230}Th)/(^{238}U). Overall uncertainty of measurements is quantified by replicate measurements of rock standards which return values within 2% of secular equilibrium.

3.4 RESULTS

For each eruption, most of the glass and plagioclase samples have (^{230}Th)/(^{232}Th) and (^{238}U)/(^{232}Th) activity ratios within 2% (i.e. within uncertainty) of each other. Results are presented in Table 3.1 and Figure 3.4. All samples are referenced to their processing step, which is listed in italics after the sample name.

Table 3.1: Concentrations, isotopic ratios, and activities for Okataina Volcanic Center samples

Sample	Grain size (mm)	Eruption date (ka)	Process step	Th (ppm)	U (ppm)	^{230}Th/^{232}Th (x10^{-6})	SE (%)	(^{234}U)/(^{238}U)	(^{238}U)/(^{232}Th)	(^{230}Th)/(^{232}Th)	(^{230}Th)/(^{238}U)
Kakapiko Dome gl-1	0.063–0.125	~120	2a	13.70	3.20	3.93	0.16	0.995	0.718	0.726	1.01
Kakapiko Dome gl-2	0.125–0.25	~120	2a	13.04	2.95	3.94	0.10	0.979	0.696	0.729	1.05
Kakapiko Dome plg-1	0.063–0.125	~120	3a	0.22	0.05	4.15	0.23	0.997	0.714	0.767	1.07
Rotoiti WR-1	<0.063	~45-60	1	9.37	2.23	4.04	0.57	1.001	0.731	0.747	1.02
Rotoiti WR-2	<0.063	~45-60	1	9.54	2.28	3.99	0.12	1.000	0.737	0.738	1.00
Rotoiti gl-2	0.063–0.125	~45-60	2a	9.63	2.28	3.98	0.13	1.003	0.729	0.736	1.01
Rotoiti gl-3	0.5–1	~45-60	2c	9.11	2.19	4.00	0.18	1.011	0.740	0.740	1.00
Rotoiti gl-4	0.5–1	~45-60	2a	8.93	2.13	4.01	0.12	0.997	0.734	0.742	1.01
Rotoiti gl-5	0.25–0.5	~45-60	2b	9.39	2.25	3.98	0.14	0.993	0.736	0.736	1.00
Rotoiti plg-1	0.25–0.5	~45-60	3a	0.660	0.145	3.96	0.10	0.983	0.676	0.732	1.08
Rotoiti plg-2	0.25–0.5	~45-60	3b	0.713	0.171	3.98	0.13	0.989	0.738	0.736	1.00
Rotoiti plg-3	1–2	~45-60	3c	0.075	0.018	3.99	0.21	0.995	0.738	0.739	1.00
Rotoiti plg-4	0.25–0.5	~45-60	3c	0.455	0.109	3.98	0.12	1.003	0.737	0.736	1.00
Rotoiti plg-5	1–2	~45-60	3a	0.734	0.183	3.95	0.12	1.002	0.767	0.731	0.95
Rotoiti plg-6	0.25–0.5	~45-60	3a	0.766	0.184	3.99	0.14	1.002	0.739	0.739	1.00
EQF WR-1	<0.063	~45-60	1	12.82	3.00	3.96	0.11	0.998	0.721	0.732	1.02
EQF gl-1	0.25–0.5	~45-60	2a	13.02	3.01	3.95	0.13	1.002	0.711	0.731	1.03
EQF gl-2	0.125–0.25	~45-60	2a	13.83	3.25	3.97	0.11	1.003	0.723	0.734	1.02
EQF gl-4	0.25–0.5	~45-60	2a	14.31	3.39	3.95	0.18	1.001	0.728	0.730	1.00
EQF gl-5	0.25–0.5	~45-60	2b	14.30	3.40	3.93	0.16	1.002	0.731	0.727	0.99
EQF plg-1	0.25–0.5	~45-60	3a	1.13	0.26	3.98	0.48	1.007	0.719	0.736	1.02
EQF plg-2	0.25–0.5	~45-60	3b	0.72	0.17	3.99	0.18	1.000	0.713	0.739	1.04
EQF plg-3	1–2	~45-60	3c	0.08	0.02	3.98	0.22	1.002	0.688	0.736	1.07
EQF plg-4	0.25–0.5	~45-60	3c	0.24	0.05	3.95	0.12	0.997	0.704	0.731	1.04
EQF plg-5	1–2	~45-60	3a	2.66	0.63	3.99	0.14	0.993	0.727	0.739	1.02
EQF plg-6	0.063–0.125	~45-60	3a	1.03	0.24	4.00	0.26	--	0.720	0.741	1.03
EQF bte -1	1–2	~45-60	4a	2.18	0.57	4.77	0.14	0.993	0.805	0.882	1.10
EQF bte - 2	1–2	~45-60	4b	0.91	0.19	3.95	0.29	1.011	0.654	0.730	1.12
EQF hbl - 1	1–2	~45-60	5a	1.90	0.45	3.93	0.21	1.004	0.730	0.727	1.00
EQF hbl -2	1–2	~45-60	5b	0.54	0.08	5.19	0.22	0.999	0.473	0.960	2.03
Hauparu gl-1	0.125–0.5	~35	2a	7.41	1.81	4.02	0.11	1.003	0.750	0.744	0.99
Hauparu gl-2	0.063–0.125	~35	2a	6.55	1.60	4.00	0.13	1.002	0.750	0.740	0.99
Hauparu gl-3	0.125–0.5	~35	2a	7.63	1.87	3.99	0.30	0.997	0.754	0.738	0.98
Hauparu mt-1	0.125–0.5	~35	6	0.41	0.09	3.76	0.22	1.000	0.656	0.695	1.06
Hauparu mt-2	0.125–0.5	~35	6	0.18	0.04	3.92	0.30	0.997	0.670	0.725	1.08
Hauparu plg-1	0.063–0.125	~35	3a	0.08	0.02	4.01	0.35	--	0.741	0.742	1.00

Table 3.2: Average concentrations, isotopic ratios, and activities of USGS rock standards

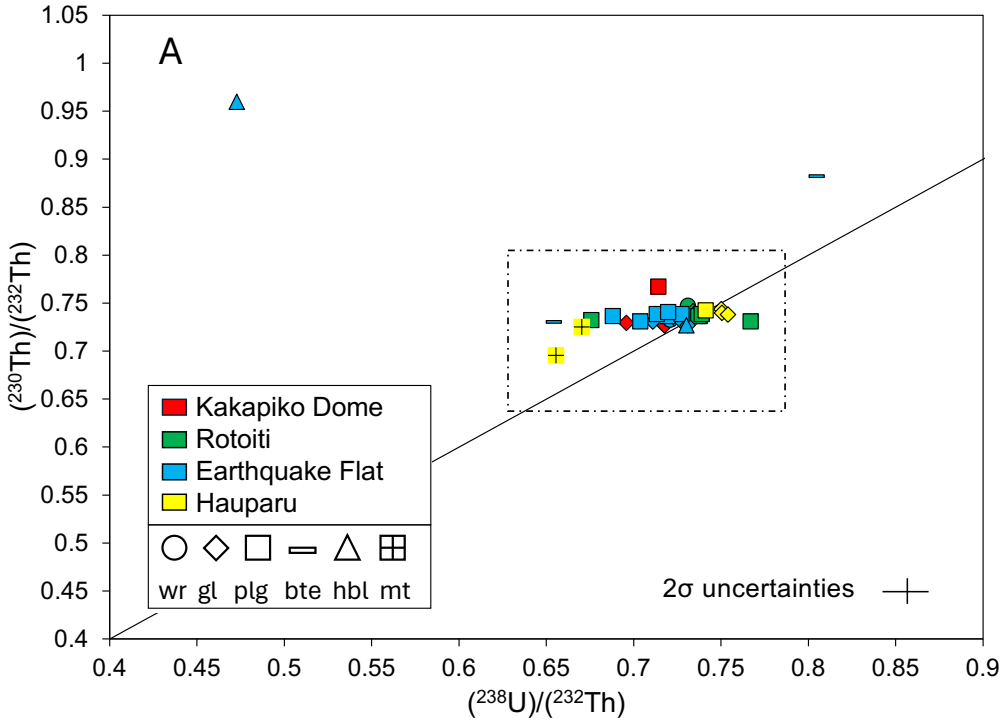
USGS Standard	Th (ppm)	U (ppm)	$^{230}Th/^{232}Th$ ($x10^{-6}$)	SE (%)	$(^{234}U)/(^{238}U)$	$(^{238}U)/(^{232}Th)$	$(^{230}Th)/(^{232}Th)$	$(^{230}Th)/(^{238}U)$
AGV2 (7)	5.917	1.859	5.125	0.14	0.991	0.968	0.948	0.981
AGV2 - UCD avg	6.043	1.868	5.112	0.13	0.997	0.9373	0.946	1.009
BCR2 (7)	5.778	1.656	4.755	0.14	0.994	0.900	0.880	0.980
BCR2 - UCD avg	5.847	1.670	4.712	0.13	1.003	0.8661	0.872	1.006
BCR2 Sims (08)	--	--	4.740	--	--	--	--	--
W2 (4)	2.130	0.490	3.820	0.14	1.003	0.706	0.707	1.002
W2 - UCD avg	2.141	0.498	3.833	0.16	1.003	0.7054	0.70899	1.005
W2 Sims (08)	--	--	3.870	--	--	--	--	--

Reproducibility of the USGS standards for this study compared to the UC Davis long-term average (UCD avg from 2011-2024): relative 1σ analytical uncertainty, including instrumental uncertainty and spike calibration, for Th and U concentration measurements is <0.28%; reproducibility of the USGS rock standards is <12% for $(^{238}U)/(^{232}Th)$, $(^{230}Th)/(^{232}Th)$, and $(^{230}Th)/(^{238}U)$; reproducibility of known secular equilibrium for USGS rock standards is within 2%; reproducibility of the WUN solution standard is <1% for $(^{238}U)/(^{232}Th)$ using values from Pietruszka et al. (2002) and Sims (2008); decay constants used for calculation are λ_{232} = 4.9511 (± 0.01) x 10^{-11} yr^{-1} (Holden et al. 1990), λ_{230} = 9.1705 (± 0.0138) x 10^{-6} yr^{-1} (Cheng et al. 2013), λ_{234} = 2.82206 (± 0.00302) x 10^{-6} yr^{-1} (Cheng et al. 2013), λ_{238} = 1.551 x 10^{-10} yr^{-1} (Jaffey et al. 1971); samples with (n) are replicate measurements, number of replicates listed in parentheses.

Table 3.3: Concentrations, isotopic ratios, and activities from Charlier et al. (2003)

Sample	Th (ppm)	U (ppm)	$^{230}Th/^{232}Th$ ($x10^{-6}$)	SE (%)	$(^{234}U)/(^{238}U)$	$(^{238}U)/(^{232}Th)$	$(^{230}Th)/(^{232}Th)$	$(^{230}Th)/(^{238}U)$
Rotoiti - WR	7.55	1.83	6.173	0.7	1.005	0.735	0.738	1.004
Rotoiti - plg	2.26	0.45	6.173	0.7	1.003	0.611	0.684	1.119
EQF - WR	9.63	2.30	6.173	0.7	1.010	0.725	0.748	1.032

WR - whole rock; plg- plagioclase; OVC, Okataina Volcanic Center; From Charlier et al. (2003) external reproducibility is ± <1.5% for $(^{238}U)/(^{232}Th)$ and ± <2% for $(^{230}Th)/(^{232}Th)$; decay constants used for cacluations are λ_{232} = 4.94752 x 10^{-11} yr^{-1}, λ_{230} = 9.19525 x 10^{-6} $yr^{-1,}$ λ_{238} = 1.55125 x 10^{-10} yr^{-1}


A
Kakapiko Dome
Rotoiti
Earthquake Flat
Hauparu
wr gl plg bte hbl mt
2σ uncertainties
(230Th)/(232Th)
(238U)/(232Th)
1.05
1
0.95
0.9
0.85
0.8
0.75
0.7
0.65
0.6
0.55
0.5
0.45
0.4
0.4
0.45
0.5
0.55
0.6
0.65
0.7
0.75
0.8
0.85
0.9

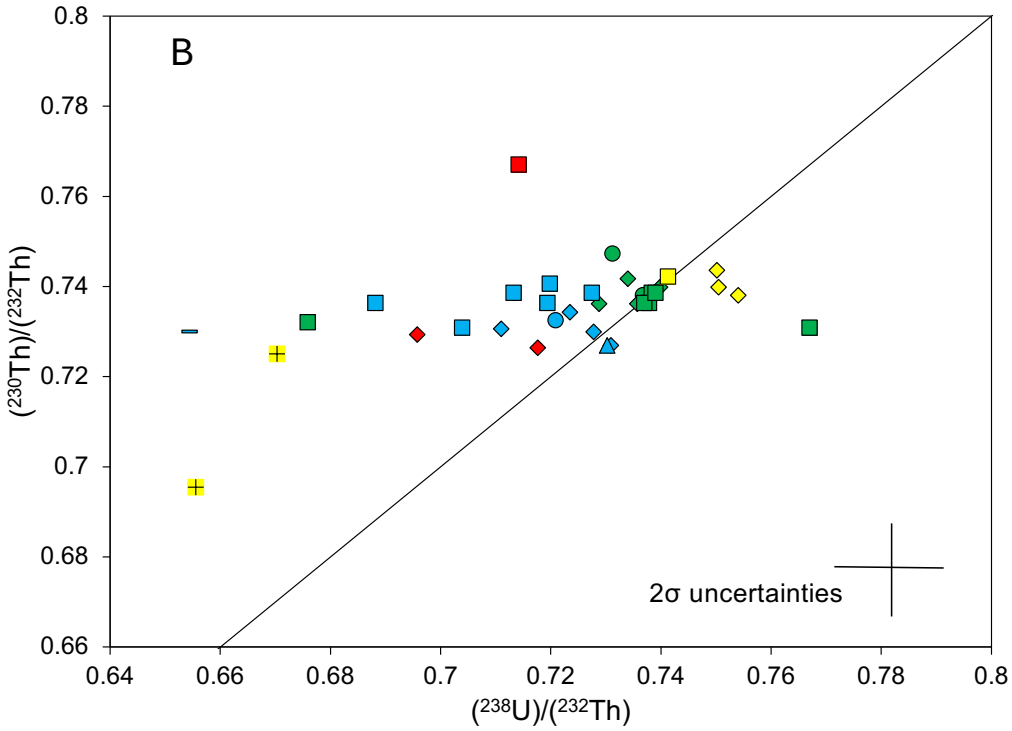


Figure 3.4*: Panel A: ^{238}U-^{230}Th isochron diagrams for all of the Okataina Volcanic Center (OVC) mineral, glass and whole rock data; Panel B: Inset from panel A shows the bulk of the data in more detail; Symbols as follows, circles: whole rock, diamonds: glass, squares: plagioclase, rectangles: biotite, triangles: hornblende, boxed plus sign: magnetite; red symbols: Kakapiko Dome samples, green symbols: Rotoiti samples, blue symbols: Earthquake Flat (EQF) samples, and yellow symbols: Hauparu samples; characteristic 2σ uncertainties are presented for (^{238}U)/(^{232}Th) and (^{230}Th)/(^{232}Th). Fine black line represents secular equilibrium equiline.*

3.4.1 Kakapiko Dome

(^{230}Th)/(^{232}Th) and (^{238}U)/(^{232}Th) ratios for the two Kakapiko glass separates (gl-1 (*2a*) and gl-2 (*2a*)) are within uncertainty of each other, yielding (^{230}Th)/(^{232}Th) = 0.726 and 0.729 and (^{238}U)/(^{232}Th) = 1.01 and 1.05, respectively (Table 3.1, Fig. 3.4). Kakapiko gl-2 (*2a*) is indistinguishable from EQF and Rotoiti glasses and WR within uncertainty, but measurably different from those of the Hauparu glasses. Kakapiko gl-1 (*2a*) data are indistinguishable from

all EQF, Rotoiti, and Hauparu glass and plagioclase analyses. Although the Kakapiko plagioclase is within uncertainty of the Kakapiko glasses, it plots at (^{230}Th)/(^{232}Th) = 0.767, which is a higher (^{230}Th)/(^{232}Th) ratio than the Kakapiko glasses as well as the general data cloud. Both Kakapiko Dome glass samples and the plagioclase sample were processed to steps *2a* and *3a*, respectively, Kakapiko gl-1 (*2a*), Kakapiko gl-2 (*2a*), Kakapiko plg-1 (*3a*) (Fig. 3.3); these samples were separated by Frantz magnetic separation but no further processing beyond that.

3.4.2 Rotoiti

The Rotoiti whole rock, glass, and plagioclase data all plot within uncertainty of each other, with the exception of Rotoiti plg-1, which plots at lower (^{238}U)/(^{232}Th) ratio (0.676) (Table 3.1, Fig. 3.4). Despite different levels of processing, four of the six Rotoiti plagioclase samples (plg-2 (*3b*), plg-3 (*3c*), plg-4 (*3c*), and plg-6 (*3a*)), and all of the Rotoiti glass samples plot within uncertainty of the equiline and are therefore within uncertainty of secular equilibrium. The Rotoiti plagioclase plg-1 (*3a*) and plg-5 (*3a*) do not plot within uncertainty of the equiline; these samples were separated by the Frantz Magnetic Separator according to magnetic susceptibility and were not processed any further (Fig. 3.3*, 3a*). Both of the Rotoiti whole-rock samples, WR-1 (*1*) and WR-2 (*1*), plot within uncertainty of each other at (^{230}Th)/(^{232}Th) = 0.747 and 0.738, and (^{238}U)/(^{232}Th) = 0.731 and 0.733, respectively, as well as within uncertainty of the equiline.

3.4.3 Earthquake Flat

All of the EQF whole rock and glass samples are within uncertainty of each other and range from (^{238}U)/(^{232}Th) = 0.711–0.731, and (^{230}Th)/(^{232}Th) = 0.727–0.734, and despite being the most

processed, EQF gl-5 (*2b*) has the highest (^{238}U)/(^{232}Th) ratio, (^{238}U)/(^{232}Th) = 0.731 (Table 3.1, Fig. 3.4). EQF plagioclase samples EQF plg-1 *(3a),* plg-2 *(3b),* plg-4 *(3c),* plg-5 *(3a),* and plg-6 *(3a)* are all within uncertainty of each other as well as the whole rock and glass samples and range from (^{230}Th)/(^{232}Th) = 0.731–0.741 and (^{238}U)/(^{232}Th) = 0.704–0.727. EQF plg-3 (3c) plots at the lowest (^{238}U)/(^{232}Th) value outside of uncertainty of the other plagioclase, glass, and whole-rock samples. EQF bte-2 (*4b*) is within uncertainty of all EQF whole rock, glass, and plagioclase samples at (^{230}Th)/(^{232}Th) = 0.730, but plots on the far left at (^{238}U)/(^{232}Th) = 0.654 and is only within uncertainty of samples with (^{238}U)/(^{232}Th) < 0.674 (Rotoiti plg-1 (*3a*) and Hauparu magnetite samples (*6*)). EQF bte-1 (*4a*) is not within uncertainty of any of the OVC samples at (^{238}U)/(^{232}Th) = 0.805 and (^{230}Th)/(^{232}Th) = 0.882. EQF hbl-1 (*5a*) plots within uncertainty of all OVC whole rock, glass, and plagioclase samples at (^{238}U)/(^{232}Th) = 0.730 and (^{230}Th)/(^{232}Th) = 0.727, but EQF hbl-2 (*5b*) does not plot with uncertainty of any of the OVC samples at (^{238}U)/(^{232}Th) = 0.473 and (^{230}Th)/(^{232}Th) = 0.960.

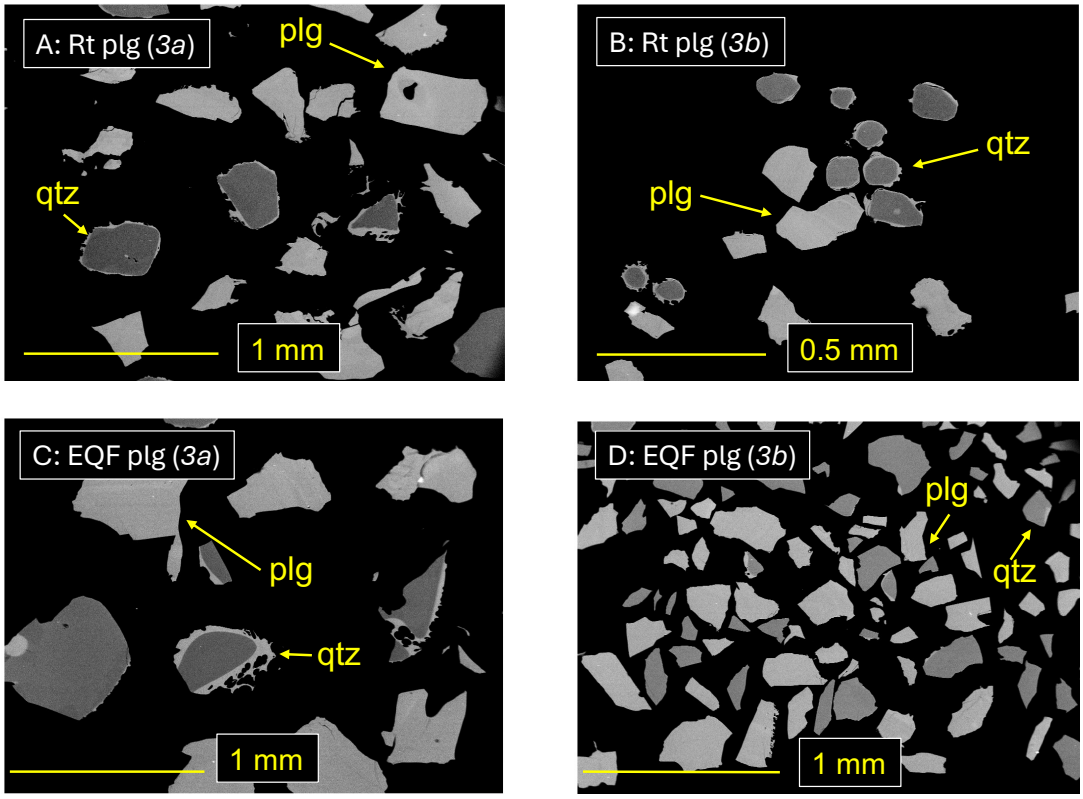
3.4.4 Hauparu

All three Hauparu glass samples and the Hauparu plagioclase sample plot within uncertainty of each other and range from (^{238}U)/(^{232}Th) = 0.741–0.750, and (^{230}Th)/(^{232}Th) = 0.738–0.744 (Table 3.1, Fig. 3.4). The three glasses plot to the right of the equiline, while Hauparu plg-1 (*3a*) plots on the equiline. Hauparu mt-1 (*6*) and mt-2 (*6*) plot within uncertainty of each other at (^{230}Th)/(^{232}Th) = 0.695 and 0.725 and (^{238}U)/(^{232}Th) = 0.656 and 0.670, respectively.

3.4.5 BSE Imaging

BSE images of Rotoiti plg-1 (*3a*) and EQF plg-1 (*3a*) are illustrated in Fig. 3.5A and 3.5C, respectively, and show that these plagioclase bulk separates contain a near equal proportion of quartz and plagioclase. Samples processed one step further, Rotoiti plg-2 (*3b*) and EQF plg-2 (*3b*), in Fig. 3.5B and 3.5D, respectively, are smaller sized grains but still contain a high proportion of quartz. The increased grain angularity and smaller size of the more processed grains of Rotoiti plg-2 (*3b*) and EQF plg-2 (*3b)* compared to the less processed samples Rotoiti plg-1 (*3a*) and EQF plg-1 (*3a*) is due to the re-crushing step (Fig. 3.3). Rotoiti plg-3 (*3c*), plg-4 (*3c*) (Fig. 3.5E-G), and EQF plg-3 (*3c*), plg-4 (*3c*) (Fig. 3.5H–J) contain proportionally less quartz than splits only processed to the *3a* and *3b* levels, suggesting that additional diamagnetic processing could further remove quartz. In samples processed to step *3a*, plagioclase grains typically contain variable amounts of glass, zircon, and apatite inclusions, and grains processed to step *3b* contain fewer mineral inclusions, but abundant glassy melt inclusions. Wormy textures in plagioclase grains (Fig. 3.5E, F, H–J) are calcic zones, or regions dominated by glassy melt inclusions that have been successfully dissolved by the acid leach (arrays of melt inclusions are often coincident with the more calcic zones within plagioclase grains). The acid leaching was not entirely effective, however, as some grains retain both recrystallized melt inclusions as well as glassy melt inclusions (Fig. 3.5G). EQF bte-1 (*4a*) (Fig. 3.5K–L) contains numerous inclusions including zircon, apatite, glass, and Fe-Ti oxides. The highly processed sample EQF bte-2 (*4b*) (Fig. 3.5M) has significantly fewer inclusions than less processed splits, but the process was not completely effective in separating the liberated inclusions from the bulk sample; we observed both Fe-Ti oxides and glass in the bulk separate post-processing. EQF hbl-1 (*5a*) (Fig. 3.5N–O) contains glass, zircon, apatite, Fe-Ti oxides, and biotite inclusions, while the highly processed samples EQF hbl-2 (*5b*) (Fig. 3.5P) contains mostly apatite inclusions. However, given the

relatively large size (0.25 mm) of the post-processed grains in EQF hbl-2 (*5b*), it is possible that the grains still contain other inclusions that were not visible in the plane of the section.



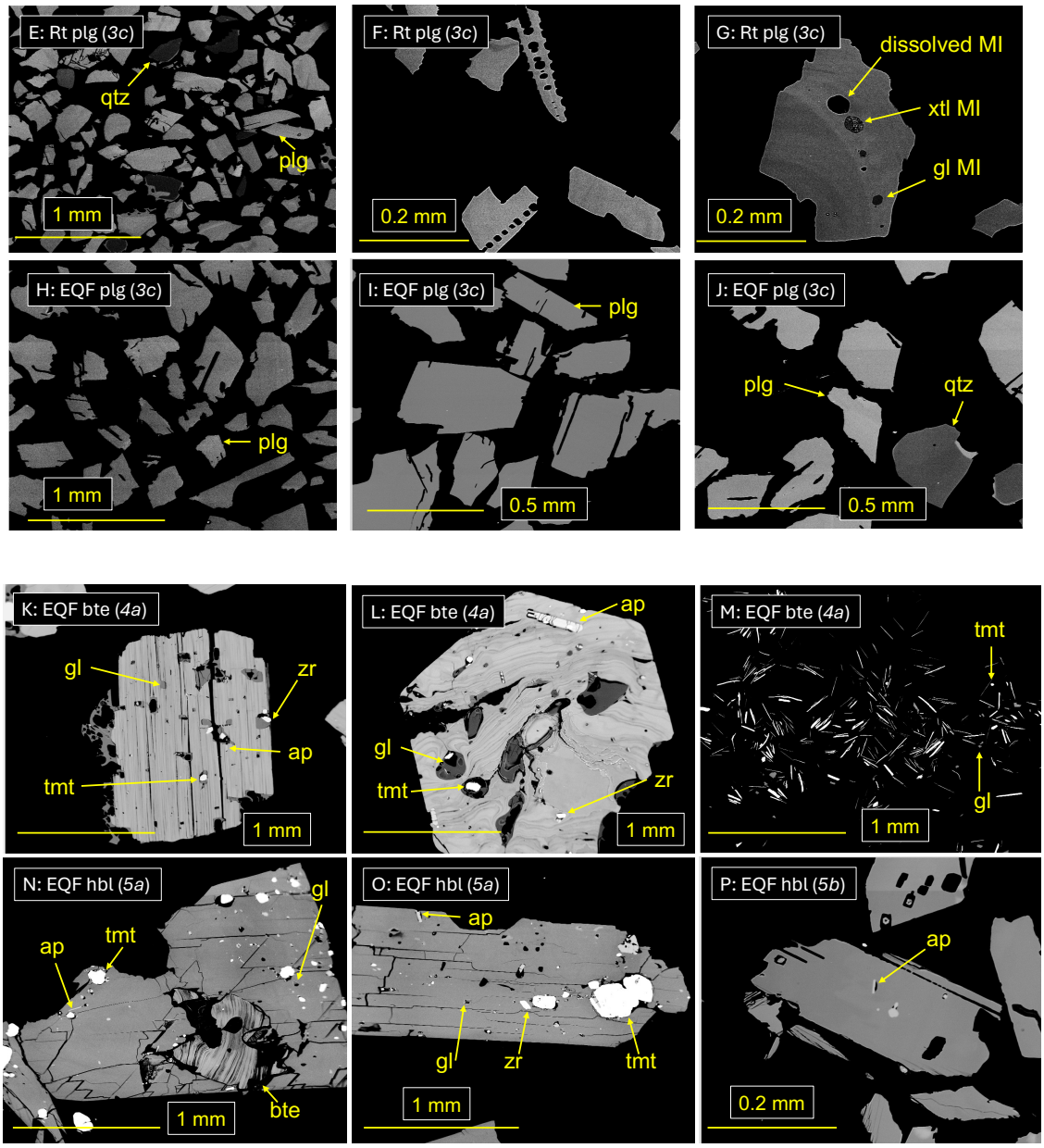


***Figure 3.5**: Back-scattered electron (BSE) images of post-processed samples, qtz quartz, plg plagioclase, bte biotite, zr zircon, ap apatite, tmt titanomagnetite (Fe-Ti oxides), hbl hornblende, gl MI glass/melt inclusion; Panel A: The Rotoiti plg (3a) sample contains plagioclase (light gray) and quartz (dark gray) which is rimmed with glass; Panel B: The Rotoiti plg (3b) sample contains smaller grains than sample 3a, and also contains a large proportion of quartz rimmed with glass; Panel C: The Earthquake Flat (EQF) plg (3a) sample contains plagioclase (light gray) mixed with quartz rimmed by glass (dark gray with light gray*

filigree); Panel D: The EQF plg (3b) sample contains smaller grains due to the re-crush and a mixture of plagioclase and quartz; Panel E: The Rt plg (3c) sample is chiefly plagioclase and contains less quartz than samples 3a and 3b; Panel F: Grains from the Rt plg (3c) sample show how the acid leach step was effective in removing some zones within the plagioclase; Panel G: A grain from the Rt plg (3c) sample shows that the acid leach was effective in removing some melt inclusions (MI), but not all, as this image shows an array of closely spaced melt inclusions, including dissolved melt inclusions, crystallized (xtl) and undissolved melt inclusions, and glassy undissolved melt inclusions; Panel H: The EQF plg (3c) sample is chiefly plagioclase, with only a few quartz grains in the mounted aliquot (Panel J); Panel I: Wormy textures in EQF plg (3c) plagioclase grains follow more calcic zones within the plagioclase and/or regions of melt inclusion arrays; Panel J: A few quartz grains are still present in EQF plg (3c) despite the high level of sample processing; Panels K and L: Biotite grains from EQF bte (4a) contain glass, zircon, apatite, and titanomagnetite inclusions; Panel M: The processed sample EQF bte (4b) contains small biotite flakes with liberated inclusions of glass and titanomagnetite; Panels N and O: Hornblende grains from EQF hbl (4a) contain glass, zircon, apatite, titanomagnetite, and biotite inclusions; Panel P: The processed hornblende split, EQF hbl (4b), experienced effective removal of some inclusion but still contains apatite inclusions.

3.5 DISCUSSION

3.5.1 Expected behavior of U-series nuclides in mineral separates

U-series bulk mineral ages can help to contextualize magmatic processes by revealing simple growth histories from a single magma, complicated growth involving antecrystic cores, or incorporation of xenocrystic material of varying isotopic composition, among other insights. This information can help to better understand how and when minerals grow in a magma reservoir. In order to evaluate the effectiveness of the mineral purification process and to interpret the apparent U-Th ages calculated from the measured data, we compare our results to the results expected in the case of simple crystallization from a single melt, followed by aging.

U and Th concentrations in minerals together with the U/Th ratio control the resolution of ^{238}U-^{230}Th crystallization ages. U and Th concentrations and the U/Th ratio are based on a mineral's affinity to incorporate U and Th into the crystal lattice. Minerals with high concentrations of U and Th can yield more precise ^{238}U-^{230}Th crystallization ages than minerals

with low U and Th concentrations. For example, zircon have high concentrations of U and Th (10^2–10^3 ppm) which yield analytically precise U-series dates with small uncertainties. Conversely, plagioclase are expected to contain low concentrations of U and Th (~10^{-3} ppm) (as predicted by U and Th partitioning from a characteristic OVC glass) which must be analyzed by a bulk analysis of thousands of grains and which typically has larger uncertainties than in-situ mineral measurements (i.e. zircon). In addition, because analyses of bulk separates that contain impurities will have isotopic ratios that reflect the mixture, understanding the behavior of elemental partitioning is key to understanding what phases might be present in a bulk separate, and therefore, to interpreting the resulting the ^{238}U-^{230}Th isochron. To better understand the U-series systematics of mineral separates, it is helpful to first understand U and Th partitioning in minerals. Each mineral partitions U and Th into its crystal lattice based on each element's chemical compatibility within a given mineral (quantified by the mineral-melt partition coefficients for U and Th), thereby producing elemental fractionation.

While some partition coefficients are relatively well understood, others are poorly understood and are the subject of active research. We use partition coefficients from Blundy and Wood (2003) and compiled by Cooper and Reid (2008), with the exception of apatite partition coefficients which are from Luhr et al. (1984) and Mahood and Stimac (1990), and titanomagnetite (oxide) partition coefficients from Luhr et al. (1984). Given the general expectations of U and Th partitioning into minerals, we can predict the (^{238}U)/(^{232}Th) ratio of pure mineral separates. Using EQF glass U and Th concentrations, and the predicted partition coefficients as above, we can calculate the theoretical concentration of U and Th in each solid mineral using the equation:

$$K_D^i = \frac{C_s^i}{C_l^i}$$

where K_D^i is the partition coefficient of element, *i*, and C_s^i is the concentration of element *i* in the solid, ratioed to C_l^i, the concentration of element *i* in the liquid. The predicted concentrations of U and Th in the solid are used to calculate predicted (^{238}U)/(^{232}Th) ratios for each mineral, and we assume that (^{230}Th)/(^{232}Th) ratios at the time of crystallization are equal to those of the glass. From the experimental and theoretical studies, plagioclase is expected to have a Th/U partition coefficient ratio ($K_{D(Th)}/K_{D(U)}$) of 1.8; biotite and amphibole are expected to have $K_{D(Th)}/K_{D(U)}$ ratios of 1 and 0.94, respectively; apatite is expected to have a $K_{D(Th)}/K_{D(U)}$ ratio of 0.6; titanomagnetite is expected to have a $K_{D(Th)}/K_{D(U)}$ ratio of 0.5; and zircon is expected to have a $K_{D(Th)}/K_{D(U)}$ ratio of 0.167 (Blundy and Wood 2003, Cooper and Reid 2008, Luhr et al. 1984, Mahood and Stimac 1990). U and Th are both strongly incompatible elements in major minerals (Cooper and Reid 2008) and will preferentially remain in the melt. Given the differences in partitioning behavior between minerals, a suite of minerals that crystallizes simultaneously (at time t = 0) should contain different concentrations of U and Th, and therefore would plot at different (^{238}U)/(^{232}Th) ratios on an isochron diagram (Fig. 3.6). Through time, the decay of ^{238}U and ^{230}Th will alter the (^{230}Th) activity such that it begins to approach the (^{238}U) activity, which will drive a sample closer to the equiline as it returns to secular equilibrium (Fig. 3.6).

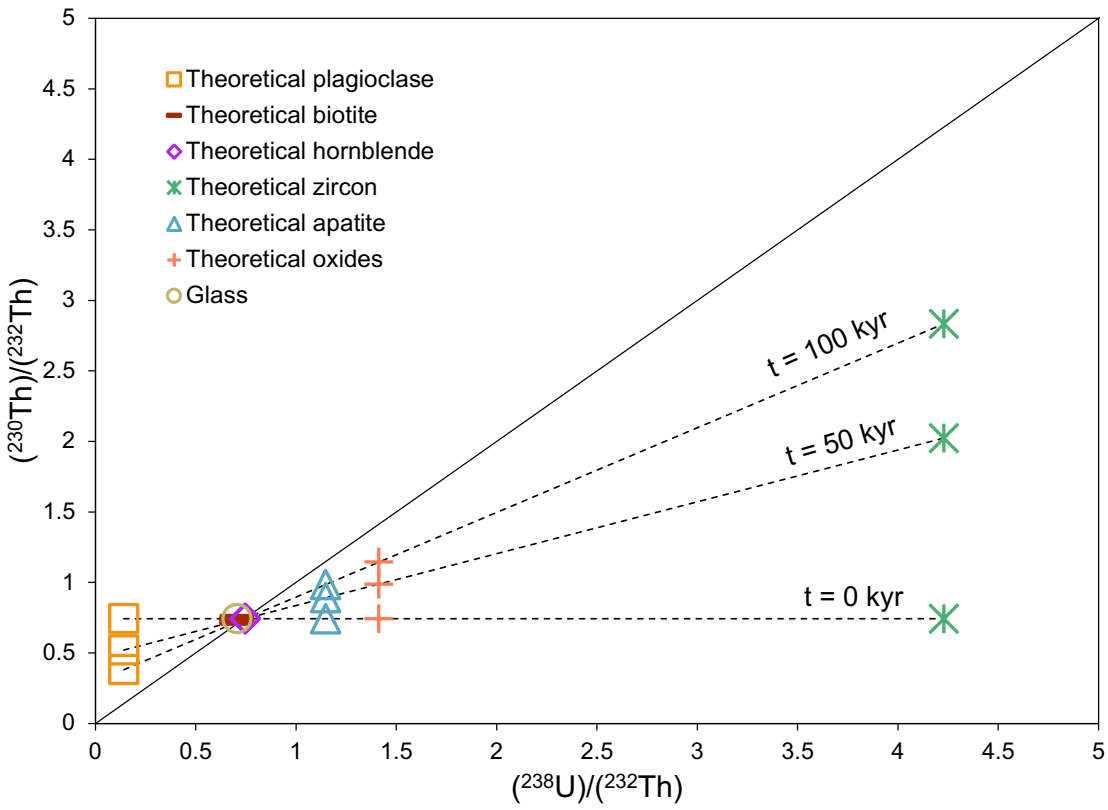


Figure 3.6: *^{238}U-^{230}Th isochron plot illustrating the theoretical position of minerals based on U and Th partition coefficients assuming Earthquake Flat glass U and Th concentrations. Symbols: plagioclase (orange square), biotite (red rectangle), hornblende (purple diamond), glass (brown circle), apatite (blue triangle), titanomagnetite (red-orange plus), zircon (green star). The equiline is illustrated as a solid black line. At time = 0, all minerals plot on a horizontal array. Through time the linear array will rotate about the intersection with the equiline. Mineral abbreviations: plagioclase, plg; glass, gl; biotite, bte; hornblende, hbl; apatite, ap; titanomagnetite, tmt; zircon, zrc.*

The multi-phase ^{238}U-^{230}Th isochron is a useful tool for understanding crystallization ages of minerals on magmatic timescales but requires several foundational assumptions: 1) the mineral suite must be cogenetic, having crystallized from the same host melt at the same time; 2) minerals are closed systems, once they crystallize there is no exchange of U and Th into or out of

the crystals, and; 3) the crystallization timescales are short relative to the half-life of the daughter isotope ^{230}Th ($t_{1/2}$ = 75690 ± 230 kyrs) (Bourdon et al. 2003, Cooper and Reid 2008).

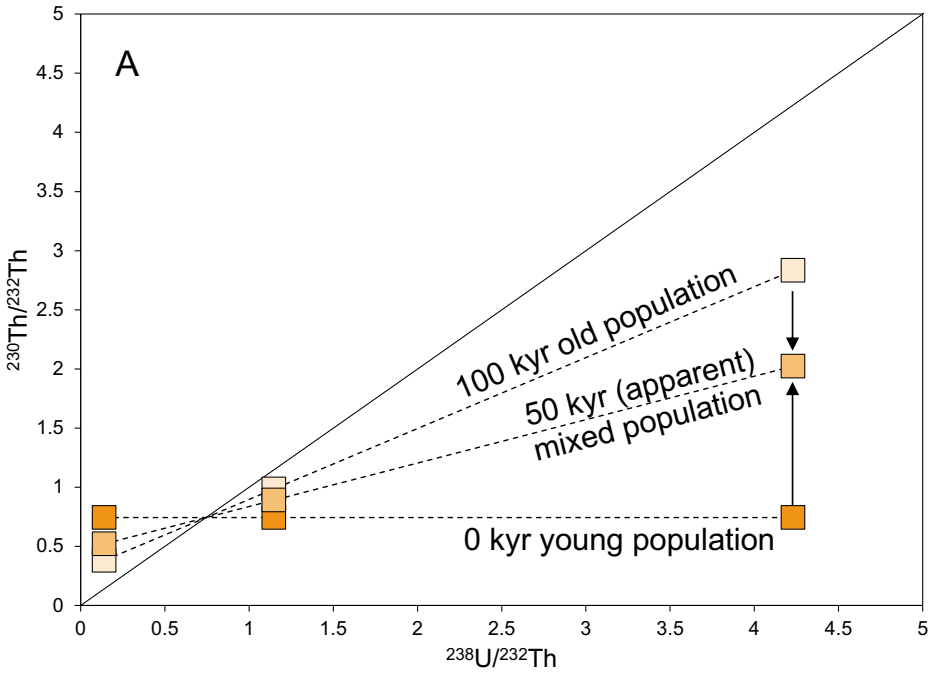
Assumptions 2 and 3 are generally thought to be robust in magmatic systems. With respect to the second assumption, diffusion studies at high temperature (1350–1500 ºC) in basaltic melts have shown that U and Th diffusivities are among the lowest for some trace elements (logD = -10 – -11(m^2/s) (LaTourette et al. 1996, LaTourette and Wasserburg 1997), and extrapolation of U and Th diffusivities to lower temperatures and in more viscous rhyolitic melts are predicted to be even lower. Additionally, Cherniak et al. (1996) and Giletti and Casserly (1994) show that U and Th in intermediate composition feldspars have high closure temperatures, and therefore diffusive re-equilibration of U and Th in plagioclase with the host melt is unlikely (Reid 2003). Therefore, once mineral crystallization has occurred, the total U and Th abundance in the mineral is fixed. One caveat is that at low temperatures α-recoil forces can eject daughters from the mineral lattice rim, but this is not a major concern at magmatic temperatures as mineral annealing occurs on faster timescales than decay (Bourdon et al 2003, Schoene et al. 2014). Additionally, the half-life of ^{238}U is sufficiently long and the decay constant sufficiently small ($t_{1/2}$ = 4.47 Ga; $\lambda = 1.551 \times 10^{-10}$ yr^{-1}; Jaffey et al. 1971) such that it will not appreciably affect measured (^{238}U)/(^{232}Th) ratios on the timescales of the investigated magmatic processes, and therefore will not move the plotted samples appreciably on the horizontal axis of the isochron diagram.

A co-crystallized suite of minerals will have the same initial Th isotopic composition as the host glass, and therefore all should initially plot at the same (^{230}Th)/(^{232}Th) ratio. Variation in the initial (^{238}U)/(^{232}Th) ratio stems from U and Th partition coefficient reflecting a mineral's affinity for those particular elements. A ^{238}U-^{230}Th isochron with a slope at (or near) zero would

be expected from crystallization of minerals shortly before eruption for geologically young eruptions. In such cases, minerals that crystallize during magma eruption ascent or immediately prior to eruption will define a "zero-age" isochron (Fig. 3.6, t = 0); in this scenario, the apparent crystallization age will represent the youngest period of growth. Older co-genetic suites of minerals should yield linear arrays where the slope increases with age (Fig. 3.6) until secular equilibrium is reached.

Non-cogenetic minerals can lead to more complicated isochrons due to a difference in the initial Th isotopic composition and ingrowth of daughter product and decay of initial daughter. If a population of young (~eruption age) minerals are mixed with an older population of the same mineral, or if young rims grow on older antecrystic cores, and all minerals crystallized from the same (or similar) host liquid, the isochron will appear as a linear array that plots between those two end members isochrons (young rim isochron and old core isochron) (Fig. 3.7A). The exact location of the mixed isochron will depend on the relative proportions of the two endmember components. In the case of mixed populations of the same minerals, the mixed isochron can yield information about the relative proportion of old and young component in the bulk mineral split. If mineral phases are mixed (i.e. one mineral included in another), but both minerals crystallized from the same host liquid, then the two minerals will plot on the same linear array but will plot as a mixture in between the end members (Fig. 3.7B). In the case of mixed populations of different minerals, only relative age information can be gleaned from the isochron. For example, plagioclase with zircon inclusions should plot between the theoretical plagioclase and zircon end members, but if they maintain a horizontal array, it can be inferred that there are some "young" (~eruption age) plagioclase in the population (Fig. 3.7A, Cooper and Reid 2008). Only a small percentage of U- and Th-rich minerals such as zircon are needed to dominate the U and Th

signatures of mineral separates for low concentration minerals such as plagioclase. OVC plagioclase U concentrations are on the order of 10^{-2}–10^{-1} ppm, whereas OVC zircon U concentrations range from 10^{1}–10^{2}. Based on mass balance calculations assuming a mixture of zircon and plagioclase and using U concentration calculated for a theoretically pure plagioclase separate and U concentration measured in a OVC zircon, we calculate that the plagioclase bulk separate U budget is 0.1–0.4% of a single zircon U budget. Thus, a single zircon crystal could dominate the U-Th systematics of the bulk plagioclase separate. In such cases, the bulk mineral separate would have U-series characteristics that are similar to those expected for zircon rather than plagioclase.



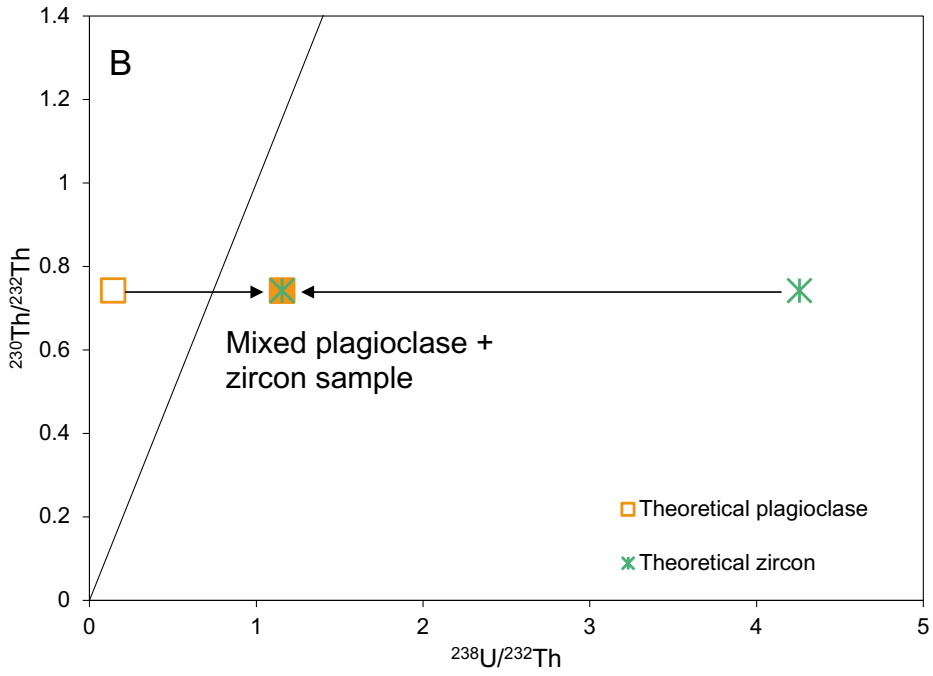


Figure 3.7*: Panel A: Illustrates a mixed population of the same mineral will yield isochrons between the two mixing components, depending on the relative proportions of the mixture. Panel B: Illustrates the placement of a mixed cogenetic pair of minerals; symbols as in Figure 3.6. The plagioclase separate that contains cogenetic zircon will plot between pure plagioclase and zircon, often to the right of the equiline depending on the amount of zircon contamination. Fine black line represents secular equilibrium equiline.*

Minerals that crystallize at different times and from different host liquids may have different Th isotopic compositions because the melts from which they crystallized would not necessarily have had the same initial Th isotopic composition. Such mineral suites will not define a linear array (except in special cases), and any apparent age information will be inconclusive. In these cases where bulk ^{238}U-^{230}Th crystallization ages do not yield much useful information it is helpful to pair these data with other datasets such as ^{230}Th-^{226}Ra crystallization ages or in-situ ^{238}U-^{230}Th crystallization ages in order gain insights into crystallization dynamics in the magma reservoir.

Previous studies have successfully resolved bulk major mineral ^{238}U-^{230}Th crystallization ages in hotspot and some arc volcanic settings (i.e. Hawaii, Yellowstone, Mt. Hood, South Sister, Mount. St. Helens; Cooper et al. 2001, Cooper and Reid 2003, Eppich et al. 2012, Schlieder et al. 2022, Stelten et al. 2012, Stelten et al. 2015), but results from the TVZ have been mixed. Rubin (2016) found that mineral inclusions and antecrystic minerals produced non-linear arrays that obfuscated ^{238}U-^{230}Th crystallization ages. Charlier et al. (2003) were able to construct five- and six-point isochrons (whole rock, plagioclase, Fe-Ti oxides, zircon, and "ferromags:" cummingtonite, orthopyroxene, hornblende, and biotite) for Rotoiti, both resulting in resolvable ^{238}U-^{230}Th crystallization ages assuming the same age of all of the component minerals. Given these mixed results, the goal of our work was to remove some of the complicating factors (i.e. mineral and glass inclusions) in order to resolve crystallization ages as consistent with other age determinations from the TVZ (i.e. eruption age, in-situ ^{238}U-^{230}Th ages on zircon).

3.5.2 Okataina Volcanic Center minerals

Previous studies have found that OVC glasses yield $(^{238}U)/(^{232}Th)$ ratios between 0.683 – 0.755 and $(^{230}Th)/(^{232}Th)$ of 0.701 – 0.748 (Charlier et al. 2003; Charlier and Wilson 2010). Our glass data from the four OVC eruptions presented here are consistent with activity ratios from these other studies (Table 3.3). There are very few published datasets that present U-series data for OVC plagioclase. A study by Charlier et al. (2003) measured U-Th disequilibria in a Rotoiti plagioclase separate, yielding $(^{238}U)/(^{232}Th) = 0.611$ and $(^{230}Th)/(^{232}Th) = 0.684$ (Fig.10). Our OVC plagioclase data plot from 0.676 – 0.767 in $(^{238}U)/(^{232}Th)$ and 0.731 – 0.767 in $(^{230}Th)/(^{232}Th)$ (Table 3.3, Fig. 3.8).

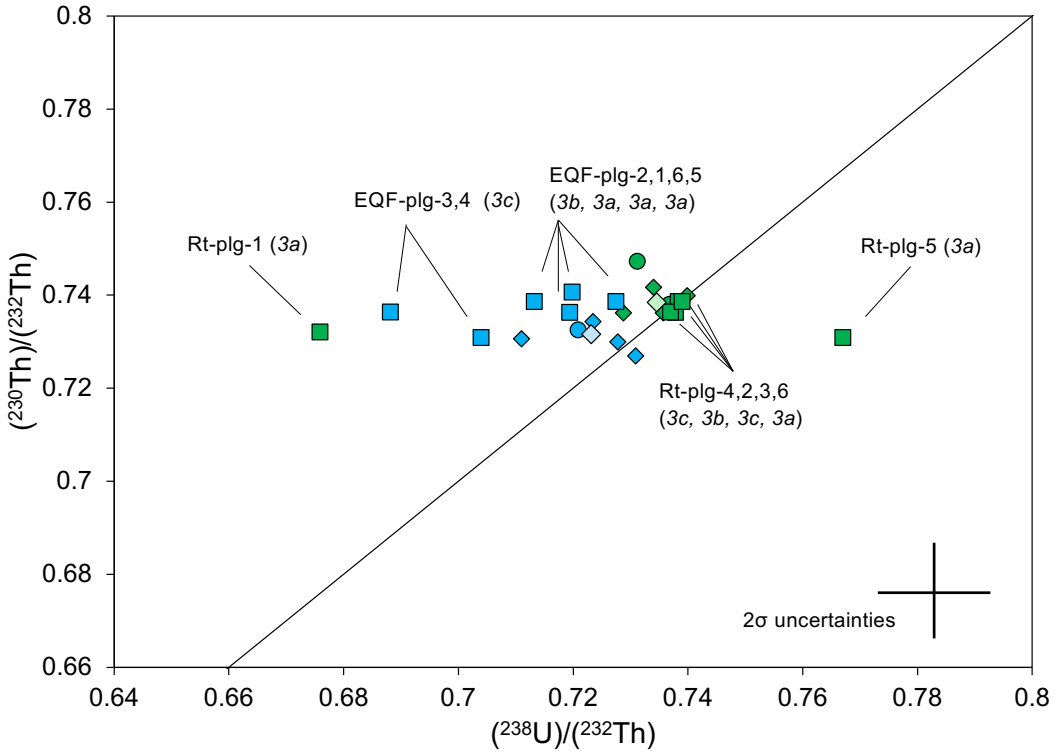


***Figure 3.8**: ^{238}U-^{230}Th isochron diagrams for all of the Okataina Volcanic Center (OVC) mineral, glass and whole rock data; Panel B: Inset from panel A shows a detailed ^{238}U-^{230}Th isochron diagram; Symbols as follows, circles: whole rock, diamonds: glass, squares: plagioclase, rectangles: biotite, triangles: hornblende, boxed plus sign: magnetite; red symbols: Kakapiko Dome samples, green symbols: Rotoiti samples, blue symbols: Earthquake Flat (EQF) samples, and yellow symbols: Hauparu samples; characteristic 2σ uncertainties are presented for (^{238}U)/(^{232}Th) and (^{230}Th)/(^{232}Th). Fine black line represents secular equilibrium equiline.*

While we do not expect plagioclase samples from different eruptions within the same volcanic center to necessarily plot within uncertainty of each other, it is reasonable to expect that the samples would have similar (^{238}U)/(^{232}Th) and (^{230}Th)/(^{232}Th) ratios. The spread in glass and plagioclase data from this study are likely caused by the compositional and volumetric diversity of inclusions within the samples. All of the Rotoiti glass samples (gl-2 (*2a*), gl-3 (*2c*), gl-4 (*2c*), gl-5 (*2b*)) and Rotoiti plg-2 (*3b*), plg-3 (*3c*), plg-4 (*3c*), and plg-6 (*3a*) plot within uncertainty of

each other (Fig. 3.8). The overlapping glass samples suggests that the processing between steps *2a, 2b*, and *2c*, did not greatly affect the glass measurements. The two whole rock samples are within uncertainty of all the glass samples, which suggests that the U-series data in the whole rock are dominated by glass. The fact that most of the Rotoiti plagioclase separates (plg-2 (*3b*), plg-3 (*3c*), plg-4 (*3c*), and plg-6 (*3a*)) all plot within uncertainty of each other, and the glasses (Fig. 3.8), suggests that the processing was ineffective at removing melt inclusions from the plagioclase bulk separate for these samples. Rotoiti plg-1 (*3a*) has the lowest (^{238}U)/(^{232}Th) ratio of all of the measured Rotoiti plagioclase samples (i.e., more similar to the U/Th ratio expected for pure plagioclase) despite having the least amount of processing, which suggests that this sample had fewer inclusions by chance. Rotoiti plg-5 (*3a*) has the highest (^{238}U)/(^{232}Th) ratio of all the plagioclase data and plots to the right of the equiline, which suggests that this sample might have contained a micro-inclusion of a high concentration U phase such as zircon that dominated the U-Th systematics.

The EQF whole rock, glass, and plagioclase samples are entirely within uncertainty of each other despite being processed to different levels, with the exception of EQF plg-3 *(3c)* which has the lowest (^{238}U)/(^{232}Th) ratio of all of the EQF samples and is only within uncertainty of two EQF plagioclase samples and one EQF glass sample. EQF plg-3 (*3c*) and plg-4 (*3c*) have lower (^{238}U)/(^{232}Th) ratios than the other plagioclase samples, the glass, and the whole-rock, and were both processed to stage *3c* (Fig. 3.3), although it is clear that EQF plg-4 (*3c*) must have had more inclusions relative to EQF plg-3 (*3c*) (Fig. 3.8). The low (^{238}U)/(^{232}Th) Earthquake Flat plagioclase samples suggest some success in sample processing. Although we can estimate theoretical plagioclase activity ratios, it remains somewhat unclear where the true EQF plagioclase should plot if the plagioclase matrix were free of inclusions due to highly albitic EQF

plagioclase and the uncertainty in U and Th partition coefficients in albitic plagioclase. Rotoiti plg-1 (*3a*) plots to the left of EQF plg-3 (*3c*) and is less processed, but some natural variation between eruptions from the same volcanic center should be expected, and therefore without knowing the true (^{238}U)/(^{232}Th) ratios for the Rotoiti and EQF plagioclase, we cannot compare these sample from these two eruptions. Figure 3.9 illustrates where the OVC minerals plot relative to the theoretical mineral separates and suggests that the OVC minerals from this study are dominated by glass inclusions.

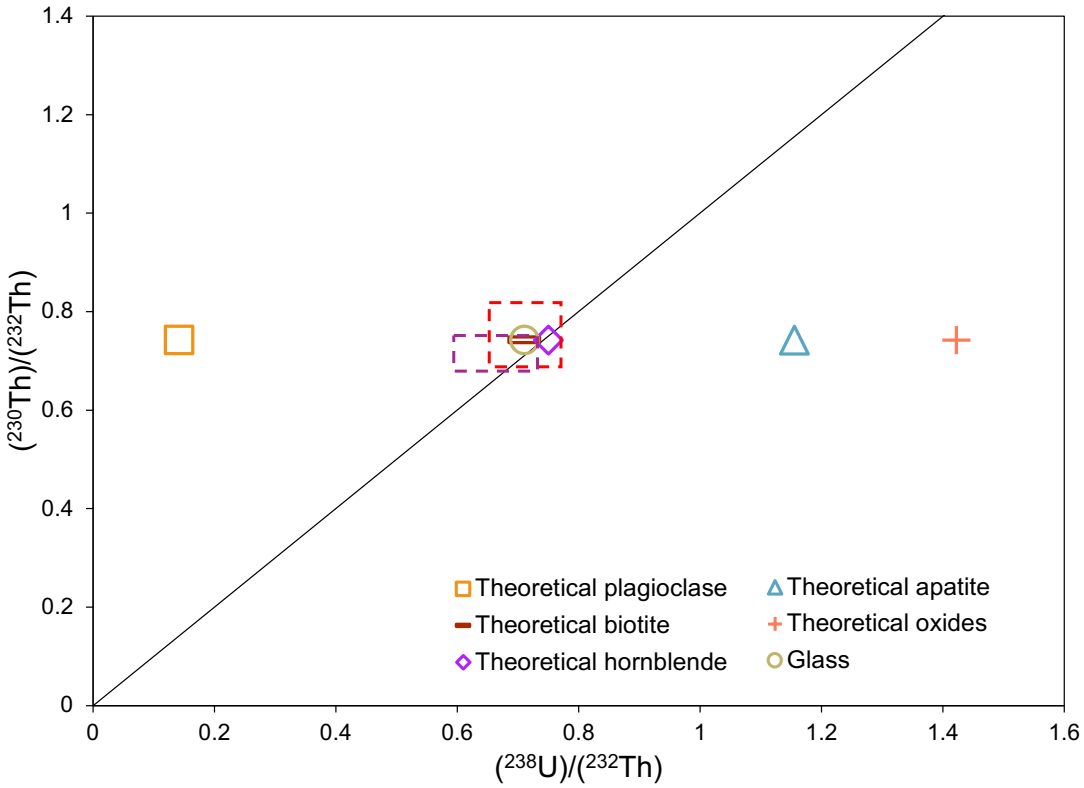


Figure 3.9: *^{238}U-^{230}Th diagram illustrating the theoretical location of minerals at the time of crystallization, based on U and Th partitioning. Symbols as in Figure 3.6; Red dashed box illustrates the range of OVC minerals from this study with the exception of EQF bte-1 and*

EQF hbl-2; Purple dashed box illustrates the range of plagioclase and glass (^{238}U)/(^{232}Th) and (^{230}Th)/(^{232}Th) ratios for Rotoiti and EQF glass and plagioclase.

Based on estimations of partitioning, the U and Th partition coefficients are predicted to be similar to each other in hornblende and biotite, and the two minerals are therefore expected to plot very close to the glass data (Fig. 3.6). This is the case for some samples (Fig. 3.4), however, some of the measured hornblende and biotite do not follow this pattern and plot to the left of the equiline (i.e. enriched in ^{230}Th relative to ^{238}U) and with anomalously high (^{230}Th)/(^{232}Th) ratios compared to glass. Samples with these characteristics should evolve toward lower (^{230}Th)/(^{232}Th) ratios over time, therefore the high (^{230}Th)/(^{232}Th) ratios compared to glass cannot be explained by aging. Instead, high (^{230}Th)/(^{232}Th) values relative to glass require the addition of an isotopically different Th component in order to explain the data (e.g. crystallization from a melt with higher (^{230}Th)/(^{232}Th)). Such a component could be due to the assimilation of xenocrystic materials of different isotopic composition. A Th isotopic compositional study of the mafic phases is needed to quantify the extent to which xenocrystic materials might be incorporated in the OVC minerals.

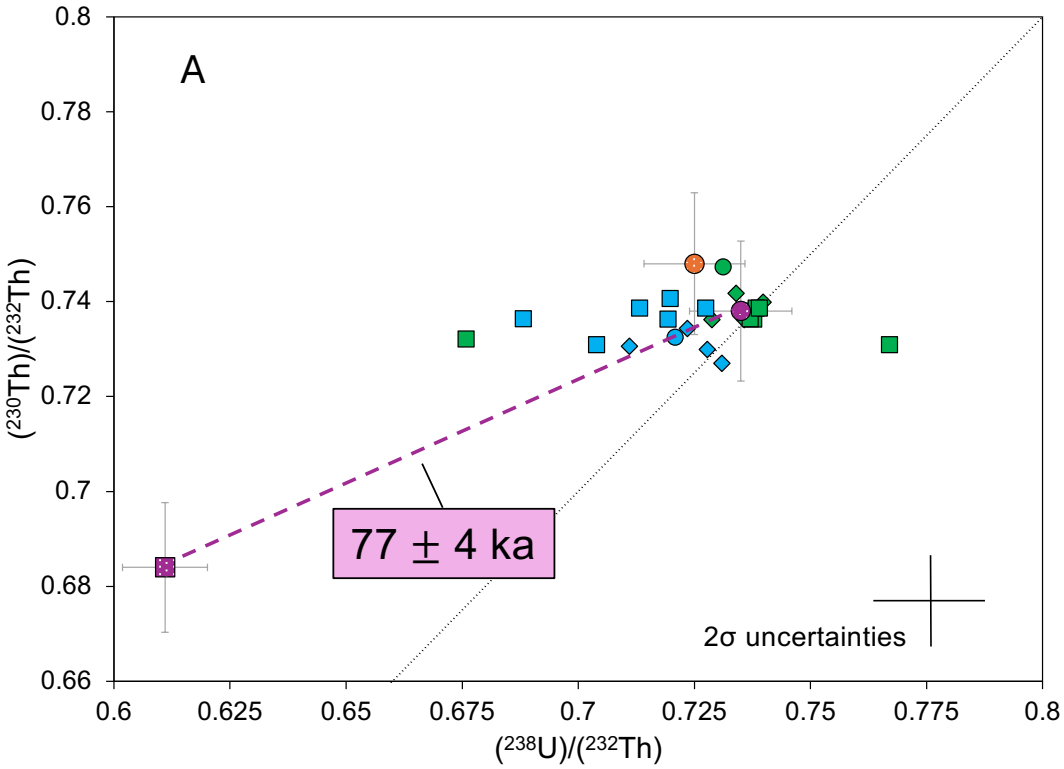
EQF bte-1 (*4a*) also plots at higher (^{230}Th)/(^{232}Th) ratios than the EQF glass and plagioclase data (Fig. 3.4). The high (^{230}Th)/(^{232}Th) ratio suggests that the biotite sample is derived from a different source material or that the inclusions within the biotite were sourced from an isotopically distinct material. EQF bte-2 (*4b*) plots along the same horizontal array as the plagioclase and glass samples but at a lower (^{238}U)/(^{232}Th) ratio of 0.654. Although EQF bte-2 (*4b*) plots along a horizontal array with EQF plagioclase and glass it is inconsistent with the ~45 ka eruption age. EQF hbl-1 (*5a*) plots within uncertainty of the EQF glass and whole rock, which suggests that the EQF hbl-1 (*5a*) measurement follows the expected pattern of U and Th

partitioning (Fig. 3.4). However, BSE images of EQF hbl-1 (*5a*) (Fig. 3.5N) reveal numerous mineral and glass inclusions within the sample. This finding highlights the need for a rigorous study that quantifies U and Th partitioning into mafic phases such as hornblende. EQF hbl-2 (*5b*) plots at (^{238}U)/(^{232}Th) = 0.473 and (^{230}Th)/(^{232}Th) = 0.960, which is the lowest (^{238}U)/(^{232}Th) ratio and the highest (^{230}Th)/(^{232}Th) of all the OVC samples, far above the cloud of glass and plagioclase data (Fig. 3.4). Similar to EQF bte-1 (*4a*), this sample might contain material that is from an isotopically distinct source, which would explain the high (^{230}Th)/(^{232}Th) ratio. It is interesting that the more processed of the two hornblende samples contains the isotopically heterogeneous material, but as we only ran one aliquot of hornblende for each step in the purification process (Fig. 3.3), it is possible that this unexpected result is due to sampling bias. Additional measurements would be required to determine the source of the isotopically heterogenous material.

3.5.3 Comparison to other studies

Charlier et al. (2003) presented U-series data for Rotoiti whole rock and plagioclase, and EQF whole rock. Our glass and whole rock data plot within uncertainty of the Charlier et al. (2003) whole rock data, but none of our plagioclase are within uncertainty of the Charlier et al. (2003) plagioclase data (Table 3.3, Fig. 3.10A). The Charlier et al. (2003) Rotoiti plagioclase was separated in a bulk sieving process (0.063 – 0.25 mm), and zircon were removed using a heavy liquid separation. It is unclear how the plagioclase separate was processed beyond that. They used between 0.1 and 1 g of material for their TIMS analysis, and their resulting measurements were (^{238}U)/(^{232}Th) = 0.611 and (^{230}Th)/(^{232}Th) = 0.684. The Charlier et al. (2003) plagioclase measurement is closer to theoretical U/Th ratio of plagioclase than are our plagioclase samples

(Fig. 3.9), and although it is unlikely that pure OVC plagioclase would fall exactly on the theoretical plagioclase point defined in figure 3.6 because the U and Th partition coefficients in plagioclase are anorthite dependent and the OVC plagioclase are more albitic than those plagioclase on which the theoretical partition coefficients were based (Blundy and Wood 1991, Blundy and Wood 2003), pure OVC plagioclase is likely closer to the Charlier et al. (2003) plagioclase data than to ours. The construction of a five- and six-point isochron between the mineral separate measurements from Charlier et al. (2003) produces a geologically reasonable date of 77 ± 4 ka, although attaching age significance to such an isochron would require that all phases including plagioclase, "ferromags," magnetite, and zircon crystallized at the same time.



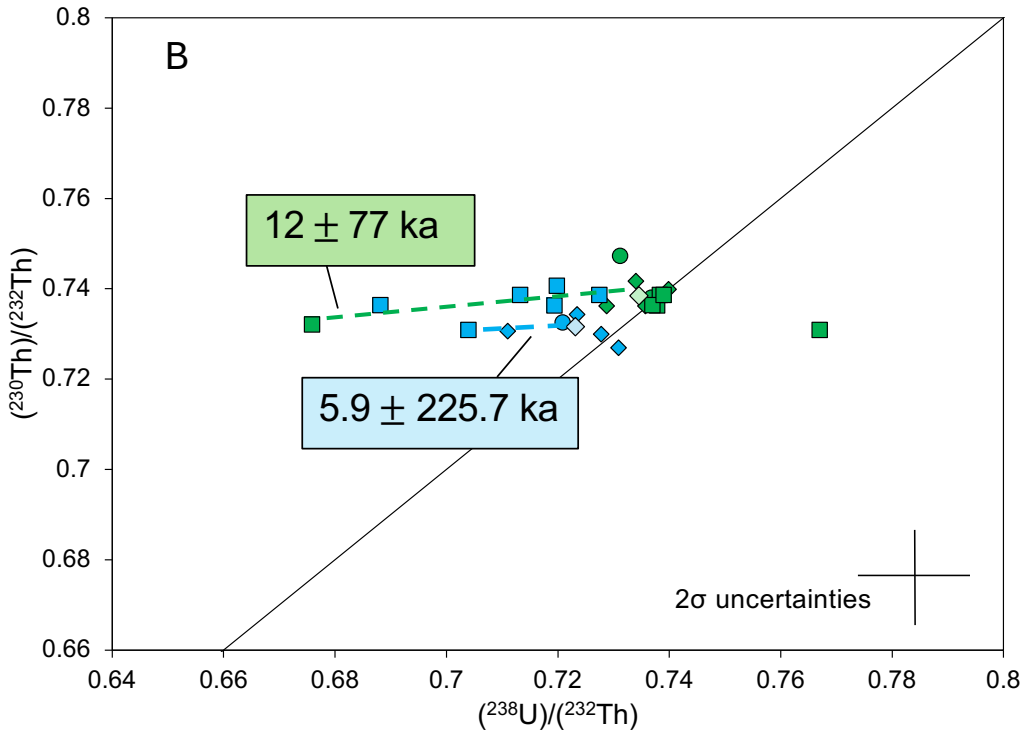


***Figure 3.10**: ^{238}U-^{230}Th isochron diagrams of the Rotoiti and Earthquake Flat (EQF) whole rock (circles), glass (diamonds), and plagioclase (squares) from this study; Panel A: Includes Rotoiti whole rock (purple stippled circle) and plagioclase (purple stippled square), and the EQF whole rock (orange stippled circle) from Charlier et al. (2003), uncertainties are 1.5% for (^{238}U)/(^{232}Th) and 2% for (^{230}Th)/(^{232}Th); six-point isochron between Rotoiti whole rock and plagioclase of Charlier et al. (2003) yields a crystallization age of 77 ± 4 ka; Panel B: Two-point isochrons constructed between the lowest (^{238}U)/(^{232}Th) ratio plagioclase samples and an average of the glass samples for each eruption (Rotoiti average glass is light green diamond; EQF average glass is light blue diamond); characteristic 2σ uncertainties are presented (^{238}U)/(^{232}Th) and (^{230}Th)/(^{232}Th); Fine black dotted line represents secular equilibrium equiline.*

We used IsoplotR to construct two-point isochrons using an average of the Rotoiti glass samples and the EQF glass samples and the plagioclase samples with the lowest measured (^{238}U)/(^{232}Th) ratio (we used EQF plg-4 (*3c*) to avoid a negative slope isochron, as negative slope isochrons in IsoplotR yield a null result) (Fig. 3.10B). Our Rotoiti and EQF isochrons yield

apparent ^{238}U-^{230}Th crystallization ages of 12 ± 77 ka for Rotoiti, and 5.9 ± 225.7 for EQF, which are highly imprecise but technically within uncertainty of eruption (~45 ka). The large uncertainties on the isochron are largely due to the proximity of the plagioclase and glass data, likely reflecting the presence of glass within the bulk separate. If plagioclase plotted at lower (^{238}U)/(^{232}Th), as predicted by U and Th partitioning, then the uncertainties on the isochron would yield a more precise result, as with the Charlier et al. (2003) data. Due to the abundance of glass and other inclusions observed in BSE within the plagioclase grains and the large proportion of quartz grains (which contain abundant and large melt inclusions) in the plagioclase bulk splits, the plagioclase split does not plot where it is expected to based on theory. Thus, we can be confident that the plagioclase analyses were dominantly measuring a glass signature, rather than a true plagioclase signature. Due to the low concentration of the U and Th in the plagioclase lattice, relative to glass, even a very small amount of glass (or a larger amount of melt inclusion-bearing quartz) will dominate the U and Th signature. Our two-point isochron date, while technically resolvable within uncertainty of eruption, does not fit with evidence from other studies and sources. The geologically syn-eruptive Rotoiti and EQF eruptions occurred between ~45 and ~62 ka (Charlier et al. 2003, Danišík et al. 2012, Rubin et al. 2016, Wilson et al. 1992), which at the very minimum precludes a <45 ka crystallization age, since this would post-date eruption. The preponderance of data points plotting within uncertainty of glass, suggests that glass is still a major component in the mineral separates despite the efforts to rid the samples of impurities.

The methodologies followed by Rubin (2016) and Charlier et al. (2003) are reported as identical. So why is it that plagioclase ^{238}U-^{230}Th crystallization ages are only sometimes successful in the OVC? One explanation for this disparity in ^{238}U-^{230}Th crystallization age results

could be the sample from which the plagioclase were derived. Pyroclastic deposits in the OVC are unwelded, massive, matrix-supported flows, oftentimes, intercalated with ash beds (Davis 1985, Schmitz and Smith 2004); they are voluminous (0.1–100 km^3), not always well exposed, and wide-reaching, extending from the OVC caldera to the Bay of Plenty (Fig. 3.1) (Jurado-Chichay and Walker 2000, Schmitz and Smith 2004, Smith et al. 2005). The Rotoiti caldera-forming eruption, and Earthquake Flat (EQF) syn-caldera-forming eruption are both reported as unzoned or weakly zoned (Schmitz and Smith 2004, Molloy et al. 2008), and are inconsistent with the zoned stratigraphy from other major ignimbrite deposits such as the Bishop Tuff (Hildreth and Wilson 2007). Given that the tuff deposits are heterogeneous, and the magma reservoir highly complexity, it is possible that different sampling locations could result in the sampling of different crystal cargos. If this is the case, it is also possible that different samples from a chaotic pyroclastic deposit would result in different ^{238}U-^{230}Th crystallization ages.

3.5.4 Complexities of growth from a magma mush

Evidence from in-situ U-series measurements on zircon surfaces show that zircon crystals generally do not crystallize in a single episode but have protracted crystallization records that range from within uncertainty of eruption to secular equilibrium (Chapter 2; Reid et al. 1997, Reid and Vazquez 2017, Rubin et al. 2016, Stelten et al. 2013, Stelten et al. 2015, Storm et al. 2011, Storm et al. 2012, Storm et al. 2014, Vazquez and Reid 2002), suggesting that for these systems zircon is within the threshold of its saturation parameters throughout much of the duration of the its magma residence time. Similar results from other studies show protracted growth of major minerals, which is captured by complicated records of plagioclase growth zones. Rotoiti and EQF plagioclase contain resorbed calcic cores, sometimes with patchy zoning,

and with overgrowths of oscillatory zoning (Grant et al. 2024, Molloy et al. 2008), suggesting that plagioclase was on the liquidus for most of the magma's history (Sas et al. 2021, Schmitz and Smith 2004). Collectively these observations suggest that TVZ mineral growth was sustained throughout the magma reservoir history. One key interpretation is that many of the OVC magmas, especially Rotoiti, EQF, and Kakapiko Dome, were likely stored in highly crystalline mush environments. Evidence from petrography shows large (>2 mm) grains, euhedral–subhedral mineral habits, idiomorphic rims, and abundant glomerocrysts, all of which suggest that minerals were stored in a crystal-rich environment where evolved melts occupied interstitial space within the crystalline framework (Deering et al. 2011, Grant et al. 2024, Sas et al. 2021, Storm et al. 2014).

Given the long durations over which these minerals can crystallize, and the proximity of various mineral phases either growing or nucleating on neighboring minerals, it is unsurprising that the OVC minerals contain abundant inclusions. The OVC bulk major mineral splits are complicated by the abundance of mineral inclusions within major phases resulting in a U-series signature that is dominated by glass, as well as antecrystic cores and younger rims resulting in a mixed ^{238}U-^{230}Th age. Although the ^{238}U-^{230}Th crystallization ages are technically within uncertainty of eruption age (given the large uncertainties), the combination of mineral inclusions and mixed populations complicate the ^{238}U-^{230}Th crystallization ages, making the results difficult to interpret and precluding any insightful observations.

3.6 CONCLUSIONS

Despite our new workflow, the bulk of the OVC glass and plagioclase data are within uncertainty of each other, suggesting that we were unable to sufficiently rid the plagioclase mineral separate

of glass (and possibly other) inclusions. The ^{238}U-^{230}Th two-point isochron ages yield apparent ages within uncertainty of eruption, given the uncertainties. Purifying mineral separates that contain abundant and diverse inclusions is challenging, and it is recommended to all future U-series workers to pre-screen their samples with BSE imaging to determine the type and volume of inclusions. In the case of plagioclase grains with abundant melt inclusions, it is recommended to hand pick plagioclase samples to ensure that all grains are free of inclusions. It is possible and feasible to measure an accurate and precise ^{238}U-^{230}Th crystallization age for TVZ major minerals, but it will take careful observation of the minerals and thorough and methodical separation of the inclusion-free grains.

3.7 REFERENCES

Blundy, J., & Wood, B. (2003). Mineral-melt partitioning of uranium, thorium and their daughters. *Reviews in Mineralogy and Geochemistry*, *52*(1), 59-123.

Bourdon, B., Turner, S., Henderson, G. M., & Lundstrom, C. C. (2003). Introduction to U-series geochemistry. *Reviews in mineralogy and geochemistry*, *52*(1), 1-21.

Cashman, K. V. (1992). Groundmass crystallization of Mount St. Helens dacite, 1980–1986: a tool for interpreting shallow magmatic processes. *Contributions to Mineralogy and Petrology*, *109*(4), 431-449.

Charlier, B. L., Peate, D. W., Wilson, C. J., Lowenstern, J. B., Storey, M., & Brown, S. J. (2003). Crystallisation ages in coeval silicic magma bodies: 238U–230Th disequilibrium evidence from the Rotoiti and Earthquake Flat eruption deposits, Taupo Volcanic Zone, New Zealand. *Earth and Planetary Science Letters*, *206*(3-4), 441–457.

Charlier, B. L. A., & Wilson, C. J. N. (2010). Chronology and evolution of caldera-forming and post-caldera magma systems at Okataina Volcano, New Zealand from zircon U–Th model-age spectra. *Journal of Petrology*, *51*(5), 1121–1141.

Cheng, H., Edwards, R. L., Shen, C. C., Polyak, V. J., Asmerom, Y., Woodhead, J., Hellstorm, J., Wang, Y., Kong, X., Spötl, C., Wang, X., & Alexander Jr, E. C. (2013). Improvements in ^{230}Th dating, ^{230}Th and ^{234}U half-life values, and U–Th isotopic measurements by multi-collector

inductively coupled plasma mass spectrometry. *Earth and Planetary Science Letters*, *371*, 82–91.

Cherniak, D. J. (1996). Strontium diffusion in sanidine and albite, and general comments on strontium diffusion in alkali feldspars. *Geochimica et Cosmochimica Acta*, *60*(24), 5037-5043.

Cole, J. W., Deering, C. D., Burt, R. M., Sewell, S., Shane, P. A. R., & Matthews, N. E. (2014). Okataina Volcanic Centre, Taupo Volcanic Zone, New Zealand: A review of volcanism and synchronous pluton development in an active, dominantly silicic caldera system. *Earth-Science Reviews*, *128*, 1-17.

Cooper, K. M., Reid, M. R., Murrell, M. T., & Clague, D. A. (2001). Crystal and magma residence at Kilauea Volcano, Hawaii: 230Th–226Ra dating of the 1955 east rift eruption. *Earth and Planetary Science Letters*, *184*(3-4), 703-718.

Cooper, K. M., & Donnelly, C. T. (2008). ^{238}U-^{230}Th-226Ra disequilibria in dacite and plagioclase from the 2004–2005 eruption of Mount St. Helens. *A volcano rekindled: the renewed eruption of Mount St. Helens*, *2006*, 827–846.

Cooper, K. M., & Reid, M. R. (2008). Uranium-series crystal ages. *Reviews in Mineralogy and Geochemistry*, *69*(1), 479-544.

Danišík, M., Shane, P., Schmitt, A. K., Hogg, A., Santos, G. M., Storm, S., Evans, N. J., Fifield, L. K., & Lindsay, J. M. (2012). Re-anchoring the late Pleistocene tephrochronology of New Zealand based on concordant radiocarbon ages and combined 238U/230Th disequilibrium and (U–Th)/He zircon ages. *Earth and Planetary Science Letters*, *349*, 240-250.

Davis WJ (1985). Geochemistry and petrology of the Rotoiti and Earthquake Flat pyroclastic deposits. Unpublished MSc thesis, University of Auckland, New Zealand.

Deering, C. D., Cole, J. W., & Vogel, T. A. (2011). Extraction of crystal-poor rhyolite from a hornblende-bearing intermediate mush: a case study of the caldera-forming Matahina eruption, Okataina volcanic complex. *Contributions to Mineralogy and Petrology*, *161*, 129-151.

Eppich, G. R., Cooper, K. M., Kent, A. J., & Koleszar, A. (2012). Constraints on crystal storage timescales in mixed magmas: Uranium-series disequilibria in plagioclase from Holocene magmas at Mount Hood, Oregon. *Earth and Planetary Science Letters*, *317*, 319-330.

Grant, E. R., Blatter, D. L., Sisson, T. W., & Cooper, K. M. (2024). Shallow storage of the explosive Earthquake Flat Pyroclastics magma body, Okataina Volcanic Center, Taupo Volcanic Zone, New Zealand: evidence from phase-equilibria experiments. *Contributions to Mineralogy and Petrology*, *179*(8), 81.

Giletti, B. J., & Casserly, J. E. D. (1994). Strontium diffusion kinetics in plagioclase feldspars. *Geochimica et Cosmochimica Acta*, *58*(18), 3785-3793.

Hammer, J. E., Cashman, K. V., Hoblitt, R. P., & Newman, S. (1999). Degassing and microlite crystallization during pre-climactic events of the 1991 eruption of Mt. Pinatubo, Philippines. *Bulletin of Volcanology*, *60*, 355-380.

Hammer, J. E., Cashman, K. V., & Voight, B. (2000). Magmatic processes revealed by textural and compositional trends in Merapi dome lavas. *Journal of Volcanology and Geothermal Research*, *100*(1-4), 165-192.

Hildreth W, Wilson CJ (2007). Compositional zoning of the Bishop Tuff. Journal of Petrology 48(5): 951-999. https://doi.org/10.1093/petrology/egm007

Holden, N. E. (1990). Total half-lives for selected nuclides. *Pure and Applied Chemistry*, *62*(5), 941–958.

Jaffey, A. H., Flynn, K. F., Glendenin, L. E., Bentley, W. T., & Essling, A. M. (1971). Precision measurement of half-lives and specific activities of ^{235}U and ^{238}U. *Physical review C*, *4*(5), 1889.

Jurado-Chichay, Z., & Walker, G. P. L. (2000). Stratigraphy and dispersal of the Mangaone Subgroup pyroclastic deposits, Okataina Volcanic Centre, New Zealand. *Journal of Volcanology and Geothermal Research*, *104*(1-4), 319-380.

Langridge, R.M., Ries, W.F., Litchfield, N.J., Villamor, P., Van Dissen, R.J., Barrell, D.J.A., Rattenbury, M.S., Heron, D.W., Haubrock, S., Townsend, D.B., Lee, J.M., Berryman, K.R., Nicol, A., Cox, S.C., Stirling, M.W. (2016). The New Zealand Active Faults Database. *New Zealand Journal of Geology and Geophysics 59*: 86-96. doi: 10.1080/00288306.2015.1112818.

LaTourrette, T., Wasserburg, G. J., & Fahey, A. J. (1996). Self diffusion of Mg, Ca, Ba, Nd, Yb, Ti, Zr, and U in haplobasaltic melt. *Geochimica et Cosmochimica Acta*, *60*(8), 1329-1340.

LaTourrette, T., & Wasserburg, G. J. (1997). Self diffusion of europium, neodymium, thorium, and uranium in haplobasaltic melt: The effect of oxygen fugacity and the relationship to melt structure. *Geochimica et Cosmochimica acta*, *61*(4), 755-764.

Luhr, J. F., Carmichael, I. S., & Varekamp, J. C. (1984). The 1982 eruptions of El Chichón Volcano, Chiapas, Mexico: mineralogy and petrology of the anhydrite-bearing pumices. *Journal of Volcanology and Geothermal Research*, *23*(1-2), 69-108.

Mahood, G. A., & Stimac, J. A. (1990). Trace-element partitioning in pantellerites and trachytes. *Geochimica et Cosmochimica Acta*, *54*(8), 2257-2276.

Marcaida, M., Vazquez, J. A., Stelten, M. E., & Miller, J. S. (2019). Constraining the early eruptive history of the Mono Craters rhyolites, California, based on ^{238}U-^{230}Th isochron dating of

their explosive and effusive products. *Geochemistry, Geophysics, Geosystems*, *20*(3), 1539–1556.

Molloy C, Shane P, Nairn I (2008). Pre-eruption thermal rejuvenation and stirring of a partly crystalline rhyolite pluton revealed by the Earthquake Flat Pyroclastics deposits, New Zealand. Journal of the Geological Society 165(1): 435–447. https://doi.org/10.1144/0016-76492007-071

Pietruszka, A. J., Carlson, R. W., & Hauri, E. H. (2002). Precise and accurate measurement of ^{226}Ra–^{230}Th–^{238}U disequilibria in volcanic rocks using plasma ionization multicollector mass spectrometry. *Chemical Geology*, *188*(3–4), 171–191.

Reid, M. R., Coath, C. D., Harrison, T. M., & McKeegan, K. D. (1997). Prolonged residence times for the youngest rhyolites associated with Long Valley Caldera: ^{230}Th—^{238}U ion microprobe dating of young zircons. *Earth and Planetary Science Letters*, *150*(1-2), 27–39.

Reid, M. R., & Vazquez, J. A. (2017). Fitful and protracted magma assembly leading to a giant eruption, Youngest Toba Tuff, Indonesia. *Geochemistry, Geophysics, Geosystems*, *18*(1), 156–177.

Rubin, A. E. (2016). *Constraining the thermal and chemical evolution of large silicic volcanic centers: Insights from the crystal record at Okataina Caldera Center, New Zealand* (Order No. 10244174). Available from Dissertations & Theses @ University of California; ProQuest Dissertations & Theses A&I. (1872339951). Retrieved from https://www.proquest.com/dissertations-theses/constraining-thermal-chemical-evolution-large/docview/1872339951/se-2

Rubin, A., Cooper, K. M., Leever, M., Wimpenny, J., Deering, C., Rooney, T., Gravley, D., & Yin, Q. Z. (2016). Changes in magma storage conditions following caldera collapse at Okataina Volcanic Center, New Zealand. *Contributions to Mineralogy and Petrology*, *171*, 1–18.

Ruprecht, P., & Cooper, K. M. (2012). Integrating the uranium-series and elemental diffusion geochronometers in mixed magmas from Volcán Quizapu, Central Chile. *Journal of Petrology*, *53*(4), 841-871.

Sas, M., Shane, P., Kuritani, T., Zellmer, G. F., Kent, A. J., & Nakagawa, M. (2021). Mush, melts and metasediments: a history of rhyolites from the Okataina Volcanic Centre, New Zealand, as captured in plagioclase. *Journal of Petrology*, *62*(8), egab038.

Schlieder, T. D., Cooper, K. M., Kent, A. J., Bradshaw, R., & Huber, C. (2022). Thermal storage conditions and origin of compositional diversity of plagioclase crystals in magmas from the 1980 and 2004–2005 eruptions of Mount Saint Helens. *Journal of Petrology*, *63*(8), egac064.

Schmitz MD, Smith IEM (2004). The petrology of the Rotoiti eruption sequence, Taupo Volcanic Zone: An example of fractionation and mixing in a rhyolitic system. Journal of Petrology 45(10): 2045–2066. https://doi.org/10.1093/petrology/egh047

Schoene, B. (2014). U–Th–Pb Geochronology. *Treatise on geochemistry*, *4*, 341-378.

Sims, K. W., Gill, J. B., Dosseto, A., Hoffmann, D. L., Lundstrom, C. C., Williams, R. W., Ball, L., Tollstrup, D., Turner, S., Prytulak, J., Glessner, J.G., Standish, J.J., Elliott, T. (2008). An inter-laboratory assessment of the thorium isotopic composition of synthetic and rock reference materials. *Geostandards and Geoanalytical Research*, *32*(1), 65–91.

Smith VC, Shane P, Nairn IA (2005). Trends in rhyolite geochemistry, mineralogy, and magma storage during the last 50 kyr at Okataina and Taupo Volcanic Centres, Taupo Volcanic Zone, New Zealand. Journal of Volcanology and Geothermal Research, 148(3-4): 372-406. https://doi.org/10.1016/j.jvolgeores.2005.05.005

Stelten, M. E., & Cooper, K. M. (2012). Constraints on the nature of the subvolcanic reservoir at South Sister volcano, Oregon from U-series dating combined with sub-crystal trace-element analysis of plagioclase and zircon. *Earth and Planetary Science Letters*, *313*, 1-11.

Stelten, M. E., Cooper, K. M., Vazquez, J. A., Reid, M. R., Barfod, G. H., Wimpenny, J., & Yin, Q. Z. (2013). Magma mixing and the generation of isotopically juvenile silicic magma at Yellowstone caldera inferred from coupling 238 U–230 Th ages with trace elements and Hf and O isotopes in zircon and Pb isotopes in sanidine. *Contributions to Mineralogy and Petrology*, *166*, 587-613.

Stelten, M. E., Cooper, K. M., Vazquez, J. A., Calvert, A. T., & Glessner, J. J. (2015). Mechanisms and timescales of generating eruptible rhyolitic magmas at Yellowstone caldera from zircon and sanidine geochronology and geochemistry. *Journal of Petrology*, *56*(8), 1607–1642.

Storm, S., Shane, P., Schmitt, A. K., & Lindsay, J. M. (2011). Contrasting punctuated zircon growth in two syn-erupted rhyolite magmas from Tarawera volcano: Insights to crystal diversity in magmatic systems. *Earth and Planetary Science Letters*, *301*(3-4), 511-520.

Storm, S., Shane, P., Schmitt, A. K., & Lindsay, J. M. (2012). Decoupled crystallization and eruption histories of the rhyolite magmatic system at Tarawera volcano revealed by zircon ages and growth rates. *Contributions to Mineralogy and Petrology*, *163*, 505-519.

Storm, S., Schmitt, A. K., Shane, P., & Lindsay, J. M. (2014). Zircon trace element chemistry at sub-micrometer resolution for Tarawera volcano, New Zealand, and implications for rhyolite magma evolution. *Contributions to Mineralogy and Petrology*, *167*, 1-19.

Waters, L. E., Andrews, B. J., & Lange, R. A. (2015). Rapid crystallization of plagioclase phenocrysts in silicic melts during fluid-saturated ascent: phase equilibrium and decompression experiments. *Journal of Petrology*, *56*(5), 981-1006.

Wilson, C. J. N., Houghton, B. F., Lanphere, M. A., & Weaver, S. D. (1992). A new radiometric age estimate for the Rotoehu Ash from Mayor Island volcano, New Zealand.

CHAPTER FOUR

Trace element diffusion modeling in plagioclase from the Okataina Volcanic Center, Taupo Volcanic Zone, New Zealand

Elizabeth R. G. Grant
Kari M. Cooper
Darren M. Gravley
Chad D. Deering
Adam J.R. Kent

4.1 ABSTRACT

Diffusion chronometry is a useful tool that can place timescales on magmatic processes such as magma ascent, recharge, mixing, and storage. Quantifying timescales of magma processes can help to understand how magma bodies assemble in the shallow crust prior to eruption. Plagioclase is a ubiquitous silicate mineral present in a wide compositional range of magmas and is thus a useful target for trace element diffusion studies. Here we use Sr in plagioclase diffusion to quantify the timescales that plagioclase crystals could have been stored at a range of temperatures (600–850 ºC). Our results show that for many of the Okataina Volcanic Center plagioclase, there is a strong positive correlation between Sr and anorthite content and flat Sr profiles, which suggests that crystals grew rapidly enough such that Sr did not have the time to equilibrate prior to eruption, and/or that the plagioclase grew in the presence of a compositionally changing magma. While such crystals provide information about magma processes, they are not candidates for trace element diffusion modeling. For the crystals that contained relaxed Sr profiles (i.e. sufficiently relaxed for modelling purposes), we modeled diffusive timescale around the rheological lock-up temperature of 750 ºC. At the rheological lock-up temperature where magma convection is inhibited by the formation of a crystalline framework, storage conditions should be more dominant. If crystals are stored for a long duration below the rheological lock-up temperature of 750 ºC then we would expect to see more Sr profiles reflecting more relaxation during storage. At 750 ºC our modeled timescales are between 10^0–10^2 years. The two high crystallinity eruptions (Kakapiko Dome and Earthquake Flat) yield longer diffusion timescales (10^1–10^2 years) than the moderate (Rotoiti) and low (Hauparu) crystallinity eruptions (10^1 years, and 10^0 years, respectively). Our results show that the magma processes dominant in the Okataina Volcanic Center magma reservoir are complicated and unlike

other systems that yield more straight-forward results (Mount St. Helens, Mt. Hood, Yellowstone, etc.). Further study of the Okataina Volcanic Center deposits could shed light on some of the more complicated nuances of this system.

4.2 OVERVIEW

Magma assembly and storage timescales are important constraints in understanding the life cycle of caldera-forming eruptions (CFEs) and are critical parameters in volcanic hazard planning and mitigation. Understanding how CFEs build to eruption and how they are stored in the crust is thus a matter of community-wide active research. One aspect of this research is to quantify the residence time of the magma prior to eruption. Variation in temperature will have a strong effect on the residence time of magmas as higher temperature hotter magmas are not sustainable for long timescales relative to lower temperature cooler (<750 ºC) magmas. At crystallinities of ~50%, magmas typically reach a rheological lock-up point where the development of a crystalline framework impedes magma convection (Marsh 1981). In rhyolitic magmas, R-MELTs modeling estimates that ~40-50% crystallinity is reached around 750 ºC (e.g., Cooper and Kent 2014, Schlieder 2022). Therefore, at temperatures <750 ºC we can assume to a first order that the magma had reached rheological lock-up and that minerals were stored as part of a relatively rigid crystal framework. Diffusion chronometry can quantify the residence time as the duration that individual mineral grains and/or mineral populations were stored at a given temperature, which can be related to the physical conditions of magma storage – i.e., a locked crystal mush vs. a liquid-dominated system. Understanding this aspect of magma storage history is important because it facilitates the quantification of storage timescales in different physical states.

Diffusion chronometry is an effective tool to assess magmatic processes such as residence times, mixing, recharge, and ascent, and has been used in numerous recent studies (e.g., Cooper and Kent 2014, Moshrefzadeh et al. 2023, Shamloo et al. 2021, Shea et al. 2015, Zellmer 1999). Here we use Sr diffusion in plagioclase to quantify the timescales on which a crystal (or group of crystals) resided at the modeled temperatures. Diffusive relaxation timescales of Sr in plagioclase coupled with plagioclase crystallization ages are powerful tools that can provide an assessment of thermal histories, defined as the duration the plagioclase were stored at a model temperature prior to eruption (Cooper and Kent 2014). This has major implications for our understanding of how magma reservoirs are assembled and stored in the crust. For example, a study by Cooper and Kent (2014) showed how Sr diffusion profiles and crystallization ages can successfully determine the residence time of plagioclase populations at Mount Hood in liquid-dominated magmas. The quantified thermal histories of the plagioclase grains allowed them to propose that Mount Hood magma was dominantly stored in a crystal-rich, cool environment prior to eruption. This is a significant finding that differs from other work that supports relative relatively high temperature magma storage (Barboni et al. 2016).

Another successful example of thermal history quantification using Sr diffusion modelling in plagioclase comes from Schlieder et al. (2022). The authors presented a summary of thermal histories for plagioclase from Mount St. Helens for a range of scenarios (Fig. 4.2). In scenario 1, a maximum diffusion time was modeled at 173 years (at 750 ºC), but the crystal age was unconstrained, which resulted in an unconstrainted thermal history. In scenario 2, the maximum diffusion time of >10 kyr and a crystal age of >40 kyr resulted in a thermal history calculation of 25% residence time at 750 ºC. In scenario 3, the modeled diffusion profile traversed an interior zone of the crystal that preserved a sharp step function in Sr and anorthite.

The maximum diffusion time of 600 years (at 750 ºC) and crystal age of >20 kyrs resulted in a thermal history of 3% residence time at 750 ºC in order to preserve the observed Sr profile. This type of study is powerful because it allows us to place constraints on the length of time that melt bodies must exist in order to explain the range of observed crystal chemistries. It is worth noting that some volcanic systems are too complicated for similar thermal history calculations, but the diffusion data alone provide important insights into magma reservoir processes (example refs of diffusion studies that didn't do crystal ages).

Here we present model results for Sr diffusion in plagioclase grains from four eruptions from the Okataina Volcanic Center, Taupo Volcanic Zone, New Zealand (Fig. 4.1). The Okataina Volcanic Center (OVC) has complicated crystals that contain sieve textures, a combination of patchy, oscillatory, and normal zoning, resorbed rims, glomerocrystic clusters, and mineral and glass inclusions, all of which makes them difficult for mineral-based study. For this study we were unable to obtain resolvable plagioclase crystallization ages in the OVC, and while we therefore cannot determine the thermal histories for plagioclase crystals, we can instead look at the relative rates of Sr diffusion in the plagioclase grains to understand variations in the thermal conditions of the reservoir during magma storage. Isothermal modelling of Sr diffusion in plagioclase at multiple temperatures allows us to understand possible residence times over a range of temperatures. We can further compare this to rheological lock-up conditions to understand the interplay between crystallinity and temperature in the magma reservoir.

4.3 SAMPLES

We present diffusion modeling results for four erupted units from the OVC: Kakapiko Dome, Rotoiti tuff, EQF tuff, and Hauparu tuff (Fig. 4.1). The Rotoiti eruption produced ~100

km^3 of fall and pyroclastic flow material causing caldera collapse around ~45 ka (Shane et al. 2005a). EQF erupted immediately after Rotoiti (Nairn and Kohn 1973, Molloy et al. 2008) producing ~10 km^3 of fall and pyroclastic flow materials. Rotoiti deposits are crystal-moderate at ~20% crystals, and EQF is crystal-rich, between 25–45% crystals (Molloy et al. 2008). The Kakapiko Dome preceded both Rotoiti and EQF by >100 ka and erupted as an effusive lava with a high crystallinity (~45%). Hauparu erupted 3.9 km^3 of fall and pyroclastic flow materials around 36 ka, ~10–15 ka after the Rotoiti caldera-forming eruption (and the syn-eruptive EQF) (Smith et al. 2005, Shane et al. 2005b). For each eruption, zircon compositional and thermal data shows that heterogenous melt environments existed throughout the magma residence period (Chapter 2; Allan et al. 2013, Bégué et al. 2014, Charlier et al. 2003, Charlier et al. 2005, Charlier et al. 2010, Cooper and Wilson 2014, Cooper et al. 2014, Shane et al. 2005a, Smithies et al. 2023). For Kakapiko Dome, Rotoiti, and EQF, the compositional and thermal diversity recorded in zircon are similar, whereas Hauparu records a wider ranger in both compositional and thermal conditions. Collectively, these data suggest that the post-caldera magma reservoir might have been hotter or accessed melts from hotter regions in the crust (Shane et al. 2005b, Shane et al. 2007, Shane et al. 2008a). Given this background and the existing understanding of the OVC magma reservoir, we model Sr diffusion in plagioclase at a range of temperatures (600–850 ºC) for each eruption that is supported by other work (i.e. Ti-in-zircon thermometry from Chapter 2).

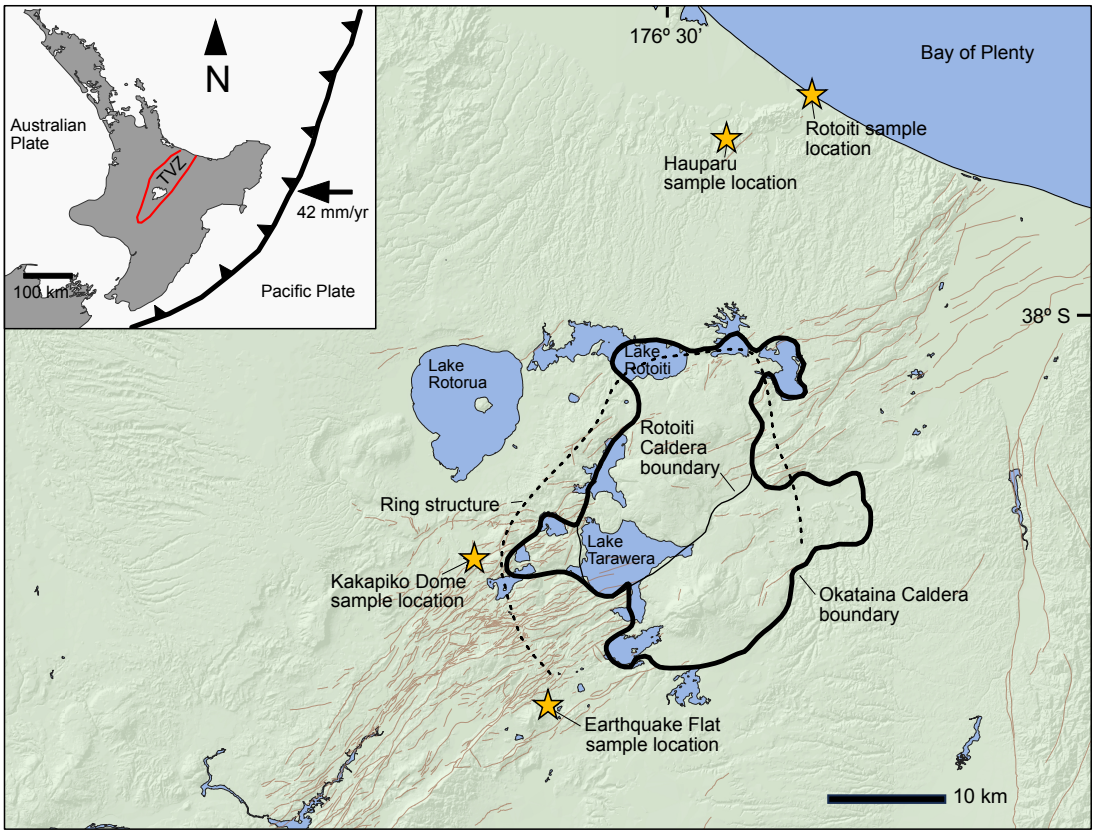


***Figure 4.1**: Map of the Okataina Volcanic Center (OVC) (thick black line), Rotoiti Caldera boundary (thin black line), and OVC ring structure (dashed black Line) from Nairn 2002 and Sas et al. 2021; sampling locations from this study indicated by yellow stars; hillshade and lake polygon layer publicly available at linz.govt.nz; regional fault layer from Langridge et al. (2016); Inset regional tectonic map, Pacific Plate trench location and convergence rate from Deering et al. 2011.*

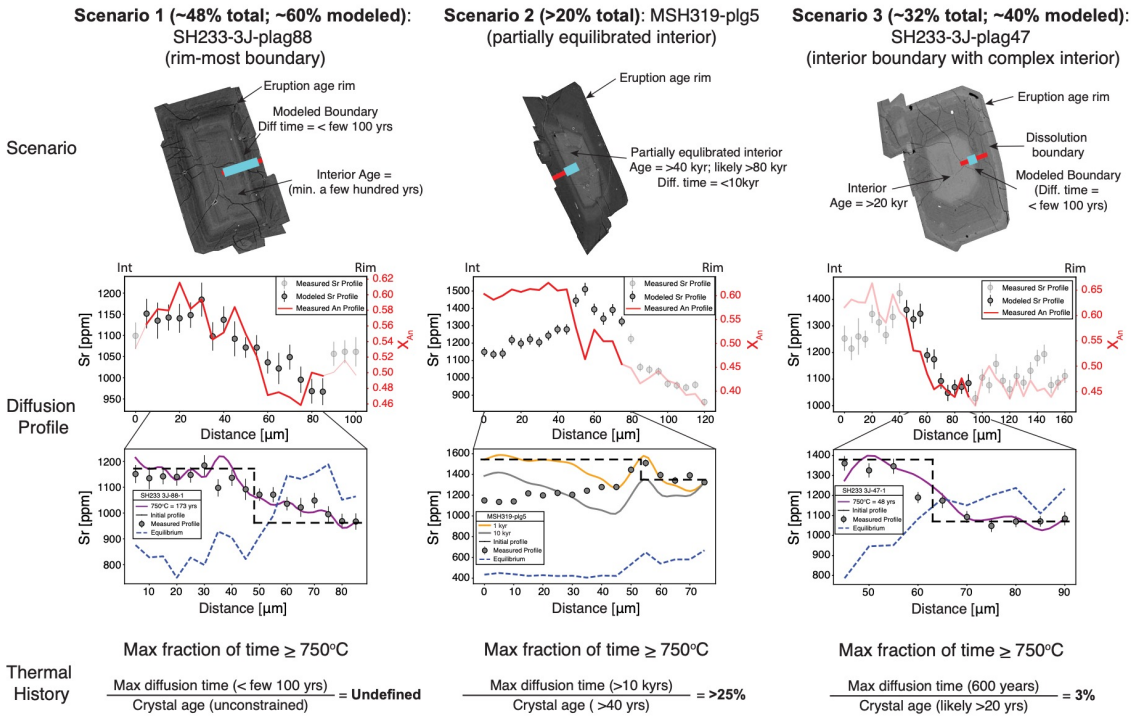


Figure 4.2*: Figure from Schlieder et al. 2022 illustrating three scenarios of thermal history calculations. The top row shows BSE images of Mount St. Helens plagioclase and the location of the measured profile; the red portion of the line illustrates the measured profile, and the blue portion illustrates the modeled portion of the profile. The middle row shows the model output including the initial profile (gray dots) and anorthite profile (red line), the modeled profile (purple line) and the calculated equilibrium anorthite profile (dashed blue line). The bottom row shows thermal histories calculations using the modeled diffusion time and the crystal age.*

4.4 METHODS

While diffusion chronometry is an effective tool for assessing the timescales of magmatic processes there are some assumptions and initial conditions that must first be identified. First, there are numerous minerals that can be used to quantify diffusive timescales, here we used plagioclase for the following reasons: 1) plagioclase is a common igneous minerals that crystallizes throughout a wide compositional range in silicate melts (Nielsen et al. 2017); 2)

plagioclase is a solid-solution mineral and will capture the growth history through zoning patterns, which reflect changes in pressure, temperature, magma composition, water concentrations, and growth kinetics (Zellmer et al. 1999); 3) compositional diffusion via CaAl-NaSi coupled substitution occurs very slowly even at magmatic temperatures and therefore anorthite content can be considered as unmodified through the duration of a mineral's residence time in a magma (Costa et al. 2003); and 4) trace element partitioning into plagioclase is relatively well understood and can be used to understand the thermal history of an individual grain through diffusion chronometry (Costa et al. 2003). We use Sr because: 1) Sr is strongly compatible in plagioclase (An_{40}–An_{80}) (Bindeman et al. 1998); 2) Sr concentrations in plagioclase follows well-described Henrian behavior, acting as a sufficiently dilute species such that its behavior is captured by Henry's law; and 3) Sr diffusion in plagioclase is isotropic and therefore does not need rigorous controls on crystallographic axis orientation (Giletti and Casserly 1994).

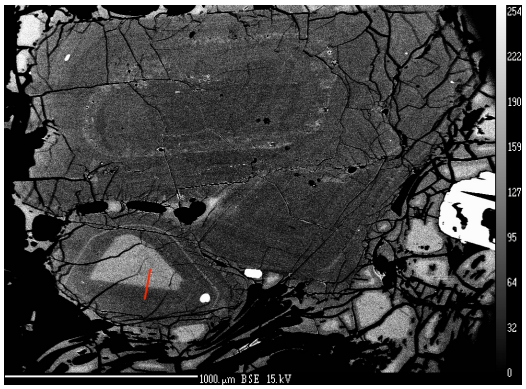
One complication with using plagioclase is that trace element diffusion in plagioclase is dependent on anorthite content. Sr partitioning is inversely correlated with anorthite content (Blundy and Wood 1991, Bindeman et al. 1998) such that Sr is more compatible in albitic plagioclase than anorthitic plagioclase due to increased elasticity of the crystal lattice (Blundy and Wood 1991). Costa et al. (2003) developed a diffusion law that incorporates anorthite dependency in plagioclase. They documented that with time trace element diffusion will seek equilibrium with the anorthite content in each crystal, but at equilibrium conditions, anorthite content and Sr concentration are inversely correlated. A full discussion of trace element diffusive relaxation in plagioclase as governed by Fick's laws can be found in Costa et al. (2003).

Plagioclase grains were analyzed on a Photon Machines Analyte G2193 ArF Excimer and ThermoFisher Scientific iCAP-RQ ICP-MS laser ablation system at the Keck Collaboratory for Plasma Spectrometry, Oregon State University (OR, USA). We measured ^{7}Li, ^{24}Mg, ^{29}Si, ^{43}Ca, ^{48}Ti, ^{57}Fe, ^{86}Sr, ^{88}Sr, ^{137}Ba, ^{138}Ba, ^{139}La, ^{140}Ce, ^{153}Eu, ^{208}Pb in plagioclase. ^{24}Mg, ^{48}Ti, and ^{57}Fe are used as filters for mineral and glass inclusions. Spot sizes were 6 µm by 50 µm spaced every 5 µm, which collectively made up the transect. Spot pits were 8–10 µm deep, and analysis time of each spot ran for 10 seconds at 15 Hz. Transects locations were oriented normal to zones and crystal faces as per Shea et al. (2015), avoiding as many cracks and inclusions as possible. Count rate data were reduced to concentrations using the methodology of Lubbers et al. (2022) and the LaserTRAM-DB software package of Lubbers et al. (2021). Anorthite content of plagioclase was calculated using an iteration of the methodology used in Kent et al. (2008), which compares measured $^{43}Ca^{+}$ and $^{29}Si^{+}$ ratios to those known by NIST standards and calculates a CaO/SiO_2 ratio. We used ATHO-G, BCR-2G, and BHVO-2G standards, which were run as blocks of two analyses at the beginning and end of each analytical session and after every 10 unknowns within the session. Errors are presented as one standard error of the mean concentration data. Precision of replicate measurements of the standards is <13%.

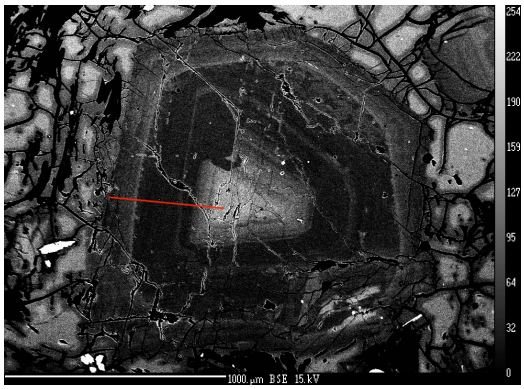
We used the Python code developed by Schlieder (2022) to model Sr diffusion in plagioclase isothermally at temperatures between 600 and 850 ºC. The basis of the code is from the anorthite-dependent diffusion equation of Costa et al. (2003) and uses the Sr in plagioclase partitioning parameters of Nielsen et al. (2017). The code uses ^{88}Sr concentrations (ppm), measurement errors (ppm), and calculated anorthite content (wt.%) for each point in transects across plagioclase grains together with Sr concentration in glass to model isothermal Sr diffusion. Although the eruption temperature can be constrained using Fe-Ti oxide thermometry,

we modeled each profile at a range of temperatures because the modeled Sr profiles are located across sectioned grains from interior to rim and may have experienced thermal conditions different from those leading to eruption. Model temperatures were chosen based on available data from Ti-in-zircon thermometry, Fe-Ti oxide thermometry, and modeled rheological lock-up temperatures (Cooper and Kent 2014), and were run at a range of temperatures for each profile (600–850 ºC). BSE images for all analyzed plagioclase grains from this study are presented in figure 4.3; BSE images of the modeled from Bradshaw (2017) can be found in that publication. The code assumes an initial condition that is a step function in Sr concentration across a profile. Input parameters require the user to select the initial step conditions, as well as the Sr glass concentration. We used Sr glass concentrations from Rocco (2020) and Sas et al. (2021). For each profile, we modeled core to rim profiles and adjusted the initial conditions for each profile by eye (i.e. starting and ending concentration, and step location). We only modeled grains that retained a step-function or a relaxed diffusive profile that retained a slope with an inflection point and a difference greater than 100 ppm Sr between the starting and ending points in the profile. The output products are presented in figure 4.4 (all of the model results are available in appendix B): the upper left figure plots Sr concentration versus distance (core to rim) of the modeled portion of the profile, where the measured profile is in gray, the initial step function is in solid black, the best fit profile is solid purple, and the equilibrium profile is in dashed blue. The equilibrium profile is calculated using partition coefficients and constants derived from determined by Nielsen et al. (2017) and determined using an Arrhenius expression. The Sr equilibrium profile reflects the expected behavior of Sr in equilibrium with the calculated anorthite content. The upper right figure is the sum of the best fit curves (goodness of fit chi-squared curves) versus time, which extracts the best fit time. The lower left figure plots Sr

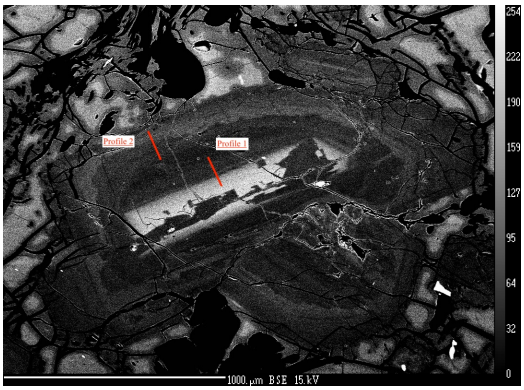
concentration versus distance (core to rim) of the entire profile. The filled gray dots represent the modeled portion of the profile, and the transparent gray dots represent the portion of the profile that was not modeled. The user selects which portion of the code they want to model. For this study, we chose to model only sections of the curve that approximate a step-function. The solid red line represents the measured anorthite content and the blue dashed line is the equilibrium profile. The bottom right figure plots Sr concentration (left axis) and distance in grain (core to rim, right axis) versus anorthite content. The solid black line with gray regions represents equilibrium partitioning of Sr with anorthite content. Locations of modeled profiles for each grain from this study are presented in figure 4.3.



Kakapiko Dome MD_TS1_21



Kakapiko Dome SM_TS1_2



Kakapiko Dome SM_TS1_3 (profile 1)



Kakapiko Dome SM_TS1_10

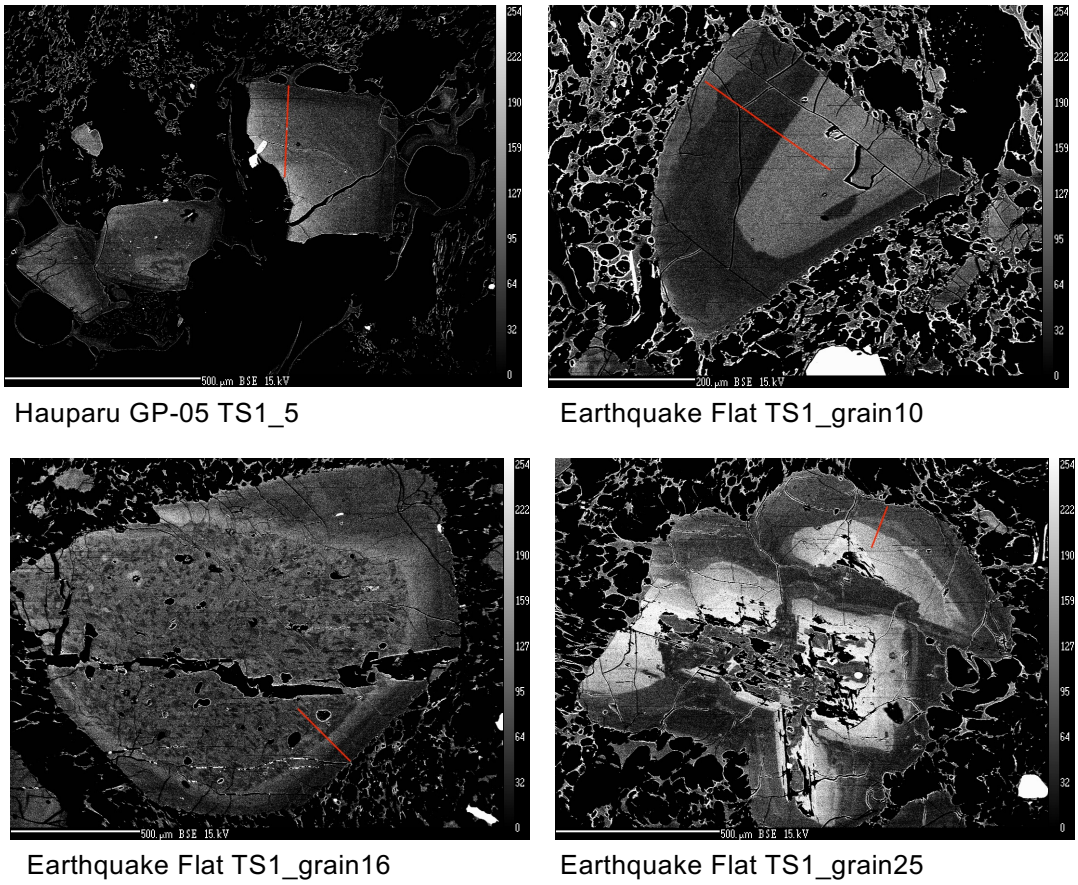


***Figure 4.3**: BSE images of plagioclase grains measured for this study (Kakapiko Dome, Earthquake Flat, and Hauparu) with measured transects illustrated in red.*

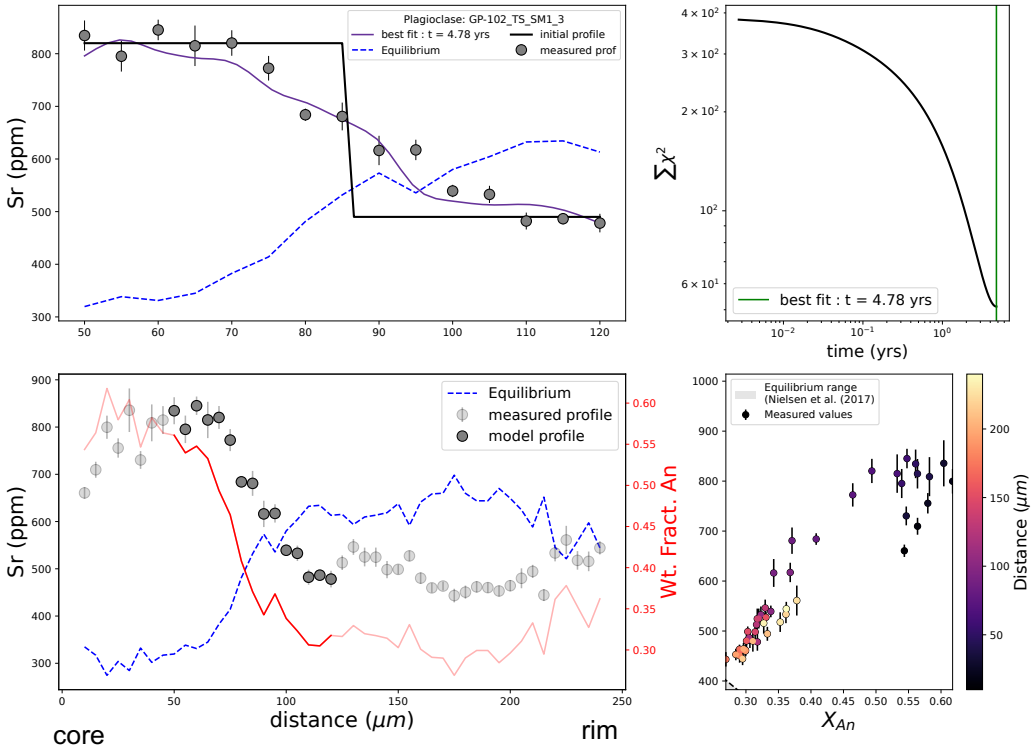
4.5 RESULTS

We present modeled profiles for four eruptions from the OVC, Kakapiko Dome, Rotoiti, EQF, and Hauparu, in addition to modeled profiles using data from Bradshaw (2017) who have additional transects on plagioclase from Rotoiti and EQF. Although Bradshaw (2017) already reported diffusive timescales for their data, we use a different code and therefore get slightly different results. We measured Sr concentration profiles in 19 plagioclase grains from Kakapiko Dome, four of which had distinct step function profiles that we could model to obtain time

information. Given the wide range in Ti-in-zircon temperatures, we modeled Kakapiko Dome plagioclase at a range of 600–850 ºC. Only one of the 49 measured Hauparu plagioclase grains retained distinct Sr profiles from which we could extract diffusive relaxation timescales. All of the other 47 Sr profiles did not have a large enough difference in Sr concentration across the transect to model. We measured 16 EQF plagioclase grains, and modeled Sr profiles in three of those grains. Of the 11 Rotoiti plagioclase grains, none had Sr profiles suitable for modeling (i.e. all lacked a steep step in Sr and anorthite content, see methods). Figure 4.4 presents examples of isothermal diffusion modelling of Sr in plagioclase from the OVC volcanics. All other modeled profiles are in appendix B. Using data from Bradshaw (2017), we modeled five of the 15 measured Rotoiti plagioclase profiles that showed a slope in the Sr profiles. We modeled eight of the 12 profiles measured for EQF. Figure 4.5 shows the apparent diffusion timescales from 600 to 850 ºC.

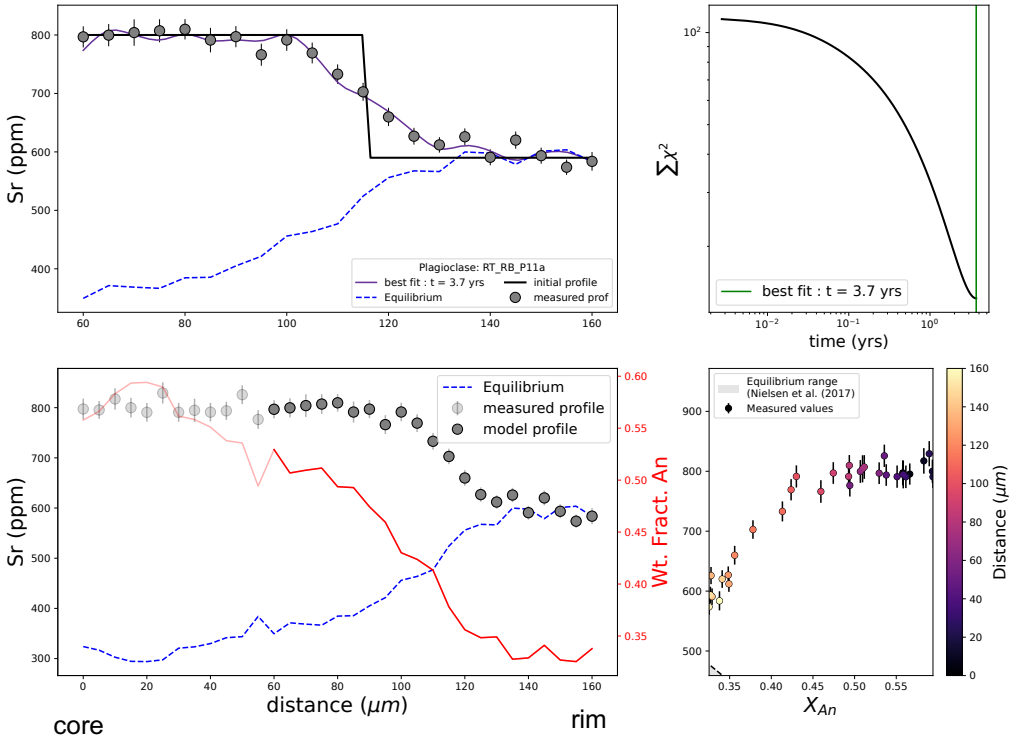
Bradshaw (2017) obtained timescales of 10^0–10^1 for Rotoiti and EQF plagioclase modeled at 750 ºC. This is slightly different than our modeled results at 750 ºC using the Bradshaw (2017) dataset, for which we get timescales of 10^1–10^2 for Rotoiti and 10^0–10^2 for EQF. Slight differences in the diffusion code, model set-up, and Sr glass concentration used could account for these slight differences, and the discrepancy provides a measure of the reproducibility of the diffusion results.

Kakapiko Dome grain 3



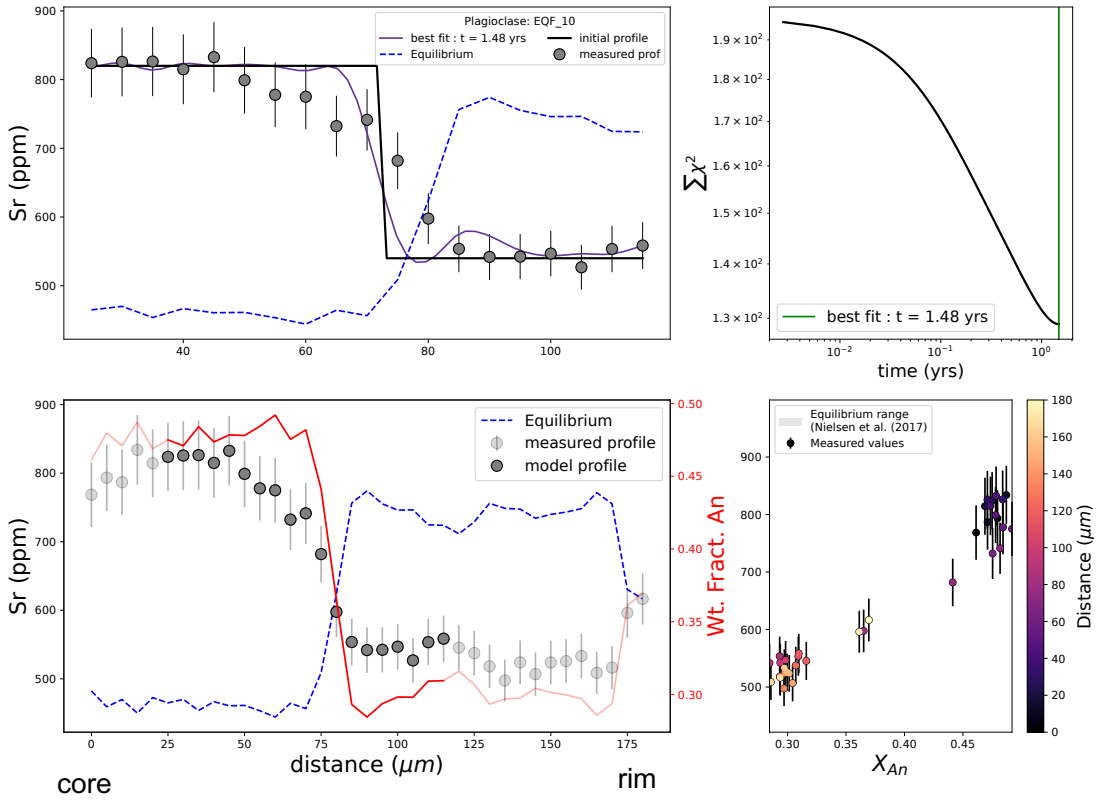
T = 850 ºC

Rotoiti grain 11a



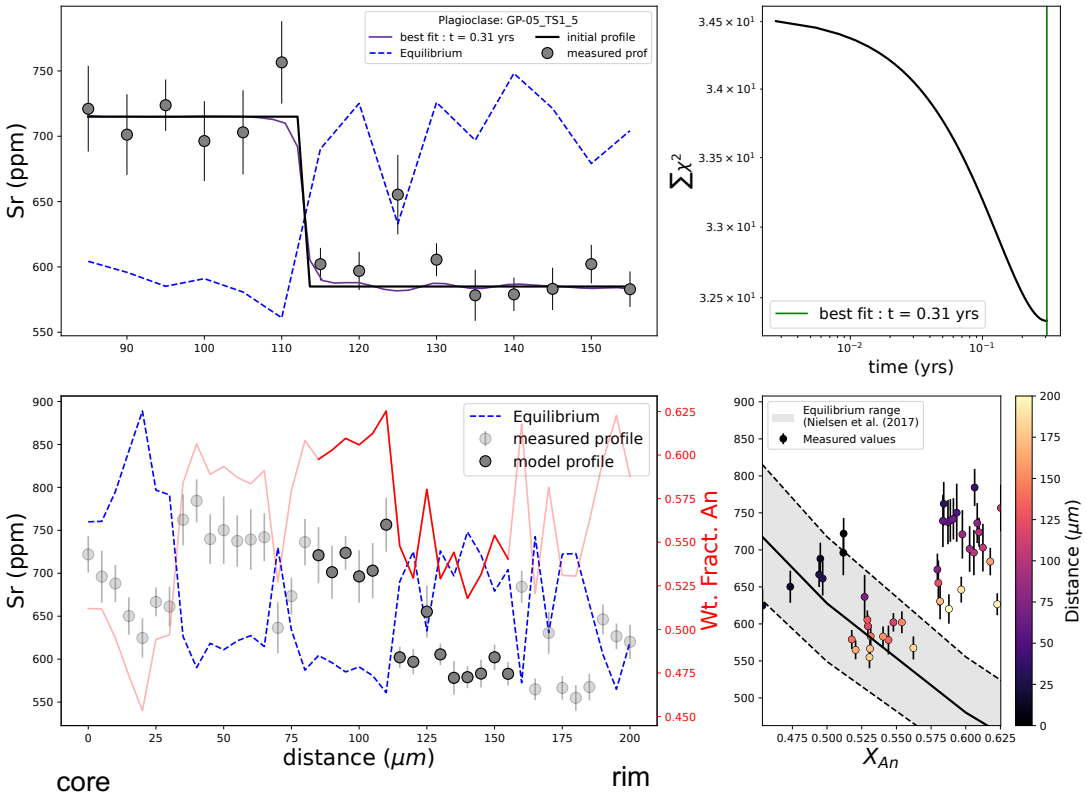
T = 850 ºC

EQF grain 10



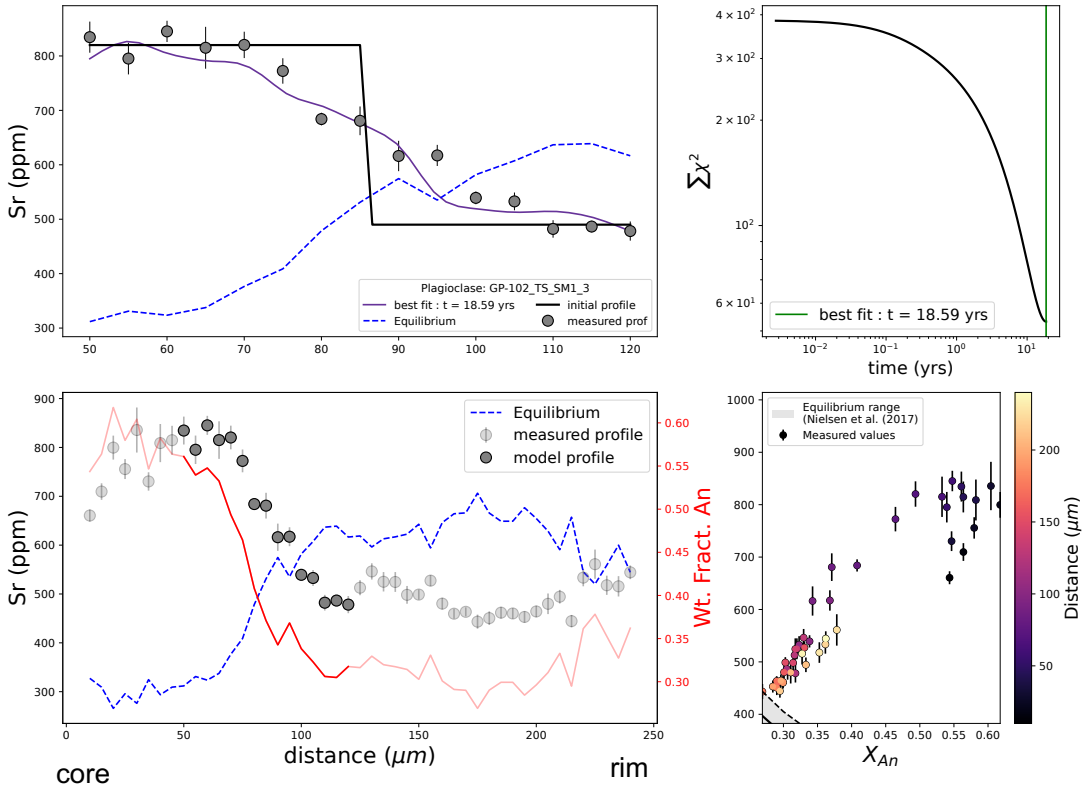
T = 850 °C

Hauparu grain 5



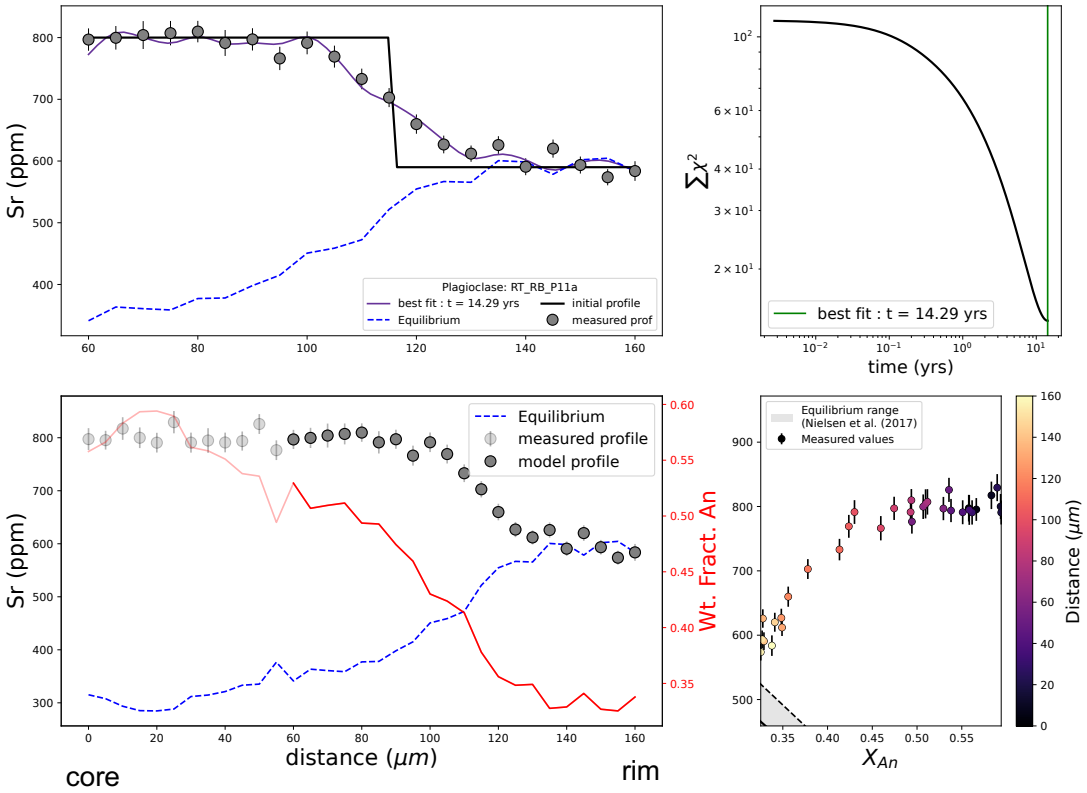
T = 850 ºC

Kakapiko Dome grain 3



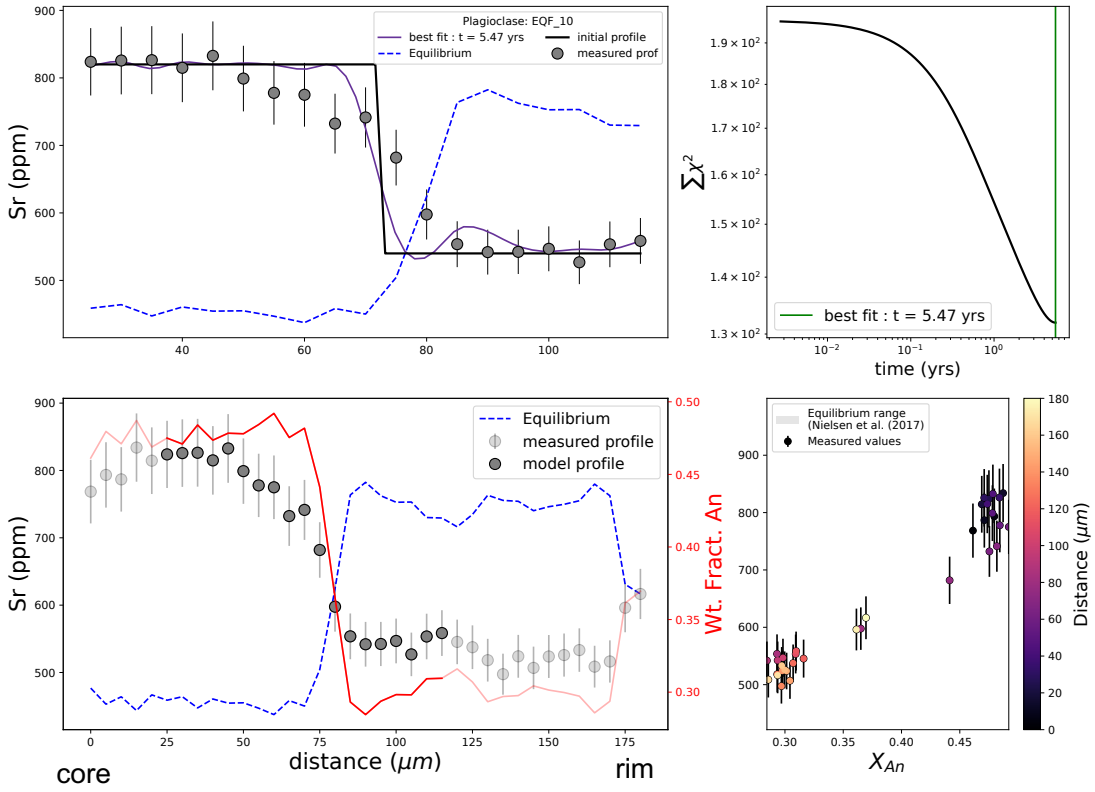
T = 800 °C

Rotoiti grain 11a



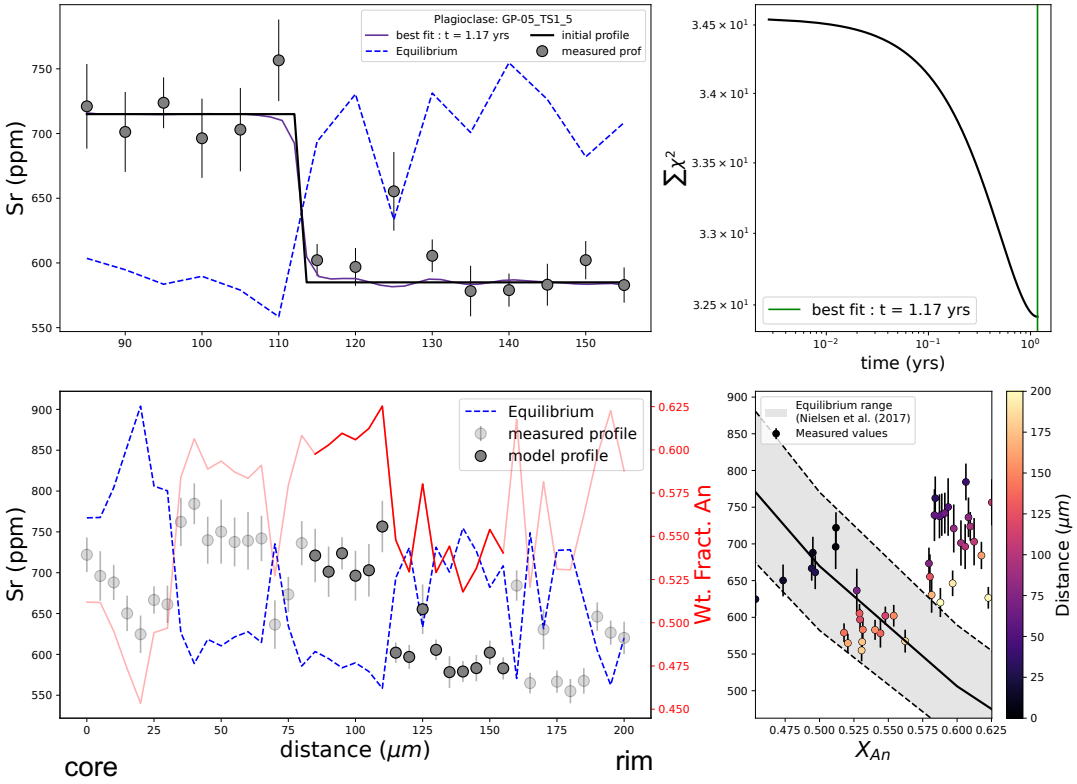
T = 800 ºC

EQF grain 10



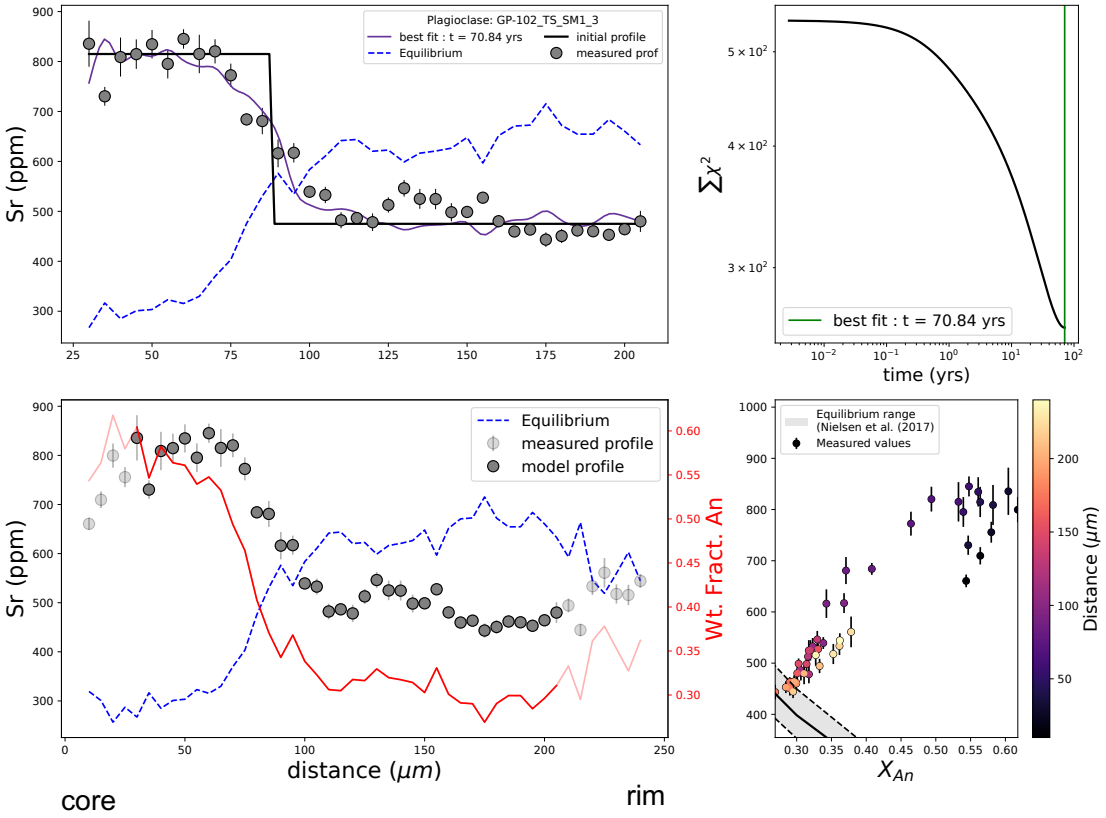
T = 800 °C

Hauparu grain 5



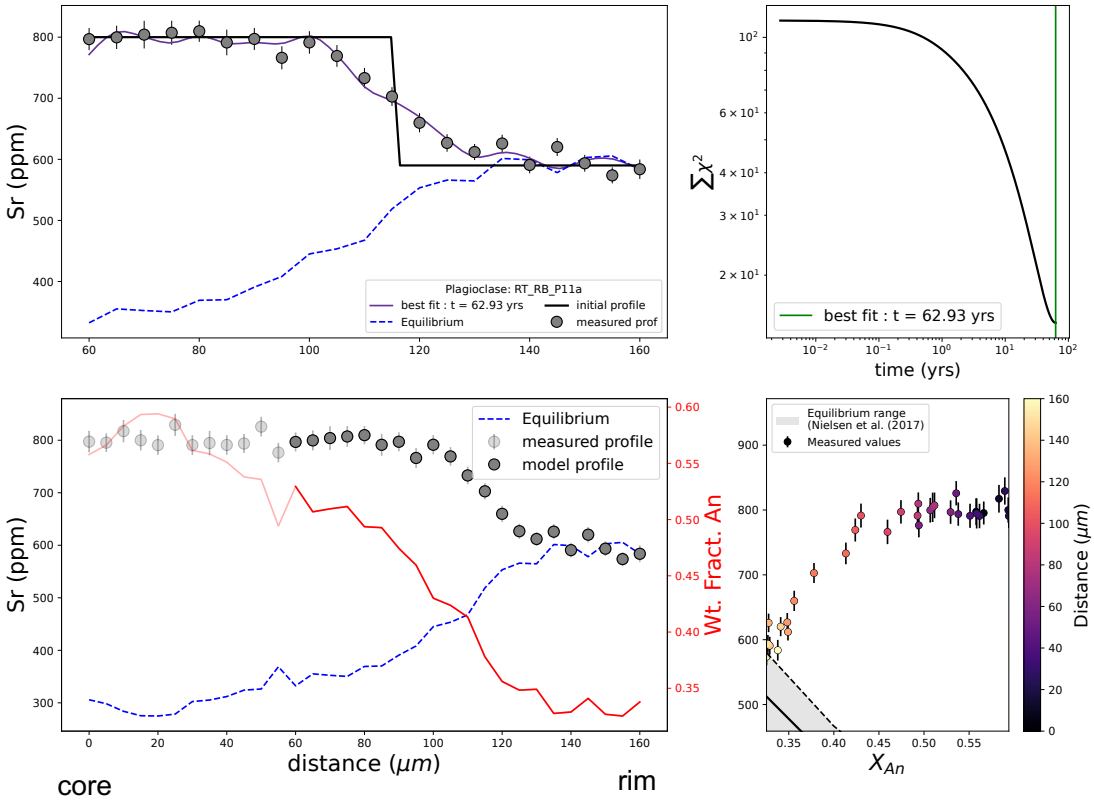
T = 800 °C

Kakapiko Dome grain 3



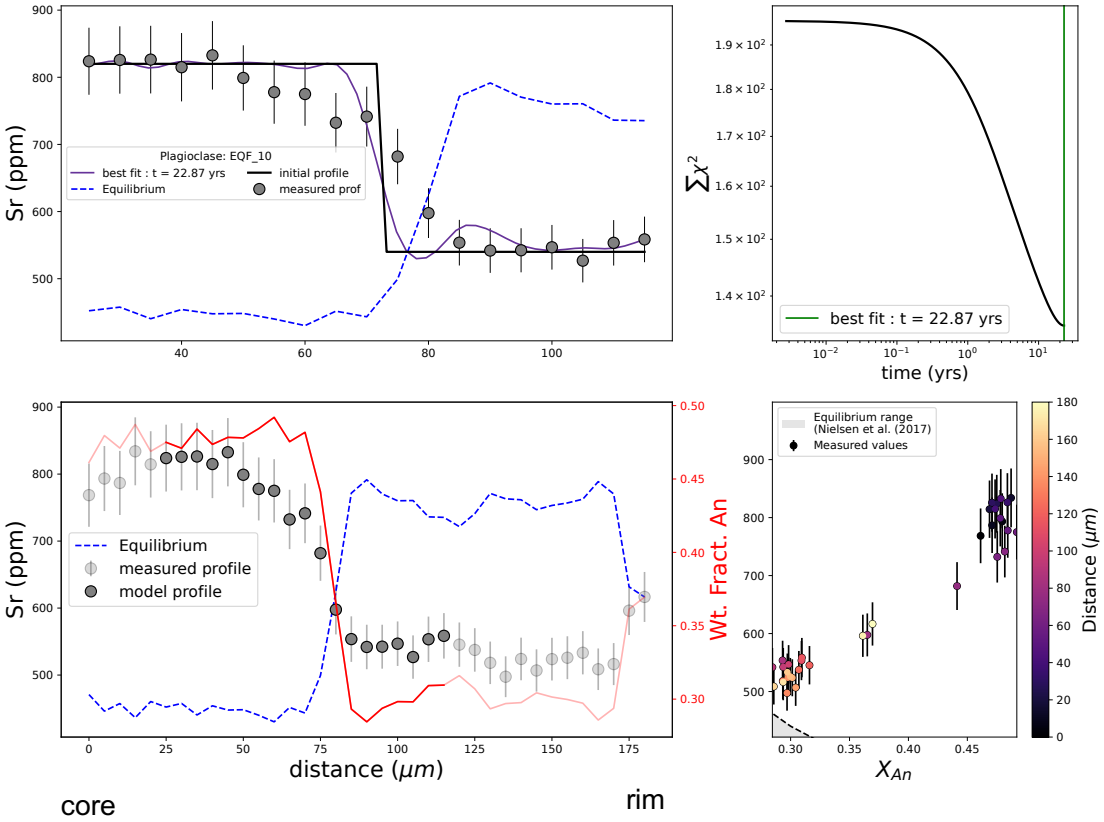
T = 750 ºC

Rotoiti grain 11a



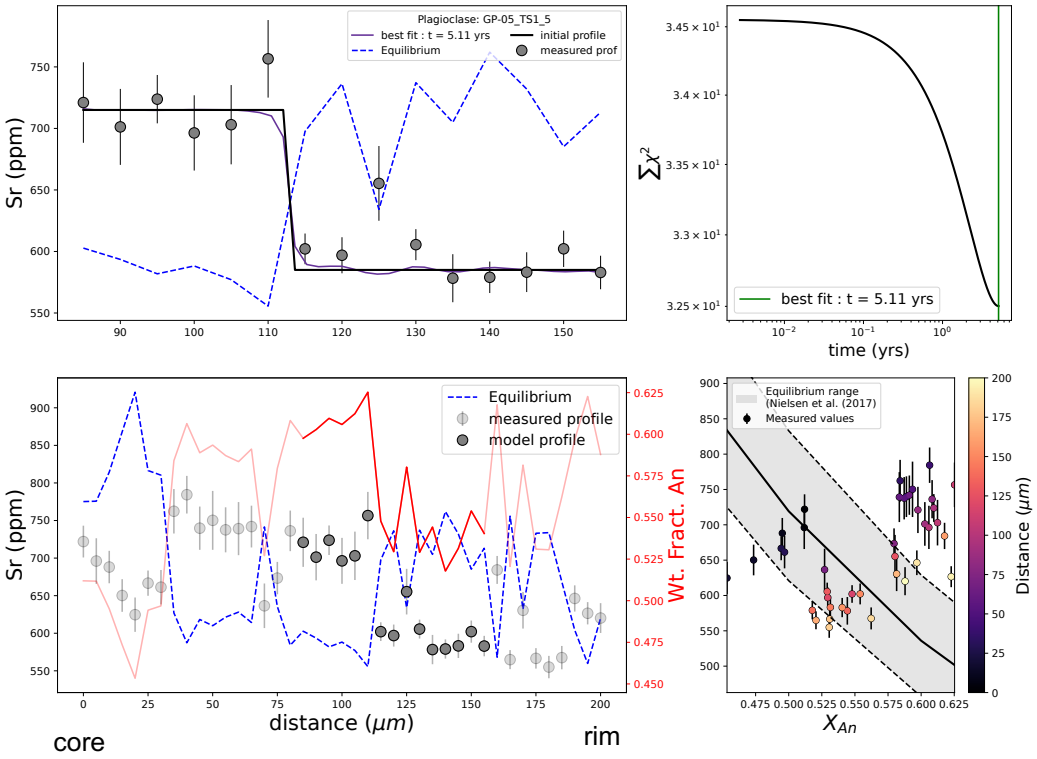
T = 750 ºC

EQF grain 10



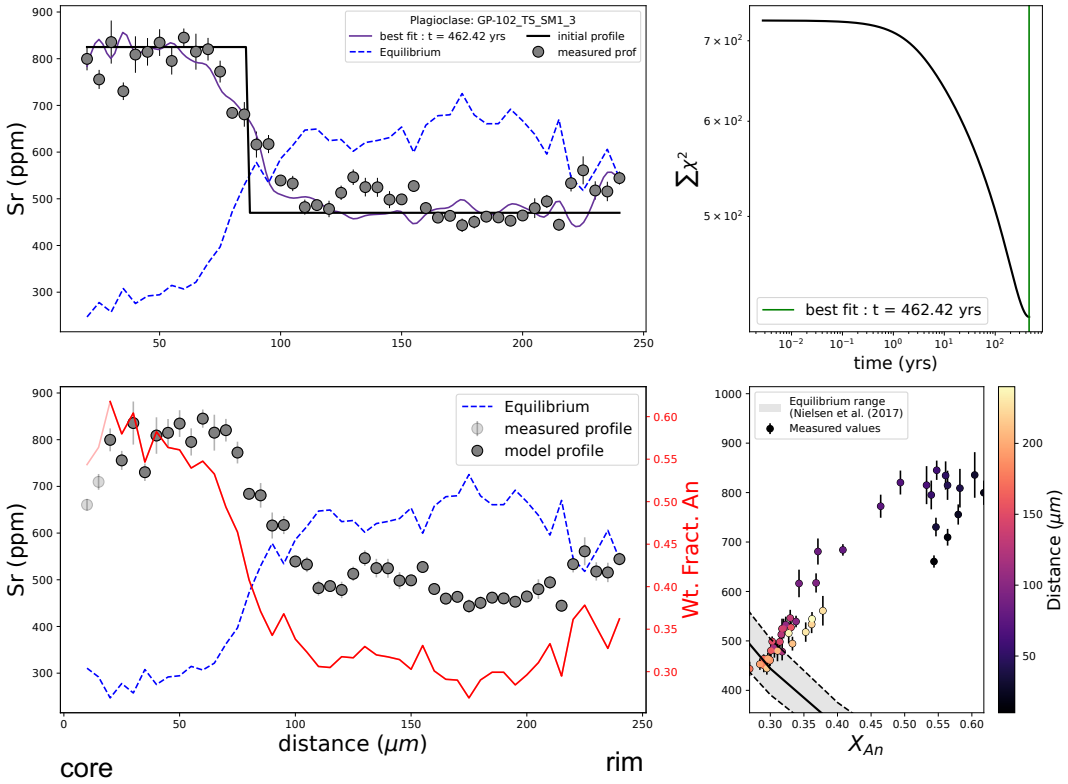
T = 750 ºC

Hauparu grain 5



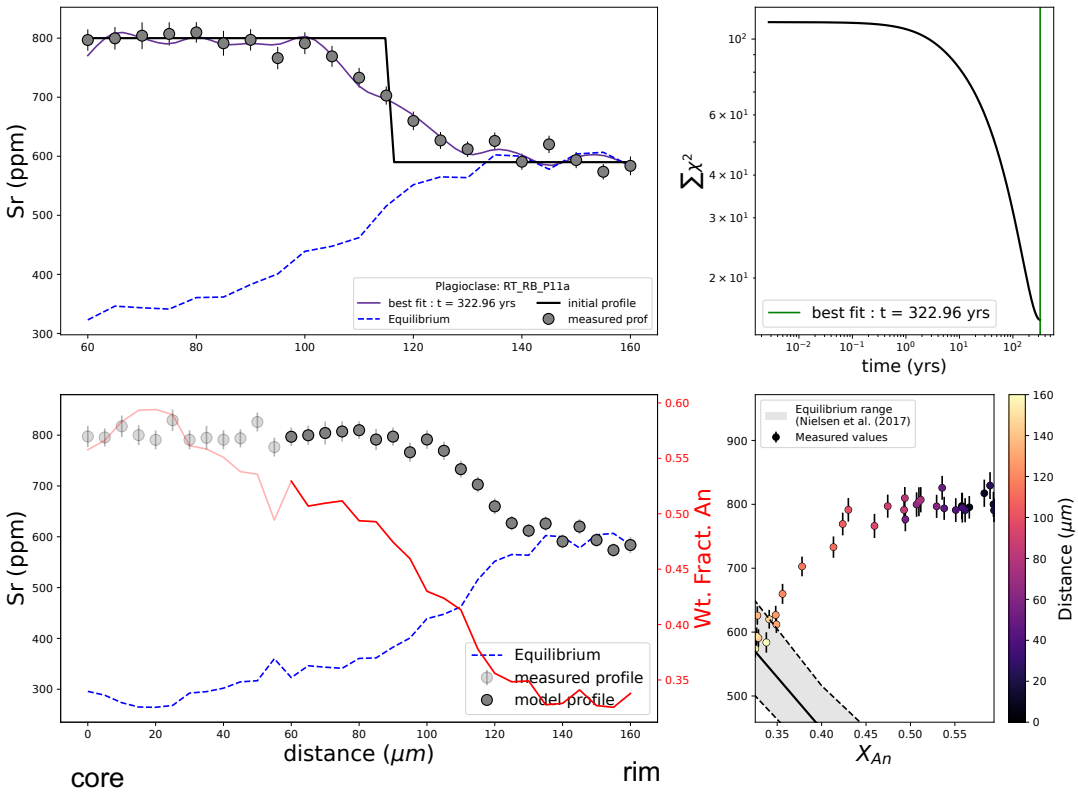
T = 750 ºC

Kakapiko Dome grain 3



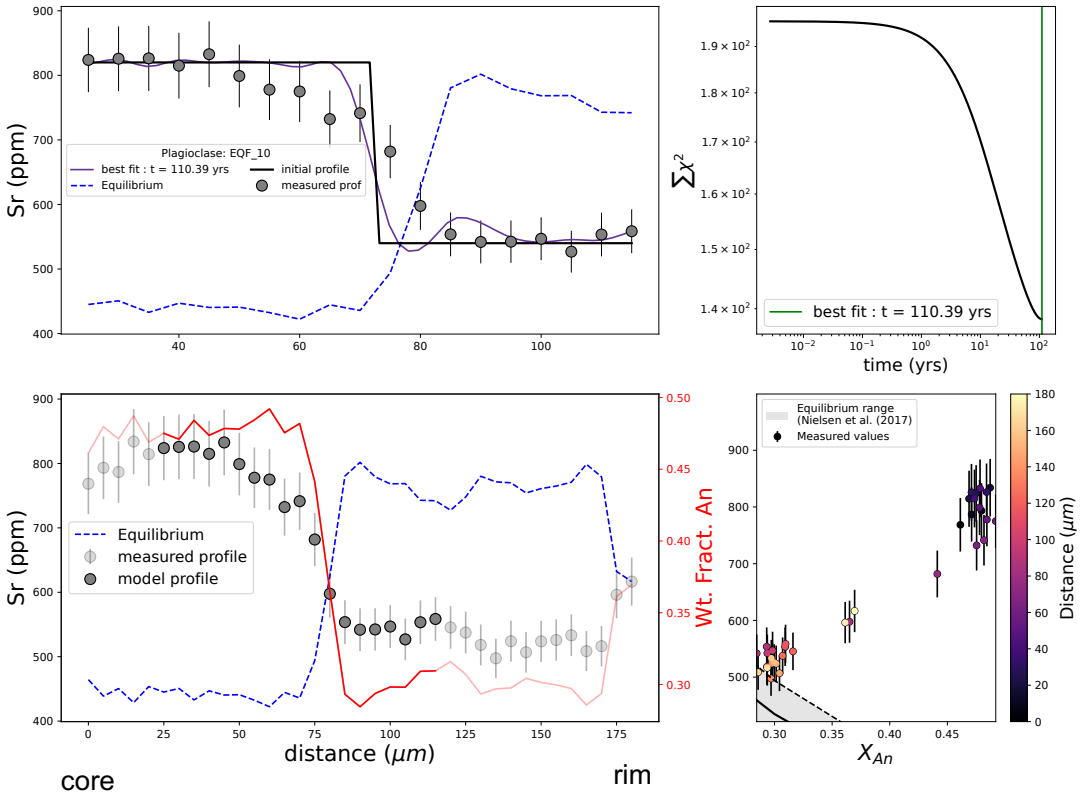
T = 700 ºC

Rotoiti grain 11a



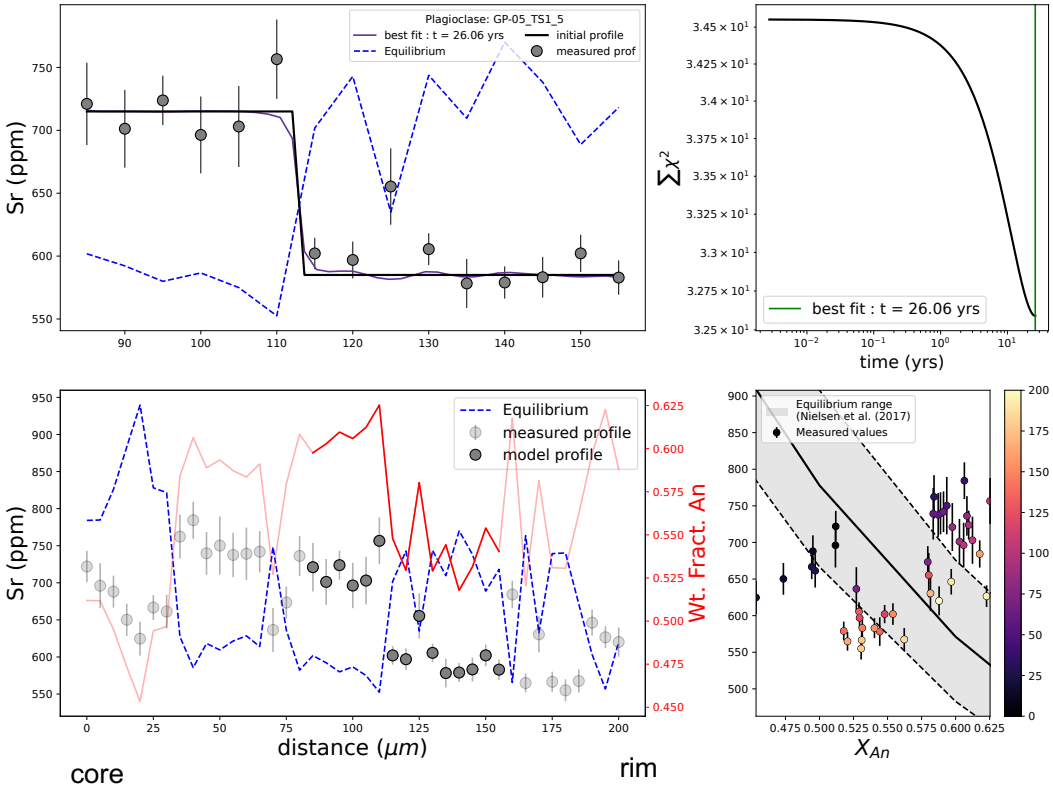
T = 700 °C

EQF grain 10



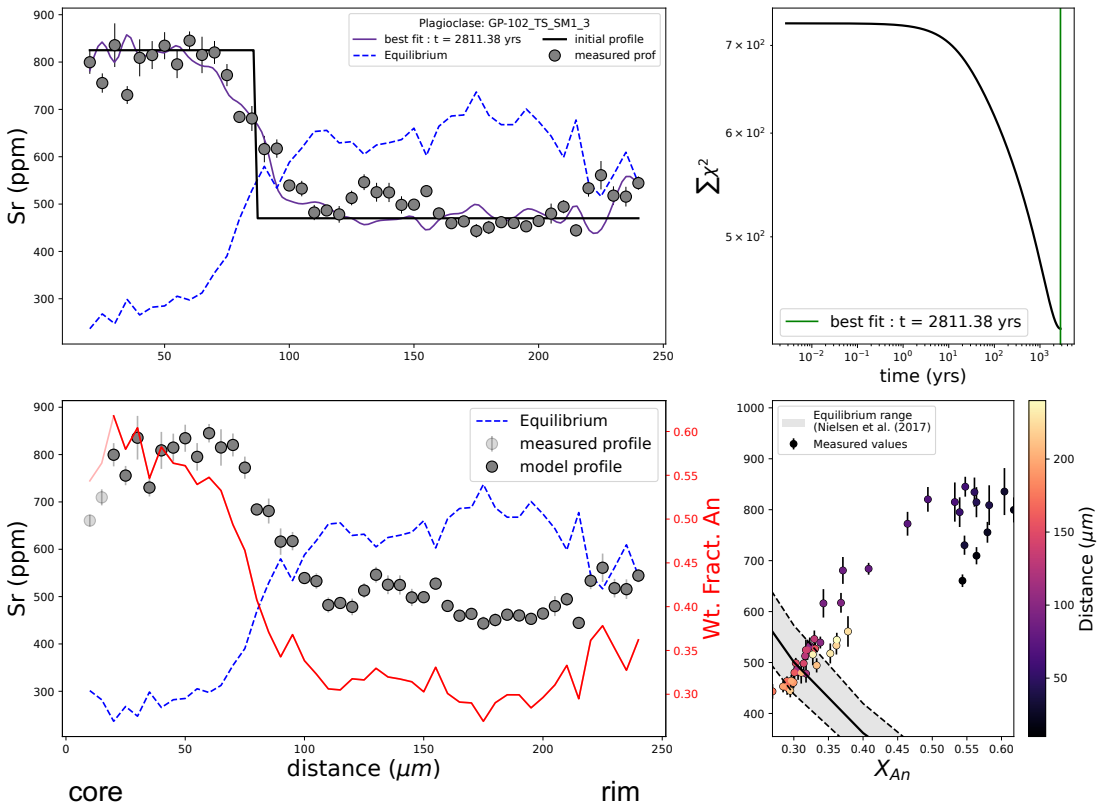
T = 700 ºC

Hauparu grain 5



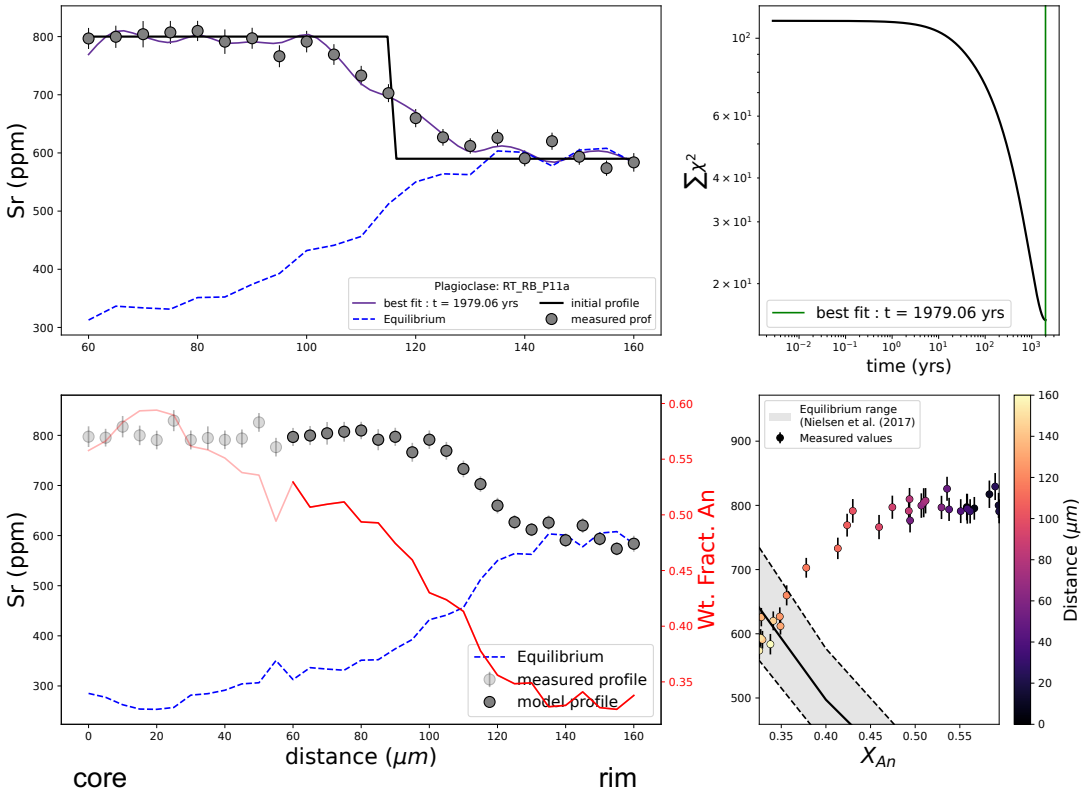
T = 700 ºC

Kakapiko Dome grain 3



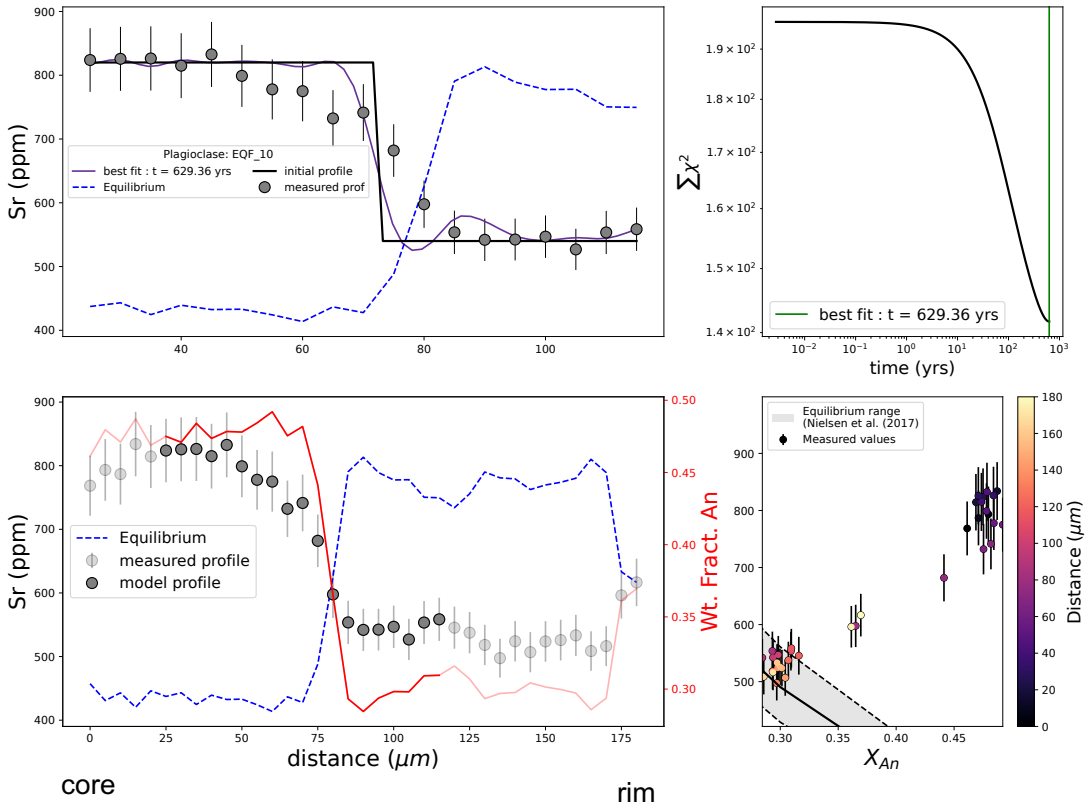
T = 650 ºC

Rotoiti grain 11a



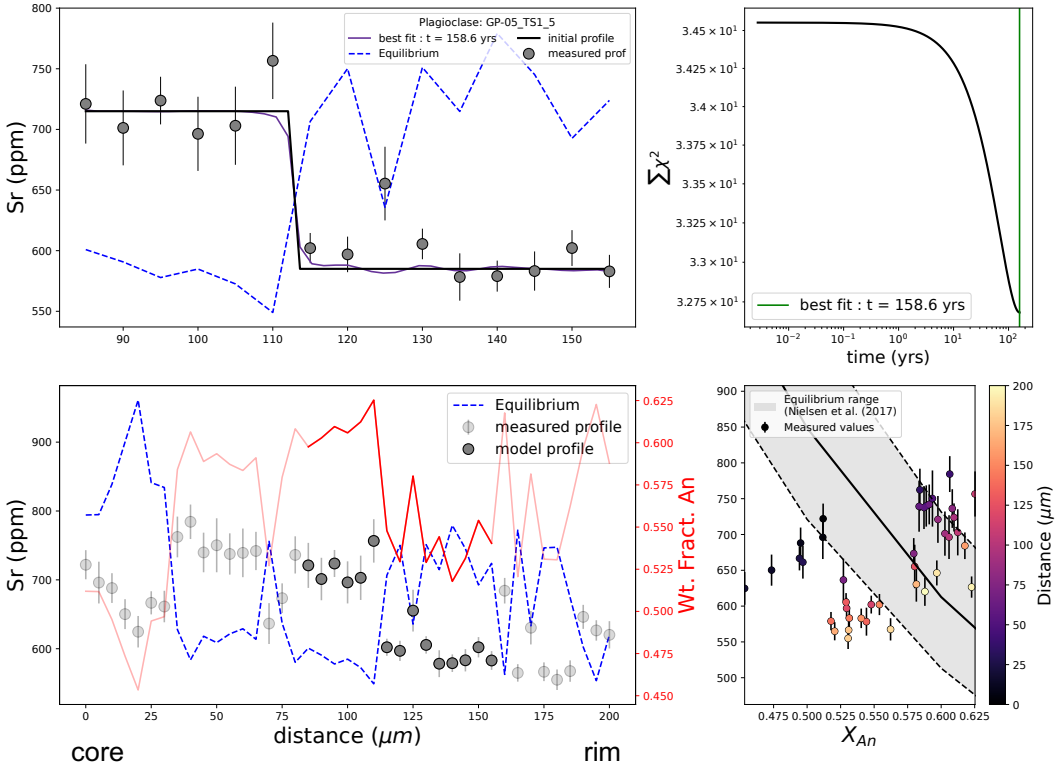
T = 650 ºC

EQF grain 10



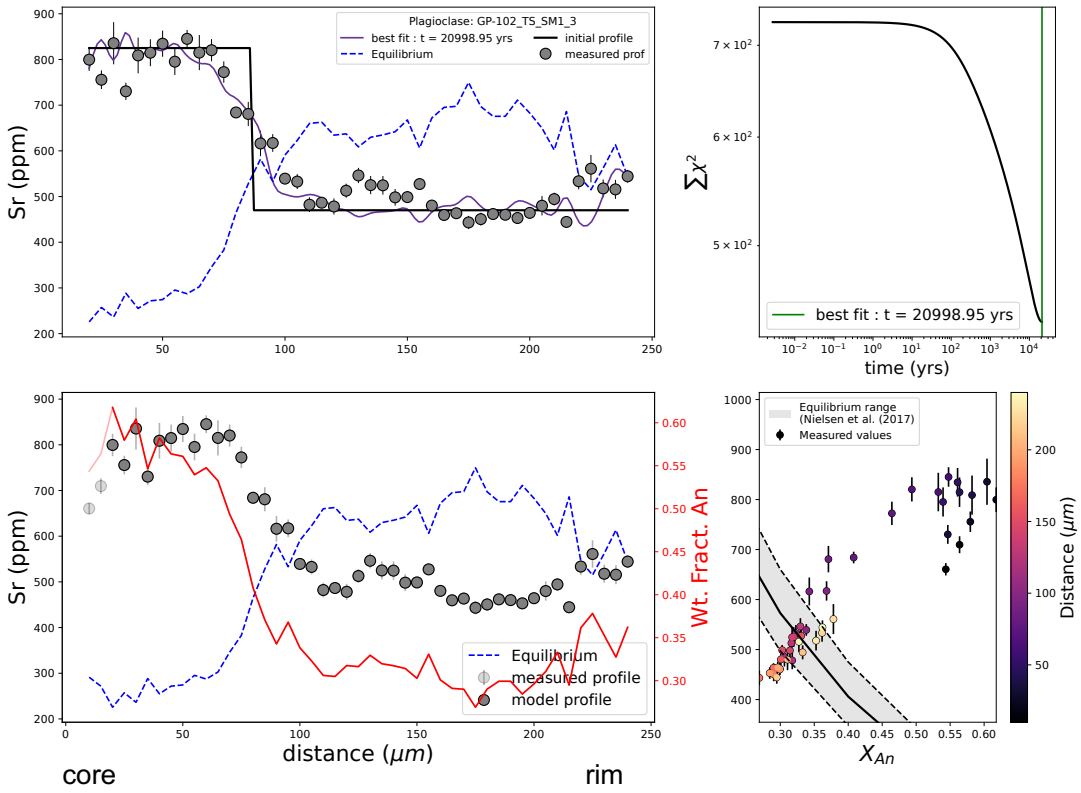
T = 650 ºC

Hauparu grain 5



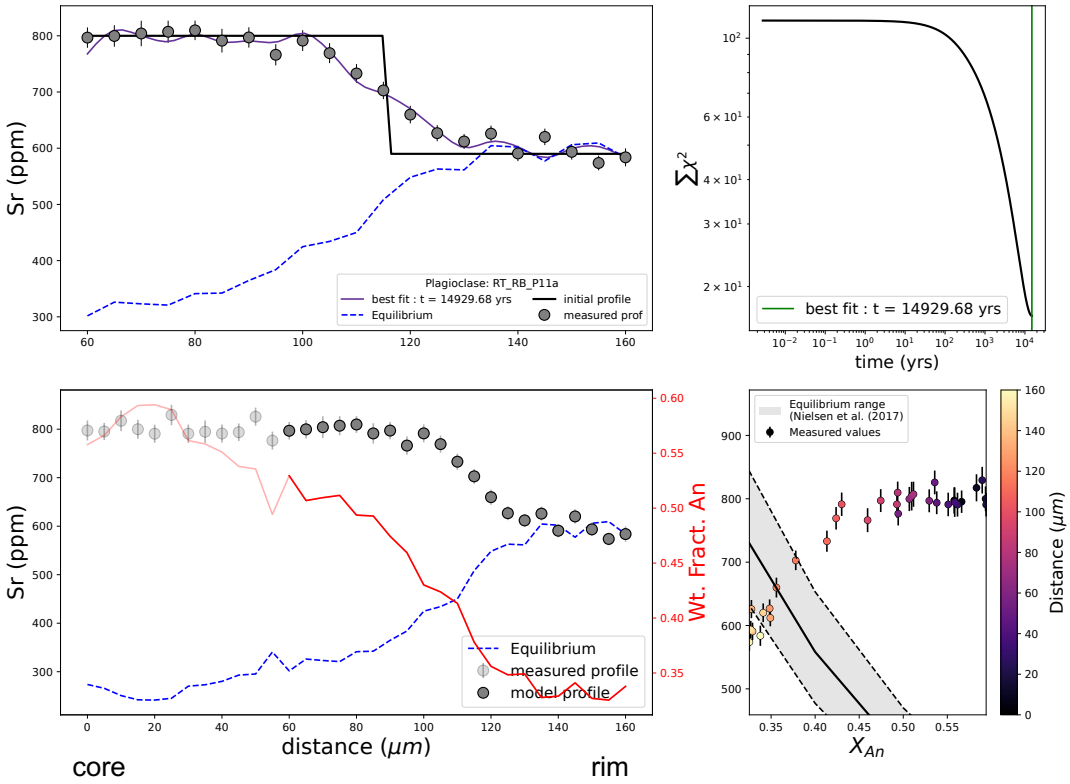
T = 650 ºC

Kakapiko Dome grain 3



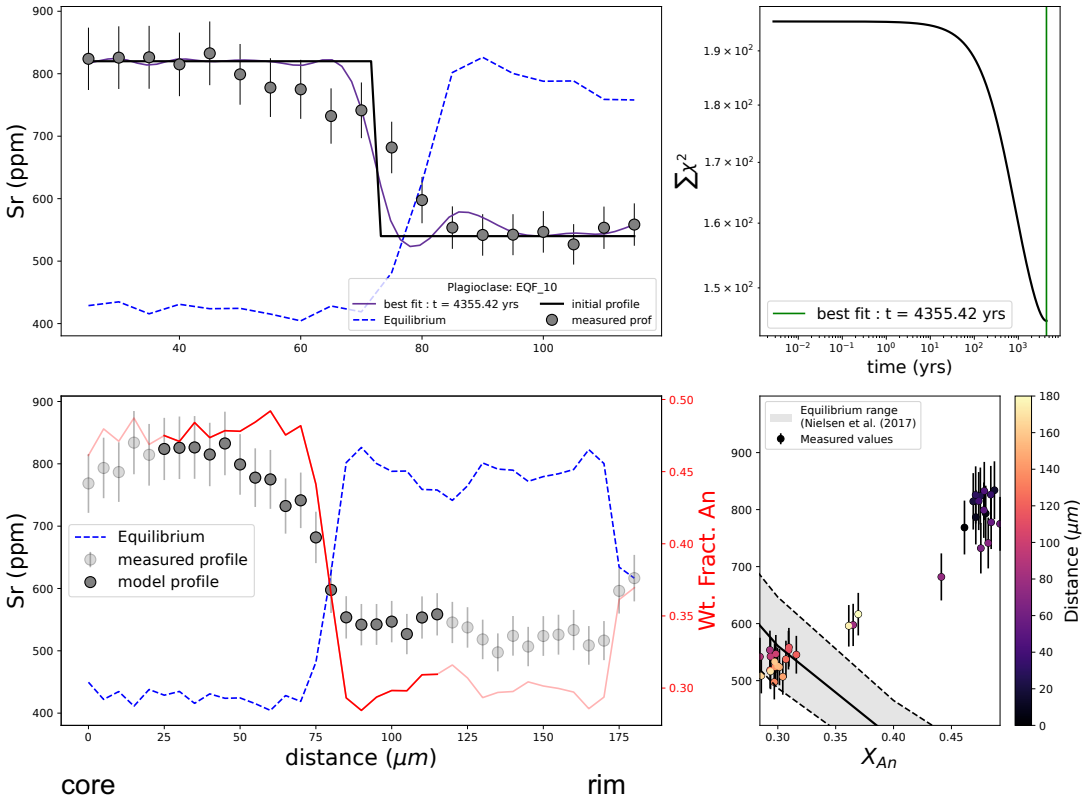
T = 600 ºC

Rotoiti grain 11a



T = 600 ºC

EQF grain 10



T = 600 ºC

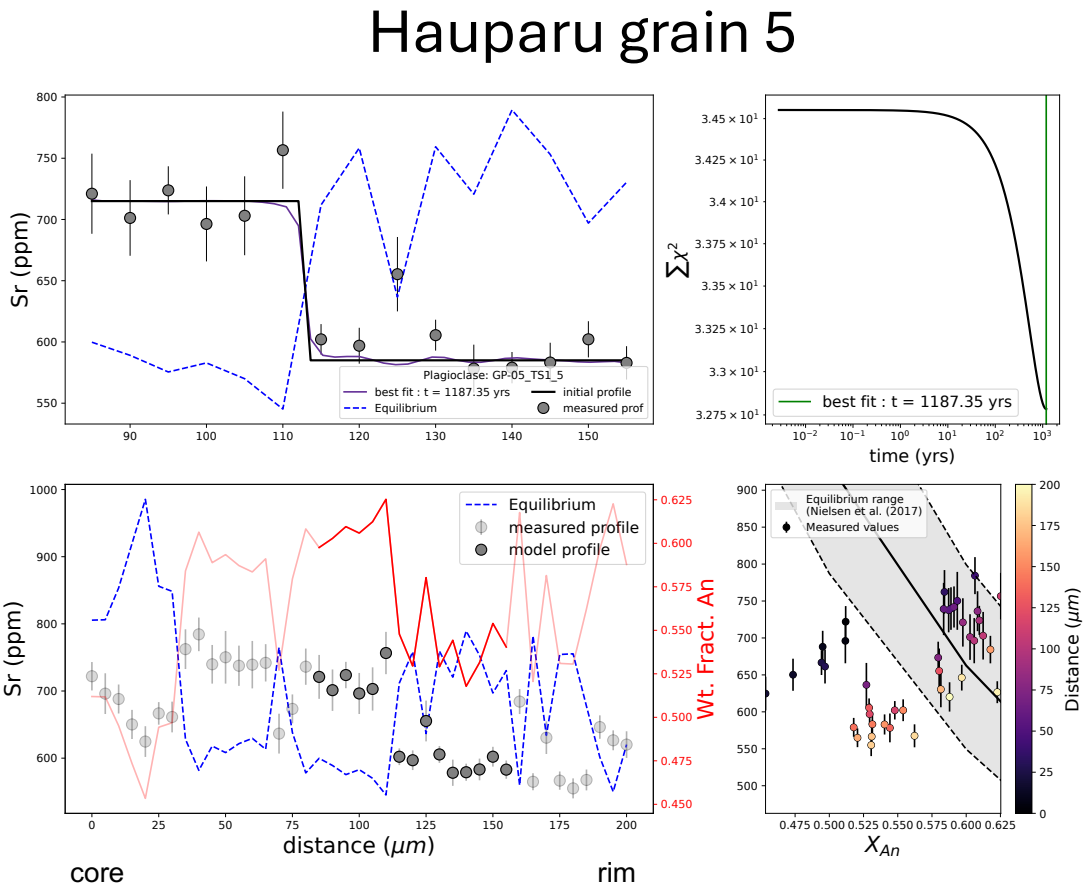


***Figure 4.4**: Model results for a characteristic plagioclase grain from Kakapiko Dome, Rotoiti, Earthquake Flat, and Hauparu at 600, 650, 700, 750, 800, and 850 ºC. Each model result includes four panels: The upper left panel illustrates the modeled section of the profile; the purple line shows the modeled diffusion profile, and the dashed blue line shows the equilibrium profile. The upper right figure illustrates the best fit calculation results. The lower left illustrates the entire initial profile, dark gray dots are included in the model and light gray dots are excluded, the anorthite profile is illustrated red, and the anorthite equilibrium profile in dashed blue. The lower right figure illustrates the equilibrium range of anorthite compositions versus temperature (gray region) and the measured anorthite content of the plagioclase grain color-scaled to distance from core to rim.*

4.6 DISCUSSION

Sr diffusive relaxation timescales can provide the durations that a population of crystals spent at a modeled temperature. Such models are useful especially when paired with existing temperature estimates from mineral thermometers because together the data can reveal realistic storage temperatures and time scales for the magma body. We have modeled Sr diffusion in plagioclase over a range of 600–850 ºC. Our dataset is somewhat (21 modeled profiles) small due to the limitations required for "modellable" grains (see methods). Across all four eruptions and in every modeled plagioclase grain, including those grains that were measured but not modeled, the Sr concentration and anorthite content curves are positively correlated, suggesting that Sr and anorthite have not equilibrated. We can use these Sr diffusive profiles to understand broad thermal conditions and pair them with data from other thermometers to understand likely storage scenarios.

4.6.1 Diffusive modelling with Ti-in-zircon thermometry

The diffusive storage timescales are modeled isothermally. We ran the model multiple times for each profile at a range of temperatures between 600 and 850 ºC. Although the storage temperature is difficult to define given the complexity of magma mush systems, this temperature range likely encompasses the true storage temperature(s) and we can compare the diffusive timescales at the modeled storage temperatures to Ti-in-zircon thermometry (Chapter 2). This comparison allows us to juxtapose zircon crystallization temperatures with the modeled storage temperatures for plagioclase. In rhyolitic magmas of compositions similar to those of the OVC, plagioclase and zircon will co-crystallize across a wide range of compositions, therefore we use the Ti-in-zircon thermometry as a guide of likely storage temperatures for plagioclase diffusion. Zircon from all four eruptions lack resorption rims on the surfaces confirming that they were

mostly below their respective zircon saturation temperatures. For the continuing discussion we assume that all zircon are under the zircon saturation threshold.

The Ti-in-zircon temperatures for Kakapiko Dome, Rotoiti and EQF are broadly similar (excluding a few outliers), which made our choice of model temperatures fairly straight-forward. The EQF Ti-in-zircon temperatures range from 640–799 ºC (Chapter 2). Of the 77 EQF zircon measured in Chapter 2, only seven record temperatures >750 ºC, and at the same temperature Sr diffusion profiles in plagioclase yield timescales of 10^1–10^2 years (Fig. 4.5). Only two zircon record temperatures <650 ºC. The other 68 zircon record temperatures between 650 and 750 ºC which corresponds with a fairly large range in Sr diffusion timescales at 10^1–10^3 years (Fig. 4.5). Ti-in-zircon temperatures from Rotoiti range from 620 – 792 ºC excluding three outliers. Of the 110 measured Rotoiti zircon, only eight record temperatures >750 ºC, and seven record temperatures <650 ºC. The other 95 grains record temperatures between 650 and 750 ºC, which corresponds with a fairly large range in Sr diffusion timescales at 10^1–10^3 years. The range in Ti-in-zircon thermometry from the Kakapiko Dome is from 573 to 748 ºC (one outlier at 990 ºC). Only two of the 45 measured zircon grains record temperatures >750 ºC, and 12 record temperatures <650 ºC. The other 31 grains record temperatures between 650 and 750 ºC, which corresponds with a fairly large range in Sr diffusion timescales at 10^1–10^4 years.

Hauparu zircon record much hotter temperatures than the preceding eruptions. Ti-in-zircon thermometry from Hauparu zircon range from 669–929 ºC, with one outlier at 1211 ºC. These data show that Hauparu zircon crystallized at a wider range of temperatures than Kakapiko Dome, Rotoiti and EQF, and lack of dissolution rims on Hauparu zircon surfaces suggests that the grains were dominantly stored below the zircon saturation threshold (790–848 ºC). Of the 53

Hauparu zircon grains measured, 32 record temperatures >750 ºC and none record temperatures <650 ºC. Only eight of the grains record temperatures >850 ºC.

For all four eruptions, there are broad similarities in the mineral textures. While the zircon show no obvious signs of disequilibrium on their surfaces, many of the zircon have resorbed interior zones. Similarly, plagioclase have patchy zoned interiors with resorption zones that are overgrown by thick normally zoned rims. Many of the plagioclase grains are preserved as glomerocrystic clusters with twinned grains, rather than individual phenocrysts. Collectively, these observations suggest that the melt from which the zircon and plagioclase surfaces grew was both cool (below zircon saturation temperature threshold) and evolved (thick, sodic rims on plagioclase), consistent with co-crystallization. In the plagioclase grains, the measured Sr profiles are positively correlated with the anorthite profile (Sr and An are not in equilibrium) suggesting that either the plagioclase grew rapidly enough such that the Sr did not have time to diffuse even at magmatic temperatures, or the plagioclase were stored in very cool environments such that Sr diffusion was slower than the magma assembly and mobilization timescales.

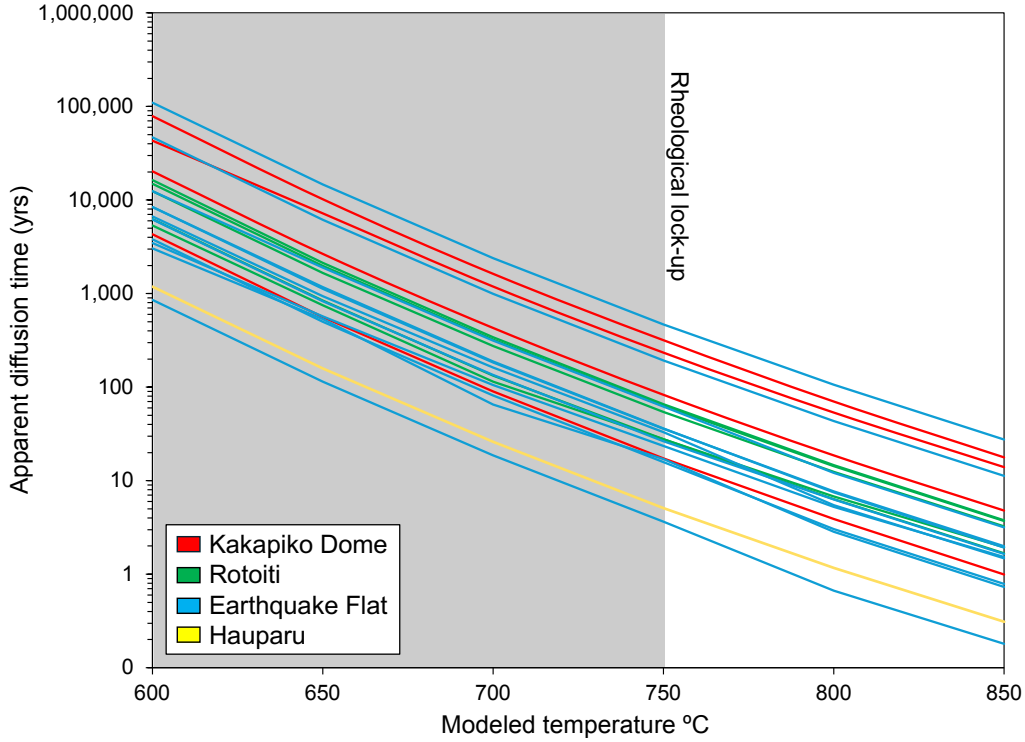


Figure 4.5*: Modeled diffusion timescales versus modeled temperature. Kakapiko Dome timescales are illustrated in red, Rotoiti timescales are illustrated in green, Earthquake Flat timescales are illustrated in blue, and Hauparu timescales are illustrated in yellow. The gray region represents the rheological lock-up regime, approximated as temperatures below 750 ºC from (Cooper and Kent 2014).*

4.6.2 Diffusive modelling with Fe-Ti oxide thermometry

Given the complexity of magma mush storage, and the lack of equilibrated grains, a different proxy for storage temperature could be pre-eruptive temperature recorded by Fe-Ti oxides. Fe-Ti oxide thermometry is a measure of temperature in the reservoir immediately prior to eruption. Fe-Ti oxide diffusion can reset grains on timescales of hours to weeks (Devine et al. 2003, Hou et al. 2021, Venezky and Rutherford 1999). An experimental study by Hou et al. (2021) shows that after ~100 hours at magmatic temperatures, Fe-Ti oxides approach compositional equilibrium. Their study has important implication for volcanic application of Fe-

Ti oxides; their work implies that effusively erupted volcanics and many lavas will have re-equilibrated Fe-Ti oxides that represent cooling. Therefore, the use of Fe-Ti oxide thermometry in Plinian eruptions is a better proxy for pre-eruptive temperature of the magma rather than dome eruptions, as Fe-Ti oxides pre-eruptive temperatures are preserved in rapidly quenched eruptive products. If the plagioclase grew very rapidly prior to eruption, then the Fe-Ti oxides temperatures could be a good guide for Sr diffusive modelling temperatures. We cannot rule out rapid plagioclase growth, therefore we examine the Fe-Ti oxide temperatures at a possible range of temperatures for Sr diffusive modelling. One exception is the Kakapiko Dome, which was an effusive dome eruption and probably contains Fe-Ti oxides that were reset by slow cooling; thus we apply the Kakapiko Dome Fe-Ti oxide temperatures with caution.

Kakapiko Dome Fe-Ti oxides record pre-eruptive temperatures of 708–751 ºC (Sas et al. 2021). At temperatures coincident with the Fe-Ti oxide thermometry (700 and 750 ºC), best-fit diffusion profiles for modeled plagioclase grains range from 10^1–10^3 years. This wide range in diffusive relaxation timescales could reflect the mushy nature of the reservoir and the range of storage conditions (pressure, temperature, composition) in which the magma was stored; grains stored at cooler conditions would preserve less relaxed Sr diffusion profiles than those stored in hotter conditions. The Kakapiko Dome plagioclase are normally zoned, with few inner calcic zones, and sodic margins. There is no evidence from the plagioclase to suggest that the Kakapiko Dome plagioclase were reheated prior to eruption. The few grains that were modellable according to the criteria above preserve anorthite profiles with a slightly relaxed step function which is closely matched by the Sr profiles (i.e. the anorthite and Sr profiles are not in equilibrium). The similarity in the anorthite and Sr profile suggests that either the plagioclase grew rapidly prior to eruption such that Sr did not have time to diffuse, or the plagioclase were

stored at cool enough temperatures that Sr diffusion is very slow. Zircon age spectra from Kakapiko Dome show protracted crystallization between eruption age and secular equilibrium (Chapter 2); given the ubiquity of plagioclase in volcanic rocks, and the cooler temperatures recorded by zircon, plagioclase crystallization can be expected throughout the duration of the zircon crystallization. Therefore, it is difficult to assess whether Sr profiles are due to antecrystic grains held at cooler temperatures for long durations, or autocrystic grains held at hotter temperatures for short durations, although cooler storage temperatures are more likely given the zircon temperatures.

Hauparu Fe-Ti oxide pre-eruptive temperatures are between 890–990 ºC (Shane et al. 2005b). For the single plagioclase grain that had a profile appropriate to model, we found diffusive timescales of 10^{-1} years at temperatures >850 ºC. Thus, if plagioclase were stored at the Fe-Ti oxide temperatures, Sr diffusion times suggest very short storage times. Lack of modellable plagioclase grains restricts our ability to thoroughly examine the Hauparu plagioclase storage conditions beyond that observation. There are multiple Hauparu plagioclase morphologies: some crystals have normal and oscillatory zoning patterns with intact cores; and some crystals have sieved cores with patchy zoning and resorption rims that are overgrown by generally thick normally zoned rims. Most of the Hauparu plagioclase anorthite profiles appear to be either relaxed to some degree, or record little to no variation in anorthite content across the transect. The Sr profiles track with the anorthite profiles showing little equilibration with anorthite content. None of the grains preserve a distinct step in anorthite content suggesting that kinetic or growth effects were controlling anorthite content as the plagioclase crystallized as suggested by Chamberlain et al. (2014). Zircon ages and trace element concentrations from Hauparu show protracted crystallization and storage at a range of temperature and compositional

environments, which suggests that the plagioclase crystals in the Hauparu eruption might be antecrysts harvested from a large mush reservoir of different thermal and compositional environments. Antecrystic plagioclase grains stored for longer durations at cooler temperatures could yield the same profile as autocrystic grains stored for shorter durations but at hotter temperatures (Fig 4, Fig 5).

Although erupted at essentially the same time, the Rotoiti Fe-Ti oxides yield hotter eruptive temperatures than the EQF Fe-Ti oxides. The EQF Fe-Ti oxide temperatures range from 694–722 ºC (Grant et al. 2024), and at 700 to 750 ºC the diffusive relaxation timescales range from 10^0 to 10^3 years. The Rotoiti oxide temperatures range from 751 – 863 ºC (Schmitz and Smith 2004) and the at 750 to 850 ºC the modeled diffusive relaxation timescales range from 10^0 to 10^1 years. There is a much larger spread in the modeled apparent diffusive timescales in EQF plagioclase than in Rotoiti plagioclase (Fig. 4.5). The profiles from Rotoiti in both this study and Bradshaw (2017) do not preserve sharp anorthite or Sr profiles. In nearly all cases, the anorthite and Sr profiles are not in equilibrium, instead they appear to positively correlated (Fig. 4.4). In a small subset of grains, there are gently sloping profiles of Sr from core to rim, but in all cases anorthite content and Sr concentration are correlated with each other – that is, none of the profiles have fully equilibrated. The EQF profiles from this study and from Bradshaw (2017) also have a number of plagioclase grains nearly flat profiles (or constant) anorthite and Sr profiles, and a small subset of grains that preserve distinct step-functions in Sr concentration and anorthite content. The observation that anorthite content and Sr concentration are not in equilibrium requires that the plagioclase grains either grew quickly, and/or the grains were stored in a cool portion of the reservoir such that Sr diffusion was significantly slowed. Alternatively, studies by Till et al. (2015) and Shamloo and Till (2019) show that gently sloping profiles of Mg

concentration are the result of changing composition magma rather than Mg diffusion. Therefore, it is also possible that the relatively flat Sr profiles observed in the OVC plagioclase could represent crystallization from a magma that is changing composition.

Unsurprisingly, these OVC data suggest that plagioclase residence times are short (10^0–10^2) if held at moderate temperatures (750 ºC) although they could be longer if held at cooler temperatures (10^2–10^4 at 650 ºC) (Fig 5). For the Taupo Volcanic Center (TVC), Schlieder (2022) found a larger range of Sr diffusive timescales (of 10^1–10^4 years) when modeled at 750 ºC. One interesting observation is that the two caldera-forming eruptions, Rotoiti (OVC) and Oruanui (TVC), have different modeled Sr diffusion timescales. The Oruanui eruption yields model timescales of 10^1–10^3 years at 750 ºC, and the Rotoiti eruption yields model timescales of 10^0–10^1 years at 750 ºC. However, there are 116 modellable grains for the TVC (Schlieder (2022)), and only 22 modellable grains for the OVC, so some of this difference in range might be due to sample bias. Nevertheless, if supported by additional data, this observation could have important implications for understanding the timescales on which CFEs build to eruption. In the case of Oruanui, the plagioclase grains in the magma reservoir preserve diverse thermal conditions, which suggests that the Oruanui eruption could have sourced its crystal cargo from a magma mush. In the case of Rotoiti, short diffusive apparent timescales suggest that plagioclase storage at moderate temperatures was short-lived, suggesting that the body was amalgamated rapidly prior to eruption. On the other hand, there is other evidence to suggest that Rotoiti stored its crystals long-term in a magma mush (Chapter 2), which suggests that the apparent diffusive timescales of 10^0–10^1 years might be minimum estimates of storage timescales.

Overall, the diffusive relaxation timescales for the four eruptions in the OVC are consistent with the body of existing data supporting the model that OVC magmas are stored in a

highly crystalline mush state, with interstitial pockets of melt that record different thermal and compositional parameters (Chapter 2; Molloy et al. 2008, Reid et al. 2011, Stelten et al. 2015, Till et al. 2019). Given the wide range in Sr diffusive apparent timescales for Kakapiko Dome, Rotoiti, and EQF, these data suggest storage as a magma mush with varied thermal and compositional zones is likely.

4.6.3 Implications for hazard mitigation

Other diffusion chronometers reveal similarly short timescales of magma assembly prior to eruption. Allan et al. (2017) use Fe-Mg diffusion in orthopyroxene to infer that magma assembly for the Oruanui eruptible melt body occurred on timescales of decades to millennia, and a study by Barker et al. (2016) show that Fe-Mg diffusion in orthopyroxene reveal magma assembly timescales of decades to centuries for post-Oruanui eruptions in the Taupo Volcanic Center. Similarly, Gualda et al. (2018) show that high Ti concentrations in quartz rims suggests that quartz grains grew <100 years prior to eruption for TVZ eruptions, and Pamukçu et al. (2015) also found quartz Ti diffusion timescales of <120 years. There is general agreement between mineral diffusion chronometers and geothermal modelling (Kelly et al. 2021) in support of long-lived crystal mush systems but rapidly assembled eruptible melt bodies. This has important implications for hazard mitigation and volcano monitoring. Geophysical monitoring efforts (ground deformation, gas emissions, etc.) can detect volcanic unrest shortly prior to eruption, but it is often difficult to discern the difference between ambient unrest and an imminent eruption, as unrest does not require an eruption. It has been shown that high volatile contents in magmas can indicate imminent large eruptions (Stix 2018) which is consistent with the “fermentation” phase of caldera cycles described by Bouvet de Maisonneuve et al. (2021).

Heightened gas monitoring and geodetic surveys could serve as useful and pragmatic indicators of eruption. The knowledge that large magma bodies can assemble in years to centuries heightens the needs for consistent monitoring at major volcanic centers.

4.7 CONCLUSIONS

Quantifying magma assembly and storge timescales is an important parameter in understanding the timescales on which magmas reservoir build to eruption. Assessing thermal histories of mineral grains and populations in individual eruptions is a powerful tool that can help to understand residence timescales at different thermal conditions. We modeled Sr diffusion in volcanic plagioclase for four eruptions from the Okataina Volcanic Center, placing general thermal constraints on each eruption. When combined with other thermometric data, this result allows us to generally understand thermal conditions of the reservoir. In general, plagioclase residence times are short (10^0–10^2) if held at moderate temperatures (750 ºC) and longer (10^2–10^4) if held at cooler temperatures (650 ºC) and are different than those of the neighboring volcanic center (the TVC).

4.8 REFERENCES

Allan, A. S., Morgan, D. J., Wilson, C. J., & Millet, M. A. (2013). From mush to eruption in centuries: assembly of the super-sized Oruanui magma body. *Contributions to Mineralogy and Petrology*, *166*, 143-164.

Allan, A. S., Barker, S. J., Millet, M. A., Morgan, D. J., Rooyakkers, S. M., Schipper, C. I., & Wilson, C. J. (2017). A cascade of magmatic events during the assembly and eruption of a super-sized magma body. *Contributions to Mineralogy and Petrology*, *172*, 1-34.

Barboni, M., Boehnke, P., Schmitt, A. K., Harrison, T. M., Shane, P., Bouvier, A. S., & Baumgartner, L. (2016). Warm storage for arc magmas. *Proceedings of the National Academy of Sciences*, *113*(49), 13959-13964.

Barker, S. J., Wilson, C. J., Morgan, D. J., & Rowland, J. V. (2016). Rapid priming, accumulation, and recharge of magma driving recent eruptions at a hyperactive caldera volcano. *Geology*, *44*(4), 323-326.

Bégué, F., Deering, C. D., Gravley, D. M., Kennedy, B. M., Chambefort, I., Gualda, G. A., & Bachmann, O. (2014). Extraction, storage and eruption of multiple isolated magma batches in the paired Mamaku and Ohakuri eruption, Taupo Volcanic Zone, New Zealand. *Journal of Petrology*, *55*(8), 1653-1684.

Bindeman, I. N., Davis, A. M., & Drake, M. J. (1998). Ion microprobe study of plagioclase-basalt partition experiments at natural concentration levels of trace elements. *Geochimica et Cosmochimica Acta*, *62*(7), 1175-1193.

Blundy, J. D., & Wood, B. J. (1991). Crystal-chemical controls on the partitioning of Sr and Ba between plagioclase feldspar, silicate melts, and hydrothermal solutions. *Geochimica et Cosmochimica Acta*, *55*(1), 193-209.

Bouvet de Maisonneuve, C., Forni, F., & Bachmann, O. (2021). Magma reservoir evolution during the build up to and recovery from caldera-forming eruptions–a generalizable model?. *Earth-Science Reviews*, *218*, 103684.

Bradshaw, R. W. (2017). Crystal records of the origin, evolution, and thermal histories of magmas.

Chamberlain, K. J., Morgan, D. J., & Wilson, C. J. (2014). Timescales of mixing and mobilisation in the Bishop Tuff magma body: perspectives from diffusion chronometry. *Contributions to Mineralogy and Petrology*, *168*, 1-24.

Charlier, B. L., Peate, D. W., Wilson, C. J., Lowenstern, J. B., Storey, M., & Brown, S. J. (2003). Crystallisation ages in coeval silicic magma bodies: 238U–230Th disequilibrium evidence from the Rotoiti and Earthquake Flat eruption deposits, Taupo Volcanic Zone, New Zealand. *Earth and Planetary Science Letters*, *206*(3-4), 441-457.

Charlier, B. L. A., Wilson, C. J. N., Lowenstern, J. B., Blake, S., Van Calsteren, P. W., & Davidson, J. P. (2005). Magma generation at a large, hyperactive silicic volcano (Taupo, New Zealand) revealed by U–Th and U–Pb systematics in zircons. *Journal of Petrology*, *46*(1), 3-32.

Charlier, B. L. A., & Wilson, C. J. N. (2010). Chronology and evolution of caldera-forming and post-caldera magma systems at Okataina Volcano, New Zealand from zircon U–Th model-age spectra. *Journal of Petrology*, *51*(5), 1121-1141.

Cooper, G. F., Wilson, C. J., Charlier, B. L., Wooden, J. L., & Ireland, T. R. (2014). Temporal evolution and compositional signatures of two supervolcanic systems recorded in zircons from

Mangakino volcanic centre, New Zealand. *Contributions to Mineralogy and Petrology*, *167*, 1-23.

Cooper, G. F., & Wilson, C. J. (2014). Development, mobilisation and eruption of a large crystal-rich rhyolite: the Ongatiti ignimbrite, New Zealand. *Lithos*, *198*, 38-57.

Cooper, K. M., & Kent, A. J. (2014). Rapid remobilization of magmatic crystals kept in cold storage. *Nature*, *506*(7489), 480-483.

Costa, F., Chakraborty, S., & Dohmen, R. (2003). Diffusion coupling between trace and major elements and a model for calculation of magma residence times using plagioclase. *Geochimica et Cosmochimica Acta*, *67*(12), 2189-2200.

Deering, C. D., Cole, J. W., & Vogel, T. A. (2011). Extraction of crystal-poor rhyolite from a hornblende-bearing intermediate mush: a case study of the caldera-forming Matahina eruption, Okataina volcanic complex. *Contributions to Mineralogy and Petrology*, *161*, 129-151.

Devine, J. D., Rutherford, M. J., Norton, G. E., & Young, S. R. (2003). Magma storage region processes inferred from geochemistry of Fe–Ti oxides in andesitic magma, Soufriere Hills Volcano, Montserrat, WI. *Journal of Petrology*, *44*(8), 1375-1400.

Ferry, J. M., & Watson, E. B. (2007). New thermodynamic models and revised calibrations for the Ti-in-zircon and Zr-in-rutile thermometers. *Contributions to Mineralogy and Petrology*, *154*(4), 429-437.

Grant, E.R.G., Blatter, D.L., Sisson, T.W., Cooper, K.M.. Shallow storage of the explosive Earthquake Flat Pyroclastics magma body, Okataina Volcanic Center, Taupo Volcanic Zone, New Zealand: evidence from phase-equilibria experiments. *Contributions to Mineralogy and Petrology* **179**, 81 (2024). https://doi.org/10.1007/s00410-024-02151-y

Gualda, G. A., Gravley, D. M., Connor, M., Hollmann, B., Pamukcu, A. S., Bégué, F., Ghiorso, M., & Deering, C. D. (2018). Climbing the crustal ladder: Magma storage-depth evolution during a volcanic flare-up. *Science Advances*, *4*(10), eaap7567.

Hou, T., Botcharnikov, R., Moulas, E., Just, T., Berndt, J., Koepke, J., Zhang, Z., Wang, M., Yang, Z., & Holtz, F. (2021). Kinetics of Fe–Ti oxide re-equilibration in magmatic systems: implications for thermo-oxybarometry. *Journal of Petrology*, *61*(11-12), egaa116.

Kelly, L. J., Gualda, G. A., Gravley, D. M., & Dempsey, D. E. (2021). Hydrothermal cooling as a requirement for short storage of silicic magmas. *Geochemistry, Geophysics, Geosystems*, *22*(9), e2021GC009794.

Kent, A. J., Rowe, M. C., Thornber, C. R., & Pallister, J. S. (2008). Trace element and Pb isotope composition of plagioclase from dome samples from the 2004–2005 eruption of Mount St. Helens, Washington. *US Geological Survey Professional Paper*, *1750*, 809-826.

Langridge, R.M., Ries, W.F., Litchfield, N.J., Villamor, P., Van Dissen, R.J., Barrell, D.J.A., Rattenbury, M.S., Heron, D.W., Haubrock, S., Townsend, D.B., Lee, J.M., Berryman, K.R., Nicol, A., Cox, S.C., Stirling, M.W. (2016). The New Zealand Active Faults Database. *New Zealand Journal of Geology and Geophysics 59*: 86-96. doi: 10.1080/00288306.2015.1112818.

Lubbers, J., Kent, A. J., & Russo, C. (2021). LaserTRAM-DB: a time resolved analysis module for the complete reduction of laser ablation inductively coupled plasma mass spectrometry data.

Lubbers, J., Kent, A. J., & de Silva, S. (2022). Thermal budgets of magma storage constrained by diffusion chronometry: the Cerro Galán ignimbrite. *Journal of Petrology*, *63*(7), egac048.

Marsh, B. D. (1981). On the crystallinity, probability of occurrence, and rheology of lava and magma. *Contributions to Mineralogy and Petrology*, *78*, 85-98.

Moshrefzadeh, J., Izbekov, P., Loewen, M., Larsen, J., & Regan, S. (2023). Dating individual zones in phenocrysts from the 2016–2017 eruption of Bogoslof volcano provides constraints on timescales of magmatic processes. *Journal of Volcanology and Geothermal Research*, *435*, 107741.

Nairn, I. A., & Kohn, B. P. (1973). Relation of the Earthquake Flat Breccia to the Rotoiti Breccia, central North Island, New Zealand. *New Zealand journal of geology and geophysics*, *16*(2), 269-279.

Nielsen, R. L., Ustunisik, G., Weinsteiger, A. B., Tepley III, F. J., Johnston, A. D., & Kent, A. J. (2017). Trace element partitioning between plagioclase and melt: An investigation of the impact of experimental and analytical procedures. *Geochemistry, Geophysics, Geosystems*, *18*(9), 3359-3384.

Pamukçu, A. S., Wright, K. A., Gualda, G. A., & Gravley, D. (2020). Magma residence and eruption at the Taupo Volcanic Center (Taupo Volcanic Zone, New Zealand): insights from rhyolite-MELTS geobarometry, diffusion chronometry, and crystal textures. *Contributions to Mineralogy and Petrology*, *175*, 1-27.

Reid, M. R., Vazquez, J. A., & Schmitt, A. K. (2011). Zircon-scale insights into the history of a Supervolcano, Bishop Tuff, Long Valley, California, with implications for the Ti-in-zircon geothermometer. *Contributions to Mineralogy and Petrology*, *161*, 293-311.

Rocco, N. D. (2020). Isotopic and geochemical signatures of mantle and crustal contributions in rhyolites from Okataina and Taupo volcanoes, New Zealand.

Sas, M., Shane, P., Kuritani, T., Zellmer, G. F., Kent, A. J., & Nakagawa, M. (2021). Mush, melts and metasediments: a history of rhyolites from the Okataina volcanic centre, New Zealand, as captured in plagioclase. *Journal of Petrology*, *62*(8), egab038.

Schlieder, T. D. (2022). *Combining U-series crystal ages with trace element and isotopic information to evaluate the thermal and chemical evolution of silicic magmatic systems* (Order No. 29211943). Available from Dissertations & Theses @ University of California; ProQuest Dissertations & Theses A&I. (2718673894). Retrieved from https://www.proquest.com/dissertations-theses/combining-u-series-crystal-ages-with-trace/docview/2718673894/se-2

Schmitz, M. D., & Smith, I. E. (2004). The petrology of the Rotoiti eruption sequence, Taupo Volcanic Zone: an example of fractionation and mixing in a rhyolitic system. *Journal of Petrology*, *45*(10), 2045-2066.

Shamloo, H. I., & Till, C. B. (2019). Decadal transition from quiescence to supereruption: petrologic investigation of the Lava Creek Tuff, Yellowstone Caldera, WY. *Contributions to Mineralogy and Petrology*, *174*(4), 32.

Shamloo, H. I., Till, C. B., & Hervig, R. L. (2021). Multi-mode magnesium diffusion in sanidine: Applications for geospeedometry in magmatic systems. *Geochimica et Cosmochimica Acta*, *298*, 55-69.

Shane, P., Nairn, I. A., & Smith, V. C. (2005a). Magma mingling in the~ 50 ka Rotoiti eruption from Okataina Volcanic Centre: implications for geochemical diversity and chronology of large volume rhyolites. *Journal of Volcanology and Geothermal Research*, *139*(3-4), 295-313.

Shane, P., Smith, V. C., & Nairn, I. A. (2005b). High temperature rhyodacites of the 36 ka Hauparu pyroclastic eruption, Okataina Volcanic Centre, New Zealand: Change in a silicic magmatic system following caldera collapse. *Journal of Volcanology and Geothermal Research*, *147*(3-4), 357-376.

Shane, P., Martin, S. B., Smith, V. C., Beggs, K. F., Darragh, M. B., Cole, J. W., & Nairn, I. A. (2007). Multiple rhyolite magmas and basalt injection in the 17.7 ka Rerewhakaaitu eruption episode from Tarawera volcanic complex, New Zealand. *Journal of Volcanology and Geothermal Research*, *164*(1-2), 1-26.

Shane, P., Nairn, I. A., Smith, V. C., Darragh, M., Beggs, K., & Cole, J. W. (2008a). Silicic recharge of multiple rhyolite magmas by basaltic intrusion during the 22.6 ka Okareka Eruption Episode, New Zealand. *Lithos*, *103*(3-4), 527-549.

Shea, T., Costa, F., Krimer, D., & Hammer, J. E. (2015). Accuracy of timescales retrieved from diffusion modeling in olivine: A 3D perspective. *American Mineralogist*, *100*(10), 2026

Smith, V. C., Shane, P., & Nairn, I. A. (2005). Trends in rhyolite geochemistry, mineralogy, and magma storage during the last 50 kyr at Okataina and Taupo volcanic centres, Taupo Volcanic Zone, New Zealand. *Journal of Volcanology and Geothermal Research*, *148*(3-4), 372-406.

Smithies, S. L., Harmon, L. J., Allen, S. M., Gravley, D. M., & Gualda, G. A. (2023). Following magma: the pathway of silicic magmas from extraction to storage during an ignimbrite flare-up, Taupō volcanic zone, New Zealand. *Earth and Planetary Science Letters*, *607*, 118053.

Stelten, M. E., Cooper, K. M., Vazquez, J. A., Calvert, A. T., & Glessner, J. J. (2015). Mechanisms and timescales of generating eruptible rhyolitic magmas at Yellowstone caldera from zircon and sanidine geochronology and geochemistry. *Journal of Petrology*, *56*(8), 1607-1642.

Stix, J. (2018). Understanding fast and slow unrest at volcanoes and implications for eruption forecasting. *Frontiers in Earth Science*, *6*, 56.

Till, C. B., Vazquez, J. A., & Boyce, J. W. (2015). Months between rejuvenation and volcanic eruption at Yellowstone caldera, Wyoming. *Geology*, *43*(8), 695-698.

Till, C. B., Vazquez, J. A., Stelten, M. E., Shamloo, H. I., & Shaffer, J. S. (2019). Coexisting discrete bodies of rhyolite and punctuated volcanism characterize Yellowstone's post-Lava Creek Tuff caldera evolution. *Geochemistry, Geophysics, Geosystems*, *20*(8), 3861-3881.

Venezky, D. Y., & Rutherford, M. J. (1999). Petrology and Fe–Ti oxide reequilibration of the 1991 Mount Unzen mixed magma. *Journal of Volcanology and Geothermal Research*, *89*(1-4), 213-230.

Watson, E. B. (1996). Dissolution, growth and survival of zircons during crustal fusion: kinetic principals, geological models and implications for isotopic inheritance. *Earth and Environmental Science Transactions of the Royal Society of Edinburgh*, *87*(1-2), 43-56.

Zellmer, G. F., Blake, S., Vance, D., Hawkesworth, C., & Turner, S. (1999). Plagioclase residence times at two island arc volcanoes (Kameni Islands, Santorini, and Soufriere, St. Vincent) determined by Sr diffusion systematics. *Contributions to Mineralogy and Petrology*, *136*, 345-357.

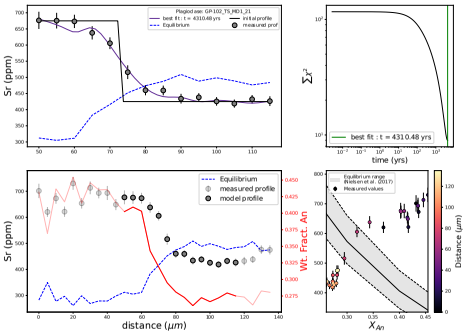
Chapter 4 Appendix A
Table of diffusion model results

Best-fit times (in years) from isothermal modeling							
		Isothermal model temperature					
Sample	Grain #	600 ºC	650 ºC	700 ºC	750 ºC	800 ºC	850 ºC
Kakapiko Dome	EG-MD-21	4310	561	90	17	3.9	1.0
Kakapiko Dome	EG-SM-3	20242	2652	428	83	19	4.8
Kakapiko Dome	EG-SM-10	78701	10192	1627	318	70	18
Kakapiko Dome	EG-SM-2	43118	7217	1192	235	54	14
Hauparu	EG-5	1187	159	26	5.1	1.2	0.3
Rotoiti	RB-3	6249	843	133	28	6.4	1.7
Rotoiti	RB-11a	14930	1979	323	63	14	3.7
Rotoiti	RB-11b	12397	1664	275	54	12	3.2
Rotoiti	RB-18	16392	2132	342	66	15	3.8
Rotoiti	RB-20	5319	752	114	28	6.8	1.9
Earthquake Flat	RB-4 pr2	3040	533	65	17	2.8	0.7
Earthquake Flat	RB-4 pr1	3788	500	81	16	3.0	0.8
Earthquake Flat	RB-7	3463	570	105	23	5.2	1.5
Earthquake Flat	RB-8	12469	1901	314	62	12	3.2
Earthquake Flat	RB-10	6216	827	135	27	6.3	1.7
Earthquake Flat	RB-12	859	114	19	3.7	0.7	0.2
Earthquake Flat	RB-13	8411	1121	184	36	7.7	2.0
Earthquake Flat	RB-15	109528	14631	2399	469	107	28
Earthquake Flat	EG-10	6664	939	162	33	5.5	1.5
Earthquake Flat	EG-16	8394	1174	188	36	7.5	1.9
Earthquake Flat	EG-25	46708	6140	995	193	43	11.2

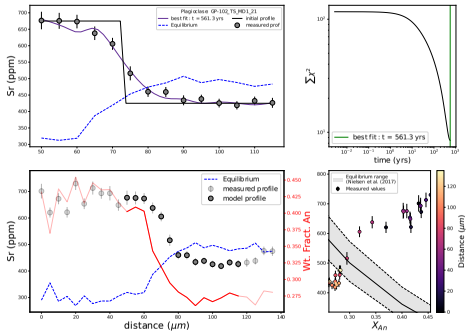
Grain # identifiers use initals "RB" to indicate data from Bradshaw (2017) and "EG" to indidate data from this study. Model results are in years.

Chapter 4 Appendix B
Model results

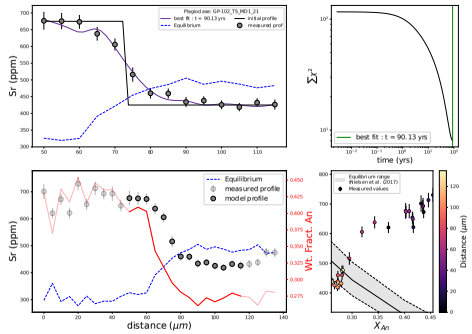
Kakapiko Dome grain 21 (MD)



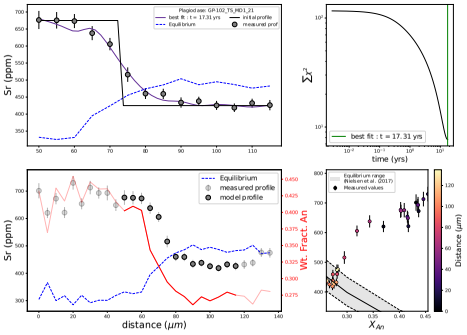
T = 600 ºC



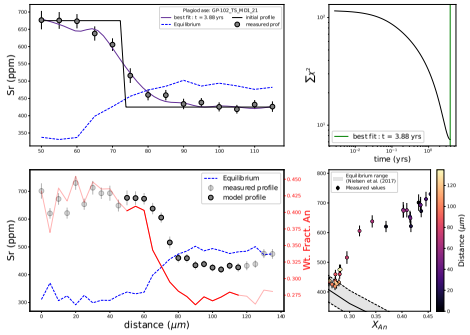
T = 650 ºC



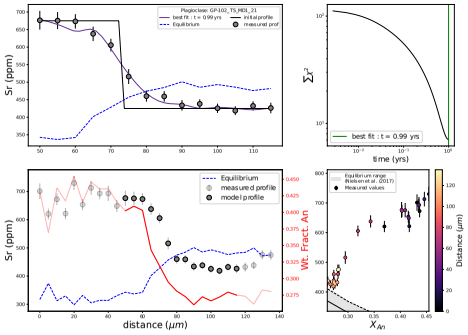
T = 700 ºC



T = 750 ºC

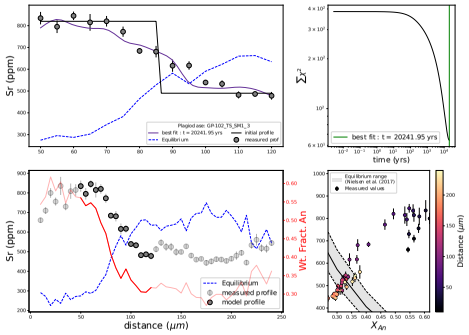


T = 800 ºC

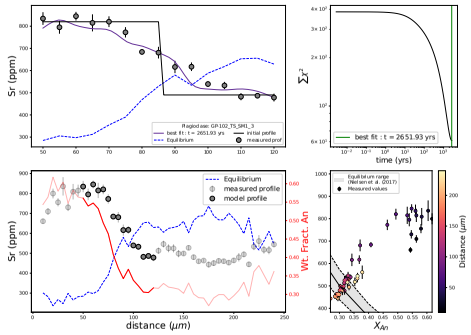


T = 850 ºC

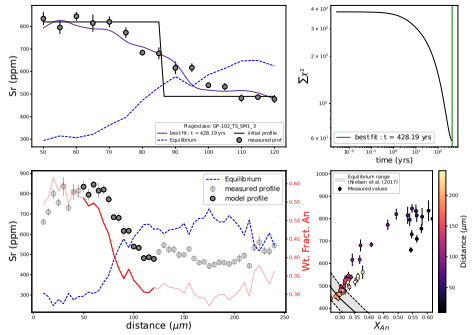
Kakapiko Dome grain 3 (SM)



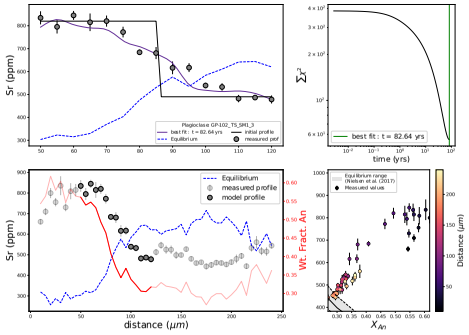
T = 600 ºC



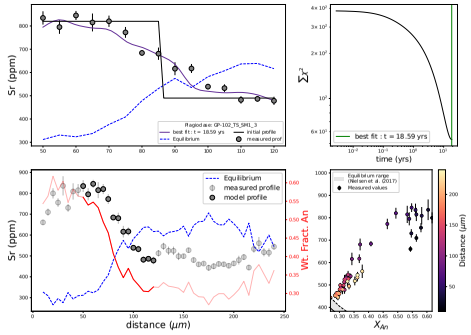
T = 650 ºC



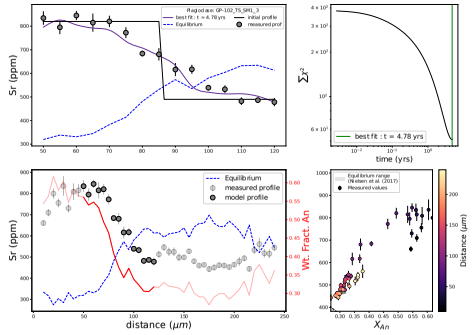
T = 700 ºC



T = 750 ºC

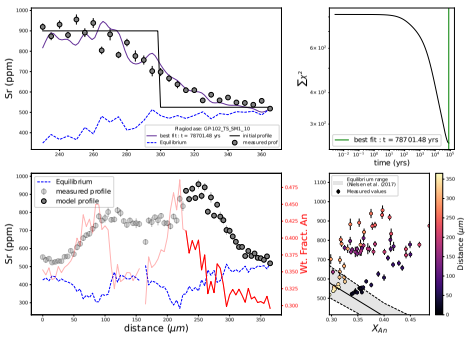


T = 800 ºC

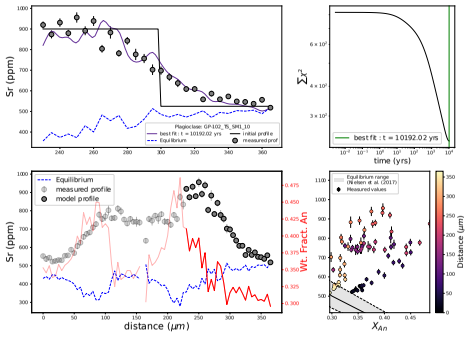


T = 850 ºC

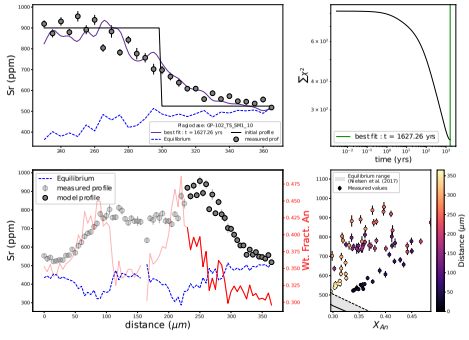
Kakapiko Dome grain 10 (SM)



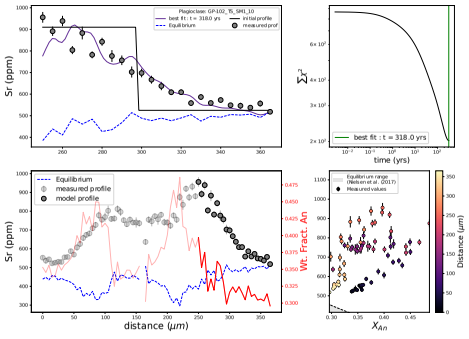
T = 600 ºC



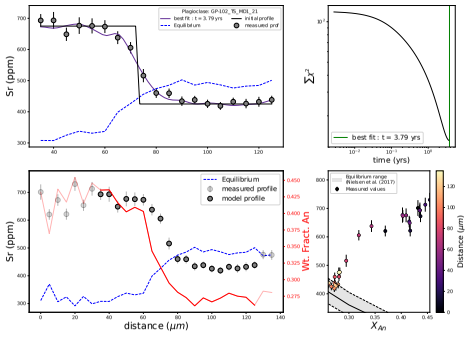
T = 650 ºC



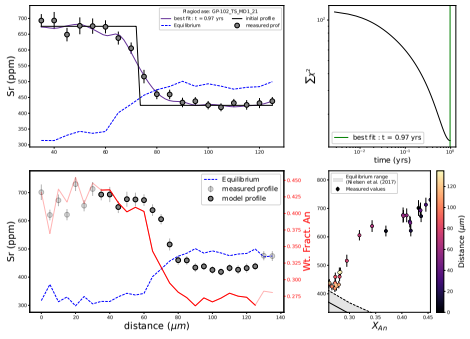
T = 700 ºC



T = 750 ºC

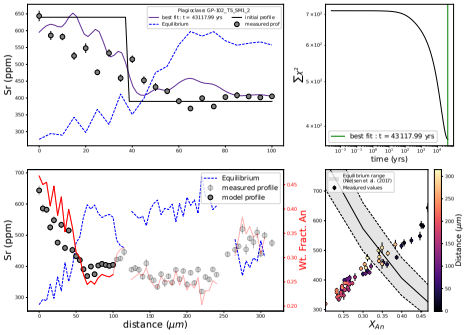


T = 800 ºC

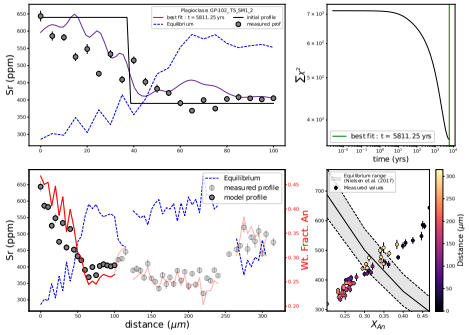


T = 850 ºC

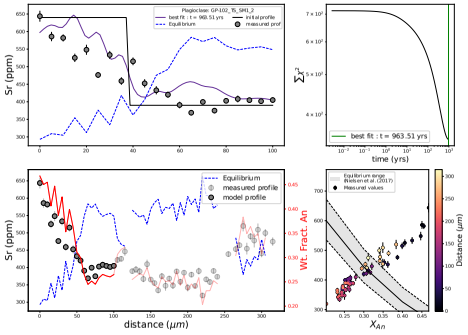
Kakapiko Dome grain 2 (SM)



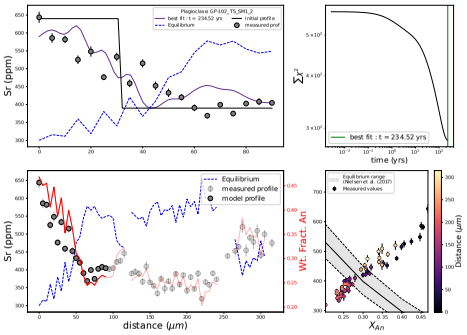
T = 600 ºC



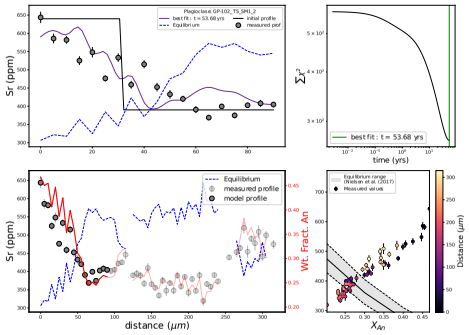
T = 650 ºC



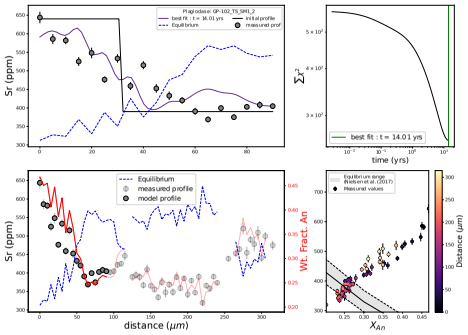
T = 700 ºC



T = 750 ºC

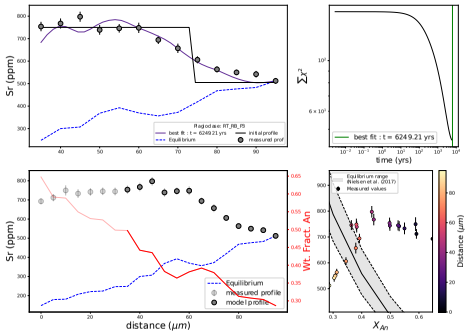


T = 800 ºC

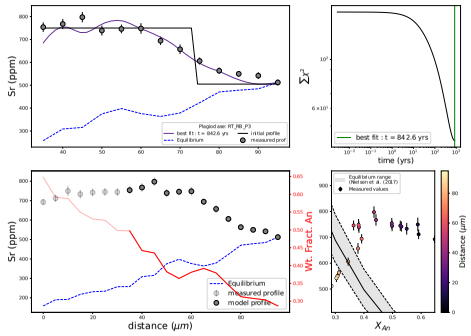


T = 850 ºC

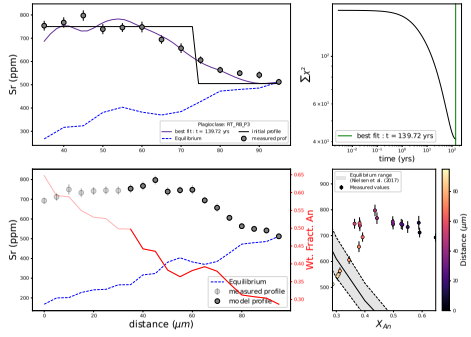
Rotoiti (R. Bradshaw 2017) grain 3



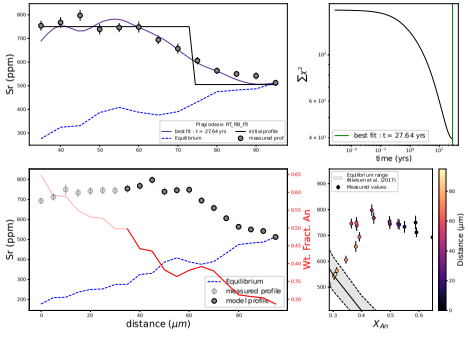
T = 600 ºC



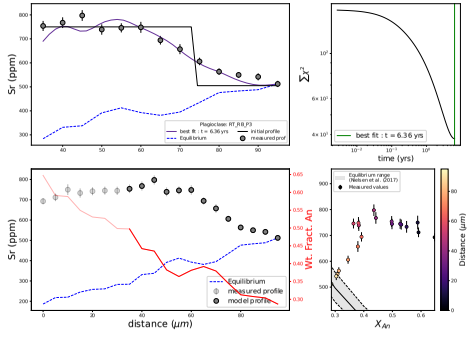
T = 650 ºC



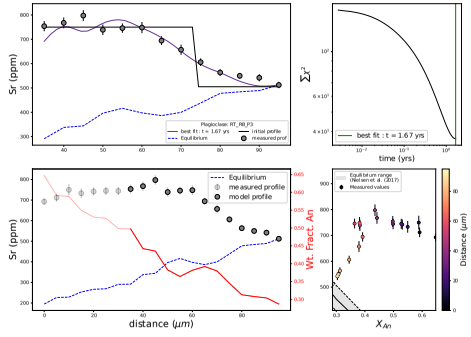
T = 700 ºC



T = 750 ºC

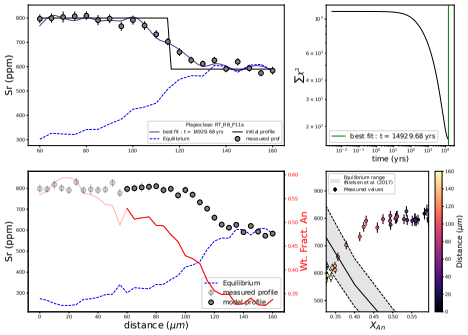


T = 800 ºC

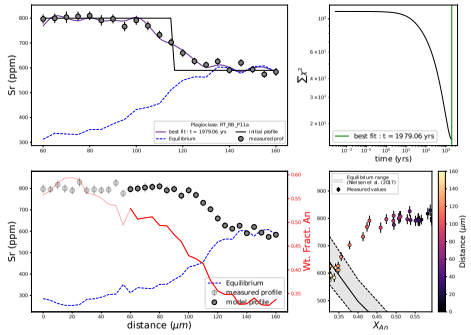


T = 850 ºC

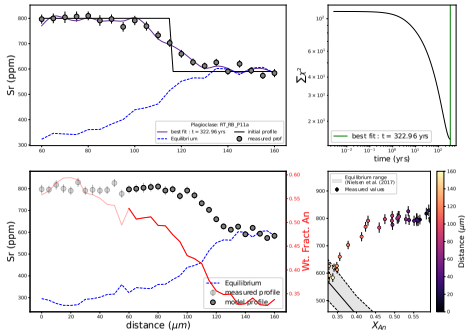
Rotoiti (R. Bradshaw 2017) grain 11a



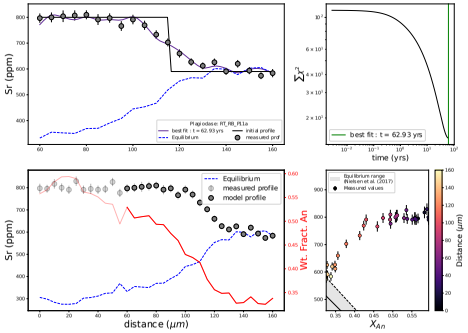
T = 600 ºC



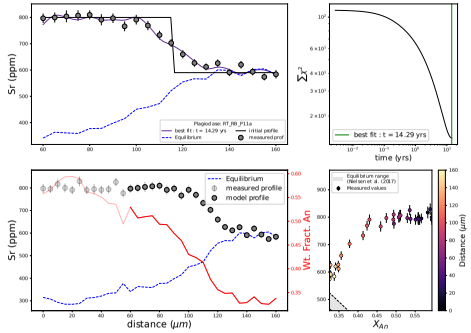
T = 650 ºC



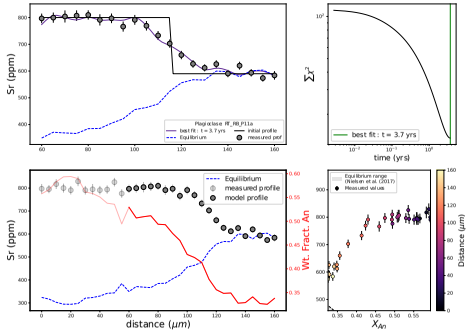
T = 700 ºC



T = 750 ºC

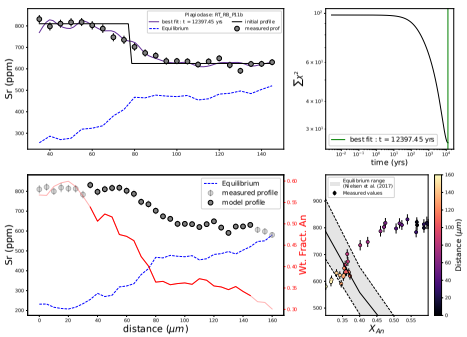


T = 800 ºC

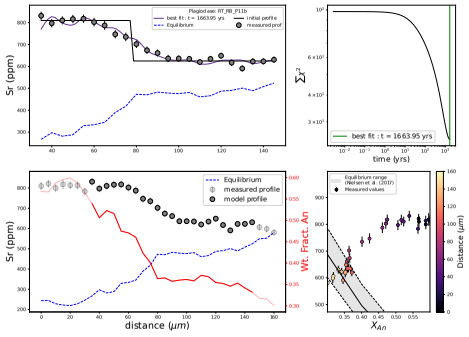


T = 850 ºC

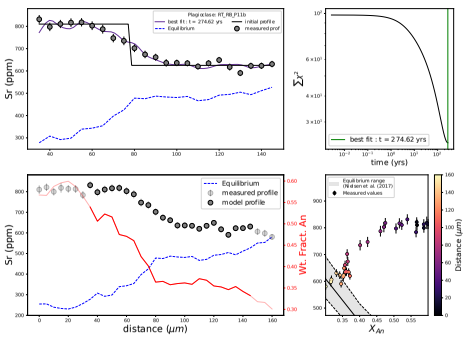
Rotoiti (R. Bradshaw 2017) grain 11b



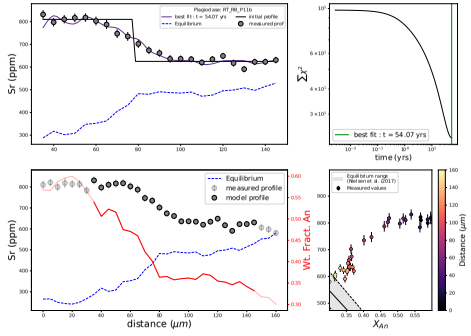
T = 600 ºC



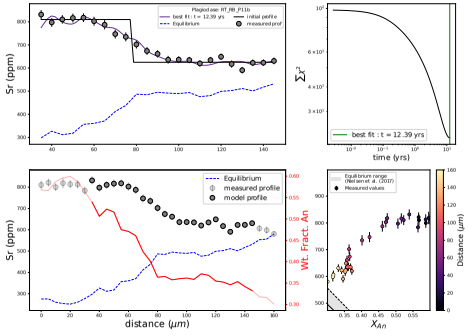
T = 650 ºC



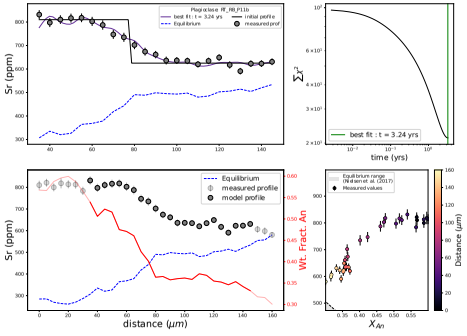
T = 700 ºC



T = 750 ºC

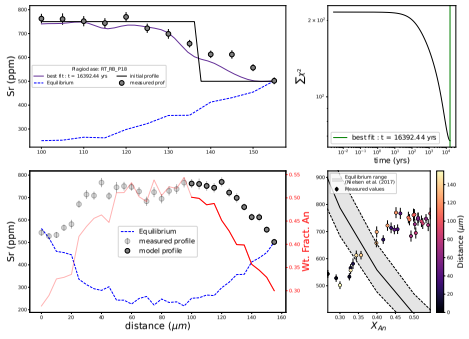


T = 800 ºC

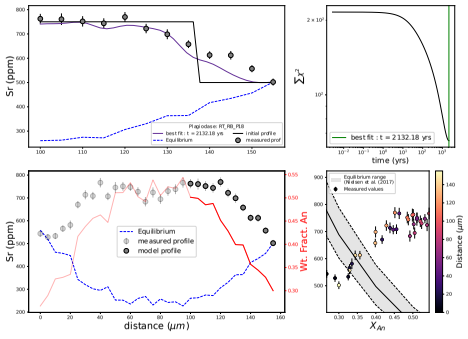


T = 850 ºC

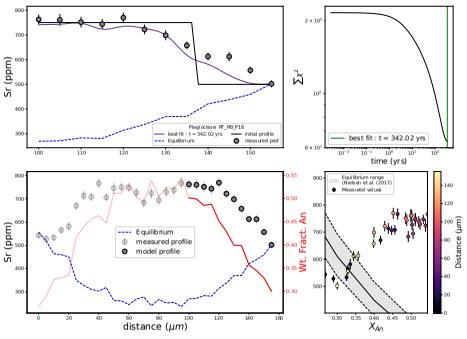
Rotoiti (R. Bradshaw 2017) grain 18



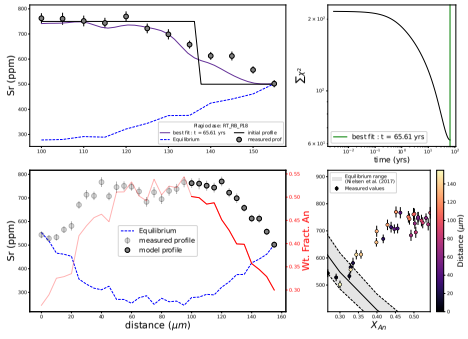
T = 600 ºC



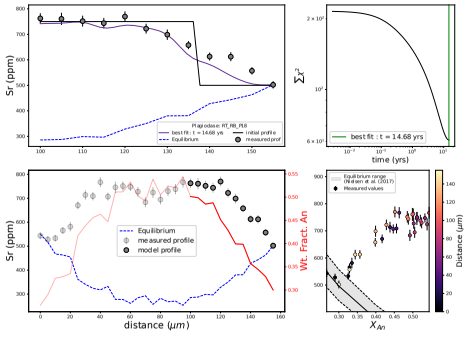
T = 650 ºC



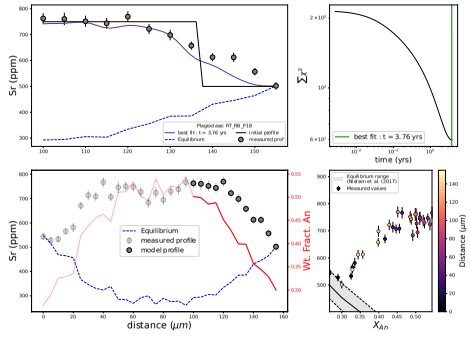
T = 700 ºC



T = 750 ºC

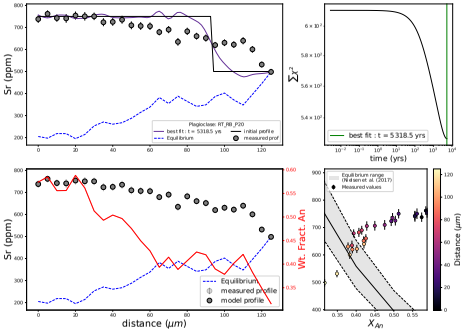


T = 800 ºC

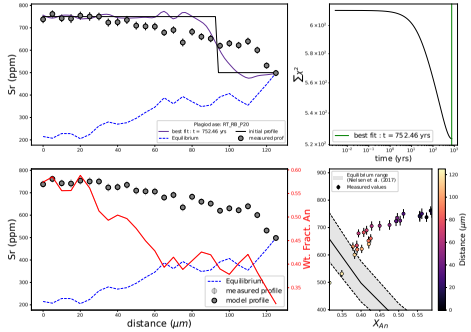


T = 850 ºC

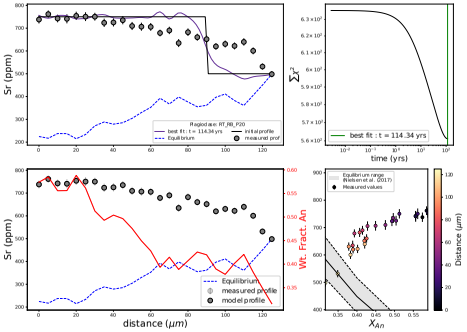
Rotoiti (R. Bradshaw 2017) grain 20



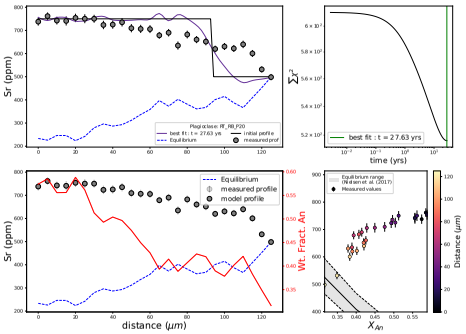
T = 600 ºC



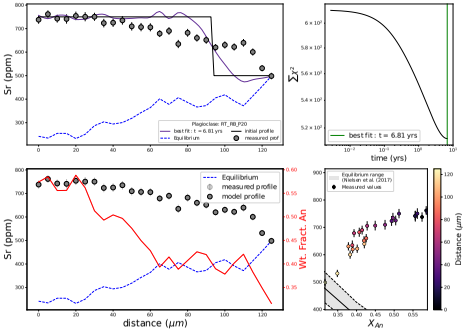
T = 650 ºC



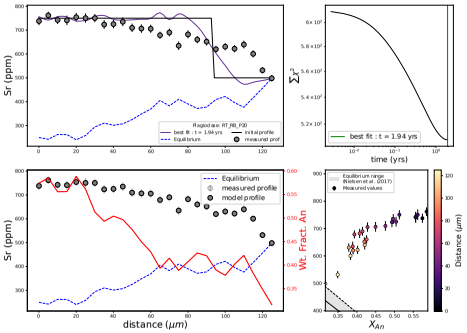
T = 700 ºC



T = 750 ºC

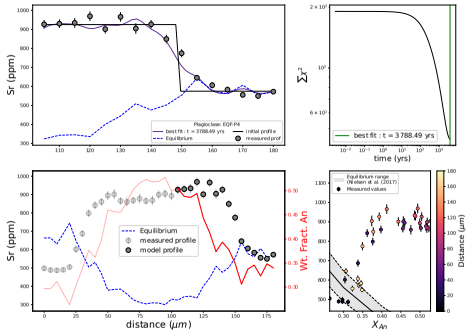


T = 800 ºC

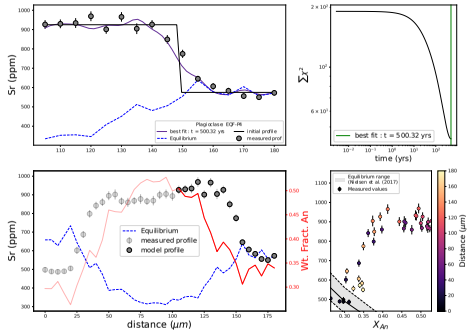


T = 850 ºC

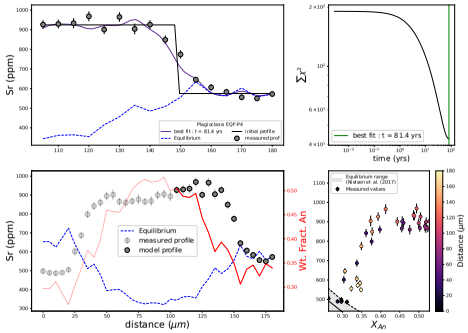
Earthquake Flat (R. Bradshaw 2017) grain 4 profile 1



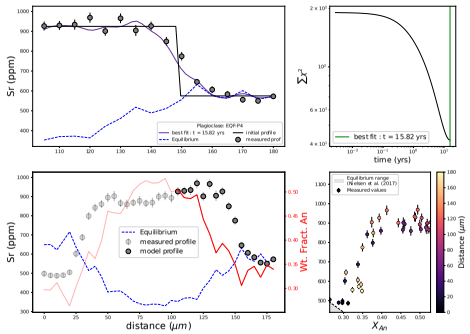
T = 600 ºC



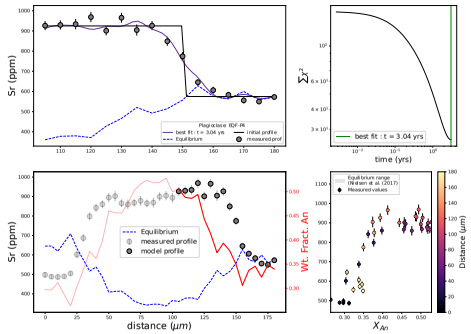
T = 650 ºC



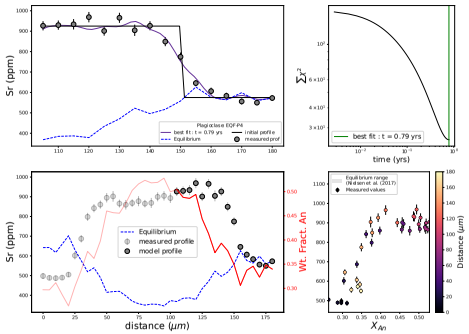
T = 700 ºC



T = 750 ºC

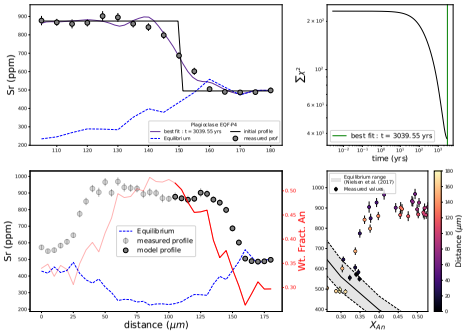


T = 800 ºC

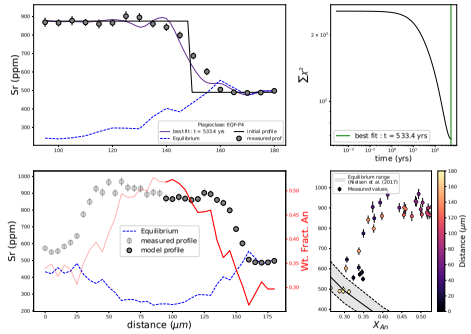


T = 850 ºC

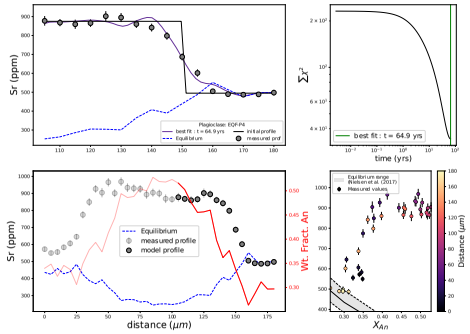
Earthquake Flat (R. Bradshaw 2017) grain 4 profile 2



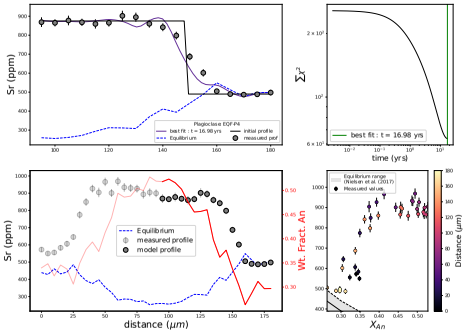
T = 600 ºC



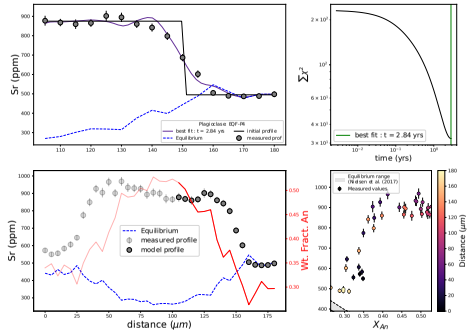
T = 650 ºC



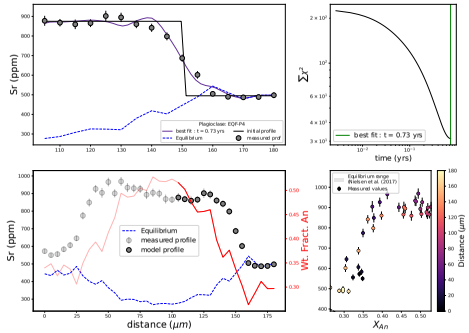
T = 700 ºC



T = 750 ºC

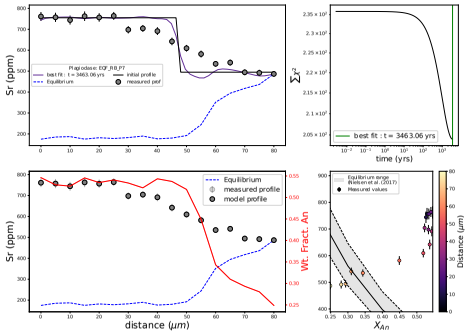


T = 800 ºC

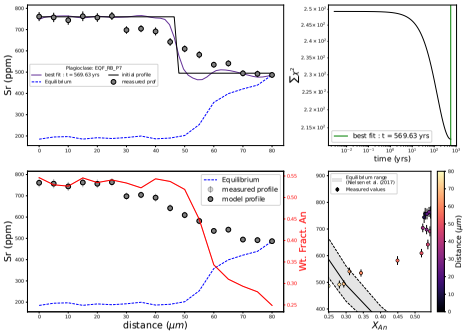


T = 850 ºC

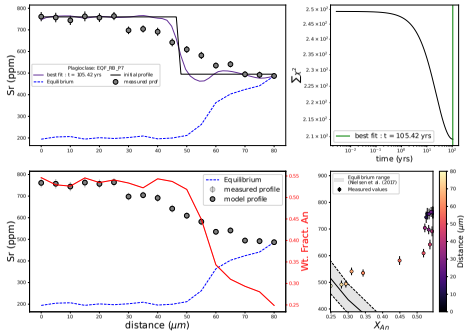
Earthquake Flat (R. Bradshaw 2017) grain 7



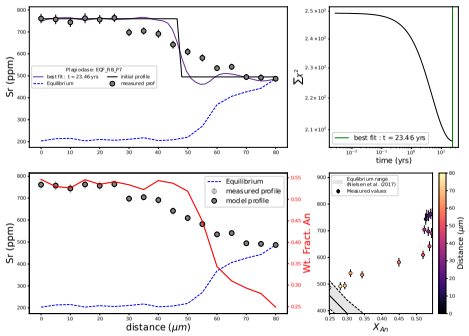
T = 600 ºC



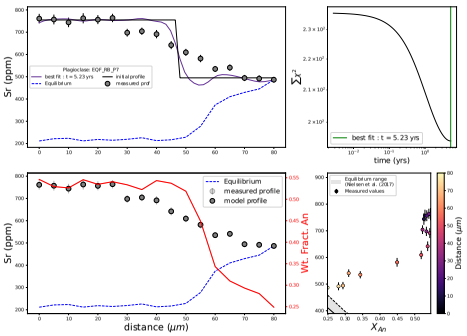
T = 650 ºC



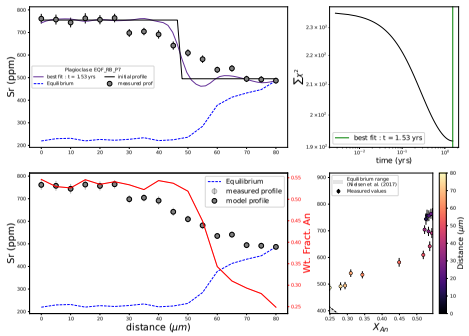
T = 700 ºC



T = 750 ºC

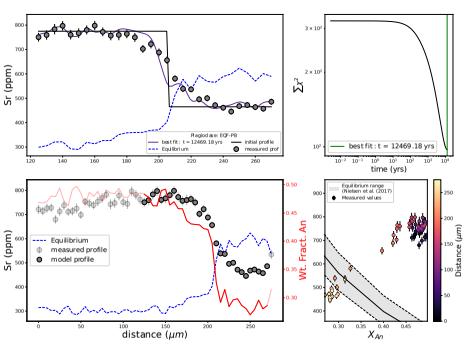


T = 800 ºC

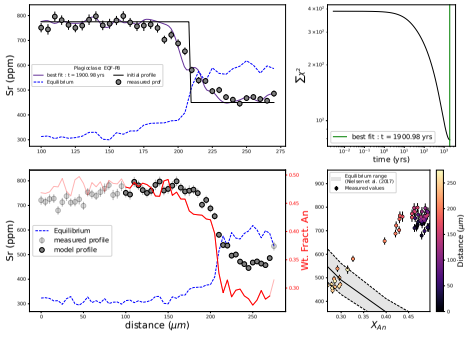


T = 850 ºC

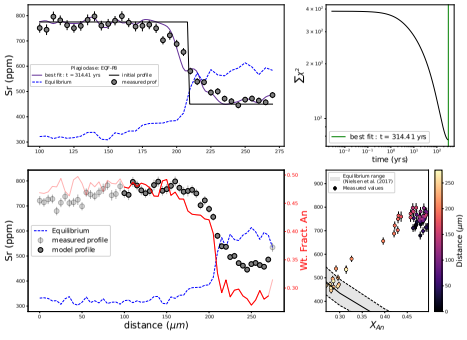
Earthquake Flat (R. Bradshaw 2017) grain 8



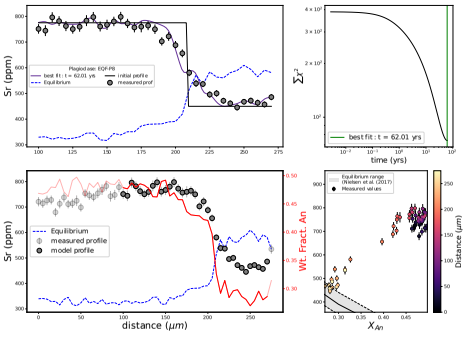
T = 600 ºC



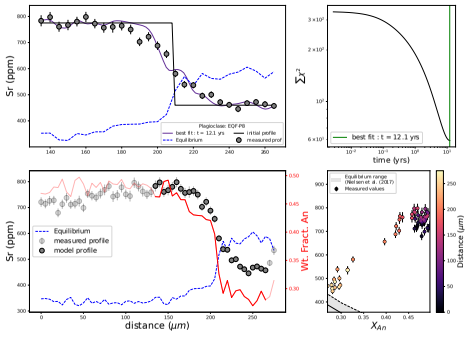
T = 650 ºC



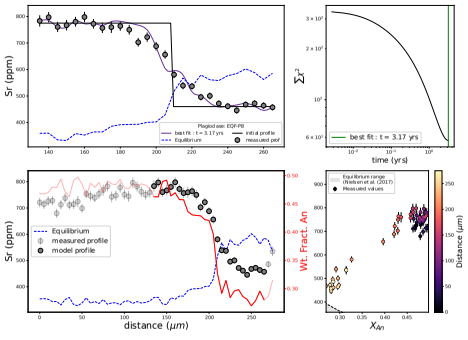
T = 700 ºC



T = 750 ºC

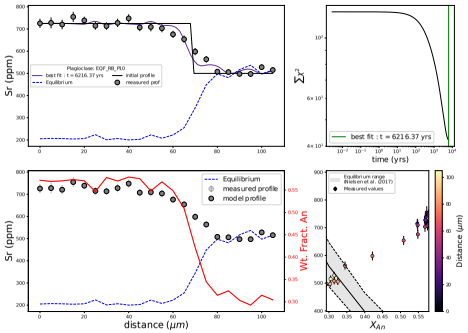


T = 800 ºC

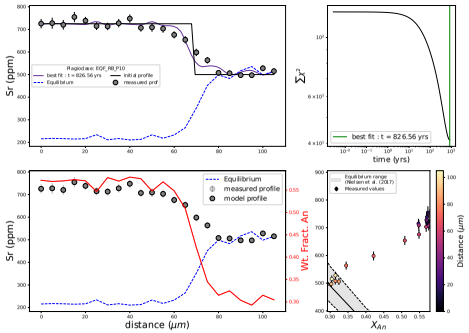


T = 850 ºC

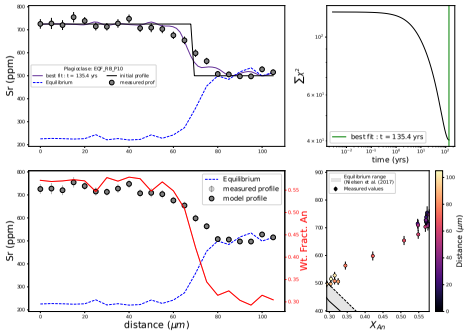
Earthquake Flat (R. Bradshaw 2017) grain 10



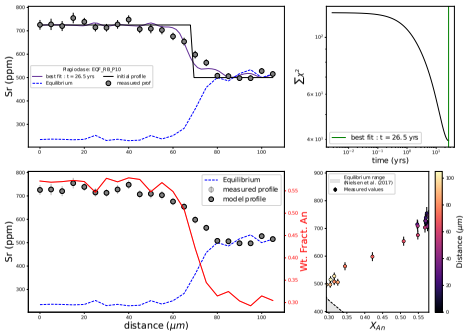
T = 600 ºC



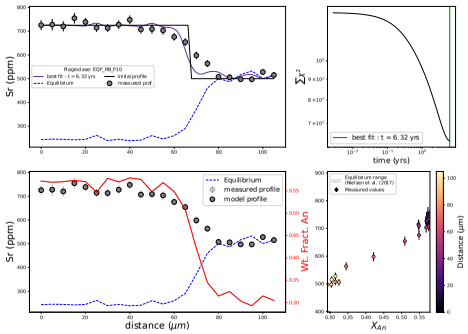
T = 650 ºC



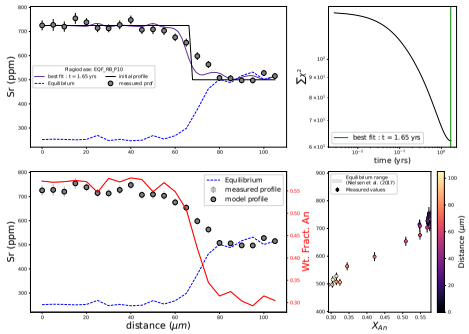
T = 700 ºC



T = 750 ºC

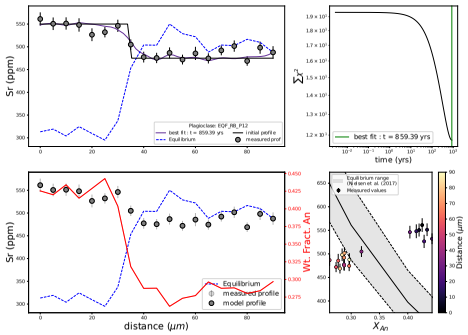


T = 800 ºC

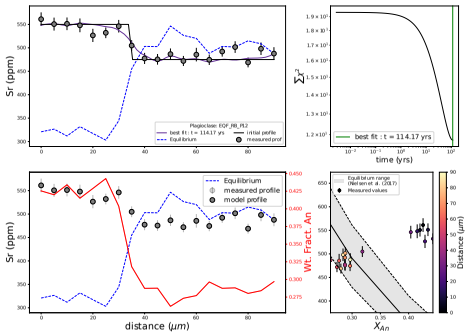


T = 850 ºC

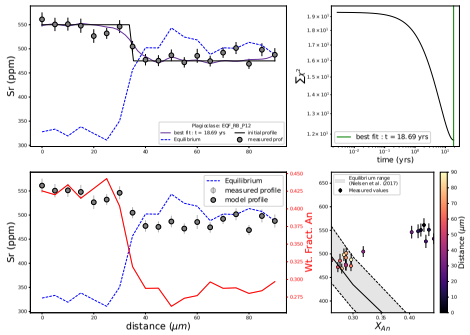
Earthquake Flat (R. Bradshaw 2017) grain 12



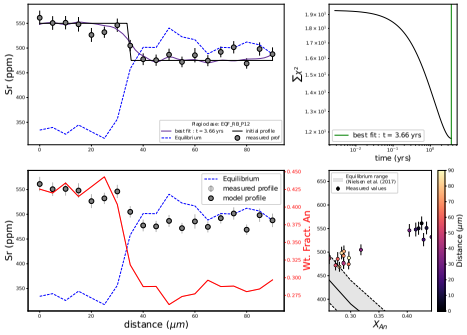
T = 600 ºC



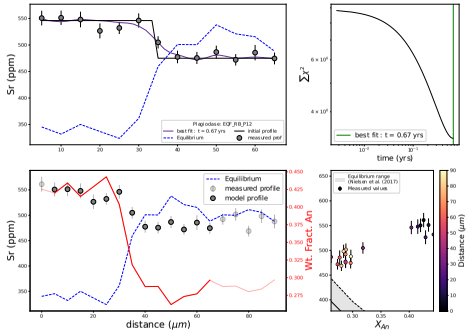
T = 650 ºC



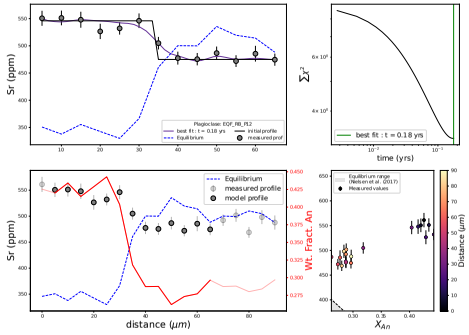
T = 700 ºC



T = 750 ºC

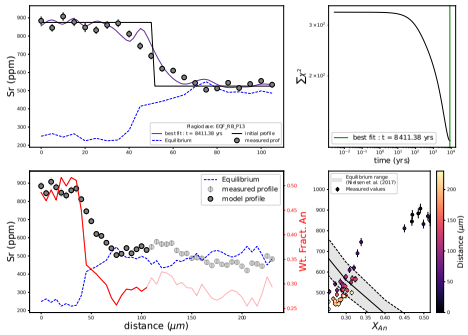


T = 800 ºC

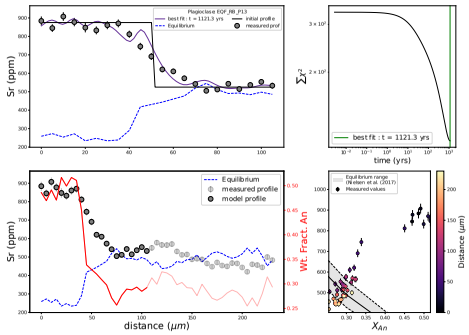


T = 850 ºC

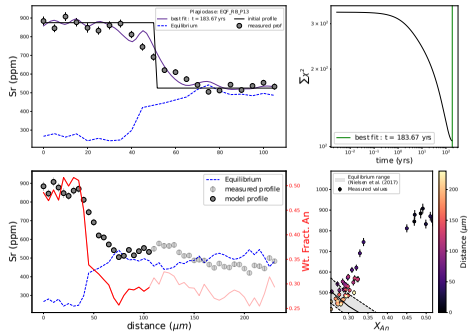
Earthquake Flat (R. Bradshaw 2017) grain 13



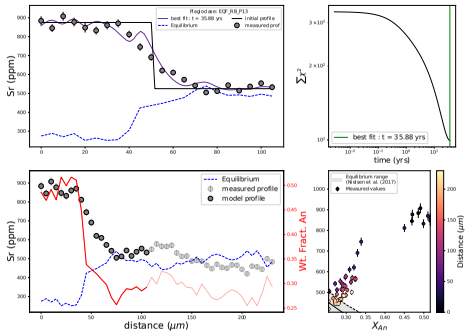
T = 600 ºC



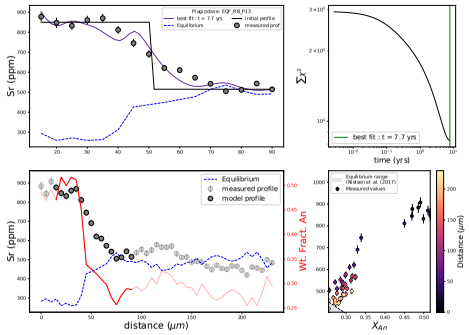
T = 650 ºC



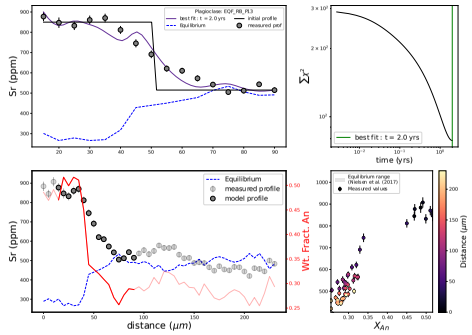
T = 700 ºC



T = 750 ºC

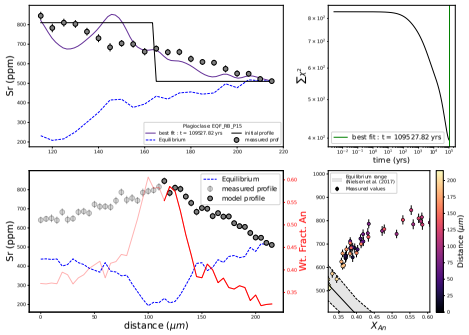


T = 800 ºC

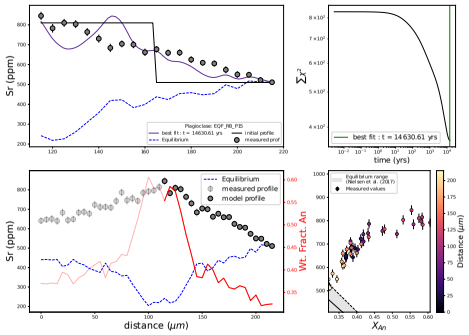


T = 850 ºC

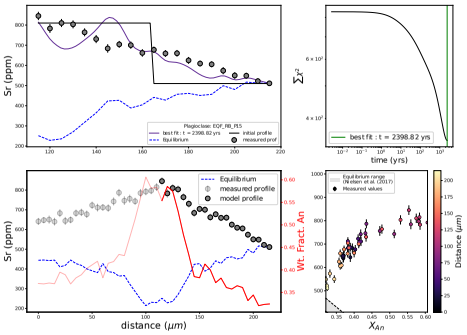
Earthquake Flat (R. Bradshaw 2017) grain 15



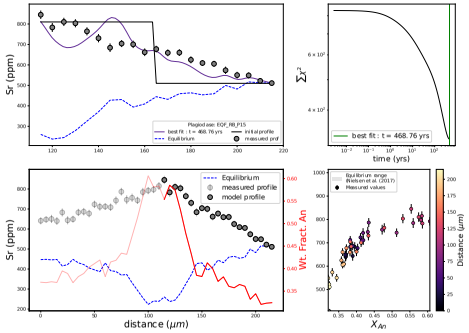
T = 600 ºC



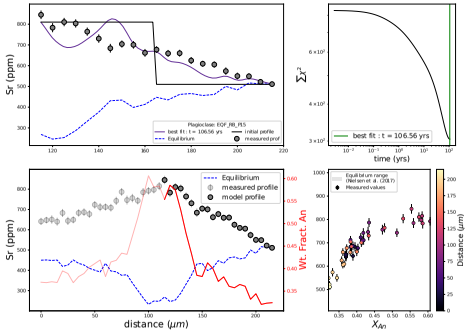
T = 650 ºC



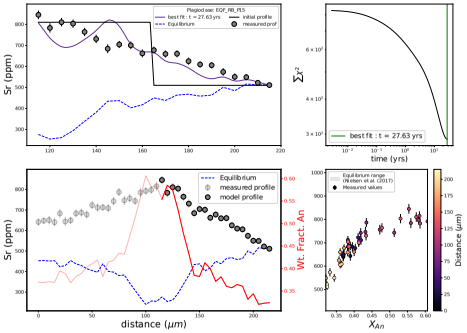
T = 700 ºC



T = 750 ºC

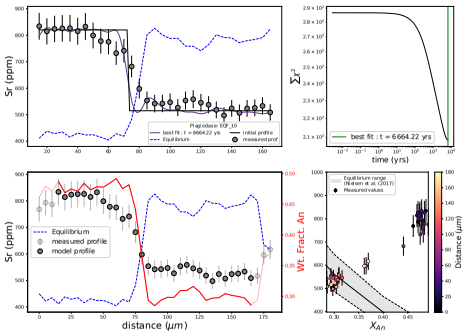


T = 800 ºC

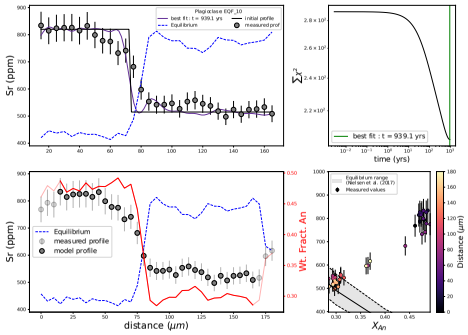


T = 850 ºC

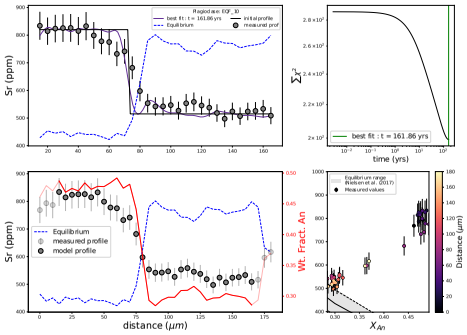
Earthquake Flat grain 10



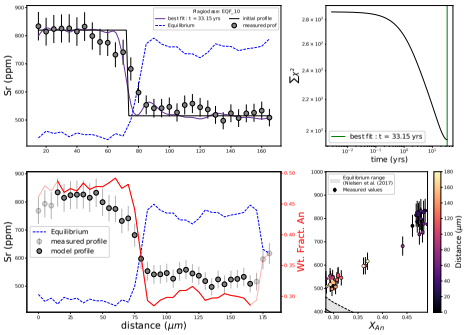
T = 600 ºC



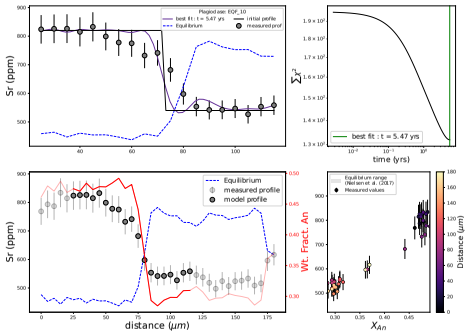
T = 650 ºC



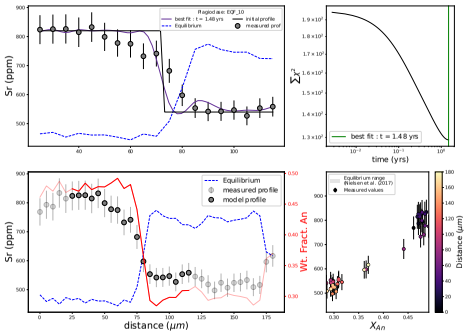
T = 700 ºC



T = 750 ºC

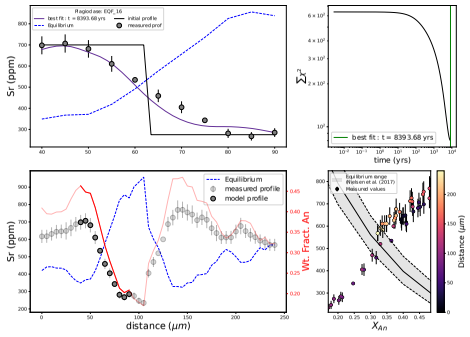


T = 800 ºC

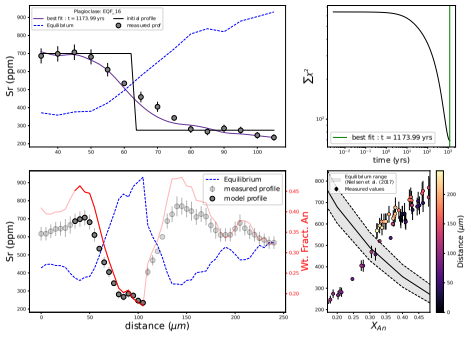


T = 850 ºC

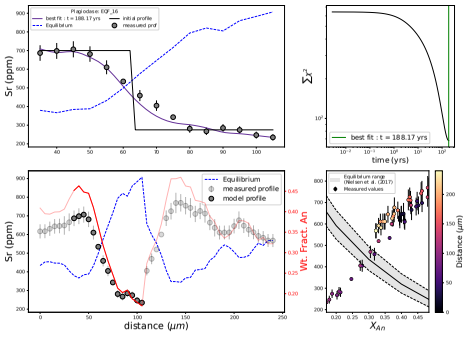
Earthquake Flat grain 16



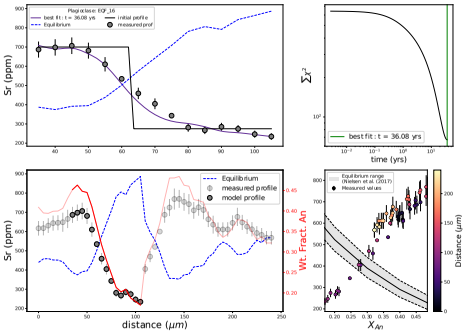
T = 600 ºC



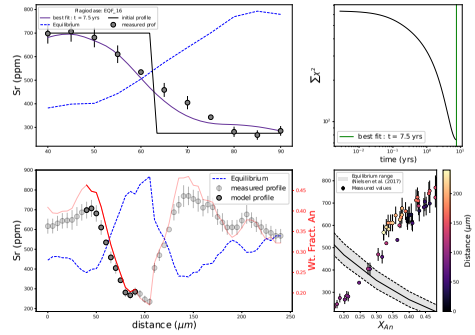
T = 650 ºC



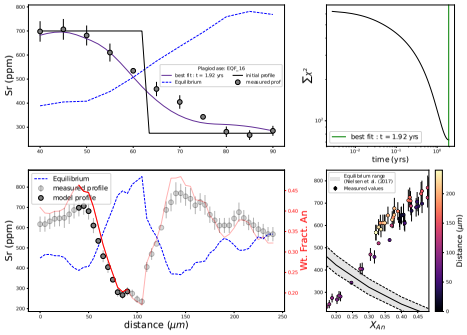
T = 700 ºC



T = 750 ºC

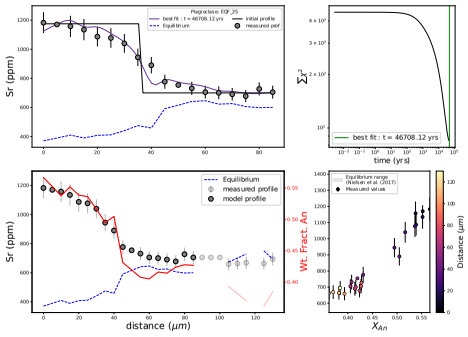


T = 800 ºC

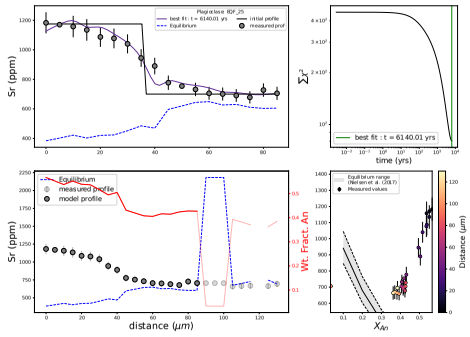


T = 850 ºC

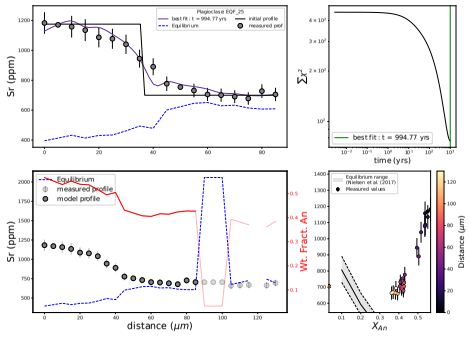
Earthquake Flat grain 25



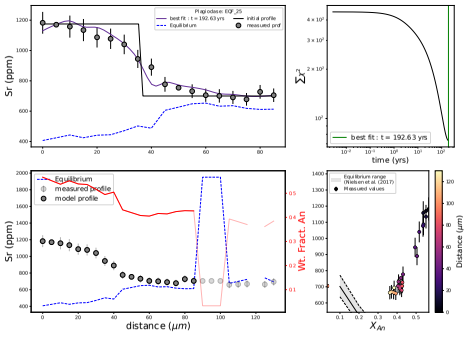
T = 600 ºC



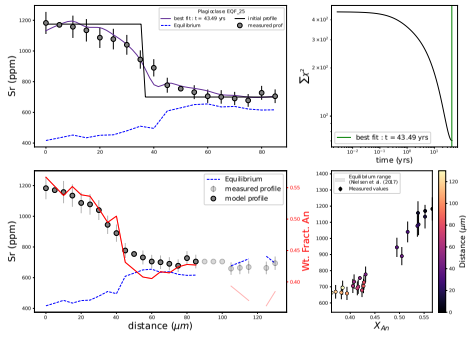
T = 650 ºC



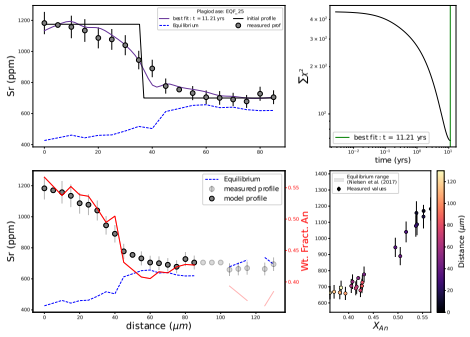
T = 700 ºC



T = 750 ºC

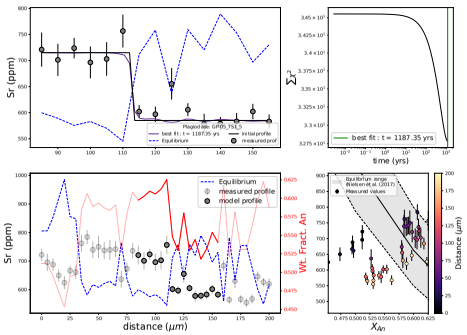


T = 800 ºC

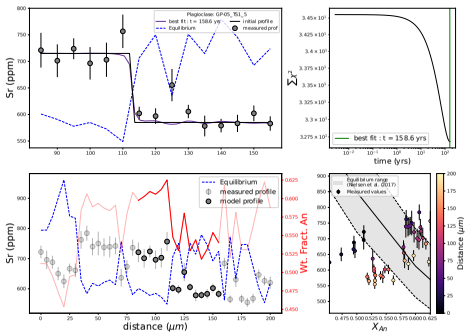


T = 850 ºC

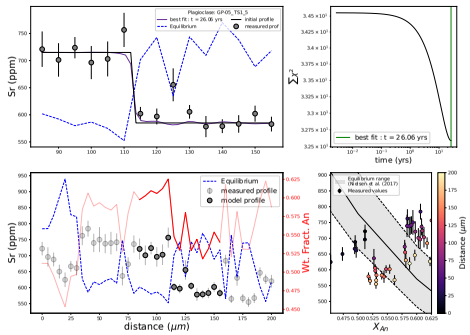
Hauparu grain 5



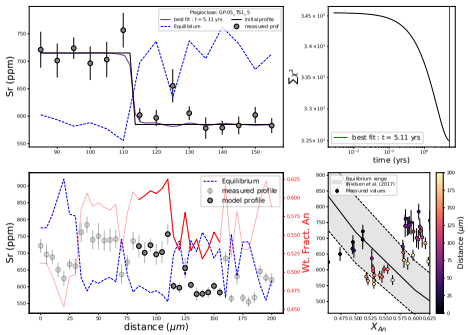
T = 600 ºC



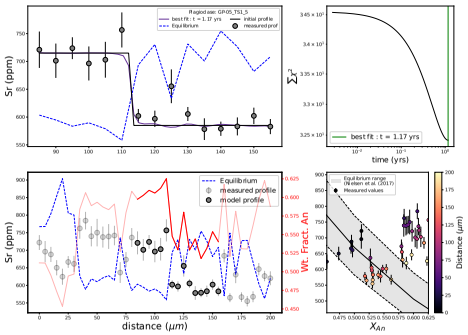
T = 650 ºC



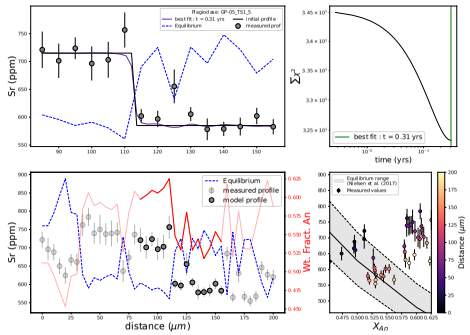
T = 700 ºC



T = 750 ºC

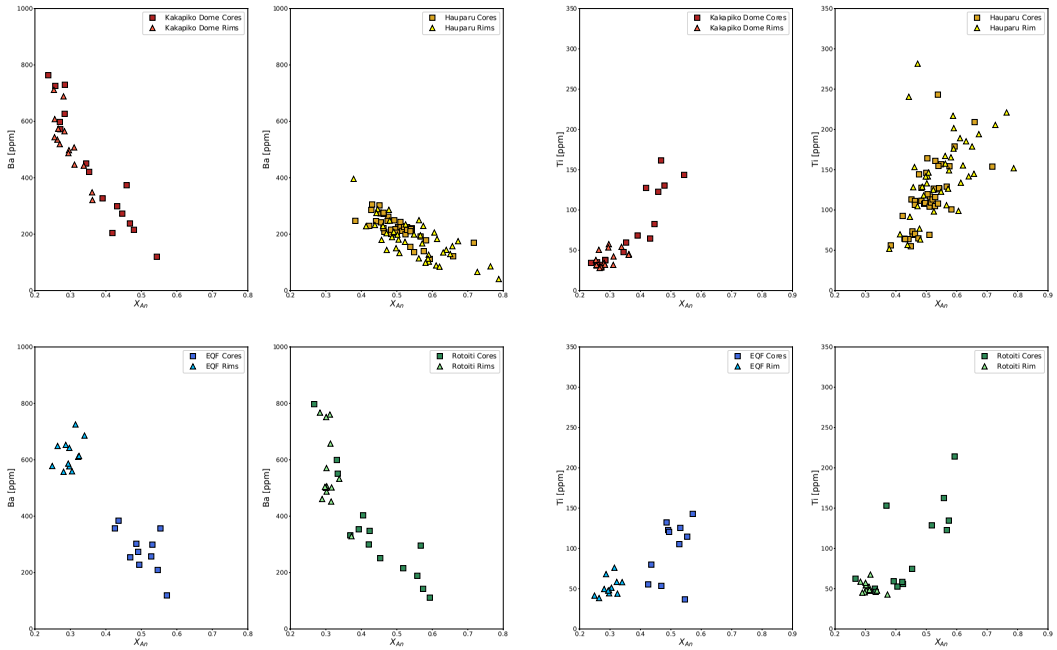


T = 800 ºC

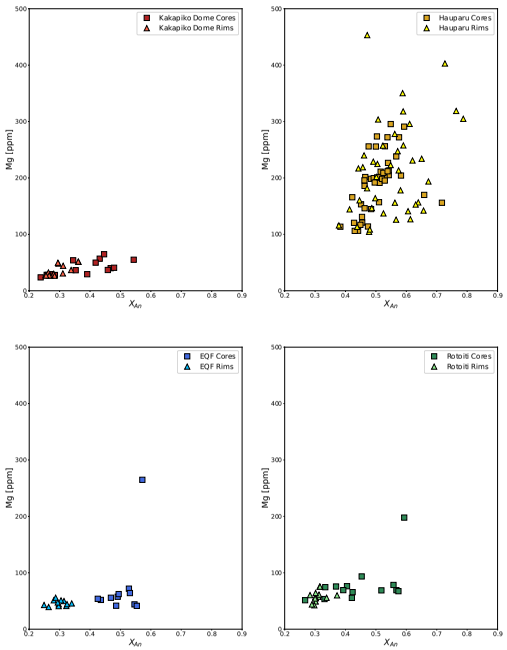


T = 850 ºC

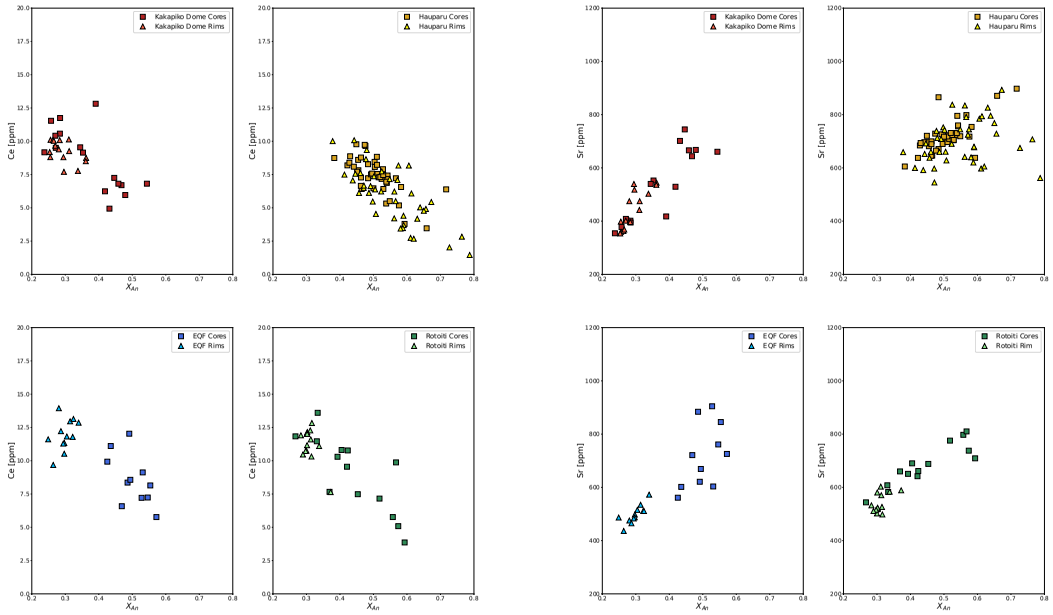
Chapter 4 Appendix C
Trace element plots



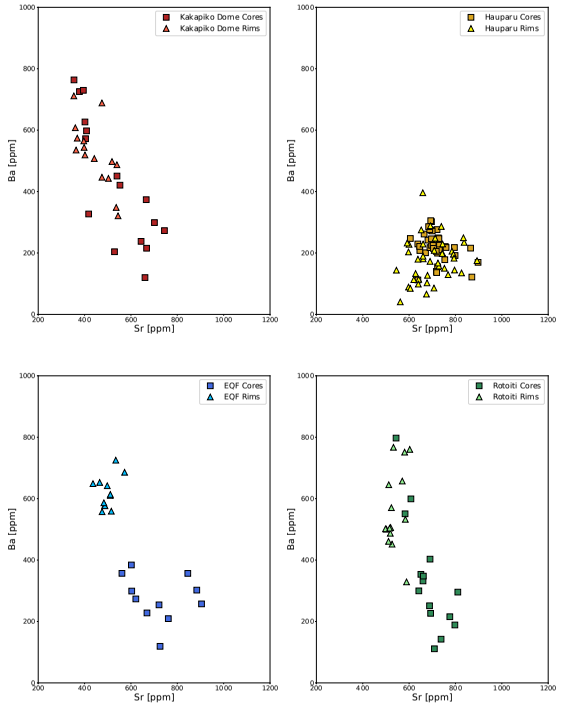
Trace element (Ba, Ti) concentration versus anorthite content for Okataina Volcanic Center plagioclase: Kakapiko Dome (red), Hauparu (yellow), Earthquake Flat (blue), Rotoiti (green). For each sample, the lighter colored triangles represent rim analyses and the darker colored squares represent core analyses. Rims and cores are the rim-most and interior-most spot analyzed during each plagioclase transect analysis.



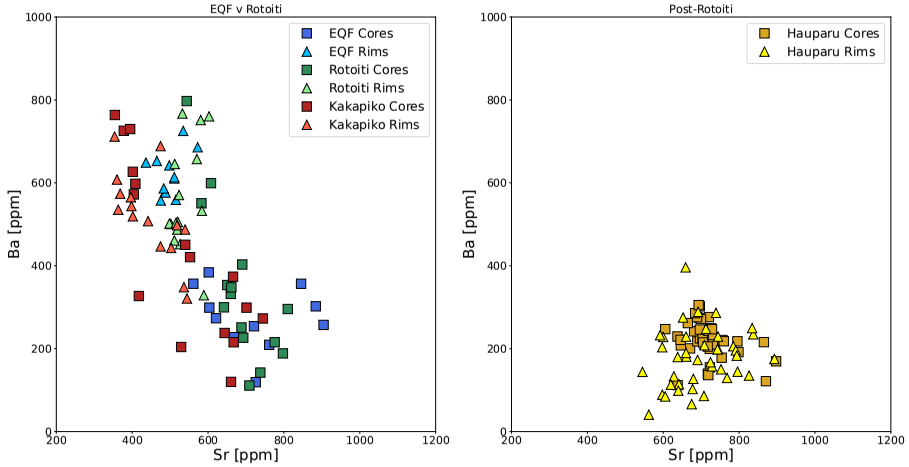
Trace element (Mg) concentration versus anorthite content for Okataina Volcanic Center plagioclase: Kakapiko Dome (red), Hauparu (yellow), Earthquake Flat (blue), Rotoiti (green). For each sample, the lighter colored triangles represent rim analyses and the darker colored squares represent core analyses. Rims and cores are the rim-most and interior-most spot analyzed during each plagioclase transect analysis.



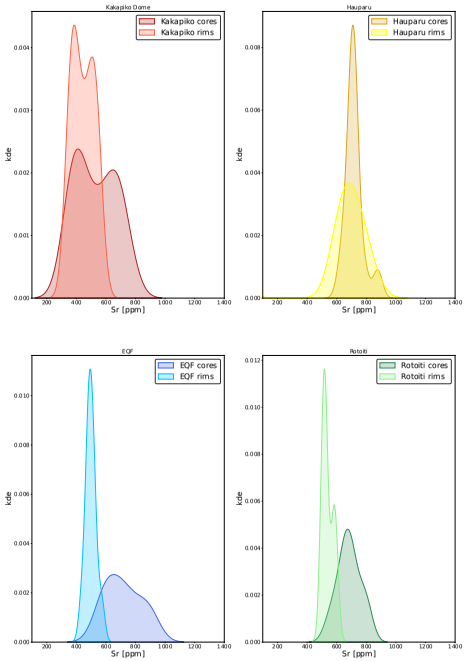
Trace element (Ce, Sr) concentration versus anorthite content for Okataina Volcanic Center plagioclase: Kakapiko Dome (red), Hauparu (yellow), Earthquake Flat (blue), Rotoiti (green). For each sample, the lighter colored triangles represent rim analyses and the darker colored squares represent core analyses. Rims and cores are the rim-most and interior-most spot analyzed during each plagioclase transect analysis.



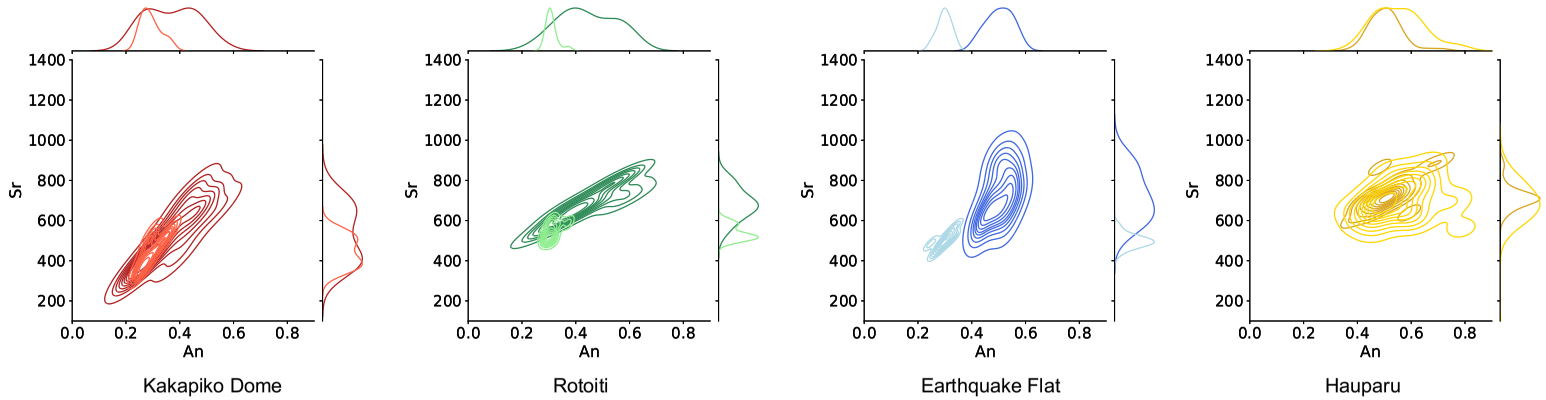
Ba versus Sr concentration for Okataina Volcanic Center plagioclase: Kakapiko Dome (red), Hauparu (yellow), Earthquake Flat (blue), Rotoiti (green). For each sample, the lighter colored triangles represent rim analyses and the darker colored squares represent core analyses. Rims and cores are the rim-most and interior-most spot analyzed during each plagioclase transect analysis. Figure shows the Ba vs Sr relationship for individual eruptions.



Ba versus Sr concentration for Okataina Volcanic Center plagioclase: Kakapiko Dome (red), Hauparu (yellow), Earthquake Flat (blue), Rotoiti (green). For each sample, the lighter colored triangles represent rim analyses and the darker colored squares represent core analyses. Rims and cores are the rim-most and interior-most spot analyzed during each plagioclase transect analysis. Figure plots Kakapiko Dome, Earthquake Flat, and Rotoiti on a single plot to show their similarity, and Hauparu on a single plot to show it's relative different to the pre-caldera eruption and caldera-forming eruptions.



Kernel density estimates (kde) for Okataina Volcanic Center plagioclase Sr composiitions: Kakapiko Dome (red), Hauparu (yellow), Earthquake Flat (blue), Rotoiti (green). For each sample, the lighter color represents rim analyses and the darker color represents core analyses.



Density plots of Sr concentration versus anorthite content for Okataina Volcanic Center plagioclase: Kakapiko Dome (red), Hauparu (yellow), Earthquake Flat (blue), Rotoiti (green). For each sample, the lighter color represents rim analyses and the darker color represents core analyses. Kernel density estimates (kde) for Sr and An content are located opposite each axis.